



01 Mar 2000

Modeling EMI Resulting from a Signal Via Transition Through Power/Ground Layers

Wei Cui

Xiaoning Ye

Bruce Archambeault

Missouri University of Science and Technology, archamb@mst.edu

Doug White

et. al. For a complete list of authors, see https://scholarsmine.mst.edu/ele_comeng_facwork/1144

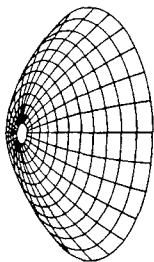
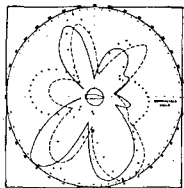
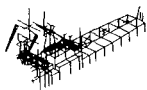
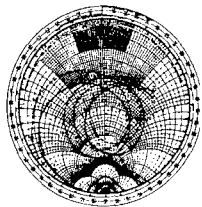
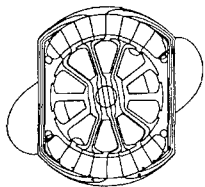
Follow this and additional works at: https://scholarsmine.mst.edu/ele_comeng_facwork

 Part of the [Electrical and Computer Engineering Commons](#)

Recommended Citation

W. Cui et al., "Modeling EMI Resulting from a Signal Via Transition Through Power/Ground Layers," *Proceedings of the 16th Annual Review of Progress in Applied Computational Electromagnetics (2000, Monterey, CA)*, vol. 1, pp. 436-443, Applied Computational Electromagnetics Society (ACES), Mar 2000.

This Article - Conference proceedings is brought to you for free and open access by Scholars' Mine. It has been accepted for inclusion in Electrical and Computer Engineering Faculty Research & Creative Works by an authorized administrator of Scholars' Mine. This work is protected by U. S. Copyright Law. Unauthorized use including reproduction for redistribution requires the permission of the copyright holder. For more information, please contact scholarsmine@mst.edu.



16th Annual Review of Progress in

APPLIED

COMPUTATIONAL

ELECTROMAGNETICS

at the

Naval Postgraduate School

Monterey, CA

March 20-24, 2000

CONFERENCE PROCEEDINGS

20000502 133

CONFERENCE PROCEEDINGS

VOLUME I

16th Annual Review of Progress in

APPLIED

COMPUTATIONAL

ELECTROMAGNETICS

at the

Naval Postgraduate School

Monterey, CA

March 20-24, 2000

TECHNICAL PROGRAM CHAIRMAN

Douglas Werner

Sponsored by

The Applied Computational Electromagnetics Society,

**Naval Postgraduate School, Penn State University,
Utah State University, University of Wisconsin-Madison,
Michigan State University, Southwest Research Institute**

DISTRIBUTION STATEMENT A
Approved for Public Release
Distribution Unlimited

Table of Contents	i
2001 Call for Papers	xii
2000 Symposium Program Committee	xiv
Technical Program Chairman's Statement	xv
ACES President's Statement	xvi
ACES 2000 Short Courses	xvii
Agenda	xix

PLENARY SESSION I

"Efficient Extraction of S-parameters of Transmission Line Discontinuities for RF and Wireless Circuit Design", Raj Mittra	2
--	---

SESSION 1: FINITE ELEMENT METHODS Chairs: Jianming Jin and Peter Monk

"Transient Electromagnetic Scattering from Curved Dielectric/lossy 3D Bodies Using Covariant Projection Elements", R. Ordoas, S.P. Walker and M.J. Bluck	4
"Towards an <i>hp</i> -adaptive Finite Element Method for Full-Wave Analysis of Waveguides" L. Vardapetyan and L. Demkowicz	11
"An <i>hp</i> -Adaptive Finite Element Method for Maxwell's Equations" L. Demkowicz	19
"Finite Element Method for Designing Plasma Reactors" Leo Kempel, Paul Rummel, Tim Grotjohn and John Amrhein	28
"Finite-Element Domain Decomposition Through an Iterative Algorithm: Coupling Between Cavity-Backed Slots" Anastasis C. Polycarpou and Constantine A. Balanis	35
"Investigation of the Bunting/Davis Functional When Used with Vector Finite Elements for Waveguide Analysis", Andrew F. Peterson and Sharib Wasi	43
"Numerical Methods for High Frequency Problems" T. Huttunen and P. Monk	49

Table of Contents	i
2001 Call for Papers	xii
2000 Symposium Program Committee	xiv
Technical Program Chairman's Statement	xv
ACES President's Statement	xvi
ACES 2000 Short Courses	xvii
Agenda	xix

PLENARY SESSION I

"Efficient Extraction of S-parameters of Transmission Line Discontinuities for RF and Wireless Circuit Design", Raj Mittra	2
--	---

SESSION 1: FINITE ELEMENT METHODS Chairs: Jianming Jin and Peter Monk

"Transient Electromagnetic Scattering from Curved Dielectric/Lossy 3D Bodies Using Covariant Projection Elements", R. Ordoas, S.P. Walker and M.J. Bluck	4
"Towards an hp-adaptive Finite Element Method for Full-Wave Analysis of Waveguides" L. Vardapetyan and L. Demkowicz	11
"An hp-Adaptive Finite Element Method for Maxwell's Equations" L. Demkowicz	19
"Finite Element Method for Designing Plasma Reactors" Leo Kempel, Paul Rummel, Tim Grotjohn and John Amrhein	28
"Finite-Element Domain Decomposition Through an Iterative Algorithm: Coupling Between Cavity-Backed Slots" Anastasis C. Polycarpou and Constantine A. Balanis	35
"Investigation of the Bunting/Davis Functional When Used with Vector Finite Elements for Waveguide Analysis", Andrew F. Peterson and Sharib Wasi	43
"Numerical Methods for High Frequency Problems" T. Huttunen and P. Monk	49

SESSION 2: OPTIMIZATION IN ELECTROMAGNETICS

Chairs: Eric Michielssen and Dan Weile

"Design of Dual Band Frequency Selective Surfaces Using Genetic Algorithms" A. Monorchio, R. Mittra, and G. Manara	56
"A Study of Cauchy and Gaussian Mutation Operators in the Evolutionary Programming Optimization of Antenna Structures" Ahmad Hoofar and Yuan Liu	63
"A Statistical Intercomparison of Binary and Decimal Genetic Algorithms" Yee Hui Lee, Stuart J. Porter and Andrew C. Marvin	70
"The Compact Genetic Algorithm: A Litmus Test for Genetic Algorithm Applicability" Daniel S. Weile, Eric Michielssen and David E. Goldberg	78
"Dipole Equivalent Circuit Optimization Using Genetic Algorithm" Bruce Long, Ping Werner, and Doug Werner	86
"Computing the Electromagnetic Field in a Perturbed Configuration Using Modified" Reduced-Order Models" R.F. Remis and P.M. van den Berg	93
"Some Further Results from FARS: Far-Field Analysis of Radiation Sources" Edmund K. Miller	99

SESSION 3: NUMERICAL TECHNIQUES FOR PACKAGING AND INTERCONNECTS

Chairs: Omar Ramahi and Andreas C. Cangellaris

"A New Methodology for the Direct Generation of Closed-Form Electrostatic Green's Functions in Layered Dielectrics" Andreas C. Cangellaris	108
"The Treatment of Narrow Microstrips and PCB Tracks in the FDTD Method Using Empirically Modified Coefficients", Chris J. Ralston	115
"Time-Domain-Analysis of QTEM Wave Propagation and Crosstalk on Lossy Multiconductor Transmission Lines with Terminal Coupling" Georg Mueller, Jan Wendel, and Karl Reiss	123
"An MPIE-Based Circuit Extraction Technique and its Applications on Power Bus Modeling in High-Speed Digital Designs" Kim Fan, Hao Shi, James L. Knighten, and James L. Drewniak	130
"Non-Resonant Electromagnetic Simulation of Some Resonant Planar Circuits" Yuriy O. Shlepnev	138
"FDTD Analysis of Conventional and Novel Delay Lines", Omar M. Ramahi	146
"Complementary Operators for Frequency-Domain Methods: A Single Simulation Implementation", Omar M. Ramahi	152

SESSION 4: STUDENT PAPER COMPETITION Chair: Perry Wheless

"Systematic Studies in Annular Ring PBG Structures" Todd M. Lammers, Shawn W. Staker, and Melinda Pike-May	160
"Fast Electromagnetic Analysis Using the Asymptotic Waveform Evaluation Method" Dan Jiao and Jianming Jin	166
"A Domain-Decomposition/Reciprocity Technique for the Analysis of Arbitrarily-Shaped Microstrip Antennas with Dielectric Substrates and Superstrates Mounted on Circularly-Cylindrical Platforms" R.J. Allard, D.H. Werner, and J.S. Zmysto	173
"A New FDTD Scheme to Model Chiral Media" A. Akyurtlu, D.H. Werner, and K. Aydin	181
"T-Matrix Computer Code Applied to Electromagnetic Field Penetration in Magnetic Resonance Imaging" Rafael R. Canales, Luis F. Fonseca, Fredy R. Zypman	189

SESSION 5: INTERACTIVE POSTER SESSION

"Characteristics of Silicon Photoconductivity Under Near-Infrared Illumination" Preston P. Young, Robert Magnusson, and Tim R. Holzheimer	198
"Characteristics of Fractal Antennas", Haruo Kawakami, Yasushi Ojio, Yasushi Lizuka, Satoshi Kogiso and Gentai Sato	206
"Feigenbaum Encryption of Computer Codes" R.M. Bevensee	214
"Extension of SuperNEC to Calculate Characteristic Modes", Thomas Abbott	221
"Review of Basic 3-D Geometry Considerations for Intelligent CEM Pre-Processor Applications", Kurt V. Sunderland	226
"Modelling of Loaded Wire Conductor Above Perfectly Conducting Ground by Using 3D TLM Method" Nebojsa S. Doncov, Bratislav D. Milovanovic, and Vladica M. Trenkic	233
"Evanescent Tunneling and Quantile Motion of Electromagnetic Waves in Wave Guides of Varying Cross Section", E. Gjonaq	241
"A Modal Approach for the Calculation of Scattering Parameters in Lossfree and Lossy Structures Using the FI-Technique" Rolf Schuhmann, Peter Hammes, Stefan Setzer, Bernd Trapp, Thomas Weiland	247
"A Modular Technique for the Calculation of Wave Guide Structures" Johannes Borkes, Adalbert Beyer, and Oliver Pertz	255

SESSION 5: INTERACTIVE POSTER SESSION (cont)

"Wave Propagation Through 2D Clusters of Coupled Cylindrical Resonators" Ross A. Speciale	263
"Design Software for Cylindrical Helix Antennas" M. Slater and C.W. Trueman STUDENT PAPER COMPETITION	281
"The Analysis of a Center-Fed Helical Microstrip Antenna Mounted on a Dielectric-Coated Circular Cylinder Using the Reciprocity Theroem" R.A. Martin and D.H. Werner	286
"Near to Far Field Transformation for a FDTD BOR with PML ABC and Sub-Grid Capability" Vicente Rodriguez-Pereyra, Atef Z. Elsherbeni, and Charles E. Smith	294
"Computer Simulation of Radar Images of PEC Models of Complicated Objects" Nickolai Zh. Kolev PAPER WITHDRAWN - PAGES 302 THROUGH 307	302

PLENARY SPEAKER II

"Design on Computer - A Coming of Age Tom Cwik	308
--	-----

SESSION 6: COMPUTATIONAL BIO-ELECTROMAGNETICS Chairs: Ray Luebbers and Susan Hagness

"Numerical Investigation of Two Confocal Microwave Imaging Systems for Breast Tumor Detection" Susan C. Hagness, Xu Li, Elise C. Fear, and Maria A. Stuchly	310
"FDTD Studies on SAR in Biological Cells Exposed to 837 and 1900 MHz in a TEM Cell" A.W. Guy	317
"Modelling of Personnel Electromagnetic Radiation Hazards", Alan Nott	325
"Modeling Interference Between Very Low Frequency Electromagnetic Fields and Implanted Cardiac Pacemakers" Trevor W. Dawson and Maria A. Stuchly	333
"Using Computational Electromagnetics to Solve an Occupational Health and Safety Incident" Timothy Priest, Kevin Goldsmith, and Dean DuRieu	341
"Analysis of Permanent Magnet Type of MRI Taking Account of Hysteresis and Eddy Current and Experimental Verification", Norio Takahashi, Siti Zubaidah, Takeshi Kayano, Koji Miyata and Ken Ohashi	349

SESSION 7: VIRTUAL REALITY IN REAL WORLD APPLICATIONS Chairs: Stan Kubina and Dennis DeCarlo

"A Virtual Radiation Pattern Range and Its Uses - C-130/Hercules HF Notch Antenna" Stanley J. Kubina, Christopher W. Trueman, and David Gaudine	356
"HP Towel-Bar Antenna Location Study Aboard an H-3 Sikorsky Helicopter" Saad N. Tabet, Carl D. Myers, and Dennis DeCarlo	365
"Improving Model Confidence through Metamorphosis" Douglas R. Munn and C.W. Trueman	373
"Model Morphing for Insight into the HF Assessment Parameters" Douglas R. Munn and C.W. Trueman	381
"3D Modeling of Complex Helicopter Structures: Predictions and Measurements" Anastasis C. Polycarpou, Dong-Ho Han, Stavros V. Georgakopoulos, Constantine Balanis	387
"Increasing the Productivity of NEC Analysis with Virtual Reality and 3D Laser Scanners" Kevin J. Cybert and Daniel D. Reuster	395
"An Interactive HTML Based Multimedia Course on Antennas" Ulrich Tuerk and Peter Russer	401

SESSION 8: EMC Chairs: Bruce Archambeault and Jim Drewniak

"Adding Imperfections to EMC FDTD Models as a Means of Increasing Accuracy" Colin E. Brench	410
"Power Conversion Techniques for Portable EMI Sensitive Applications" Reinaldo Perez	416
"Using the Partial Element Equivalent Circuit (PEEC) Simulation Technique to Properly Analyze Power/Ground Plane EMI Decoupling Performance" Bruce Archambeault	423
"EMI Model Validation and Standard Challenge Problems" Bruce Archambeault and James L. Drewniak	431
"Modeling EMI Resulting from a Signal Via Transition Through Power/Ground Layers" Wei Cui, Xiaoning Ye, Bruce Archambeault, Doug White, James Drewniak	436
"Techniques for Optimizing FEM/MoM Codes" Y. Ji, T.H. Hubing, and H. Wang	444
"Numerical Modeling of Shielding by a Wire Mesh Box" Gerald J. Burke and David J. Steich	452

SESSION 9: PROPAGATION Chairs: Steve Fast and Frank Ryan

"A Fast Quasi Three-Dimensional Propagation Model for Urban Microcells" Joseph W. Schuster and Raymond J. Luebbers	462
"FDTD Techniques for Evaluating the Accuracy of Ray-Tracing Propagation Models for Microcells" Joseph W. Schuster and Raymond J. Luebbers	470
"A Building Database Features Pre-Processor for 3D SBR/GTD Urban EM Propagation Models" James Pickelsimer and Raymond Luebbers	477
"Toward a New Model for Indoor and Urban Propagation Using Percolation Theory" G. Franceschetti, S. Marano, N. Pasquino, and I.M. Pinto	485
"Ray Tracing Algorithm for Indoor Propagation" C.W. Trueman, R. Paknys, J. Zhao, D. Davis, and B. Segal	493
"Modeling Large and Small-Scale Fading on the DPSK Datalink Channel Using a GTD Ray-Tracing Model" Kent Chamberlin, Mikhailo Seledtsov, and Petar Horvatic	501
"Rough Surface Forward Scatter in the Parabolic Wave Equation Model" Frank Ryan	507
"A Comparison of Electromagnetic Parabolic Equation Propagation Models Used by the U.S. Navy to Predict Radar Performance" Donald de Forest Boyer and Huong Pham	515

AUTHOR INDEX	523
---------------------------	------------

SESSION 10: WAVELET AND TLM MODELING TECHNIQUES

Chairs: Wolfgang J.R. Hoefer and Peter Russer

"The Implementation of a High Level (1st-order) Haar Wavelet MRTD Scheme" Enqiu Hu, Poman P.M. So, Masafumi Fujii, Wei Liu, and Wolfgang J.R. Hoefer	526
"Multi-Resolution Based TLM Technique Using Haar Wavelets" Ismael Barba, Jose Represa, Masafumi Fujii, and Wolfgang J.R. Hoefer	534
"Formulation and Study of an Arbitrary Order Haar Wavelet Based Multi-resolution Time Domain Technique" Costas D. Sarris and Linda P.B. Katehi	540
"Computational Optimization of MRTD Haar-Based Adaptive Schemes Used for the Design of RF Packaging Structures", Manos M. Tentzeris	548
"Time-Domain Simulation of Electromagnetic Wave Propagation in a Magnetized Plasma" J. Paul, C. Christopoulos, and D.W.P. Thomas	556

SESSION 10: WAVELET AND TLM MODELING TECHNIQUES (cont)

"TLM Simulation of Patch Antenna on Magnetized Ferrite Substrate" M.I. Sobhy, M.W.R. Ng, R.J. Langley, and J.C. Batchelor	562
"On the Practical Use of Layered Absorbers for the Simulation of Planar Microwave Circuits Using the SCN-TLM Method" Juergen Rebel, Tobias Mangold and Peter Russer	570
"A Numerical Study of MEMS Capacitive Switches Using TLM" Fabio Cocceffi, Larissa Vietzorreck, Vitali Chitchekatourov, and Peter Russer	580
"Thin Wire Modeling with the TLMIE-Method" S. Lindenmeier, C. Christopoulos, and P. Russer	587
"What Determines the Speed of Time-Discrete Algorithms?" Tobias Mangold, Jurgen Rebel, Wolfgang J.R. Hoefer, Poman P.M. So, and Peter Russer	594

SESSION 11: TIME DOMAIN METHODS Chairs: Amelia Rubio Bretones and R. Gomez Martin

"Introducing a New Time-Domain Electromagnetic Field Solver LSFEM™ TD-3D" Craig C. Ouyang, B.N. Jiang, and Nina Liao	604
"Characteristic-Based Time-Domain Method for Antenna Analysis" Dan Jiao, Jianming Jin and J.S. Shang	611
"Modeling of Thin-Wire Structures by Solving the EFIE in Time Domain" Friedrich Schunn and Hermann Singer	619
"Time-Domain Analysis of Thin-Wire Loaded Antennas Using Integral Equations" M. Fernandez Pantoja, A. Rubio Bretones, and R. Gomez Martin	627
"Haar MRTD Wave Propagation Through Isotropic Plasmas" Ismael Barba, Jose Represa, Masafumi Fujii, and Wolfgang J.R. Hoefer	635
"Time-Domain Scattering from arbitrarily Shaped Metallic Shelters with Apertures: Numerical and Experimental Analysis" Giuliano Manara and Agostino Monorchio	640
"Integral Equation Based Analysis of Transient Electromagnetic Scattering From Three Dimensional Inhomogeneous Dielectric Objects" N.T. Gres, A.A. Ergin, B. Shanker, and E. Michielssen	647
"Computational Properties of Wavelet Based PEEC Analysis in Time Domain" G. Antonini and A. Orlandi	654
"Time Domain Modeling of a Pulsed Horn-Dish Antenna" M.J. Bluck, S.P. Walker and C. Thomas	662

PLENARY SPEAKER III

"Fast Solvers for Electromagnetic Simulations - A New Age Analysis Tool"	
W.C. Chew	668

SESSION 12: MOMENT METHODS Chairs: Zach Baharav and Ramakrishna Janaswamy

"Iterative Solvers for Dense Matrices - Application to Moment Method Matrices"	
Juergen v. Hagen and Werner Wiesbeck	670
"Convergence Properties of the CFIE for Several Conducting Scatterers"	
William Wood Jr., Kueichien Hill, William Kent, Robert Layden & Lisa Cravens	677
"Modeling of General Surface Junctions of Composite Objects in an SIE/MoM Formulation"	
Joon Shin, Allen W. Glisson, and Ahmed A. Kishk	683
"A Novel Grid-Robust Higher-Order Vector Basis Function for the Method of Moments"	
G. Kang, J.M. Song, W.C. Chew, K. Donepudi, and J.M. Jin	691
"Analytical Treatment of Green's Functions Singularities in Microstrip Structures"	
E. Jimenez, F.J. Cabrera, J.G. Cuevas del Rio	699
"A Two-Stage Numerical Procedure for Extraction of Surface Wave Poles for Multilayered Media"	
Ya-Xun Liu, Le-Wei Li, Tai-Seen Yeo, Pand-Shyan Kooi, and Meek-Seng Leong	707
PAPER WITHDRAWN - PAGES 707 THROUGH 715	
"Higher-Order Electromagnetic Modeling of Multilayer Microstrip Structures"	
Feng Ling, Kalyan Donepudi, and Jianming Jin	716

SESSION 13: CONFORMAL ANTENNAS Chairs: Leo Kempel and Douglas Werner

"A Conformal, Flexible, Multifunction Communications Antenna"	
T.R. Holzheimer	726
"Finite Printed Antenna Array Modeling Using an Adaptive Multi-Resolution Approach"	
Lars S. Anderson, Yunus E. Erdemil, and John L. Volakis	734
"A Technique for Analyzing Radiation from Conformal Antennas Mounted on Arbitrarily-Shaped Conducting Bodies"	
Dean Arakaki, Douglas H. Werner, and Raj Mittra	742
"Using Computational Electromagnetics and Monte-Carlo Methods to Locate Antennas on Aircraft"	
Kevin Goldsmith, Paul Johnson, and Timothy Priest	750
"Coupling Phenomena in Horizontal and Vertical Polarized Aperture Coupled Patch Antennas on Cylindrical Surfaces"	
D. Loffler, J. von Hagen, and W. Wiesbeck	758

SESSION 13: CONFORMAL ANTENNAS (cont)

"Modeling and Analysis of Wideband Conformal Antennas" Keith D. Trott, Rene D. Guidry, and Leo C. Kempel	765
"Curvature Effects on a Conformal Log-Periodic Antenna" Charles Macon, Leo Kempel, Keith Trott, and Stephen Schneider	772

SESSION 14: ANTENNA ARRAYS Chairs: Keith Lysiak and Nathan Cohen

"Problems of Characterising Array Manifolds for Naval Platform in HF Environments" Linda Holtby	780
"Designing A VHF Wrap-Around DF Antenna Array Using NEC", Keith Lysiak	790
"Specifying A Direction Finding Antenna with Examples" T.R. Holzheimer	798
"A High Efficiency Broad Band Wire Antenna System " Kevin J. Cybert and Daniel D. Reuster	806
"Comparison of Calculations and Measurements of an Electronically Scanned Circular Array" James M. Stamm, Michael W. Jacobs, and James K. Breakall	814
"Array Sidelobe Reduction by Small Position Offsets of Fractal Elements" Nathan Cohen and Robert G. Hohlfeld	822
"The Radiation Characteristics of Recursively Generated Self-Scalable and Self-Similar Arrays" D.H. Werner and P.L. Werner	829

SESSION 15: FAST AND EFFICIENCY METHODS Chairs: Weng C. Chew and Jiming Song

"Three Dimensional Scattering Analysis in Stratified Medium Using Fast Inhomogeneous Plane Wave Algorithm" Bin Hu and Weng Cho Chew	838
"Multilevel Fast Multipole Algorithm for Analysis of Large-Scale Microstrip Structures" Feng Ling, Jiming Song, and Jianming Jin	845
"A Novel Implementation of Multilevel Fast Multipole Algorithm for Higher-Order Galerkin's Method" K.C. Donepudi, J.M. Song, Jianming Jin, G. Kang, and W.C. Chew	851
"Incomplete LU Preconditioner for FMM Implementation" Kubilay Sertel and John L. Volakis	859
"A Fast, High-Order Scattering Code for Solving Practical RCS Problems" J.J. Ottusch, J.L. Visher, and S.M. Wandzura	867

SESSION 15: FAST AND EFFICIENCY METHODS (cont)

"An Efficient Integral Equation Based Solution Method for Simulation of Electromagnetic Fields in Inhomogeneous Dielectric (Biological) Media" E. Bleszynski, M. Bleszynski, and T. Jaroszewicz	874
"Efficient Solution of Large-Scale Electromagnetic Eigenvalue Problems Using the Implicitly Restarted Arnoldi Method" Daniel White and Joseph Koning	882
"Fast Fourier Transform of Functions with Jump Discontinuities" Guo-Xin Fan and Qing Huo Liu	890
"Applications of Nonuniform Fast Transform Algorithms in Numerical Solutions of Integral Equations " Q.H. Liu, X.M. Xu, and Z.Q. Zhang	897

SESSION 16: APPLICATIONS OF THE FIXED TECHNIQUE Chairs: Atef Elsherbeni and Wenhua Yu

"A Non-Dissipative Staggered Fourth-Order Accurate Explicit Finite Difference Scheme for the Time-Domain Maxwell's Equations" A. Yefet and P.G. Petropoulos	906
"FDTD Method for Maxwell's Equations in Complex Geometries" A. Ditekowski, K. Dridi, and J.S. Hesthaven	917
"FDTD Analysis of Tapered Meander Line Antennas for RF and Wireless Communications" Chun-Wen Paul Huang, Atef Z. Elsherbeni, and Charles E. Smith	924
"FDTD Modeling of an Electron Cyclotron Resonance Reactor Driven by a Lisitano Coil" Gaetano Marrocco, Fernando Bardati, and Francesco De Marco	930
"Modelling Microwave and Hybrid Heating Using FDTD" J. Haala and W. Wiesbeck	936
"A Conformal Finite Difference Time Domain (CFDTD) Algorithm for Modeling Perfectly Conducting Objects" Wenhua Yu, Raj Mittra, Dean Arakaki, and Douglas H. Werner	944
"A Finite-Difference Algorithm for Modeling of Conductive Wedges in 2D" Piotr Przybyszewski 8 pages	951
"Advanced Techniques of Geometrical Modelling and CFDTD" F. Rivas, J.P. Roa, and M.V. Catedra 7 pages	959

SESSION 17: HYBRID TECHNIQUES Chairs: Agostino Monorchio and P.H. Pathak

"A Three-Dimensional Hybrid Techniques for Combining the Finite Element and Finite Difference Methods in Time Domain" Agostino Monorchio and Raj Mittra	968
"Vertical Antenna Near-Field Computation in Complex Environments by a Hybrid Method" F. Bardati, E. Di Giampaolo, A. Durantini, and G. Marrocco	975
"3-D EM Problem Modelling by Geometry Decomposition and Combination of the FE, FDTD and BIE Techniques" Hendrik Rogier, Daniel De Zutter, and Frank Olyslager	981
"Hybrid FDTD-Frequency Dependent Network Simulations Using Digital Filtering Techniques" Ian Rumsey and Melinda Picket-May	988
"Study of Electrically-Short Thin-Wire Antennas Located in the Proximity of Inhomogeneous Scatterers Using a Hybrid NEC/FDTD Approach" A. Rubio Bretones, R. Mittra, and R. Gomez Martin	995
"A Review of Some Hybrid High Frequency and Numerical Solutions for Radiation/Scattering Problems" P.H. Pathak and R.J. Burkholder	1001
"An Hybrid Method Combining Integral Equations and Modal Expansion Applied to the RCS Modulation of Antennas and Rotating Fans" Andre Barka and Paul Soudais	1006
"A 2D TLM and Haar MRTD Real-Time Hybrid Connection Technique" Masafumi Fujii, Poman P.M. So, Enqiu Hu, Wei Liu, and Wolfgang J.R. Hoefer	1013
AUTHOR INDEX	1021



CALL FOR PAPERS

THE APPLIED COMPUTATIONAL ELECTROMAGNETICS SOCIETY



**The 17th Annual Review of Progress in Applied Computational Electromagnetics
March 19 - 23, 2001**

**Naval Postgraduate School, Monterey, California
Share Your Knowledge and Expertise with Your Colleagues**

The Annual ACES Symposium is an ideal opportunity to participate in a large gathering of EM analysis enthusiasts. The purpose of the Symposium is to bring analysts together to share information and experience about the practical application of EM analysis using computational methods. The symposium offerings include technical presentations, demonstrations, vendor booths, short courses, and hands-on workshops. All aspects of electromagnetic computational analysis are represented.

The ACES Symposium is a highly influential outlet for promoting awareness of recent technical contributions to the advancement of computational electromagnetics. Attendance and professional program paper participation from non-ACES members and from outside North America are encouraged and welcome.

Papers may address general issues in applied computational electromagnetics, or may focus on specific applications, techniques, codes, or computational issues of potential interest to the Applied Computational Electromagnetics Society membership.

Areas and topics

Computational studies of basic physics	Computer hardware issues
Examples of practical code application	Code validation
New codes, algorithms, code enhancements, and code fixes	Code performance analysis

Partial list of applications

Communications systems	Microwave components	Wireless	Radar Imaging
Remote sensing & geophysics	EMP EMI/EMC	Shielding	Radar cross section
Dielectric & magnetic materials	MIMIC technology	Visualization	Fiberoptics
Non-destructive evaluation	Wave propagation	Eddy currents	Direction finding
Propagation through plasmas	Bioelectromagnetics	Inverse scattering	Antennas

Partial list of techniques

Diffraction theories	Moment methods	Physical optics
Frequency-domain & Time-domain techniques	Hybrid methods	Modal expansions
Finite difference & finite element analysis	Numerical optimization	
Integral equation & differential equation techniques	Perturbation methods	

INSTRUCTIONS FOR AUTHORS AND TIMETABLE

Submission Deadline - November 1, 2000: Electronic submission preferred (Microsoft Word). Otherwise submit three copies of a full-length, camera-ready paper to the Technical Program Chairman. Please supply the following data for the corresponding authors: name, address, email address, FAX, and phone numbers.

Authors notified of acceptance by December 1, 2000.

PAPER FORMATTING REQUIREMENTS

The recommended paper length is 6 pages, with 8 pages as a maximum, including figures. The paper should be camera-ready (good resolution, clearly readable when reduced to the final print of 6x9 inch paper). The paper should be printed on 8-1/2x11 inch papers with 13/16 side margins, 1-1/16 inch top margin, and 1 inch on the bottom. On the first page, place title 1-1/2 inches from top with authors, affiliations, and e-mail addresses beneath the title. Single spaced type using 10 or 12 point font size, entire text should be justified (flush left and flush right). No typed page numbers, but number your pages lightly in pencil on the back of each page.

For all questions regarding the ACES Symposium please contact:

Leo C. Kempel, Technical Program Chair

Michigan State University, ECE Engr,

2120 Engineering Bldg, E. Lansing, MI 48824-1126

Tel: (517) 353-9944, Fax: (517) 353-1980,

E-mail: lkempel@ieee.org

or visit ACES on line at: <http://aces.ee.olemiss.edu>.

EARLY REGISTRATION FEES

ACES member	\$300	Student/Retired/Unemployed	\$130 (no proceedings)
Non-member	\$350	Student/Retired/Unemployed	\$165 (includes proceedings)

Each conference registration is entitled to publish two papers in the proceedings free of charge. Excess pages over a paper limit of 8 will be charged \$15/page.

\$500 BEST-PAPER PRIZE

A \$500 prize will be awarded to the authors of the best non-student paper accepted for the 16th Annual Review. Papers will be judged by a special ACES prize-paper Committee according to the following criteria:

- | | |
|---|--------------------------------------|
| 1. Based on established electromagnetic (EM) theory | 4. Practical applications |
| 2. Reliable data | 5. Estimates of computational errors |
| 3. Computational EM results | 6. Significant new conclusions |

\$200 BEST STUDENT PAPER CONTEST

This will be for the best student paper accepted for the 17th Annual Review. (Student must be the presenter on the paper chosen). Submissions will be judged by three (3) members of the BoD. The prizes for the student presenter and his/her principal advisor will consist of: (1) free Annual Review registration for the following year; (2) one free short course taken during the 2001 or 2002 Annual Review; and (3) \$200 cash for the paper.

2001 ACES Symposium Sponsored by: ACES, NPS, PSU, MSU, SWRI
In cooperation with: The IEEE Antennas and Propagation Society,
The IEEE Electromagnetic Compatibility Society and USNC/URSI

2000 Symposium Program Committee
for the
16th Annual Review of Progress
in
Applied Computational Electromagnetics
at the
Naval Postgraduate School
Monterey, CA

Technical Program Chairman
Douglas H. Werner
EE Department
Penn State University
211A Electrical Engineering East
University Park, PA 16802
Phone: (814) 863-2946
Fax: (814) 865-3359
Email: dhw@psu.edu

Short Course Chairman
Susan C. Hagness
ECE Department
University of Wisconsin-Madison
1415 Engineering Drive
Madison, WI 53706-1691
Phone: (608) 265-5739
Fax: (608) 262-1267
Email: hagness@engr.wisc.edu

Symposium Administrator
Richard W. Adler
ECE Dept/Code EC/AB
Naval Postgraduate School
Monterey, CA 93943-5121
Phone: (831) 646-1111
Fax: (831) 649-0300
Email: rwa@attglobal.net

Technical Co-Chair
Pingjuan L. Werner
EE Department
Penn State University
211A Electrical Engineering East
University Park, PA 16802
Phone: (814) 865-2364
Fax: (814) 865-3359
Email: plw7@psu.edu

Vendor Chairman
Leo C. Kempel
ECE Department
Michigan State University
2120 Engineering Bldg.
E. Lansing, MI 48824-1126
Phone: (517) 353-9944
Fax: (517) 353-1980
Email: l.kempel@ieee.org

Conference Secretary
Mrs. Pat Adler
822 Devisadero Street
Monterey, CA 93940-1913
Email: pba@attglobal.net

Advisory Committee:
Richard W. Adler, Naval Postgraduate School
Bruce Archambeault, IBM
Robert Bevensee, Borna Enterprises
Anthony Brown, Chilworth, UK
Andreas Cangelaris, University of Illinois
Allen W. Glisson, University of Mississippi
Eric Michielssen, University of Illinois
Guiseppe Pelosi, University of Florence
Ray Perez, Jet Propulsion Lab.
Andrew Peterson, Georgia Institute of Technology
Norio Takahashi, Okayama University
W. Perry Wheelless, Jr., University of Alabama

Technical Co-Chair
Randy L. Haupt
ECE Department
Utah State University
4120, Old Main Hill
Logan, UT 84322-4120
Phone: (435) 797-2840
Fax: (435) 797-3054
Email: haupt@ieee.org

Publicity Chair:
Keith Lysiak
Southwest Research Institute
6220 Culebra Road
San Antonio, TX 78238-5166
Phone: (210) 522-5776
Fax: (210) 522-2709
Email: klysiak@swri.edu

PREFACE

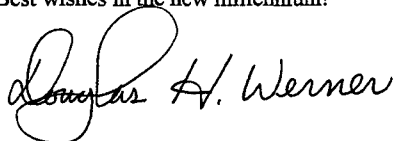
On behalf of the Conference Technical Committee, I would like to personally welcome all of you, especially those from overseas, to the 16th Annual Review of Progress in Applied Computational Electromagnetics – the first ACES Conference of the new millennium, here at the Naval Postgraduate School in beautiful Monterey.

We are fortunate to have with us this year three highly-regarded plenary speakers, Raj Mittra, Tom Cwik and Weng Chew, who will be discussing the challenges in computational electromagnetics that await as we move into the new millennium. The technical sessions this year cover a wide variety of topics ranging from *Wavelet and TLM Modeling Techniques* to *Virtual Reality in Real-World Applications*. Of special significance this year are the good number of international participants, some of whom have organized sessions and will also be chairing and presenting papers in the conference. This will also be the first year that there will be a special session devoted to the Student Paper Competition. We hope that you will all take advantage of the interactive poster session, vendor exhibits and the excellent program of short courses that have been organized for this years' conference.

We would also like to take this opportunity to thank the Naval Postgraduate School for serving as the host for the ACES 2000 conference. Special thanks goes to Dick and Pat Adler for their unending dedication and tireless efforts on behalf of ACES. We want to specifically thank all those who have helped to make ACES 2000 possible by organizing and chairing sessions. Finally, I would like to extend my personal thanks to my technical program committee team members -- including co-chairs Randy Haupt and Ping Werner, vendor chair Leo Kempel, short course chair Susan Hagness, publicity chair Keith Lysiak, and ACES webmaster Etef Elsherbeni -- for all their hard work and dedication throughout the past year.

We hope that the conference will provide a unique opportunity for all of you to come together from around the world to share your knowledge in computational electromagnetics by renewing old acquaintances and forming new collaborations. We also hope that ACES 2000 will be a memorable and productive conference for each and every participant.

Best wishes in the new millennium!

A handwritten signature in dark ink, reading "Douglas H. Werner". The signature is fluid and cursive, with the first name "Douglas" being more prominent and the last name "Werner" following in a similar style.

Douglas H. Werner
Technical Program Chair
ACES 2000 Conference

ACES PRESIDENT'S STATEMENT

Welcome to the ACES 2000 conference! The *ACES Annual Review of Progress in Applied Computational Electromagnetics* now has a 16-year tradition of excellence that guarantees a pleasant and educational experience. CEM specialists worldwide, both members and non-members of ACES, know they can find our conference in Monterey during the third week of March. The Naval Postgraduate School has been a gracious host and afforded excellent accommodations to ACES over the years, but a school calendar change has brought into question the week or location for our future conferences. The ACES Board of Directors will study this issue carefully before recommending any change, as both our date and place have been so well known for so many years.

We again express our continuing gratitude and debt to Dick and Pat Adler for their (perennial) long hours devoted to ACES, including the conference local arrangements. Doug Werner and his capable conference team have put together an excellent technical program. I won't attempt to credit all his enthusiastic and capable assistants here, but please come hear Doug's opening remarks on Tuesday morning. Because the majority of our conference registrants continue to prefer a limited number of parallel sessions, ACES has restricted the number of accepted papers for the technical program this year. I hope you will appreciate and enjoy this distinctive feature of our conference. The ACES 2000 conference is more than just paper sessions, short courses, and award banquets, and ACES is actively striving to enhance your opportunities to have some quality time available for colleagues and friends, both old and new. If you see a way that we can further improve the structure and conduct of the conference, please do let us hear from you!

For all the news about ACES 2001 as it becomes available, remember to visit our Web site at aces.ee.olemiss.edu on a regular basis!

Perry Wheless
ACES President

ACES 2000 SHORT COURSES/WORKSHOPS

MONDAY 20 MARCH 2000

- 0830-1630 **SHORT COURSE #1 (FULL-DAY)**
"Computational Electromagnetic Methods in Mobile Wireless Communication Design"
Ray Perez, Jet Propulsion Laboratory
- 0830-1630 **SHORT COURSE #2 (FULL-DAY)**
"XML and Modern Internet Technologies for Scientific Applications"
Furrukh S. Kahn, Ohio State University.
- 0830-1630 **SHORT COURSE #3 (FULL-DAY)**
"The Basics of The Finite Difference Time Domain Technique for Electromagnetic Application"
Atef Z. Elsherbeni and Allen W. Glisson, University of Mississippi
- 0830-1630 **SHORT COURSE #4 (FULL-DAY)**
"Techniques for Electromagnetic Visualization"
Edmund K. Miller, Santa Fe, NM, and John Shaeffer, Marietta Scientific, Inc.
- 0830-1630 **SHORT COURSE #5 (FULL-DAY)**
"EIGER - Electromagnetic Interactions Generalized: An Introduction to and Tutorial on the Software Suite"
Robert M. Sharpe and Nathan J. Champagne, Lawrence Livermore National Laboratory
William A. Johnson, Sandia National Laboratories, Donald R. Wilton, University of Houston, and J. Brian Grant, ANT-S.
- 0830-1130 **HANDS-ON-WORKSHOP #6 (HALF-DAY, MORNING)**
"MATHCAD BASICS", Jovan Lebaric, Naval Postgraduate School.
- 1330-1630 **HANDS-ON-WORKSHOP #7 (HALF-DAY, AFTERNOON)**
"MATLAB BASICS", Jovan Lebaric, Naval Postgraduate School.
- 0830-1630 **SHORT COURSE #8 (FULL-DAY)**
"EMI/EMC Computational Modeling for Real-World Engineering Problems"
Omar Ramahi, Compaq Corporation, and Bruce Archambeault, IBM

PLEASE NOTE THAT A 10% DISCOUNT IS IN EFFECT FOR ALL WORKSHOPS TAKEN AFTER ATTENDING AN INITIAL WORKSHOP.
THIS APPLIES TO THE GROUP OF WORKSHOPS FOR MATLAB AND MATHCAD.

FRIDAY 24 MARCH 2000

- 0830-1630 **SHORT COURSE #9 (FULL-DAY)**
"Why is There Electromagnetic Radiation and Where Does It Come From?"
John Shaeffer, Marietta Scientific Inc., and Edmund K. Miller, Santa Fe, NM
- 0830-1630 **SHORT COURSE #10 (FULL-DAY)**
"Recent Advances in Fast Algorithms for Computational Electromagnetics"
Weng Cho Chew, Jianming Jin, Eric Michielssen, and Jiming Song, University of Illinois at Urbana Champaign

ACES 2000 SHORT COURSES/WORKSHOPS (cont)

FRIDAY 24 MARCH 2000

- 0830-1630 **HANDS-ON-WORKSHOP #11 (FULL-DAY)**
 "Method of Moments (MoM) Using MATHCAD"
 Jovan Lebaric, Naval Postgraduate School
- 0830-1130 **SHORT COURSE #12 (HALF-DAY, MORNING)**
 "Computational Electromagnetics Using Beowulf-Cluster Computers"
 Tom Cwik and Daniel S. Katz, Jet Propulsion Laboratory
- 1330-1630 **SHORT COURSE #13 (HALF-DAY AFTERNOON)**
 "Multiresolution FEM: Introduction and Antenna Applications"
 John L. Volakis, University of Michigan and Lars Anderson, Agilent

SATURDAY 25 MARCH 2000

- 0830-1630 **HANDS-ON-WORKSHOP #14 (FULL-DAY)**
 "FD/FDTD Using MATLAB"
 Jovan Lebaric, Naval Postgraduate School, Monterey, CA
- 0830-1630 **SHORT COURSE #15 (FULL-DAY)**
 "An Introduction to Radar Cross Section"
 John Shaeffer, Marietta Scientific Inc.

AGENDA

The Sixteenth Annual Review of Progress in Applied Computational Electromagnetics

NAVAL POSTGRADUATE SCHOOL, MONTEREY, CALIFORNIA, U.S.A.
20-25 March 2000

Douglas Werner, Technical Program Chair

Randy Haupt, Symposium Co-Chair

Pingjuan Werner, Symposium Co-Chair

Susan Hagness, Short Course Chair

Leo Kempel, Vendor Chair

Keith Lysiak, Publicity Chair

Richard Adler, Symposium Administrator

Pat Adler, Conference Secretary

MONDAY MORNING 20 MARCH 2000

0700 – 0730	CONTINENTAL BREAKFAST (For short course and hands-on-workshop attendees only)	Glasgow Courtyard
0730 – 0820	SHORT COURSE/HANDS-ON-WORKSHOP REGISTRATION	Glasgow 103
0830-1630	SHORT COURSE #1 (FULL-DAY) "Computational Electromagnetic Methods in Mobile Wireless Communication Design" Ray Perez, Jet Propulsion Laboratory	Ingersoll 280
0830-1630	SHORT COURSE #2 (FULL-DAY) "XML and Modern Internet Technologies for Scientific Applications" Fumukh S. Khan, Ohio State University	Glasgow 102
0830-1630	SHORT COURSE #3 (FULL-DAY) "The Basics of The Finite Difference Time Domain Technique for Electromagnetic Application" Atef Z. Elsherbeni and Allen W. Glisson, University of Mississippi	Ingersoll 122
0830-1630	SHORT COURSE #4 (FULL-DAY) "Techniques for Electromagnetic Visualization" Edmund K. Miller, Santa Fe, NM, and John Shaeffer, Marietta Scientific, Inc	Engr Auditorium
0830-1630	SHORT COURSE #5 (FULL-DAY) "EIGER – Electromagnetic Interactions Generalized: An Introduction to and Tutorial on the Software Suite" Robert M. Sharpe and Nathan J. Champagne, Lawrence Livermore National Laboratory William A. Johnson, Sandia National Laboratories, Donald R. Wilton, University of Houston, And J. Brian Grant, ANT-S	Ingersoll 265
0830-1130	HANDS-ON-WORKSHOP #6 (HALF-DAY, MORNING) "MATHCAD Basics" Jovan Lebaric, Naval Postgraduate School	
0830-1630	SHORT COURSE #8 (FULL-DAY) "EMI/EMC Computational Modeling for Real-World Engineering Problems" Omar Ramahi, Compaq Corporation, and Bruce Archambeault, IBM	Spanagel 101A
0900-1200	CONFERENCE REGISTRATION	Glasgow 103

MONDAY AFTERNOON

1330-1630	HANDS-ON-WORKSHOP #7 (HALF-DAY, AFTERNOON) "MATLAB Basics" Jovan Lebaric, Naval Postgraduate School	
1400-1800	CONFERENCE REGISTRATION	Glasgow 103
1700	BOD MEETING	SP 101A
1900	PUBLICATION DINNER	

TUESDAY MORNING 21 MARCH 2000

0715 – 0745	CONTINENTAL BREAKFAST		Glasgow Courtyard
0740	ACES BUSINESS MEETING	President Perry Wheless	Glasgow 102
0745	ACES Website Demo	Atef Elsherbeni	Glasgow 102
0800	WELCOME	Douglas Werner, Penn State University	Glasgow 102
0815	PLENARY SPEAKER: "Efficient Extraction of S-parameters of Transmission Line Discontinuities for RF and Wireless Circuit Design"	Raj Mittra, Penn State University	Glasgow 102

SESSION 1: FINITE ELEMENT METHODS

Chairs: Jianming Jin and Peter Monk

Parallel with Sessions 2, 3 & 4)

0920	"Transient Electromagnetic Scattering from Curved Dielectric/Lossy 3D Bodies Using Covariant Projection Elements"	R. Ordovas, S.P. Walker & M.J. Bluck
0940	"Towards an <i>hp</i> -Adaptive Finite Element Method for Full-Wave Analysis of Waveguides"	L. Vardapetyan & L. Demkowicz
1000	"An <i>hp</i> -Adaptive Finite Element Method for Maxwell's Equations: A Progress Report"	L. Demkowicz
1020	BREAK	
1040	"Finite Element Method for Designing Plasma Reactors"	Leo Kempel, Paul Rummel, Tim Grotjohn & John Amrhein
1100	"Finite-Element Domain Decomposition Through an Iterative Algorithm: Coupling Between Cavity-Backed Slots"	Anastasis C. Polycarpou & Constantine A. Balanis
1120	"Investigation of the Bunting/Davis Functional when used with Vector Finite Elements for Waveguide Analysis"	Andrew F. Peterson & Sharib Wasi
1140	"Numerical Methods for High Frequency Problems"	T. Huttunen & P. Monk
1200	LUNCH	

SESSION 2: OPTIMIZATION IN ELECTROMAGNETICS

Chairs: Eric Michielssen and Dan Weile

(Parallel with Sessions 1, 3 & 4)

0920	"Design of Dual Band Frequency Selective Surfaces Using Genetic Algorithm"	A. Monorchio, R. Mittra & G. Manara
0940	"A Study of Cauchy and Gaussian Mutation Operators in the Evolutionary Programming Optimization of Antenna Structures"	Ahmad Hoorfar & Yuan Liu
1000	"A Statistical Intercomparison of Binary and Decimal Genetic Algorithms"	Yee Hui Lee, Stuart J. Porter & Andrew C. Marvin
1020	BREAK	
1040	"The Compact Genetic Algorithm: A Litmus test for Genetic Algorithm Applicability"	Daniel S. Weile, Eric Michielssen & David E. Goldberg
1100	"Dipole Equivalent Circuit Optimization Using Genetic Algorithm"	Bruce Long, Ping Werner & Doug Werner
1120	"Computing the Electromagnetic Field in a Perturbed Configuration Using Modified Reduced-Order Models"	R.F. Remis & P.M. van den Berg
1140	Some Further Results From FARS: Far-Field Analysis of Radiation Sources"	Edmund K. Miller
1200	LUNCH	

SESSION 3: NUMERICAL TECHNIQUES FOR PACKAGING AND INTERCONNECTS

Chairs: Omar Ramahi and Andreas Cangelaris

(Parallel with Sessions 1, 2, & 4)

0920	"A New Methodology for the Direct Generation of Closed-Form Electrostatic Green's Functions in Layered Dielectrics"	Andreas C. Cangelaris
0940	"The Treatment of Narrow Microstrips and PCB Tracks in the FDTD Method Using Empirically Modified Coefficients"	Chris J. Railton
1000	"Time-Domain-Analysis of QTEM Wave Propagation and Crosstalk on Lossy Multiconductor Transmission Lines with Terminal Coupling"	Georg Müller, Jan Wendel & Karl Reiß

TUESDAY MORNING 21 MARCH 2000

SESSION 3: NUMERICAL TECHNIQUES FOR PACKAGING AND INTERCONNECTS (cont)

1020 **BREAK**

1040 "An MPIE-Based Circuit Extraction Technique and Its Applications on Power Bus Modeling in High-Speed Digital Designs" Jun Fan, Hao Shi, James L. Knighten
James L. Drewniak

1100 "Non-resonant Electromagnetic Simulation of Some Resonant Planar Circuits" Yuriy O. Shlepnev

1120 "FDTD Analysis of Conventional and Novel Delay Lines" Omar M. Ramahi

1140 "Complementary Operators for Frequency-Domain Method: A Single Simulation Implementation" Omar M. Ramahi

1200 **LUNCH**

SESSION 4: STUDENT PAPER COMPETITION

Chair: Perry Wheless

(Parallel with Sessions 1, 2 & 3)

0920 "Systematic Studies in Annular Ring PBG Structures" Todd Lammers, Shawn W. Staker, & Melinda Piket-May

0940 "Fast Electromagnetic Analysis Using the Asymptotic Waveform Evaluation Method" Dan Jiao & Jianming Jin

1000 "A Domain-Decomposition/Reciprocity Technique for the Analysis Of Arbitrarily-Shaped Microstrip Antennas with Dielectric Substrates and Superstrates Mounted on Circularly-Cylindrical Platforms" R.J. Allard, D.H. Werner, & J.S. Zmysto

1020 **BREAK**

1040 "A New FDTD Scheme to Model Chiral Media" A. Akyurtlu, D.H. Werner, & K. Aydin

1100 "T-Matrix Computer Code Applied to Electromagnetic Field Penetration in Magnetic Resonance Imaging" Rafael R. Canales, Luis F. Fonseca & Fredy R. Zypman

1200 **LUNCH**

TUESDAY AFTERNOON

1300-1530 **INTERACTIVE POSTER SESSION** Ballroom, Hermann Hall

1300-1900 **VENDOR EXHIBITS** Ballroom, Hermann Hall

1500-1700 **WINE AND CHEESE TASTING** Ballroom, Hermann Hall

SESSION 5: INTERACTIVE POSTER SESSION Ballroom, Hermann Hall

"Characteristics of Silicon Photoconductivity Under Near-Infrared Illumination" Preston P. Young, Robert Magnusson
Tim R. Holzheimer

"Characteristics of Fractal Antennas" Haruo Kawakami, Yasushi Ojio, Yasushi Iizuka,
Satoshi Kogiso & Gentel Sato

"Feigenbaum Encryption of Computer Codes" R.M. Bevensee

"Extension of SuperNEC to Calculate Characteristic Modes" Thomas Abbott

(THE PAPER "XPATCH 4...", BELOW IS BEING PRESENTED HERE ONLY; IT WAS NOT RELEASED IN TIME FOR INCLUSION IN THE PROCEEDINGS)

"Xpatch 4: The Next Generation in High Frequency Electromagnetic Modeling and Simulation Software" J. Hughes, J. Moore, S. Kosanovich, D. Kapp,
R. Bhalla, R. Kipp, T. Courtney, A. Nolan, D. Andersh,
F. German and J. Cook

"Review of Basic 3D Geometry Considerations for Intelligent CEM Pre-Processor Applications" Kurt V. Sunderland

"Modelling of Loaded Wire Conductor Above Perfectly Conducting Ground by Using 3D TLM Method" Nebojša S. Dončov, Bratislav D. Milovanović,
Vladica M. Trenkić

TUESDAY AFTERNOON 21 MARCH 2000

1300-1530 INTERACTIVE POSTER SESSION (cont)

"Near to Far Field Transformation for a FDTD BOR with PML ABC and Sub-Grid Capability"

"Evanescence Tunneling and Quantile Motion of Electromagnetic Waves in Wave Guides of Varying Cross Section"

"A Modal Approach for the Calculation of Scattering Parameters in Lossfree and Lossy Structures Using the FI-Technique"

"A Modular Technique for the Calculation of Wave Guide Structures"

"Wave Propagation Through 2D Clusters of Coupled Cylindrical Resonators"

"Design Software for Cylindrical Helix Antennas"

"The Analysis of a Center-Fed Helical Microstrip Antenna Mounted on a Dielectric-Coated Circular Cylinder Using the Reciprocity Theorem"

"Near to Far Field Transformation for a FDTD BOR with PML ABC and Sub-Grid Capability"

WEDNESDAY MORNING

0715 - 0800 CONTINENTAL BREAKFAST

0815 PLENARY SPEAKER Tom Cwik, Jet Propulsion Laboratory
"Design on Computer - A Coming of Age"

Ballroom, Hermann Hall

Vicente Rodriguez-Pereyra, Atef Z. Elsherbeni, Charles E. Smith

E. Gjonaj

Rolf Schuhmann, Peter Hammes, Stefan Setzer, Bernd Trapp, & Thomas Weiland

Johannes Borkes, Adalbert Beyer, & Oliver Pertz

Ross A. Speciale

M. Slater, C.W. Trueman

R.A. Martin, & D.H. Werner

Vicente Rodriguez-Pereyra, Atef Elsherbeni & Charles Smith

SESSION 6: COMPUTATIONAL BIO-ELECTROMAGNETICS Chairs: Ray Luebbers and Susan Hagness

0920 "Numerical Investigation of Two Confocal Microwave Imaging Systems for Breast Tumor Detection"

0940 "FDTD Studies on SAR in Biological Cells Exposed to 837 and 1900 MHz in a TEM Cell"

1000 "Modelling of Personnel Electromagnetic Radiation Hazards: Deliberation of a Novice"

1020 BREAK

1040 "Modeling Interference Between Very Low Frequency Electromagnetic Fields and Implanted Cardiac Pacemakers"

1100 "Using Computational Electromagnetics to Solve an Occupational Health and Safety Incident"

1120 "Analysis of Permanent Magnet Type of MRI Taking Account of Hysteresis and Eddy Current and Experimental Verification"

SESSION 7: VIRTUAL REALITY IN REAL-WORLD APPLICATIONS Chairs: Stan Kubina and Dennis DeCarlo

0920 "A Virtual Radiation Pattern Range and Its Uses - C-130/Hercules HF Notch Antenna"

0940 "HF Towel-Bar Antenna Location Study Aboard an H3 Sikorsky Helicopter"

1000 "Improving Model Confidence through Metamorphosis"

1020 BREAK

1040 "Model Morphing for Insight into the HF Assessment Parameters"

1100 "3D Modeling of Complex Helicopter Structures: Prediction and Measurements"

Parallel with Sessions 7 & 8)

Susan C. Hagness, Xu Li, Elise C. Fear & Maria A. Stuchly

A.W. Guy

Alan Nott

Trevor W. Dawson & Maria A. Stuchly

Timothy Priest, Kevin Goldsmith & Dean DuRieu

Norio Takahashi, Siti Zubaedah, Takeshi Kayano Koji Miyata & Ken Ohashi

(Parallel with Sessions 6 & 8)

Stanley J. Kubina, Christopher W. Trueman David Gaudine

Saad N. Tabet, Carl D. Myers & Dennis DeCarlo

Douglas R. Munn and Chris Trueman

Douglas R. Munn and Chris Trueman

Anastasis C. Polycarpou, Dong-Ho Han Stavros V. Georgakopoulos & Constantine A. Balanis

WEDNESDAY MORNING 22 MARCH 2000

SESSION 7: VIRTUAL REALITY IN REAL-WORLD APPLICATIONS (cont)

- | | | |
|------|--|-------------------------------------|
| 1120 | "Increasing the Productivity of NEC Analysis with Virtual Reality and 3D Laser Scanners" | Kevin J. Cybert & Daniel D. Reuster |
| 1140 | "An Interactive HTML Based Multimedia Course on Antennas" | Ulrich Türk & Peter Russer |

SESSION 8: EMC

Chairs: Bruce Archambeault and Jim Drewniak

(Parallel with Sessions 6 & 7)

- | | | |
|------|--|--|
| 0920 | "Adding Imperfections to EMC FDTD Models as a Means of Increasing Accuracy" | Colin E. Brench |
| 0940 | "Power Conversion Techniques for Portable EMI Sensitive Applications" | Reinaldo Perez |
| 1000 | "Using the Partial Element Equivalent Circuit (PEEC) Simulation Technique to Properly Analyze Power/Ground Plane EMI Decoupling Performance" | Bruce Archambeault |
| 1020 | BREAK | |
| 1040 | "EMI Model Validation and Standard Challenge Problems" | Bruce Archambeault & James L. Drewniak |
| 1100 | "Modeling EMI Resulting from a Signal via Transition Through Power/Ground Layers" | Wei Cui, Xiaoning Ye, Bruce Archambeault
Doug White, Min Li & James L. Drewniak |
| 1120 | "Techniques for Optimizing FEM/MoM Codes" | Y. Ji, T.H. Hubing, & H. Wang |
| 1140 | "Numerical Modeling of Shielding by a Wire Mesh Box" | Gerald J. Burke & David J. Steich |

LUNCH

WEDNESDAY AFTERNOON

SESSION 9: PROPAGATION

Chairs: Steve Fast and Frank Ryan

(Parallel with Sessions 10 & 11)

- | | | |
|------|--|--|
| 1320 | "A Fast Quasi Three-Dimensional Propagation Model for Urban Microcells" | Joseph W. Schuster & Raymond J. Luebbers |
| 1340 | "FDTD Techniques for Evaluating the Accuracy of Ray-Tracing Propagation Models for Microcells" | Joseph W. Schuster & Raymond J. Luebbers |
| 1400 | "A Building Database Features Pre-Processor for 3-D SBR/GTD Urban EM Propagation Models" | James Pickelsimer & Raymond J. Luebbers |
| 1420 | "Toward a New Model for Indoor and Urban Propagation Using Percolation Theory" | G. Franceschetti, S. Marano, N. Pasquino, & I.M. Pinto |
| 1440 | "Ray Tracing Algorithm for Indoor Propagation" | C.W. Trueman, R. Paknys, J. Zhao, D. Davis, & B. Segal |
| 1500 | BREAK | |
| 1520 | "Modeling Large and Small-Scale Fading on the DPSK Datalink Channel Using a GTD Ray-Tracing Model" | Kent Chamberlin, Mikhailo Seledtsov & Petar Horvatic |
| 1540 | "Rough Surface Forward Scatter in the Parabolic Wave Equation Model" | Frank J. Ryan |
| 1600 | "A Comparison of Electromagnetic Parabolic Equation Propagation Models Used by the U.S. Navy to Predict Radar Performance" | Donald de Forest Boyer & Huong Pham |

SESSION 10: WAVELET AND TLM MODELING TECHNIQUES

Chairs: Wolfgang J.R. Hoefer and Peter Russer

(Parallel with Sessions 9 & 11)

- | | | |
|------|---|---|
| 1320 | "The Implementation of a High Level (1st-order) Haar Wavelet MRTD Scheme" | Enqiu Hu, Poman P.M. So, Masafumi Fujii, Wei Liu
Wolfgang J. R. Hoefer |
| 1340 | "Multi-Resolution Based TLM Technique Using Haar Wavelets" | Ismael Barba, Jose Represa, Masafumi Fujii,
Wolfgang J.R. Hoefer |
| 1400 | "Formulation and Study of an Arbitrary Order Haar Wavelet Based Multi-Resolution Time Domain Technique" | Costas D. Sarris & Linda P.B. Katehi |

WEDNESDAY AFTERNOON 22 MARCH 2000

SESSION 10: WAVELET AND TLM MODELING TECHNIQUES (cont)

- | | | |
|------|--|---|
| 1420 | "Computational Optimization of MRTD Haar-Based Adaptive Schemes Used for the Design of RF Packaging Structures" | Manos M. Tentzeris |
| 1440 | "Time-Domain Simulation of Electromagnetic Wave Propagation in a Magnetized Plasma" | J. Paul, C. Christopoulos & D.W.P. Thomas |
| 1500 | BREAK | |
| 1520 | "TLM Simulation of Patch Antenna on Magnetized Ferrite Substrate" | M.I. Sobhy, M.W. R. Ng, R.J. Langley & J.C. Batchelor |
| 1540 | "On the Practical Use of Layered Absorbers for the Simulation of Planar Microwave Circuits Using the SCN-TLM Method" | Jürgen Rebel, Tobias Mangold, & Peter Russer |
| 1600 | "A Numerical Study of MEMS Capacitive Switches Using TLM" | Fabio Coccetti, Larissa Vletozreck, Vitali Chitcheatourov, Peter Russer |
| 1620 | "Thin Wire Modeling with the TLMIE-Method" | S. Lindenmeier, C. Christopoulos & P. Russer |
| 1640 | "What Determines The Speed of Time-Discrete Algorithms" | Tobias Mangold, Jürgen Rebel, Wolfgang J.R. Hoefer, Poman P.M. So, & Peter Russer |

SESSION 11: TIME DOMAIN METHODS AND APPLICATIONS Chairs: Amelia Rubio Bretones and R. Gomez Martin

(Parallel with Sessions 9 & 10)

- | | | |
|------|--|---|
| 1320 | "Introducing a New Time-Domain Electromagnetic Field Solver LSFEM™TD-3D" | Craig C. Ouyang, B.N. Jiang & Nina Liao |
| 1340 | "Characteristic-Based Time-Domain Method for Antenna Analysis" | Dan Jiao, Jianming Jin & J.S. Shang |
| 1400 | "Modeling of Thin-Wire Structures by Solving the EFIE in Time Domain" | Friedrich Schunn & Hermann Singer |
| 1420 | "Time-Domain Analysis of Thin-Wire Loaded Antenna Using Integral Equations" | M. Fernandez Pantoja, A. Rubio Bretones R. Gomez Martin |
| 1440 | "Haar MRTD Wave Propagation Through Isotropic Plasmas" | Ismael Barba, Jose Represa, Masafumi Fujii, Wolfgang J. R. Hoefer |
| 1500 | BREAK | |
| 1520 | "Time-Domain Scattering from Arbitrarily Shaped Metallic Shelters with Apertures: Numerical and Experimental Analysis" | Giuliano Manara & Agostino Monorchio |
| 1540 | "Integral Equation Based Analysis of Transient Electromagnetic Scattering from Three Dimensional Inhomogeneous Dielectric Objects" | N.T. Gres, A.A. Ergin, B. Shanker, & E. Michieleson |
| 1600 | "Computational Properties of Wavelet Based PEEC Analysis in Time Domain" | G. Antonini & A. Orlandi |
| 1620 | "Time Domain Modeling of a Pulsed Horn-Dish Antenna" | M.J. Bluck, S.P. Walker & C. Thomas |

THURSDAY MORNING 23 MARCH 2000

0715 – 0800 **CONTINENTAL BREAKFAST**

- | | |
|------|---|
| 0815 | PLENARY SPEAKER: W.C. Chew, University of Illinois at Urbana-Champaign
"Fast Solvers for Electromagnetic Simulations – A New Age Analysis Tool" |
|------|---|

SESSION 12: MOMENT METHODS Chairs: Zach Baharav and Ramakrishna Janaswamy

(Parallel with Sessions 13 & 14)

- | | | |
|------|--|--|
| 0920 | "Iterative Solvers for Dense Matrices – Applications to Moment Method Matrices" | Jürgen v. Hagen & Werner Wiesbeck |
| 0940 | "Convergence Properties of the CFIE for Several Conducting Scatterers" | William D. Wood, Jr., Kueichien C. Hill
William J. Kent, Robert G. Layden & Lisa A. Cravens |
| 1000 | "Modeling of General Surface Junctions of Composite Objects in an SIE/MoM Formulation" | Joon Shin, Allen W. Glisson, & Ahmed A. Kishk |
| 1020 | BREAK | |

THURSDAY MORNING 23 MARCH 2000

SESSION 12: MOMENT METHODS (cont)

- | | | |
|------|--|--|
| 1040 | "A Novel Grid-Robust Higher-Order Vector Basis Function for the Method of Moments" | G. Kang, J.M. Song, W.C. Chew, K. Donepudi, & J.M. Jin |
| 1100 | "Analytical Treatment of Green's Functions Singularities in Microstrip Structures" | E. Jiménez, F.J. Cabrera & J.G. Cuevas del Río |
| 1120 | "Higher-Order Electromagnetic Modeling of Multilayer Microstrip Structures" | Feng Ling, Kalyan Donepudi & Jianming Jin |

SESSION 13: CONFORMAL ANTENNAS

Chairs: Leo Kempel and Douglas Werner

- | | | |
|------|---|---|
| 0920 | "A Conformal, Flexible, Multifunction Communications Antenna" | T.R. Holzheimer |
| 0940 | "Finite Printed Antenna Array Modeling Using an Adaptive Multi-Resolution Approach" | Lars S. Andersen, Yunus E. Erdemli & John L. Volakis |
| 1000 | "A Technique for Analyzing Radiation from Conformal Antennas Mounted on Arbitrarily-Shaped Conducting Bodies" | Dean Arakaki, Douglas H. Werner & Raj Mittra |
| 1020 | BREAK | |
| 1040 | "Using Computational Electromagnetics and Monte-Carlo Methods to Locate Antennas on Aircraft" | Kevin Goldsmith, Paul Johnson & Timothy Priest |
| 1100 | "Coupling Phenomena in Horizontal and Vertical Polarized Aperture Coupled Patch Antennas on Cylindrical Surfaces" | D. Löffler, J. von Hagen & W. Wiesbeck |
| 1120 | "Modeling and Analysis of Wideband Conformal Antennas" | Keith D. Trott, Rene D. Guidry & Leo C. Kempel |
| 1140 | "Curvature Effects on a Conformal Log-Periodic Antenna" | Charles Macon, Leo Kempel, Keith Trott, Stephen Schneider |

(Parallel with Sessions 12 & 14)

SESSION 14: ANTENNA ARRAYS

Chairs: Keith Lysiak and Nathan Cohen

- | | | |
|------|--|---|
| 0920 | "Problems of Characterising Array Manifolds for Naval Platforms in HF Environments" | Linda Holtby |
| 0940 | "Designing a VHF Wrap-Around DF Antenna Array Using NEC" | Keith Lysiak |
| 1000 | "Specifying a Direction Finding Antenna with Examples" | T. R. Holzheimer |
| 1020 | BREAK | |
| 1040 | "A High Efficiency Broad Band Wire Antenna System" | Kevin J. Cybert & Daniel D. Reuster |
| 1100 | "Comparison of Calculations and Measurements of an Electronically Scanned Circular Array" | James M. Stamm, Michael W. Jacobs & James K. Breakall |
| 1120 | "Array Sidelobe Reduction by Small Position Offsets of Fractal Elements" | Nathan Cohen & Robert G. Hohlfield |
| 1140 | "The Radiation Characteristics of Recursively Generated Self-Scalable and Self-Similar Arrays" | D.H. Werner & P.L. Werner |

(Parallel with Sessions 12 & 13)

THURSDAY AFTERNOON

SESSION 15: FAST AND EFFICIENT METHODS

Chairs: Weng C. Chew and Jiming Song

- | | | |
|------|--|--|
| 1320 | "Three Dimensional Scattering Analysis in Stratified Medium Using Fast Inhomogeneous Plane Wave Algorithm" | Bin Hu, & Weng Cho Chew |
| 1340 | "Multilevel Fast Multipole Algorithm for Analysis of Large-Scale Microstrip Structures" | Feng Ling, Jiming Song & Jianming Jin |
| 1400 | "A Novel Implementation of Multilevel Fast Multipole Algorithm for High-Order Galerkin's Method" | K.C. Konepudi, J.M. Song, J.M. Jin, G Kang & W.C. Chew |
| 1420 | "Incomplete LU Preconditioner for FMM Implementation" | Kubilay Sertel, & John L. Volakis |

(Parallel with Sessions 16 & 17)

THURSDAY AFTERNOON 23 MARCH 2000

SESSION 15: FAST AND EFFICIENT METHODS (cont)

- | | | |
|------|--|---|
| 1440 | "A Fast, High-Order Scattering Code for Solving Practical RCS Problems" | J.J. Ottusch, J.L. Visher & S.M. Wandzura |
| 1500 | BREAK | |
| 1520 | "An Efficient Integral Equation Based Solution Method for Simulation of Electromagnetic Fields in Inhomogeneous Dielectric (Biological) Media" | E. Bleszynski, M. Bleszynski & T. Jaroszewicz |
| 1540 | "Efficient Solution of Large-Scale Electromagnetic Eigenvalue Problems Using the Implicitly Restarted Arnoldi Method" | Daniel White & Joseph Koning |
| 1600 | "Fast Fourier Transform of Functions with Jump Discontinuities" | Guo-Xin Fan, & Qing Huo Liu |
| 1620 | "Applications of Non-Uniform Fast Transform Algorithms in Numerical Solutions of Integral Equations" | Q.H. Liu, X.M. Xu, & Z.Q. Zhang |

SESSION 16: APPLICATIONS OF THE FDTD TECHNIQUE

Chairs: Atef Elsherbeni and Wenhua Yu

(Parallel with Sessions 15 & 17)

- | | | |
|------|---|---|
| 1320 | "A Non-Dissipative Staggered Fourth-Order Accurate Explicit Finite Difference Scheme for the Time-Domain Maxwell's Equations" | A. Yefet & P.G. Petropoulos |
| 1340 | "FDTD Method for Maxwell's Equation in Complex Geometries" | A. Ditkowski, K. Dridi & J.S. Hesthaven |
| 1400 | "FDTD Analysis of Tapered Meander Line Antennas for RF and Wireless Communications" | Chun-Wen Paul Huang, Atef Z. Elsherbeni
Charles E. Smith |
| 1420 | "FDTD Modeling of an Electron Cyclotron Resonance Reactor Driven by an Lsitano Coil" | Gaetano Marrocco, Fernando Baardati
Francesco De Marco |
| 1440 | "Modeling Microwave and Hybrid Heating Using FDTD" | J. Haala & W. Wiesbeck |
| 1500 | BREAK | |
| 1520 | "A Conformal Finite Difference Time Domain (CFDTD) Algorithm for Modeling Perfectly Conducting Objects" | Wenhua Yu, Raj Mittra, Dean Arakaki, & Doug Werner |
| 1540 | "A Finite-Difference Algorithm for Modeling of Conductive Wedges in 2D" | Piotr Przybyszewski |
| 1600 | "Advanced Techniques of Geometrical Modelling and CFDTD" | F. Rivas, J.P. Roa & M.F. Catedra |

SESSION 17: HYBRID TECHNIQUES

Chairs: Agostino Monorchio and P. H. Pathak

(Parallel with Sessions 15 & 16)

- | | | |
|------|--|---|
| 1320 | "A Three-Dimensional Hybrid Technique for Combining the Finite Element and Finite Difference Method in Time Domain" | Agostino Monorchio & Raj Mittra |
| 1340 | "Vertical Antenna Near-Field Computation in Complex Environments by a Hybrid Method" | F. Bardati, E. Di Giampaolo, A. Durantini, & G. Marrocco |
| 1400 | "3D EM Problem Modeling by Geometry Decomposition and Combination of the FE, FDTD and BIE Techniques" | Hendrik Rogier, Daniël De Zutter & Frank Olyslager |
| 1420 | "Hybrid FDTD-Frequency Dependent Network Simulations Using Digital Filtering Techniques" | Ian Rumsey & Melinda Piket-May |
| 1440 | "Study of Electrically-Short Thin-Wire Antennas Located in the Proximity of Inhomogeneous Scatterers Using a Hybrid NEC/FDTD Approach" | A. Rubio Bretones, R. Mittra & R. Gómez Martín |
| 1500 | BREAK | |
| 1520 | "A Review of Some Hybrid High Frequency and Numerical Solutions for Radiation/Scattering Problems" | P.H. Pathak & R.J. Burkholder |
| 1540 | "An Hybrid Method Combining Integral Equations and Modal Expansion Applied to the RCS Modulation of Antennas and Rotating Fans" | Andre Barka & Paul Soudais |
| 1600 | "A 2D TLM and Haar MRTD Real-Time Hybrid Connection Technique" | Masafumi Fujii, Poman P.M. So, Enqiu Hu, Wei Liu
Wolfgang J. R. Hoefer |

FRIDAY 24 MARCH 2000

0700 – 0730	CONTINENTAL BREAKFAST (For Short Course and hands-on-workshop attendees only)	Glasgow Courtyard
0730 – 0820	SHORT COURSE/HANDS-ON-WORKSHOP REGISTRATION	Glasgow 103
0830-1630	SHORT COURSE #9 (Full Day) Why is There Electromagnetic Radiation and Where Does It Come From?" John Shaeffer, Marietta Scientific Inc and Edmund K. Miller, Santa Fe, NM.	Engr Auditorium
0830-1630	SHORT COURSE #10 (FULL-DAY) "Recent Advances in Fast Algorithms for Computational Electromagnetics" Weng Cho Chew, Jianming Jin, Eric Michielssen and Jiming Song, University of Illinois at Urbana-Champaign	Ingersoll 265
0830-1630	HANDS-ON-WORKSHOP #11 (FULL-DAY) "Method of Moments (MoM) Using MATHCAD" Jovan Lebaric, Naval Postgraduate School	
0830-1630	SHORT COURSE #12 (HALF-DAY, MORNING) "Computational Electromagnetics using Beowulf-Cluster Computers" Tom Owik and Daniel S. Katz, Jet Propulsion Laboratory	Ingersoll 122
1330-1630	SHORT COURSE #13 (HALF-DAY, AFTERNOON) "Multiresolution FEM: Introduction and Antenna Applications" John L. Volakis, University of Michigan, and Lars Andersen, Agilent	Ingersoll 122

PLEASE NOTE THAT A 10% DISCOUNT IS IN EFFECT FOR ALL WORKSHOPS TAKEN AFTER ATTENDING AN INITIAL WORKSHOP. THIS APPLIES TO THE GROUP OF WORKSHOPS FOR MATLAB AND MATHCAD.

SATURDAY 25 MARCH 2000

0700 – 0730	CONTINENTAL BREAKFAST (For Short Course and hands-on-workshop attendees only)	Glasgow Courtyard
0730 – 0820	SHORT COURSE/HANDS-ON-WORKSHOP REGISTRATION	Glasgow 103
0830-1630	HANDS-ON-WORKSHOP #14 (FULL-DAY) "FD/FDTD Using MATLAB" Jovan Lebaric, Naval Postgraduate School	
0830-1630	SHORT COURSE #15 (FULL-DAY) "An Introduction to Radar Cross Section" John Shaeffer, Marietta Scientific, Inc.	Engr Auditorium

PLENARY SESSION I

Raj Mittra

Efficient Extraction of S-parameters of Transmission line discontinuities for RF and Wireless Circuit Design

Raj Mittra

Electromagnetic Communication Laboratory
319 EE East, Pennsylvania State University
University Park, PA 16802

Virtual prototyping of RF and wireless circuits plays an important role in the cost-effective and timely development of new products. However, this task may be very time-consuming because these circuits typically contain a large number of linear and non-linear components, and the procedures for the circuit simulation and optimization can be very computer-intensive.

Typically, one resorts to EM field solvers for extracting the S-parameters or Spice-equivalent circuits for the circuit components that are discontinuities in various transmission lines, e.g., microstrip lines, striplines and coplanar guides. However, if one runs a frequency sweep for each choice of parameter sets, e.g., the width and height of the etch and the dielectric constant of the substrate, and uses full wave solvers for this purpose, the time required to develop the design may be prohibitively large, because a large number of iterations of the parameters may be needed to achieve the requisite frequency response and the impedance match. To circumvent this difficulty, one frequently resorts to using closed-form expressions that are extremely fast to compute, are available in a number of published papers and texts, and even in commercially-available softwares. The caveat in following this approach is that the closed-form expressions for the lumped-circuit parameters representing the transmission line discontinuities are based on quasi-static analyses and are, therefore, often quite limited in their range of application if accurate models are desired over a broad span of physical parameters and wide frequency interval. To-date, no simple alternatives seem to be available for bridging the gap between the quasi-static and full wave models. What is needed is an approach that can be used to derive the desired S-parameters almost as numerically efficiently as those based on the closed-form expressions, but one that does not compromise the accuracy of the models of the discontinuities in the process.

The objective of this paper is to propose one such approach that utilizes the neural networks in combination with quasi-electrostatic and -magnetostatic analyses to create models for the frequently-used microstrip discontinuities, e.g., bends, gaps, stubs, and so on.

Illustrative examples will be provided in the paper to demonstrate the usefulness of the approach by comparing its accuracy and computation times with full-wave solvers for a number of representative circuit components.

SESSION 1

FINITE ELEMENT METHODS

Chairs: Jianming Jin and Peter Monk

Transient electromagnetic scattering from curved dielectric/lossy 3D bodies using covariant projection elements

R Ordovas, S P Walker, M J Bluck

Imperial College of Science, Technology and Medicine, London
r.ordovas@ic.ac.uk, s.p.walker@ic.ac.uk, m.bluck@ic.ac.uk

Abstract

A novel transient finite element (FE) method is developed to study electromagnetic scattering from curved, dielectric/lossy 3-D bodies. The analysis is in terms of the E field. The test/trial spaces are modelled using Covariant Projection Elements (CPE). A description of the CPE properties -built-in avoidance of spurious modes and curvilinear modelling of rich geometries- is given. Their nature is then discussed in the context of differential geometry. Problem geometry is mapped via curvilinear (quadratic) modelling, providing accurate representation of arbitrarily curved bodies. The spatial representation of the field is quadratic tangential/linear normal (QT/LN), as a consequence of the CPE. Spatial integration is performed using Gaussian quadrature. A second-order implicit formulation is employed using Galerkin's method. The algebraic formulation is 'clean', without penalty terms or constraints being required. Time integration is accomplished using a unified set of double-step algorithms, meaning that the solution of a sparse matrix equation is involved at each timestep. Scattering results from a sphere are presented and compared with analytical and previous transient integral equation treatments. Good agreement and accuracy is shown.

1. Introduction

In this paper we present a finite-element time-domain (FETD) technique for the solution of wave scattering from electromagnetically complex (dielectric/lossy) 3-D bodies of arbitrary shape. The use of FETD methods still trails the popularity of finite-difference time-domain (FDTD) approaches, although [1] FETD methods seem to have an advantage in certain problems.

The analysis developed herein fully exploits the assets of FETD and expands them further by introducing a covariant projection element (CPE) [2,3] treatment for the vector test/trial functions. This allows curvilinear modelling of the geometry and includes naturally a quadratic tangential/normal linear (QT/LN) representation of the field spatial variation.

The material is structured as follows. In section 2 we introduce the CPE which we employ in the time domain. Their inherent ability to avoid the so-called spurious modes is reviewed and understood within a wider mathematical framework. The *weak inclusion* condition defined by Crowley [3] as the property to rule out spurious solutions is identified with the fulfilment of the De Rham-Whitney complex appearing in discrete differential geometry [4]. In section 3 the semi-discrete algebraic formulation for the problem is derived. Galerkin's method is applied to the *curl curl* equation for E. Two possibilities are considered for dealing with the exterior solution; an "exact" hybrid treatment with IETD or a truncation scheme implemented via absorbing boundary conditions. Section 4 is concerned with time integration and the final form of the system of equations to be solved. Finally, in section 5 the accuracy and efficiency of the present method are shown. Comparison is made with previously published results.

2. Covariant Projection Elements

The CPE is a form of hexahedral vector elements with the property that the associated degrees of freedom (DOF's) and interpolation polynomials are arranged to represent adequately a 1-form. They were first introduced by Crowley et al. [2,3]. Their major characteristic is the built-in

capability for removing spurious modes, but they also have the ability to support naturally abrupt material interfaces and to handle efficiently edges and sharp points. Spurious corruptions of the solution are avoided by fulfilling the so called *weak inclusion condition* [3] and we shall now see that the *weak inclusion condition* is strongly related to the fulfilment of the De Rham-Whitney complex.

Maxwell's equations are most elegantly expressed in the language of differential forms [5,6]. The E and H fields are 'ordinary' vectors (*1-forms*) but the induction, B, for instance, is a 'polar' vector (*2-form*) and does not change under transformations in the same way that E does. A *1-form* and a *2-form* are radically different objects in differential geometry, both from each other, and from *0-forms* and therefore, they cannot be modelled using the same 'elements' employed for scalar functions (*0-forms*).

In the continuum this geometrical structure is automatically fulfilled by Maxwell's equations but it is not generally satisfied when the fields (inductions) are arbitrarily discretised. Representation of E or H we must replicate the underlying structure of *1-forms*, and that algebraic structure is induced by the *exterior derivative*. This essential observation is not appreciated when the FE are implemented using a node-based discretisation with explicit continuity in all components. The elements required to deal with *1-forms* (*2-forms*) have their DOF's associated with edges (faces) rather than with nodes. Nodal elements are appropriate for *0-forms*.

Having identified E and H as *1-forms*, we seek the properties of the vector elements required to model them. First it is explained why the DOF's must be associated with edges and then conditions on how to model the irrotational space are given. Finally we show that CPE exhibit these characteristics.

1-forms can be considered as 'machines' [6] which yield a number out of a line integral. So *1-forms* have integrals over edges (circulations or line integrals). Therefore, the unknowns associated with the finite elements for differential *1-forms* are tangential magnitudes related with edges. Since the manifold where *1-forms* live is split

into elements and ultimately we represent the *1-forms* within these elements, the *only* unknowns to be fixed in the interelement boundary conditions are the tangential ones (edges), which determine the *1-form* throughout the element. From this point of view it is easier to understand why the essential boundary conditions encountered in ordinary EM vector analysis are always tangential to the surfaces and the natural boundary conditions are normal. This difference between essential and natural boundary conditions is present in EM just because the fields are *1-forms*, whose nature is 'tangential'. It is obvious then why natural interelement conditions are unconstrained and left to take care of themselves, given that *1-forms* are geometrical objects affected only by line integrals.

The exterior derivative d has the property that when it is applied twice it yields zero $d \circ d = 0$ (i.e. $\text{curl grad} = 0$) and therefore it divides the p -form space where it acts into two orthogonal sets: the kernel, $\ker(d^p F)$, of the exterior derivative (subspace mapped to zero upon the application of d) and its orthogonal counterpart. The relations and algebraic structures arising from this constitute the De-Rham complex [6,8].

The irrotational space of a vector, I , can then be interpreted as the kernel, $\ker(d^1 F)$, of the exterior derivative d for the space of *1-forms*, 1F . This kernel contains the image of the space of *0-forms* (associated with the scalar potential in EM) through the exterior derivative. In vector language we can say it contains elements of the type $E \propto \nabla \phi$.

Our goal is to generate two orthogonal trial spaces M and M_1 , such that $M \subset I$ and $M_1 \subset I_1$, as shown in figure 1. Practically we shall accomplish our goal only up to the order of the interpolation and the degree of refinement of the mesh.

To reproduce these orthogonal spaces correctly under the action of d using a discrete approximation let us start by defining a set of arbitrary vector basis functions which interpolate the *1-forms* through polynomials. Let us call this set $T = \{W_i\}$. The W_i 's are assumed element-independent and of the form,

$$\begin{aligned} W_{i \leftrightarrow \{l,m,n;u\}} &= h_l(u)h_m(v)h_n(w)du \\ W_{i \leftrightarrow \{l,m,n;v\}} &= h_l(u)h_m(v)h_n(w)dv \\ W_{i \leftrightarrow \{l,m,n;w\}} &= h_l(u)h_m(v)h_n(w)dw \end{aligned} \quad (1)$$

The natural coordinates are assumed. The subindices l, m, n stand for the order of the polynomial h 's and in order to establish a unique numbering for the W_i 's a global number i is given to every tetrad $\{l, m, n; u\}, \{l, m, n; v\}, \{l, m, n; w\}$. Let us recall the exterior derivative d is identified with curl in the case of 1-forms. We wish to express the E field with the trial space T and since it is a 1-form we must be able to reproduce both rotational and irrotational fields. The following expansion is adopted when trying to span the fields by the set T ,

$$E = \sum v_i W_i \quad (2)$$

Given a member of M , $v \in M$, we must have, by definition $dv = 0$. Also, from eq. (2) the expansion $v = \sum v_i W_i$ must hold. With these definitions we reach the homogeneous system of equations for the v_i 's,

$$d(\sum v_i W_i) = 0 \quad (3)$$

after applying the exterior derivative d . If a non-trivial solution is sought and $v \in M$, equation (3) has no solution, unless some v_i are zero. Taking the u component of expression (3) and expanding the notation, it is found,

$$\begin{aligned} 0 &= \sum_{\text{tetrads}} e_{\{l,m,n;w\}} h_l(u) \partial_u h_m(v) h_n(w) - \\ &\quad - \sum_{\text{tetrads}} e_{\{l,m,n;v\}} h_l(u) h_m(v) \partial_v h_n(w) \end{aligned} \quad (4)$$

If no restriction is made on the interpolating polynomials, there will be terms in eq. (4) proportional to $v^{c-m-1} w^m, v^m w^{c-m-1}$ without counterpart. These cannot be cancelled by any choice of $e_{\{l,m,n;w\}}$ or $e_{\{l,m,n;v\}}$ and represent corruptions to the modelling of 1-forms. Essentially one is then unable to model nullspaces of the d operator, $\ker(d^1 F)$, which in ordinary vector language constitute respectively the curl and div nullspaces. In the case of 1-forms, the fact that no solution can be found to (4) (except by setting some coefficients to zero) signifies that no terms like $\mathbf{E} \propto \nabla \phi$ can exist. Spurious modes are then inevitable; transient analysis, which contains zero frequencies in the spectrum, will be corrupted. Similarly, in quasistatic problems, where the field tends to be irrotational, no

solution can be found. The source of spurious modes is identified as the inability in the discrete world to accommodate and represent the action of the exterior derivative. From another point of view, having no solution for (4) is equivalent to stating that the size of the irrotational trial functions relative to the total trial space is too small. This is the link to the inclusion condition introduced by Crowley, which can be interpreted as a condition on the minimum relative size that the irrotational trial space can take.

A suitable restriction to use in (4) is to make the h 's complete up to one order lower in the normal direction (eg. in the first order, they would be tangentially quadratic and normally linear). This means that for the discrete irrotational space to be modelled, the 1-form space employed must have different orders of interpolation depending on the direction.

Let us recall that the discretisation accomplished so far is for use in a FE formalism which contains an associated error. The FE will provide the best fit to the space F up to its degree of accuracy. The creation of a trial space satisfying weak orthogonality moves the error due to spurious solutions into the 'higher order' error space which is the error space of the FE method itself. Therefore, within the order of the FE method, corruptions are nonexistent.

Covariant Projection Elements

Now we present the CPE as conceived by Crowley, but bearing in mind they can be derived according to the theoretical mathematical framework described above. The CPE are geometrically based on ordinary 27-noded, Lagrangian, curvilinear hexahedra. The 'real' brick Cartesian coordinates (x, y, z) are mapped into a reference cube with curvilinear coordinates (u, v, w) . This mapping entitles us to introduce a local curvilinear covariant basis $u^{\hat{a}} v^{\hat{b}} w^{\hat{c}}$ defined to be $\partial x / \partial u, \partial x / \partial v, \partial x / \partial w$ respectively. Here \mathbf{r} is the position vector and $u^{\hat{a}} v^{\hat{b}} w^{\hat{c}}$ are tangential to the axis shown in the subindices. The electric field can be expanded in this system as,

$$\mathbf{E}(u, v, w) = E_u \mathbf{a}^u + E_v \mathbf{a}^v + E_w \mathbf{a}^w \quad (5)$$

where $a^u a^v a^w$ are the contravariant basis (reciprocal in some literature) and E_u, E_v, E_w the covariant components. The covariant components along the axis are expressed also through the projection

$$(E_u, E_v, E_w) = (a_u \cdot E, a_v \cdot E, a_w \cdot E) \quad (6)$$

and from (6) it is seen to be easy to apply boundary or interelement conditions to the faces of the brick by just matching or fixing the covariant projections.

The way in which E is represented in an element according to Crowley (lowest order) [3] and Webb (hierarchical generalisation) [7] is,

$$\begin{aligned} E_u &= \sum_{i=0}^n \sum_{j=0}^n \sum_{k=0}^n e_{ijk} h_i(u) h_j(v) h_k(w) \\ E_v &= \sum_{i=0}^n \sum_{j=0}^n \sum_{k=0}^n e_{vjk} h_i(u) h_j(v) h_k(w) \\ E_w &= \sum_{i=0}^n \sum_{j=0}^n \sum_{k=0}^n e_{wjk} h_i(u) h_j(v) h_k(w) \end{aligned} \quad (7)$$

Working in the lowest possible order for CPE, we have $m=1$ $n=2$, and the parallelism with the above derivation for CPE is evident by identifying $W_{\{i,j,k,a^*\}} = h_i(u) h_j(v) h_k(w) a^*$ with (1).

3. EM scattering formulation

In this section we apply the Galerkin formulation to obtain a semi-discrete system of equations which approximate the Maxwell's time-dependent problem. Time discretisation will be discussed in next section.

The domain where the FETD (from now on CPETD) analysis will govern is named as a CPE (dielectric/lossy) region CPE with isotropic material properties ϵ, μ, σ , surrounded by an artificial surface S over which boundary conditions are later enforced (be they ABC's or a BIE hybrid treatment).

Taking the *curl* of the *curl* E Maxwell equation,

$$\nabla \times \nabla \times E + \mu \sigma \frac{\partial E}{\partial t} + \mu \epsilon \frac{\partial^2 E}{\partial t^2} = 0 \quad (8)$$

gives us our starting point. In a second order formulation one has the freedom to choose E or H as the working variable, as both procedures are analogous. To eq. (8) we apply Galerkin's method. A Galerkin formulation is particularly well suited for our formulation because it

provides us with a weak statement of the problem. In the previous section it has been seen that continuity conditions at material / interelement interfaces require only edge continuity, while leaving the normal conditions to be imposed weakly in an appropriate formalism. Therefore the weighted residual methods, especially the Galerkin method, prove to be a natural setting for a CPE treatment.

For simplicity we use a single-index notation to represent the E field using the vector basis functions W_i provided by the CPE, with i ranging from 1 to n , where n is the total number of DOF's. It is important to note that no penalty terms or constraints in the form of Lagrange multipliers need be included in the formulation.

To determine fully the CPETD problem, a treatment for the exterior solution, here the surface term, must be given. In [11] three possible choices are shown. For simplicity ABC's will be enforced. Nevertheless, it is important to recall that hybridisation with efficient BIETD is exact and that dispersion effects stemming from the CPE discretisation are diminished.

Zeroth order ABC's are applied to the scattered field in the surface term. The ABC operator is,

$$\mathbf{n} \times \nabla \times E = -\frac{1}{c} \mathbf{n} \times \mathbf{n} \times \frac{\partial E}{\partial t} = \frac{1}{c} \frac{\partial E_{\text{sc}}}{\partial t} \quad \text{on } S_{\text{sc}} \quad (9)$$

being equivalent to the Sommerfeld radiation condition on the surface of the truncated mesh. The final semi-discrete system of equations to deal with is then,

$$\begin{aligned} 0 &= e_j(t) \int_{\Omega_{\text{CPE}}} (\nabla \times W_i) \cdot (\nabla \times W_j) d\Omega \\ &+ \dot{e}_j(t) \int_{\Omega_{\text{CPE}}} \mu \sigma W_i \cdot W_j d\Omega \\ &+ \ddot{e}_j(t) \int_{\Omega_{\text{CPE}}} \mu \epsilon W_i \cdot W_j d\Omega \\ &+ \dot{e}_j(t) \oint_S (\mathbf{n} \times W_i) \cdot (\mathbf{n} \times W_j) dS \\ &+ \oint_S W_i \cdot (\mathbf{n} \times \nabla \times E_j^{\text{incident}}) dS \\ &+ \oint_S (\mathbf{n} \times W_i) \cdot (\mathbf{n} \times \dot{E}_j^{\text{incident}}) dS \end{aligned} \quad (10)$$

Different regions are taken into account by specifying the ϵ, μ, σ values at each element in the assembly process. Interelement boundary conditions are automatically fulfilled even across different regions.

4. Time integration and profiling

With the appropriate definitions for the matrices the system of equation (10) takes the form,

$$[M_y]\ddot{e}_j + [C_y]\dot{e}_j + [K_y]e_j = \tilde{f}_j \quad (11)$$

which can be tackled either via a single-step algorithm [9] or a double-step algorithm [1]. Performance from a double-step code is preferable. M_y is not diagonal, thus making the problem implicit. Stability is unconditional and the timestep size can be selected to suit the temporal variation being modelled. In particular, local mesh refinement to model geometrical detail does not require a corresponding timestep reduction.

The problem is reduced at each timestep to the implicit form $[A]x = b$, which is then solved via a bi-conjugate gradient method. Previous timestep solutions are used as a guess. A solution is typically reached with $\leq (N)^{1/3}$ iterations when the bulk of the wave/pulse crosses the scatterer, dropping considerably when the field is being radiated away. This shows the bulk of the computational effort is the time integration, with a scaling $\propto N^{1/3}$. (f), whereas the cost of building the matrices in eq. (11) scales as N (f). The storage cost comes mainly from the matrices present in the stepping algorithm. These are banded matrices with a number of entries $\approx Nb$, where $b \leq 180$. Storage scales as N (f). Note that all the above scalings are increased to the extent that discretisation needs to be made finer at high frequencies to accommodate dispersion.

5. Numerical results

The results and validation of this new CPETD method are described. The geometry for the test case considered is a sphere.

Defining λ as the characteristic Gauss pulsewidth, the problem considered for the dielectric(lossy) sphere is a $3\lambda \times 3\lambda \times 3\lambda$ one. However the 'interesting' part concerning the scatterer is only a $1\lambda \times 1\lambda \times 1\lambda$ region, making a hybrid treatment eventually desirable to model the surrounding vacuum region. The number of DOF's needed for a converged solution (15,000) is relatively small, and considerably smaller than has been reported using other FE formulations.

This is a consequence of the QT/LN mixed-order interpolation approximation and curvilinear modelling.

Dielectric sphere

Results have been published for a dielectric sphere by Vechinski, Rao and Sarkar [11] and Pocock, Bluck and Walker. A unit radius sphere is illuminated with an incident pulse given by,

$$E^{inc}(r, t) = E_0 \frac{1}{\sqrt{\pi}} \exp\left(-\frac{1}{2}(ct - ct_0 - r \cdot \hat{k})^2\right) \quad (12)$$

with $E_0 = \pm \hat{a}_z$, $ct_0 = 12m$, $\hat{k} = -\hat{a}_z$. Timestep size is $\Delta t = 0.6 \cdot 10^{-9} s$. The standard spherical-polar coordinate system is adopted. Figures 3 and 2 show the equivalent surface currents θ and J_ϕ , at $\theta = 90^\circ$, $\phi = 90^\circ$ and $\theta = 90^\circ$, $\phi = 0^\circ$, for the dielectric case with material properties are $\epsilon_r = 2.0$, $\mu_r = 1.0$. Good agreement with the results of Bluck [11] and Vechinski et al.[10] is displayed.

Figure 5 also shows the static case of a dielectric sphere immersed in a 1V/m uniform electric field. A uniform field is obtained in the interior with a value of 0.75V/m, in accord with the analytical result. Discontinuity is also represented accurately, yielding a jump in the normals of 2. No spurious modes are present.

Lossy sphere

Figure 4 shows the E_z component of the front, side and rear nodes of the lossy sphere. The material properties are $\epsilon_r = 3$, $\sigma = 0.01 S/m$. Comparison is made with an IETD code (Bluck[13]) using the pulse,

$$E^{inc}(r, t) = E_0 \exp\left(-\frac{1}{b^2}(ct - ct_0 - r \cdot \hat{k})^2\right) \quad (13)$$

with $E_0 = \hat{a}_z$, $ct_0 = 12m$, $\hat{k} = -\hat{a}_z$, $b = 2m$. and the same mesh given in the dielectric case. Again, agreement is good.

6. Conclusions

A successful implementation of curvilinear modelling, free of spurious modes, has been derived for a finite element treatment of dielectric/lossy targets. Further, a simple and clean formulation can be employed as a consequence of the freedom of the CPE from spurious mode problems. Solutions obtained are in very good agreement to previously published results.

References

[1] J.F.Lee, R.Lee, A.Cangellaris, 'Time-domain finite-element methods', *IEEE Trans. Antennas Propag.*, vol.45, no.3, pp.430-442, March 1997

[2] C.W.Crowley, P.P.Silvester, H.Hurwitz, 'Covariant projection elements for 3D vector field problems', *IEEE Trans. Magn.*, vol.24, no.1, pp.397-400, January 1988

[3] C.W.Crowley, *Mixed order covariant projection finite elements for vector fields*, PhD dissertation, McGill University, 1988

[4] A.Bossavit, 'Whitney forms: a class of finite elements for three-dimensional computations in electromagnetism', *IEE Proc.*, vol. 135, Pt. A, no.8, November 1988

[5] D.Baldomir, 'Differential forms and electromagnetism in 3-dimensional Euclidean space R', *IEE Proc.*, vol.133, Pt.A, no.3, pp.139-143, May 1986

[6] H.Flanders, *Differential forms with applications to the physical sciences*, Dover Publications, New York, 1989

[7] P.T.S.Liu, J.P.Webb, 'Analysis of 3D microwave cavities using hierarchical vector finite elements', *IEE Proc.-Microw. Antennas Propag.*, vol.142, no.5, pp.373-378, October 1995

[8] T.V. Yioultsis, T.D.Tsiboukis, 'A generalized theory of higher order vector finite elements and its applications in three-dimensional electromagnetic scattering problems', *Electromagnetics*, vol.18, no.5, pp.467-480, September-October 1998

[9] O.C.Zienkiewicz, W.L.Wood, N.W.Hine, 'A unified set of single step algorithms', *Int. J. numer. Methods eng.*, vol.20, 1529-1552, 1984

[10] D.A. Vechinski, S.M. Rao, T.K. Sarkar, 'Transient scattering from three-dimensional arbitrarily shaped dielectric bodies', *J. Opt. Soc. Am. A*, vol.11, No.4, April 1994

[11] J.L.Volakis, T. Ozdemir, J.Gong, 'Hybrid finite element methodologies for antennas and

scattering', *IEEE Trans. Antennas Propag.*, vol.45, no.3, pp.493-504, March 1997

[12] M. D. Pocock, M. J. Bluck, and S. P. Walker, 'Electromagnetic scattering from 3D, curved, dielectric bodies using time domain integral equations', *IEEE Transactions on Antennas and Propagation*, 46, pp. 1212-1219, 1998.

[13] M. J. Bluck, M. D. Pocock, and S. P. Walker, 'The extension of time domain integral equation analysis to scattering from imperfectly conducting bodies', *IEEE Transactions on Antennas and Propagation* (submitted), 1999

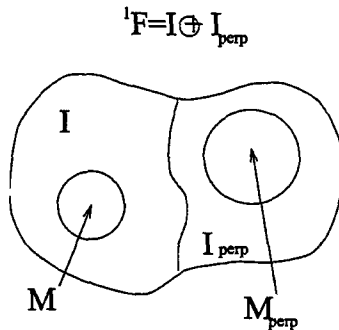


Figure 1. Orthogonal decomposition into the irrotational and non-irrotational parts of the 1-forms space.

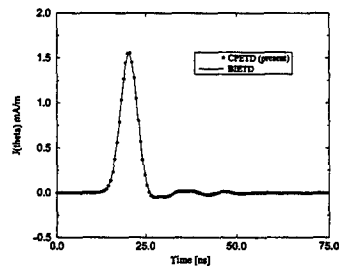


Figure 2. J_0 current for dielectric sphere.

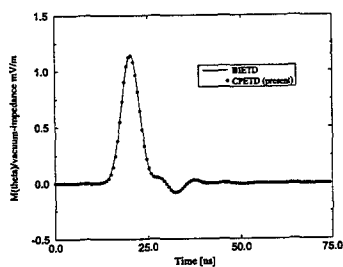


Figure 3. M_θ current for dielectric sphere.

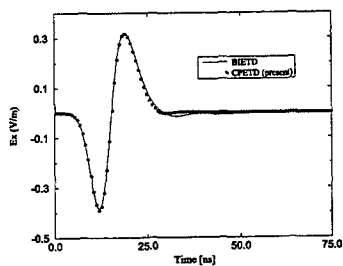


Figure 4. E_x for front node for lossy sphere.

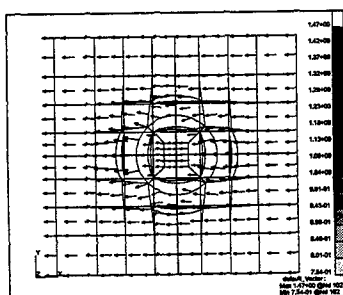


Figure 5. Dielectric sphere, $\epsilon_r = 2.0$, in a static electric 1V/m field

Towards an hp -adaptive Finite Element Method for Full-wave Analysis of Waveguides

L. Vardapetyan, L. Demkowicz

Texas Institute for Computational and Applied Mathematics

The University of Texas at Austin,

leon@ticam.utexas.edu, leszek@ticam.utexas.edu

Support: Air Force Grant F49620-98-1-0255

Abstract

A new stable variational formulation for full-wave analysis of waveguides is presented. Reported theoretical results apply to a wide class of vector finite elements including two families of Nedelec [11, 12] and their generalization, hp -edge elements [2, 15]. Numerical experiments fully support theoretical estimates for convergence rates.

1 Introduction.

In this short communication, we consider the numerical full-wave eigenmode analysis of an inhomogeneously loaded waveguide, at a given frequency ω . An existing approach to this problem allows for an infinite dimensional subspace of spurious modes corresponding to propagation constant $\beta = 0$, see [9, 10]. These spurious modes may pollute numerical TEM-like solutions, especially as $\omega \rightarrow 0$, if no extra care is taken in the numerical scheme. Our goal has been to develop a variational formulation applicable for quasistatic regimes and to provide a comprehensive mathematical analysis of a suitable finite element discretization with convergence rate estimates. The proposed variational formulation of the appropriate eigenvalue problem (although less memory-efficient than in [9, 10]) is uniformly stable as $\omega \rightarrow 0$, does not suffer from spurious modes¹ and, leading to the spectral analysis of a compact operator, greatly simplifies the mathematical analysis. As a practical advantage, zero is not an eigenvalue and all (non-infinite) eigenvalues have finite multiplicities. In this note, we outline our approach to the problem, present convergence rates for Nedelec elements [11, 12] and show sample numerical experiments with Nedelec elements and their generalization, the hp -edge elements [2, 15]. We refer to [14] for theoretical details and additional numerical examples.

¹One might argue that now $\beta = \infty$, not $\beta = 0$ as in [9, 10], has infinite multiplicity and spurious eigenmodes. However, the fields corresponding to $\beta = \infty$ are completely eliminated from actual computations.

2 Maxwell's equations.

Let us consider a closed waveguide defined by a right cylinder with polyhedral simply-connected cross section $\Omega \in \mathbb{R}^2$. Perfect electric conductor boundary condition are applied at $\partial\Omega$. The waveguide is loaded with a non-lossy dielectric described by scalar piece-wise continuous functions ϵ and μ . The general ansatz for electromagnetic fields in waveguides is given by

$$\begin{aligned}\mathcal{E}(\mathbf{x}, x_3, t) &= (\mathbf{E}(\mathbf{x}), E_3(\mathbf{x})) e^{j(\omega t \mp \beta x_3)}, \\ \mathcal{H}(\mathbf{x}, x_3, t) &= (\mathbf{H}(\mathbf{x}), H_3(\mathbf{x})) e^{j(\omega t \mp \beta x_3)},\end{aligned}\quad (2.1)$$

where t is time, $\mathbf{x} \in \Omega$, and x_3 -axis is along the waveguide. \mathbf{E} and \mathbf{H} are the electric and the magnetic vectors in the plane of the cross section, and E_3 and H_3 are the fields' components along the waveguide. With this ansatz, second order Maxwell's equations expressed in terms of electric field (\mathbf{E}, E_3) lead to a system of three equations:

$$\begin{cases} \nabla \times \left(\frac{1}{\mu} \nabla \times \mathbf{E} \right) - \omega^2 \epsilon \mathbf{E} + \frac{\beta^2}{\mu} \mathbf{E} - \frac{j\beta}{\mu} \nabla E_3 = 0 \\ \nabla \circ \left(\frac{1}{\mu} \nabla E_3 \right) + \omega^2 \epsilon E_3 + j\beta \nabla \circ \left(\frac{1}{\mu} \mathbf{E} \right) = 0 \\ \nabla \circ (\epsilon \mathbf{E}) - j\beta \epsilon E_3 = 0, \end{cases} \quad (2.2)$$

with boundary conditions imposed on $\partial\Omega$:²

$$\mathbf{E} \times \mathbf{n} = 0; \quad E_3 = 0. \quad (2.3)$$

We note that for $\beta \neq 0$ system (2.2) is overdetermined and either (2.2)₂ or (2.2)₃ can be dropped. By the logic of [2, 15], we retain the divergence constraint (2.2)₃. By rescaling E_3 as $E_3^{new} = j\beta E_3$, we can reduce system (2.2) to:

$$\begin{cases} \nabla \times \left(\frac{1}{\mu} \nabla \times \mathbf{E} \right) - \omega^2 \epsilon \mathbf{E} - \frac{1}{\mu} \nabla E_3^{new} = -\frac{\beta^2}{\mu} \mathbf{E}, \\ \nabla \circ (\epsilon \mathbf{E}) - \epsilon E_3^{new} = 0. \end{cases} \quad (2.4)$$

3 Variational eigenvalue problem. Continuous level.

To get a weak formulation of (2.4) with boundary conditions (2.3), we take test and trial functions from functional space $\mathbf{X} = \mathbf{H}_0(\text{curl}, \Omega) \times \mathbf{H}_0^1(\Omega)$:

$$\mathbf{X} = \{(\mathbf{F}, F_3) : \nabla \times \mathbf{F} \in \mathbf{L}^2(\Omega), \mathbf{F} \in \mathbf{L}^2(\Omega); \quad \nabla F_3 \in \mathbf{L}^2(\Omega)\}, \quad (3.5)$$

endowed with the norm:

$$\|(\mathbf{F}, F_3)\|_{\mathbf{X}}^2 = (\nabla \times \mathbf{F}, \nabla \times \mathbf{F}) + (\epsilon \mathbf{F}, \mathbf{F}) + (\epsilon \nabla F_3, \nabla F_3). \quad (3.6)$$

²To get a system on (\mathbf{H}, H_3) , interchange ϵ and μ and impose $\mathbf{H} \circ \mathbf{n} = 0$, $\partial_n H_3 = 0$ on $\partial\Omega$.

In this note, (\cdot, \cdot) stands for the $L^2(\Omega)$ -inner product: $(f, g) = \int_{\Omega} f \bar{g} d\Omega$.

Following the standard procedure, we recast (2.4), (2.3) into the following variational eigenvalue problem:

Find $(E, E_3^{new}) \in X$, $\beta \in \mathbb{C}$, such that $\forall (F, q) \in X$:

$$\begin{cases} (\frac{1}{\mu} \nabla \times E, \nabla \times F) - \omega^2 (\epsilon E, F) - (\frac{1}{\mu} \nabla E_3^{new}, F) = -\beta^2 (\frac{1}{\mu} E, F), \\ (\epsilon E, \nabla q) + (\epsilon E_3^{new}, q) = 0. \end{cases} \quad (3.7)$$

We assume that ω^2 is not an eigenvalue of

$$\begin{cases} (\frac{1}{\mu} \nabla \times E, \nabla \times F) = \omega^2 (\epsilon E, F) \\ (\epsilon E, \nabla q) = 0, \end{cases} \quad \text{or} \quad \begin{cases} (\frac{1}{\mu} \nabla E_3, \nabla F_3) = \omega^2 (\epsilon E_3, F_3). \end{cases} \quad (3.8)$$

It can be shown then that $\beta = 0$ is not an eigenvalue of (3.7). Owing to the divergence constraint (3.7)₂, the formulation is uniformly stable as $\omega \rightarrow 0$. Moreover, spectral analysis of (3.7) can be equivalently conducted on the solution operator T defined in accordance with (3.7), see [1]. Operator T is not only bounded, but also is compact on $L^2(\Omega) \times L^2(\Omega)$ due to the constraint (3.7)₂ and properties of X .

Compactness of operator T ensures that the spectrum of (3.7) is comprised only of eigenvalues and that any eigenvalue $\beta \neq \infty$ has finite multiplicity.

Generally, operator T is not self-adjoint; consequently its eigenvalues may have nonzero imaginary parts, and its eigenfields are not expected to form an orthogonal basis in $L^2(\Omega) \times L^2(\Omega)$.

4 Variational eigenvalue problem. Discrete level.

Let $\{\mathcal{T}_h\}_{h>0}$ be a family of discretizations of the computational domain Ω by triangles or quads, with parameter h reflecting the mesh size. For each \mathcal{T}_h , we construct W_h and V_h , finite dimensional internal approximations to $H_0(\text{curl}, \Omega)$ and $H_0^1(\Omega)$, and approximate X of (3.5) with $X_h = W_h \times V_h$. We note that system (3.7) involves constraint (3.7)₂ which needs to be properly modeled on the discrete level. The following three sufficient conditions, taken from [4], ensure convergence of numerical eigenpairs to the physical ones:

- (C1) Compatibility of spaces V_h and W_h such that:

$$\nabla V_h = \{E_h \in W_h : \nabla \times E_h = 0\}, \quad (4.9)$$

- (C2) Approximability of X by X_h such that:

$$\lim_{h \rightarrow 0} \inf_{(F_h, q_h) \in X_h} \|(E, E_3) - (F_h, q_h)\|_X = 0, \quad (4.10)$$

- (C3) Discrete compactness of \mathbf{W}_h in $L^2(\Omega)$ as defined in [5]:

Any bounded $\{\mathbf{E}_h\}_{h>0} \in \mathbf{H}_0(\text{curl}, \Omega)$, such that $\mathbf{E}_h \in \mathbf{W}_h$ and

$(\epsilon \mathbf{E}_h, \nabla q_h) = 0, \forall q_h \in V_h, \forall h$, contains a subsequence which

converges in the $L^2(\Omega)$ -norm to a function $\mathbf{E} \in \mathbf{H}_0(\text{curl}, \Omega)$.

For shape-regular affine meshes, Nedelec triangles and quads of [11] and triangles of [12] have been shown to possess discrete compactness, see [6, 7, 3]. The hp -edge elements (which generalize Nedelec quads of [11] and triangles of [12]) possess the discrete compactness as well [3], provided that p remains uniformly bounded. Conditions (C1)-(C3) are sufficient to show that there exists such $h_0 > 0$ that, for all $0 < h < h_0$, discretized version of (3.7) considered on \mathbf{X}_h is uniformly stable as $\omega \rightarrow 0$ and uniquely defines compact solution operators \mathbf{T}_h which converge to \mathbf{T} not only pointwise but also in the operator norm. This makes applicable the results of mathematical analysis for eigenvalue problems [1].

5 Convergence Rates for Nedelec Elements.

The estimates of convergence rates are necessary for the analysis and design of successful adaptive schemes. Since the hp -edge elements [2, 15] generalize Nedelec elements [11, 12], we consider the Nedelec elements first with the intention of using these results for further study of the hp -convergence mechanism and hp -adaptivity. To get the rates of convergence for propagation constant β , we need to know the regularity of the eigenmodes (\mathbf{E}, E_3) and the adjoint eigenmodes (\mathbf{E}^*, E_3^*) which correspond to β^2 , see [1]. Let us assume that all the eigenmodes and the adjoint eigenmodes for β^2 of multiplicity m and ascent α ³ are such that

$$\begin{aligned} \mathbf{E} &\in \mathbf{H}^r(\Omega), \quad \nabla \times \mathbf{E} \in \mathbf{H}^r(\Omega), \quad E_3 \in H^{r+1}(\Omega), \\ \mathbf{E}^* &\in \mathbf{H}^r(\Omega), \quad \nabla \times \mathbf{E}^* \in \mathbf{H}^r(\Omega), \quad E_3^* \in H^{r+1}(\Omega), \end{aligned} \quad (5.11)$$

where \mathbf{H}^r is Sobolev space of order r . If we use H^1 -conforming scalar elements of order p , then for shape-regular affine meshes with N -degrees of freedom,

$$|\beta - \beta_{i,h}|^\alpha \leq \mathcal{O}(N^{-s}), \quad (5.12)$$

where $s = \min(p, r)$, provided that the compatible Nedelec triangles or quads of the first family [11] are used.

In general, if the compatible Nedelec triangles of the second family [12] are used, then $s = \min(p - 1, r)$. However, if we solve for (\mathbf{E}, E_3) and the modes corresponding to β^2 are all TM or TEM, or if we solve for (\mathbf{H}, H_3) and all the modes are TE or TEM, then the triangles of both families offer the same rate of convergence.

³Ascent α is defined as the smallest integer such that $\dim \text{Ker}(\mathbf{T} - \beta^2)^\alpha = \dim \text{Ker}(\mathbf{T} - \beta^2)^{\alpha+1}$. If \mathbf{T} is self-adjoint, $\alpha = 1$.

6 Sample Numerical Examples.

We confirm convergence rates (5.12) by applying our method to homogeneously loaded waveguides with known exact solutions derived from eigenfunctions for the Laplace operator with Dirichlet or Neumann boundary conditions. For all considered cases, solution operators are such that ascent $\alpha = 1$, and all adjoint eigenspaces have the same regularity as the corresponding eigenspaces. To confirm (5.12), we implement Nedelec quads of [11] and Nedelec triangles of [12] on uniform meshes. We use 2Dhp90_EM, a FE package for electromagnetics [13], designed to support the hp -edge elements which generalize these quads and triangles of Nedelec.

For plots in Figures 5 and 6, cross section Ω is taken as 1×2 rectangle at $k = 0.2$ with $\sigma = 0$. The slopes are in full agreement with (5.12).

In Figure 6, eigenvalues λ_1 and λ_2 correspond to the TE-modes. This implies that $\nabla \times \mathbf{H} = 0$. Therefore, as predicted by theory and now seen in the plots, solving Maxwell's equations for (\mathbf{H}, H_3) , not for (\mathbf{E}, E_3) , provides for higher rates of convergence.

For plots in Figure 7, cross section Ω is taken as $1\text{mm} \times 2\text{mm}$ rectangle at 100KHz with $\epsilon_r = 1$, $\mu_r = 1$, $\sigma = 5.8 \cdot 10^4 \text{S/mm}$. Although the theoretical results apply only to non-lossy waveguides, the rates of convergence are as expected.

For an example of domains with singular eigenmodes, we take cross section Ω as a $3/2\pi$ -sector of unit radius. The eigenmode with the lowest regularity of $r = 2/3 - \delta$, $\delta > 0$ corresponds to λ_1 , the smallest eigenvalue. Since Ω is not a polygon, a map isoparametric with respect to the scalar element is used to model curved elements. The rates of convergence given in Figure 8 are as expected in all plots but one: for λ_1 the rate is higher then expected if $p_s = 2$.

Figure 1 depicts the cross section of a shielded microstrip line, taken from [16], which can support complex modes. We use symmetry of the domain and impose the perfect magnetic conductor boundary conditions along the y -axis. The dispersion curves in Figure 2 for some representative modes, including a complex mode, are produced using non-uniform hp -meshes with scalar hp -quads of order $p_s = 2, 3, 4$ linked with the compatible hp -edge elements. Two levels of h -refinement, performed at the tip of the perfectly conducting strip, result in 3041 degrees of freedom. Electric field (\mathbf{E}, E_3) is solved for.

In conclusion, we show that the formulation is indeed stable as $\omega \rightarrow 0$. Dimensionless numerical frequency corresponding to the domain used to compute attenuation constants of the microstrip depicted in Figure 3 can drop below 10^{-6} on the global level, and below 10^{-8} on the element level. In Figure 4, we observe that the FE-method based on formulation (3.7) and implemented using the hp -elements yields the attenuation curve marked "FE" which is in a good agreement with the curve computed by means of a conformal mapping technique taken from [8]. The hp -elements are of the same type as in the previous example. Two levels of h -refinement at the strip's corners result in 3412 degrees of freedom.

References

- [1] I. Babuška and J. Osborn, *Eigenvalue Problems*, in Handbook of Numerical Analysis, vol.2, Elsevier-North Holland, Amsterdam, 1991.
- [2] L. Demkowicz, L. Vardapetyan, "Modeling of Electromagnetic Absorption/Scattering Problems Using *hp*-adaptive Finite Elements", *Computer Methods in Applied Mechanics and Engineering*, **152**, 1-2, 103-124, 1998.
- [3] L. Demkowicz, P. Monk, Ch. Schwab, and L. Vardapetyan, "Maxwell Eigenvalues and Discrete Compactness in Two Dimensions", *TICAM Report 99-12*, The University of Texas at Austin, Austin, TX 78712.
- [4] P. Joly, C. Poirier, J. E. Roberts, and P. Trounev, "A New Nonconforming Finite Element Method for the Computation of Electromagnetic Guided Waves I: Mathematical Analysis", *SIAM Journal of Numerical Analysis*, **33** 4, 1494-1525, 1996.
- [5] F. Kikuchi, "Mixed and Penalty Formulations for Finite Element Analysis of an Eigenvalue Problem in Electromagnetism", *Computer Methods in Applied Mechanics and Engineering*, **64**, 509-521, 1987.
- [6] F. Kikuchi, "On a Discrete Compactness Property for the Nedelec Finite Elements", *J. Fac. Sci., Univ. Tokyo, Sect. IA Math*, **36**, 479-490, 1989.
- [7] F. Kikuchi, "Discrete Compactness of the Linear Rectangular Nedelec Element", *Abstracts of Presentations at 1999 Spring Meeting of Math. Soc. Japan*, 108-111, 1999.
- [8] B.-T., Lee, *Efficient Series Impedance Extraction Using Effective Internal Impedance*, Ph.D. thesis, Graduate School of The University of Texas at Austin, August 1996.
- [9] J.-F. Lee, D.K. Sun, and Z.J. Cendes, "Full-Wave Analysis of Dielectric Waveguides Using Tangential Vector Finite Elements", *IEEE Transactions on Microwave Theory and Techniques*, **39**, 8, 1262-71, 1991.
- [10] J.-F. Lee, "Finite Element Analysis of Lossy Dielectric Waveguides", *IEEE Transactions on Microwave Theory and Techniques*, **MTT-42**, 1025-1031, 1994
- [11] J.C. Nedelec, "Mixed Finite Elements in \mathbb{R}^3 ", *Numerische Mathematik*, **35**, 315-341, 1980.
- [12] J.C. Nedelec, "A New Family of Mixed Finite Elements in \mathbb{R}^3 ", *Numerische Mathematik*, **50**, 57-81, 1986.
- [13] W. Rachowicz, L. Demkowicz, "A Two-Dimensional *hp*-Adaptive FE Package for Electromagnetics", *TICAM Report 98-15*, July 1998.

- [14] L. Vardapetyan, *hp-Adaptive Finite Element Method for Electromagnetics with Applications to Waveguiding Structures*, Ph.D. thesis, Graduate School of The University of Texas at Austin, December 1999.
- [15] L. Vardapetyan and L. Demkowicz, "hp-Adaptive Finite Elements in Electromagnetics", *Computer Methods in Applied Mechanics and Engineering*, **169**, 331-344, 1999.
- [16] E. Yamashita and K. Atsuki, "Analysis of microstrip-like transmission lines by nonuniform discretization of integral equations", *IEEE Trans., Microwave Theory and Tech.*, **MTT-24**, 195-200, April 1976.

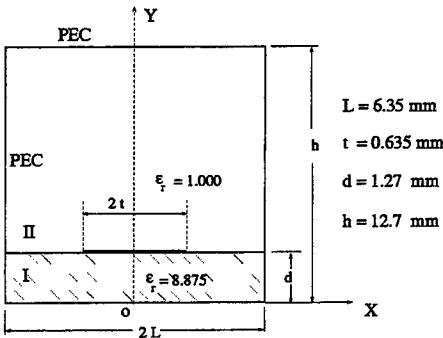


Figure 1: Shielded microstrip.

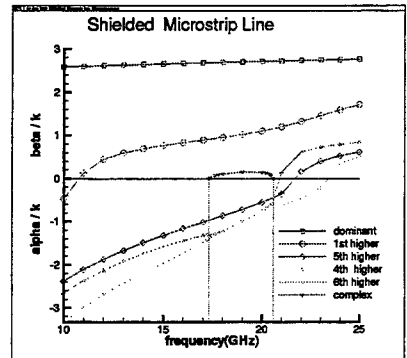


Figure 2: Dispersion curve.

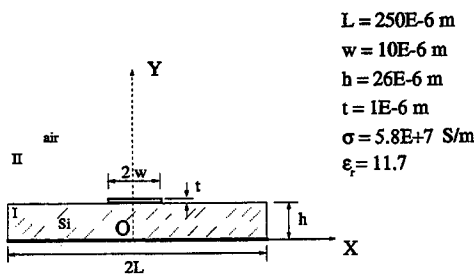


Figure 3: Microstrip, DC-limit reached.

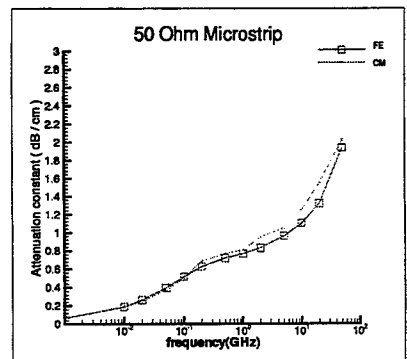


Figure 4: Attenuation curves for dominant mode.

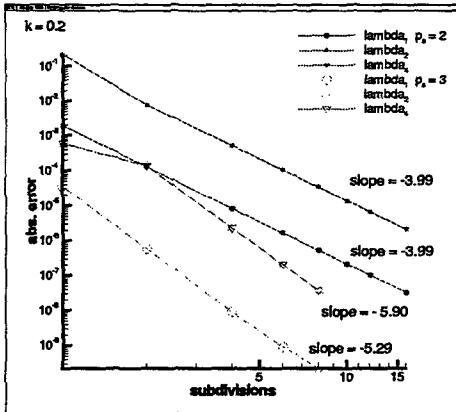


Figure 5: Dielectric rectangle: h -refinement by quads.

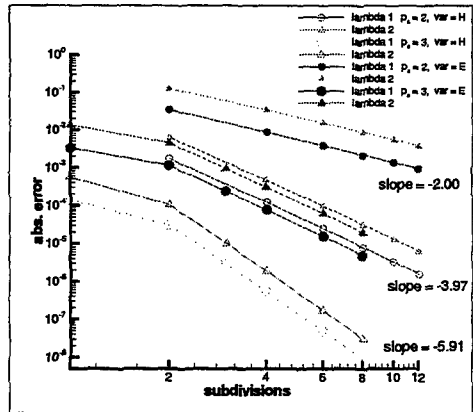


Figure 6: Dielectric rectangle: h -refinement by triangles.

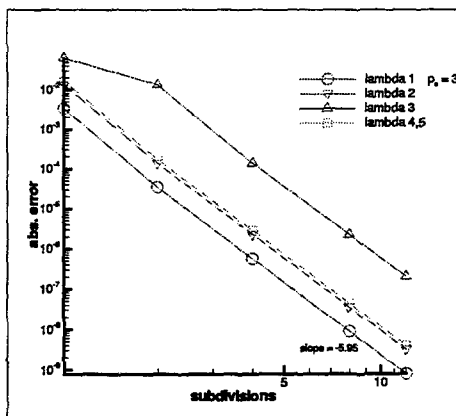


Figure 7: Conducting rectangle: h -refinement by quads.

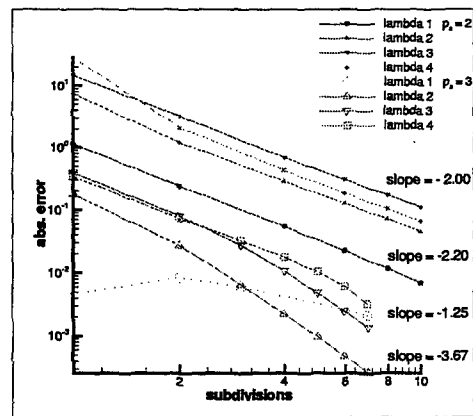


Figure 8: Dielectric sector: h -refinement by isoparametric triangles.

AN hp -ADAPTIVE FINITE ELEMENT METHOD FOR MAXWELL'S EQUATIONS A Progress Report

L. Demkowicz

Texas Institute for
Computational and Applied Mathematics
The University of Texas at Austin

Abstract

I review the main results of the research on hp -adaptive finite element modeling for Maxwell's equations done at TICAM for the last three years, and summarize open problems.

Introduction. It has been almost three years since we have proposed in [16] a generalization of Nédélec's edge elements allowing to vary *locally* in a mesh, element order of approximation p . The variable order of approximation allows to combine in the same mesh large elements of high order, optimal from the point of view of minimizing the pollution (phase) error [21, 22, 23, 24], and small elements of low order, necessary to capture geometrical details. The variable order of approximation is also indispensable in constructing geometrically graded meshes to capture singularities in the electric and magnetic fields [35] and, finally, offers the general framework for constructing approximations that converge *exponentially* fast to the exact solutions. With a generous support of Dr. Arje Nachman from Air Force (Contract F49620-98-1-0255) and the National Science Foundation through *National Partnership for Advanced Computational Infrastructure* (NPACI), we have been able to focus on the subject for the last three years. In this note, I will review the main results of our work for the last three years and state the most important open problems.

Time harmonic Maxwell's equations. We consider the following formulation of time-harmonic Maxwell's equations in terms of electric field E . Given a *bounded* domain $\Omega \subset \mathbb{R}^3$, with boundary Γ consisting of two disjoint parts Γ_1 and Γ_2 , we wish to find electric field $E(x)$, $x \in \bar{\Omega}$, that satisfies the reduced wave equation in Ω , Dirichlet (ideal conductor) boundary condition on Γ_1 , and Neumann (magnetic field) boundary condition on Γ_2 . The standard variational formulation is obtained by multiplying the wave equation with a vector test function \bar{F} , integrating over domain Ω , integrating by parts, and using the Neumann boundary condition.

$$\left\{ \begin{array}{l} \text{Find } E \in W \text{ such that} \\ \int_{\Omega} \frac{1}{\mu} (\nabla \times E) \cdot (\nabla \times \bar{F}) dx - \int_{\Omega} (\omega^2 \epsilon - j\omega\sigma) E \cdot \bar{F} dx = \\ \qquad -j\omega \int_{\Omega} J^{imp} \cdot \bar{F} dx + j\omega \int_{\Gamma_2} H^P \cdot \bar{F} dS \quad \text{for all } F \in W \end{array} \right. \quad (0.1)$$

In the above W is the *space of admissible solutions*,

$$W := \{E \in L^2(\Omega) : \nabla \times E \in L^2(\Omega), n \times E = 0 \text{ on } \Gamma_1\}, \quad (0.2)$$

ω is an angular frequency, ϵ, μ, σ denote dielectric permittivity, magnetic permeability and conductivity of the medium, \mathbf{J}^{imp} is a prescribed, impressed (source) current. \mathbf{H}^p is interpreted as a tangent component of a magnetic field \mathbf{H} to be enforced on Γ_2 , $\mathbf{H}^p = \mathbf{n} \times \mathbf{H}$, with \mathbf{n} denoting the outward unit normal vector to boundary Γ_2 . Finally, j is the imaginary unit.

The second order part of the operator, $\nabla \times (\nabla \times \mathbf{E})$ is not elliptic, as it has a infinite dimensional null space consisting of all gradient fields. This is the main reason why the solution of the Maxwell equations is more difficult than the solution of the Helmholtz equation. The lack of ellipticity has an immediate effect on the stability properties of the equation. The L^2 -norm of the electric field \mathbf{E} depends continuously on data $\mathbf{J}^{imp}, \mathbf{H}^p$, but the stability constant is frequency dependent and it blows up to infinity as frequency $\omega \rightarrow 0$ [16]. This corresponds to the fact that the formulation is *not valid* for the zero frequency case.

Introducing a *space of Lagrange multipliers* (scalar potentials):

$$V := \{q \in H^1(\Omega) : q = 0 \text{ on } \Gamma_1\}, \quad (0.3)$$

we employ a special test function $\mathbf{F} = \nabla q, q \in V$, to learn that solution \mathbf{E} to (0.1) must *automatically* satisfy the weak form of the continuity equation,

$$-\int_{\Omega} (\omega^2 \epsilon - j\omega\sigma) \mathbf{E} \cdot \nabla \bar{q} \, dx = j\omega \int_{\Omega} \mathbf{J}^{imp} \cdot \nabla \bar{q} \, dx + j\omega \int_{\Gamma_2} \mathbf{H}^p \cdot \nabla \bar{q} \, dS. \quad (0.4)$$

The idea behind the *stabilized formulation* [16] is to enforce this continuity equation *explicitly* at the expense of introducing an additional variable, the Lagrange multiplier $p \in V$:

$$\left\{ \begin{array}{l} \text{Find } \mathbf{E} \in \mathbf{W}, p \in V \text{ such that} \\ \int_{\Omega} \frac{1}{\mu} (\nabla \times \mathbf{E}) (\nabla \times \bar{\mathbf{F}}) \, dx - \int_{\Omega} (\omega^2 \epsilon - j\omega\sigma) \mathbf{E} \cdot \bar{\mathbf{F}} \, dx - \int_{\Omega} (\omega^2 \epsilon - j\omega\sigma) \nabla p \cdot \bar{\mathbf{F}} \, dx = \\ \quad -j\omega \int_{\Omega} \mathbf{J}^{imp} \cdot \bar{\mathbf{F}} \, dx + j\omega \int_{\Gamma_2} \mathbf{H}^p \cdot \bar{\mathbf{F}} \, dS, \quad \forall \mathbf{F} \in \mathbf{W} \\ - \int_{\Omega} (\omega^2 \epsilon - j\omega\sigma) \mathbf{E} \cdot \nabla \bar{q} \, dx = j\omega \int_{\Omega} \mathbf{J}^{imp} \cdot \nabla \bar{q} \, dx + j\omega \int_{\Gamma_2} \mathbf{H}^p \cdot \nabla \bar{q} \, dS \quad \forall q \in V. \end{array} \right. \quad (0.5)$$

The Lagrange multiplier p *identically vanishes*, and for that reason, it is frequently called the *hidden variable*. In contrary to the original formulation, the stability constant for the regularized formulation converges to one, as $\omega \rightarrow 0$. The regularized formulation works because gradients of the scalar-valued potentials from V form precisely the null space of the curl-curl operator. The variable order edge elements [16] are constructed precisely in this way. We start with a standard, H^1 -conforming, variable order element, (triangle, quad in 2D, tetrahedron, hexahedron, or prism in 3D), identify the corresponding *space of shape functions*, and consider its image through the gradient operator. For instance, for a triangle, if the space of scalar potentials V_h consists of polynomials of order $p+1$ whose restrictions to element edges e are of *lower or equal* order p_e+1 , the space of vector-valued functions \mathbf{W}_h to approximate the \mathbf{E} -field will consist of vector-valued polynomials whose *tangential components* (and tangential only) on the element boundary will reduce to the lower order p_e . This corresponds to the fact that only the differentiation *along* the boundary lowers the order of the polynomial.

The same assumption that \mathbf{W}_h should include gradients of functions from V_h lies behind the construction of the parametric element [38].

De Rham diagram. Spaces $H^1, H(\text{curl})$ and their discrete counterparts V_h, \mathbf{W}_h can be put into a more general context of the de Rham diagram [14] involving additionally the curl and div operators. The de Rham sequence shown below not only can be reproduced on the discrete level using the variable order spaces, but also can be completed with corresponding *hp* interpolation operators to make the diagram commute.

$$\begin{array}{ccccccc}
 H^1 & \xrightarrow{\nabla} & H(\text{curl}) & \xrightarrow{\nabla \times} & H(\text{div}) & \xrightarrow{\nabla \cdot} & L^2 \\
 \downarrow \Pi_{hp} & & \downarrow \Pi_{hp}^{\text{curl}} & & \downarrow \Pi_{hp}^{\text{div}} & & \downarrow P_{hp} \\
 V_{hp} & \xrightarrow{\nabla} & \mathbf{W}_{h,p-1} & \xrightarrow{\nabla \times} & \mathbf{X}_{h,p-2} & \xrightarrow{\nabla \cdot} & Y_{h,p-3}
 \end{array} \quad (0.6)$$

For a uniform order of approximation, the diagram reduces to the classical one [1], involving the Nedelec and Raviart-Thomas elements. The *hp* interpolation operators reduce then to those used by Nedelec but the generalization is non-trivial as the Nedelec interpolation procedures *do not* generalize directly to the variable order elements. The de Rham diagram applies to all standard elements, including curved (parametric) elements as well, and forms a mathematical foundation for stability and convergence analysis not only for Maxwell's equations but also for *acoustics* and various *mixed formulations*. For *h*-refinements, the corresponding interpolation error estimates reduce to those for Nedelec and Raviart-Thomas elements. One of the still open challenges (in 3D only) is to lower maximally the regularity assumptions on interpolated functions so that the interpolation error estimates could be applied to problems involving non-smooth, non-convex domains with singular solutions. But the main open problem in this context is to prove interpolation error estimates for the *p*-method. Such estimates have so far been investigated only for H^1 -conforming elements by Babuška, Suri, Guo et al, but they remain unknown for the remaining $H(\text{curl})$ and $H(\text{div})$ -conforming elements. As the definitions of the interpolation procedures involve mixed problems [14], analysis of the *p*-interpolation properties reduce to a *p*-stability analysis of a mixed method for Maxwell-like problem on a *single* element. Numerical experiments for $p = 1, \dots, 9$ indicate that the stability is there but the question of a general proof for arbitrary elements remains open (the case of square and hexahedral elements was successfully analyzed by Monk [28]).

Fortran 90 implementations. In the past three years we developed four *hp* research codes, written in Fortran 90. The choice of language was motivated, among other reasons, with recycling portions of earlier, Fortran 77 implementations, dynamic memory allocation, possibility of using long, self-explanatory names, and user-defined data types. The fundamental data structure for each of the implemented *hp*-adaptive discretizations [11, 17, 32, 9, 33] reduces to just two arrays of two kinds of objects: *elements* and *nodes*. The 2D code uses both triangular and quadrilateral elements, the 3D code works (currently) on hexahedra only. In both 2D and 3D we have used the same strategy, starting with a *generic* version for continuous elements (2Dhp90, 3Dhp90) and then customizing it to the edge elements and Maxwell's equations (2Dhp90_EM, 3Dhp90_EM).

The codes support not only the variable order approximations but the *constrained approximation* (hanging nodes) on anisotropically refined, *one-irregular* meshes. These refinements allow to produce long, needle-like elements to handle edge singularities and geometrically graded meshes for corner singularities. The source codes, along with manuals, have been placed on the Web, and are being updated regularly.

Convergence. Maxwell's eigenvalues. Stability and convergence analysis for the time-harmonic Maxwell equations leads quickly to the related (and important for itself) problem of convergence of Maxwell's eigenvalues [29]. Due to the lack of ellipticity, the problem is not covered by the standard theory for elliptic equations. Over a decade ago, Kikuchi [25] introduced the notion of *discrete compactness* that provides a sufficient condition for a convergence analysis for Maxwell's eigenvalues. In a recent contribution, Caorsi et al. [5] demonstrate that, in a sense, the discrete compactness is not only sufficient but also necessary to assure good convergence properties. In turn, Boffi [2, 3] has linked that discrete compactness with the commutativity of the de Rham diagram showing, in essence, that the two are equivalent. This strongly suggests that, eventually, we can prove the optimal *hp*-error estimates for all kinds of elements and the most general 3D problems. Our contributions to the subject include a 2D *h*-convergence analysis for shape regular, variable order meshes (geometrically graded meshes included) [13], and a 3D *h*-convergence analysis for standard Nedelec's elements of higher order on quasi-uniform meshes [29]. A general proof, including the *p*-convergence analysis, is linked to the *p* interpolation estimates discussed above, and it remains open.

A posteriori error estimation. Any adaptive procedure is based on estimating residuals. Since the \mathbf{E} field, as the solution to Maxwell's equations, with or without the Lagrange multiplier, satisfies the continuity equation automatically, one may be tempted to estimate the residual corresponding to the curl-curl equation only. This is wrong, and this fact is well known in the EE community [36]. The residual of the continuity equations can indeed be bounded by the residual corresponding to the curl-curl equation, but the constant is *not frequency independent* and it blows up to infinity as $\omega \rightarrow 0$. This is, again, related to the stability properties of the standard variational formulation discussed earlier. Consequently, one *has to* estimate the error corresponding to *both* equations even if one chooses to use the standard variational formulation only. We have developed and implemented 2D a-posteriori *element implicit error estimators* based on locally equilibrated residuals [8, 10]. As opposed to most popular *explicit* error estimates, the method works for general *hp* meshes without use of any ad hoc constants. The main drawback of the technique is the complexity of the coding, prohibitive in a 3D implementation. A number of other techniques will have to be investigated, including explicit error estimates, element implicit error estimates based on a solution of local Dirichlet problems, duality estimates, estimates based on patches etc. [31].

Automatic *hp*-Adaptivity. One of the 'holy grails' of the *hp* methods is the search for a fully *automatic hp* refinement/unrefinement procedure. The idea is well known. There is a consensus that refinements should be based on *local* residuals. Elements with largest residuals must be refined.

The question is whether to go then with h - or p -refinement. The main principle is as follows: for a 'regular' solution we should use the p -refinement, for less regular, the h -refinement. The big question is how to access the regularity of the solution through the data to the problem and the FE solution in a sufficiently quantitative way, so we could select the right type of the refinement. The automatic refinements procedure is expected to reproduce the optimal meshes known for a few classes of problems: the p -refinements for analytical (very regular) solutions, geometrically graded meshes of Babuška and Guo for vertex and edge singularities, see e.g. [19, 20], optimal hp meshes for boundary layers investigated by Schwab, Suri and Melenk, see e.g. [26]. In all these cases we *do know* how the meshes should look like and, therefore, the optimal procedure should at least asymptotically produce the same grids.

We emphasize that the continued research on the subject of automatic hp -adaptivity, does not preclude using hp methods to solve practical problems. Most of the time we can identify the boundary layers, vertex and edge singularities, and start with meshes that capture those irregularities from the very beginning. The pollution analysis suggests to use higher order, large elements whenever possible and, finally, h -refinements can be used to control the residual error. This is indeed the procedure that we currently use.

Infinite Elements. Most of the practical problems are formulated in unbounded domains (exterior problems, infinite waveguides), and the computational domain has to be truncated with the rest of the domain modeled by means of an Absorbing Boundary Condition (ABC). This is a huge subject by itself and even a short review of it would have taken several pages. Continuing our research on Helmholtz equation [18, 12], we proposed in [15] an infinite element for Maxwell's equations, proving an exponential convergence with respect to number of terms N used in the asymptotic expansion. The element has been implemented in both 2D and 3D codes [6, 7]. The good news is that the computational results are promising, and that we have been able to confirm optimal h -convergence rates. The bad news, at least on the theoretical side, is that we could not observe exponential convergence, neither in order of approximation p , nor in number of terms N . We blame the conditioning for it, but the issue needs a more careful analysis and further investigation. Besides, rapid advances in fast Boundary Element Methods, suggest to look at the possibility of coupling the hp finite elements with (fast) boundary element methods.

Iterative solvers. No adaptive code will ever have a practical impact if it does not come with a good iterative solver to tackle large problems and take advantage of the sequence of solutions on consecutively adapted meshes. Recent advances of Hiptmair, and Arnold, Falk and Winther, on multigrid solvers for the *positive definite* case pave the way for constructing a solver for the time-harmonic case but, according to our best knowledge, the problem still remains open. Following the idea of Cai and Widlund [4], we presented in [34] a two-grid solver based on the idea of regularization. We begin with a slightly modified version of the regularized problem in the form:

$$\begin{cases} (\nabla \times \mathbf{u}, \nabla \times \mathbf{v}) - k^2(\mathbf{u}, \mathbf{v}) + (\nabla p, \mathbf{v}) &= (\mathbf{J}, \mathbf{v}) \quad \forall \mathbf{v} \\ -k^2(\mathbf{u}, \nabla w) &+ \frac{1}{2}(\nabla p, \nabla w) = 0 \quad \forall w \end{cases} \quad (0.7)$$

where (\cdot, \cdot) denotes the L^2 -inner product, k is the wave number and, for simplicity, the Dirichlet boundary condition is used only. Notice the additional Laplace operator in the continuity equation acting on the Lagrange multiplier. The problem can be rewritten then in the operator form:

$$\begin{cases} Au - k^2 u + Bp = J \\ -k^2 B^T u + \frac{1}{2} Dp = 0 \end{cases} \quad (0.8)$$

The additional Laplace operator D allows us to eliminate the multiplier and we arrive at a *regularized* equation in the form:

$$\left(A + k^2 \underbrace{(2BD^{-1}B^T)}_{\text{new term}} - I \right) u = J \quad (0.9)$$

We solve then the equation using a two-grid method that consists of a block-Jacobi smoother coupled in a *multiplicative way* with a coarse grid solve. The method converges and, actually, we can even prove the convergence theoretically. The difficulty is that the regularization involves the (global) inverse Laplacian operator which makes the whole idea rather academic. Replacing the inverse Laplacian with an appropriate preconditioner [34] helps in terms of the efficiency but it still does not make the method competitive. Numerical experiments indicate that, as long as we couple the smoother with the coarse grid solve in a multiplicative way, the method will converge *without any regularization* but we cannot prove it yet. That leaves us with another open problem...

Waveguides. We refer to a parallel talk of Vardapetyan in this session on our recent results on full wave analysis for waveguides, using the *hp* edge elements. For a given frequency ω , the problem reduces to the solution of a generalized eigenvalue problem on the constants of propagation. For *nonhomogeneous* waveguides, the corresponding operator is non self-adjoint (even for the lossless case), and the propagation constant may be complex. In his dissertation, Vardapetyan proved that the problem is well-posed and, following the recent results on Maxwell eigenvalues, derived *h*-convergence error estimates [39, 37]. The theoretical analysis has been confirmed with numerical experiments. Finally, solutions of non-trivial examples illustrate the generality and the potential of the method.

Potential of the *hp* method. Implementational bells and whistles. The potential of the finite element method for Maxwell's equations is best visible for problems with non-homogeneous media. As long as the grid is aligned with material interfaces, contrary to other discretization techniques, the finite element method offers a general framework for constructing schemes of arbitrarily high order. The possibility to vary the order of approximation p and mesh size h makes the *hp* edge elements a very powerful method of discretization. A-posteriori error control allows to construct optimal meshes and guarantees the reliability of computations.

All these advantages do not come for free, however. *hp*-adaptive finite element codes are much more complicated than the standard codes and, at least in my opinion, have to be written from scratch, as the corresponding data structures differ considerably from those for the classical methods. In this note, I have tried to outline the main open problems and research issues that we face

in our work. I believe, that the most critical issue is to construct a robust iterative solver for the hp meshes that would considerably accelerate the computations and make possible the solution of large scale problems, also on small platforms. The element computations should be accelerated using recent advances in fast integration schemes and an optimal choice of shape functions [27]. It is worth to mention perhaps that, for affine elements and piecewise constant material data, the element matrices can be computed by rescaling corresponding contributions from the master element. In this context, the hp elements are competitive in terms of efficiency with implicit finite differences. Finally, the construction of fully explicit time integration schemes that could be combined with hp -discretization, remains an open research subject.

References

- [1] A. Bossavit, "Un nouveau point de vue sur les éléments finis mixtes", *Matapli* (bulletin de la Société de Mathématiques Appliquées et Industrielles), 23-35, 1989.
- [2] D. Boffi, "Discrete Compactness and Fortin Operator for Edge Elements", Preprint, March 1999.
- [3] D. Boffi, "A Note on the Discrete Compactness Property and the de Rham Diagram", Preprint, April 1999.
- [4] X.C. Cai, O. Widlund, "Domain Decomposition Algorithms for Indefinite Elliptic Problems", *SIAM J. Sci. Stat. Comput.*, 13, 243-258, 1992.
- [5] S. Caorsi, P. Fernandes, M. Raffetto, "On the Convergence of Galerkin Finite Element Approximations of Electromagnetic Eigenproblems", preprint 1999.
- [6] W. Cecot, L. Demkowicz, and W. Rachowicz, "A Two-Dimensional Infinite Element for Maxwell's Equations", *Computer Methods in Applied Mechanics and Engineering*, in print.
- [7] W. Cecot, L. Demkowicz, and W. Rachowicz, "A Three-Dimensional Infinite Element for Maxwell's Equations", *TICAM Report*, in preparation.
- [8] L. Demkowicz, "A Posteriori Error Analysis for Steady-State Maxwell's Equations", in *Advances in Adaptive Computational Methods in Mechanics*, eds. P. Ladaveze and J.T. Oden, Elsevier Science Ltd., 513-526, 1998.
- [9] L. Demkowicz, A. Bajer, W. Rachowicz, and K. Gerdes, "3D hp -Adaptive Finite Element Package. Fortran 90 Implementation (3Dhp90)", *TICAM Report 29*.
- [10] L. Demkowicz, Chang-Wan Kim, "An Implementation of the Implicit Element Residual Method for One-Irregular hp Meshes in Two Dimensions", *TICAM Report*, in preparation.
- [11] L. Demkowicz, K. Gerdes, C. Schwab, A. Bajer, and T. Walsh, "HP90: A General and Flexible Fortran 90 hp -FE Code", *Computing and Visualization in Science*, 1, 145-163, 1998.

- [12] L. Demkowicz and F. Ihlenburg, "Analysis of a Coupled Finite-Infinite Element Method for Exterior Helmholtz Problems", *TICAM Report 96-52*, in review in *Numerische Mathematik*.
- [13] L. Demkowicz, P. Monk, Ch. Schwab, and L. Vardapetyan "Maxwell Eigenvalues and Discrete Compactness in Two Dimensions" *TICAM Report 99-12*, accepted to *Mathematics and Computers with Applications*.
- [14] L. Demkowicz, P. Monk, L. Vardapetyan, and W. Rachowicz. "De Rham Diagram for hp Finite Element Spaces" *TICAM Report 99-06*, accepted to *Mathematics and Computers with Applications*.
- [15] L. Demkowicz and M. Pal, "An Infinite Element for Maxwell's Equations", *Computers Methods in Applied Mechanics and Engineering*, **164**, 77-94, 1998.
- [16] L. Demkowicz, L. Vardapetyan, "Modeling of Electromagnetic Absorption/Scattering Problems Using hp-Adaptive Finite Elements", *Computer Methods in Applied Mechanics and Engineering*, **152**, 1-2, 103-124, 1998.
- [17] L. Demkowicz, T. Walsh, K. Gerdes, and A. Bajer, "2D hp-Adaptive Finite Element Package. Fortran 90 Implementation", *TICAM Report 98-14*, July 1998.
- [18] K. Gerdes and L. Demkowicz, "Solution of 3D-Laplace and Helmholtz Equation in Exterior Domains Using hp Infinite Elements", *Computer Methods in Applied Mechanics and Engineering*, **137**, 239-274, 1996.
- [19] B. Guo, "The hp Version of the Finite Element Method for Solving Boundary Value Problems in Polyhedral Domains", in *Boundary Value Problems and Integral Equations in Nonsmooth Domains*, M. Costabel, M. Dauge & C. Nicaise ed., 101-120, Marcel Dekker Inc., 1994.
- [20] B. Guo, "The h-p Version of the Finite Element Method in R^3 : Theory and Algorithm", *Proceeding of ICOSAHOM'95*, A. Il'in & R. Scott ed., 487-500, 1995.
- [21] F. Ihlenburg and I. Babuška, "Dispersion Analysis and Error Estimation of Galerkin Finite Element Methods for the Helmholtz Equation", *Int. J. Numer. Methods Eng.*, **38**, 3745-3774, 1995.
- [22] F. Ihlenburg and I. Babuška, "Finite Element Solution to the Helmholtz Equation with High Wave Numbers - Part I: the h-Version of the FEM", *Computers & Mathematics with Applications*, **30**, 9, 9-37, 1995.
- [23] F. Ihlenburg and I. Babuška, "Finite Element Solution to the Helmholtz Equation with High Wave Numbers - Part II: the h-p-Version of the FEM", *SIAM J. Numer. Anal.*, **34**, 1, 315-358, 1997.
- [24] F. Ihlenburg, *Finite Element Analysis of Acoustic Scattering*, Springer-Verlag, New York, 1998
- [25] F. Kikuchi, "On a Discrete Compactness Property for the Nedelec Finite Elements", *J. Fac. Sci. Univ. Tokyo, Sect. IA, Math.*, **36**, 479-490, 1989.

- [26] J.M. Melenk, "On the Robust Exponential Convergence of *hp* Finite Element Methods for Problems with Boundary Layers", *IMA Journal of Numerical Analysis*, **17**, 577-601, 1997.
- [27] J.M. Melenk, K. Gerdes, Ch. Schwab, "Fully Discrete *hp* Finite Elements: Fast Quadrature", preprint 1999.
- [28] P. Monk, "On the *p*- and *hp*-extension of Nédélec's Curl-Conforming Elements", *Journal of Computational and Applied Mathematics*, **53**, 117-137, 1994.
- [29] P. Monk, L. Demkowicz, and L. Vardapetyan, "Discrete Compactness and the Approximation of Maxwell's Equations in \mathbb{R}^3 " *Mathematics of Computation*, accepted.
- [30] J.C. Nédélec, "Mixed Finite Elements in \mathbb{R}^3 ", *Numerische Mathematik*, **35**, 315-341, 1980.
- [31] J.T. Oden, L. Demkowicz, W. Rachowicz and T.A. Westermann, "Toward a Universal *hp* Adaptive Finite Element Strategy, Part 2. A Posteriori Error Estimation", *Computer Methods in Applied mechanics and Engineering*, **77**, 113-180, 1989.
- [32] W. Rachowicz and L. Demkowicz, "A Two-Dimensional *hp*-Adaptive Finite Element Package for Electromagnetics", *TICAM Report 98-15*, July 1998, *Computer Methods in Applied Mechanics and Engineering*, in print.
- [33] W. Rachowicz and L. Demkowicz, "A Three-Dimensional *hp*-Adaptive Finite Element Package for Electromagnetics", *TICAM Report*, in preparation.
- [34] W. Rachowicz, L. Demkowicz, A. Bajer, and T. Walsh, "A Two-Grid Iterative Solver for Stationary Maxwell's Equations", *Iterative Methods in Scientific Computation II* David R. Kincaid et al. (eds.), IMACS, 1999.
- [35] W. Rachowicz, L. Demkowicz, L. Vardapetyan, "hp-Adaptive FE Modeling for Maxwell's Equations. Evidence of Exponential Convergence" ACES' 99, Monterey, CA, March 16-20, 1999.
- [36] M. Salazar-Palma, T.K. Sarkar, L.E. Garcia-Castillo, T. Roy, and A. Djordjević, *Iterative and Self-Adaptive Finite Elements in Electromagnetic Modeling*, Artech House 1998.
- [37] L. Vardapetyan, "hp-Adaptive Finite Element Method for Electromagnetics with Applications to Waveguiding Structures", *Ph.D. Dissertation*, The University of Texas at Austin, Austin, TX 78712, December 1999.
- [38] L. Vardapetyan and L. Demkowicz, "hp-Adaptive Finite Elements in Electromagnetics", *Computers Methods in Applied Mechanics and Engineering*, **169**, 331-344, 1999.
- [39] L. Vardapetyan and L. Demkowicz, "Full-Wave Analysis of Dielectric Waveguides at a Given Frequency", *TICAM Report 99-22*.

Finite Element Method for Designing Plasma Reactors
Leo Kempel, Paul Rummel, Tim Grotjohn, and John Amrhein
Department of Electrical and Computer Engineering
Michigan State University

Abstract

The finite element method has proven to be versatile in the analysis of various electromagnetic phenomena. In this paper, we investigate the utility of the finite element method for guiding the design of plasma reactors. These reactors are used for processing integrated circuit substrates. The design of such reactors is based on the complex interactions between the electromagnetic fields and a plasma-filled region. The reactor geometry, the feed mechanism, and the current state of the plasma determine the electromagnetic fields. This paper investigates the details and difficulties of modeling plasmas within a closed cavity.

Introduction

The finite element-boundary integral method has been used in the electromagnetics analysis community for more than two decades, especially for electrostatics and magnetostatics analysis. Solution of dynamic problems, such as antenna characterization, radar cross section calculation, and closed cavity analysis, require the introduction of edge-based (also known as vector) finite elements. However, even with the use of vector finite elements, implementations of a hybrid finite element method were scarce and limited in their utility.

Hybrid finite element methods utilize a boundary integral to close the finite element mesh by providing the relationship between the tangential electric and magnetic fields on the surface of the mesh. The boundary integral explicitly couples each unknown (or edge) on the surface to all the other unknowns resulting in a fully-populated matrix. Hence, this hybrid finite element-boundary integral (FE-BI) method had limited utility in an era of Intel 386-based computers with up to 32 MB of RAM. Fortunately, for modeling plasma-loaded cavities, the feed coaxial aperture requiring a boundary integral is of limited extent and hence results in a relatively light memory demand. However, the relatively large volume of a plasma reactor results in a large number of unknowns to characterize the electric field within the cavity. This led to a intractable computational demand for average plasma reactor users even five years ago.

As computer resources have improved (today, one can purchase a dual processor computer with 1 GB of RAM for less than \$10,000) making what was once called a supercomputer available to average users. Significant effort has been spent over the past few years to make user-friendly computer programs that allow significant simulation capability with a minimal user effort. Specifically, computer program designers are utilizing triangular surface meshes and either right prism or tetrahedra meshes to solve rather complex electromagnetic design problems.

This paper presents the formulation, problem to be solved, and preliminary results for plasma reactor cavities.

Hybrid Finite Element-Boundary Integral Method

The FE-BI equations ([1],[2]) for a total electric field formulation may be written as

$$\int_V [\nabla \times \mathbf{W}_i \cdot \bar{\mu}_r^{-1} \cdot \nabla \times \mathbf{W}_j] dV - k_0^2 \int_V [\mathbf{W}_i \cdot \bar{\epsilon}_r \cdot \mathbf{W}_j] dV + jk_0 \int_{S_R} \left[\frac{(\hat{n}_R \times \mathbf{W}_i) \cdot (\hat{n}_R \times \mathbf{W}_j)}{R_e} \right] dS \\ - k_0^2 \int_{S_a} \int_{S_a} [\mathbf{W}_i \cdot \hat{z} \times \bar{\mathbf{G}}_{e2} \times \hat{z} \cdot \mathbf{W}_j] dS' dS = f_i^{\text{int}} + f_i^{\text{ext}}$$

where the first term is associated with the curl of the basis function (the magnetic field), the second term is associated with the basis function itself (the electric field), the third term is necessary to account for any resistive transition conditions present (e.g. to model thin dielectrics such as glue), and the last term on the left-hand side is the boundary integral term (involving a second kind electric field dyadic Green's function). As shown, the placement of the material parameters ($\bar{\epsilon}_r, \bar{\mu}_r$) suggests that the basis functions (\mathbf{W}_j) and test functions (\mathbf{W}_i) should be chosen so that the dot products with the material tensors are accomplished readily. The basis functions presented herein were chosen to accomplish this goal.

An additional observation is that the boundary integral term does not involve the material parameters. Accordingly, since the basis functions and test functions are functionally identical (e.g. Galerkin's testing procedure was used) and the dyadic Green's function is symmetric, $G_{e2}^{xy} = G_{e2}^{yx}$ and $\bar{\mathbf{G}}_{e2}(\mathbf{r}, \mathbf{r}') = \bar{\mathbf{G}}_{e2}(\mathbf{r}', \mathbf{r})$, then the boundary integral sub-matrix is symmetric. Therefore, it is not necessary to store either the lower or upper triangle of that matrix.

On the other hand, since it is desirable to allow for the possibility of anisotropic materials within the computational volume, the sparse finite element matrix should be stored without symmetry considerations. Accordingly, it is recommended that the finite element and boundary integral matrices be stored separately and hence that an iterative solver (e.g. BiCG, CG, GMRES) be used. The most significant source of computational cost in an iterative solver is the matrix-vector multiply. This operation can be accomplished with separate matrix storage by realizing

$$\begin{bmatrix} \mathbf{A}_{BB} + \mathbf{Y}_{BB} & \mathbf{A}_{BI} \\ \mathbf{A}_{IB} & \mathbf{A}_{II} \end{bmatrix} \begin{bmatrix} \mathbf{E}_B \\ \mathbf{E}_I \end{bmatrix} = \begin{bmatrix} \mathbf{A}_{BB} & \mathbf{A}_{BI} \\ \mathbf{A}_{IB} & \mathbf{A}_{II} \end{bmatrix} \begin{bmatrix} \mathbf{E}_B \\ \mathbf{E}_I \end{bmatrix} + \begin{bmatrix} \mathbf{Y}_{BB} & 0 \\ 0 & 0 \end{bmatrix} \begin{bmatrix} \mathbf{E}_B \\ \mathbf{E}_I \end{bmatrix}$$

where "A" matrices denote finite element interactions and the "Y" matrix indicates the boundary integral matrix. The subscript "B" denotes a boundary edge while "I" indicates an interior edge. This decomposition of the finite element and boundary integral matrices allows the computer program designer to use optimized matrix storage and multiplication schemes for each portion.

Another common aspect to these hybrid finite element computer programs is the need for a volumetric mesh. If tetrahedra are used for the volume mesh, a commercial mesh generating package such as SDRC IDEAS may be used. However, for many applications, an extruded mesh will work perfectly well without the need for additional investment. Extrusion is accomplished by forming elements for each layer of the mesh by replicating the nodal distribution of the top layer for all lower layers of the mesh. Hence, to form the first layer of elements, the top layer nodes are replicated at the interface of the first and second layer. Elements are formed from those nodes (and the previous layer's "bottom"

nodes) and edges are then formed based on the chosen finite element such as right prisms. Such meshes are fairly rigid and hence cannot represent the wide range of geometries that can be modeled using a free mesh (such as that produced by SDRC IDEAS); however, they are often sufficient and considerably simplifies the analysis procedures.

Vector edge-based expansion functions used for right prisms are developed by multiplying the traditional Rao-Wilton-Glisson (RWG) basis function [3] with a function of the prism height for the transverse (e.g. x- and y-component) functions. The normal functions are simply the node-based simplex basis function (see for example [4]) multiplied by \hat{z} . Hence, the transverse basis functions for edges on the top of the prism are given by

$$W_\chi = \left(\frac{z}{\Delta z} \right) S_k = \left(\frac{z}{\Delta z} \right) \frac{d_i}{2S^e} [(x - x_i)\hat{y} - (y - y_i)\hat{x}] \quad \chi = 1, 2, 3$$

where χ is the local edge number and i is the global edge number. Note that the local edge numbers are defined so that the edge is opposite the local node number as shown in Figure 1.

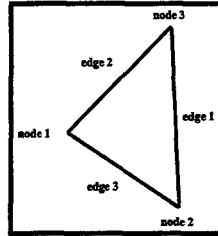


Figure 1. Illustration of local node and edge numbering for a triangle.

Transverse expansion functions on the bottom of the prism are given by:

$$M_\chi = \left(\frac{\Delta z - z}{\Delta z} \right) S_k = \left(\frac{\Delta z - z}{\Delta z} \right) \frac{d_i}{2S^e} [(x - x_i)\hat{y} - (y - y_i)\hat{x}] \quad \chi = 4, 5, 6$$

Finally, the normal (z-directed) expansion functions are given by:

$$K_\chi = \hat{z} \frac{(x_{k1}y_{k2} - x_{k2}y_{k1}) + (y_{k1} - y_{k2})x + (x_{k2} - x_{k1})y}{2S^e} \quad \chi = 7, 8, 9$$

where the indices $k1$ and $k2$ are given in the following table

χ	$k1$	$k2$
7	2	3
8	3	1
9	1	2

As stated previously, the choice of basis functions is dictated by the physical constraints of the geometry, the requirements for representation of a field, and convenience for implementation. The later

consideration is understood by considering a version of the basis functions given in Chapter 5 of [2]. In that presentation, the basis functions are represented in a *local coordinate system* rather than the *global* treatment given above. Although the solutions are identical, inclusion of anisotropic materials is more difficult if the basis functions are expressed in local coordinates since a transformation back to global coordinates is required to perform the necessary dot products. Hence, the form of the basis functions given above is more convenient for implementation than the form given in [2].

Plasma Reactors

Plasma reactors are closed cavities energized by high power microwaves to form the desired plasma that is used to perform a desired processing procedure [5]. Figure 2 illustrates Michigan State University's plasma reactor design.

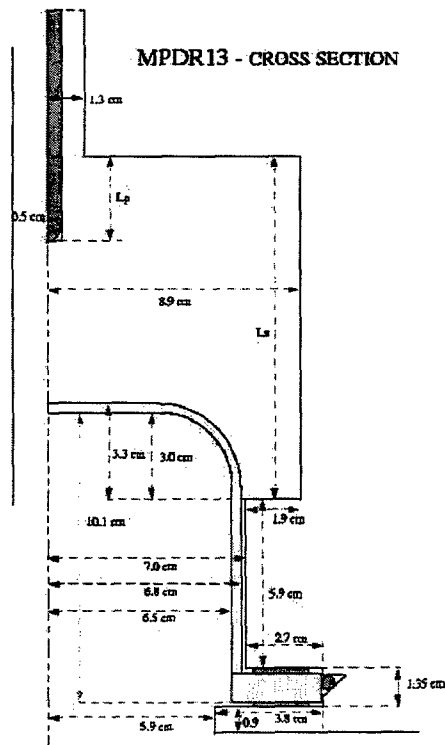


Figure 2. Plasma reactor design used at Michigan State University. (Compliments of Mark Perrin)

This reactor is constructed of brass with adjustable cavity height (L_s), adjustable probe length (L_p), and a quartz bell jar to contain the plasma formed by a high power microwave source tuned to 2.45 GHz.

The design challenge is to determine the cavity length and probe length so that the maximum energy is coupled to the plasma. The resonant frequency of the cavity is determined by the cavity dimensions as well as the material within the cavity. For our case, the cavity fill is comprised of air, quartz, and plasma. The finite element method is ideal for including this inhomogeneous material fill.

Plasma is formed by the excitation of the cavity by a high power microwave source. This plasma is very difficult to characterize due to the complex physics associated with plasmas as well as its non-stationary behavior. However, we assume that the time scale associated with the evolution of the plasma is much longer than the time it takes to form standing waves within the reactor. Hence, we can assume the reactor state is stationary and consider the plasma in its various excitation states separately.

For our investigation, we are assuming isotropic plasma whose dielectric parameters are given by

$$\epsilon_r = 1 + \frac{\omega_p^2}{-\omega^2 + j\omega\nu}$$

where the plasma frequency is given by $\omega_p = \sqrt{Ne^2/(m\epsilon_0)}$, N is the electron density, and ν is the collision frequency responsible for dampening. We note that for a conducting medium,

$$\epsilon_r = 1 - j\frac{\sigma}{\omega\epsilon_0}$$

which leads to the equivalent conductivity (σ) of

$$\frac{\sigma}{\epsilon_0} = \frac{\omega_p^2}{\nu + j\omega}$$

Note that unless $\omega \ll \nu$, the conductivity is a function of frequency.

Depending on the state of the plasma, it can have a dielectric constant that is greater than zero, less than zero, and even zero! This leads questions as to the conditioning of the finite element matrix as the plasma evolves into its various states. We will discuss our findings regarding modeling plasma at the meeting.

To test our cavity model, including the finite probe thickness, we simulated the TM_{012} fields within a closed cavity of the dimensions shown in Figure 2 where $L_s = 14.4$ cm. Figure 3 illustrates the change in resonance frequency as the probe length (L_p) is changed. Figure 4 illustrates the axial fields at the base of the cavity (where the plasma will form) at 2.474 GHz.

Closing Remarks

In this paper, we have presented the finite element method and an application of the method to the design of plasma reactors. The finite element method permits the simulation of a closed cavity with all of the important physics. The plasma reactor's structure, quartz bell jar, plasma load, and feed probe is

included in the model. An extruded right prism mesh is utilized to simplify the analysis task. Results for various configurations will be presented at the conference.

References

- [1] J.M. Jin and J.L. Volakis, "A hybrid finite element method for scattering and radiation by microstrip patch antennas and arrays residing in a cavity, *IEEE Trans. Antennas Propagat.*, **39**, pp. 1598-1604, Nov. 1991.
- [2] J.L. Volakis, A. Chatterjee, and L.C. Kempel, *Finite Element Method for Electromagnetics*, New York: *IEEE Press*, 1998.
- [3] S.M. Rao, D.R. Wilton, and A.W. Glisson, "Electromagnetic scattering by surfaces of arbitrary shape," *IEEE Trans. Antennas Propagat.*, **30**, pp. 409-418, May 1982.
- [4] O.C. Zienkiewicz and R.L. Taylor, *The Finite Element Method*, 4th Ed., New York: *McGraw-Hill*, 1989.
- [5] J. Asmussen, T.A. Grotjohn, P. Mak, and M.A. Perrin, "The design and application of electron cyclotron resonance discharges," *IEEE Trans. Plasma Sci.*, **25**, pp. 1196-1221, 1997.

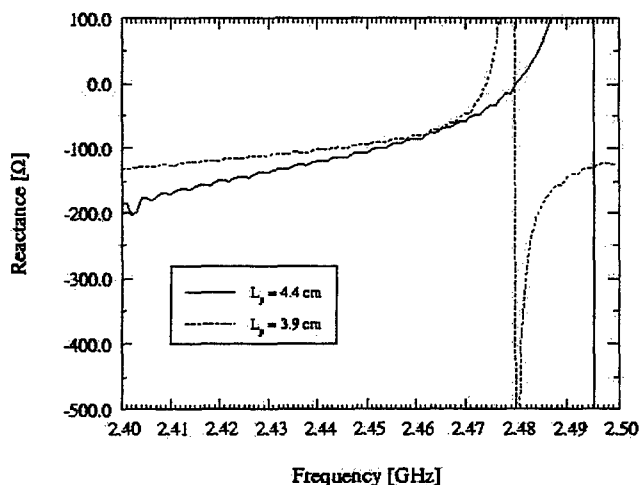


Figure 3. Input reactance for a circular cavity as a function of feed probe length.

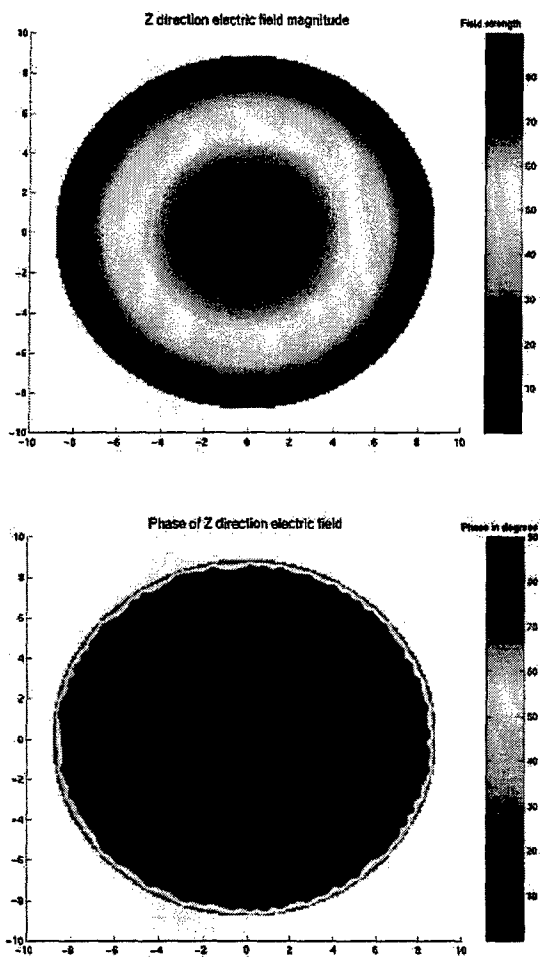


Figure 4. Magnitude and phase of the axial field at the base of the cavity.

Finite-Element Domain Decomposition Through an Iterative Algorithm: Coupling Between Cavity-Backed Slots *

Anastasis C. Polycarpou and Constantine A. Balanis

Tel: (480) 965-3909, Fax: (480) 965-8325, E-mail: balanis@asu.edu

Department of Electrical Engineering, Telecommunications Research Center
Arizona State University, Tempe, AZ 85287-7206

I. Introduction

Cavity-backed slot (CBS) antennas mounted on an infinite perfectly conducting ground plane have been analyzed in the past [1] using a hybrid finite element-moment method (FE-MM) approach which is also referred to as the finite element-boundary integral (FE-BI) method. Based on the FE-BI method, the interior of the cavity is discretized using finite elements (tetrahedrons, prisms, bricks, etc.) whereas the exterior region is treated using a spectral or spatial domain moment method. As a result, the overall system matrix consists of the finite element matrix $[A]$, which is highly sparse, and the admittance matrix $[Y]$, which is dense; the two matrices are coupled through the unknowns in the aperture.

The FE-BI method has enormous advantages over a pure FE method because the exterior region of the cavity is not discretized thereby saving memory storage and improving overall computational time. Computational savings are even more profound when calculating coupling parameters of multiple CBS antennas on an infinite ground plane. Although the FE-BI method is computationally more efficient than a pure FE method, the overall computational effort required to solve for coupling among multiple CBS antennas is not acceptable. The resulting FE matrix $[A]$ and the admittance matrix $[Y]$ are often large enough to solve for this problem effectively.

In this paper, a *new iterative* FE-BI approach in conjunction with domain decomposition is proposed in order to compute effectively coupling among multiple CBS antennas placed arbitrarily with respect to each other on a flat conducting surface. Each cavity is treated as an isolated FE-BI domain whereas interaction among these radiating elements is taken into account through an iteration algorithm. For simplicity, assume that there exist two cavity-backed slots spaced a given distance apart, as shown in Figure 1. For coupling computations, one antenna is excited with a constant voltage V_0 whereas the other one is left open circuit. The new algorithm is as follows: in the first iteration, the transmitting antenna radiates in space in the absence of the second antenna. The radiated field induces a field in the aperture of the second antenna which propagates through its cavity. The second antenna, in turn, scatters the incident field in all directions thus affecting the field distribution in the aperture of the radiating slot. This perturbation in the field of the radiating element changes its input impedance. The new field distribution is re-radiated toward the second antenna and the iteration process continues until convergence of the field in the two domains is achieved. Once convergence is reached, the self and mutual impedances can be computed in a straightforward manner.

*This work was sponsored by the Advanced Helicopter Electromagnetics Industrial Associates Program and NASA Grand NAG-1-1082.

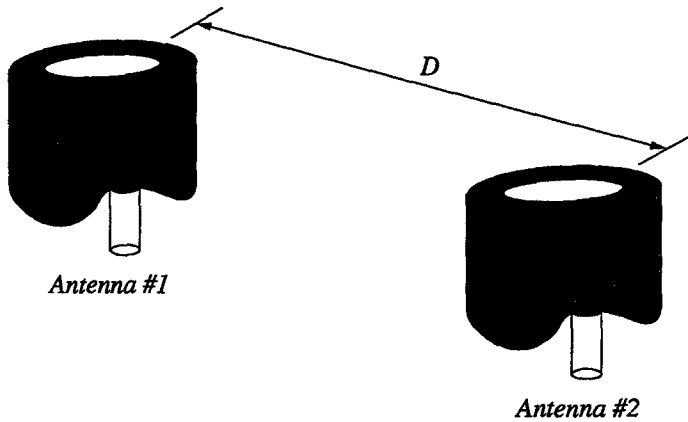


Figure 1: Geometry of two cavity-backed slot antennas mounted on an infinite ground plane.

This iterative algorithm becomes extremely useful when the two CBS antennas are identical; thus, reducing, as it will be shown later in this paper, memory requirements and CPU time. It also provides a mechanism to achieve full hybridization of the FE-BI method with other numerical techniques such as the GTD and PO. In this paper, the formulation of this iterative FE-BI method will be presented and applied to the problem of computing coupling parameters of two identical CBS antennas flushmounted on an infinite conducting ground plane. The results obtained using the proposed iterative algorithm will be compared with results obtained using the direct FE-BI approach. A comparison of CPU times and memory storage will also be provided.

II. Formulation

The problem under investigation is coupling among multiple CBS antennas flushmounted on a conducting ground plane. For simplicity, let us consider the problem of coupling between two CBS antennas similar to the ones shown in Figure 1. In order to compute the coupling parameters for such a configuration, one antenna is usually excited at the input terminal using a constant current I_1 whereas the input terminal of the second antenna is left as an open circuit. Radiation by the first antenna induces a voltage V_2 at the input terminal of the second antenna. Thus, the mutual impedance Z_{21} can be calculated using

$$Z_{21} = \frac{V_2}{I_1} \quad (1)$$

Similarly, the self impedance Z_{11} is equal to

$$Z_{11} = \frac{V_1}{I_1} \quad (2)$$

Due to reciprocity, $Z_{12} = Z_{21}$ and $Z_{22} = Z_{11}$. Knowing the complete set of Z-parameters, the corresponding S-parameters can be computed in a straightforward manner using standard transformation formulas [2].

Using the hybrid FE-BI approach to solve this coupling problem, the interior of the two cavities, including the apertures, is discretized using tetrahedral elements. The free space in between the two slots is not discretized but rather the interaction between the two slots is taken into account through an integral formulation using the respective half-space Green's function. This approach certainly provides an advantage over a pure FE method since the latter requires a brute-force discretization of free space. By renumbering the unknowns inside the finite element volume so that the unknowns in the aperture appear first, whereas the unknowns inside the cavity appear last, the corresponding matrix system for a single radiating antenna is given by

$$\begin{bmatrix} M^{a/a} & M^{a/c} \\ M^{c/a} & M^{c/c} \end{bmatrix} \begin{bmatrix} E^a \\ E^c \end{bmatrix} = \begin{bmatrix} 0 \\ b^c \end{bmatrix} \quad (3)$$

where the superscript a represents the aperture while c identifies the cavity. The non-zero excitation vector b^c is part of the finite element volume inside the cavity. In addition, the matrix $M^{a/a}$ is a pure method of moments matrix and is dense; $M^{c/c}$ is a pure finite element matrix and is highly sparse; the other two matrices $M^{a/c}$ and $M^{c/a}$ provide coupling between the field inside the cavity and the field in the aperture. Now, in case there are two cavity-backed slots in close proximity, the combined matrix system, after renumbering the unknowns, is given by

$$\begin{bmatrix} M_1^{a/a} & M_1^{a/c} & T_{12}^{a/a} & 0 \\ M_1^{c/a} & M_1^{c/c} & 0 & 0 \\ T_{21}^{a/a} & 0 & M_2^{a/a} & M_2^{a/c} \\ 0 & 0 & M_2^{c/a} & M_2^{c/c} \end{bmatrix} \begin{bmatrix} E_1^a \\ E_1^c \\ E_2^a \\ E_2^c \end{bmatrix} = \begin{bmatrix} 0 \\ b_1^c \\ 0 \\ 0 \end{bmatrix} \quad (4)$$

The subscript 1 denotes *antenna #1* and 2 denotes *antenna #2*. Note that for coupling calculations, when *antenna #1* is excited, *antenna #2* is left open circuit and vice versa. Thus, the right-hand side vector of the matrix system for *antenna #2* is zero. The above matrix system can be written in a more compact and convenient form as follows:

$$\begin{bmatrix} M_1 & T_{12} \\ T_{21} & M_2 \end{bmatrix} \begin{bmatrix} E_1 \\ E_2 \end{bmatrix} = \begin{bmatrix} b_1 \\ 0 \end{bmatrix} \quad (5)$$

Matrix M_1 is the self matrix of *antenna #1*, M_2 is the self matrix of *antenna #2*, T_{12} and T_{21} are the interaction matrices between slots 1 and 2, and b_1 is the right-hand side vector corresponding to the excitation of *antenna #1*. It is important to mention here that the matrices T_{12} and T_{21} are transpose of each other, thus only one of them is stored in memory. In case the two cavities/slots are identical, and therefore their mesh information is also identical, these two matrices are square and symmetric which means only half of the matrix needs to be stored in memory.

As seen from the matrix system in (5), the electric fields E_1 and E_2 are coupled only through the dense interaction matrices T_{12} and T_{21} . If those interaction matrices were to be zero, matrices M_1 and M_2 would be completely decoupled, therefore, allowing us to solve for E_1 and E_2 independently and more efficiently. However, since these matrices are obviously not zero, we need to take into account the interaction between the two slots.

The matrix system in (5) can be efficiently solved through an iteration algorithm. The iteration starts by setting the field E_2 to zero. This implies that *antenna #1* radiates in space as if *antenna #2* was not present. In other words, for iteration $k = 0$

$$E_2^{(0)} = 0 \quad (6)$$

and, therefore, we can write that

$$M_1 \cdot E_1^{(0)} + T_{12} \cdot E_2^{(0)} = b_1 \quad (7)$$

$$M_1 \cdot E_1^{(0)} = b_1 - T_{12} \cdot E_2^{(0)} \quad (8)$$

$$M_1 \cdot E_1^{(0)} = b_1 - 0 \quad (9)$$

where the superscript (0) indicates iteration $k = 0$. Thus, once the matrix system in (9) is solved, we obtain $E_1^{(0)}$, which corresponds to the governing field distribution of *antenna #1* in the absence of *antenna #2*. Then, from (5), it can be shown that

$$M_2 \cdot E_2^{(1)} = 0 - T_{21} \cdot E_1^{(0)} \quad (10)$$

where the product of $T_{21} \cdot E_1^{(0)}$ requires $N_1^2 \times N_2^2$ operations (multiplications plus additions); N_1^2 is the number of unknowns in the aperture of *antenna #1* and N_2^2 is the number of unknowns in the aperture of *antenna #2*. Once the value of E_2 is updated, the iteration algorithm may continue on by updating E_1 using

$$M_1 \cdot E_1^{(1)} = b_1 - T_{12} \cdot E_2^{(1)} \quad (11)$$

The updating of the vectors E_1 and E_2 will continue until an acceptable convergence tolerance is obtained. A measure of convergence can be defined based on the 2-norm residual given by

$$\rho_1 = \|E_1^{(k)} - E_1^{(k-1)}\|_2 \quad (12)$$

$$\rho_2 = \|E_2^{(k)} - E_2^{(k-1)}\|_2 \quad (13)$$

When both ρ_1 and ρ_2 are less than a given tolerance, it means that convergence has been achieved.

This hybrid method, which takes into account coupling between antennas through an iterative algorithm, is even more attractive when needed to compute coupling parameters of two identical antennas as a function of distance. For two identical CBS antennas, only one geometry needs to be discretized since $M_1 = M_2 = M$. Also, $T_{12} = T_{21} = T$ which, in this case, is a square symmetric matrix. Thus, when coupling versus distance is calculated, the system matrix M does not change as a function of distance; the only matrix that changes versus distance is the interaction matrix T , which is relatively small ($N_a \times N_a$) and calculated using a spatial or spectral domain method of moments. As a result of this observation, the matrix M needs to be inverted only once, possibly using a sparse LU decomposition, whereas the updating of the fields E_1 and E_2 is done relatively fast using a simple backward substitution. Even when the relative distance between the two antennas is varied, the matrix M does not need to be inverted again. Consequently, the coupling parameters as a function of distance may be computed with only minimum computational effort which corresponds to the CPU time needed by the sparse LU algorithm to factorize the matrix M . In addition, the memory requirements for storing the system matrix and other information are reduced considerably, compared to a brute-force discretization of the original problem which consists of two cavity-backed slots.

III. Results

In the previous section, the idea of field interaction between two distant cavity-backed slots through an iterative hybrid approach has been introduced and formulated. Initially, each cavity-backed slot is treated separately using the FE-BI approach, whereas EM interaction between the two slots is accounted for at subsequent iterations to correct the field distribution obtained from a previous iteration step. This approach is innovating and potentially powerful because it allows field interaction not only between two FEM domains, or an FEM and a MM domain, but also between FEM and GTD or FEM and PO.

As a first step, this idea is applied to the problem of coupling between two identical CBS antennas mounted on an infinite ground plane, as is shown in Figure 2. The two cavity-backed slots are placed a distance D apart whereas the transverse dimensions of each slot correspond to those of an X-band waveguide. The depth of the cavity is 7.7559 cm and the probe is located in the center of the horizontal dimension at a distance of 1.905 cm from the bottom face. The length of the probe is 0.6985 cm.

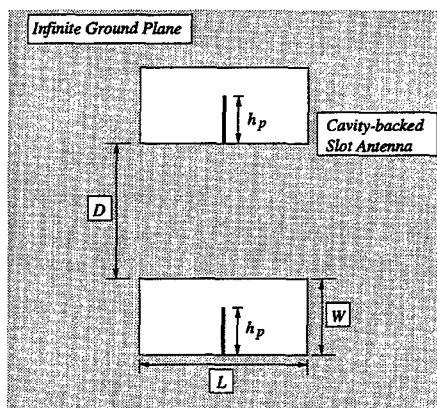


Figure 2: E-plane configuration of two identical cavity-backed slot antennas mounted on an infinite ground plane ($L = 2.286$ cm, $W = 1.016$ cm, $h_p = 0.6985$ cm).

The most obvious approach to solve for the coupling parameters of the two slots is to perform a brute-force discretization in both cavities and apply the direct hybrid FE-BI approach. The interaction between the two slots is implicitly taken into account in the hybrid formulation. This approach has the disadvantage of creating twice as many unknowns, compared to the proposed iterative method, therefore requiring excessive memory storage and a long CPU time to solve the final matrix system. Besides, the matrix system needs to be re-solved every time the separation distance D between the slots is changed. In contrast, using the iterative approach, only one cavity needs to be discretized, thus saving memory storage and generating a smaller matrix system, which can be solved faster and more efficiently. Also, every time the separation distance is changed, the new field distribution can be conveniently computed using a simple back-substitution since the original self matrix is not a function of separation distance. This back-substitution can be performed provided the sparse LU factorization of the original matrix was obtained at the first iteration step. More substantial computational savings, both in terms of memory and CPU time, can be obtained when coupling among more than two CBS antennas is computed.

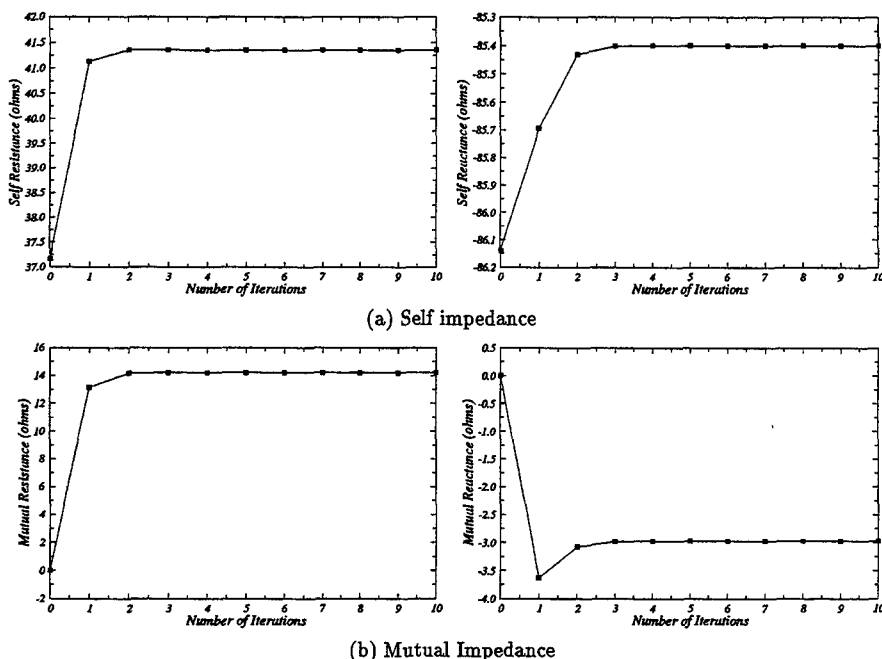


Figure 3: Real and imaginary parts of the self and mutual impedance as a function of iteration number. The two slots are placed in an E-plane configuration with separation distance of 1 cm. The frequency of operation is 8 GHz.

Using the iterative approach to calculate coupling, the two antennas are simply treated separately whereas the field interaction between the slots is accounted for through an iteration procedure. It is not clear, however, how many iterations it takes for the field distribution in the two domains to actually converge. The first experiment performed in this study was to calculate the real and imaginary parts of the self and mutual impedances as a function of iteration number k at a frequency of 8 GHz and a separation distance of 1 cm along the E-plane. These results are illustrated in Figure 3. In both these figures, it is clear that the self and mutual impedances converge to a final value at $k = 3$. For $k = 0$, which basically means that there is no interaction between the two antennas, the real part of the self impedance was found to be 37.2 ohms whereas the imaginary part was -86.15 ohms; the converged values, however, at $k = 3$ are 41.3 and -85.4 ohms, respectively. For a smaller separation distance D , the discrepancy between first and second iterations is even larger. Similar observations are made for the mutual impedance, too. For $k = 0$, the mutual impedance is zero since the interaction between the two slots has not yet been accounted for. As the iteration number increases, both real and imaginary parts of the mutual impedance converge to a final value.

This iterative technique was applied to the same antenna configuration, however with slot separation $D = 2$ cm, to calculate the Z-matrix as a function of frequency. From the Z-matrix, one may obtain

the S-matrix by using a simple transformation. The return loss and mutual coupling as a function of frequency are depicted in Figure 4 for a separation distance of 2 cm along the E-plane. The iteration technique is compared with the hybrid FE-BI direct approach which was found to be quite accurate [3]. As illustrated, the agreement between the two methods is excellent. Even after one iteration the mutual coupling as a function of frequency compares very well. However, since the computational effort required for subsequent iterations is minimal, we often choose to compute the coupling parameters after a total of 5 iterations.

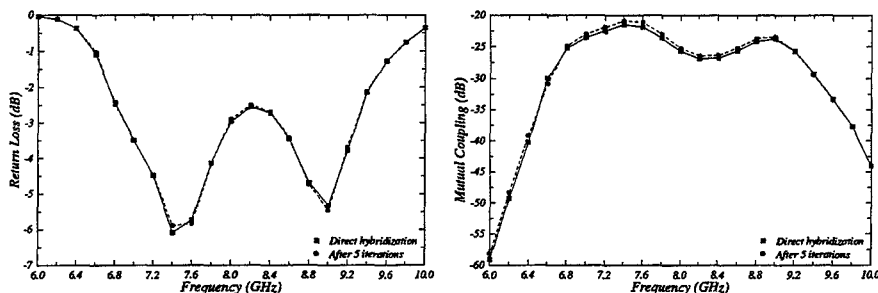


Figure 4: Return loss and mutual coupling as a function of frequency. The two slots are placed in an E-plane configuration with separation distance $D = 2$ cm.

The most noticeable computational savings in terms of CPU time are realized when computing coupling parameters as a function of distance. The reason for achieving such computational speed-up is because the system matrix is factorized (using sparse LU) only once. As the separation distance is varied, the updated field distribution inside the cavities and slots is computed by using only a simple back-substitution which involves order of N operations, where N is the number of unknowns for the self matrix.

The mutual coupling (S_{12}) as a function of distance is compared with the direct FE-BI approach in Figure 5. The two slots are oriented along the E-plane with separation distance varying between 30 and 160 mm. As illustrated, both methods (iterative FE-BI and direct FE-BI) give almost identical results. As far as the iterative technique is concerned, the difference in the predictions when using only 1 iteration versus when using 5 iterations is more noticeable for relatively small separation distances.

For the case of computing coupling as a function of distance, it is important that the computational requirements of the direct and iterative techniques be discussed. The number of tetrahedrons used in the direct FE-BI approach was 39,046 and the number of unknowns was 41,120. For the iterative FE-BI approach, assuming the same element mesh size, the number of tetrahedrons used in the computational domain was 19,543 and the total number of unknowns was 20,583. Solving the matrix system for the direct FE-BI approach, a Conjugate Gradient Square (CGS) algorithm was used. The total CPU time spent to compute the mutual coupling between the two slots for a total of 14 points, as shown in Figure 5, was 288 minutes. For the iterative FE-BI approach, we had the choice of either using a sparse LU decomposition to first factorize the matrix and then use back-substitutions for the remaining iteration process, or using the CGS algorithm in every iteration. Both options were followed. When the sparse LU decomposition was used, it took 134 minutes to obtain the matrix factorization; all remaining computations were performed with only a fraction of time (1-2 minutes, assuming 1 iteration per point). When the CGS was used, again assuming only 1 iteration per point, the total CPU time

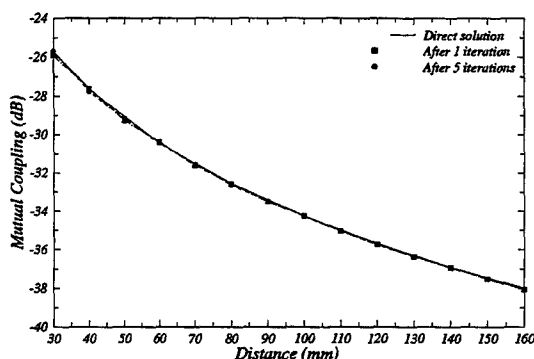


Figure 5: Mutual coupling as a function of distance. The two slots are placed in an E-plane configuration and the frequency of operation is 8 GHz.

for 14 evaluation points was 83 minutes. However, as the number of iterations increases, the CPU time increases accordingly. For example, if 5 iterations are used, the total CPU time increases to 265 minutes.

IV. Conclusions

A novel iterative algorithm in conjunction with domain decomposition and the FE-BI method was introduced in this paper to efficiently compute coupling between two or more CBS antennas mounted on an infinite ground plane. Each cavity is independently analyzed using the hybrid FE-BI approach, whereas the field interaction between the slots is taken into account through an iteration algorithm. This results in substantial computational savings both in terms of memory storage and CPU time. It was observed that this algorithm converges within only a few iterations. The results compare favorably with the hybrid FE-BI direct approach.

References

- [1] A. C. Polycarpou, C. A. Balanis, J. T. Aberle, and C. Birtcher, "Radiation and scattering from ferrite-tuned cavity-backed slot antennas: Theory and experiment," *IEEE Trans. Antennas Propagat.*, vol. 46, no. 9, pp. 1297-1306, Sep. 1998.
- [2] D. M. Pozar, *Microwave Engineering*. Massachusetts: Addison-Wesley Publishing Company, Inc., 1990.
- [3] C. A. Balanis, A. C. Polycarpou, C. R. Birtcher, S. Georgakopoulos, D.-H. Han, and G. Ballas, "Advanced electromagnetic methods for helicopter applications," Tech. Rep. TRC-EM-CAB-9903, Telecommunications Research Center, Arizona State University, Oct. 1999.

Investigation of the Bunting/Davis Functional when used with Vector Finite Elements for Waveguide Analysis

*Andrew F. Peterson and Sharib Wasi
School of Electrical and Computer Engineering
Georgia Institute of Technology
Atlanta, GA 30332-0250
peterson@ee.gatech.edu*

Introduction

In a recent paper [1], Bunting and Davis proposed a new functional for finite element analysis that reportedly eliminates spurious solutions of Maxwell's equations. Although [1] presented an implementation involving node-based scalar finite elements, it is well-known that node-based elements are problematical when used to represent vector fields at material discontinuities and complicate the satisfaction of boundary conditions at boundaries that do not align with a Cartesian axis. Since the functional in [1] involves the fields and their curls, it appears that these drawbacks could be alleviated through the use of an edge-based curl-conforming vector finite element representation such as that described in [2]. This paper details a vector finite element approach based on the Bunting/Davis equations, in order to assess the utility of the approach.

The motivation for pursuing alternative formulations such as [1] must ultimately be to improve the trade-off between accuracy and efficiency. For specificity, we focus on the problem of a heterogeneous waveguide, and the task of determining the propagation constant β of a waveguide mode versus frequency. A number of approaches involving scalar or vector representations have been proposed for this problem, and as a baseline for comparison purposes we select a minor variation on the approach of Lee, Sun, and Cendes [3]. The formulation of [3] involves a single unknown field (three vector components) within the waveguide, and uses vector finite elements to represent the transverse (x-y) part of the field and scalar finite elements to represent the longitudinal (z) component of the field. Coupled weak differential equations for this problem lead to a matrix eigenvalue equation of the form

$$\mathbf{Q}\mathbf{u} = \beta^2 \mathbf{R}\mathbf{u} \quad (1)$$

The full details of the formulation leading to this equation may be found in [3] or [4]. The unknown fields appearing in equation (1) have been scaled to produce a real-valued matrix when the medium is lossless and to eliminate terms involving the first power of β . Consequently, (1) has the form of a generalized matrix eigenvalue equation that can be solved by standard procedures (eg., EISPACK, LAPACK, simultaneous iteration) for the eigenvalue β^2 . The matrix order in (1) is equal to the sum of the transverse unknowns

and the longitudinal unknowns, and the equation exhibits a nullspace equal to the number of longitudinal unknowns (which typically accounts for at least 25% of the eigenvalues).

Formulation

The formulation of [1] is a special case of a coupled system of weak equations constructed from Maxwell's equations

$$-j\omega\epsilon_0 \nabla \times \bar{\mathbf{E}} + \omega^2 \mu_0 \epsilon_0 \mu_r \bar{\mathbf{H}} = 0 \quad (2)$$

$$j\omega\mu_0 \nabla \times \bar{\mathbf{H}} + \omega^2 \mu_0 \epsilon_0 \epsilon_r \bar{\mathbf{E}} = 0 \quad (3)$$

and their curls:

$$\nabla \times \left(\frac{1}{\mu_r} \nabla \times \bar{\mathbf{E}} \right) + j\omega\mu_0 \nabla \times \bar{\mathbf{H}} = 0 \quad (4)$$

$$\nabla \times \left(\frac{1}{\epsilon_r} \nabla \times \bar{\mathbf{H}} \right) - j\omega\epsilon_0 \nabla \times \bar{\mathbf{E}} = 0 \quad (5)$$

From a linear combination of equations (3) and (4) and a linear combination of equations (2) and (5) we obtain

$$C_1 \nabla \times \left(\frac{1}{\mu_r} \nabla \times \bar{\mathbf{E}} \right) + C_2 \omega^2 \mu_0 \epsilon_0 \epsilon_r \bar{\mathbf{E}} + j\omega\mu_0 (C_1 + C_2) \nabla \times \bar{\mathbf{H}} = 0 \quad (6)$$

$$C_3 \nabla \times \left(\frac{1}{\epsilon_r} \nabla \times \bar{\mathbf{H}} \right) + C_4 \omega^2 \mu_0 \epsilon_0 \mu_r \bar{\mathbf{H}} - j\omega\epsilon_0 (C_3 + C_4) \nabla \times \bar{\mathbf{E}} = 0 \quad (7)$$

where arbitrary constants C_1 , C_2 , C_3 , and C_4 have been introduced. The vector Helmholtz equations can be obtained by choosing $C_1 = -C_2$ and $C_3 = -C_4$, but here the idea is to include the other factors which provide additional constraints on the field solution.

For the waveguide problem identified above, we seek a solution of the form

$$\bar{\mathbf{E}}(x, y, z) = \{\hat{t} \bar{\mathbf{E}}_t(x, y) + \hat{z} \bar{\mathbf{E}}_z(x, y)\} e^{-j\beta z} \quad (8)$$

$$\bar{\mathbf{H}}(x, y, z) = \{\hat{t} \bar{\mathbf{H}}_t(x, y) + \hat{z} \bar{\mathbf{H}}_z(x, y)\} e^{-j\beta z} \quad (9)$$

After substituting (8) and (9) into equations (6) and (7), we obtain the vector equations

$$\begin{aligned} C_1 \nabla_t \times \left\{ \frac{1}{\mu_r} \nabla_t \times \bar{\mathbf{E}}_t \right\} - C_1 \frac{1}{\mu_r} (j\beta \nabla_t \bar{\mathbf{E}}_z - \beta^2 \bar{\mathbf{E}}_t) + C_2 \omega^2 \mu_0 \epsilon_0 \epsilon_r \bar{\mathbf{E}}_t \\ - j\omega\mu_0 (C_1 + C_2) \hat{z} \times (j\beta \bar{\mathbf{H}}_t + \nabla_t \bar{\mathbf{H}}_z) = 0 \end{aligned} \quad (10)$$

$$C_3 \nabla_t \times \left\{ \frac{1}{\epsilon_t} \nabla_t \times \bar{H}_t \right\} - C_3 \frac{1}{\epsilon_t} (j\beta \nabla_t H_z - \beta^2 \bar{H}_t) + C_4 \omega^2 \mu_0 \epsilon_0 \mu_t \bar{H}_t \\ + j\omega \epsilon_0 (C_3 + C_4) \hat{z} \times (j\beta \bar{E}_t + \nabla_t E_z) = 0 \quad (11)$$

and the scalar equations

$$C_1 \nabla_t \cdot \left\{ \frac{1}{\mu_t} (\nabla_t E_z + j\beta \bar{E}_t) \right\} - C_2 \omega^2 \mu_0 \epsilon_0 \epsilon_t E_z \\ - j\omega \mu_0 (C_1 + C_2) \hat{z} \cdot \nabla_t \times \bar{H}_t = 0 \quad (12)$$

$$C_3 \nabla_t \cdot \left\{ \frac{1}{\epsilon_t} (\nabla_t H_z + j\beta \bar{H}_t) \right\} - C_4 \omega^2 \mu_0 \epsilon_0 \mu_t H_z \\ + j\omega \epsilon_0 (C_3 + C_4) \hat{z} \cdot \nabla_t \times \bar{E}_t = 0 \quad (13)$$

where ∇_t is used to denote the transverse part of the appropriate operator. This system of four coupled equations can be converted into weak form by introducing scalar and vector testing functions, integrating over the computational domain Γ , and performing suitable manipulations to shift certain derivatives onto the testing functions. The result is the coupled system

$$\iint_{\Gamma} C_1 \frac{1}{\mu_t} \nabla_t \bar{T} \cdot \nabla_t \bar{E}_t + C_2 \omega^2 \mu_0 \epsilon_0 \epsilon_t \bar{T} \cdot \bar{E}_t - (C_1 + C_2) \omega \mu_0 \bar{T} \cdot \hat{z} \times \nabla_t h_z \\ - \beta \iint_{\Gamma} C_1 \frac{1}{\mu_t} \bar{T} \cdot \nabla_t e_z - (C_1 + C_2) \omega \mu_0 \bar{T} \cdot \hat{z} \times \bar{H}_t \\ + \beta^2 \iint_{\Gamma} C_1 \frac{1}{\mu_t} \bar{T} \cdot \bar{E}_t = 0 \quad (14)$$

$$\iint_{\Gamma} C_1 \frac{1}{\mu_t} \nabla_t T \cdot \nabla_t e_z + C_2 \omega^2 \mu_0 \epsilon_0 \epsilon_t T e_z - (C_1 + C_2) \omega \mu_0 T \hat{z} \cdot \nabla_t \times \bar{H}_t \\ - \beta \iint_{\Gamma} C_1 \frac{1}{\mu_t} \nabla_t T \cdot \bar{E}_t = 0 \quad (15)$$

$$\iint_{\Gamma} C_3 \frac{1}{\epsilon_t} \nabla_t \bar{T} \cdot \nabla_t \bar{H}_t + C_4 \omega^2 \mu_0 \epsilon_0 \mu_t \bar{T} \cdot \bar{H}_t + (C_3 + C_4) \omega \epsilon_0 \bar{T} \cdot \hat{z} \times \nabla_t e_z \\ - \beta \iint_{\Gamma} C_3 \frac{1}{\epsilon_t} \bar{T} \cdot \nabla_t h_z + (C_3 + C_4) \omega \epsilon_0 \bar{T} \cdot \hat{z} \times \bar{E}_t \\ + \beta^2 \iint_{\Gamma} C_3 \frac{1}{\epsilon_t} \bar{T} \cdot \bar{H}_t = 0 \quad (16)$$

$$\begin{aligned} \iint_{\Gamma} C_3 \frac{1}{\epsilon_r} \nabla_t T \cdot \nabla_t h_z + C_4 \omega^2 \mu_0 \epsilon_0 \mu_r T h_z + (C_3 + C_4) \omega \epsilon_0 T \hat{z} \cdot \nabla_t \times \bar{E}_t \\ - \beta \iint_{\Gamma} C_3 \frac{1}{\epsilon_r} \nabla_t T \cdot \bar{H}_t = 0 \end{aligned} \quad (17)$$

where $e_z = jE_z$ and $h_z = jH_z$. Boundary integrals arising in the above have been omitted since all boundaries under consideration are perfect conductors. We believe (14)–(17) are weak equations corresponding to the Bunting/Davis functional in [1]. However, note the appearance of β^0 , β^1 , and β^2 in the equations. An alternate scaling using $e_z = j\beta E_z$, $h_z = jH_z$, and $h_t = \beta H_t$ produces the system

$$\begin{aligned} \iint_{\Gamma} C_1 \frac{1}{\mu_r} \nabla_t \times \bar{T} \cdot \nabla_t \times \bar{E}_t + C_2 \omega^2 \mu_0 \epsilon_0 \epsilon_r \bar{T} \cdot \bar{E}_t - (C_1 + C_2) \omega \mu_0 \bar{T} \cdot \hat{z} \times \nabla_t h_z \\ + \iint_{\Gamma} -C_1 \frac{1}{\mu_r} \bar{T} \cdot \nabla_t e_z + (C_1 + C_2) \omega \mu_0 \bar{T} \cdot \hat{z} \times \bar{h}_t \\ + \beta^2 \iint_{\Gamma} C_1 \frac{1}{\mu_r} \bar{T} \cdot \bar{E}_t = 0 \end{aligned} \quad (18)$$

$$\begin{aligned} \iint_{\Gamma} C_1 \frac{1}{\mu_r} \nabla_t T \cdot \nabla_t e_z + C_2 \omega^2 \mu_0 \epsilon_0 \epsilon_r T e_z - (C_1 + C_2) \omega \mu_0 T \hat{z} \cdot \nabla_t \times \bar{h}_t \\ - \beta^2 \iint_{\Gamma} C_1 \frac{1}{\mu_r} \nabla_t T \cdot \bar{E}_t = 0 \end{aligned} \quad (19)$$

$$\begin{aligned} \iint_{\Gamma} C_3 \frac{1}{\epsilon_r} \nabla_t \times \bar{T} \cdot \nabla_t \times \bar{h}_t + C_4 \omega^2 \mu_0 \epsilon_0 \mu_r \bar{T} \cdot \bar{h}_t + (C_3 + C_4) \omega \epsilon_0 \bar{T} \cdot \hat{z} \times \nabla_t e_z \\ - \beta^2 \iint_{\Gamma} C_3 \frac{1}{\epsilon_r} \bar{T} \cdot \nabla_t h_z + (C_3 + C_4) \omega \epsilon_0 \bar{T} \cdot \hat{z} \times \bar{E}_t \\ + \beta^2 \iint_{\Gamma} C_3 \frac{1}{\epsilon_r} \bar{T} \cdot \bar{h}_t = 0 \end{aligned} \quad (20)$$

$$\begin{aligned} \iint_{\Gamma} C_3 \frac{1}{\epsilon_r} \nabla_t T \cdot \nabla_t h_z + C_4 \omega^2 \mu_0 \epsilon_0 \mu_r T h_z + (C_3 + C_4) \omega \epsilon_0 T \hat{z} \cdot \nabla_t \times \bar{E}_t \\ - \iint_{\Gamma} C_3 \frac{1}{\epsilon_r} \nabla_t T \cdot \bar{h}_t = 0 \end{aligned} \quad (21)$$

Discretization

We now consider a triangular-cell discretization of the waveguide cross section, in which cells are assumed to have uniform permittivity and permeability, and embedded conductors are excluded from the computational domain. In this formulation there is no need to restrict the material parameters; in particular ϵ_r and μ_r can change at the same material interface without difficulty. The transverse components of electric and magnetic field are to be represented by curl-conforming vector basis functions (eg., the Whitney

elements), while the longitudinal components are to be represented by first-order scalar Lagrangian functions. Similar representations are used for the testing functions.

The result is a matrix eigensystem with the form of equation (1), where matrices \mathbf{Q} and \mathbf{R} have the structure

$$\mathbf{Q} = \begin{bmatrix} C_1 \mathbf{A}_\mu + C_2 \mathbf{B}_\varepsilon & -C_1 \mathbf{C}_\mu & (C_1 + C_2) \mathbf{D}_\mu & -(C_1 + C_2) \mathbf{E}_\mu \\ 0 & C_1 \mathbf{G}_\mu + C_2 \mathbf{H}_\varepsilon & -(C_1 + C_2) \mathbf{I}_\mu & 0 \\ 0 & (C_3 + C_4) \mathbf{E}_\varepsilon & C_3 \mathbf{A}_\varepsilon + C_4 \mathbf{B}_\mu & 0 \\ (C_3 + C_4) \mathbf{I}_\varepsilon & 0 & -C_3 \mathbf{J}_\varepsilon & C_3 \mathbf{G}_\varepsilon + C_4 \mathbf{H}_\mu \end{bmatrix} \quad (22)$$

$$\mathbf{R} = \begin{bmatrix} -C_1 \mathbf{F}_\mu & 0 & 0 & 0 \\ C_1 \mathbf{J}_\mu & 0 & 0 & 0 \\ (C_3 + C_4) \mathbf{D}_\varepsilon & 0 & -C_3 \mathbf{F}_\varepsilon & C_3 \mathbf{C}_\varepsilon \\ 0 & 0 & 0 & 0 \end{bmatrix} \quad (23)$$

and

$$\mathbf{u} = \begin{bmatrix} \mathbf{E}_t \\ e_z \\ \mathbf{h}_t \\ \mathbf{h}_z \end{bmatrix} \quad (24)$$

It is obvious that the matrix \mathbf{R} is singular, and the block row and column of zeros suggests that this eigenvalue equation also exhibits a nullspace (in contrast to what is implied in [1]). Despite the singular nature of \mathbf{R} , this equation is amenable to solution by one of the standard approaches or by a customized iterative scheme based on the shifted inverse power method [5-6].

Results to be presented

The preceding formulation extends the approach of [1] to the realm of vector finite elements. In the presentation, numerical results will be used to assess the relative accuracy of the preceding approach compared to the method of references [3-4], using the identical expansion functions and identical triangular-cell models of various waveguide cross sections. The trade-off between computational effort and accuracy will be investigated. In addition, the presence of a nullspace will be verified, and the impact of the parameters C_1 , C_2 , etc. will be explored.

References

- [1] C. F. Bunting and W. A. Davis, "A functional for dynamic finite-element solutions in electromagnetics," *IEEE Trans. Antennas Propagat.*, vol. 47, pp. 149-156, January 1999.
- [2] R. D. Graglia, D. R. Wilton, and A. F. Peterson, "Higher-order interpolatory vector bases for computational electromagnetics," *IEEE Trans. Antennas Propagat.*, vol. 45, pp. 329-342, March 1997.
- [3] J. F. Lee, D. K. Sun, and Z. J. Cendes, "Full wave analysis of dielectric waveguides using tangential vector finite elements," *IEEE Trans. Microwave Theory Tech.*, vol. 39, pp. 1262-1271, August 1991.
- [4] A. F. Peterson, S. L. Ray, and R. Mittra. *Computational Methods for Electromagnetics*. New York: IEEE Press, 1998, pp. 388-392.
- [5] Y. Li, S. Zhu, and F. A. Fernandez, "The efficient solution of large sparse nonsymmetric and complex eigensystems by subspace iteration," *IEEE Trans. Magnetics*, vol. 30, pp. 3582-3585, September 1994.
- [6] B. R. Crain and A. F. Peterson, "Analysis of dielectric-loaded waveguides using covariant projection vector finite elements," *Proceedings of the 10th Annual Review of Progress in Applied Computational Electromagnetics*, Monterey, CA, vol. 1, pp. 144-151, March 1994.

NUMERICAL METHODS FOR HIGH FREQUENCY PROBLEMS

T. HUTTUNEN AND P. MONK*

1. Introduction. Finite element methods are a convenient means of approximating acoustic or electromagnetic fields due to their geometric flexibility and ability to approximate fields in heterogeneous media. Unfortunately, as the wave number for the field increases, the size of the elements must decrease more rapidly in order to maintain accuracy [6]. Thus finite elements become very expensive for large problems. One way to help control this is to use higher order schemes, but then the need to change the order of the approximation in different elements complicates the programming of the scheme [4]. An alternative approach is to replace the piecewise polynomials used by the finite element method by solutions of the underlying differential equation on each element. The hope is that the use of exact solutions will help the accuracy of the scheme. The problem with this approach is that the approximate solution will be discontinuous between elements.

To describe these methods in more detail we shall use a simple model problem which we give next. Let $D \subset \mathbb{R}^2$ be a bounded domain with two boundaries Γ and Σ such that $\partial D = \Gamma \cup \Sigma$ and $\Gamma \cap \Sigma = \emptyset$. Then we seek to compute an approximation to the solution u of the following boundary value problem.

$$(1.1a) \quad \Delta u + k^2 u = 0 \text{ in } D,$$

$$(1.1b) \quad u = g \text{ on } \Gamma,$$

$$(1.1c) \quad \frac{\partial u}{\partial \nu} - iku = 0 \text{ on } \Sigma,$$

where k is the wave-number of the time harmonic field, g is a given function and ν is the unit outward normal on Γ . Obviously we are interested in more complex scattering problems, but problem (1.1) is an easy model problem for the schemes we shall discuss.

Now let D be covered by a mesh consisting of N_h elements $\{\Omega_n\}_{n=1}^{N_h}$ of maximum diameter h . This need not be a finite element mesh, but $\Omega_1 \dots \Omega_k$ are assumed disjoint and

$$\bar{D} = \bigcup_{n=1}^{N_h} \bar{\Omega}_n.$$

For our calculations we do, in fact, employ a finite element grid. We also assume the elements are regular and quasi-uniform. On each element Ω_n we approximate the field u using plane-waves (Bessel functions are also possible). Let $p > 0$ be fixed then the approximate field u_h is defined by

$$(1.2) \quad u_h|_{\Omega_n} = \sum_{\ell=1}^p u_{n,\ell} \exp(ik\mathbf{x} \cdot \mathbf{d}_\ell), \quad n = 1, \dots, N_h$$

where $\mathbf{d}_\ell = (\cos(2\pi\ell/p), \sin(2\pi\ell/p))$, $\ell = 1, \dots, p$. The coefficients $\{u_{n,\ell}\}$ are unknown and determined by the method. For a heterogeneous medium the wave number k would

*Department of Mathematical Sciences, University of Delaware, Newark, DE 19716

also vary from element to element. Next we shall describe two approaches to computing u_h . For completeness we note a third approach which uses plane waves. In this scheme (due to Babuska and Melenk [8, 1]) the expansion (1.2) uses a finite element function in place of $u_{n,e}$. This results in a partition of unity method that preserves the continuity of the field from place to place in the grid. It has been tested for example in [7]. We will not consider it further here since we want to have discontinuous basis elements.

2. Least Squares. The simplest way to compute u_h is to compute the least squares fit across edges in the mesh. This has been suggested by many people (see for example [5, 10]) and analyzed in [9]. Let the edges in the mesh be divided into three disjoint sets

$$e \in \begin{cases} E_0 & \text{if } e \text{ is in the interior of } D, \\ E_\Gamma & \text{if } e \text{ is on } \Gamma, \\ E_\Sigma & \text{if } e \text{ is on } \Sigma. \end{cases}$$

For a given edge $e \in E_0$ let, for $x \in e$,

$$[f](x) = \lim_{\epsilon \rightarrow 0} (f(x + \epsilon \nu_e) - f(x - \epsilon \nu_e))$$

where ν_e is normal to e . Then let

$$\vec{u} = (u_{1,1}, u_{1,2}, \dots, u_{1,p}, u_{2,1}, u_{2,2}, \dots, u_{2,p}, \dots, u_{N_h,p})$$

and define

$$(2.1) \quad \begin{aligned} J(\vec{u}) = & \sum_{e \in E_0} \int_e (|\nabla u_h|^2 + k^2 |u_h|^2) ds \\ & + \sum_{e \in E_\Gamma} \int_e k^2 |u_h - g|^2 ds + \sum_{e \in E_\Sigma} \int_e \left| \frac{\partial u_h}{\partial \nu} - i k u_n \right|^2 ds. \end{aligned}$$

The coefficients in (1.2) are obtained by minimizing $J(\vec{u})$ so

$$\vec{u}^* = \underset{\vec{u} \in \mathbb{C}^M}{\operatorname{argmin}} J(\vec{u})$$

where $M = pN_h$. The vector \vec{u}^* gives the coefficients for (1.2). The discrete minimization problem can be solved using the standard conjugate gradient method.

In [9] it is shown that convergence occurs so that $u_h \rightarrow u$ in the $L^2(D)$ norm as $h \rightarrow 0$ at the rate $h^{(p-1)/2-1}$. Thus for $p = 11$ we get an $O(h^4)$ scheme. Alternatively the scheme converges as $p \rightarrow \infty$ for fixed h . Computational results in [9] show that the method can provide an accurate discretization. However the conditioning of the matrices derived from (2.1) increases rapidly as p increases. For this reason we have also investigated the method described in the next section.

3. The Ultra Weak Variational Formulation (UWVF). This method was proposed and analyzed by Cessenat and Despres in [2, 3]. Our goal is to extend this testing of their method to more complex scattering problems. We also will provide detailed comparisons between the UWVF and the finite element method.

Let us outline the UWVF [3]. Let $\Sigma_{\ell,j}$ denote the edge between element Ω_ℓ and element Ω_j , and let ν_ℓ denote the unit outward normal to Ω_ℓ . Let

$$x_\ell = \left((-\partial/\partial\nu_\ell + ik)u_h|_{\Omega_\ell} \right) \Big|_{\partial\Omega_\ell}, \quad 1 \leq \ell \leq N_h.$$

Then x_ℓ satisfies

$$\begin{aligned} & \sum_{\ell=1}^{N_h} x_\ell \overline{(-\partial/\partial\nu_\ell + ik)e_\ell} ds - \left(\sum_{\ell=1}^{N_h} \sum_{j=1}^{N_h} \int_{\Sigma_{\ell,j}} x_j \overline{(\partial/\partial\nu_\ell + ik)e_\ell} ds \right. \\ & \left. + \sum_{\ell=1}^{N_h} \int_{\partial\Omega_\ell \cap \partial\Omega} Q x_\ell \overline{(\partial/\partial\nu_\ell + ik)e_\ell} ds \right) = \sum_{\ell=1}^{N_h} \int_{\partial\Omega_\ell \cap \partial\Omega} g \overline{(\partial/\partial\nu_\ell + ik)e_\ell} ds \end{aligned}$$

for all functions e of the form (1.2) where $e_\ell = e|_{\Omega_\ell}$. Here $Q = 0$ and $g = 0$ on Σ and $Q = -1$ on Γ . Cessenat and Despres [3] suggest a method for solving this system, prove convergence and discuss conditioning. In fact the rate of convergence is the same as for the least squares method outlined in the previous section. Our contribution is so far limited to an independent verification of some of the properties of the scheme and a comparison with finite element methods which we give next.

4. Numerical Experiments.

4.1. Wave Propagation. First we show some results for simple wave propagation in the unit square. So

$$\Omega = [0, 1] \times [0, 1], \quad \Sigma = \phi, \quad \text{and} \quad \Gamma = \partial\Omega.$$

We take $k = 16\pi$ and

$$g = ((1+Q)\partial/\partial\nu + (1-Q)ik) e^{i\xi \cdot x}, \quad Q = 0, 1,$$

where $\xi = (\cos(\pi/p), \sin(\pi/p))$. This direction is midway between d_p and d_1 , and is the direction giving maximum error for the problem. The exact solution is $u = \exp(i\xi \cdot x)$. Figure 4.1 shows a contour plot of error (discrete L_2 error at the nodes in the grid) against $N = \sqrt{N_h/2}$ and p using a uniform triangular mesh on Ω consisting of right triangles. Clearly for this problem the error can be decreased by either increasing p or increasing N (or presumably both simultaneously). Timing studies show that increasing p reaches a given error in less computer time than increasing N . Thus the method has similar features to the $h-p$ finite element method.

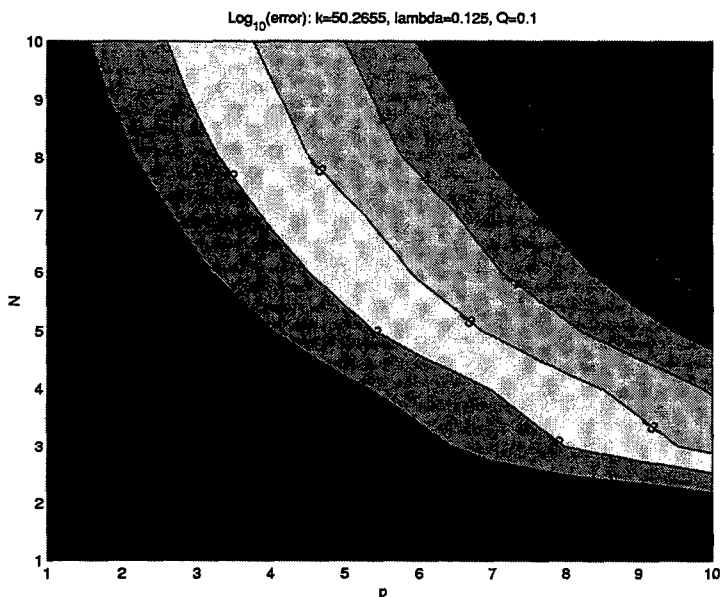


FIG. 4.1. The logarithm (base 10) of the discrete relative $L^2(D)$ error against $N = \sqrt{N_h}$ and p for the plane wave propagation problem. The results suggest that increasing p decreases the error effectively.

4.2. "Scattering". Here we test the UWVF compared to finite elements for a problem that approximates a scattering problem. The domain Ω is the annular region between the circle $|\mathbf{x}| = 0.4$ and $|\mathbf{x}| = 1$. The boundary Γ is the inner circle $|\mathbf{x}| = 0.4$ and the boundary Σ is the circle $|\mathbf{x}| = 1$.

To simulate scattering of a plane wave from Γ we take $g = -\exp(ikx_1)$. Using special functions we can easily write down a series solution to problem (1.1) or to the true scattering problem posed on an infinite domain. By meshing the annulus (using curved elements near Σ and Γ in the case of the UWVF) we can compare results for the piecewise linear finite element method and the UWVF.

In Figure 4.2, we show the relative error (in the discrete L_2 norm computed at the nodes) for both methods as k is varied. For the finite element method, the domain is remeshed at each k to keep approximately eight elements per wavelength (i.e. $2\pi/kh \simeq 8$). For the UWVF we take $p = 10$ and the domain is remeshed to keep approximately one geometric element per wavelength (i.e. $2\pi/kh \simeq 1$). Irregularities in the data are due to detailed charges in the meshes. As expected [6] the error in the FEM increases as k increases and by $k = 45$ the method is unreliable. More surprisingly the UWVF results do not show an increase as k increases (are a much wider range than used for the FE results). This insensitivity to k is an interesting feature of the UWVF and needs to be investigated in

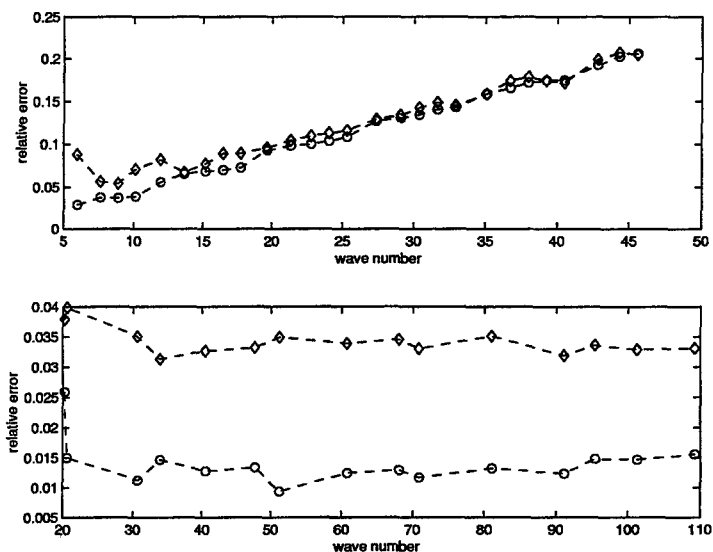


FIG. 4.2. In this figure we show the relative discrete $L^2(D)$ error for the finite element method and the UWVF. In the top panel we show results for the FE method (diamonds mark the error compared to the true solution of the scattering problem and circles show the error against the exact solution of (1.1) — the difference is due to the absorbing boundary condition). As expected the FE error increases with k . In the lower panel we show results for the UWVF. Surprisingly the error doesn't increase with k (over a much larger range of wave numbers than for the FEM).

more detail. In particular at high wave number the Bessel function series used to compute the "exact" solution may become inaccurate which may bias the results for the UWVF for large k .

5. Conclusion. The UWVF or least squares method can both produce convergent approximations to the Helmholtz equation. Our numerical experiments show that the UWVF has characteristics similar to hp finite element methods, but since the solution is discontinuous mesh (h) and interpolation (p) adaptivity might be easier to implement. For high frequency problems the UWVF shows much less sensitivity to increases in the wave number k than the FEM.

More testing of the UWVF and least squares methods are needed, particularly on domains with corners, and for transmission problems. We hope to report on this shortly.

REFERENCES

- [1] I. BABUŠKA AND J. MELENK, *The partition of unity method*, International Journal for Numerical Methods in Engineering, 40 (1997), pp. 727–758.
- [2] O. CESSENAT, *Application d'une nouvelle formulation variationnelle aux équations d'ondes harmoniques. Problèmes de Helmholtz 2D et de Maxwell 3D.*, PhD thesis, Université Paris IX Dauphine, 1996.
- [3] O. CESSENAT AND B. DESPRES, *Application of the ultra-weak variational formulation of elliptic PDEs to the 2-dimensional Helmholtz problem*, SIAM J. Numer. Anal., 35 (1998), pp. 255–299.
- [4] L. DEMKOWICZ AND L. VARDAPETVAN, *Modelling electromagnetic absorption/scattering problems using hp-adaptive finite elements*, Compu. Methods Appl. Mech. Engrg., 152 (1998), pp. 103–124.
- [5] T. DRISCOLL, *Eigenmodes of isospectral drums*, SIAM Review, 39 (1997), pp. 1–17.
- [6] H. IHLENBURG AND I. BABUŠKA, *Finite element solution of the Helmholtz equation with high wavenumber Part I: The h-version of the FEM*, Computers Math. Applic., 30 (1995), pp. 9–37.
- [7] O. LAGHROUCHE AND P. BETTESS, *Short wave modelling using special finite elements*. to appear in *Journal of Computational Acoustics*.
- [8] J. MELENK AND I. BABUŠKA, *The partition of unity finite element method: Basic theory and applications*, Computer Methods in Applied Mechanics and Engineering, 139 (1996), pp. 289–314.
- [9] P. MONK AND D. WANG, *A least squares method for the helmholtz equation*, Computer Methods in Applied Mechanics and Engineering, 175 (1999), pp. 121–136.
- [10] M. STOJEK, *Least-squares Trefftz-type elements for the Helmholtz equation*, International journal for numerical methods in engineering, 41 (1998), pp. 831–849.

SESSION 2

**OPTIMIZATION
IN
ELECTROMAGNETICS**

Chairs: Eric Michielssen and Dan Weile

Design of Dual Band Frequency Selective Surfaces Using Genetic Algorithms

A. Monorchio¹, R. Mittra² and G. Manara¹

¹Department of Information Engineering, University of Pisa, Pisa, Italy
via Diotisalvi 2, I-56126 Pisa, Italy.
E-mail: mono@iet.unipi.it, manara@iet.unipi.it

²Electromagnetic Communication Laboratory, Pennsylvania State University,
319 Electrical Engineering East, University Park, PA 16802.
E-mail: rxm53@psu.edu

Abstract- In this paper, an optimization procedure based on the genetic algorithm (GA) is utilized to design Frequency Selective Surfaces (FSSs) for dual frequency applications. The FSS is analyzed by employing the Method of Moments (MoM) procedure with sub-domain basis functions. This formulation allows us to include the shape of the mask defining the unit cell of the FSS in the set of parameters controlling the optimization scheme. Such a GA-based synthesis procedure enables us to develop new and unconventional elements that attempt to achieve the specified frequency and polarization characteristics, which would be difficult to realize by using well-known element shapes, e.g., patches, crosses, loops and Jerusalem crosses.

I INTRODUCTION

Frequency Selective Surfaces (FSSs) find widespread use in a variety of applications, e.g., bandpass radomes and subreflectors for dual-band reflector antennas, to name just a few. An FSS comprises a two-dimensional periodic array of apertures or patch elements that resonate at certain frequencies, and provide the characteristics of spatial filters to the screen [1]. To realize a particular frequency behavior, one varies several design parameters, such as the element shape, size, lattice geometry and dielectric properties of the substrate [2-4]. In this paper we utilize an optimization procedure, based on the use of an evolutionary scheme [5-7], called the Genetic Algorithm (GA), to accomplish this task. The analysis module of the GA synthesis procedure is based on the Method of Moments (MoM) formulation utilizing sub-domain basis functions. The MoM is particularly suited for the analysis of doubly-periodic screens, comprising printed metallic elements that are sandwiched between different

layers of dielectrics [8]. A key step in the design procedure consists in choosing the parameters that control the optimization procedure. For the problem at hand, we select these to be the dimensions of the unit cell along the principal directions, the dielectric substrate properties (thickness and relative permittivity) and the shape of the printed elements in a unit cell. In order for the design to be realistically manufacturable, the substrate permittivity is chosen from among a set of commercially-available products. In a previous work, we opted to assign a great deal of flexibility to the optimization program designing an FSS [9] that meets the prescribed frequency specifications. However, such a strategy resulted in a random and scattershot pattern for the FSS element, and this then led us to consider the possibility of imposing certain constraints on the element geometry so as to realize a more "structured" design, one in which the symmetry and connectivity conditions on the mask have been incorporated.

II MOM MODELING OF THE FSS

A MoM-based computer code has been employed in this work to perform the electromagnetic simulations of the FSS. The numerical analysis follows the well-established procedure of solving the Electric Field Integral Equation (EFIE) for the current distribution on the perfectly conducting patches, derived by enforcing the Floquet's periodicity condition in an elementary cell [1]. Consider a screen lying in the x - y plane, with cell periodicities d_x and d_y along the x - and y -directions, respectively. We can cast the EFIE in the form:

$$\begin{bmatrix} E_x^s(x, y) \\ E_y^s(x, y) \end{bmatrix} = \frac{2\pi}{d_x d_y} \sum_n \sum_m \frac{1}{j\omega\epsilon_0} \begin{bmatrix} k_0^2 - \alpha_n^2 & -\alpha_n \beta_m \\ -\alpha_n \beta_m & k_0^2 - \beta_m^2 \end{bmatrix} \underline{G}(\alpha_n, \beta_m) \begin{bmatrix} J_x(\alpha_n, \beta_m) \\ J_y(\alpha_n, \beta_m) \end{bmatrix} e^{j\alpha_n x} e^{j\beta_m y}. \quad (1)$$

In (1), E_x^s and E_y^s represent the x - and y -components, respectively, of the electric field scattered by the screen, and α_n and β_m are expressed in terms of the periodicity of the screen and the incident wavenumber. Specifically, we have

$$\alpha_n = (2\pi/d_x)n + k_x^{inc}, \quad (2a)$$

$$\beta_m = (2\pi/d_y)m + k_y^{inc}, \quad (2b)$$

where k_x^{inc} and k_y^{inc} are the projections of the incident plane-wave wave vector k_0 along the x - and y -directions, respectively. Finally, $\underline{G}(\alpha_n, \beta_m)$ is the dyadic spectral Green's function that accounts for the presence of the lossy dielectric substrate of thickness τ upon which the patches are printed. Equation (1) must be solved for the unknown current distributions J_x and J_y , after imposing the boundary condition on the surface of the conductor.

If we assume that the patch material is a perfect electric conductor (PEC), the tangential components of the total electric field must vanish on the surface of the patch, i.e., $\vec{E}^s \times \hat{z} = -\vec{E}^{inc} \times \hat{z}$, where \hat{z} is the normal to the screen. Next, we express the current distribution in terms of a set of basis functions, that can be defined either on the entire domain [10], or on the sub-domains of the periodic cell. The

latter type of basis functions are commonly known as "rooftops" and are particularly suited for handling arbitrarily-shaped patches [11], which we expect to synthesize by using the GA approach. Our next step is to derive a matrix equation by applying the Galerkin's procedure and to solve it for the current distribution. The final steps are to compute the FSS response from the knowledge of this distribution, and to link this analysis module to the GA optimization algorithm.

III OPTIMIZATION PROCEDURE

The specific GA adopted in this work employs a standard proportionate selection, also referred to as the weighted roulette wheel selection scheme. Moreover, it applies both a simple single-point crossover operator and a mutation operator with probabilities $p_{cross}=80\%$ and $p_{mutation}=0.1\%$, respectively. The chromosomes are a set of genes, representing coded versions of individual optimization parameters. In particular, once the desired frequency response of the screen is assigned, the design procedure can be reduced to that of determining the following control parameters: the shape (mask) of the printed element in the basic periodicity cell; the electrical characteristics of the dielectric substrate (relative permittivity ϵ_r and conductivity σ) and its thickness t ; and, finally, the dimensions of the FSS element, *i.e.*, the cell periodicities d_x and d_y along the x - and y -directions. All of the above-mentioned parameters can be assigned to a different field in the chromosome. As mentioned earlier, the dielectric substrate parameters are selected for among a set of commercially-available products to achieve a realistic design. To model the mask of the printed element, we subdivide the basic periodic cell into elementary pixels, and represent each pixel by either a 1 or a 0 depending on whether it is covered by a printed metallic element or not. This provides the GA the flexibility it needs to choose the shape of the basic periodic cell, which can be quite arbitrary. The objective function is defined as the root mean square difference of the actual and the desired FSS transfer functions, evaluated at different frequencies within the operational band of the filter.

The choice of the objective function strongly affects the performance of the resulting design, as well as the rate of convergence of the algorithm; hence this choice should be made with great care. In our case, we found excellent results by using an objective function:

$$F = (F_{B1} + F_{B2}) / 2. \quad (3)$$

where F_{B1} and F_{B2} correspond to the transmission and reflection bands, respectively, and are defined below. For each of these bands, we calculate the objective function as the mean square value of the difference between the desired and computed frequency responses of the screen. In particular, for the transmission band we set:

$$F_{B1} = \frac{1}{4N_f} \sum_{i=1}^{N_f} \sqrt{[100 - P_{TE}^{trans}(f_i)]^2} + \sqrt{[100 - P_{TM}^{trans}(f_i)]^2} + |P_{TE}^{refl}(f_i)| + |P_{TM}^{refl}(f_i)|. \quad (4)$$

In (4), N_f is the total number of frequencies in the transmission band B1, while $P_{TE}^{trans}(f_i)$ is the transmitted power for the TE polarization, at the frequency f_i , evaluated as a percentage of the incident total power. The other terms can be interpreted similarly.

For the reflection band, the objective function is complementary, *i.e.*, it reads:

$$F_{B2} = \frac{1}{4N_{f2}} \sum_{i=1}^{N_{f2}} \left[\sqrt{[100 - P_{TE}^{ref}(f_i)]^2} + \sqrt{[100 - P_{TM}^{ref}(f_i)]^2} + |P_{TE}^{trans}(f_i)| + |P_{TM}^{trans}(f_i)| \right]. \quad (5)$$

The objective function F given in (3), and derived by using (4) and (5), can assume values between 0 and 100. It is minimized by using the GA to derive the desired solution of the FSS system problem.

IV NUMERICAL RESULTS

We now present some illustrative numerical results to demonstrate the effectiveness of the proposed synthesis procedure. We choose an example where the design specifications call for the dual-band FSS to perform simultaneously in the S- and X-bands. Specifically, it is desirable for the FSS to provide a transmission coefficient in the S-band (2-3 GHz) that is as high as possible. Concurrently, we require a high reflection coefficient in the X-band (7-8 GHz), at an incidence angle of 45°. Additionally, these requirements are imposed on both the TE- and TM-polarized incident fields.

The optimization problem is defined as that of determining the following design parameters: (i) the substrate characteristics, *i.e.*, dielectric permittivity and thickness; (ii) periodicities d_x and d_y along the two main axes; and, (iii) the map of the mask representing the FSS element, which comprises 16×16 pixels represented by a 256 bit chromosome and characterized by either a 1 or a 0, depending on whether it is metallic or not. A finer discretization can also be used, if desired.

As mentioned earlier, if the distribution of 1's and 0's is totally random, the resulting mask has a scattershot character. Since the isolated pixels contribute little to the frequency response, and since the roof top basis functions span a pair of subdomains, we can carry out a final editing of the mask *post fact* and eliminate these isolated pixels [9]. However, in this paper we have chosen to implement this editing step on the fly, at each step of defining the chromosomes, by imposing connectivity constraints on the geometry of the random mask generated during the optimization cycle. In particular, the isolated pixels are removed from the mask and the resulting holes are filled with metal instead, leading to a relatively structured design in the process. In addition, we impose one of the two reflection symmetry constraints on the geometry of the mask, and only optimize one fourth of the mask as illustrated in Fig. 1. This, in turn, reduces the original problem to one-fourth the size, comprising only 8×8 pixels, with a chromosome field, which is 64 bits long.

The chromosome can now be constructed by using the genes associated with the four control parameters mentioned above. In particular, 4 bits are used to code the database of the materials and the d_x and d_y dimensions are coded with 13 bits each, so that the total length of the chromosome is 94

bits. A map of 40 chromosomes is used and the objective function is evaluated at 5 frequencies within the transmission and reflection bands.

Figures 2 through 4 present some results derived by using the GA approach. Figures 2(a) and 3(a) display the elementary cells obtained by imposing the symmetry strategy illustrated in Fig. 1(a). The thickness and material parameters of the substrate are included in the figure captions. Figures 2(b) and 3(b) present the frequency responses of the corresponding FSSs, and plot the reflected and transmitted powers normalized with respect to the incident power. In Fig. 4, we present the elementary cell and the frequency response of another FSS screen, which is designed with the symmetry strategy shown in Fig. 1(b). Before closing, we mention that all of the results presented herein have been obtained in 800 to 1000 generations steps, which were sufficient to achieve the convergence of the GA.

V CONCLUSIONS

An optimization procedure based on the genetic algorithm has been applied to design FSSs for dual frequency applications. The MoM analysis of the FSS, employing sub-domain basis functions, has enabled us to include the shape of the mask in the set of parameters controlling the optimization scheme. This has led to the development of some new and perhaps unconventional FSS element geometries, synthesized by the GA, that were found to exhibit good performance, and meet the design specifications for both the frequency and polarization characteristics. It was found that the imposition of reflection symmetries leads to structured geometrical shapes for the FSS elements, rather than totally random ones that emerge when the unconstrained GA optimization process is used.

REFERENCES

- [1] T. K. Wu Ed., *Frequency Selective Surface and Array*, John Wiley & Sons, 1995.
- [2] E.A. Parker and S.M.A. Hamdy, "Rings as elements for frequency selective surfaces," *Electron.Lett.*, vol 17, pp.612 - 614, 1981.
- [3] E. L. Pelton and B. A. Munk, "Scattering from periodic arrays of crossed dipoles," *IEEE Trans. on Antennas and Propagat.*, vol.AP-27, n. 3, pp. 323-330, Mar. 1979.
- [4] S.M.A. Hamdy and E.A. Parker, "Influence of lattice geometry on transmission of electromagnetic waves through arrays of crossed dipoles," *IEE Proc., Part H*, vol.129, pp.7 -10, 1982.
- [5] R. L. Haupt, "An introduction to genetic algorithms for electromagnetics," *IEEE Antennas and Propagat. Mag.*, vol. 37, pp. 7-15, April 1995.
- [6] D. S. Weile and E. Michielssen, "Genetic algorithm optimization applied to electromagnetics: a review," *IEEE Trans. on Antennas and Propagat.*, vol.AP-45, pp. 343-353, March 1997.
- [7] J. M. Johnson and Y. Rahmat-Samii, "Genetic algorithms in engineering electromagnetics," *IEEE Antennas and Propagat. Mag.*, vol. 39, n. 4, pp. 7-21, Aug. 1997.
- [8] R. Mittra, C. Chan, and T. Cwik, "Techniques for analyzing frequency selective surfaces - a review," *IEEE Proc.*, vol.76, n.23, pp. 1593-1615, 1988.

- [9] G. Manara, A. Monorchio, R. Mittra, "Frequency selective surface design based on genetic algorithm," *Electronics Letters*, Vol. 35, No.17, pp.1400-1401, August 19 1999.
- [10] S.M.A Hamdy, and E.A. Parker: 'Current distribution on the elements of a square loop frequency selective surface', *Electron. Lett.*, vol. 18, pp. 624 - 626, 1982.
- [11] C. H. Chan and R. Mittra, "On the analysis of frequency selective surfaces using subdomain basis functions," *IEEE Trans. on Antennas and Propagat.*, vol.AP-38, pp. 40-50, Jan. 1990.

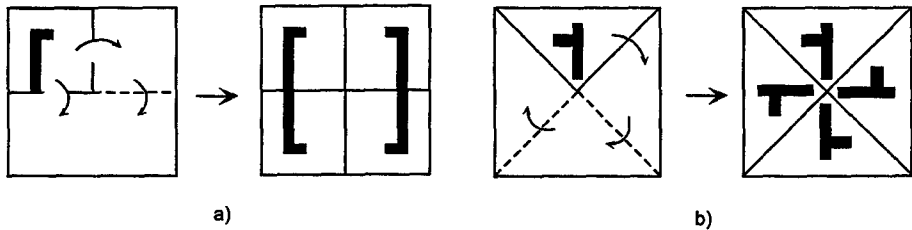


Fig. 1 – Two possible strategies for imposing symmetry constraints on the shape of the mask.

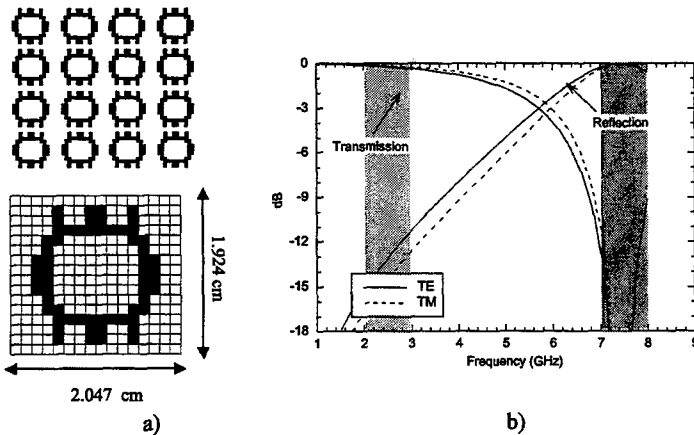


Fig. 2 – a) Shape of the elementary cell derived by the GA and complete view of the screen.
b) Frequency characteristics of the FSS screen for both the TE and TM polarizations. Substrate thickness: 25 μm , $\epsilon_r=2.8$.

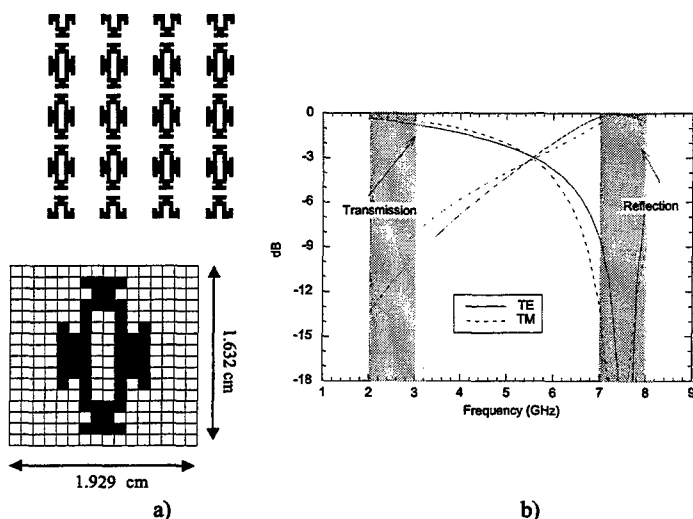


Fig. 3 – a) Shape of the elementary cell derived by the GA and complete view of the screen.
b) Frequency characteristics of the FSS screen for both the TE and TM polarizations. Substrate thickness: 2 mm, $\epsilon_r=3.3$.

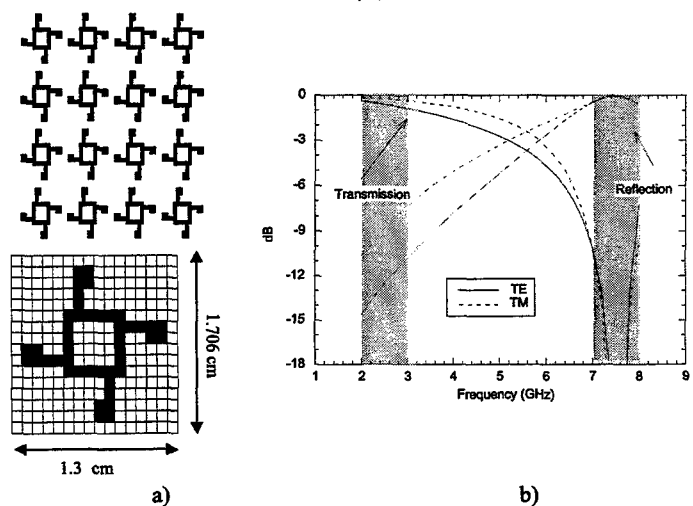


Fig. 4 – a) Shape of the elementary cell derived by the GA and complete view of the screen.
b) Frequency characteristics of the FSS screen for both the TE and TM polarizations. Substrate thickness: 2 mm, $\epsilon_r=3.3$.

A Study of Cauchy and Gaussian Mutation Operators in the Evolutionary Programming Optimization of Antenna Structures

Ahmad Hoorfar and Yuan Liu

ECE Department, Villanova University, Villanova, PA 19085;

E-mails: hoorfar@ece.vill.edu ; Yuan@ece.vill.edu

I. Introduction

Recent research in various parameter optimization problems have clearly demonstrated that the evolutionary computational techniques can yield robust globally optimized solutions to problems that otherwise are not amenable to traditional gradient-based local-search optimization methods. These probabilistic techniques, collectively known as Evolutionary Algorithms (EAs), try to emulate, in one way or the other, the Darwinian model of natural evolution on a computer. Even though there are many branches of EA's, one can in general find three main trends in the literature: Evolutionary Programming (EP)[1], Evolution Strategies (ES)[2] and Genetic Algorithms (GAs)[3]. All these algorithms are multi-agent stochastic search methods that incorporate random variation and selection. They all operate on a population of candidate solutions and rely on a set of variation operators to generate new offspring population. Selection is then used to probabilistically advance better solutions to the next generation and eliminate less-fit solution according to the objective function being optimized. Of the three paradigms of EAs, GAs are well-known to the electromagnetic community and have been extensively used in optimization of antenna and microwave structures[4,5,6], whereas the application of EP in electromagnetics appeared more recently [7,8,9].

One can identify the following major differences among the aforementioned three branches of EAs. i) The conventional GAs require the continuous design parameters to be digitized and represented as binary strings, whereas EP and ES can both directly work with the continuous, discrete or mixed parameters. ii) The variation operator used in GAs is a combination of crossover and mutation with the former being the main mechanism of change. The evolution process in ES uses both recombination and mutation with the latter being the dominant operator. On the other hand, mutation is the only operator used in EP. iii) The selection of the crossover and mutation probabilities in GAs is rather arbitrary and they are not adapted during evolution. The selection of the initial values for the so-called strategy parameters for EP and ES are well defined and efficient adaptive and self-adaptive techniques exist for adapting these parameters during evolution.

Mutation-based reproduction process in EP may provide a versatile tool in design of the problem specific operators and facilitate easy integration with available apriori knowledge about the problem. Conventional implementation of EP for continuous parameter optimization uses Gaussian mutations. Recently, an implementation of EP with Cauchy mutation operator was shown to outperform EP using the Gaussian mutations for optimizations of multi-modal functions with many local minima, whereas on multi-modal functions with few local minima, the differences in performances of the two mutation operators were statistically insignificant [10].

In this paper, we present details of the implementations of EP algorithms using Gaussian and Cauchy mutation operators and apply them to various unconstrained as well as constrained antenna optimization problems. The objective here is to perform a comparative study of the two mutation operators in terms of the rate of convergence and the quality of the solutions produced for selected antenna optimization problems. The examples include optimization of aperiodic non-uniform antenna arrays and the challenging gain optimization problem of a Yagi-like array of multi-layered stacked microstrip antennas. For the latter problem the objective function is highly non-linear due to the presence of surface-waves and strong mutual coupling effects.

II. EP Algorithms with Gaussian and Cauchy Mutation Operators

The EP algorithm with self-adaptive mutation operator for global optimization of an n-dimensional objective function $\phi(\vec{x})$, $\vec{x} = [x(1), x(2), \dots, x(n)]$ consists of five basic steps: initialization, fitness evaluation,

mutation, tournament and selection. Here we concentrate on the mutation step; the details on the other steps can be found in [1,2]

Design of efficient mutation operators is presently an ongoing topic of research in evolutionary computation. Here we present two algorithms, which use different mutation operators in the evolution process. First let us assume an initial population of μ individuals is formed through a uniform random or a biased distribution. Each individual is taken as a pair of real-valued vectors, $(\bar{x}_i, \bar{\eta}_i)$, $\forall i \in \{1, \dots, \mu\}$ where $\bar{x}_i = [x_i(1), x_i(2), \dots, x_i(n)]$ and $\bar{\eta}_i$ are the n -dimensional solution and its corresponding strategy parameter (variance) vectors, respectively. In EP with Gaussian mutation operator (GMO), each parent $(\bar{x}_i, \bar{\eta}_i)$ creates a single offspring $(\bar{x}_i', \bar{\eta}_i')$ by:

$$x_i'(j) = x_i(j) + \sqrt{\eta_i(j)} N_j(0,1) ; \quad \eta_i'(j) = \eta_i(j) e^{[\tau' N(0,1) + \tau N_j(0,1)]} \quad (2)$$

for $j = 0, 1, 2, \dots, n$, where $x_i(j)$ and $\eta_i(j)$ are the j th components of the solution vector and the variance vector, respectively. $N(0,1)$ denotes a one-dimensional random variable with a Gaussian distribution of mean zero and standard deviation one. $N_j(0,1)$ indicates that the random variable is generated anew for each value of j . The scale factors τ and τ' are commonly set to $(\sqrt{2/n})^{-1}$ and $(\sqrt{2n})^{-1}$, respectively, where n is the dimension of the search space. Self-adaptive mechanism of the second equation in (2), borrowed from ES, enables the meta-EP to evolve its own variance parameters during the search, exploiting an implicit link between internal model and good fitness values. The logarithmic normally distributed process for the variances in (2) guarantees positive values of standard deviations. The global factor $\tau' N(0,1)$ allows for an overall change of mutability and guarantees the preservation of all degrees of freedom, whereas the factor $\tau N_j(0,1)$ allows for individual changes of the variances $\eta_i(j)$ [2].

In EP with Cauchy mutation operator (CMO), the offsprings are still generated according to (2), but with a Cauchy mutation replacing the Gaussian mutation in the first equation, i.e.,

$$x_i'(j) = x_i(j) + \sqrt{\eta_i(j)} C_j(0,1) \quad (3)$$

where $C(0,1)$ is a random variable with a Cauchy distribution operator, G , centered at the origin and with the scale parameter $t = 1$,

$$G_t(x) = \frac{1}{2} + \frac{1}{\pi} \tan^{-1}\left(\frac{x}{t}\right) ; \quad -\infty < x < \infty \quad (4)$$

We note that the inverse of the operator in (4), needed in generation of the random variables in (3), is given in closed form.

After the offspring's population is formed, a tournament/selection process is performed in which a pairwise comparison with respect to the fitness values over the union of parents and offspring populations is conducted. For each individual \bar{x}_k in the union, $k \in \{1, \dots, 2\mu\}$, q opponents are chosen at random with equal probability from the total membership 2μ of the union. For each comparison, if the individual fitness is no greater than the opponent's, it receives a "win". The best individual is guaranteed a maximum "win" score of q and its survival to the next generation. We note that this tournament process differs from the one in conventional GAs and is 'elitist' in nature. The μ individuals out of the union of $(\bar{x}_i, \bar{\eta}_i) \cup (\bar{x}_i', \bar{\eta}_i')$, $\forall i \in \{1, \dots, 2\mu\}$, with the most "win" score are then selected to be the parents of the next generation.

For objective functions with few local minima the differences between the performances of EP with GMO and EP with CMO are statistically insignificant. For multi-modal functions with many local minima, however, CMO outperforms GMO. To demonstrate the latter, we consider the n -dimensional Ackley function [2]:

$$f_n(\bar{x}) = -20 \exp\left(-0.2 \sqrt{\frac{1}{n} \sum_{i=1}^n x_i^2}\right) - \exp\left(\frac{1}{n} \sum_{i=1}^n \cos(2\pi x_i)\right) + 20 + e \quad (5)$$

This function has a global minimum at 0 and a total of about $(2a+1)^n$ in the range $[-a, a]$. The 3-D mesh plot of the function for $n = 2$ is given in Figure 1. We have applied EP algorithms in the range $[-5, 5]$ to the above function when $n=2$ and 20. The population size and the number of opponents were set to $\mu = 50$ and $q = 10$, respectively. The results are shown in Figures 2-5. Figure 2 shows the function-value trajectory, for $n = 2$, of the best population member over 100 trials. The corresponding histogram in Figure 3 depicts the number of occurrences of various function values when CMO and GMO are used. As can be seen, CMO performs slightly better than GMO but there is not a significant convergence rate difference between the two algorithms. For $n=20$, however, CMO easily outperforms GMO as evident from Figures 4 and 5. We note that the very large number of local minima, which in this case is about 11^{20} , would trap any gradient-based, hill climbing method.

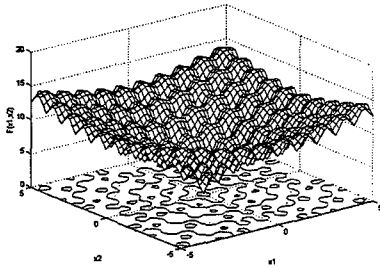


Fig. 1: Mesh plot of Ackley function for $n = 2$

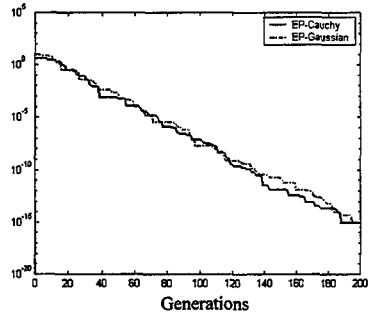


Fig. 2: Convergence rate for $n = 2$

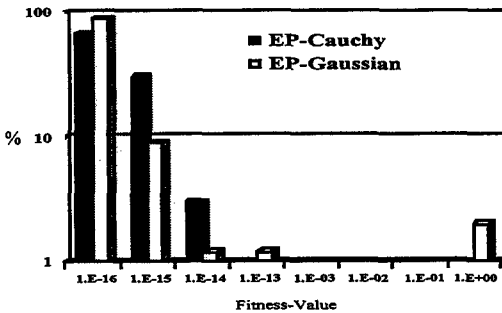


Fig. 3: Histogram for $n = 2$

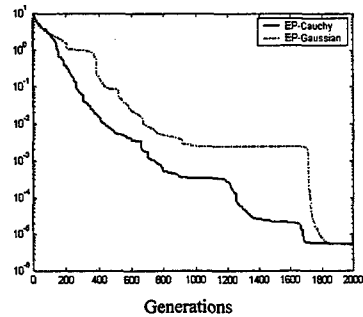


Fig. 4: Convergence rate for $n = 20$

The above results for the convergence rates of these mutation operators can be explained if we compare their corresponding probability density functions,

$$g(x) = \frac{1}{\sqrt{2\pi}\sigma} e^{-\frac{(x-\mu)^2}{2\sigma^2}} ; \quad c(x) = \frac{t}{\pi(t^2 + x^2)} \quad (6)$$

which are plotted in Figure 6 for $\mu_0 = 0$, standard deviation $\sigma = 1$ and the scale parameter $t = 1$. As seen the Cauchy distribution has fatter tails, which suggests that it should converge faster than the Gaussian distribution to the global optimum because of an increased probability of escaping from a local optimum.

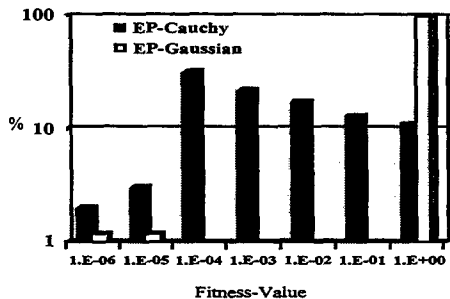


Fig. 5: Histogram for $n = 20$

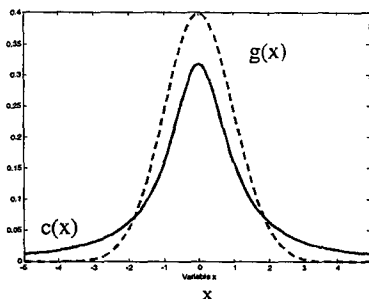


Fig. 6: Cauchy and Gaussian Probability density functions

III. Applications of EP algorithms with GMO and CMO to Antenna Structures

A. Optimization of Aperiodic Array

The array factor for an N element aperiodic array of isotropic radiating elements with non-uniform amplitude and spacing can be written as:

$$AF = \sum_{n=1}^N I_n e^{j(n-1)(kd_n \cos\theta + \beta)} \quad I_n \in [0,1] \quad d_n \in [0,\lambda] \quad (7)$$

where I_n and d_n are the normalized excitation amplitude and the spacing of the n th element; θ is the elevation angle measured from the array axis. Assuming a symmetric pattern with $N=21$, we have used the EP algorithms to minimize the side-lobe levels (SLL) subject to the constraint of $10^\circ < \text{HPBW} < 10.5^\circ$ where HPBW is the 3-dB half power beam-width. A parents' population size of $\mu = 50$ and opponents' size of $q = 10$ are used to optimize I_n and d_n , $n = 1, 2, \dots, 10$. Fifty independent trials and 200 generations per trials were performed. The fitness-value trajectory of the best population member and the histogram (in percentage) of the 50 trials are shown in Figure 7 and 8, respectively. For this constraint optimization problem, GMO results in a faster convergence rate than CMO. Maximum side-lobe levels of -33 dB and -43 dB are obtained after about 75 and 170 generations, respectively. The pattern for the former case is shown in Figure 9; the corresponding HPBW is about 10.4° .

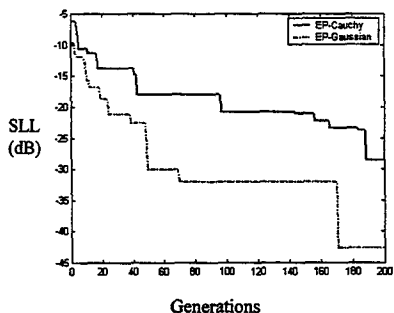


Fig. 7: Convergence rate for Cauchy and Gaussian mutations

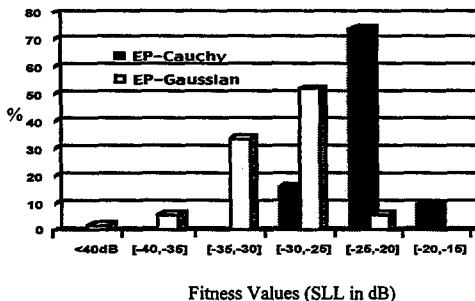


Fig. 8: Histogram for Cauchy and Gaussian mutations

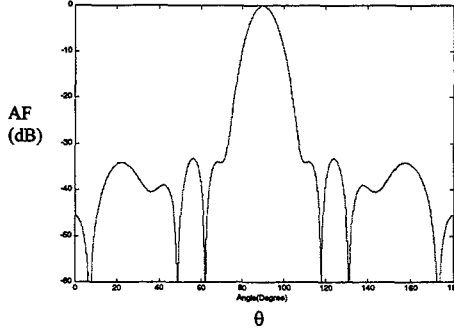


Fig. 9: Optimized far-field pattern with SLL = -33.2 dB and HPBW = 10.4°

B. Optimization of Yagi-like Array of Microstrip Antennas

The printed Yagi-like structure in Figure 10 consists of a driver and a finite number of embedded director strip elements printed in an N-layer dielectric medium. To optimize the gain the structure is modeled using a mixed-potential integral equation:

$$\left(\frac{j\eta_0 k_0^2}{2\pi} \right) \sum_{i=1}^N \iint_{S_i} \left[\bar{G}_{Mi}^{(p)}(\bar{x}, \bar{x}') \bar{J}_{si}(\bar{x}') + \frac{1}{k_0^2} \nabla_t \bar{G}_{Ei}^{(p)}(\bar{x}, \bar{x}') \nabla_t' \cdot \bar{J}_{si}(\bar{x}') \right] dS' - Z_{sp} \bar{J}_{sp}(\bar{x}) = -\bar{E}_{inc}^{(p)} \quad (8)$$

$\bar{x} = (x, y) \in S ; p = 1, 2, \dots, N$

where \bar{J}_{si} and Z_{si} are the electric surface current and the surface impedance of S_i , respectively; $\bar{E}_{inc}^{(p)}$ is the tangential (incident) electric field impressed at the p-th surface. $\bar{G}_{Mi}^{(p)}$ and $\bar{G}_{Ei}^{(p)}$ are the Green's Functions of Magnetic and Electric types, respectively, evaluated at the p-th layer due to a source at the i-th layer. The Green's functions are of the Sommerfeld integral type and can be expressed as the inverse Bessel transformation,

$$\bar{G}_{E,M}(z, \rho) = 2\pi \int_0^{\infty} \tilde{\bar{G}}_{E,M}(z, \lambda) J_0(k_0 \rho \lambda) \lambda d\lambda ; \quad \rho = \sqrt{(x-x')^2 + (y-y')^2} \quad (9)$$

where the spectral-domain Green's functions $\tilde{\bar{G}}_{E,M}(z, \lambda)$ satisfy the voltage distribution in an equivalent multi-section transmission line. Our implementation of MPIE utilizes an efficient technique for semi-analytical evaluation of the corresponding Green's functions and is, therefore, well suited for optimization of printed antennas in a medium with many dielectric layers [11]. A Galerkin moment method approach is used to numerically solve the integral equation (8) for the unknown current densities. For the present problem, each strip conductor is assumed to have an electrically small width, thus the current on the strip is primarily flowing along its length.

To optimize the gain, the printed Yagi-like structure is represented by a column vector as given below:

$$\bar{X} = [L_{dri}, L_{dir}(1), \dots, L_{dir}(N), \epsilon_r(1), \dots, \epsilon_r(N), dl(1), \dots, dl(N)]^T \quad (10)$$

where L_{dri} and $L_{dir}(i)$, $\epsilon_r(i)$ and $dl(i)$ are length of the driver element, length of the ith director element, dielectric constant and thickness of the ith dielectric layer, respectively. Length of the vector in (10), in view of the mutations (2)-(3), is in general $n = 6N+1$. For the gain optimization we construct the Fitness function as,

$$F(\bar{X}) = -Gain(\theta, \phi; \bar{x}) + \sum_m P_m(\bar{x}) \quad (11)$$

where *Gain* is the power gain in (θ, ϕ) direction obtained from the moment method solution of the integral equation in (8); P_m , $m = 1, 2, \dots$, are the penalty criteria for violating a set of constraints chosen to ensure that the optimized solutions are practically feasible.

In the first example, we present the performances of the EP algorithms with CMO and GMO in an unconstrained optimization of a five-layer Yagi array with air dielectric layers. The population size and the number of opponents were set to $\mu = 100$ and $q = 10$, respectively. Optimization was performed with respect to lengths of the elements and thickness of the layers. Figure 11 shows the mean fitness-value trajectory of the best population member after 10 trial runs were performed. As seen CMO performs much better than GMO in terms of convergence rate. A gain of better than 17dBi was obtained after 155 generations.

In the second example, a Yagi-like array in a 3 layer medium was optimized with $\mu = 20$, $q = 8$ and subject to the constraints of $D = d_1 + d_2 + d_3 < 0.15\lambda_0$ and radiation efficiency, $e_s > 95\%$. The optimization parameters in this case were lengths of the elements, thickness of the layers and the dielectric constants, which were allowed to vary in the range of 2 to 4. It was observed that ϵ_{r1} and ϵ_{r2} always tended to 2 while ϵ_{r3} tended to 4; this is consistent with the high gain condition for an embedded dipole [12]. The corresponding mean fitness trajectories for EP algorithms with CMO and GMO over 10 trials are plotted in Figure 12. EP with GMO performs better than EP with CMO for this constrained optimization case. Gain of about 13 dBi with $D = 0.12\lambda_0$ and $e_s = 99\%$ was obtained within 200 generations. It is noteworthy that the same structure without the director elements has a gain of only about 7.5 dBi. Gain and surface-wave powers of this structure are plotted as a function of normalized frequency in Figure 13. As can be seen at the maximum gain, the power coupled into the surface waves is minimized.

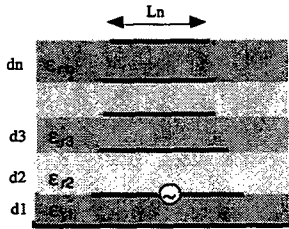


Fig. 10: A multi-layered printed Yagi array

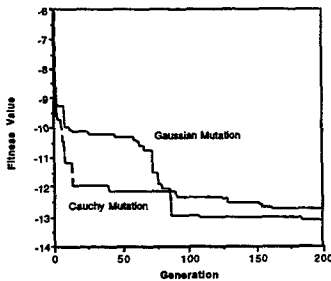


Fig. 12: A multi-layered printed Yagi array

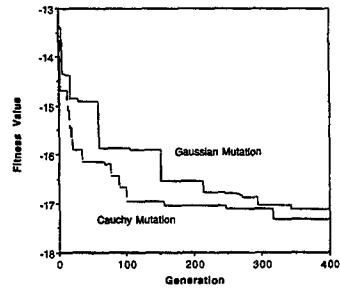


Fig. 11: Convergence rates for an air dielectric

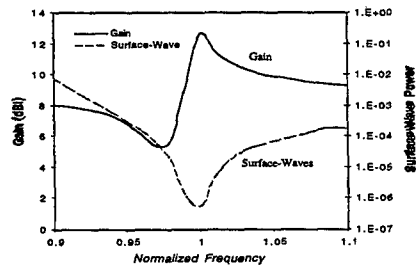


Fig. 13: Gain and surface-wave power vs frequency

IV. Conclusions

In this paper we presented the implementations of two Evolutionary Programming algorithms with two different mutation operators for global optimization of multimodal objective functions. We then performed a comparative study of these algorithms in optimization of selected antenna problems. It was shown that EP with a Cauchy operator result in a much faster convergence than EP with a Gaussian operator for unconstrained or weakly-constrained optimizations of objective functions with many local optima. The performance of Cauchy operator, however, degrades when antenna objective function is subjected to sever design constraints in which case the Gaussian operator performs better. A hybrid EP optimization technique that combines these two operators and its application to electromagnetic problems is presently under investigation.

References

- [1] D. B. Fogel, *Evolutionary Computation: Toward a New Philosophy of Machine Intelligence*, Piscataway, NJ: IEEE Press, 1994.
- [2] T. Bäck, *Evolutionary Algorithms in Theory and Practice*, Oxford Univ. Press, 1996.
- [3] D. E. Goldberg, *Genetic Algorithms in Search, Optimization and Machine Learning*, 1989.
- [4] D.S.Weile and E. Michielssen, "Genetic algorithm optimization applied to electromagnetics: A review," *IEEE Trans. Antennas Propagat.*, March 1997.
- [5] J. M. Johnson and Y. Rahmat-Samii, "Genetic algorithms in engineering electromagnetics," *AP-S Magazine*, August 1997.
- [6] *Electromagnetic Optimization by Genetic Algorithms*, edited by Y. Ramat-Samii and E. Michielssen, John Wiley & Sons, 1999.
- [7] K. Chellapilla and A. Hoorfar, "Evolutionary programming: an efficient alternative to genetic algorithms for electromagnetic optimization problems," *IEEE AP-S Int. Symp.*, Atlanta, June 1998.
- [8] A. Hoorfar and K. Chellapilla "Gain optimization of a multi-layer printed dipole array using evolutionary programming," *Proceedings of the IEEE AP-S International Symposium*, Atlanta, GA, pp. 46-49, June 1998.
- [9] K. Chellapilla, A. Hoorfar and S.S. Rao, "Optimization of thinned phased arrays using evolutionary programming," *Proceedings of EP'98 : The Seventh Intl. Conf. on Evolutionary Programming*, March 1998.
- [10] X. Yao and Y. Liu, "Fast evolutionary programming," *Proc. of 5th Conf. on Evol. Prog.*, L. J. Fogel, P.I. Angeline, T. Bäck (editors), MIT Press, Cambridge, MA, 1996.
- [11] A. Hoorfar and D. C. Chang, "Semi-analytical solutions for microstrip Green's functions in multi-layered media," *Proceedings of the 1998 International Symposium on Electromagnetic Theory*, pp. 618-620, May 1998, Thessaloniki, Greece.
- [12] D. R. Jackson and N. G. Alexopoulos, "Gain enhancement methods for printed circuit antennas," *IEEE Trans. Antennas Propagat.*, Vol. AP-33, pp. 976-987, Sept. 1985.

A Statistical Intercomparison of Binary and Decimal Genetic Algorithms.

Yee Hui Lee, Stuart J Porter, Andrew C Marvin.
Department of Electronics, University of York
York, YO10 5DD, United Kingdom
Fax: (+44) 1904 43 3224, E-mail: yhl100@york.ac.uk

Abstract— The use of genetic algorithms for the design of antennas has become increasingly popular in recent years. This is due to their versatility and ability to perform a rigorous search in complex multi modal search spaces. Much attention has been placed on binary genetic algorithms. In this paper, a real parameter genetic algorithm [3] for the optimisation of antenna design is presented. A statistical comparison is made between real and binary genetic algorithms for the design of array antennas. It is shown that by using real parameters, the problem space can be better defined, and a higher fitness value can be obtained. With the crossover adopted here, the problem space is searched more thoroughly than with the binary genetic algorithms. The paper shows that the real parameter genetic algorithms perform much better than the binary genetic algorithms for the optimisation of array antennas. The different genetic algorithms are applied to practical antenna design problems to verify the performance of the real parameter genetic algorithms.

I. INTRODUCTION

In the field of antenna design [1]-[2], much work has been done on the use of binary genetic algorithms [7]-[13] as a search tool. Few have looked into the use of the continuous parameter genetic algorithm. In this paper, an in depth look into the difference between the binary and decimal genetic algorithms (GAs) is presented. Statistical comparison was done using a realistic array antenna design problem. Statistics show that the decimal GAs perform relatively better than the binary GAs.

There are many advantages of using decimal GAs over binary GAs. As is well-known, most practical problems which require optimisation consist of a number of real parameters. Traditionally, in order to apply the genetic algorithm onto these problems, the real parameters have to be encoded into binary form. By using real parameter GAs, this process can be eliminated. Furthermore, in the binary GAs, the resolution of the parameters is determined by the number of bits in which the parameters are encoded. As the decimal GAs eliminate this encoding and decoding process, the results obtained have a higher resolution. Another advantage of real parameter GAs is that, by using appropriate real value crossover, it is shown that the problem space is searched more thoroughly.

The paper will look at how real parameter GAs are similar to the binary GAs. This is then followed by the statistical comparison of various binary coding methods and decimal coding methods using an antenna design problem. Through the example, it has been shown that the decimal GAs perform better than the binary GAs.

II. THE GENETIC ALGORITHMS

When applying the binary genetic algorithm to an antenna design problem, the following steps are taken:

1. Decimal to binary coding.
2. Selection.

3. Crossover.

4. Mutation.

These steps are repeated over a number of iterations until the GA converges to a desired fitness value. If the values do not converge, these steps are repeated until a total number of generations is reached. In this case, the total number of generations is set to 50. When applying the decimal GA, similarly, the above mentioned steps are repeated. The following describes the differences and similarities of the binary and decimal GA.

A. Decimal to binary coding

When a GA is applied to a real parameter problem such as array antenna design, the real parameters have to be coded into binary bit strings. One of the advantages of using real parameters GA is to reduce the computational complexity of coding the real parameters into binary bit strings in order to form the chromosomes. In the real parameter GA, the chromosomes are formed by placing the parameters to be optimised directly in the form $(x_1 \ x_2 \ x_3 \ \dots \ x_i)$.

B. Selection schemes

Selection introduces the influence of the fitness function to the GA optimization process [15]. The selection scheme can not be based solely on choosing the best chromosome, because the best chromosome may not be very close to the optimal solution. Therefore, there should be some chance that relatively unfit chromosomes are selected, so as to ensure that genes carried by unfit chromosomes are not lost permanently from the population. In general, the selection scheme should be one which relates the fitness of the chromosomes to the average fitness of the population.

Many selection schemes have been developed [4]-[5]. Two of the more widely used selection schemes are presented in this paper. These two selection schemes are used for both the decimal and binary GAs.

Elitism Roulette Wheel Selection - The Elitism Roulette Wheel Selection (ERWS), is a combination of the elitism and roulette wheel selections. In ERWS, all the chromosomes are ranked according to their fitness values. The fittest top 10% of the population is taken and put directly into the new population. The remaining population is filled up by a roulette wheel selection scheme [4]. In this scheme, all the members are allocated a section on the wheel. The proportion of the section allocated depends on the fitness of the chromosome. The wheel is then spun and a chromosome is selected into the new population.

Tournament Selection - The tournament selection uses the tournament method as described in [5]. In this process, a sub-population of N individuals is chosen at random from the original population. The individuals in this sub-population compete using their fitness value. The fittest individual in the sub-population wins the tournament and is selected into the new population. All the members in the sub-population are then placed back into the original population and this process is repeated until the new population is filled up. The most common binary tournament selection scheme, where N equals 2, is used.

C. Binary Crossover Methods

After obtaining the new population, the next step is to perform crossover. The crossover operator takes two parent chromosomes from the new population and generates two child chromosomes. By performing crossover, good characteristics from the parents can be passed on to the children. Like the selection scheme, many variations of crossover have been developed [16]. In this paper, the more effective crossover methods are examined.

Traditional Single-Point Crossover - A single random location in the parent chromosomes is selected. Bits in the parent chromosomes preceding the crossover point are copied directly into the children, whereas bits after the crossover point are swapped.

Multi-Point Crossover - The multi-point crossover is a natural extension of the single-point crossover. Instead of choosing a single crossover point at which the genes are swapped, more than one point is chosen (in this study eight points are chosen), breaking the chromosomes into segments. The segments at the randomly chosen crossover points are exchanged to produce children. This reduces the positional bias of a single-point crossover.

Uniform Crossover - Uniform crossover exchanges bits rather than segments [14]. For each bit in the chromosome, the bits from the two parents are exchanged with a fixed probability p . Since the probability of exchanging two bits in each position is independent of the choice made with regard to any other position, uniform crossover has no positional bias.

D. Decimal Crossover Method

As was shown in [3], a simple one point binary crossover can be seen as a perturbation of the parents. This can be illustrated using a simple example. Taking the range of the parameters to be optimised to be between 0 and 1, and the parameters to be encoded into 4 bit strings, two arbitrary parents, 0.5 and 0.875, are chosen. The corresponding binary form would be 10 00 and 11 10 respectively. During crossover, a random crossover point is taken, in this case, between bits 2 and 3. The children obtained through a single-point crossover from the parents would then be 10 10 and 11 00, which correspond to decimal values 0.625 and 0.75. The interchange of the less significant bits 10 and 00 correspond to a difference of 0.125. Looking back at the two child chromosomes produced from the parents, this is simply a perturbation of ± 0.125 where child one is obtained from parent one through $(0.5 + 0.125)$ and child two from parent two through $(0.875 - 0.125)$.

If the size range of the two parents, P_1 and P_2 , is $R = P_2 - P_1$, then the two children, C_1 and C_2 , will be given by

$$C_1 = P_1 + F(R) \quad (1)$$

$$C_2 = P_2 - F(R). \quad (2)$$

By substituting R , we find that, in the real parameter crossover, the two children can now be written as,

$$C_1 = (1 - F)P_1 + F(P_2) \quad (3)$$

$$C_2 = (1 - F)P_2 + F(P_1). \quad (4)$$

where F is a factor to be chosen. This is similar to the random crossover point chosen in the binary GA. In this particular example, the factor, F , has a value of $\frac{1}{3}$.

The fundamental and most meaningful part of coding a real parameter problem into binary code for genetic algorithm is the conservation of the schemata, "similarity template", in the chromosomes. From the example above, it has been shown that the schemata in the parent chromosomes can also be preserved even in a real parameter genetic algorithm. This is done by doing perturbation to the real parameter parents during the crossover stage. For one point crossover, a single factor value F is chosen as the crossover factor, in place of the crossover point.

In the decimal GA, the factor F determines how well the search space is being searched. In the single-point crossover, very often, the more significant bits in the chromosome are not altered due to the lower probability of a high crossover point. However, with an appropriate factor F chosen, the probability of crossover at more significant bits is increased. This results in a more rigorous search of the entire problem space.

E. Mutation

In GAs, mutation is performed to ensure that the population is not caught in a local minimum and also to ensure a diversity in the population. In the binary GAs, mutation is performed by randomly flipping a bit from its original

state to its complementary state, from 0 to 1 or 1 to 0. Similarly, in the decimal GA, mutation can be performed by randomly altering the value of the parameter. This is done by doing a perturbation of the original parameter.

For example, if a particular parameter (P_i) is chosen to undergo mutation, then a factor (F_{mut}) of the parameter range (R) is added or subtracted from the parameter. This results in a new parameter ($P_i \pm F_{mut}R$). In order to maintain a fair comparison of the two genetic algorithms, the probability of mutation for the decimal GA is lowered. For example, if the 5 parameters are represented by a chromosome of length 100, and the probability of mutation of each bit is 1%, then the probability of mutation for the decimal GA will be reduced to 0.2% for each parameter.

III. ADVANTAGES OF DECIMAL GA

From the above analysis, it can be seen that the real parameter genetic algorithm can be viewed as a binary genetic algorithm by means of perturbation. Notice that the conservation of schemata is still preserved. There are many advantages of using real parameter genetic algorithms in antenna optimisation:

1. The real parameter need not be converted from decimal to binary every single time the fitness function is calculated. This increases the efficiency of the code.
2. In the binary GA, the precision of the parameters are determined by the number of bits in which the parameters are coded, the resolution. However, with the use of real parameters, there will be increased precision as there will be no loss in resolution during coding.
3. The problem space can be searched more rigorously by choosing a larger value of factor F .

IV. ANTENNA DESIGN PROBLEM

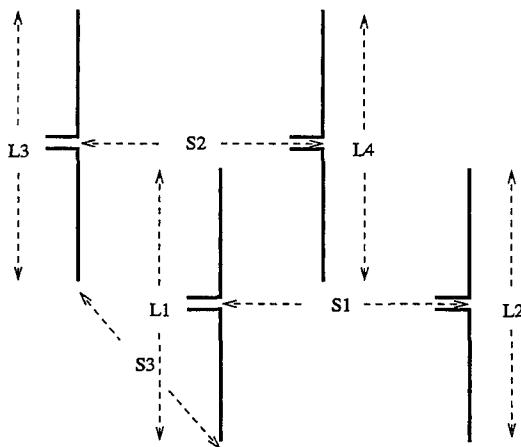


Fig. 1. Antenna structure used for comparison.

The example used for comparison of the methods described is a simplified antenna design problem shown in Fig. 1. This antenna is designed for immunity and susceptibility testing. Therefore, it was designed to satisfy the following criteria.

1. Radiate a uniform near electric field over a $5m$ by $3m$ plane situated at a distance of $3m$ in front of the antenna. The field magnitude must not vary by more than $+0dB$ and $-3dB$ over the frequency range $30MHz$ to $100MHz$.
2. The uniform near electric field is required to be as close to $10V/m$ as possible.
3. Transmitted power is maximised for the limited input power.

In order to ensure field uniformity, 77 uniformly distributed grid points on the plane of interest is taken. The fitness function maximises the number of points which are within $3dB$ range of each other. In order to ensure that the desired field intensity is achieved, the difference between the simulated near field strength and the desired field strength ($10V/m$) is minimised. Finally, the fitness function has to maximise the power transmitted by the antenna. The higher the fitness value, the better the fitness of the chromosome.

The antenna design consists of four individual dipoles, two dipoles in front and two behind (Fig. 1). There are 8 parameters to be optimised: the individual length of the dipoles (L_1 , L_2 , L_3 and L_4); the spacing between the front dipole pair (S_1); the spacing between the back dipole pair (S_2); the spacing (S_3) and phase (L_o) between the front and back dipole pairs.

A. Simulation

The eight different decimal and binary algorithms described in the above section were used to optimise the structure in Fig. 1. Simulations were done using the Numerical Electromagnetic Code (NEC). For each algorithm, the simulation was performed on a population of 50 chromosomes over 50 generations. Each algorithm was run 50 separate times and results generated from all 50 runs were compared and tabulated in Table. I.

B. Comparison of Different GAs

TABLE I
COMPARISON OF DIFFERENT GENETIC ALGORITHMS

Name	ERW_{DEC}	ERW_{SP}	ERW_{MP8}	ERW_{UNI}
Max. Pts. in $3dB$	1.000	1.000	1.000	1.000
Ave. Pts. in $3dB$	0.940	0.888	0.896	0.910
Max. Power Trans.	0.966	0.977	0.977	1.000
Ave. Power Trans.	1.000	0.919	0.929	0.908
Min. E.Field from $10V/m$	1.000	0.756	0.778	0.827
Ave. E.Field from $10V/m$	0.919	0.953	0.933	1.000
Max. Fitness	1.000	0.968	0.986	0.994
Ave. Fitness	1.000	0.936	0.944	0.958

Name	$Tourn_{DEC}$	$Tourn_{SP}$	$Tourn_{MP8}$	$Tourn_{UNI}$
Max. Pts. in $3dB$	1.000	1.000	1.000	1.000
Ave. Pts. in $3dB$	0.900	0.858	0.866	0.862
Max. Power Trans.	0.971	0.971	0.995	0.975
Ave. Power Trans.	0.911	0.896	0.882	0.854
Min. E.Field from $10V/m$	0.882	0.754	0.745	0.831
Ave. E.Field from $10V/m$	0.913	0.846	0.845	0.793
Max. Fitness	0.998	0.953	0.967	0.979
Ave. Fitness	0.904	0.889	0.893	0.874

The values in Table I are all normalised for easy comparison. They are normalised to the maximum value achieved by the eight different algorithms. In Table I, ERW represents elitism roulette wheel selection, $Tourn$ is tournament

selection, *DEC* is decimal crossover, *SP* is single-point crossover, *MP8* is 8 point multi-point crossover and *UNI* is uniform crossover with 0.5 exchange rate. The overall fitness function optimises 3 objectives. To maximise the number of points, of the 77 points, on the plane of interest which lie within 3dB of each other. The first two rows in the table show the maximum and average number of points which lies within a 3dB range; secondly, maximum power transmission; the next two rows in the table show the maximum and average power transmission for the 125000 simulations; finally, ensure that the near electric field on the plane of interest is as close to 10V/m as possible. The following two rows shows the minimised and average electric field strength. And the final two rows show the maximum and the average of the overall fitness function.

In [16], it has been shown that the 8 point multi-point crossover is the best crossover operator when used to optimise five different functions, and the uniform crossover with a 0.5 exchange rate is one of the better performers. From the results obtained here, it can be seen that the decimal outperforms the other algorithms. The decimal crossover has found higher overall fitness values for both the ERWS and the tournament selection. Looking at the maximum fitness value, it can be seen that most of the algorithms were able to come to a relatively high fitness value at least once over the 50 runs. This is shown by the maximum fitness value achieved in Table I, where the normalised maximum fitness value for all the algorithms are close to 1. However, when the average fitness value is calculated, it can be seen that the average fitness of the decimal algorithms is much higher then the other algorithms. From this, we can conclude that on average, the decimal algorithm performs much better then the binary algorithms. Looking at each individual objective function and the overall fitness function, it can be seen that for the ERW selection, the decimal crossover has the best performance. This is followed by the uniform crossover, which is performing quite well. The single-point crossover has the worst performance. For the tournament selection, the decimal GA performs predominantly better, whereas the different binary GAs have more or less similar performance with the multi-point crossover performing slightly better then the rest.

The table also shows that there is a compromise between the different objectives in the overall fitness function. For example, the decimal GA has found designs which have good performance in near electric field strengths by getting designs with many near field points within 3dB range and as close to 10V/m as possible. However, these designs seem to be less efficient in power transmission. It is clear that the ERW selection is a comparatively better selection method than the tournament selection. Almost all the objective and fitness values found from the tournament selection are less then those found by the ERW selection.

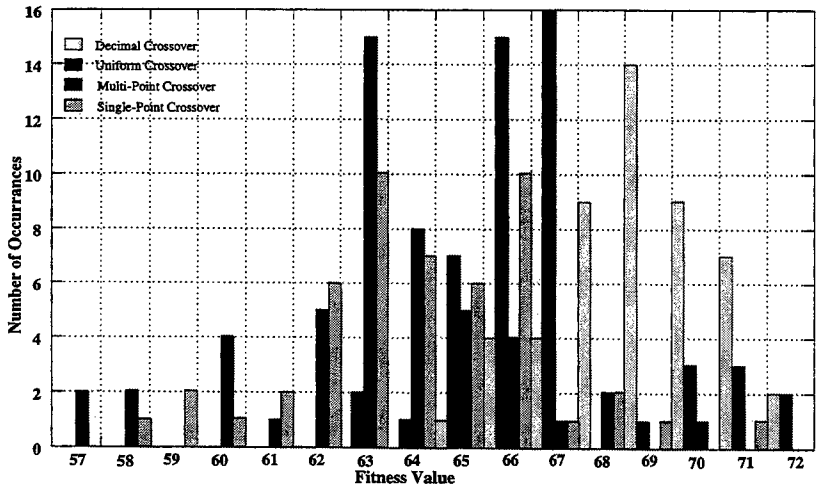


Fig. 2. Probability distribution of fitness function.

Fig. 2 shows the probability distribution for the 50 runs of the four different algorithms. The relatively higher performance of the decimal GA becomes obvious in this plot. Most of the runs of the decimal GA ended up with a high fitness value. The uniform crossover GA is producing very promising results as well. However, the single-point and multi-point crossover are less effective in coming to a high fitness value. From the results shown in the table and the bar chart, it has been shown that the decimal GA is performing much better than the rest of the binary GAs. This is true for array antenna optimisation.

C. Convergence Trend

These results produced from a total of 125000 simulations show that the decimal algorithms give significantly better fitness values. When looking into the details of each new run of the simulation, a few details were noted.

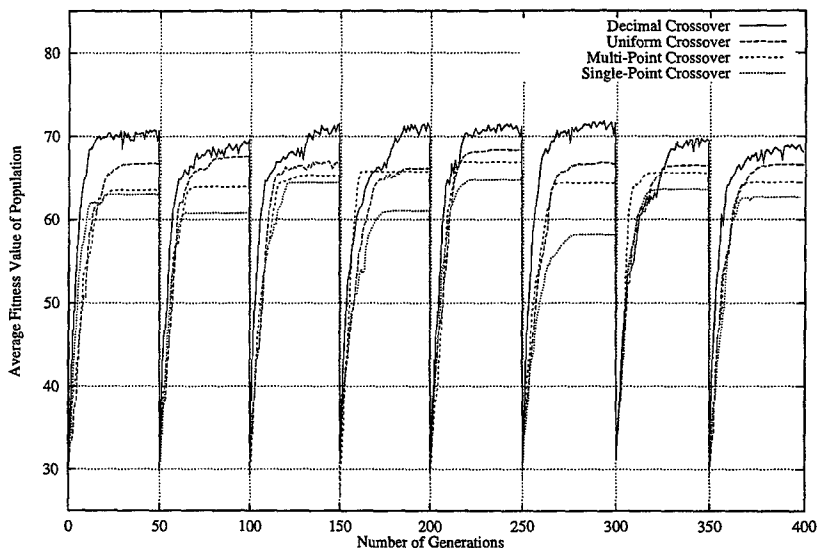


Fig. 3. Average fitness of a population of 50 for a single run.

Fig. 3 shows 8 separate runs of each of the four GAs using ERW selection. The average value of the population of 50 chromosomes for each generation is plotted. Each run of the algorithms consists of 50 generations. Firstly, the convergence of the binary GA is faster as compared to the decimal GA. This can be seen from Fig. 3, where the multi-point crossover and the single-point crossover GAs converge to a single value relatively soon (after 20 generations) and then levels out. The uniform crossover and the decimal crossover tends to converge later. The single-point crossover, on average converges to a lower fitness value, although it converges faster. Although the uniform crossover converges later, it converges to a much fitter population. When the GA converges to a single value before the 50 generations are up, the mutation rate is increased to ensure a varied population is maintained. In the case of the decimal GA, it tends to converge relatively slower. This is due to a more varied population maintained by the decimal GAs while performing its rigorous search. This can clearly be seen from Fig. 3, where the fitness value of the decimal crossover seems to vary quite a bit even after 30 generations. The decimal crossover, on the average, comes to a relatively higher fitness value. Therefore, although the decimal GA converges at a later stage, it approaches a fitter final population. From Fig. 3, the binary GA reaches a final fitness value and levels

out after about 20 iterations. However, even after 30 iterations, the decimal GA still seems to be maintaining a highly varied population as compared to the binary GAs.

There is no known solution to this antenna design problem and thus no known global optima. However, through statistics, running the algorithms 50 times each time with a different randomly chosen initial population, it can be seen that the decimal GA is able to reach a better fitness value as compared to the binary GA.

V. SUMMARY

In this paper, the link between decimal genetic algorithms and binary genetic algorithms has been studied. The use of decimal genetic algorithm for array antenna design has been examined. This is done using statistics collected from fifty runs of each algorithm. The statistics obtained have been analysed and it has been found that the decimal GA performs better for array antenna designs. Various aspects such as the speed of convergence and the trend of convergence have also been analysed. A statistical comparison was also done for the different selection schemes.

Finally, a practical antenna design problem was optimised using the better of the two selection schemes. Four antenna designs were arrived at: one obtained from the decimal GA; one from the uniform crossover GA; one from the multi-point crossover GA; and the one from the single-point crossover GA. Results show that the antenna design from the decimal GA performs much better than that from the binary GA. This again confirms that the decimal GA performs better than the binary GA for array antenna design.

REFERENCES

- [1] J. D. Klaus, *Antennas*, McGraw-Hill, 1988.
- [2] T. Gilligan, *Modern Antenna Design*, McGraw-Hill, 1985.
- [3] A. H. Wright, "Genetic Algorithms for Real Parameter Optimization," *Foundation of Genetic Algorithms*, San Mateo, CA: Morgan Kaufmann, 1991.
- [4] D. E. Goldberg, *Genetic Algorithms in search, optimization & Machine Learning*, Reading, MA: Addison-Wesley, 1989.
- [5] J. M. Johnson and Y. R. Sam ii, "Genetic Algorithms in Engineering Electromagnetics," *IEEE Antennas Propag. Mag.*, vol.39, No. 4, pp.7-25, Aug. 1997.
- [6] R. L. Haupt, "An Introduction to Genetic Algorithms for Electromagnetics," *IEEE Antennas Propag. Mag.*, vol.37, No. 2, pp.7-15, April 1995.
- [7] E. E. Altshuler and D. S. Linden, "Wire-Antenna Designs Using Genetic Algorithms," *IEEE Antennas Propag. Mag.*, vol.39, No. 2, pp.33-43, April 1997.
- [8] E. A. Jones and W. T. Joines, "Design of Yagi-Uda Antennas Using Genetic Algorithms," *IEEE Trans. Antennas Propag.*, vol.45, No. 9, pp.1386-1392, Sep. 1997.
- [9] R. L. Haupt, "Thinned Arrays Using Genetic Algorithms," *IEEE Trans. Antennas Propag.*, vol.42, No. 7, pp.993-999, July 1994.
- [10] A. Boag, E. Michielssen and R. Mittra, "Design of Electrically Loaded Wire Antennas Using Genetic Algorithms," *IEEE Trans. Antennas Propag.*, vol.44, No. 5, pp.687-695, May 1996.
- [11] E. E. Altshuler and D. S. Linden, "Design of a Loaded Monopole Having Hemispherical Coverage Using a Genetic Algorithm," *IEEE Trans. Antennas Propag.*, vol.45, No. 1, pp.1-4, January 1997.
- [12] Z. Altman, R. Mittra and A. Boag, "New Design of Ultra Wide-Band Communication Antennas Using Genetic Algorithm," *IEEE Trans. Antennas Propag.*, vol.45, No. 10, pp.1494-1501, Oct. 1997.
- [13] B. Kemp, S. J. Porter and J. F. Dawson, "Optimization of Wire Antennas Using Genetic Algorithms and Simulated Annealing," *ACES Symposium Proceedings*, vol. II, pp.1350-1357, March 1997.
- [14] D. H. Ackley, *A Connectionist Machine for Genetic Hillclimbing*, Kluwer Academic Publishers, Boston, MA, 1987.
- [15] D. E. Goldberg, and K. Deb, "A Comparative Analysis of Selection Schemes Used in Genetic Algorithms," *Foundations of Genetic Algorithms*, Morgan Kaufmann, pp.69-93, 1991.
- [16] L. J. Eshelman, R. A. Caruana and J. D. Schaffer, "Biases in the Crossover Landscape," *Proc. 3rd Int. Conf. on Genetic Algorithms*, pp.10-19, 1989.
- [17] G. J. Burke and A. J. Poggio, *Numerical Electromagnetic Code (NEC) - Method of Moments*, Lawrence Livermore National Laboratory Rept. UCID-18834, January 1981.

The Compact Genetic Algorithm: A Litmus Test for Genetic Algorithm Applicability

Daniel S. Weile* and Eric Michielssen

David E. Goldberg

Center for Computational Electromagnetics
Department of Electrical and Computer
Engineering
University of Illinois at Urbana-Champaign
1406 W. Green St., Urbana, IL 61801, USA
dsw@decwa.ece.uiuc.edu

Illinois Genetic Algorithm Laboratory
Department of General Engineering
University of Illinois at Urbana-Champaign
104 S. Mathews Av., Urbana, IL 61801, USA

Abstract

The compact genetic algorithm is introduced both as a new optimization method for general electromagnetics design problems and as a tool for determining the applicability of evolutionary optimization methods to a given problem. Unlike the simple genetic algorithm, which guides an entire population of solutions toward an optimal design, the compact genetic algorithm operates on a vector of probabilities representing the distribution of alleles in a virtual population. Because of its simplicity, the compact genetic algorithm may be a better choice than the "simple genetic algorithm" for many problems. Moreover, because the compact genetic algorithm mimics the behavior of the simple genetic algorithm, its failure for a given problem may indicate a need for more advanced techniques. Numerical results demonstrate both of these uses for the compact genetic algorithm with applications to problems of electromagnetic interest.

1. Introduction

Since the early 1990's, genetic algorithms (GAs) have steadily gained popularity as synthesis tools for electromagnetic device design [1-3]. The rapid growth of interest in GAs is a direct result of their remarkable qualities as optimization methods:

- They return global or strong local optima for a wide variety of multimodal optimization problems,
- They work only with objective function values and thus require no derivative information,
- They have the ability to optimize functions of both discrete and continuous variables, and
- They are simple to implement and are broadly applicable.

Despite these beneficial qualities, however, GA practitioners have found that the picture is not always so rosy. GAs are often lethargic in success and inscrutable in failure. Given a specific electromagnetic design problem, it is generally impossible to tell if it is amenable to optimization by a simple GA (SGA) without extensive experimentation. Worse yet, the SGA is a stochastic algorithm depending on a plethora of parameters and operators, making it difficult to determine if the failure of the algorithm is a result of parameter choice, poor operator design, insufficient run time, or the inapplicability of the SGA technique altogether.

In this paper, a compact genetic algorithm (cGA) is introduced into electromagnetic optimization to help answer these questions [4]. The cGA, which is an interesting optimization algorithm in its own right, mimics the behavior of an SGA using tournament selection and uniform crossover. Because it does not operate on a population in the usual sense, but instead represents the population by a vector of Bernoulli random variables, its operation depends on only a small number of parameters. This permits a more thorough study of GA applicability as the parameter space is quite small. Moreover, as will be seen below, convergence of the cGA to a single, well-defined solution is all but inevitable, removing the necessity of altering algorithm parameters to see if the GA has "really" converged. The description of the algorithm and numerical examples will show that these qualities of the cGA make it useful not only as an optimizer, but also as a diagnostic tool for GA applicability.

The remainder of this paper will proceed as follows: Section 2 presents the cGA itself, and discusses its relation to the SGA. Section 3 then demonstrates the usefulness of the cGA both as an optimizer and as a diagnostic. Finally, Section 4 presents the conclusions of the study.

2. The Compact Genetic Algorithm

Much like the SGA, an application of the cGA to a given problem first involves encoding design parameters into a bit string (of length l) called a chromosome. This process is well documented in the literature and is not discussed here; the interested reader is referred to Goldberg [5] for a description. Once such a coding has been fixed, the optimization problem of interest (assuming it is a maximization problem) can be stated in mathematical terms: Find a chromosome c^* such that $f(c^*) \geq f(c)$ for a given objective function f and for all chromosomes c of length l .

To solve this optimization problem, the cGA begins by initializing all components of a real-valued *probability vector* p of length l to a value of 0.5. This probability vector can be thought of as representative of the population of a virtual SGA: Each component p_i of the vector p represents the fraction of the population which contains the allele (bit) "1" in locus (component) i , $i = 1, \dots, l$. The initialization of the components of p to 0.5 is thus equivalent to choosing alleles in the starting SGA population at random with equal probability.

A chromosome $c = [c_1 \dots c_l]$ may be generated at random using this vector of probabilities with the following procedure: For each locus in the vector, a random number $0 \leq r_i < 1$ is generated and compared to p_i . If $r_i \leq p_i$, c_i is set to 1, otherwise c_i is set to 0. The cGA "generation" thus begins by generating s chromosomes c^j , $j = 1, \dots, s$. Each of these chromosomes is then evaluated by the objective function f , and assigned an objective function value $f^j = f(c^j)$.

The objective function values can be used to update the population vectors in the direction of the best chromosome of the bunch. First, the best of the s chromosomes is located. (Without loss of generality, assume the best chromosome is c^1 .) This chromosome is then compared, bit by bit, to the other (inferior) $s-1$ chromosomes, and the probability vector is updated using a very simple rule: Define integers $2 \leq j \leq s$ and $N > 1$. Then, for each inferior chromosome j , if $c^1_i = 1$ and $c^j_i = 0$, p_i is incremented by $1/N$. On the other hand, if $c^1_i = 0$ and $c^j_i = 1$, p_i is decremented by $1/N$. Finally if $c^1_i = c^j_i$, p_i is left unaltered.

This process of generating chromosomes, evaluating them, and updating the probability vector is continued until all components of \mathbf{p} are either 0 or 1. This final probability vector is the solution returned by the cGA. A flowchart of the process is shown in Figure 1.

Like the probability vector \mathbf{p} , which functions as a compact representation of the SGA population, the parameters N and s also have SGA analogues. Specifically, N is equivalent to the SGA's population size, and s is represented of the tournament size in an SGA using tournament selection and uniform crossover [4]. To see this, consider a cGA with $s = 2$. At each stage of the algorithm, two chromosomes are generated, and the proportion of the better chromosome's alleles at each position is increased by $1/N$. This is exactly the behavior that would be expected from an SGA using binary tournament selection. Similarly, increasing s simulates an increase of selection pressure in an SGA. It should be mentioned, however, that unlike the relationship between the cGA parameter N and population size, the relationship between s and tournament size is more complex.

Because of its simplicity and similarity to the SGA, the cGA can be an invaluable tool for the evolutionary optimization of electromagnetic devices in two complementary fashions. First, the cGA is useful in its own right as an optimization method. If it works for a given optimization problem, the cGA will generally give results comparable to those delivered by an SGA. Moreover, because the cGA depends on only two parameters, less experimentation is required to determine its applicability to a given problem than for an SGA.

On the other hand, if for a given problem, the cGA fails completely, or if results for a high selection rate are much better than those for a low selection rate, the SGA is likely to return poor results for that problem. In such cases, advanced genetic methods are needed. Such methods include, but are not limited to, physics-based domain decomposition methods, hybridization with local optimizers, and genetic algorithms with more advanced schema processing abilities [3].

3. Numerical Results

To demonstrate the claims of the last section, the cGA was applied to two design problems: thinned antenna arrays and polarizers. These are now discussed in turn.

The first problem comprised the thinning of a symmetric, 200-element linear antenna array of isotropic elements to reduce sidelobe levels as much as possible. The chromosome for this problem represented each of the 100 independent array elements by a single bit that indicated whether a given pair of elements in the array was turned on or off. The objective function value for a given array was taken as the decibel reduction in the highest sidelobe relative to the main lobe. The cGA was applied to this problem with 25 different values of N ranging from 20 to 500, and with s values of 2 and 4. For each parameter combination, the cGA was run 100 times, for a total of 5000 experiments. Results are presented in Figures 2 through 5. Figures 2 and 3 respectively show the average and best results obtained for each parameter combination averaged over its 100 experiments. Figure 4 shows the average number of function evaluations until convergence for each combination of parameters, and Figure 5 shows the pattern of the best design found in all 5000 runs.

Many interesting results can be gleaned from these four graphs. First, we note that while increasing the selection rate from 2 to 4 can give better results for a large enough population, the results do not improve all that much. This implies that this problem is rather easy for a GA to solve,

if one is satisfied with a very good (but not necessarily the best) solution. Moreover, though the number of function evaluations required until convergence is a roughly linear function of N , the average (and best) result returned becomes nearly constant in the vicinity of $N=100$. This lends credence to the rule of thumb that states that population size should be on the order of chromosome length [3]. Finally, it is noted that the original result for this problem reported in the literature [6] resulted in sidelobes reduced 22.09dB—about 1.4 dB less than the result shown in Figure 5, and less than the average results for $N=80$.

The second problem considered in this study involved the design of a polarizing screen. The design of periodic structures in general is known to cause difficulty for the SGA [7, 8], so this problem will demonstrate the applicability of the cGA as a litmus test. The screen (assumed to be situated in the $z=0$ plane) was to be designed to reflect the y component and transmit the x component of a plane electromagnetic wave travelling in the z direction. To solve this problem, the cGA was applied to decide which pixels in a square 16×16 grid of side Δ , periodically repeated in the $z=0$ plane, should be metallized to achieve the polarization effect.

The chromosome for this problem consisted of 128 bits used to code the metallization status of the top half of the screen, with the bottom half of the screen assumed to be the "mirror image" of the top (Figure 6). A spectral Galerkin code using rooftop basis functions [9] was used to analyze the screens using a 32×32 grid, and return the reflection coefficients Γ_x and Γ_y due to x and y polarized waves at ten frequencies between DC and c/Δ , where c is the speed of light in vacuum and Δ denotes the screen periodicity. The objective function was taken as the minimum value of the quantity

$$|\Gamma_y|^2 \left| \frac{\Gamma_y}{\Gamma_x} \right|^2 \quad (1)$$

at the ten test frequencies. Five cGA runs were executed, with $N=150$ and $s=2$. Results are shown in Figures 6, 7, and 8.

Unlike the thinning problem, the polarizer design problem has a well-known solution: the screen should be composed of thin, tightly-packed vertical strips. This solution, which is depicted in Figure 6, achieves an objective function value of 330.85. The solution achieved by the cGA, depicted in Figure 7, only achieves an objective function value of 26.78. Figure 8 compares the polarization response of the two screens by showing the ratio of the power reflection coefficient for the y -polarized wave to that for the x -polarized wave versus the "normalized frequency," defined as

$$f_{norm} = \frac{f\Delta}{c} \quad (2)$$

Clearly, the screen designed by the cGA is not a very good polarizer!

The poor result indicates that this problem would be extremely difficult for an SGA. Indeed, the authors' previous work on the GA optimization of periodic screens indicated very clearly that the SGA was not an option [8]. This of course does not imply that GAs cannot be used for these types of problems, but instead that the SGA need to be modified to force it to work. For instance, by using symmetric properties of the screen and a special GA carefully hybridized with a local search method, the authors were able to produce a three-screen FSS with two pass bands between normalized frequencies of 0.09 and 0.11 and between 0.64 and 0.74, and a stop band between normalized frequencies of 0.45 and 0.5 [8]. The response of this screen is shown as Figure 9.

For the polarizer problem presented here, a GA capable of solving the problem could be created by coding changes (such as assuming at the start that the solution will be composed of strips), or by operator modifications (such as using a single point crossover operator likely to preserve such strips). Alternatively, extended cGA-like methods that employ more powerful population representations may be used [10, 11]. In any case, the cGA has demonstrated that no amount of SGA experimentation is likely to make this problem work, and thus may be used to indicate the need for such alterations to the optimization method.

4. Conclusions

This work has introduced the cGA as a useful tool in the evolutionary optimization of electromagnetic devices. Because the cGA is a simple algorithm that mimics the behavior of the more complex SGA, it can be used as a litmus test for the applicability of the SGA, or as a useful optimization algorithm in its own right. Its usefulness as an optimization algorithm was demonstrated by application to an array thinning problem, and its importance as a litmus test was shown in a polarizer example. Numerous extensions to the technique are also possible and will be discussed in the presentation.

5. References

- [1] R. L. Haupt, "An introduction to genetic algorithms for electromagnetics," *IEEE Antennas and Propagation Magazine*, vol. 37, 1995.
- [2] J. M. Johnson and Y. Rahmat-Samii, "Genetic algorithms in engineering electromagnetics," *IEEE Antennas and Propagation Magazine*, vol. 39, pp. 7-21, 1997.
- [3] D. S. Weile and E. Michielssen, "Genetic algorithm optimization applied to electromagnetics: A review," *IEEE Transactions on Antennas and Propagation*, vol. 45, pp. 343-353, 1997.
- [4] G. Harik, F. Lobo, and D. E. Goldberg, "The compact genetic algorithm," *Proceedings of the IEEE Conference on Evolutionary Computation*, pp. 523-528, 1998.
- [5] D. E. Goldberg, *Genetic Algorithms in Search, Optimization and Machine Learning*. Reading, MA: Addison-Wesley, 1989.
- [6] R. L. Haupt, "Thinned arrays using genetic algorithms," *IEEE Transactions on Antennas and Propagation*, vol. 42, pp. 993-999, 1994.
- [7] R. Mittra, "Genetic algorithms: the last word for solving all of your design problems?," presented at IEEE Antennas and Propagation Society International Symposium, Montréal, July 1997.
- [8] D. S. Weile and E. Michielssen, "The use of domain decomposition genetic algorithms exploiting model reduction for the design of frequency selective surfaces," *Computer Methods in Applied Mechanics and Engineering*, vol. to be published, 1999.
- [9] R. Mittra, C. H. Chan, and T. Cwik, "Techniques for analyzing frequency selective surfaces-A review," *Proceedings of the IEEE*, vol. 76, pp. 1593-1615, 1988.
- [10] M. Pelikan, D. E. Goldberg, E. Cantú-Paz, "BOA: The Bayesian optimization Algorithm," *IlligAL Report No. 99003*, Illinois Genetic Algorithm Laboratory, University of Illinois at Urbana-Champaign.
- [11] G. Harik, "Linkage learning via probabilistic modeling in the ECGA," *IlligAL Report No. 99010*, Illinois Genetic Algorithm Laboratory, University of Illinois at Urbana-Champaign.

Figures

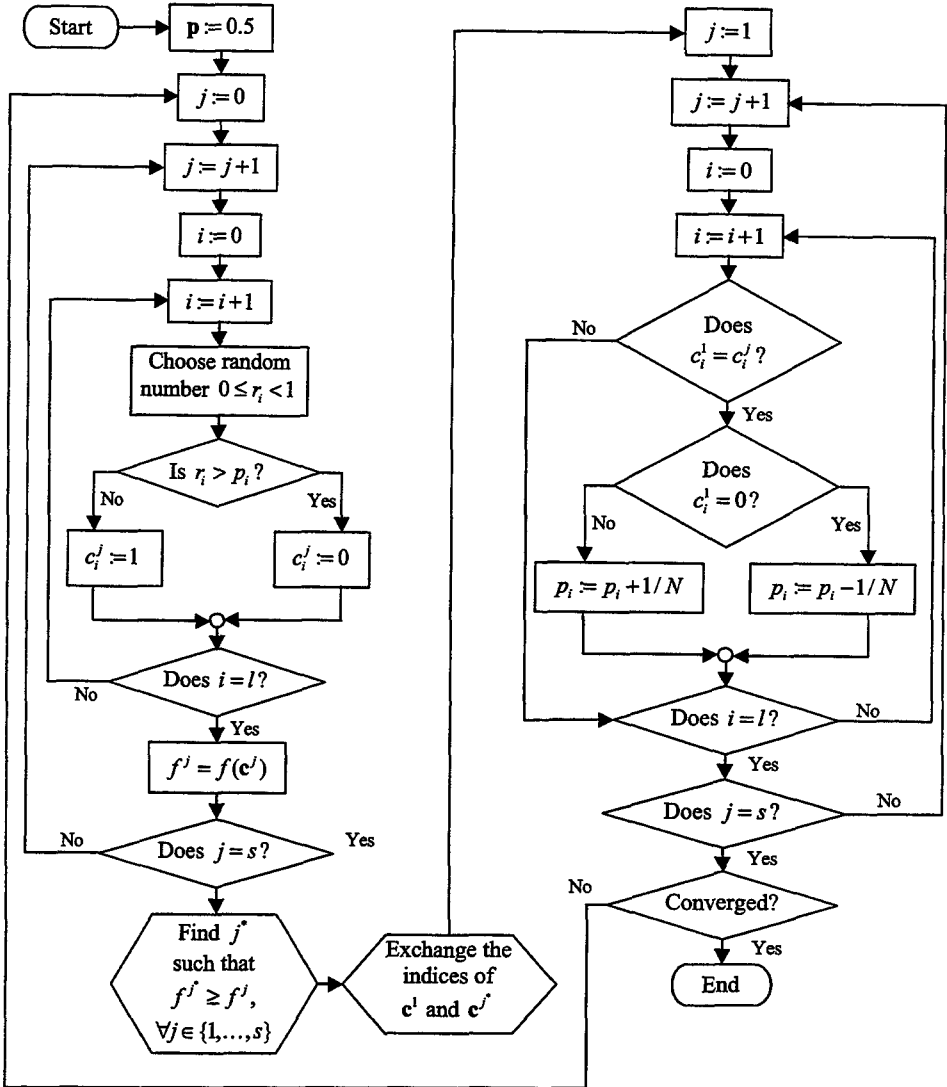


Figure 1. Flowchart of the cGA.

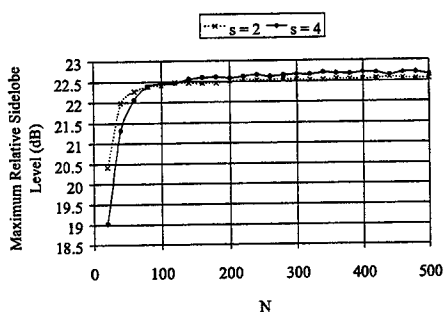


Figure 2. Average cGA results over 100 runs per parameter set.

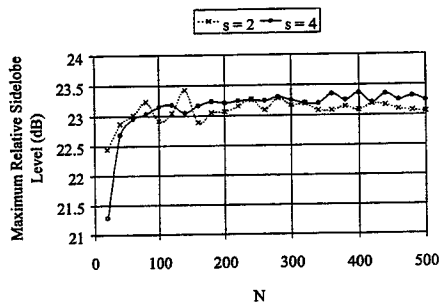


Figure 3. Best cGA results over 100 runs per parameter set.

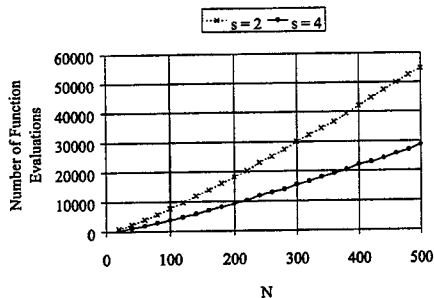


Figure 4. Average number of function evaluations required by the cGA until convergence over 100 runs per parameter set.

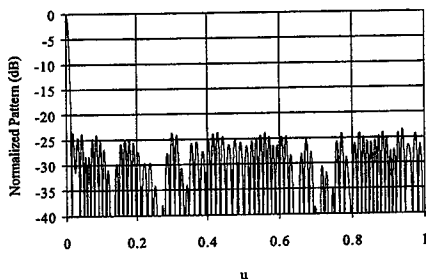


Figure 5. Pattern of the best thinned array found in 5000 cGA runs. The parameter u is the sine of the angle from broadside.

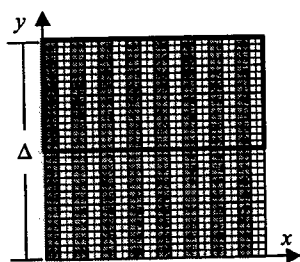


Figure 6. The optimal solution of the polarizer problem. The black lines indicate the pixel boundaries metallized by the cGA, and the gray lines show the grid used for the spectral Galerkin analysis.

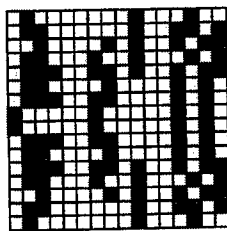


Figure 7. The "best solution" to the polarizer problem returned by the cGA.

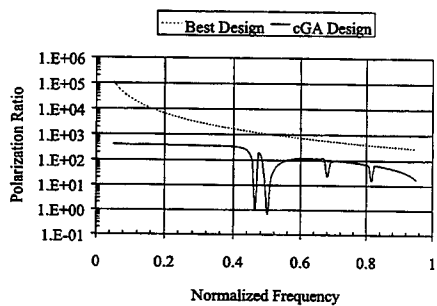


Figure 8. The response of the polarizers of Figures 6 and 7. Here, normalized frequency is the frequency in Hertz divided by c/Δ .

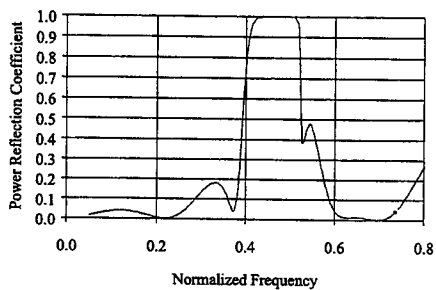


Figure 9. The response of a hybrid GA designed, three-screen FSS.

Dipole Equivalent Circuit Optimization Using Genetic Algorithm

Bruce Long, Ping Werner, and Doug Werner
Department of Electrical Engineering
The Pennsylvania State University
University Park, PA 16802

Abstract—Two broadband equivalent circuit models with component values optimized by use of a genetic algorithm are presented. The first is a conventional LCR network. The second uses transmission line segments as well as lumped components. Both exhibit good impedance fidelity over a bandwidth exceeding five octaves including the fundamental through the forth overtone response.

I. Introduction

It is often convenient to have an accurate yet simple representation of antenna self-impedance over a broad frequency band. One example that comes to mind is the evaluation of a transmitter output amplifier, harmonic filter, and antenna system. Lumped constant equivalent circuit models are typically called into service in such cases. An equivalent circuit in this sense is a network of components that has terminal frequency-impedance function essentially equivalent to an actual antenna. Of course the accuracy required to be "essentially equivalent" depends upon the application at hand.

In this paper the authors demonstrate the use of a genetic algorithm to optimize a conventional lumped component antenna equivalent circuit model for best impedance fidelity over a broad band. We also introduce an antenna circuit model, based upon transmission line segments and believed to be novel, that is simpler and has better broadband fidelity than the lumped component model.

The equivalent circuit models presented here represent wire dipoles although they should be useful in the representation of other antennas having similar frequency-impedance characteristics. While not investigated by the authors a simple alteration of the proposed models, specifically replacement of a series capacitor with a shunt inductor, allows representation of loop antennas.

II. Lumped Component Equivalent Circuit

Our interest in equivalent antenna models arose from a need to find a convenient broadband dipole antenna impedance representation that was computationally efficient. While the literature has many references to antenna equivalent circuits, most are narrowband representations. References [1] and [2] are exceptions to this general rule. The first reference describes an antenna equivalent circuit model design technique, suitable for broadband representation but having limited accuracy. The authors describe a simple circuit synthesis technique, based upon point matching at critical frequencies. A series capacitor is selected to match antenna reactance at a very low frequency. A series inductor generates the reactance zero at half-wave resonance. A parallel resonant LCR networks creates the full-wave resonance with an additional LCR network required for each additional overtone response to be represented.

The second reference describes more complex equivalent antenna circuit models having better broadband accuracy. This model, shown in Figure 1, has a shunt network for each half-wave type resonance. Reactance poles representing full wave resonances arise from the parallel resonance of adjacent shunt networks. The authors provide a table of normalized circuit element values, for a thin, center fed dipole. Our target antenna, with ½ meter (total) length and a radius of 1 cm did not quite qualify as thin. Consequently the fidelity of the equivalent circuit was poor. Target antenna impedance in this comparison came from Method of Moments (MoM) computer calculation [3]. Clearly some form of circuit optimization is called for.

III. Genetic Optimization

While many optimization methods are applicable to the problem at hand, we decided to use a genetic algorithm [4]. Because the network topology is not in doubt, only the component values are optimized. A 10 bit binary coded gene represents the value of each of the components. Upper and lower limits for each component are also set. Because all 16 component values are open to optimization they form, when strung end to end, a single 160-bit chromosome representing the antenna equivalent circuit.

The GA employed here permits a population size of 160 members. Equal population and chromosome size in this example is only a coincidence. A single optimization cycle or generation then considers 160 different candidate parameter strings or chromosomes. Standard circuit analysis determines the circuit impedance-frequency function for each member of the population.

Comparison against a suitable objective function F identifies the best performing candidates of each generation. The objective function is given by:

$$F = \sum_{n=1}^{N_f} \left[(\text{Re}^{NEC}(f_n) - \text{Re}^{GA}(f_n))^2 + (\text{Im}(f_n)^{NEC} - \text{Im}^{GA}(f_n))^2 \right]$$

where N_f is the number of frequency points, $\text{Re}^{NEC}(f_n)$ and $\text{Im}^{NEC}(f_n)$ are the real and imaginary parts of the antenna impedance computed by the NEC code. $\text{Re}^{GA}(f_n)$ and $\text{Im}^{GA}(f_n)$ are the real and imaginary components of the equivalent circuit model chosen by the GA.

After evaluating each of the design candidates in the previous population, the GA generates a new population, by means of the processes of *selection*, *crossover* and *mutation*. The candidate chromosomes with the best objective function scores are *selected*. Sections of these selected chromosomes are exchanged at random among the selected sub-population in the *crossover* process. Finally a small number of bits are altered or *mutated* at random and the optimization cycle repeated. Selection, crossover, and mutation encourage selective evolution towards ideal performance defined by the objective function. Candidate solutions that score well against the fitness criteria survive and pass on their genes to the next generation. Poorly performing solutions die out. Figure 2 shows the final result. Agreement between the impedance of the genetically optimized antenna equivalent circuit and the antenna impedance computed by MoM for a center fed, 1/2 meter long, 1 cm radius dipole is quite good, for both real and imaginary components across a bandwidth of about five octaves. Final model component values are shown below:

R11 = 3.92 K Ω	R21 = 5.36 K Ω	R31 = 4.24 K Ω	R41 = 1.24 K Ω
R12 = .903 Ω	C21 = .241 pF	C31 = .183 pF	C41 = .185 pF
C11 = 1.21 pF	C22 = .517 pF	C32 = .100 pF	C42 = .367 pF
L11 = 261 nH	L21 = 206 nH	L31 = 186 nH	L41 = 35.4 nH

One disadvantage of the lumped element model is the fact each additional overtone resonance requires another circuit branch and the recalculation of all model elements. To make matters worse, the sensitivity of the model component values seems to increase with the addition of overtone circuit branches. The problem is fundamental; antennas have overtone responses, lumped circuit elements do not.

IV. Lumped Component, Transmission Line Equivalent Model

It then makes sense to consider an antenna equivalent circuit model built around components that, like the target antenna, have periodic frequency domain impedance behavior. Figure 3 shows such a model consisting of a pair of transmission line sections, one mismatched into a high impedance load, the other mismatched into a low impedance load in series with a capacitor. This simple model has repetitive reactance poles and zeros very similar to an actual dipole. The series capacitor improves model accuracy at low frequencies. Both transmission lines are about one eighth wavelength long at the first half wave resonance. While this proposed model has intrinsic frequency periodicity, its higher order resonances fall at frequencies progressively removed from the resonant frequencies of an actual antenna and the overall impedance accuracy is only fair.

Improved model fidelity comes with increased complexity of the lumped impedance loads at both ends of the transmissions lines. Figure 4 shows an antenna equivalent circuit model with improved impedance fidelity where negative capacitors are included in the load networks. Because negative capacitors have positive reactance, they shift the full wave resonance frequencies downward and because the magnitude of this reactance decreases with frequency, the fundamental resonance is affected more strongly than the overtones thereby improving correspondence between circuit model and actual antenna impedance poles. The transmission lines themselves are allowed to be lossy with loss increasing with frequency. Increased flexibility improves model fidelity. As before, GA is applied to select the parameter values needed for model accuracy. The transmission line segments are modelled using the standard hyperbolic trigonometric relationship with a complex propagation constant γ . Figure 5 shows the optimized results. Impedance fidelity is quite good over a frequency range exceeding five octaves. Final component values are given below:

R11= 13.11 Ω	C11 = -16.25 pF	R21 = 699.7 Ω	C21 = .2938 pF
R12= 3600 Ω	C12 = .4000 pF	R22 = 1100 Ω	C22 = -.020 pF
R13= 500 Ω	C13 = .1388 pF	R23 = 330.0 Ω	C23 = -.030 pF

Cs = 2.504 pF

Line L₁ Zo = 214.8 Ω , length = .1248 M, $\alpha = .0744 + .3000 * [\text{Log}_{10}(f / 900 \text{ MHz})]$
Line L₂ Zo = 195.1 Ω , length = .1304 M, $\alpha = .0101 + .0339 * [\text{Log}_{10}(f / 90 \text{ MHz})]$

Where $\gamma = \alpha + j\beta$

While GA optimization works well, some heuristic insight is also worthwhile. Here are a few guidelines. Transmission line L1, the line having the low impedance far end load, dominates the odd order full wave resonances. Altering L1 or its associated load networks changes the first and third full wave resonances with little effect upon the second and fourth. The second line and associated lumped components effects chiefly the even order resonances. Series RC branches have increasing effect at higher frequencies.

V. Conclusions

The authors have demonstrated the use of a genetic algorithm to improve the impedance fidelity of two broadband antenna equivalent circuit models for a dipole. In the first example a GA optimizes component values in a lumped LCR network. In the second example the authors present a novel transmission line based antenna equivalent circuit model and again determine optimum model parameters with the use of a genetic algorithm. The second equivalent circuit model exhibits quite good impedance fidelity over a bandwidth exceeding five octaves including the fundamental through the forth overtone response.

References

- [1] M. Hamid, R. Hamid, "Equivalent Circuit of Dipole Antenna of Arbitrary Length" *IEEE Trans. Antennas and Propagation*, Vol. 45, No. 11, pp. 1695-1696, November 1997.
- [2] G. W. Streable, L. W. Pearson, "A Numerical Study on Realizable Broad-Band and Equivalent Admittances for Dipole and Loop Antennas" *IEEE Trans. Antennas and Propagation*, Vol. AP-29, No. 5, pp. 707-717, September 1981.
- [3] G. J. Burke, A. J. Poggio, *Numerical Electromagnetics Code-Method of Moments*. Naval Ocean Systems Center, San Diego, CA, 1981.
- [4] Y. Rahmat-Samii, E. Michielssen, *Electromagnetics Optimization by Genetic Algorithms*. John Wiley & Sons Inc., 1999.

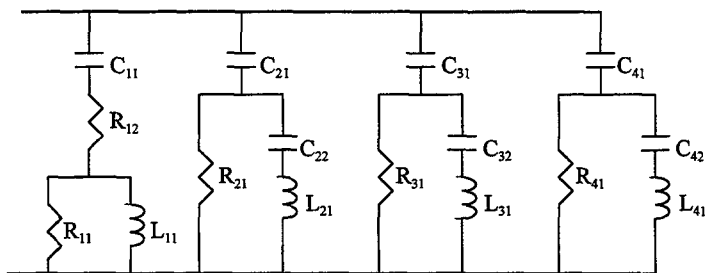


Figure 1. LCR dipole equivalent circuit model

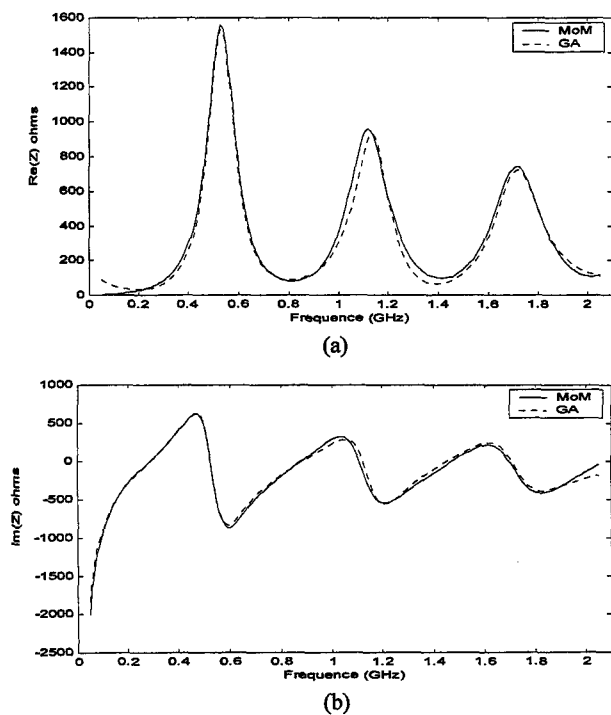


Figure 2. The impedance from MoM and from the GA optimized equivalent circuit.
(a) Real part of the impedance. (b) Imaginary part of the impedance.

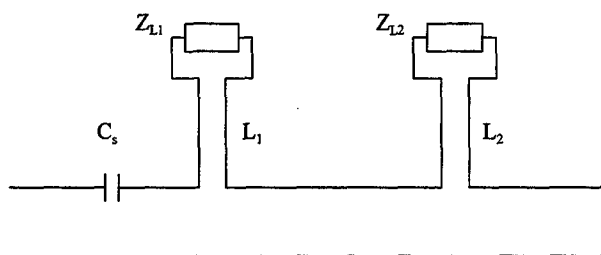


Figure 3. Simplified transmission line equivalent circuit model.

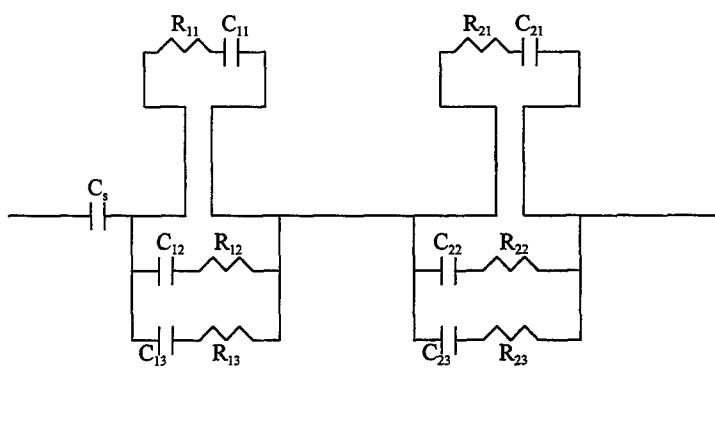
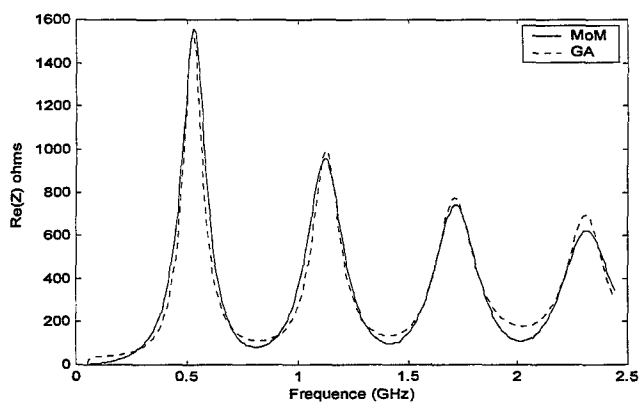
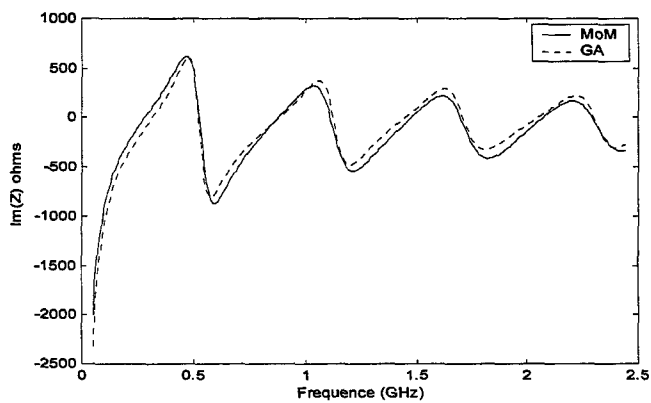


Figure 4. Antenna equivalent circuit model with improved impedance fidelity.



(a)



(b)

Figure 5. Impedance from MoM and the GA optimized transmission line based dipole equivalent circuit (a) Real part of the impedance. (b) Imaginary part of the impedance.

Computing the Electromagnetic Field in a Perturbed Configuration Using Modified Reduced-Order Models

R.F. Remis and P.M. van den Berg

Laboratory of Electromagnetic Research,

Centre for Technical Geoscience,

Delft University of Technology,

P.O. Box 5031, 2600 GA Delft, The Netherlands

1. Introduction

We consider the problem of determining the transient electromagnetic field in lossless media. One of the methods to solve these types of problems is the reduced-order modeling technique (see, for example, Zhao and Cangellaris [5] and Remis and Van den Berg [2]). In this technique a so-called reduced-order model is constructed that accurately describes the behavior of the electromagnetic field on a certain bounded interval in time. Now say that we have computed such a model for some configuration. If the medium parameters differ locally from this particular configuration, we have to start the computations all over again to obtain a new reduced-order model that accurately describes the behavior of the electromagnetic field in this new configuration. In this paper we show that this procedure can be avoided. The already computed reduced-order model can be modified and there is no need to construct a completely new model. Computing the modified reduced-order model is much more efficient than constructing a new model for the new configuration. Numerical experiments illustrating the proposed modification will be given at the conference.

The paper is organized as follows. In Section 2 briefly review Maxwell's equations and introduce our notation. In Section 3 we construct the reduced-order models for the electromagnetic field quantities if the medium under consideration is lossless. In Section 4 we show how these models can be modified such that they describe the behavior of the electromagnetic field in a perturbed configuration.

2. Basic equations

The transient electromagnetic field in an inhomogeneous, isotropic, and lossless medium is governed by Maxwell's equations

$$-\nabla \times \mathbf{H} + \epsilon \partial_t \mathbf{E} = -\mathbf{J}^e, \quad (1)$$

$$\nabla \times \mathbf{E} + \mu \partial_t \mathbf{H} = -\mathbf{K}^e. \quad (2)$$

In these equations, \mathbf{E} is the electric field strength [V/m], \mathbf{H} is the magnetic field strength [A/m], \mathbf{J}^e is the external electric-current density [A/m²], and \mathbf{K}^e is the external magnetic-current density

[V/m²]. The medium in which the electromagnetic waves propagate is characterized by the in general position dependent permittivity ϵ and permeability μ .

Written out in full, equations (1) and (2) can be arranged in the form

$$(\mathcal{D} + \mathcal{M}\partial_t)\mathcal{F} = \mathcal{Q}', \quad (3)$$

in which $\mathcal{F} = \mathcal{F}(\mathbf{x}, t)$ is the field vector given by

$$\mathcal{F} = [E_1, E_2, E_3, H_1, H_2, H_3]^T, \quad (4)$$

and the source vector $\mathcal{Q}' = \mathcal{Q}'(\mathbf{x}, t)$ consists of the components of the external electric- and magnetic-current sources as

$$\mathcal{Q}' = -[J_1^e, J_2^e, J_3^e, K_1^e, K_2^e, K_3^e]^T. \quad (5)$$

In what follows, we consider source vectors of the form

$$\mathcal{Q}'(\mathbf{x}, t) = w(t)\mathcal{Q}(\mathbf{x}), \quad (6)$$

where $w(t)$ is the source wavelet that vanishes for $t < 0$ and $\mathcal{Q} = \mathcal{Q}(\mathbf{x})$ is a time-independent vector.

The time-independent medium matrix \mathcal{M} is given by

$$\mathcal{M} = \text{diag}(\epsilon, \epsilon, \epsilon, \mu, \mu, \mu), \quad (7)$$

and, finally, the curl operators are contained in the spatial differentiation operator matrix \mathcal{D} given by

$$\mathcal{D} = \begin{pmatrix} 0 & 0 & 0 & 0 & \partial_3 & -\partial_2 \\ 0 & 0 & 0 & -\partial_3 & 0 & \partial_1 \\ 0 & 0 & 0 & \partial_2 & -\partial_1 & 0 \\ 0 & -\partial_3 & \partial_2 & 0 & 0 & 0 \\ \partial_3 & 0 & -\partial_1 & 0 & 0 & 0 \\ -\partial_2 & \partial_1 & 0 & 0 & 0 & 0 \end{pmatrix}. \quad (8)$$

We now discretize Maxwell's equations in space using a standard Yee-mesh (see, for example, Yee [4] and Taflov [3]). At the boundary of the computational domain we set the tangential components of the electric field strength to zero. After this discretization procedure we obtain the algebraic matrix equation

$$(D + M\partial_t)F(t) = w(t)Q. \quad (9)$$

The matrices D and M are both square and of order n . Matrix D is real and skew-symmetric, and matrix M is diagonal and positive definite. Notice that in two dimensions the order n is proportional to $3N^2$, where N is the number of sample points in each Cartesian direction, while in three dimensions n is proportional to $6N^3$.

If we multiply equation (9) on the left by the inverse of matrix M we obtain

$$(A + I\partial_t)F(t) = w(t)M^{-1}Q, \quad (10)$$

where I is the identity matrix and

$$A = M^{-1}D. \quad (11)$$

Solving equation (10) for the field vector gives

$$F(t) = w(t) * \chi(t) \exp(-At)M^{-1}Q, \quad (12)$$

where $\chi(t)$ is the Heaviside unit step function and the asterisk denotes convolution in time. The problem with equation (12) is that it is not feasible to evaluate the matrix exponential function by using a full decomposition of matrix A since the order of this matrix is too large. We therefore construct approximations to the field vector. These approximations, called reduced-order models, are the subject of the next section.

3. Reduced-order models

Before we discuss the construction of the reduced-order models, we introduce the M -inner product of two vectors x and y from \mathbb{R}^n as

$$\langle x, y \rangle_M = y^T Mx. \quad (13)$$

Matrix A is skew-symmetric with respect to this inner product, that is,

$$\langle x, Ay \rangle_M = -\langle Ax, y \rangle_M. \quad (14)$$

Later on we make use of this symmetry property. Furthermore, the inner product of equation (13) induces a norm given by $\|x\|_M = \langle x, Mx \rangle^{1/2}$.

The field vector given by equation (12) is approximated by the reduced-order model

$$F_m(t) = a_1(t)v_1 + a_2(t)v_2 + \dots + a_m(t)v_m, \quad (15)$$

where the expansion vectors v_i form an orthonormal set with respect to the M -inner product, and the coefficients $a_i(t)$ describe the time dependence of the reduced-order model. The reason for calling the approximation of equation (15) a reduced-order model is that m , the order of the model, is taken to be much smaller than n , the order of the original system.

Introducing the n -by- m matrix

$$V_m = (v_1, v_2, \dots, v_m), \quad (16)$$

and the m -by-1 vector

$$a(t) = [a_1(t), a_2(t), \dots, a_m(t)]^T, \quad (17)$$

the reduced-order model can also be written as

$$F_m(t) = V_m a(t). \quad (18)$$

The vectors v_i are generated as follows. The first vector v_1 is taken to be a normalized version of the source vector $M^{-1}Q$. More precisely,

$$v_1 = \|M^{-1}Q\|_M^{-1} M^{-1}Q. \quad (19)$$

From equation (19) it follows that we can also write

$$M^{-1}Q = \|M^{-1}Q\|_M v_1 = \|M^{-1}Q\|_M V_m e_1, \quad (20)$$

where e_1 is the first column of the m -by- m identity matrix I_m . The remaining vectors are constructed using the recursion

$$\beta_{i+1} v_{i+1} = A v_i + \beta_i v_{i-1} \quad \text{for } i = 1, 2, \dots, m, \quad (21)$$

with $v_0 = 0$. The coefficients $\beta_i \geq 0$ are determined from the condition $\|v_i\|_M = 1$ for $i > 1$. The above algorithm is known as the Lanczos algorithm for skew-symmetric matrices. It is not difficult to see that after m steps of this algorithm we have the summarizing equation

$$A V_m = V_m T_m + \beta_{m+1} v_{m+1} e_m^T, \quad (22)$$

where matrix T_m is a tridiagonal, skew-symmetric m -by- m matrix given by

$$T_m = \begin{pmatrix} 0 & -\beta_2 & & & \\ \beta_2 & 0 & -\beta_3 & & \\ & \beta_3 & \ddots & \ddots & \\ & & \ddots & \ddots & -\beta_m \\ & & & \beta_m & 0 \end{pmatrix}. \quad (23)$$

Moreover, we also have

$$V_m^T M V_m = I_m, \quad (24)$$

and

$$V_m^T M v_{m+1} = 0. \quad (25)$$

The right-hand side of equation (25) is the m -by-1 zero vector. The proof of the above relations is based on the fact that matrix A is skew-symmetric with respect to the M -inner product and runs along similar lines as the proof given by Golub and Van Loan [1] for a symmetric matrix A .

We substitute the reduced-order model of equation (18) in equation (10). We obtain

$$(A V_m + V_m \partial_t) a(t) = w(t) M^{-1} Q. \quad (26)$$

Using equations (20) and (22) this can be rewritten as

$$(V_m T_m + \beta_{m+1} v_{m+1} e_m^T + V_m \partial_t) a(t) = w(t) \|M^{-1} Q\|_M V_m e_1. \quad (27)$$

If we multiply equation (27) on the left by $V_m^T M$ and use the orthogonality relations (24) and (25) we end up with

$$(T_m + I_m \partial_t) a(t) = w(t) \|M^{-1} Q\|_M e_1. \quad (28)$$

Solving equation (28) for the vector $a(t)$ we obtain

$$a(t) = w(t) * \chi(t) \|M^{-1} Q\|_M \exp(-T_m t) e_1. \quad (29)$$

Substituting this result in equation (18), we arrive at our final expression for the reduced-order model

$$F_m(t) = w(t) * \chi(t) \|M^{-1} Q\|_M V_m \exp(-T_m t) e_1. \quad (30)$$

Observe that the problem of evaluating the exponent of a matrix of large order has been replaced by the problem of evaluating the exponent of a tridiagonal, skew-symmetric matrix of a much smaller order.

4. Modified reduced-order models

In this section we investigate if a modification of the reduced-order model constructed in the previous section can be used as an approximation to the field vector $\tilde{F} = \tilde{F}(t)$ that satisfies the equation

$$[D + (M + \Delta M) \partial_t] \tilde{F}(t) = w(t) Q, \quad (31)$$

where ΔM is a perturbation of matrix M . Note that matrix ΔM is taken to be a diagonal matrix.

We multiply equation (31) on the left by the inverse of matrix M . This gives

$$[A + (I + M^{-1} \Delta M) \partial_t] \tilde{F}(t) = w(t) M^{-1} Q, \quad (32)$$

where matrix A is given by equation (11). As an approximation to the field vector $\tilde{F} = \tilde{F}(t)$ we take the reduced-order model

$$\begin{aligned} \tilde{F}_m(t) &= b_1(t) v_1 + b_2(t) v_2 + \dots + b_m(t) v_m \\ &= V_m b(t), \end{aligned} \quad (33)$$

where the expansion vectors v_i are generated by the Lanczos algorithm described in the previous section, and the m -by-1 vector $b = b(t)$ is partitioned in the same way as vector a (see equation (17)). Substitution of this reduced-order model in equation (32) gives

$$[AV_m + (V_m + M^{-1} \Delta M V_m) \partial_t] b(t) = w(t) M^{-1} Q, \quad (34)$$

and with the help of equations (20) and (22) this can be written as

$$[V_m T_m + \beta_{m+1} v_{m+1} e_m^T + (V_m + M^{-1} \Delta M V_m) \partial_t] b(t) = w(t) \|M^{-1} Q\|_M V_m e_1. \quad (35)$$

If we multiply this equation on the left by $V_m^T M$ and use the orthogonality relations (24) and (25), we obtain

$$[T_m + (I_m + V_m^T \Delta M V_m) \partial_t] b(t) = w(t) \|M^{-1} Q\|_M e_1. \quad (36)$$

Introducing the scaling matrix S_m as

$$S_m = (I_m + V_m^T \Delta M V_m)^{-1} \quad (37)$$

we can rewrite equation (36) as

$$(S_m T_m + I_m \partial_t) b(t) = w(t) \|M^{-1} Q\|_M S_m e_1. \quad (38)$$

Note that the m -by- m matrix S_m is comparatively small. To compute this matrix, we only need to store those elements of the Lanczos vectors that correspond to the points where ΔM differs from zero. If we solve equation (38) for the vector $b = b(t)$ we obtain

$$b(t) = w(t) * \chi(t) \|M^{-1} Q\|_M \exp(-S_m T_m t) S_m e_1. \quad (39)$$

Substituting this result in equation (33), we obtain the modified reduced order-model

$$\tilde{F}_m(t) = w(t) * \chi(t) \|M^{-1} Q\|_M V_m \exp(-S_m T_m t) S_m e_1. \quad (40)$$

The approach outlined above is much more efficient than the standard approach as long as the scaling matrix S_m and the matrix exponent $\exp(-S_m T_m t)$ can be effectively computed.

References

- [1] G.H. Golub and C.F. Van Loan, *Matrix Computations*, The Johns Hopkins University Press, London, 1989.
- [2] R.F. Remis and P.M. van den Berg, *A modified Lanczos algorithm for the computation of transient electromagnetic wavefields*, IEEE Transactions on Microwave Theory and Techniques, vol. 45, no. 12, 1997, pp. 2139-2149.
- [3] A. Taflov, *Computational Electrodynamics: The Finite-Difference Time-Domain Method*, Artech House, Norwood, 1995.
- [4] K.S. Yee, *Numerical solution of initial boundary value problems involving Maxwell's equations in isotropic media*, IEEE Transactions on Antennas and Propagation, vol. 14, no. 3, 1966, pp. 302-307.
- [5] L. Zhao and A.C. Cangellaris, *Reduced-order modeling of electromagnetic field interactions in unbounded domains truncated by perfectly matched layers*, Microwave and Optical Technology Letters, vol. 17, no. 1, 1998, pp. 62-66.

SOME FURTHER RESULTS FROM FARS: FAR-FIELD ANALYSIS OF RADIATION SOURCES

Edmund K. Miller

3225 Calle Celestial, Santa Fe, NM 87501-9613
505-820-7371, e.miller@ieee.org

0.0 ABSTRACT

Some further results from a new approach called FARS (Far-field Analysis of Radiation Sources) are summarized here. FARS was developed in an attempt to determine how much power is contributed to the far field from a PEC object on a per-unit-length or per-unit-area basis. Examples considered here include straight, curved, and bent wires, with the FARS results appearing to be physically consistent with other expectations about radiation.

1.0 INTRODUCTION

A new method intended to address the question:

What is the quantitative contribution to the radiated power from the surface of a PEC object on a per unit length (wires) or per unit area (3D surfaces) basis?

was recently described [Miller (1999a), (1999b)]. Some further results obtained from FARS are presented here. For the sake of shortening the discussion, the FARS results will be discussed as though they do actually answer the question above, while acknowledging that so far this is only speculation. At best, the results previously presented, as well as those that follow here, can be regarded as plausibility demonstrations, for now lacking any rigorous proof of their physical meaning. However, since the FARS results do seem consistent with other observations, and do appear to offer further useful insight regarding radiation, it seems worthwhile to continue the discussion.

2. SOME BACKGROUND

When posed to electromagneticists, quite a wide a variety of responses to the radiation question above is obtained, but with most falling into two broad categories. One is that this is not really a sensible question to ask, or even if so, it's one that probably can't be answered. The other is that since solving electromagnetic problems of interest hasn't seemed to be hindered by not considering this question, what's the point of worrying about it? The first response is essentially a non-answer. If EM radiation can be quantitatively evaluated in terms of radiation patterns and radar cross sections, what can be wrong with asking where the radiated power originates? The geometrical theory of diffraction provides just one example where the contributions of edges, discontinuities and surface curvature to radiation are used explicitly and quantitatively in formulating a solution technique. Physicists who design particle accelerators and other devices involving various charge configurations must deal with this issue routinely. As for the latter response, it's one that seems to display a singular lack of intellectual curiosity. While the response may be superficially true, not having an answer to the radiation question seems to leave a big hole in our claimed understanding of electromagnetic physics.

3. THE FARS APPROACH

The approach described here, called FARS, is based on the bistatic far fields at a single fre-

quency, although a time-domain version would seem to be similarly feasible. Instead of imaging using the bistatic far fields, as described by Shaeffer et al. (1997), however, FARS seeks instead to determine the contribution made to the total power flow at a given far field observation point by each incremental source, s_i , on the PEC boundary. We first define the incremental FARS power, $P_{i,FARS}(\theta, \varphi)$ for segment s_i in observation direction θ, φ as

$$P_{i,FARS}(\theta, \varphi) = \lim_{r \rightarrow \infty} \left(r^2 \frac{1}{2\eta} \text{Re}[\mathbf{e}_i(\theta, \varphi) \cdot \mathbf{E}^*(\theta, \varphi)] \right) \quad (1)$$

where $\mathbf{e}_i(\theta, \varphi)$ is the electric field due to source i and η is the medium impedance. The total electric field for N incremental sources, denoted by $\mathbf{E}(\theta, \varphi)$ is then given as

$$\mathbf{E}(\theta, \varphi) = \sum_{i=1}^N \mathbf{e}_i(\theta, \varphi). \quad (2)$$

The total power contributed by each s_i , $P_{i,FARS}$, comes from integrating the incremental result $P_{i,FARS}(\theta, \varphi)$ over all θ, φ to obtain

$$P_{i,FARS} = \int_0^\pi \int_0^{2\pi} P_{i,FARS}(\theta, \varphi) \sin\theta d\theta d\varphi \quad (3)$$

yielding a quantity denoted in the following as the "linear power density" or LPD.

Finally, the total radiated power is obtained from integrating the LPDs over all sources, or

$$P_{FARS} = \sum_{i=1}^N P_{i,FARS}. \quad (4)$$

Note that the FARS computation differs from a conventional evaluation of the total far-field power only in defining the intermediate quantity $P_{i,FARS}$, the individual contribution of each incremental source, to the total radiated or scattered power. Although there is no constraint that each $P_{i,FARS}$ be positive, the physical significance of negative values may be unclear at this point and will be discussed elsewhere [Miller (1999a), (1999b)].

Because it provides a basis for comparison with FARS for the SCF, the induced EMF method (IEMF) for computation of boundary power is also considered. The differential IEMF power, dP_{IEMF} , for a current distribution $I(x)$ whose tangential near-electric field, $E(x)$, is given by

$$dP_{IEMF}(x) = 0.5 \text{Re}[E(x)I^*(x)dx]. \quad (5a)$$

The per-segment IEMF power can then be approximated as

$$P_{i,IEMF} = 0.5 \text{Re}[E_i \Delta_i I_i^*] \quad (5b)$$

where E_i is the tangential electric field at the center of segment i whose length is Δ_i and on which the current is I_i . The total IEMF power is then

$$P_{\text{IEMF}} = \sum_{i=1}^N P_{i,\text{IEMF}} \quad (6)$$

where, for a PEC object it is required that

$$P_{\text{FARS}} = P_{\text{IEMF}} \quad (7)$$

Note that for boundary-value problems $P_{i,\text{IEMF}}$ is non zero only on segments that are excited by some applied field, whereas for a current such as the SCF, it will generally be non zero everywhere. Castillo (1997) described a somewhat-similar approach, wherein a total far-field power value is computed using the incremental fields of all but segment i , with i sequentially scanned over the entire object. Since the fields are additive, but the incremental powers are not, the result obtained only approximates the total radiated power.

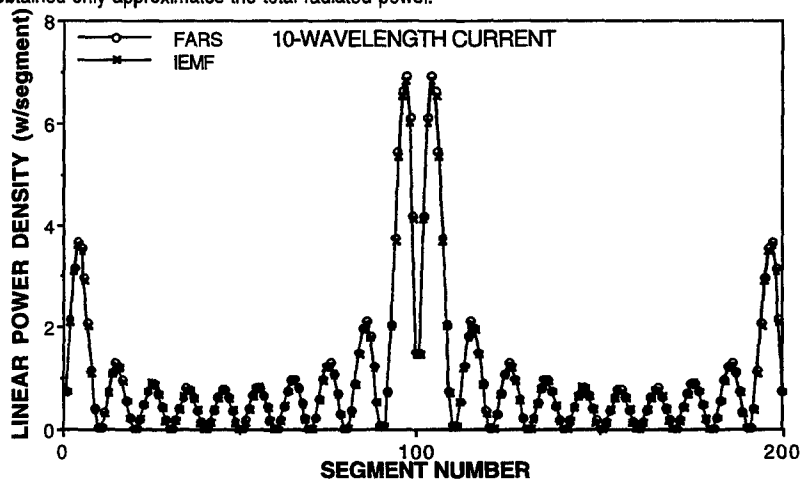


Figure 1. FARS and IEMF LPDs along a 10-wavelength, 1-A sinusoidal-current filament. The tangential electric fields for the SCF were computed at a radius of 10^{-3} wavelengths, although varying this parameter over several orders of magnitude made essentially no significant difference, numerically. Spatial integration of these results yields $P_{\text{FARS}} = 205.4$ w and $P_{\text{IEMF}} = 202.3$ w, agreeing essentially to within the integration uncertainty and the difference between the FARS and IEMF LPDs.

4.0 FARS RESULTS FOR THE SINUSOIDAL- AND UNIFORM-CURRENT FILAMENTS

Some results using FARS and the IEMF method have been developed for the SCF and the uniform-current filament (UCF). Somewhat unexpectedly, as can be seen in Fig. 1, FARS LPDs for the SCF are essentially identical to those obtained earlier [Miller (1996)] when using the IEMF method to compute the "input" power for a SCF. Note, however, that the only connection between the two procedures is that both exploit knowledge of the current distribution, but FARS uses the far field while IEMF uses the near field. It's not clear why $P_{i,\text{FARS}}$ should equal $P_{i,\text{IEMF}}$ for the SCF, besides which, as mentioned above, this agreement cannot be expected for general boundary-value problems involved PEC objects. Similar results for a UCF are presented in Fig. 2. The FARS

LPDs are seen to be nearly uniform along the current filament, while those from the IEMF method oscillate slightly around the FARS values with position, being most variable near the ends.

5.0 FARS RESULTS FOR WIRE OBJECTS

When applied to an actual wire dipole of the same length and having a 1-A maximum current magnitude, the FARS LPDs resemble those of the SCF, but are slightly smaller with increasing distance from the feedpoint. A typical result is presented in Fig. 3 where a sampling density of 20/wavelength is used. Corresponding results for a plane wave at 10 deg from axial incidence on the right end of a 10-wavelength long wire are shown in Fig. 4. While the IEMF LPDs grow monotonically towards the left, or far, end of the wire, the FARS results are largest at the ends, with the far end value having a maximum more than twice that of the near end. This result seems consistent with a geometrical-theory-of-diffraction model for such a problem with its predominant end contributions.

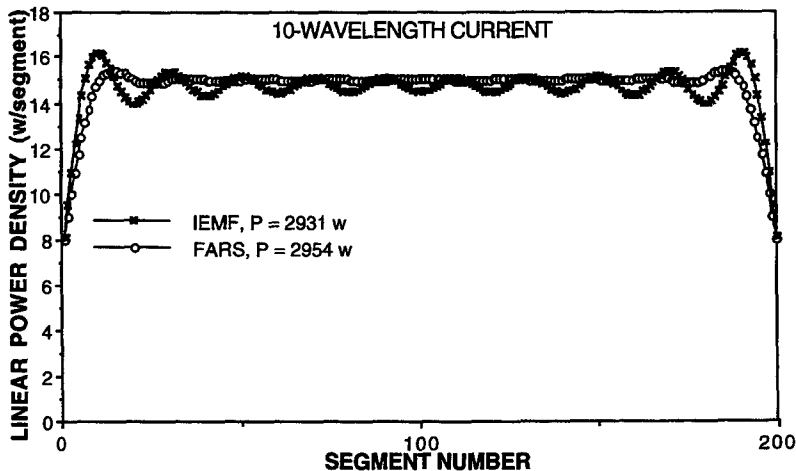


Figure 2. FARS and IEMF LPDs along a 10-wavelength, 1-A uniform-current filament. The tangential electric fields for the UCF were computed at a radius of 10^{-3} wavelengths. A spatial integral of the LPDs yields the results indicated in the figure, again agreeing essentially to within the integration uncertainty and the difference between the FARS and IEMF.

Continuing with 10-wavelength wires, FARS results are presented in Fig. 5 for a straight, centered dipole and for circular- and square-loop antennas, all having 1-A maximum current magnitude. For clarity, the LPDs are shown for only half of an object, with the feedpoint being at the right for each. For the same maximum current, the circular loop radiates about twice the power, showing the increased radiation that occurs from a curved wire compared with one that is straight as a result of charge acceleration around the curve. The square loop also radiates more power than the straight wire, with a maxima occurring at each corner, again demonstrating effect of accelerated charge, in this case moving around a right-angle corner.

Results are presented in Fig. 6 for the FARS LPDs on one arm of a two-arm, three-turn conical-spiral antenna at two different frequencies. A region of largest LPDs occurs in the area where

the circumference of the spiral is about one wavelength, which is known to be the active region.

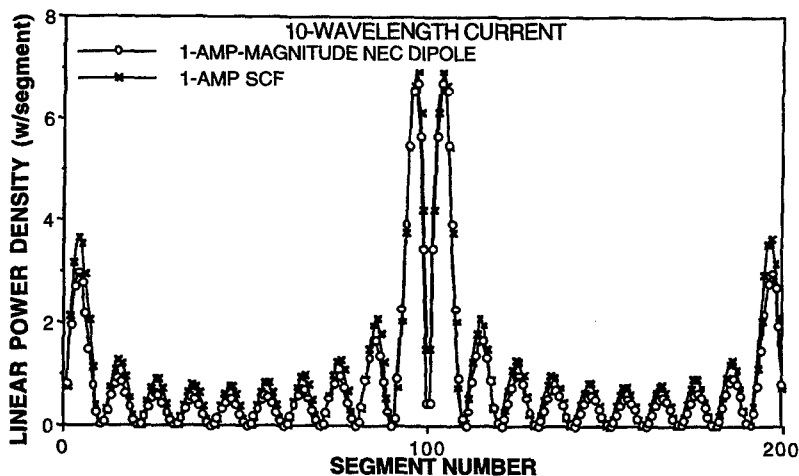


Figure 3. FARS LPDs for a 10-wavelength SCF and NEC dipole, each having a 1-A maximum current magnitude. Their respective radiated powers are 205.4 and 170.7 w.

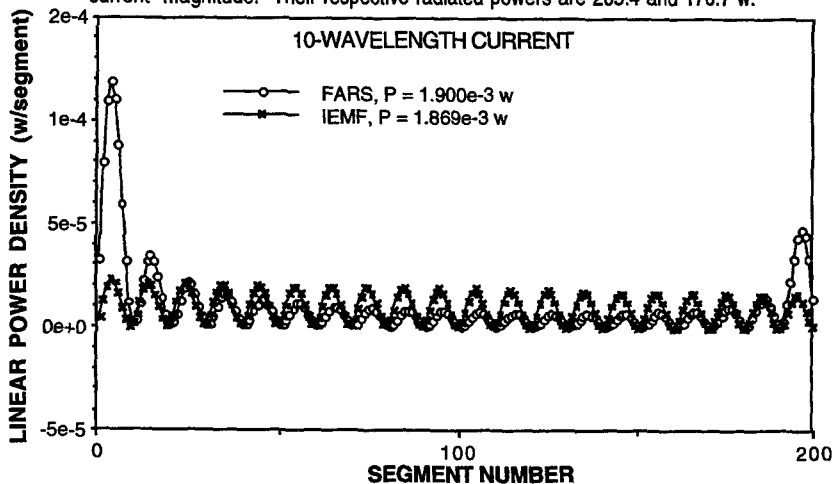


Figure 4. FARS and IEMF LPDs for a 10-wavelength wire illuminated by a 1 V/m plane at 10 deg from axial incidence on the right.

The discussion thus far has assumed that the FARS LPDs do indeed quantitatively answer the question about how much power is radiated per unit length from wire antennas and scatterers modeled with NEC. Without an answer to this question independent of FARS, the truth of this

basic assumption remains speculative.

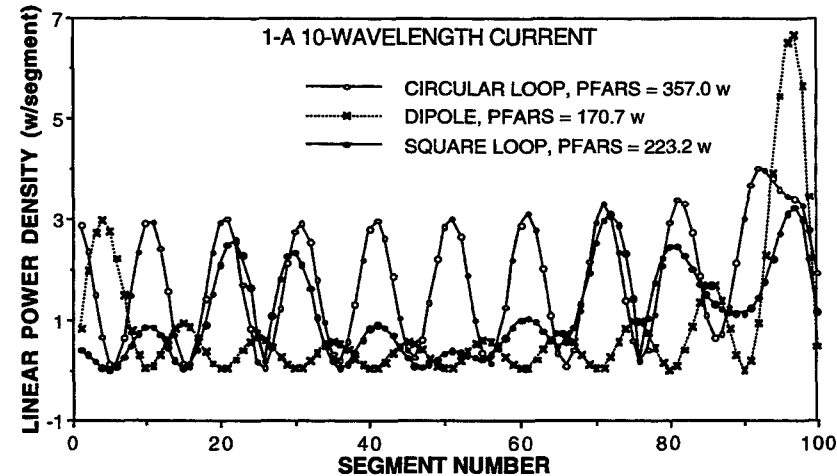


Figure 5. FARS LPDs on half of a 10-wavelength straight dipole, and circular and square loops having a 1-A maximum current magnitude with their feedpoints located at the right of the plot. The circular loop radiates most efficiently while the square loop has maxima at the corner bends.

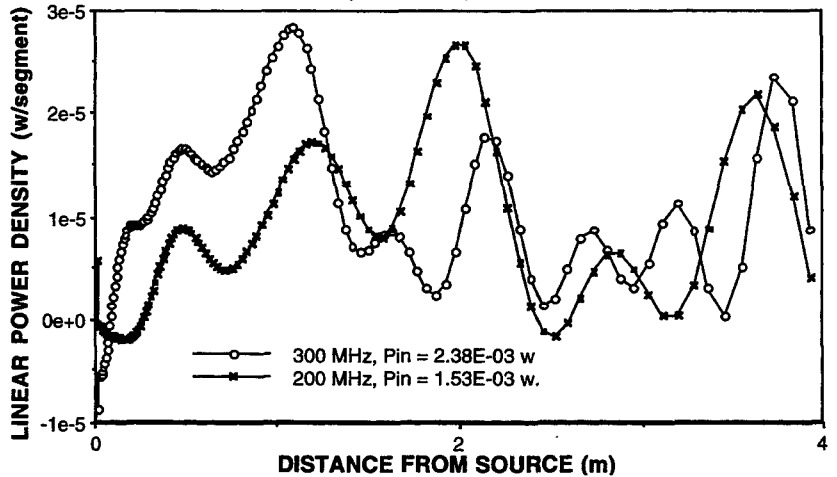


Figure 6. FARS LPDs on one arm of a two-arm conical-spiral antenna at two different frequencies. The 1-V source is at the left and segment length increases with distance, there being a constant number of segments per turn. The total power radiated over any interval is obtained by summing the LPDs.

Suppose, however, that FARS were to be applied to NEC results for a collection of antennas, small enough and far enough apart to be non-interacting. Then the integrated FARS LPDs for each antenna should be expected to match the NEC-computed input power. To test this assumption, a collinear array of nine 0.35 wavelength dipoles nonuniformly distributed over a 10-wavelength aperture was modeled using NEC. Each dipole was excited by a different voltage to vary their radiated powers, and FARS was applied to the far field produced by the array. The input power as provided by NEC is plotted together with the integrated FARS LPDs for each dipole as a function of dipole number in the array in Fig. 7. There it can be seen that the NEC and FARS powers agree to within a per cent. This agreement shows that FARS can determine the power radiated per antenna element in such an array, but does not prove that it yields the correct spatial distribution of power along each antenna. Thus, it represents a necessary, though not sufficient, condition to demonstrate that FARS can answer the question posed in the Introduction.

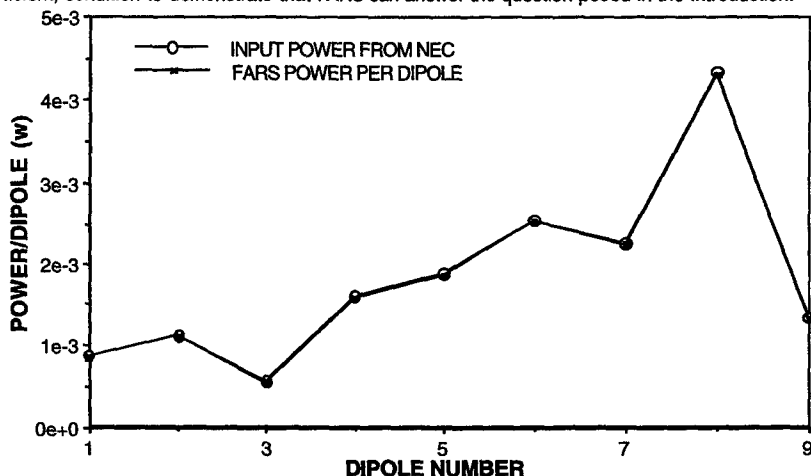


Figure 7. Comparison of the NEC-computed input power and the integrated FARS LPDs for the elements of a collinear array of nine nonuniformly spaced 0.35-wavelength dipoles. The two results agree to within one per cent, serving as a necessary, but not sufficient, test that FARS LPDs do provide a quantitative measure of the power radiated per unit length for wire antennas.

As a last example, the result of applying FARS to a 12-element log-periodic dipole array is shown in Fig. 8, where the normalized values for the current and LPDs are plotted for each element as well as the NEC-computed per-element input power. It can be clearly seen that the LPDs are not proportional to the element currents. Furthermore, some of the input powers and LPDs are negative on a given element, but this does not occur in all cases. The negative input powers for this kind of problem have been interpreted to indicate array elements that are supplying power to the connecting transmission line by absorbing it from the near fields. A comparable appears applicable to the negative LPD values.

6. CONCLUDING REMARKS

A method called FARS (Far-field Analysis of Radiation Sources) has been outlined here and its application demonstrated using a variety of current sources and wire geometries. The develop-

ment of FARS was motivated in an attempt to answer the question: **What is the quantitative contribution to the radiated power from the surface of a PEC object on a per unit length (wires) or per unit area (3D surfaces) basis?** The FARS results presented here and elsewhere seem to be physically plausible and consistent with other perspectives of radiation physics. However, a rigorous proof that FARS answers the question posed is not yet available. Nevertheless, the fact that the results obtained do appear capable of providing quantitative insight concerning where radiation originates from a PEC object suggests FARS further extension, e.g., to three-dimension conducting bodies and to time-domain solutions.

7.0 REFERENCES

- S. Castillo, "The Interpretation of Body Current Distributions in Designing Low-RCS Scatterers," 1997 North American Radio Science Meeting, Montreal, Canada, p. 736.
- E. K. Miller (1996), PCs for AP and Other EM Reflections, *IEEE AP-S Magazine*, Vol. 38, No. 5, October, pp. 70-74.
- E. K. Miller (1999a, 1999b), PCs for AP and Other EM Reflections, *IEEE AP-S Magazine*, Vol. 41, No. 2, April, pp. 82-86; Vol. 41, No. 3, June, pp. 83-88.
- J. F. Shaeffer, B. A. Cooper, K. W. Hom, R. C. Baucke, and N. A. Talcott (1997), "A Review of Bistatic k-Space Imaging for Electromagnetic Prediction Codes for Scattering and Antennas," *IEEE AP-S Magazine*, Vol. 39, No. 5, October, pp. 2121-29.

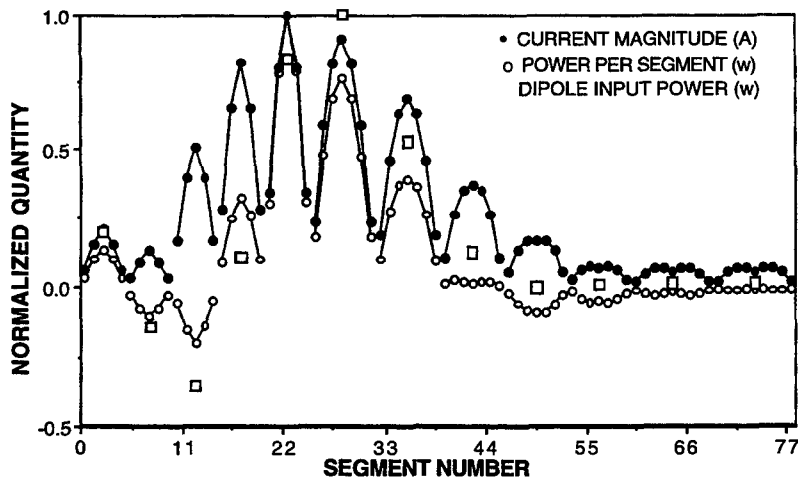


Figure 8. The FARS LPDs, current magnitudes and NEC-computed input power for a 12-element log-periodic dipole array, with the shortest dipole on the left. For clarity, these various quantities are normalized relative to their respective maximum values.

8. ACKNOWLEDGEMENT

The author gratefully acknowledges the addition of FARS to NEC by Jerry Burke.

SESSION 3

**NUMERICAL TECHNIQUES FOR
PACKAGING
AND
INTERCONNECTS**

Chairs: Omar Ramahi and Andreas Cangellaris

A New Methodology for the Direct Generation of Closed-Form Electrostatic Green's Functions in Layered Dielectrics

Andreas C. Cangellaris
Center for Computational Electromagnetics & The Electromagnetics Laboratory
Department of Electrical and Computer Engineering
University of Illinois at Urbana-Champaign
Urbana, IL 61801, USA
E-mail: cangella@uiuc.edu

Abstract

This paper introduces a new approach for the development of closed-form spatial Green's functions for electrostatic problems involving layered dielectrics. Such Green's functions are of special interest to the extraction of capacitance matrices for multi-layer electronic interconnection structures at the chip, package and printed-circuit-board level. Contrary to previous methodologies, the proposed method does not require the development of the Green's function in closed form in the spectral domain. In addition to the familiar case of a multi-layer dielectric, the new methodology is also suitable for the generation of Green's functions in planar inhomogeneous dielectrics with electric permittivity varying in the vertical direction.

1. Introduction

The availability of closed-form Green's functions for the solution of electrostatic problems in layered dielectrics is of particular interest to the development of computer-aided design tools for high-speed electronic interconnections at the chip, package and board level. For example, two-dimensional capacitance matrix extraction is needed for the development of multi-conductor transmission line models for coupled interconnections. Three-dimensional capacitance matrices are required for the prediction of interconnect capacitive coupling on chip and the subsequent quantification of delay. As the trend continues toward the implementation of more exotic multi-layer material stacking for enhancing or decreasing capacitive coupling depending on the application, use of closed-form Green's functions in integral equation-based capacitance extraction is essential for reducing computational complexity and thus increasing solution efficiency.

Closed-form expressions for the electrostatic Green's function in layered dielectrics are available and have been based on the approximation of the spectral-domain Green's function using exponential functions [1-2]. In this paper, a new methodology is proposed for the development of closed-form expressions for the electrostatic Green's function. Instead of deriving the analytic form for the spectral-domain Green's function, the proposed methodology begins with the discrete approximation of the Fourier-Bessel transform of the governing Green's function equation, and proceeds with the development of a special form of the solution of the resulting discrete problem that enables the construction of the closed-form Green's function in the space domain through a direct inverse Fourier-Bessel transform.

1. The Spectral-Domain Green's Function

Shown in Fig.1 is the layered dielectric medium of interest. It is assumed that the electric permittivity of the medium varies in the vertical direction only, $\epsilon(x,y,z) = \epsilon(z)$, in the region between the conducting plane at $z = 0$ and the planar interface at $z = d$. The medium for $z > d$ is assumed homogeneous with electric permittivity ϵ_b . Such a layered medium case is relevant to the microstrip class of interconnections.

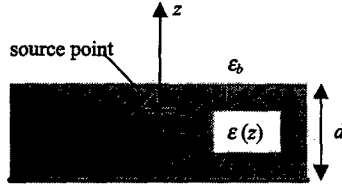


Figure 1. Geometry of a layered dielectric medium above a conducting plate.

Let $z = z'$ be the source plane. With the coordinate system selected such that the x and y coordinates of the source point are zero, the governing Green's function equation assumes the following form in cylindrical coordinates,

$$\nabla \cdot (\epsilon(z) \nabla g(\rho, z; z')) = -\frac{\delta(\rho)}{2\pi\rho} \delta(z - z') \quad (1)$$

subject to well-known boundary conditions at the conducting plate, the planar material interface, and at infinity. Using the Fourier-Bessel transform pair,

$$G(\lambda, z; z') = \int_0^\infty g(\rho, z; z') J_0(\lambda\rho) \rho d\rho \quad (2a)$$

$$g(\rho, z; z') = \int_0^\infty G(\lambda, z; z') J_0(\lambda\rho) \lambda d\lambda \quad (2b)$$

the spectral-domain form of (1) is obtained as follows,

$$\frac{d}{dz} \left[2\pi\epsilon(z) \frac{d}{dz} G(\lambda, z; z') \right] - 2\pi\epsilon(z) \lambda^2 G(\lambda, z; z') = -\delta(z - z') \quad (3)$$

Next, a discrete approximation to (3) will be developed. For this purpose, the finite difference method is employed. The discretization process is rather straightforward and well known and will not be detailed here. Perhaps the only issue that requires some discussion is the handling of the semi-infinite homogeneous medium for $z > d$.

For our purposes, a coordinate transformation is used to map the semi-infinite region $d < z < \infty$ to a finite one of length D . More specifically, the algebraic mapping proposed in [3] is used,

$$z_t = D \frac{z-d}{(z-d)+L} \quad (4)$$

where the scale factor L is a non-zero constant used to control the variation of z_t versus z . The mapping is simple and results in simple expressions for the first and second derivatives:

$$\frac{dG}{dz} = \frac{D}{L} \left[1 - \frac{z_t}{D} \right]^2 \frac{dG}{dz_t} \quad (5a)$$

$$\frac{d^2G}{dz^2} = \frac{D}{L^2} \left[1 - \frac{z_t}{D} \right]^4 \frac{d^2G}{dz_t^2} - \frac{2D}{L^2} \left[1 - \frac{z_t}{D} \right]^3 \frac{dG}{dz_t} \quad (5b)$$

As suggested in [3], standard central differencing can be used for the discretization of the resulting transformed equation. Finally, since the plane $z_t = D$ corresponds to the point at infinity, the boundary condition $G=0$ is imposed on that plane.

The finite-difference approximation of (3) results in the following matrix equation,

$$(\mathbf{A} + \lambda^2 \mathbf{B})\mathbf{g} = -\mathbf{F}\mathbf{u} \quad (6)$$

where the matrix \mathbf{A} is a tri-diagonal matrix of dimension N equal to the number of interior nodes of the finite-difference grid, \mathbf{B} is a diagonal matrix with elements values dependent on the permittivity value at the nodes, while the vector \mathbf{g} contains the values G_n of the spectral-domain Green's function at the N nodes. This discrete form of the spectral-domain equation (3) is written in such a way that it accounts for all the possible planes in the domain where source points are placed. To elaborate, let Q be the number of z planes at which source points (electric charges) are present. The development of a discrete approximation of the integral equation formulation of the problem of finding the electrostatic potential for a set of conductors requires the calculation of the spectral-domain Green's function at the Q source planes due to a point charge at each source plane. In other words, an $Q \times Q$ matrix, \mathbf{G} , of spectral-domain Green's functions is required. The vector \mathbf{u} in (6) is of length Q , identifying the Q source planes. The matrix \mathbf{F} is an $N \times Q$, with only one non-zero element per column. More specifically, for the q th source-plane a non-zero element of value 1 exists in the q th column of the matrix \mathbf{F} , at the row corresponding to the node number in the finite-difference grid assigned to the specific source plane. Multiplying both sides of (6) with the inverse of \mathbf{B} and solving for \mathbf{g} yields,

$$\mathbf{g} = -(\mathbf{B}^{-1}\mathbf{A} + \lambda^2 \mathbf{I})\mathbf{B}^{-1}\mathbf{F}\mathbf{u} \quad (7)$$

where \mathbf{I} is the identity matrix. Finally, the matrix \mathbf{G} can be obtained from the last equation by multiplying on the left with the transpose of \mathbf{F} ,

$$\mathbf{G} = -\mathbf{F}^T (\mathbf{B}^{-1}\mathbf{A} + \lambda^2 \mathbf{I})^{-1} \mathbf{B}^{-1} \mathbf{F} \quad (8)$$

The resulting equation for \mathbf{G} may be cast in a simpler form following the eigen-decomposition of the matrix $\mathbf{B}^{-1}\mathbf{A} = \mathbf{T}\mathbf{S}\mathbf{T}^{-1}$. Substitution in (8) yields,

$$\mathbf{G} = \mathbf{P}(\mathbf{S} + \lambda^2 \mathbf{I})^{-1} \mathbf{R} \quad (9)$$

where $\mathbf{P} = \mathbf{F}^T \mathbf{T}$ and $\mathbf{R} = -\mathbf{T}^{-1} \mathbf{B}^{-1} \mathbf{F}$. Since the matrix \mathbf{S} is diagonal, it follows immediately from this last equation that each element of the matrix \mathbf{G} is of the form,

$$G_{ij} = \sum_{n=1}^N \frac{P_{in} R_{nj}}{s_n + \lambda^2} \quad (10)$$

In this last equation, the constants s_n are dependent only on the properties of the layered medium and the grid size. The coefficients P_{in} and R_{nj} depend on both the layered medium properties and the position of the source planes. This step completes the development of the spectral Green's function matrix.

2. The Green's Function in the Space Domain

The final step in the construction of the Green's function in the space domain involves the calculation of the inverse Fourier-Bessel transform of (10). The relevant integral has the form

$$I = \int_0^\infty \frac{k}{a + \lambda^2} J_0(\lambda \rho) \lambda d\lambda \quad (11)$$

where k is a constant and a represents one of the eigenvalues of the matrix $\mathbf{B}^{-1} \mathbf{A}$. Using well-known properties of Bessel and Hankel functions, the above integral may be cast in the form

$$I = \frac{1}{2} \int_{-\infty}^{+\infty} \frac{k}{a + \lambda^2} H_0^{(2)}(\lambda \rho) \lambda d\lambda \quad (12)$$

It can be shown that a is always positive real; hence, the poles of the integrand in the above equation are imaginary. Considering the integral on the complex λ plane and recognizing that the integrand goes to zero for $\text{Im}\{\lambda\} < 0$, the residue theorem can be used for its calculation. The closed contour used for the integration includes the real axis and a circular arc of radius $R \rightarrow \infty$ in the lower half of the complex λ plane. This yields

$$I = \frac{1}{2} \left[\int_{-\infty}^{\infty} -2\pi j \frac{k}{-2j\sqrt{a}} \left[-j\sqrt{a} |H_0^{(2)}| \right]_{-j\sqrt{a}\rho}^{j\sqrt{a}\rho} \right] = kK_0(|\sqrt{a}\rho|) \quad (13)$$

where K_0 is the modified Bessel function of the second kind and zero order. In view of (13), the inverse Fourier-Bessel transform of (10) is

$$g_{ij}(\rho, z_i; 0, z_j) = \sum_{n=1}^N P_{in} R_{nj} K_0(|\sqrt{s_n} \rho|) \quad (14)$$

This concludes the development of the closed-form expression for the spatial Green's function in layered media.

3. Discussion and Validation

From (14) it is seen that the number of terms in the closed-form expression of the spatial Green's function is equal to the number of grid points in the finite difference grid. However, the number of terms can be reduced using model order reduction methods. Such reduction makes sense since several of the eigenvalues of the discrete system of (10) correspond to spectral lengths that are poorly resolved by the finite difference grid; hence, their contribution to the solution is insignificant. For our purposes, the so-called PRIMA algorithm [4] is used for the reduction of the order of the discrete system of (6). Our numerical experiments indicate that very accurate results are obtained using reduced models of order one fourth that of the order of the original discrete system.

In order to demonstrate the validity of the proposed method, the Green's function for a microstrip-type structure is calculated. The thickness of the dielectric substrate of relative dielectric constant 9 is taken to be 2 mm. The superstrate is free space. Two point sources are used, one at the dielectric interface ($z = 2$ mm), and the second inside the substrate at $z = 1$ mm. The algebraic mapping is implemented using $D = 1$ mm and $L = 1$ mm. A 1 mm buffer layer is used between the dielectric interface and the plane at which the mapping begins.

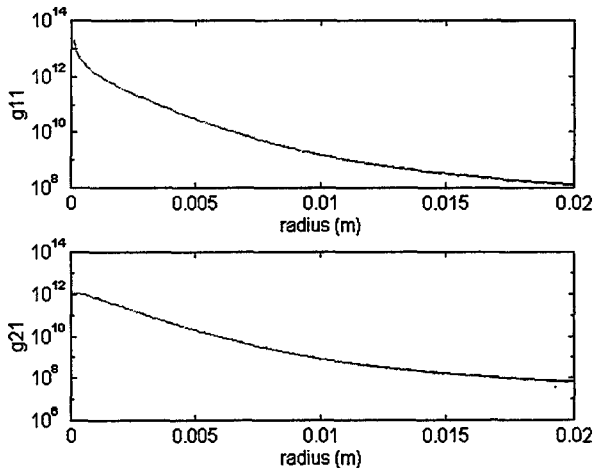


Figure 2. Calculated spatial Green's function for a microstrip structure. g_{11} is the spatial Green's function versus radial distance on the dielectric interface where the point source is located. g_{21} is the spatial Green's function versus radial distance on the plane $z = 1$ mm inside the substrate. Solid line: proposed closed-form expression; dash-dot line: analytic solution.

Closed-form expressions are easily derived for the Green's function for this simple microstrip structure, in terms of infinite series of image charges. For example, the potential due to a point source at point (x, y, z) in the superstrate at a point (X, Y, Z) inside the substrate is given by

$$g(x, y, z; X, Y, Z) = \frac{1}{2\pi(\epsilon_s + \epsilon_0)} \sum_{k=0}^{\infty} (-1)^k E^k \left[\frac{1}{\sqrt{\Delta x^2 + \Delta y^2 + (Z - z - 2kd)^2}} - \frac{1}{\sqrt{\Delta x^2 + \Delta y^2 + (Z + z + 2kd)^2}} \right] \quad (15)$$

where $\Delta X = X - z$, $\Delta Y = Y - y$, $\Delta Z = Z - z$, $E = (\epsilon_s - \epsilon_0) / (\epsilon_s + \epsilon_0)$, and d is the substrate thickness. Using this expression, analytic results for the Green's function at the dielectric interface and at plane $z = 1$ mm due to the source point at the interface are calculated and plotted versus ρ in Fig. 2. Also plotted in the same figure are the results obtained using the closed-form expressions presented in this paper. Excellent agreement is observed. Even though seventy-nine finite-difference grid points were involved in the discrete approximation, model order reduction was used to reduce the number of terms in the closed-form expression to twenty.

4. Concluding Remarks

In conclusion, a new approach has been proposed for the direct development of closed-form spatial Green's functions for electrostatic problems in layered dielectrics. Even though the mathematical development in this paper was for the three-dimensional case, the proposed methodology is directly applicable to two-dimensional problems. The only difference is that for the case of a two-dimensional geometry a one-dimensional Fourier transform pair is used in place of the Fourier-Bessel transform pair.

For the three-dimensional case, the resulting closed-form expression is in terms of a finite sum of modified Bessel functions of the second type and zero order. Once the source planes and observation planes have been selected, all required Green's functions are generated simultaneously. The z -plane information is captured by the coefficients in the finite sums, while the radial dependence is present in the argument of the modified Bessel functions. More specifically, the argument of the modified Bessel functions is of the form $(s_n)^{1/2} \rho$, where the constants s_n depend on the properties of the layered medium.

Finally, we mention that the proposed approach can be extended to the case of frequency-domain electromagnetic problems in layered media.

Acknowledgement

This work was supported in part by the Semiconductor Research Association, Contract 98-DJ-611, and an IBM Faculty Partnership Award.

References

- [1] Y. L. Chow, J. J. Yang, and G. E. Howard, "Complex images for electrostatic field computation in multilayered media," *IEEE Trans. Microwave Theory Tech.*, vol. 39, pp. 1120-1125, July 1991.

- [2] K. S. Oh, D. Kuznetsov, J. E. Schutt-Aine, "Capacitance computations in a multilayered dielectric medium using closed-form spatial Green's functions," *IEEE Trans. Microwave Theory Tech.*, vol. 42, pp. 1443 – 1453, Aug. 1994.
- [3] C. E. Grosch and S. A. Orszag, "Numerical solution of problems in unbounded regions: coordinate transforms," *J. Comput. Physics*, vol. 25, pp. 273 – 296, 1977.
- [4] A. Odabasioglou, M. Celik, and L. Pileggi, "PRIMA: Passive reduced-order interconnect macromodeling algorithm," *IEEE Trans. Computer Aided Design*, vol. 17, pp. 645 – 654, Aug. 1998.

The treatment of narrow microstrips and PCB tracks in the FDTD method using empirically modified coefficients

Chris J. Railton

**Centre for Communications Research, Faculty of Engineering
University of Bristol, Bristol,
BS8 1UB, England
chris.railton@bristol.ac.uk**

Abstract

The analysis of structures which contain narrow microstrips or PCB traces using the FDTD method and without resorting to a very fine mesh, has not yet been definitively solved despite its having been an area of intensive research for many years. The key to successful treatment of such structures is accounting for the field distribution in the vicinity of edges and wires without destroying the energy and divergence conserving properties of the FDTD mesh. In this paper the problem is dealt with by adjusting the permittivity and permeability assigned to the field nodes adjacent to the edges. These adjustments rely on a small pre-calculated look-up table and require only a negligibly small amount of extra calculation at the start of the FDTD analysis. The accuracy and robustness of the method is demonstrated for a variety of microstrip lines.

Introduction

The treatment of small geometrical detail, such as thin wires, strips or PCB traces, in the Finite Difference Time Domain (FDTD) method has been the subject of research for a number of years. Thin wires, embedded in an FDTD mesh were treated in 1981 by Holland [1] using an "in-cell inductance" concept to derive modified update equations for the magnetic, (H), field nodes which surround the wire. A simpler update formula, valid for the case where the wire is placed along a line of tangential E nodes, has been derived by applying the static field solution for the wire to the contour integral interpretation of the FDTD scheme. These formulations have been used and further investigated in a number of other publications including [2][3][4][5][6].

The conceptually similar problem of narrow microstrips has also received a considerable amount of attention in the literature. This has involved introducing static solutions into the full 3D algorithm eg. [7][8][9] and into planar models eg. [10]. Of the full-wave approaches, some early attempts at solving the problem, while achieving good levels of efficiency and accuracy, were prone to late time instability. Later contributions successfully overcame the stability problem by ensuring reciprocal interaction between nodes, but local charge conservation was not guaranteed and this limited the range of applications for the method.

In [11] a simple, effective and robust technique, without these limitations, was investigated in which the complicated field distribution around edges and wires is accounted for by modifying the permittivity and permeability assigned to the adjacent field nodes. In this contribution, this method is developed with more accurate and simpler empirical formulae for calculating the modified material parameters from the inductance and capacitance of the line to be modelled. With the use of just a small pre-calculated look-up table, accurate results can be obtained for these structures without the drawbacks of either late time instability or lack of local charge conservation. Moreover, the technique can be applied to many types of transmission line structure, such as microstrip with finite thickness, by using the appropriate empirical values.

Conductors of small cross-section in the FDTD mesh

Consider the case of a wire above a ground plane. This structure can be viewed as a transmission line which has a capacitance, C, and inductance, L, per unit length which depends on the wire radius as follows [12]:

$$L = \frac{\mu}{\pi} \cosh^{-1} \left(\frac{h}{a} \right)$$

$$C = \frac{\pi \epsilon}{\cosh^{-1} \left(\frac{h}{a} \right)} \quad (1)$$

where a is the radius of the wire and h is the height of the wire above the ground plane.

Similar equations exist, [13], from which the inductance and capacitance of a microstrip line or a PCB track can be calculated as a function of the geometry of the structure. Any transmission line which has a metal cross-section smaller than the FDTD cell size can be treated using the method described here as long as the quasi-static transmission line parameters are available.

In the standard FDTD mesh, the discretised wire will be predicted to have some value of L and C which is different from the true value. The parameters which can be adjusted in order to remedy this discrepancy are the permittivity associated with the transverse E field nodes and the permeability associated with the transverse H field nodes. If the wire is orientated along the z axis, the eight nodes which are at distances of $\delta x/2$ and $\delta y/2$ from the conductor are considered. Because these are closest to the conductor, the local nature of the conductor's influence is emphasised. In addition, since only the nodes adjacent to that conductor are modified, any spurious movement of charge, due to the introduced inhomogeneity will only happen locally to the conductor where undesirable effects are avoided. Physically, it can be seen that altering the permeability of these H field nodes is equivalent to surrounding the line with magnetic material, hence altering the inductance. Similarly altering the permittivity of the E field nodes will alter the capacitance but, due to the different field distributions for E and H fields, the extent to which the inductance and capacitance will be affected is different.

Properties of the FDTD mesh

The dependence of the transmission line parameters on the adjustments to the material parameters is complicated and depends on two geometrical parameters, (i) the number of cells between the ground plane and the strip or wire, and (ii) $h/\delta y$, and the aspect ratio of the mesh, $\delta x/\delta y$. The size of the cell in the longitudinal direction does not affect these results. This dependence can, however, be approximated by simple functions with empirically derived parameters. For instance, for metalisation which is smaller than the cell size the following approximations can be made.

$$M_\mu \approx \frac{L - a}{b}$$

$$M_\epsilon \approx \frac{1}{p(q - C)} - r \quad (2)$$

where L and C are the required inductance and capacitance for the transmission line under consideration, M_μ and M_ϵ are the factors by which the permeability and permittivity of the neighbouring E and H field nodes respectively must be multiplied. a, b, p, q, r are parameters which are derived by curve fitting to the results obtained from many FDTD runs.

It is noted that M_μ depends only on L , and M_ϵ depends only on C as would be expected. Moreover, in the case of microstrip, the value of the parameters is independent of the permittivity of the substrate. Although the capacitance of the line changes when the permittivity of the substrate changes, it is found that M_μ and M_ϵ do not. This is in accord with the principle that the asymptotic behaviour of fields around an edge are independent of the substrate. In general, it would be necessary to store a set of five coefficients for each combination of $h/\delta y$ and $\delta x/\delta y$ of

interest. In practice, $h/\delta y$ will always be an integer, usually no greater than 4, and the results for an arbitrary aspect ratio can be interpolated from a small set of pre-calculated results. Thus the total size of the look-up table is only about 200 real numbers.

These numbers have been calculated by performing a number of runs using the generic microstrip structure and FDTD arrangement described in [11].

Approximation to the transmission line inductance

An example of the calculated inductance per unit length for a thin strip whose neighbouring H field nodes have been modified, is shown in (2). It can be seen that the relationship between L and μ is approximately linear. Moreover the slope of the line is a function purely of the aspect ratio of the cell. At very small values of μ , the relationship is less linear and the slope becomes higher. The values of a and b in equation (2) are calculated by finding the best straight line fit to each set of data.

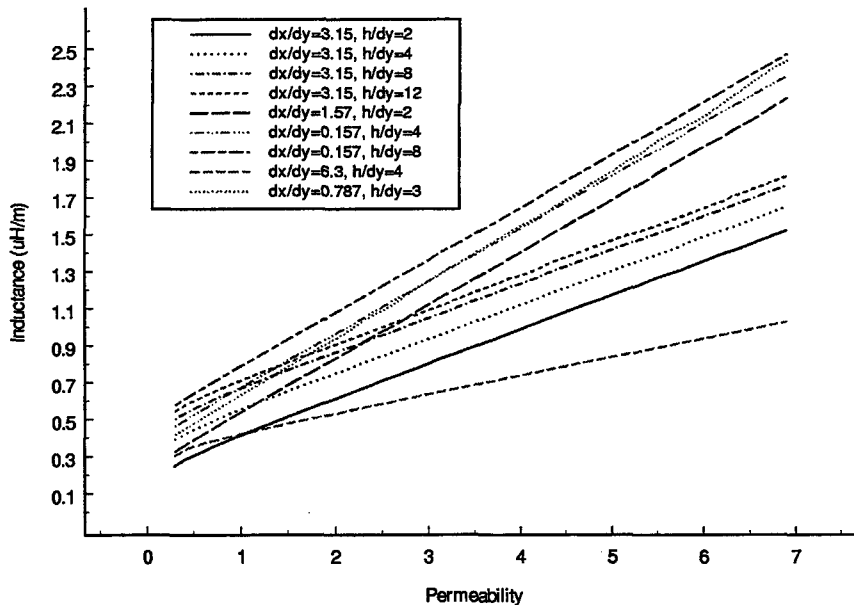


Figure 1 - The calculated inductance per unit length of a microstrip versus permeability of the adjacent H nodes

Approximation to the transmission line capacitance

An example of the calculated capacitance per unit length for a thin strip whose neighbouring E field nodes have been modified is shown in Figure 1. It can be seen that the capacitance value tends to an asymptotic limit as the permittivity gets high. These curves closely follow the form of equation (2). The parameters p, q and r are found by curve fitting to the data obtained from many FDTD runs.

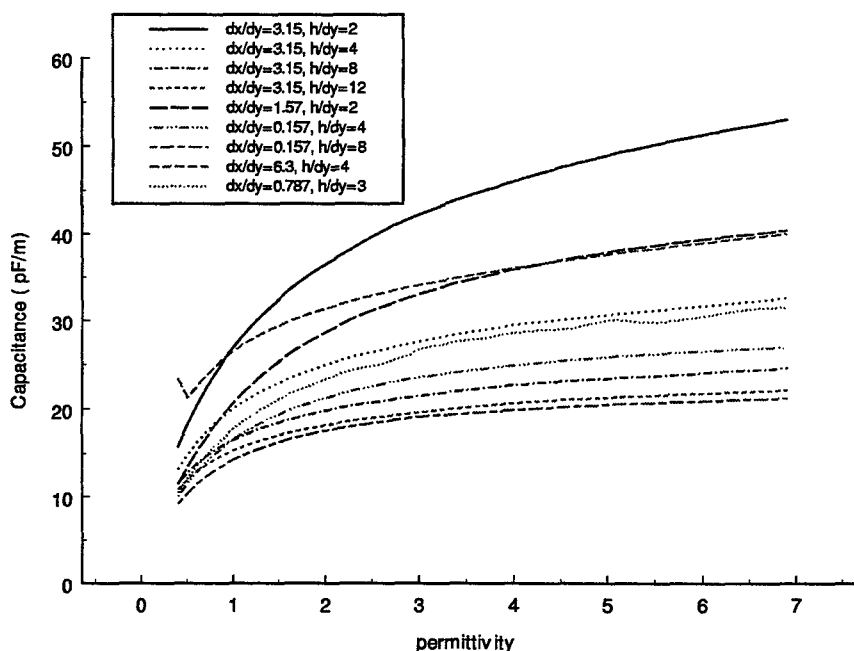


Figure 2 - The calculated capacitance per unit length of a microstrip versus permittivity of the adjacent E nodes

Analysis of wire structures using the empirical results

Using the results shown in the previous section in conjunction with equation (1), it is possible to calculate the empirical correction factors by which correct answers can be obtained for any wire radius and mesh size. The final accuracy of the computed results depend upon the accuracy of the curve fitted formulae and, of course, on the numerical accuracy of the original FDTD runs. Once the formulae have been generated, however, their use involves little or no computational overhead. In Figure 3 results calculated using the curve fitted parameters are compared to the analytical results for the case of $dx = dy = 0.3175\text{mm}$ and with the wire at a height of 0.635mm above the ground plane. It can be seen that the empirical formulae allow good accuracy to be obtained for both the propagation velocity and the characteristic impedance of the lines. The error is seen to be larger when the radius of the wire is small. It has been found that the effective permittivity, was very sensitive to errors in the node parameters. It is believed that a more painstaking derivation of the empirical formulae would allow this error to be reduced significantly.

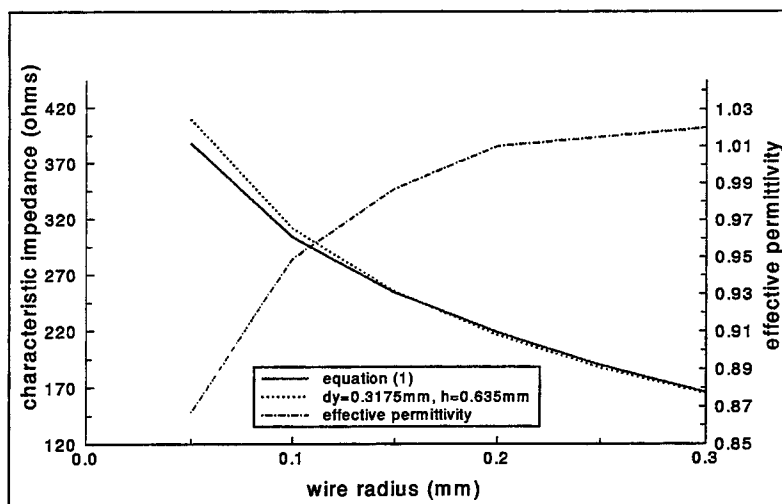


Figure 3 - Calculated parameters of wire above a ground plane compared to analytical

Analysis of microstrip lines using the empirical results

The same formulae can be used for the representation of microstrip lines. The only difference is that in this case the required capacitance and inductance are calculated using the corresponding quasi-static formulae:

Unlike the case of the wire, the edge still needs special treatment even if the width of the microstrip is large. Formulae have been calculated for the cases $\delta x < w < 2\delta x$ and $2\delta x < w < 3\delta x$. For strips wider than $3\delta x$, the latter formula can be used without significant loss in accuracy since the interaction between the two edges is then small.

In Figure 4 results for the characteristic impedance of microstrip, calculated using the empirical formulae, are compared to those calculated using the equation [13] for a variety of strip widths and mesh sizes. Again it can be seen that good accuracy is obtained. It is emphasised that, although the predicted capacitance of the transmission line is a function of the permittivity of the substrate, the required adjustment to the FDTD material parameters is not. This would be expected since the edge effects are dominated by the singular behaviour of the field which is unaffected by the presence of the dielectric. Thus the same empirical formula can be used for any substrate.

In Figure 5 and Figure 6, the calculated effective permittivity is compared to the results from [13]. It can be seen that, while not perfect, the error is much reduced from that which would have been obtained using the basic FDTD method. The latter would have predicted the same effective permittivity regardless of strip width.

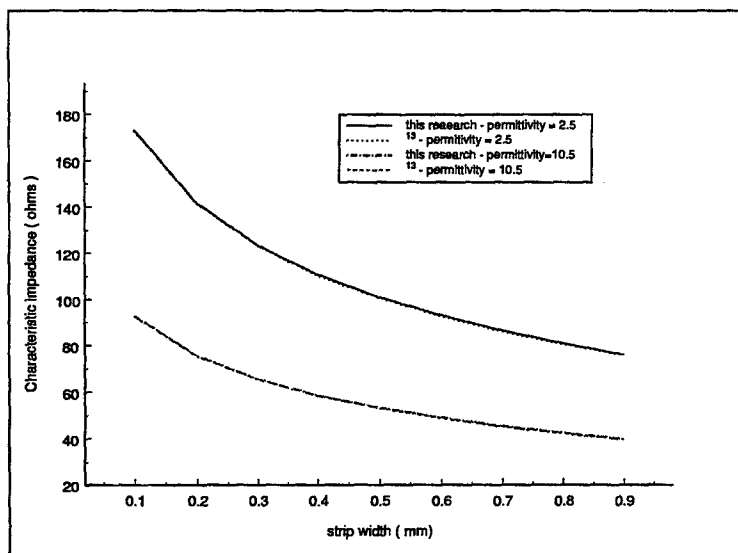


Figure 4 - Characteristic impedances using this method compared to equations from [13]

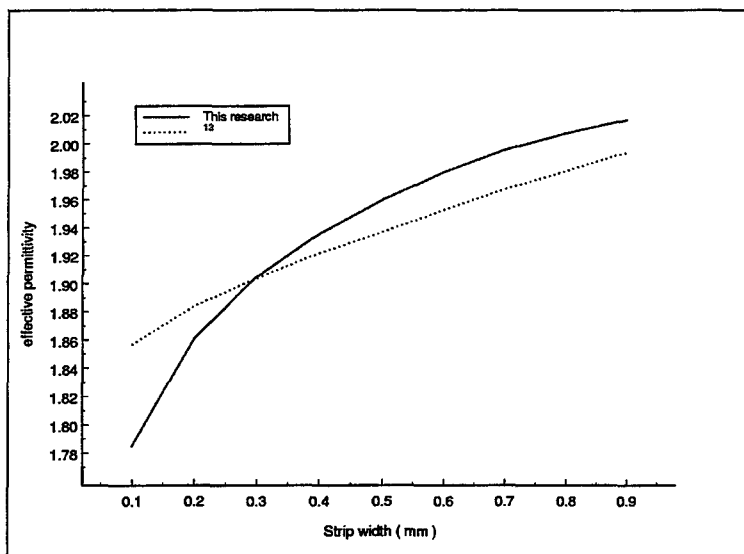


Figure 6 Effective permittivity using this method compared to equations from [13]. Substrate permittivity 2.5

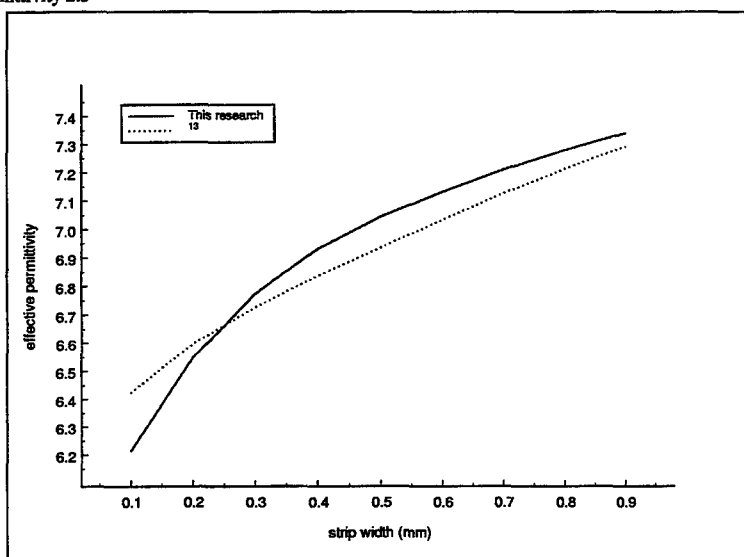


Figure 5 Effective permittivity using this method compared to equations from [13]. Substrate permittivity 10.5

Conclusions

In this contribution, a procedure has been described whereby simple analytical formulae can be derived and incorporated in the FDTD algorithm which allow the accurate treatment of wires and microstrip structures without either having to resort to a very fine mesh or to risk introducing spurious divergence or late time instability. The resulting scheme is simple, versatile, robust and readily capable of extension to more complex incidences of electrically small structures.

Acknowledgements

I wish to thank Professor Joe McGeehan for the provision of facilities within the Centre for Communications Research. I also wish to thank Dr. Ian Craddock and my colleagues in the Computational Electromagnetics Group for many helpful discussions.

References

1. R. Holland and L. Simpson "Finite Difference Analysis of EMP coupling to thin struts and wires" May 1981 IEEE Trans EMC-23 pp 88-97
2. A. Taflov and K. Umashankar, "The finite-difference time-domain method for numerical modelling of electromagnetic wave interactions", Electromagnetics, vol. 10, pp. 105-126, 1990
3. C. J. Railton, "The simple, rigorous and effective treatment of thin wires and slots in the FDTD method", 24th European Microwave Conference, Cannes, 1994, pp. 1541-1546.
4. J. Grando, F. Issac, M. Lemistre and J. C. Alliot, "Stability analysis including wires of arbitrary radius in FD-TD code", IEEE AP-S symposium, Ann Arbor, 1993, pp. 18-21.
5. P. Bonnet, X. Ferrieres, J. Grando and J. C. Alliot, "FDTD applied to dielectric or wire structures", IEEE AP-S symposium, Baltimore, 1996, pp. 2126-2129
6. J. J. Boonzaier, "The radiation and scattering by thin wires: A Finite Difference Time Domain approach", PhD thesis, University of Pretoria, South Africa, 1994.
7. D. B. Shorthouse and C. J. Railton, "Incorporation of static field solutions into the Finite Difference Time Domain algorithm", IEEE Trans MTT-40, 1992, pp. 986-994
8. C. J. Railton, D. B. Shorthouse and J. P. McGeehan, "The analysis of narrow microstrip lines using the finite difference time domain method", Electronics Letters, 1992, pp. 1168-1170.
9. I. J. Craddock and C. J. Railton, "Stable inclusion of *a priori* knowledge of field behaviour in the FDTD algorithm: Application to the analysis of microstrip lines", IEEE AP-S, Baltimore, 1996, pp. 1300-1303.
10. W. K. Gwarek, "Analysis of arbitrarily-shaped planar circuits - a time domain approach", IEEE Trans MTT-33, pp. 1067-1072, Oct. 1985.
11. C. J. Railton, "An Investigation into the properties of the FDTD mesh with application to wires and strips", Int. J. of Num. Modelling, April 1999.
12. D. Pozar, "Microwave Engineering", J. Wiley and Sons, 1998, ISBN 0-471-17096-8
13. A. Balanis, "Advanced Microwave Engineering", J. Wiley and Sons.

Time-Domain-Analysis of QTEM Wave Propagation and Crosstalk on Lossy Multiconductor Transmission Lines with Terminal Coupling

Georg Müller, Jan Wendel and Karl Reiß
Institut für Theoretische Elektrotechnik, University of Karlsruhe
76128 Karlsruhe, Germany
Tel: +49 721 608 2636, Fax: +49 721 608 2623
Email: mueller@ieee.org

Abstract – A new method for the simulation of arbitrary signals on lossy multiconductor transmission lines is presented. Coupling is considered along the lines as well as at resistive terminal networks. The algorithm works solely in the time-domain without any transforms to the frequency domain and is based on the assumption of quasi-TEM wave propagation. As first step, the time-domain MTL equations are decoupled using proper similarity transforms. An analytical solution for the wave propagation on the decoupled modal lines is derived using Riemann's method, so the solutions for all modal lines can be obtained simultaneously. These solutions contain yet unknown functions which are determined by solving a set of coupled integral equations modeling the lines' resistive terminal networks. Results are compared with those obtained using alternative methods and the effects of certain simplifications in common transmission line models are investigated.

1 Introduction

During the design process of modern high-speed electronic circuits, it is not sufficient to look at systems from a pure network-point-of-view. In addition, many electromagnetic phenomena have to be taken into account – and certainly one of the most important among them is the analysis of quasi-TEM-wave propagation on coupled multiconductor transmission lines (MTLs). This task has been dealt with mainly in the frequency domain – frequency domain techniques, however, are not very effective when applied to the simulation of very broad-band excitations (e.g. a single pulse). Furthermore, time-domain techniques often provide better insight into physical phenomena such as crosstalk and dispersion. From a time-domain point-of-view, these phenomena can be directly understood and described without falling back upon concepts like frequency-dependent phase velocities.

For these reasons, we developed and implemented an algorithm for the analysis of lossy coupled MTLs terminated by resistive networks. This algorithm works solely in the time-domain. As it is based on a modal decomposition of the coupled multiconductor transmission line equations, we will start with a review of the cases in which the decoupling of these equations is possible in the time-domain. In particular we will demonstrate under which prerequisites the MTL-equations can be decoupled without further simplifications and in which cases some simplifying assumptions have to be made.

After decoupling has succeeded, the propagation of the single modes can be described independent from each other. In [1] and [2], fundamental time-domain-solutions for quasi-TEM wave propagation in lossy media have been calculated and applied to scattering problems in stratified media. We make use of the fact that there is an isomorphism between the modal transmission line equations and the partial differential equations of quasi-TEM wave propagation in free space. Thus, the same fundamental time-domain solutions can also be used for quasi-TEM wave propagation on lossy transmission lines.

We are, however, actually dealing with multiple parallel (modal) lines coupled at their respective terminal networks. The resulting boundary conditions are specific to this problem and differ from the ones used when analyzing scattering problems in stratified media. Applying the boundary conditions leads to two sets of coupled integral expressions, one for each terminal network of the line system. An iterative scheme for evaluating these expressions is presented. By using properly adjusted spatial and temporal discretization we make sure that the iterations are performed simultaneously for all modal lines.

2 TD Modal Analysis of Lossy Lines

If we consider homogeneous n -line-systems, the physical voltages and currents on the lines can be expressed by the vectors \mathbf{u} and \mathbf{i} which are related by the well-known equations

$$-\frac{\partial \mathbf{u}}{\partial z} = \mathbf{R}\mathbf{i} + \mathbf{L}\frac{\partial \mathbf{i}}{\partial t}, \quad -\frac{\partial \mathbf{i}}{\partial z} = \mathbf{G}\mathbf{u} + \mathbf{C}\frac{\partial \mathbf{u}}{\partial t}. \quad (1)$$

The $n \times n$ -matrices \mathbf{R} , \mathbf{L} , \mathbf{G} and \mathbf{C} are constant, symmetrical and positive definite, z denotes the direction of propagation. The first step of our approach is to decouple the set of coupled partial differential equations (1), that is to determine so called *eigenmodes* v and j as linear combinations of the physical voltages and currents

$$\mathbf{u} = \mathbf{S}\mathbf{v}, \quad \mathbf{i} = \mathbf{T}\mathbf{j}, \quad (2)$$

where the transformation matrices \mathbf{S} and \mathbf{T} are chosen such that the resulting transmission line equations for the eigenmodes are decoupled, i.e.

$$\mathbf{r} = \mathbf{S}^{-1}\mathbf{R}\mathbf{T}, \quad \mathbf{l} = \mathbf{S}^{-1}\mathbf{L}\mathbf{T}, \quad \mathbf{c} = \mathbf{T}^{-1}\mathbf{C}\mathbf{S}, \quad \mathbf{g} = \mathbf{T}^{-1}\mathbf{G}\mathbf{S}, \quad (3)$$

are diagonal (in the context of this paper, diagonal matrices will be denoted by small bold letters). The matrices in (1) do – except for some particular line geometries – not commute, thus the complete system (3) is not diagonalizable except for these line geometries.

If two of the four matrices in (1) can be assumed zero (e.g. with lossless lines), decoupling of the MTL-equations is always possible. The unified line model described in [3] can then be used to determine \mathbf{S} and \mathbf{T} from associated eigenvalue-problems. In a lossy but homogenous dielectric, \mathbf{G} is a multiple of \mathbf{C} and the system can be diagonalized if only \mathbf{R} vanishes. We are interested, however, in the cases where none of these matrices can be regarded as zero and diagonalization is nonetheless possible. Solutions obtained for these cases can without problem be adopted to the more simple cases mentioned above.

Assuming $\mathbf{S} = \mathbf{T}$ in eq. (2), the expressions in (3) become similarity transforms. It is a well-known fact that symmetric positive definite matrices are diagonalized by such transforms if and only if the transformation matrices consist of the eigenvectors of the matrices to be diagonalized. Thus, diagonalization will succeed if all four matrices \mathbf{R} , \mathbf{L} , \mathbf{G} and \mathbf{C} share the same set of eigenvectors, the diagonal matrices \mathbf{r} , \mathbf{l} , \mathbf{g} and \mathbf{c} will then contain the respective eigenvalues.

There are two relevant cases where it is possible to decouple the full set of lossy MTL-equations in the time-domain:

Bus systems consist of identical parallel conductors with equidistant spacing between them above a common backplane. If coupling is considered only between adjacent conductors, all four matrices have a symmetric tri-diagonal toeplitz structure. In this case, the set of eigenvectors is completely determined by the matrices' rank (i.e. the number of conductors) and is *independent* of the actual values of the matrix elements. All matrices can be written in the form¹

$$\begin{pmatrix} a & b & 0 & 0 \\ b & a & b & 0 \\ 0 & b & a & b \\ 0 & 0 & b & a \end{pmatrix} \quad (4)$$

The Elements of \mathbf{S} can then be calculated using [4]

$$S_{ij} = \phi_{i-1} \left(-2 \cos \frac{j\pi}{n+1} \right) \quad \text{with} \quad \phi_k(x) = x\phi_{k-1}(x) - \phi_{k-2}(x), \quad \phi_0(x) = 1, \quad \phi_1(x) = x. \quad (5)$$

The elements of the corresponding diagonal matrices depend from the matrices' values:

$$\lambda_i = a - 2b \cos \left(\frac{i\pi}{n+1} \right) \quad (6)$$

¹a four-line-system is used as an example

Circular Multiconductors consist of identical conductors and a reference conductor, the conductors having a symmetry with respect to the reference conductor such that all matrices are of a circular structure [5]:

$$\begin{pmatrix} a & b & c & d \\ b & a & b & c \\ c & b & a & b \\ d & c & b & a \end{pmatrix} \quad (7)$$

Again, the eigenvectors are independent from the values of the matrix elements

$$S_{ik} = \varepsilon_k^{i-1} \quad \text{with} \quad \varepsilon_k = e^{j(k-1)\frac{2\pi}{n}} \quad (8)$$

and the corresponding eigenvalues are obtained from multiplying the eigenvector with the first line of the cyclic matrix. No couplings between lines have to be neglected in this case.

Thus, we are able to transform the set of $2n$ coupled equations (1) to n sets of 2 coupled equations each:

$$-\frac{\partial v_i}{\partial z} = r_i j_i + l_i \frac{\partial j_i}{\partial t}, \quad -\frac{\partial j_i}{\partial z} = g_i v_i + c_i \frac{\partial v_i}{\partial t}, \quad i = 1..n. \quad (9)$$

Except for the special case of non-mixing line terminations, these equations are still coupled via their boundary conditions, i.e. the system's terminal networks. If the physical lines are excited by real voltage-sources u_0 at $z = 0$ and terminated by a resistive network at $z = z_L$

$$u|_{(z=0)} = u_0 - Z_s i|_{(z=0)}, \quad u|_{(z=z_L)} = Z_t i|_{(z=z_L)}, \quad (10)$$

the excitations and terminations of the modal lines are given by

$$v_0 = S^{-1} u_0, \quad Z_{s,m} = S^{-1} Z_s S, \quad Z_{t,m} = S^{-1} Z_t S. \quad (11)$$

If any of the matrices $Z_{s/t}$ is diagonal, the respective matrix $Z_{s/t,m}$ in the modal system will again be diagonal.

3 Fundamental Solutions

The solution of (9) for a single eigenmode is calculated using Riemann's method [1]. With

$$v_{ci} = (l_i c_i)^{-1/2}, \quad Z_i = l_i^{1/2} c_i^{-1/2}, \quad \alpha_i = \frac{1}{2} \left(\frac{g_i}{c_i} + \frac{r_i}{l_i} \right), \quad \gamma_i = \frac{1}{2} \left(\frac{g_i}{c_i} - \frac{r_i}{l_i} \right) \quad (12)$$

(note that all quantities are real although we are dealing with lossy lines) we obtain

$$\begin{aligned} v_i(z, t) = e^{-\alpha_i t} \left[f_{i+}(t - \frac{z}{v_{ci}}) + f_{i-}(t + \frac{z}{v_{ci}}) \right] - \frac{\gamma_i}{2} e^{-\alpha_i t} \int_{\xi=0}^{t - \frac{z}{v_{ci}}} \left[I_0(w_+) - \gamma_i(t + \frac{z}{v_{ci}}) \frac{I_1(w_+)}{w_+} \right] f_{i+}(\xi) d\xi \\ - \frac{\gamma_i}{2} e^{-\alpha_i t} \int_{\xi=0}^{t + \frac{z}{v_{ci}}} \left[I_0(w_-) - \gamma_i(t - \frac{z}{v_{ci}}) \frac{I_1(w_-)}{w_-} \right] f_{i-}(\xi) d\xi \quad (13) \end{aligned}$$

$$\begin{aligned} j_i(z, t) = \frac{1}{Z_i} e^{-\alpha_i t} \left[f_{i+}(t - \frac{z}{v_{ci}}) - f_{i-}(t + \frac{z}{v_{ci}}) \right] + \frac{1}{Z_i} \frac{\gamma_i}{2} e^{-\alpha_i t} \int_{\xi=0}^{t - \frac{z}{v_{ci}}} \left[I_0(w_+) + \gamma_i(t + \frac{z}{v_{ci}}) \frac{I_1(w_+)}{w_+} \right] f_{i+}(\xi) d\xi \\ - \frac{1}{Z_i} \frac{\gamma_i}{2} e^{-\alpha_i t} \int_{\xi=0}^{t + \frac{z}{v_{ci}}} \left[I_0(w_-) + \gamma_i(t - \frac{z}{v_{ci}}) \frac{I_1(w_-)}{w_-} \right] f_{i-}(\xi) d\xi \quad (14) \end{aligned}$$

with

$$w_+ = w_+(\xi) = |\gamma| \sqrt{\left(t + \frac{z}{v_c}\right)\left(t - \frac{z}{v_c} - \xi\right)}, \quad w_- = w_-(\xi) = |\gamma| \sqrt{\left(t - \frac{z}{v_c}\right)\left(t + \frac{z}{v_c} - \xi\right)}. \quad (15)$$

I_0 and I_1 are the modified bessel functions of 0th and 1st order, respectively. For lossless lines, eqs. (13) and (14) become the well-known d'alambert solutions, the integral terms describe dispersion on the line due to losses, the exponential terms are responsible for attenuation. Both solutions contain the yet unknown function f_{i+} and f_{i-} which have to be determined by enforcing the boundary conditions at $z = 0$ and $z = z_L$, respectively.

4 Boundary Conditions

During numerical evaluation, the integrals in (13) and (14) are replaced by discrete sums. Thus, we first have to choose a proper temporal discretization t_0 . To get exact results, one would have to make sure that the number of discrete points in space

$$m_i = \frac{z_L/v_{ci}}{t_0} \quad (16)$$

is an integer for all modal lines i . This is virtually impossible, yet we have found that the resulting error can be neglected if we only do not choose t_0 too large. We will describe how to deal with the boundary at $z = 0$, that is how to determine

$$f_{\oplus}(t) = \begin{pmatrix} f_{i+}(t) \\ \vdots \\ f_{n+}(t) \end{pmatrix} \quad (17)$$

At the beginning of the simulation ($t = 0$) we assume that all voltages and currents along the line are zero. The lines' terminations at $z = z_L$ are passive, thus

$$f_{i+}(t) = 0, \quad t < 0 \quad \text{and} \quad f_{i-}(t) = 0, \quad t < m_i t_0. \quad (18)$$

It is important to note that when we want to determine the value of $f_{\oplus}(T)$ at the p th time-step ($t = T = p t_0$) the values of all $f_{i-}(T)$ are already known. Equations (13) and (14) yield

$$v|_{(z=0, t=T)} = [e^{-\alpha T}] \cdot (\mathcal{A} + \mathcal{C} + \mathbf{x} f_{\oplus}(T)) \quad (19)$$

$$j|_{(z=0, t=T)} = [e^{-\alpha T}] \cdot (\mathcal{B} + \mathcal{D} + \mathbf{y} f_{\oplus}(T)) \quad (20)$$

with the $(n \times 1)$ -matrices \mathcal{A}_p , \mathcal{B}_p , \mathcal{C}_p and \mathcal{D}_p given by

$$\mathcal{A}_{p,i} = -\frac{\gamma_i t_0}{2} \left[\frac{1}{2} (I_0(\gamma p t_0) - I_1(\gamma p t_0)) f_{i+}(0) + \sum_{k=1}^{p-1} \left(I_0(w_+) - \gamma_i p t_0 \frac{I_1(w_+)}{w_+} \right) f_{i+}(k t_0) \right] \quad (21)$$

$$\mathcal{B}_{p,i} = \frac{\gamma_i t_0}{2Z_i} \left[\frac{1}{2} (I_0(\gamma p t_0) + I_1(\gamma p t_0)) f_{i+}(0) + \sum_{k=1}^{p-1} \left(I_0(w_+) + \gamma_i p t_0 \frac{I_1(w_+)}{w_+} \right) f_{i+}(k t_0) \right] \quad (22)$$

$$\mathcal{C}_{p,i} = f_{i-}(p t_0) - \frac{\gamma_i t_0}{2} \left[\frac{1}{2} (I_0(\gamma p t_0) - I_1(\gamma p t_0)) f_{i-}(0) \right. \quad (23)$$

$$\left. + \sum_{k=1}^{p-1} \left(I_0(w_-) - \gamma_i p t_0 \frac{I_1(w_-)}{w_-} \right) f_{i-}(k t_0) + \frac{1}{2} \left(1 - \frac{1}{2} \gamma_i p t_0 \right) f_{i-}(p t_0) \right] \quad (24)$$

$$\mathcal{D}_{p,i} = \frac{f_{i-}(p t_0)}{Z_i} - \frac{\gamma_i t_0}{2Z_i} \left[\frac{1}{2} (I_0(\gamma p t_0) + I_1(\gamma p t_0)) f_{i-}(0) \right. \quad (25)$$

$$\left. + \sum_{k=1}^{p-1} \left(I_0(w_-) + \gamma_i p t_0 \frac{I_1(w_-)}{w_-} \right) f_{i-}(k t_0) + \frac{1}{2} \left(1 + \frac{1}{2} \gamma_i p t_0 \right) f_{i-}(p t_0) \right] \quad (26)$$

Eqs. (15) have to be evaluated at the respective points in time with ξ replaced by kt_0 , $[e^{-\alpha T}]$ is the $(n \times n)$ diagonal matrix of the exponential attenuation terms. The $(n \times n)$ diagonal matrices x and y are given by

$$x_i = 1 - \frac{1}{2}t_0 \left(\frac{\gamma}{2} - \frac{\gamma^2}{4}pt_0 \right) \quad (27)$$

$$y_i = \frac{1}{Z_i} \left[1 + \frac{1}{2}t_0 \left(\frac{\gamma}{2} + \frac{\gamma^2}{4}pt_0 \right) \right] \quad (28)$$

Substituting these into the boundary conditions (11) we get

$$f_{\oplus} = [x + Z_{s,m} \cdot y]^{-1} \cdot [e^{\alpha T}] \cdot v_0 - A - C - Z \cdot (B + D) \quad (29)$$

A similar expression is derived to determine the f_{i-} from the boundary conditions at $z = z_L$. When the new value of $f_{i-}(qt_0)$ is to be calculated, the yet unknown values of $f_{i+}(qt_0)$ do not have to be known for this calculation. Only the values of $f_{i+}(t)$ with $t < (q - m_i)t_0$ (which already have been calculated during earlier iterations) are needed. Thus, (29) and the corresponding equation for the far end of the line can be evaluated at every time-step to iteratively determine both f_{i+} and f_{i-} .

Using this algorithm, the fundamental solutions (13) and (14) have to be evaluated solely at two points in space, that is at $z = 0$ and $z = z_L$. If, however, voltages and currents are to be calculated along the line at a specified time, they can always be determined from (13) and (14) as they are needed.

5 Results

The above algorithm was implemented such that the output may be the physical or modal voltages or currents. They can be plotted as functions of time at a given point on the line or as functions of space at a given time. The program can also be used to produce animations of wave-propagation along a line system, providing immediate insight in how dispersion and speed of propagation on the modal lines influence coupling between the physical lines and how coupling is caused by the sources and terminal networks.

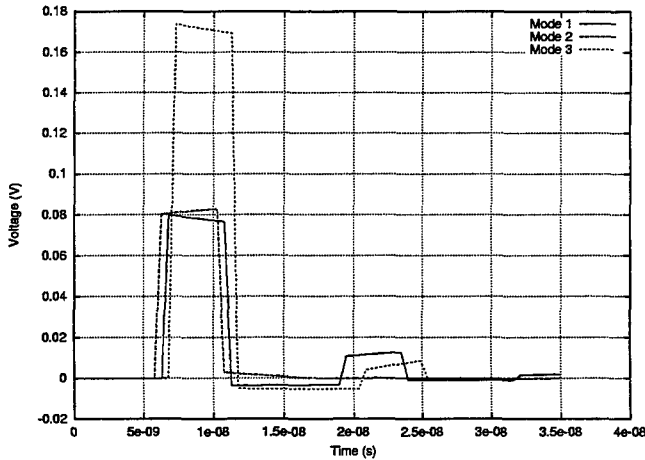


Figure 1: Modal voltages

Figure 1 shows the modal voltages at the end of a three-line bus system of which one physical line is excited by a voltage source and the others are passive. The timestep t_0 was chosen as $0.1ns$ which corresponds to a spatial

discretization of 63, 58 and 68 points, respectively, for the 1m-system. It is easy to see how all three modes are excited by the single source and how the modal properties (e.g. speed of propagation) differ. In figure 2, the same

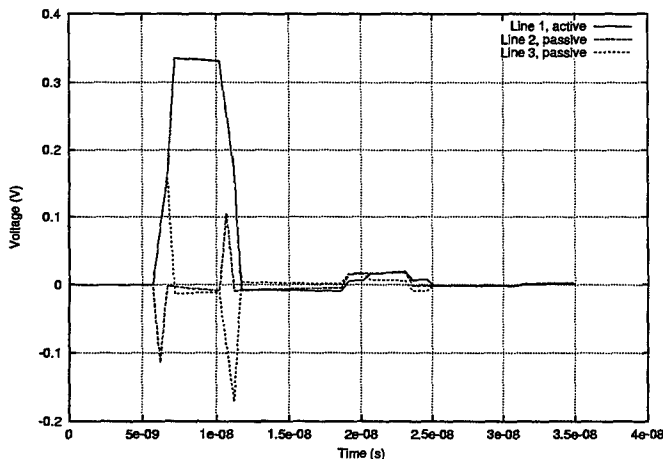


Figure 2: Physical (line) voltages

results are shown, this time for the physical lines. Crosstalk due to the different speeds of the modes can clearly be observed.

We compared our results with an FDTD-based simulation of the coupled line system (figure 3). The system was discretized using 60 points in space. The voltages exhibit the spurious oscillations typical for a disadvantageous discretization. Otherwise there is a good match with our results.

We also performed frequency-domain simulations with a limited bandwidth. In the frequency-domain, only a succession of periodic pulses can be simulated. To compare the results, we either have to increase the period between two pulses in the frequency domain or we have to excite the active line with repeating pulses in the time domain. In the last case, one can clearly observe the difference between frequency domain results and our method which are due to the fact that we actually start the simulation with completely passive lines.

When simulating bus systems, we introduce some error by the assumptions we make for the p.u.l. capacitance matrix C (and, as well, G). The main diagonal elements of C are defined as [5] the sum of the p.u.l. capacity of the corresponding line and the p.u.l. coupling capacities in that row. Thus, neglecting coupling capacities, (4) should strictly speaking be written as

$$\begin{pmatrix} a_1 & b & 0 & 0 \\ b & a_2 & b & 0 \\ 0 & b & a_2 & b \\ 0 & 0 & b & a_1 \end{pmatrix}. \quad (30)$$

Simulations showed that by choosing $a = a_1 \forall a$, the delay of the lines is underestimated as compared with choosing $a = a_2$ or not neglecting couplings at all. The difference, however, is only about 0.2ns for the given three-line system and does not need to be considered.

6 Conclusions

We developed and implemented a new time-domain algorithm for the simulation of wave propagation on coupled lossy transmission lines. The algorithm is not based on classical FD-schemes, thus stability problems do not

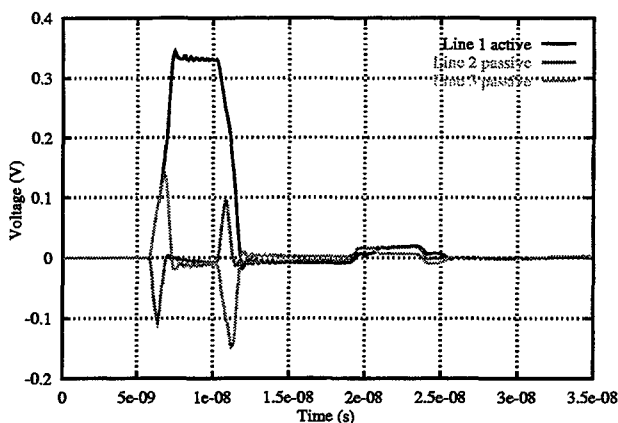


Figure 3: FDTD-simulation

arise. Combining the method with newton-raphson-iteration at the boundaries, it has been extended to deal with arbitrary nonlinear non-modemixing terminal networks. From the fundamental solutions used, dirac-shaped partial solutions can be separated analytically and might be used for convolution with arbitrary signals.

References

- [1] Michael Schinke and Karl Reiss, *Fundamental Time Domain Solutions for Plane TEM-Waves in Lossy Media and Applications*, IEICE Transactions on Electronics, vol. E78-C, No. 8, pp. 1111-1116, Aug. 1995.
- [2] Michael Weber and Karl Reiss, *A New Approach for Solving Scattering Problems in Stratified Conductive Media in Time Domain* 13th Annual Review of Progress in Applied Computational Electromagnetics (ACES97), pp. 1318-1325, Mar. 1997, Monterey, CA.
- [3] Georg Mueller, Jan Wendel and Karl Reiss, *Efficient Analysis of Coupled Multiconductor Transmission Lines*, International Symposium On Electromagnetic Compatibility (EMC 1999), pp. 646-649, May 1999, Tokyo, JAPAN.
- [4] Fabio Romeo and Mauro Santomauro, *Time-Domain Simulation of n Coupled Transmission Lines*, IEEE Trans. MTT, vol. 35, pp. 131-136, Feb. 1987.
- [5] Clayton R. Paul, *Analysis of multiconductor transmission lines*, John Wiley & Sons, 1994.

An MPIE-based Circuit Extraction Technique and its Applications on Power Bus Modeling in High-Speed Digital Designs

Jun Fan, Hao Shi*, James L. Knighten**, and James L. Drewniak

Electromagnetic Compatibility Laboratory

Department of Electrical and Computer Engineering

University of Missouri-Rolla

jfan@umr.edu

*HP-EEsof Division

Hewlett-Packard Company

** NCR Corporation

Abstract

Power bus design is a critical aspect in high-speed digital circuit designs. A circuit extraction approach based on a mixed-potential integral equation is presented to model arbitrary multilayer power bus structures including vertical discontinuities associated with surface mount (SMT) decoupling capacitor interconnects. The agreement of modeling and measurements demonstrates its effectiveness and utilization in power bus designs.

I. Introduction

Electromagnetic Interference (EMI) and Signal Integrity (SI) problems are increasingly problematic in high-speed digital designs with higher clock frequencies, faster edge rates, and dense circuit layouts. The DC power bus structure is an important design aspect [1]. Simultaneous switching noise (delta-I noise) propagates on power and ground planes in multilayer PCB designs utilizing entire planes, resulting in interference among various circuits and can couple to the chassis cavity as well to radiate through apertures and slots. There are suggested approaches for reducing the effects of this high-frequency noise in practical designs [2], such as using power island structures, placement of decoupling capacitors, using high-dielectric-constant materials in the power layer, high-loss materials, etc. However, proven guidelines are not well established. Although many power bus design aspects can be investigated by hardware trial-and-error for a certain high-speed design, this is often an inefficient and unacceptable design practice. Power bus modeling provides a cost-effective, quick-and-easy way of performing various *what-if* scenarios. Furthermore, modeling can not only provide a very suitable solution to a certain design, but also develop general guidelines for similar applications.

A full-wave power bus modeling approach, denoted as *CEMPIE*, to designate a Circuit Extraction based on a Mixed-Potential Integral Equation procedure is presented herein. Circuit models have some advantages over electromagnetic models. Their quantities are currents and voltages, which are more intuitive and easily used with other signal integrity tools than field quantities. Further, the extracted circuit model is reusable for various frequency- and time-domain modeling.

II. MPIE Formulation

Surface currents $\vec{J}(\vec{r})$ and charges $\sigma(\vec{r})$ are induced on the conducting planes of concern (power planes) and on the surfaces of vertical discontinuities as a result of an incident electric field

\vec{E}^{inc} . Ground planes and dielectric layers are assumed to be infinite in the modeling, and are incorporated into the Green's functions. When the boundary conditions on the remaining conducting surfaces are enforced, an electric field integral equation results

$$\hat{n} \times [j\omega \int_{S1+S2} \vec{\bar{G}}^A(\vec{r}, \vec{r}') \cdot \vec{J}(\vec{r}') ds' + \nabla \phi] = 0, \quad (1)$$

where ϕ is the induced scalar electric potential; $S1$ refers to horizontal planes of concern; and $S2$ refers to vertical surfaces of vias and/or ports, as shown in Figure 1; and, $\vec{\bar{G}}^A$ is a dyadic Green's function for the vector magnetic potential. The dyadic Green's function has the following form in a stratified medium [3]

$$\vec{\bar{G}}^A = G_{xx}^A(\hat{x}\hat{x} + \hat{y}\hat{y}) + G_{xx}^A\hat{z}\hat{z} + G_{xy}^A\hat{z}\hat{y} + G_{xz}^A\hat{z}\hat{z}. \quad (2)$$

The incident electric field is assumed to be zero, since the discretized problem is not solved, rather, an equivalent circuit is extracted.

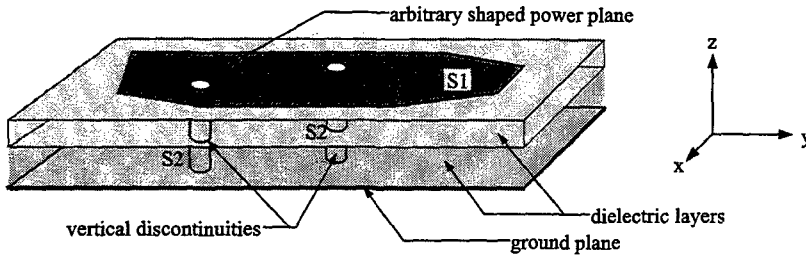


Figure 1: A typical power bus structure, with arbitrary metallization on the power layer(s).

Since triangular patches are more amenable than orthogonal patches in dealing with arbitrarily shaped structures, they are used to discretize the horizontal planes of concern. However, rectangular patches are used on the vertical surfaces, because, on these vertical surfaces, most surface currents flow axially (the height of vias and ports of interest is relatively small). Vector basis functions are employed, and anchored by the interior edges of all triangular surface patches [4], while the basis functions associated with vertical rectangular cells are chosen to have the form of one-dimensional linear functions and associated only with horizontal edges of rectangles.

After the standard Method of Moments procedure of expansion and testing, Equation (1) becomes:

$$j\omega[\mathbf{L}][\mathbf{i}] - [\mathbf{A}][\boldsymbol{\phi}] = 0, \quad (3)$$

where $[\mathbf{i}]$ is the branch current vector; $[\boldsymbol{\phi}]$ is the node (cell) scalar-potential vector; $[\mathbf{A}]$ is the connectivity matrix whose elements are determined by

$$A_{cn} = \begin{cases} 1, & \text{if } Cell_n \text{ is } Edge_c \text{'s positive side;} \\ -1, & \text{if } Cell_n \text{ is } Edge_c \text{'s negative side;} \\ 0, & \text{otherwise.} \end{cases}$$

The branch-wise inductive matrix elements are

$$L_{\alpha\gamma} = \frac{\mu}{l_{\alpha}l_{\gamma}} \int_{S_{\alpha}} d\vec{s}_{\alpha} \cdot \int_{S_{\gamma}} \vec{\bar{G}}^A \cdot \vec{f}_{\gamma} ds',$$

where \bar{f}_α and \bar{f}_γ are the testing and basis functions, respectively, l_α and l_γ are the lengths of the edges where the testing and basis functions are anchored.

On another hand, based on the continuity equation, the node currents are related to the node charges as

$$-j\omega[Q] = [I] + [I^*], \quad (4)$$

where Q_n , I_n and I_n^* are the charge, the induced current and the injected current associated with Cell n , respectively. Further, assuming the induced surface charge density is constant in every cell, then

$$[\Phi] = [K][Q], \quad (5)$$

and

$$[C] = [K]^{-1}, \quad (6)$$

where the node-wise inverse capacitive matrix elements are:

$$K_{mn} = \frac{1}{\epsilon A_m A_n} \iint_{S_m S_n} G^s ds ds',$$

where A_m and A_n are the areas of Cell m and Cell n , respectively; and G^s is the scalar electric potential Green's function. Thus, using (3), (4), (5) and (6), an mixed-potential integral equation, represented by partial circuit elements, results:

$$\begin{bmatrix} j\omega L & -\Lambda^T \\ \Lambda & j\omega C \end{bmatrix} \begin{bmatrix} i \\ \Phi \end{bmatrix} = \begin{bmatrix} 0 \\ -I^* \end{bmatrix}. \quad (7)$$

This equation has a standard form of Modified Nodal Analysis that is utilized in many circuit simulators.

III. Circuit Extraction

Equation (7) gives the nodal admittance matrix $[Y]$ of the system as:

$$[Y] = \frac{1}{j\omega} [\Lambda^T L^{-1} \Lambda] + j\omega [C]. \quad (8)$$

A circuit model can be easily extracted from this admittance matrix. The only problem results from the frequency dependency of the entities in the $[L]$ and $[C]$ matrices, which are functions of vector- and scalar-potential Green's functions that are frequency dependent. These frequency-dependent elements would make the circuit simulation for frequency response difficult and time-consuming. To overcome this problem, a quasi-static approximation of the Green's functions is employed so that the values of extracted inductance and capacitance are constant over frequency. This approximation imposes an additional mesh limitation to keep the extracted circuit valid over a given frequency range. This limitation is determined by the highest working frequency, layer stackup and dielectric materials [5].

The extracted circuit model from (8) can have an extensive netlist. There is a parallel LC branch between an arbitrary pair of two nodes, as well as a shunt capacitance between each of the nodes to the ground node, as shown in Figure 2. For a small number of nodes with their surface currents flowing to the ground associated with the via interconnects, there is also a shunt inductance connecting them to the ground node. The extracted circuit is exported into SPICE where various frequency- and time-domain simulations are performed. Well-developed SPICE models for various sources, loads, transmission lines, etc. can be easily incorporated into the extracted circuit model.

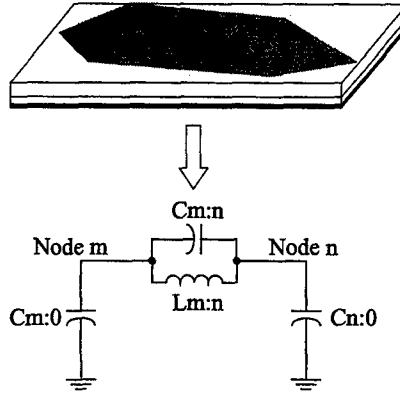


Figure 2: A type circuit model between two nodes m and n , extracted from the CEMPIE.

IV. Calculation of Green's Functions

There are two steps in calculation of the Green's functions in a stratified medium. First, the spectral-domain expressions are derived based on the concepts of the generalized reflection and transmission coefficients [6], where dielectric layers and ground planes are assumed of infinite extent so the problem is only one-dimensional (z -direction). These spectral-domain expressions are then approximated by an expansion of complex images as [7],[8]

$$\tilde{G} = \frac{1}{2\gamma} \sum_{p=1}^M \alpha_p e^{a_p \gamma}, \quad (8)$$

where $\gamma = jk_z$, M is the total number of complex images, $\alpha_1, \dots, \alpha_M$ are complex magnitudes, and a_1, \dots, a_M are complex images. The Sommerfeld identity obtains the inverse Fourier transform from spectral domain to spatial domain as [6]

$$\frac{e^{-jk_r r}}{4\pi r} = \frac{1}{4\pi} \int_{-\infty}^{\infty} k_\rho dk_\rho H_0^{(2)}(k_\rho \rho) \frac{e^{-jk_z |z|}}{2jk_z}, \quad (9)$$

i.e.

$$f^{-1}\left(\frac{e^{-jk_z |z|}}{2jk_z}\right) = \frac{e^{-jk_r r}}{4\pi r}. \quad (10)$$

Then, the desired spatial-domain expressions of Green's functions are determined from (8) and (10) as

$$G = \sum_{p=1}^M \alpha_p \frac{e^{-jk_z \sqrt{x^2 + y^2 + a_p^2}}}{4\pi \sqrt{x^2 + y^2 + a_p^2}}.$$

Several numerical methods have been developed to approximate a spectral-domain Green's function into a series of complex images, such as the original Prony's method [7], and the least-square Prony's method [9]. Prony's methods are known for their high sensitivity to noise. The generalized pencil of function (GPOF) method was then introduced to improve the performance [10]. It was observed, however, that the GPOF method was not robust for slowly converging functions with rapid

changes. A further improvement to the GPOF method, denoted the two-level approach [8], is used in the CEMPIE modeling described in this work.

V. Power Bus Modeling

The CEMPIE modeling approach was demonstrated by comparison with experiment. Figure 3 illustrates a test-board geometry, which is a two-layer printed circuit board with two solid planes representing power and ground planes, respectively. There were two vertical discontinuities. One was a shorting post connecting two planes together, and the other was an SMA test probe. The input impedance at the test port was measured using an HP4291A impedance analyzer. The reference plane was located at the input port of the test geometry. The modeled results are compared with the measurements in Figure 4. Good agreement is demonstrated up to 1.8 GHz, which is the maximum frequency of the impedance analyzer. Other $|S_{21}|$ measurements showed that CEMPIE modeled results agreed well with measurements up to 5 GHz, provided that the additional mesh limitation discussed previously was satisfied.

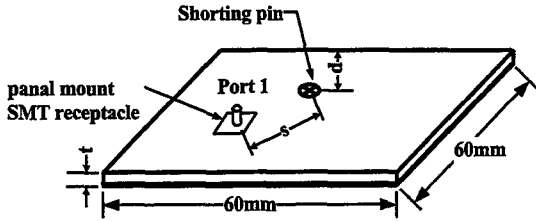


Figure 3: A power bus test geometry.

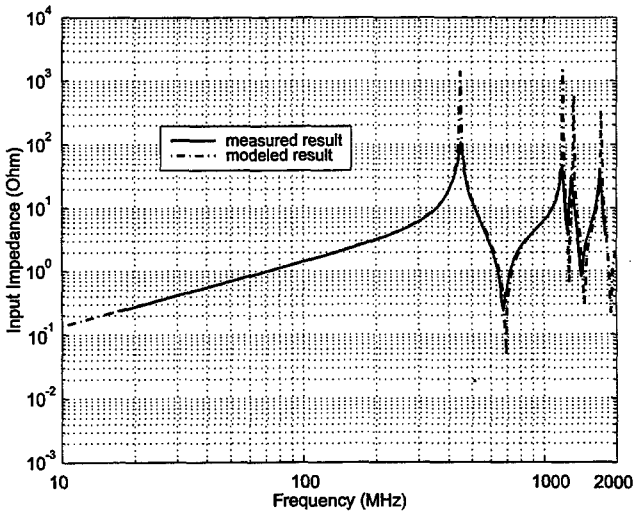


Figure 4: Comparison of modeled and measured results for the power bus structure shown in Figure 3.

An example of utilizing the modeling approach for power bus design is illustrated in Figure 5. The top plane was a gapped power layer while the bottom ground layer was solid. The rationale of placing a gap is based on introducing a series impedance between two portions to provide isolation of a noise source from the rest of the PCB design. A conducting neck was present to provide DC connections between two portions. $|S_{21}|$ was used to characterize the behavior of the power bus [11]. Figure 6 illustrates the effect on isolation when changing the neck width. The neck was located in the center of the board. The relevant dimensions were $a=100\text{ mm}$, $b=55\text{ mm}$, $c=49\text{ mm}$, $t=2\text{ mm}$, and the neck width was 2, 5 and 10 mm, respectively. The change of neck width affected the series impedance between the two segmented portions in the low frequency band so that a dramatic shift of the first resonance resulted. In the high frequency band, conductive coupling through the neck was no longer dominant and there was little difference between the three cases when the frequency is higher than 1 GHz. The low frequency responses also indicate that the power island structure with a conducting neck only marginally achieves noise isolation at low frequencies (less than 20 dB). This is consistent with some other experimental observations [11][12].

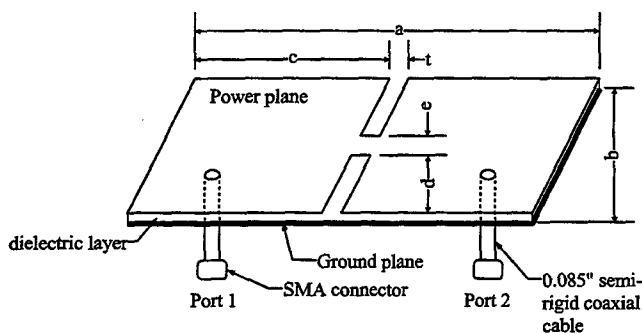


Figure 5: A power island structure with a conducting neck.

VI. Conclusion

The CEMPIE modeling approach provides a useful and powerful tool in designing power bus structures, and predicting power bus noise distribution. Measurements demonstrate the effectiveness of the modeling. It can also be used to model many SI problems, IC packaging problems and other applications with multilayer geometry.

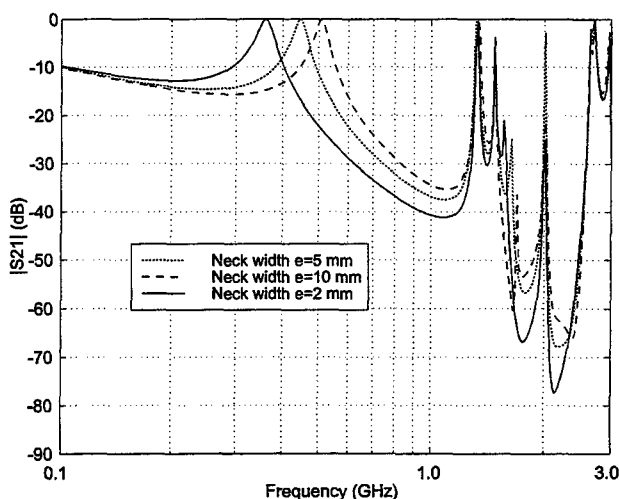


Figure 6: Modeled noise isolation versus neck width for the power island structure shown in Figure 5.

References

- [1] C. R. Paul, *Introduction to Electromagnetic Compatibility*, John Wiley, New York, 1992.
- [2] H. W. Johnson, and M. Graham, *High-Speed Digital Design, a Handbook of Black Magic*, Prentice Hall PTR, New Jersey, 1993.
- [3] K. A. Michalski, and D. Zhang, "Electromagnetic scattering and radiation by surfaces of arbitrary shape in layered media, Part I: Theory," *IEEE Trans. on Antennas and Propagation*, vol. 38, no. 3, March 1990.
- [4] S. M. Rao, D. R. Wilton, and A. W. Glisson, "Electro-magnetic scattering by surfaces of arbitrary shape," *IEEE Trans. Antennas propagat.*, Vol. 30, No. 3, pp. 409-418, May 1982.
- [5] H. Shi, "Study of printed circuit board power bus design with a circuit extraction technique based on a quasi-static MPIE/MOM formulation," Ph.D. Thesis, Department of Electrical and Computer Engineering, University of Missouri-Rolla, 1997.
- [6] W. C. Chew, *Waves and Fields in Inhomogeneous Media*, IEEE Press, New Jersey, 1995.
- [7] Y. L. Chow, J. J. Yang, D. G. Fang, and G. E. Howard, "A closed-form spatial Green's function for the thick microstrip substrate," *IEEE Trans. on Microwave Theory and Techniques*, vol. 39, no. 3, March 1991.

- [8] M. I. Aksun, "A robust approach for the derivation of closed-form Green's functions," *IEEE Transactions on Microwave Theory and Techniques*, vol. 44, pp. 651-658, no.5, May 1996.
- [9] R. M. Shubair, and Y. L. Chow, "Efficient computation of periodic Green's function in layered dielectric media," *IEEE Trans. on Microwave Theory and Techniques*, vol. 41, no. 3, March, 1993.
- [10] T. K. Sakar, and O. Pereira, "Using the matrix pencil method to estimate the parameters of a sum of complex exponentials," *IEEE Antennas and Propagation magazine*, vol. 37, pp. 48-55, no.1, 1995.
- [11] J. Fan, Y. Ren, J. Chen, D. M. Hockanson, H. Shi, J. L. Drewniak, T. H. Hubing, T. P. Van Doren, and R. E. DuBroff, "RF isolation using power islands in DC power bus design," *IEEE International Symposium on Electromagnetic Compatibility*, Seattle, WA, August 1999.
- [12] T. H. Hubing, J. Chen, J. L. Drewniak, T. P. Van Doren, Y. Ren, J. Fan, and R. E. DuBroff, "Power bus noise reduction using power islands in printed circuit board designs," *EMC'99*, Tokyo, Japan, 1999.

NON-RESONANT ELECTROMAGNETIC SIMULATION OF SOME RESONANT PLANAR CIRCUITS

Yuriy O. Shlepnev

Eagleware Corporation

4772 Stone Drive, Tucker, GA, 30084, USA

tel. 770-939-0156, fax 770-939-0157, www.eagleware.com

e-mail: yuriy@eagleware.com

Abstract.

A new resonance elimination technique is proposed to minimize a number of frequency samples in an electromagnetic simulation of some resonant planar structures over a wide frequency band. Instead of a direct interpolation of scattering matrix elements of the structure, it is suggested to create an intermediate descriptor matrix with an order higher than the order of the final scattering matrix and with non-resonant frequency behavior of the elements. The expanded descriptor can be constructed using proposed artificial internal ports and a heuristic resonance breaking approach. The elements of the expanded descriptor can be interpolated over a wide frequency range with a simple interpolation technique and minimal number of frequency samples. Elimination of the internal ports reduces the interpolated expanded descriptors to the initial scattering matrices and restores broken resonances with necessary resolution. The method of lines in its impedance interpretation is used to implement and to illustrate the resonance elimination technique.

Introduction.

The scope of this paper is interior problems of electromagnetics for microwave planar structures. The ultimate descriptor of the interior problems is usually a scattering matrix. The elements of the matrix or scattering parameters are complex functions of frequency. Typical microwave structures like filters have sometime very complex frequency dependencies of the scattering parameters. A direct electromagnetic analysis of them resolving all resonances is computationally expensive. Adaptive frequency sampling techniques as well as different curve-fitting models based on the rational function approximation are available to reduce the computational efforts [1-4]. Though their theoretical foundations are quite straightforward, numerical implementations could be difficult and unstable.

An alternative to the rational approximation of the scattering parameters is an interpolation of an impedance or Z-matrix of the method of moments (MoM) [5]. As shown in [5], the elements of this matrix are usually smooth functions of frequency over a wide band and a simple linear interpolation can suffice. For the interior problems of strip-like type, the Z-matrix elements characterize only problem housing and not the problem itself. Therefore, they could show resonance like behavior only at relatively high frequencies that are usually beyond the frequency range of the interest. In contrast, the elements of inverted Z-matrix carry the information about the problem itself, and can not be interpolated as easy as the impedance matrix elements [5]. The main drawback of the impedance matrix interpolation is the necessity to keep calculated matrices of high rank. The approach is also acceptable only if computation time of Z-matrix elements is considerably greater than the solution time of the other parts of the problem (matrix inversion or linear system solution). It could work when a problem is represented by a small number of expansion functions. With the equidistant spatial grids and pulse expansion functions like in the method of lines, the technique is computationally less efficient than the direct analysis at the frequencies of interest.

A general idea of this paper is to construct an intermediate descriptor matrix of a resonant structure, which elements are smooth functions of frequency. It can be easily subjected to a simple linear interpolation technique over a wide frequency band like the initial impedance matrix of the MoM. The order of the matrix is higher than the final scattering matrix but must be much lower than the initial impedance matrix. It is suggested here to use internal ports placed into the initial structure to break resonances. An enlarged 50-Ohm normalized scattering matrix of the structure with the external and added internal ports is used as the intermediate and supposedly non-resonant descriptor of the problem for interpolation purpose. The added ports are eliminated then in a circuit theory simulator restoring proper boundary conditions in the port regions. The internal ports are created so that they do not disturb current flow and cross - coupling. Placing of the ports is similar to a decompositional procedure in general and is relatively heuristic.

The standard GENESYS 7 suite with multilevel EM simulator =EMPOWER= is used to generate all examples for this paper¹. The simulator is based on the method of lines (MoL) that is quite similar to the MoM, and the paper gives some foundations necessary to understand the whole numerical scheme.

¹ GENESYS Suite - Eagleware Corporation, Tucker, GA, 1999.

Formulation of the EM problem. The problem of our interest can be classified as a planar 3D one. A planar structure is confined in a three dimensional rectangular volume bounded by electric or magnetic walls. The volume is filled by a stratified medium that may consist of an arbitrary number of isotropic homogeneous layers. Planes parallel to the medium layer interfaces can comprise arbitrary shaped thin or thick regions of perfect metallization, regions with complex surface impedances (lossy metal) and resistive films and can be interconnected through the media layers by via-holes. To model the external inputs of the structure and lumped element connections, auxiliary port regions are introduced into the problem domain. The desired solution of the electromagnetic problem is an immittance matrix relating the integral voltages and currents in all port regions. The immittance matrix can be transformed into a generalized Y- or S-matrix using the simultaneous diagonalization method [6]. The same kind of ports as for connection of the lumped elements is used to break resonances in the structure and to implement the resonance elimination technique thereafter.

Simulation by the MoL with fictive ports. The basic numerical technique outlined here is known as the impedance interpreted method of lines [7,8]. It forms the foundation of a commercial electromagnetic simulator =EMPOWER= [8]. Maxwell's equations are approximated on a semi-discrete grid by a differential-difference system using partial discretisation in the plane parallel to the interfaces of the medium layers (xy plane). Grid variables corresponding to the electric and magnetic fields and surface currents in the xy plane and to volumetric currents along z-axis are shown schematically on a grid cell in Fig. 1a). The finite difference scheme corresponds to a xy-plane projection of the well-known offset scheme of K.S. Yee. The grid is equidistant with $L+1$ cells along x-axis and $M+1$ cells along y-axis and with the cell size dx along x and dy along y. The 3D problem is reduced to a 2D one by means of a grid spectral representation of the fields in the homogeneous layers. A contraction of the grid Green's function (GGF) of a strip-like problem on surfaces with non-zero conductivity currents is an impedance matrix relating the grid functions of the electrical field or local voltages and the grid currents. The GGF matrix is built in the grid spectral domain using an impedance form of the solution in a layer. Each element of the GGF matrix is represented as a sum of four elements of an auxiliary array obtained using DFFT technique. The array size is in proportion to L^*M .

As soon as we have the main impedance matrix of the problem, it is possible to introduce a conceptual or informational multiport corresponding to it. The multiport is introduced to facilitate and to illustrate some boundary condition superimposing and to combine the electromagnetic simulation with the circuit theory simulation. Fig. 1b) shows a set of ports of the conceptual multiport corresponding to the points on the discretisation scheme shown in Fig. 1a). Voltages at the conceptual pairs of the terminals correspond to the grid local voltages and currents correspond to the grid conductivity currents. The total number of the ports oriented along x-axis is $M^*(L+1)$, and along y-axis is $(M+1)^*L$ per one metallization plane or level. Z-directed conceptual ports are introduced only in layers and places with non-zero conductivity currents across the layer. Note that we do not need to calculate all elements of the multiport impedance matrix and its order can be reduced taking into account that some conceptual ports are unloaded or short circuited. Fig. 2 illustrates some boundary condition superimposing in a signal plane in the conceptual multiport terms. The unloaded ports are shown as simple unloaded pairs of terminals. They correspond to regions of a signal layer without any conductivity currents. A metallization pattern in the signal layer is simulated as conceptual ports in corresponding areas either with short circuit conditions on them for lossless metal or loaded by an impedance in a general case. Fig. 2. shows a segment of a lossless microstrip line along x-axis. In the middle of the segment is a fictive port introduced to expand the final descriptor of the problem and to break resonances.

The fictive port is a simple parallel connection of the local conceptual ports across the line. In numerical electromagnetics terms, it is a simple integration across the strip conductor of the current along the strip. The only assumption is an equivalence of the local voltages at the local ports in the fictive port area. Imposing this condition, we discard the conductivity current across the strip near the fictive port. Thus, the fictive ports could be placed only in places where those currents are insignificant. The other possible solution is to introduce a set of the fictive ports across the line. The limit case for this is a situation when fictive ports correspond exactly to the local ports of the conceptual multiport. It blows up the intermediate descriptor that is not desirable here. The fictive port could be also considered as a limit case of the general internal port [8] with length equal to the grid cell size. The external ports of a microstrip structure are formed in the same way as the fictive ones near the sidewalls. To get a descriptor of the planar structure, the main impedance matrix is reduced to an immittance matrix relating currents and voltages at the external and internal ports including the fictive ones. The external ports are de-embedded then, and all ports are normalized to 50 Ohms. Here we get the extended descriptor that is converted into the scattering matrix. This matrix is used in a circuit simulator as a descriptor of a multiport. With proper positioning of the fictive ports, the matrix elements may behave smoothly over a wide frequency range. Thus, the matrix can be used as the intermediate descriptor of the structure for interpolation purpose. The short circuit conditions for ideal metallization or impedance loads for lossy surfaces,

imposed on the fictive ports in the circuit simulator, restore partially the appropriate boundary conditions. Partially, because of a fictive port spanning over a few cells suppresses currents across the port as was mentioned earlier. A procedure of placement of the fictive ports to eliminate resonances in the extended matrix is heuristic. It usually follows from the design, what part of the circuit were intended to be resonant. If so, all we need is just to disjoint the metallization corresponding to it. This procedure reminds a decomposition of the structure into some enlarged components. Though it preserves all cross couplings in the structure, including caused by interactions with the circuit enclosure.

To complete the outline of the numerical technique, we just mention some acceleration procedures. To transform the equidistant grid to a non-equidistant one, a thinning out technique together with the linear re-expansion is used. It substantially decreases the order of the main impedance matrix. Another procedure for numerical acceleration that was implemented and used in the following numerical examples is automatic detection and consideration of geometrical symmetry of a structure.

Numerical examples. To generate all examples for the paper the RF/microwave design suite GENESYS 7 from Eagleware Corporation is used. The electromagnetic simulation with the fictive ports, circuit theory co-simulation and data manipulation and post-processing are within the capabilities of the standard version of the program.

The first example is a methodical one. It demonstrates a minor influence of a fictive port on the scattering parameters of a segment of microstrip line. The problem is shown in Fig. 3. The segment to be analyzed has the following parameters: $w=0.5$ mm, $h_1=0.5$ mm, $\epsilon_1=9$, $h_2=1.5$ mm, $\epsilon_2=1$, $b=3.5$ mm, $a=4.1$ mm. Ports number 1 and 2 are external inputs. They are de-embedded and normalized to the internally calculated characteristic impedance of the line. The segment is analyzed directly without a fictive port first. The grid cell size is 0.1 mm along the line and 0.0625 mm across and is not critical for the results. The calculated elements of the generalized scattering matrix are shown in Fig. 4 (DB[S11], DB[S21]). A fictive port was added in the middle of the segment then (port number 3). It converted the structure into a three-port. The segment with the fictive port was analyzed in the EM simulator again. The resultant descriptor of the three-port is passed into the circuit simulator, where the fictive port is short circuited and eliminated. The elements of the scattering matrix calculated in this way are also shown in Fig. 4. They are different from the initial ones but both of them are at the level of the numerical noise. Angles of the transmission coefficients calculated without and with the fictive port are the same up to the fourth digit after the decimal point. They are listed in the following table.

Frequency, MHz	5000	10000	15000	20000
Angle of S21, deg.	-59.6357	-121.1883	-185.9071	-253.4355

Thus, it shows an insignificant disturbance introduced by the fictive port and proves that short circuit condition imposed in the circuit simulator restores the line segment corresponding to the fictive port. Note that it does not work like this if the fictive port is placed in a vicinity of a discontinuity in the line where transverse currents could be significant. In this case, a set of the fictive ports distributed across the line may be necessary.

The second example is a filter with three-coupled microstrip resonators in two metallization levels shown in Fig. 5. It was developed and investigated numerically and experimentally in [9]. The filter consists of two substrates with the same parameters ($h_1=0.51$ mm, $\epsilon_1=2.33$), and a foam-like dielectric between them with $h_2=3.3$ and $\epsilon_2=1.07$. Two microstrip input sections ($w=1.5$ mm, $L_1=23.09$ mm) as well as two resonators ($L_2=34.2$) are deposited on one substrate and the middle resonator ($w_1=1.6$, $L_3=33.77$) is deposited on the other substrate (inverted). The spacing parameters are $S_1=0.1$ mm, $S_2=3.2$ mm. The whole structure is in a metal box with sizes $a=40.185$ mm and $b=20$ mm. The filter has some dimensions slightly different from given in [9] because of they were rounded off to fit the structure to the grid. The different sizes are $w=w_1=1.49$, $L_1=23$, $L_3=33.94$, $a=40$. To simulate losses in the structure some loss-related parameters were guessed. The substrates tangent of loss is $3.0e-4$, the metallization resistivity is $1.7e-8$ Ohm meter, the metal thickness 0.036 mm and roughness $1.39e-3$ mm. Ports 1 and 2 are external inputs of the filter. The problem has a mirror symmetry over an xz -plane.

The filter is simulated directly on the grid with cell size 0.4275 mm along the resonators and 0.1 mm across at 101 frequency points to verify the trustworthiness of the EM analysis first. The results are shown in Fig. 7 (DB[S11], DB[S21]) and in Fig. 8 (ANG[S11], ANG[S21]). The scattering parameters are generalized. A wire thinning out algorithm with coefficient 5 was used to accelerate the simulation. It took about 2 min per frequency point on a 500 MHz Pentium III processor. The central frequency of the simulated filter is about 3032 MHz. That is 53 MHz below

the central frequency of the filter investigated in [9]. The shapes of the transmission and reflection characteristics are close to the experimental ones, taking into account the differences in sizes and possible differences in loss parameters.

To implement the resonance elimination technique, three fictive internal ports oriented along the resonators are added. They are shown in Fig. 5 as hatched areas in the middle parts of the three resonators. The port widths are the same as the resonator strip widths and the length is equal to one cell size along the resonators. The new structure with the fictive ports is a five-port and its 50-Ohm normalized scattering matrix is used as the extended or intermediate non-resonant descriptor. It was simulated at five frequency points in the same frequency range as the initial filter. Frequency dependencies of some elements of the extended scattering matrix are shown in Fig. 6. They are smooth functions of frequency and a simple linear interpolation is used to get the extended scattering parameters at the other frequency points. After the interpolation the fictive ports were simply short circuited and eliminated and the resultant scattering parameters are shown in Fig. 7 and Fig. 8 (Linear1.fictiveShort.DB[S21], Linear1.fictiveShort.DB[S21], Linear1.fictiveShort.ANG[S21], Linear1.fictiveShort.ANG[S21]). The simulation results obtained by the resonance elimination technique is almost on the top of the direct simulation results. There is just an insignificant frequency shift about 8 MHz, up, occurred due to the minor current redistribution in the fictive port areas. 20 times acceleration is achieved with the simple interpolation technique and without visible loss of accuracy.

Conclusion. An attempt to switch from the approximation of the scattering parameters of a resonant planar structure to a construction of an extended electromagnetic descriptor with smooth and predictable frequency behavior is introduced. Artificial or fictive internal ports are proposed to eliminate resonances in the structure and to obtain the extended non-resonant descriptor. The descriptor elements can be interpolated linearly over a wide frequency range and it can be converted to the scattering parameters with minimal numerical effort. This is an alternative to the multimode decomposition approach and is specifically focused on the en-bloc analysis of the planar structures and considers all possible cross-couplings. The idea is implemented on the basis of the impedance interpreted method of lines. The effectiveness of the developed resonance elimination technique (RET) is illustrated by a filter simulation example. Note that RET could be referred to as an implementation of the theory of loaded scatterers [10]. Temporary fictive ports loaded by 50-ohms are introduced to change scattering by an enclosed planar structure for interpolation purpose and then eliminated to restore the initial scattering. And finally, it must be noted, that the descriptor expansion technique works in "natural" way and does not need the fictive ports for structures with lumped elements like combline filters. The capacitors in those filters are the necessary elements to create resonances in the structure and the internal ports in the EM analysis are created to hook them up producing the non-resonant extended descriptor.

References

1. K. Kottapalli, T. Sarkar, Y. Hua, E.K. Miller, G. J. Burke, "Accurate computation of wide-band response of electromagnetic systems utilizing narrow-band information", IEEE Trans., v. MTT-39, 1991, N4, p. 682-687.
2. E.K. Miller, "Minimizing the number of frequency samples needed to represent a transfer function using adaptive sampling", in Proc. of 12th Annual Review of Progress in Applied Computational Electromagnetics, Monterey, CA, 1996, p.1132-1139.
3. T. Dhaene, J. Ureel, N. Fache, D. De Zutter, "Adaptive frequency sampling algorithm for fast and accurate S-parameter modeling of general planar structures", IEEE MTT-S Symp. Dig., 1995, p.1427-1430.
4. J.E. Bracken, D.-K. Sun, Z.J. Cendes, "S-domain methods for Simultaneous time and frequency characterization of electromagnetic devices", IEEE Trans., v. MTT-46, 1998, N9, p. 1277-1290.
5. E.H. Newman, "Generation of wide-band data from the method of moments by interpolating the impedance matrix", IEEE Trans., v. MTT-36, 1988, N12, p.1820-1824.
6. Yu.O. Shlepnev, "A new generalized de-embedding method for numerical electromagnetic analysis", in Proc. of the 14th Annual Review of Progress in Applied Computational Electromagnetics, Monterey, CA, 1998, p. 664-671.
7. Yu.O. Shlepnev, "Extension of the Method of Lines for planar 3D structures", in Proc. of the 15th Annual Review of Progress in Applied Computational Electromagnetics, Monterey, CA, 1999, p 116-121.
8. GENESYS 7, =EMPOWER= manual, Eagleware Corporation, 1999.
9. A.A. Melcon, J.R. Mosig, M.Guglielmi, "Efficient CAD of boxed microwave circuits based on arbitrary rectangular elements", IEEE Trans., v MTT-47, 1999, N 7, p.1045-1058.
10. R.F. Harrington, "Theory of loaded scatterers", Proc. IEE, v. 111, 1964, N 4, p. 617-623

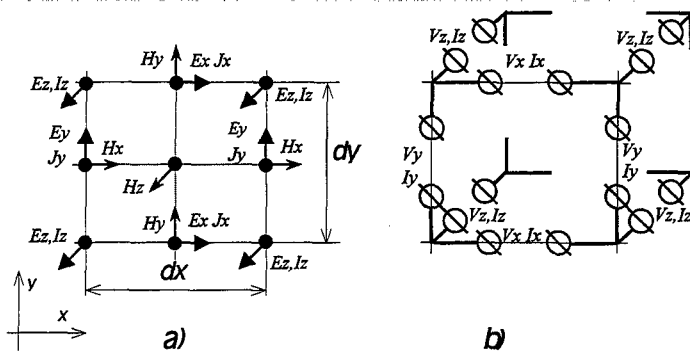


Fig. 1. A grid cell with the grid variables and corresponding to them terminals of a conceptual multiport.

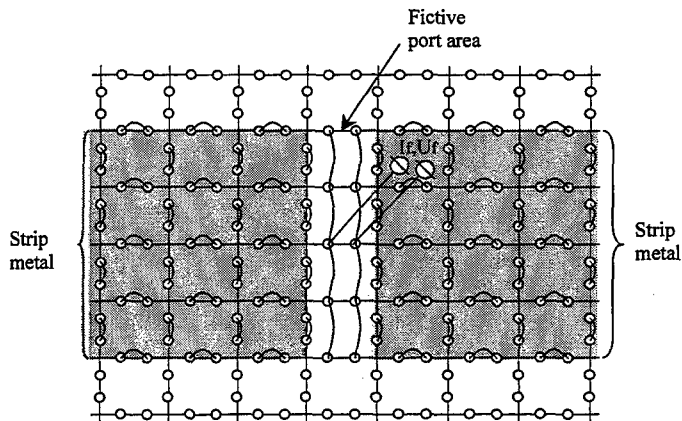


Fig. 2. A conceptual multiport representation of boundary conditions superimposing. Two areas of metallization and a fictive port between them.

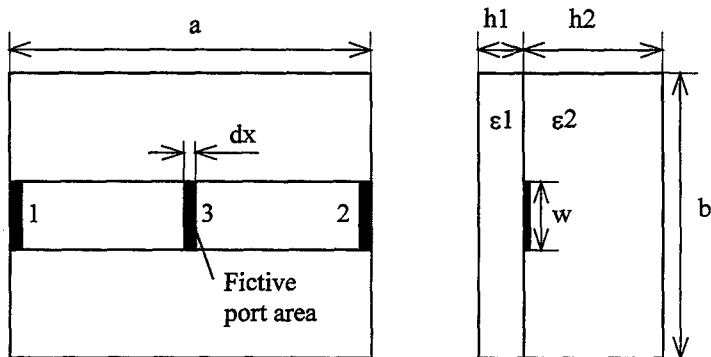


Fig. 3. A segment of microstrip line with two external ports on the opposite sides and one fictive port in the middle.

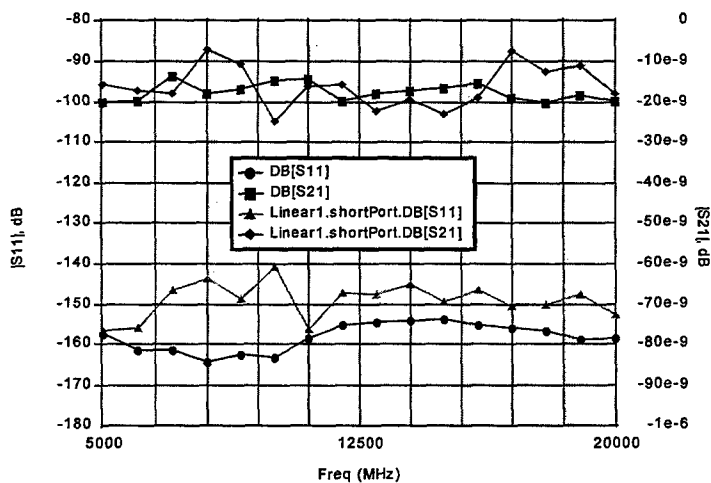


Fig. 4. Generalized reflection and transmission scattering parameters of the microstrip line segment problem solved without the fictive port ($DB[S_{11}]$ and $DB[S_{21}]$) and with the short circuited fictive port ($Linear1.shortPort.DB[S_{11}]$, $Linear1.shortPort.DB[S_{21}]$).

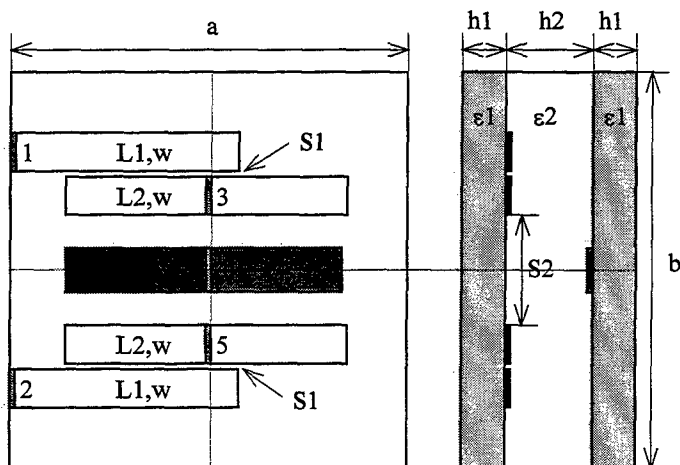


Fig. 5. A two-level three-resonator filter with two external ports and three fictive internal ports to break resonances. Two input line segments and two resonators are on one substrate and the middle resonator (hatched) is on the another (inverted) substrate.

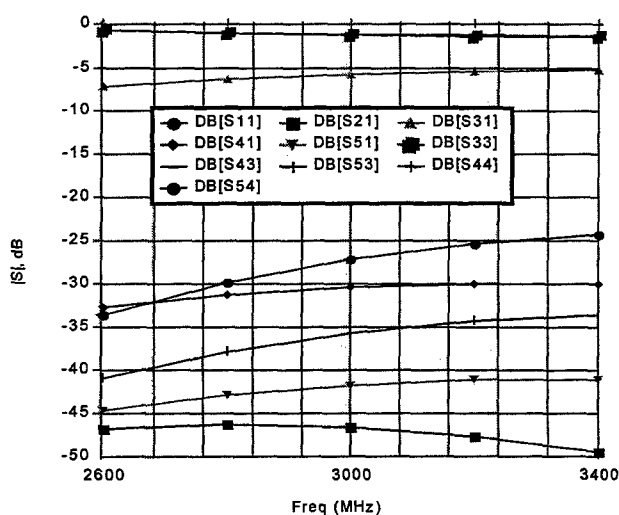


Fig. 6. Magnitudes of some elements of the extended 50-Ohm normalized scattering matrix of the two-level three-resonator filter with three fictive ports.

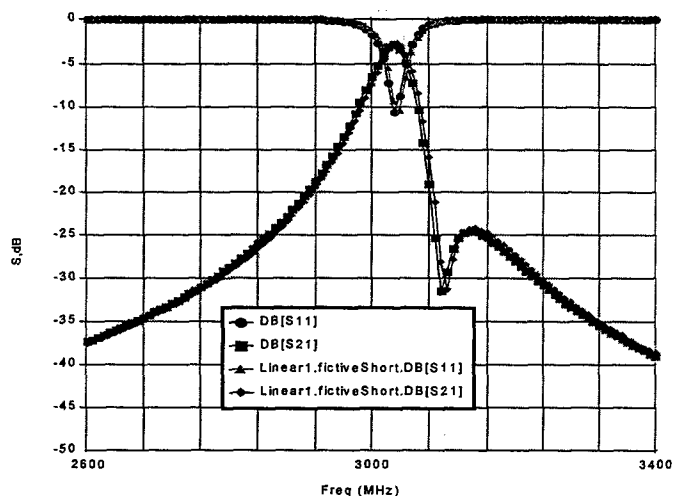


Fig. 7. Magnitudes of the transmission and reflection coefficients of the two-level three-resonator filter calculated directly (DB[S21] and DB[S11]) and trough the interpolation and reduction of the extended S-parameters (Linear1.fictiveShort.DB[S21] and Linear1.fictiveShort.DB[S11]).

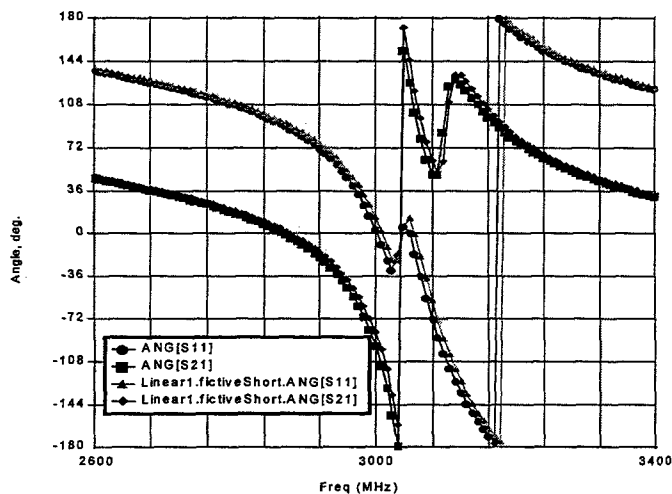


Fig. 8. Angles of the transmission and reflection coefficients of the two-level three-resonator filter calculated directly (ANG[S21] and ANG[S11]) and trough the interpolation and reduction of the extended S-parameters (Linear1.fictiveShort.ANG[S21] and Linear1.fictiveShort.ANG[S11]).

FDTD Analysis of Conventional and Novel Delay Lines

Omar M. Ramahi
Alpha Servers Development Group
Compaq Computer Corporation
MRO1-1/p5
200 Forest St.
Marlborough, MA 01752
Omar.Ramahi@compaq.com

I. INTRODUCTION

There are two mechanisms that are typically employed to achieve required signal delay between circuit components. The first mechanism of delay is achieved through internal electronic circuitry. The second mechanism, which is the most common and least expensive, is achieved through meandering a transmission line as shown in Fig. 1. The meandered line, commonly referred to as the serpentine line, consists of a number of transmission lines closely packed to each other. The objective behind the meandering is to achieve high density (of transmission line) per square inch of circuit board space while obtaining a delay in the signal that is directly proportional to the length of the line.

Serpentine lines, which are the most common of delay lines, introduce delay but also introduce a type of spurious dispersion that makes the signal appears as if it is arriving earlier than expected. Previous studies used analytic techniques and quasi-static methods to predict the delay and signal behavior on serpentine lines. These earlier studies, however, included several assumptions that can no longer be valid when the circuit becomes electrically large. Furthermore, when studying novel delay lines, such as the spiral line, earlier methods fell short of being effective.

In this work, we use the three-dimensional Finite-Difference Time-Domain (FDTD) method to analyze two types of delay lines. The first is the classical serpentine line, and the second is a the spiral delay lines. The FDTD method offers several advantages. First, it allows for easy modeling of complex geometry, and, second, since it is a three-dimensional full-wave method, it incorporates the entire coupling mechanism from the waveguide effects to the low-frequency capacitive and inductive couplings. The only drawback of the FDTD method, however, is its inflexibility in resolving finer structures while maintaining a memory-efficient simulation.

II. SERPENTINE DELAY LINES

When serpentine lines are used in high-speed digital circuit applications, the time delay through a single serpentine line can be much longer than the rise time of the pulse. Under such conditions, serpentine lines have been found to introduce a dispersion that makes the signal appears as if it is arriving earlier than would be expected

based on the total electrical length of the line. Through wave tracing, earlier work showed that this type of dispersion is caused by the crosstalk between the adjacent transmission lines section, and is related to two parameters: the first is the length of each serpentine section. The second parameter is the spacing between adjacent sections [1].

The wave tracing analysis makes several assumptions. These are:

- 1) The rise time is shorter than the round trip time along a single segment.
- 2) The coupling is small such that the multiple coupling effect induced from the crosstalk is negligible.
- 3) The forward propagating crosstalk was assumed to be zero. In practice, however, there is some forward crosstalk, which induces additional crosstalk as it propagates.
- 4) The small transmission line segments that connect the longer sections have been assumed to have zero delay (zero physical length).
- 5) Negligible multi-modal propagation.

Considering the above simplifications, the wave tracing qualitative model serves only to give an understanding of the primary crosstalk contributors. For a more accurate prediction of the performance of the serpentine line, the three-dimensional finite-difference time-domain (FDTD) method is used as it fully integrates the five constraints listed above.

The first delay line considered for study is a serpentine line, where the total electrical length of the line is 405.4 mm (15.96 in). Two variations of this line are considered, as shown in Fig. 1, and will be referred to as Case A and Case B respectively. The excitation waveform is a pulse of 1.4 nanoseconds and rise time 100 picoseconds. The cross section for both lines is shown in Fig. 2. The difference between the two is that one has shorter sections than the other. Both, however, have identical lengths, identical line separation, and both occupy equal board area.

Figure 3 shows results from the FDTD simulation, where the response of the two lines is compared to the reference line. The serpentine line designated as Case B has longer sections and consequently, its receiver signal had ladders that are longer than Case A. However, this difference is of minor importance since the low-to-high switching occurs at approximately the same time zone.

III. THE SPIRAL DELAY LINE

In the serpentine line, the crosstalk was found to accumulate synchronously. This accumulation can be significant enough to trigger false logic. Ideally, this crosstalk needs to be eliminated; however, since the crosstalk is a function of the separation between the lines, the only way to eliminate, or reduce the crosstalk would be to increase the separation between the lines. This, unfortunately requires larger circuit board area which can be either expensive, or impossible in light of the density requirements.

Given that the transmission line density to remain unchanged, the separation between the lines must be kept unchanged. An alternate design that would force the crosstalk to accumulate *asynchronously* is the spiral delay line shown in Fig. 4 (for more discussion on the spiral line, see [2]). Notice that the spiral line minimizes the

periodicity in the transmission line thus achieving the asynchronous accumulation of noise.

The most prominent feature of the spiral delay line is the spreading, over time, of the crosstalk noise. This can be seen by performing wave tracing analysis as in [2]. However, and as before, the wave tracing analysis and the multi-conductor transmission line model falls short of predicting the full-wave effects.

To demonstrate full-wave performance of the flat spiral delay line, we construct the line shown in Fig. 4, where the electrical length, line separation, and total board area, all equal to the serpentine lines shown in Fig. 1. The cross section parameters are given in Fig. 2, and the rise time and pulse duration (width) are as before.

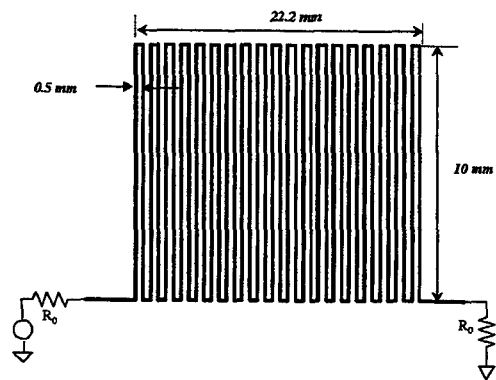
Figure 5 shows the signal at the receiving end of the spiral line as compared to the equivalent serpentine and reference lines. The outstanding performance of the spiral line is clearly visible. We observe that the crosstalk noise was spread over time ahead of the main signal resulting in a high fidelity signal. In fact, for the case considered, we notice that the maximum crosstalk stays at or below 10% of the signal level, thus the potential for triggering false logic is reduced considerably.

IV. CONCLUDING REMARKS

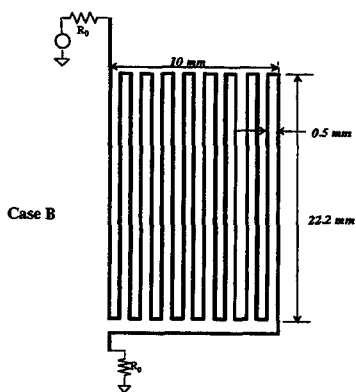
The FDTD method has been used effectively to analyse delay lines such as the conventional serpentine delay line and the spiral line. Since the FDTD method incorporates the full-wave features of the model, all coupling effects, from the low-frequency capacitive and inductive coupling to the high-frequency microwave effects are included in the model. The flexibility of the FDTD method in treating non-conventional structures such as the spiral line makes it a very viable and powerful tool in designing novel delay lines that are constrained only by the size of the printed circuit board and the imagination of the designer.

REFERENCES

- [1] R-B. Wu and F-L. Chao, Laddering wave in serpentine delay line *IEEE Trans. Components, Packaging and Manufacturing Tech., Part B: Advanced Packaging* vol. 18, no. 4, pp. 644-650, Nov. 1995.
- [2] R-B. Wu and F-L. Chao, Flat spiral delay line design with minimum crosstalk penalty, *IEEE Trans. Components, Packaging and Manufacturing Tech., Part B: Advanced Packaging* vol. 19, no. 2, pp. 397-402, May 1996.



Case A



Case B

Fig. 1. 19-section 15.96 inches long serpentine delay lines.

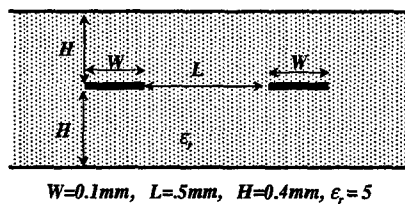


Fig. 2. Cross section of delay lines.

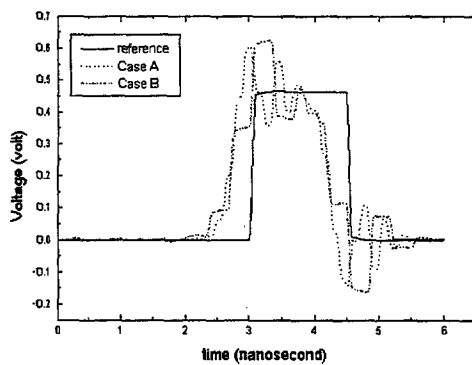


Fig. 3. Received waveform for the 15.96 inches serpentine lines.

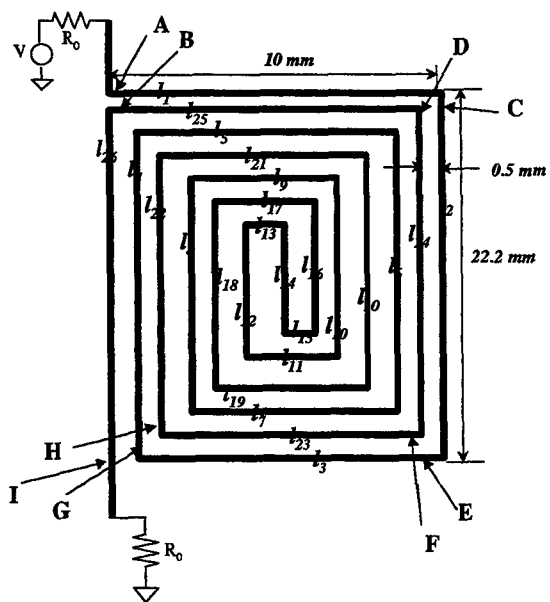


Fig. 4. Spiral delay line.

Complementary Operators for Frequency-Domain Methods: A Single Simulation Implementation

Omar M. Ramahi
Compaq Computer Corporation
MRO1-1/p5
200 Forest St.
Marlborough, MA 01752
Omar.Ramahi@compaq.com

I. ABSTRACT

The complementary operators method for mesh truncation has recently been applied to solve frequency domain (time harmonic) problems. Earlier work required multiple simulations as each of the two complementary operators was applied in every single simulation. In this work, we present a procedure by which both complementary operators are applied in a single simulation, thus achieving two objectives. First, increasing modeling efficiency, and second, allowing for the ability to solve problems involving non-linear media.

II. BACKGROUND

The past several years witnessed the development of the complementary operators method (COM) as a highly-accurate mesh-truncation technique for the solution of open-region radiation problems [1]-[3]. The COM has been applied to time-domain and frequency-domain (time harmonic) simulations, resulting in unprecedented levels of accuracy. The application of COM to frequency domain problems, however, required multiple simulations, where each of the two complementary operators was applied in each single simulation. Despite the high accuracy achieved, multiple simulations maintained a degree of inefficiency and also prevented the effective and efficient solution of radiation problems involving non-linear media.

In this work, we overcome the need for multiple simulations in frequency-domain methods by incorporating the two complementary operators in a single simulation. This is accomplished by implementing the averaging process within the frequency-

domain system matrix. Therefore, the implementation is equivalent to the concurrent implementation of COM in time-domain simulations [3]. The procedure presented is applicable to finite difference and finite element modeling.

III. COMPLEMENTARY OPERATORS

The idea behind COM is simple. Let us consider an outer boundary that is parallel to the y-axis in the Cartesian coordinates. Two auxiliary differential operators, ∂_x and ∂_t are applied on an absorbing boundary condition (ABC) B such as Higdon, Liao,...etc.. The purpose of these two auxiliary operators is to produce reflection coefficients that are 180° out of phase, not only in the analytic domain, but also in the discrete, or numerical domain. By averaging the solutions obtained from the application of each of the two operators on an ABC, we arrive at a new solution that is devoid of first-order reflections [1]-[3].

While the frequency-domain and time-domain simulation are two different representations of the same physical phenomenon, the numerical solution paradigm is not identical. For this reason, complementary operators had to be *numerically* adapted to fit the particular numerical model under consideration [3]-[5].

When the complementary operators are adapted to the frequency-domain model, the resultant two complementary boundary conditions are given by [4]:

$$D_x B = \frac{I - S^{-1}}{\Delta x} B \quad (1)$$

$$\bar{D}_x B = \frac{I + S^{-1}}{\Delta x} B, \quad (2)$$

where k_x is the wave number in the x direction, and I and S^{-1} are the identity and space shift discrete operators, respectively.

The corresponding reflection coefficients are given, respectively, by

$$R(D_x B) = -e^{jk_x \Delta x} R(B) \quad (3)$$

$$R(\bar{D}_x B) = e^{jk_x \Delta x} R(B) \quad (4)$$

where $R(B)$ is the reflection coefficient of the operator B .

Equation (3) and (4) are precisely 180° out of phase; hence, full complementariness is achieved.

IV. CONCURRENT IMPLEMENTATION OF COMPLEMENTARY OPERATORS IN FREQUENCY DOMAIN

In previous work, each of the two complementary operators were implemented in a separate simulation and the solutions of the two simulations averaged to obtain a solution devoid of first-order reflections. In this work, both operators are implemented in a single simulation.

To this end, we consider the problem of radiation in two-dimensional space. For clarity, we limit the discussion here to the finite-difference frequency-domain method. However, the implementation and application in the finite element method is similar, aside from slight implementation details that will be highlighted below.

Following similar development to the concurrent COM in time-domain simulation, we divide the computational domain into a boundary region (or layer) and an interior region as shown in Fig. 1.

Without loss of generality, we limit the discussion here to the problem of TM-polarization. Each field node in the boundary layer is assigned two field values, E_{x1} and E_{x2} . In the interior region, we assign a single field value to each node, E_x , as in conventional implementation.

Next, we apply the finite-difference equation to each node in the interior region. Let us assume that the finite-difference grid is uniform in the x and y directions, and let h be the grid spacing. Applying second-order finite-difference approximation to the free-space Helmholtz equation at the interior node (i, j) , we have:

$$E_x(i-1, j) + E_x(i+1, j) + E_x(i, j+1) + E_x(i, j-1) + (k^2 h^2 - 4)E_x(i, j) = 0 \quad (5)$$

where (i, j) is the node location.

In the boundary region, we apply the finite-difference equation to the two sets of fields:

$$E_{x1}(i-1, j) + E_{x1}(i+1, j) + E_{x1}(i, j+1) + E_{x1}(i, j-1) + (k^2 h^2 - 4)E_{x1}(i, j) = 0 \quad (6)$$

$$E_{x2}(i-1, j) + E_{x2}(i+1, j) + E_{x2}(i, j+1) + E_{x2}(i, j-1) + (k^2 h^2 - 4)E_{x2}(i, j) = 0 \quad (7)$$

The first of the two complementary operators, $D_x B$ is applied to the set of fields denoted by E_{x1} , and the second operator, $\bar{D}_x B$ is applied to the set of fields E_{x2} .

Let the interface perimeter between the boundary layer and the interior region be denoted by Γ , as illustrated in Fig. 1.

To see how the averaging process is implemented, we focus on the left-hand-side segment of the Γ . In Fig. 2 we show the grid on and in the close proximity of Γ .

On Γ , the update equation for the fields uses the average field values $0.5(E_{x1} + E_{x2})$ from the left-hand side and E_z from the interior region. Thus, the finite-difference equation for the fields on Γ is given by

$$\frac{E_{x1}(i-1, j) + E_{x2}(i-1, j)}{2} + E_z(i+1, j) + E_z(i, j+1) + E_z(i, j-1) + (k^2 h^2 - 4)E_z(i, j) = 0 \quad (8)$$

Similar equations are applied on the other three sides of Γ .

The implementation of (8) in a finite-difference code does not require any special treatment. Therefore, an existing finite-difference code requires only very minor modification to accommodate complementary operators.

It should be noted that the averaging performed by (8) does not eliminate all boundary errors, but only the first-order reflections. Analysis of boundary reflections will be discussed in a future publication.

V. CONCURRENT COM IN FINITE ELEMENTS

The extension of this development to finite element models has a high degree of similarity to the finite-difference implementation. The computational space is divided into a boundary region and an interior region. The field is *duplicated* in the boundary layer, and an interface perimeter, say Γ , is chosen as the boundary on which the fields are averaged.

In the finite element method, each row in the system matrix corresponds to the unknown field specified at a single node. The discrete equation for each node is an algebraic relationship that is obtained through the enforcement of the minimum energy variational principle. However, regardless of the complexity by which we arrive at the system matrix, we obtain an algebraic relationship between the nodes. This algebraic relationship is similar to (5) except for more added terms depending on the finite element mesh, size, and shape.

For each matrix row that involves nodes on the averaging perimeter Γ , the nodes to the exterior of Γ are averaged while the nodes in the interior remain the same. This procedure does not alter the basic finite element mesh construction but involves minor post-processing of the system matrix.

VI. NUMERICAL EXPERIMENT USING THE FINITE-DIFFERENCE METHOD

We consider the problem of a TM-polarized point source radiating in two-dimensional free space. The source is placed in the center of a 21 cell \times 21 cell computational domain. The grid spacing is $h = 0.05\lambda$. The boundary layer is taken to be 6 cells wide. We use Higdon's third-order boundary condition for B in (1) and (2). Higdon's boundary operators are well-suited for rectangular outer boundaries and thus are ideal for the finite-difference method.

Figure 3 shows comparison between the COM solution and the exact solution obtained from the analytical series solution for the point source (Hankel function series.) The solution presented in Fig. 3 corresponds to the electric field on the nodes lying across the top layer spanning 20 nodes (the corner nodes are excluded.) The COM solution is observed to compare very favorably with the exact solution. It is important to note that the COM solution includes discretization errors that are present even if the boundary condition does not generate any reflections.

VII. CONCLUSION

This short paper presented the application of concurrent COM in frequency-domain simulation. The averaging of the solutions obtained from the application of each of the complementary operators is performed within a single simulation by direct substitution in the system matrix.

The results, presented for a simple numerical experiment, testify to the validity, strength and efficiency of this new implementation.

REFERENCES

- [1] O. M. Ramahi, "Complementary operators: A method to annihilate artificial reflections arising from the truncation of the computational domain in the solution of partial differential equations," *IEEE Trans. Antennas Propagat.*, vol. AP-43, no. 7, pp. 697-704, July 1995.
- [2] O. M. Ramahi, "Complementary boundary operators for wave propagation problems," *J. Computat. Phys.*, vol. 133, pp. 113-128, 1997.

- [3] O. M. Ramahi, "The concurrent complementary operators method for FDTD mesh truncation," *IEEE Trans. Antennas Propagat.*, vol. 46, no. 10, pp. 1475-1482, Oct. 1998.
- [4] O. M. Ramahi, "Frequency-domain complementary operators for finite element simulation" in Proc. 15th Annual Progress in Applied Computational Electromagnetics Meeting, Monterey, CA, March 15-19, 1999.
- [5] O. M. Ramahi, "Frequency-domain complementary operators for finite element simulation" *IEEE Trans. Antennas Propagat.* To be published.

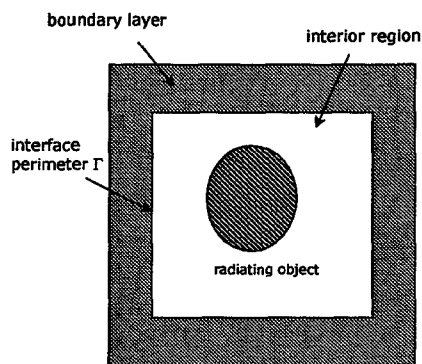


Fig. 1. Division of the computational domain showing the boundary and interior regions.

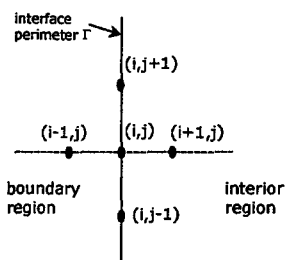


Fig. 2. The finite-difference grid shown at the interface perimeter.

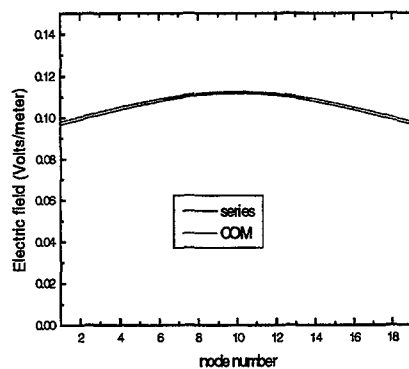


Fig. 3. The Ez field computed using the finite difference method with COM and the series solution.

SESSION 4

**STUDENT PAPER
COMPETITION**

Chair: Perry Wheless

Systematic Studies in Annular Ring PBG structures

Todd M. Lammers, Shawn W. Staker, Melinda Piket-May

Department of Electrical and Computer Engineering

Campus Box 425, University of Colorado, Boulder, CO 80309

Phone 303-492-7891, Fax 303-492-5323

Lammerst@colorado.edu, Staker@colorado.edu, mjp@colorado.edu

Abstract

Studying the use of a Photonic Band Gap Structure (PBG) as a passive filtering element in microwave devices has been well proven by both etching structures in the ground plane[1] and drilling holes in the dielectric[2]. However analyzing the destination of the propagating and mitigated energies is essential in order to completely understand the behavior of inserting such structures into any microwave device. To analyze and control the external effects of a circular 2D PBG structure in a ground plane, inner circular metal patches were inserted into the PBG and varied over a range of diameters.

I Introduction

Photonic Band Gap structures refer to the use of a repeated pattern of objects, separated in pitch by a function of λ over two. This periodicity can prohibit forward progress of a specific band of frequencies over the various vectors of propagation. This phenomenon is due to the repeated destructive back scattering of the incident wave off of the periodic lattice geometries[3]. These photonic structures can exist in 1D, 2D, and 3D space. This paper will present 2D square lattices of circular and annular rings etched in the ground plane of a microstrip.

The use of PBGs in microstrip elements has been reported in 2 distinct implementations. One by drilling actual dielectric lattices in the substrate level while not disturbing the ground plane[2]. This method, although effective, proves to be harder to fabricate since the copper strip must be laminated to the board. The second way is to etch or print a structure on to the ground plane creating disturbances in the quasi TEM propagation of a microstrip wave[1]. This method is practical for PCB designers since simple machinery can be used to achieve lattice etching. Although this type of structure can be successfully inserted into a microstrip for filtering[1], fields will exist beyond the base of the ground plane. In general, by substituting an annular ring for the regular circular PBG we can reduce the field strength below the ground plane while still achieving the same stop band frequency. However there is a relationship between the area blocked by the inner plate and the relative stop band null depth.

II. The Basic Model Design

A 2-D square lattice, was chosen to be etched on to a ground plane below a normal 50 Ω microstrip line. A 25mil thick substrate with a corresponding dielectric constant of 10.5 was used to achieve a 50 Ω line impedance with a 25mil strip width. To achieve a 12Ghz stopband, the pitch of the lattice is 200mil in both the lateral and longitudinal directions[1]. An annular ring geometry was chosen with

an outer radius (D1) of 100mil, and an inner radius of (D2) which was varied over the range 0 – 80mil by 20mil steps. The outer diameter does not effect the center frequency of the stop band, but does effect the band width of the stop band. In our case D1 was kept constant, and the inner plate became the variance on the stop band characteristics.

All models reported were designed using LC, the SGI FDTD algorithm. All models were sourced using a gaussian pulse with frequency content up to 35Ghz which was supported by the FDTD grid resolution. PML was used as the ABC to achieve the minimum amount of reflections possible.

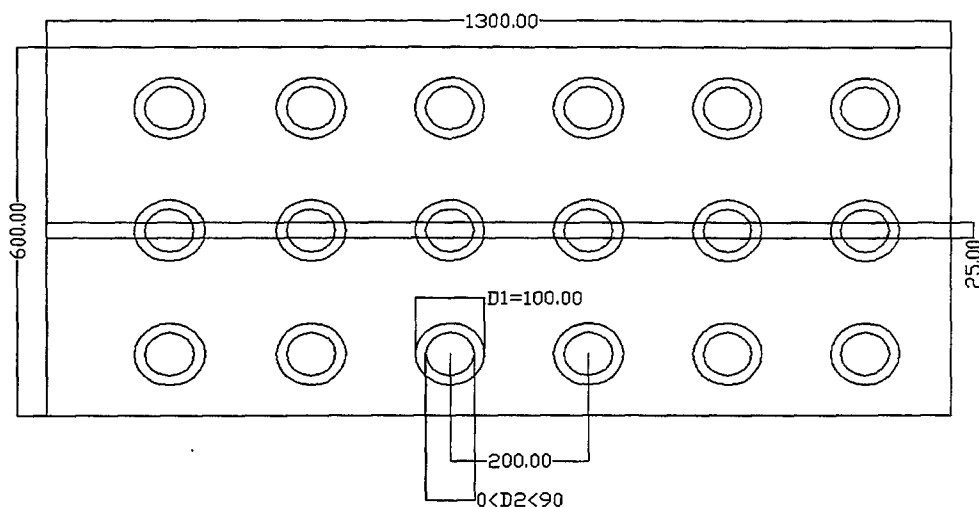


Figure 1: Physical dimensions for the annular ring PBG in FDTD.

III. PBG Stop band Analysis

In the systematic study of stop band null depth vs. annular area, the inner radii of the metal plate was varied to show trends for optimal design of the PBG. The nominal case is taken to be a PBG relief with an inner diameter of zero, or a complete circular relief. Figure X shows clean stop bands at 12Ghz and 21GHz, qualifying the sturcture as a valid PBG [1]. Figure X shows null depths below -15 dB up to a inner diameter of 80 mils. Figure X shows a -3 dB bandwidth greater than 2.5 GHz. for inner diameters up to 80 mils. These results confirm the PBG characteristics are retained with the insertion of inner diameters up to 80% of the element area. At an inner diameter of 80 mils a spike in null depth is observed. This is thought to be a result of resonances within the annular slot, and is discussed in the radiation section. Past this inner diameter the performance of the PBG sturcture degrades rapidly.

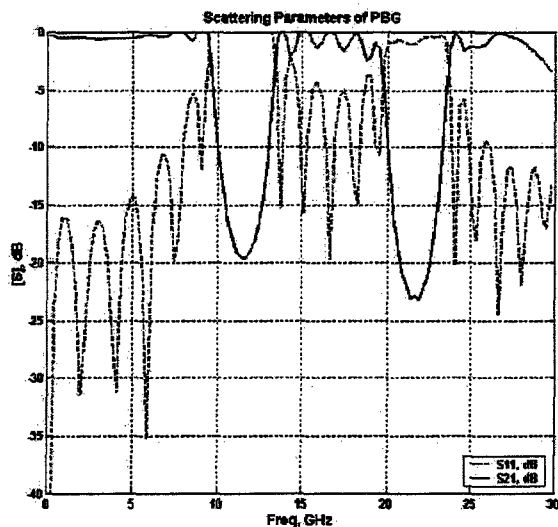


Figure 2: S parameters for the nominal PBG structure.

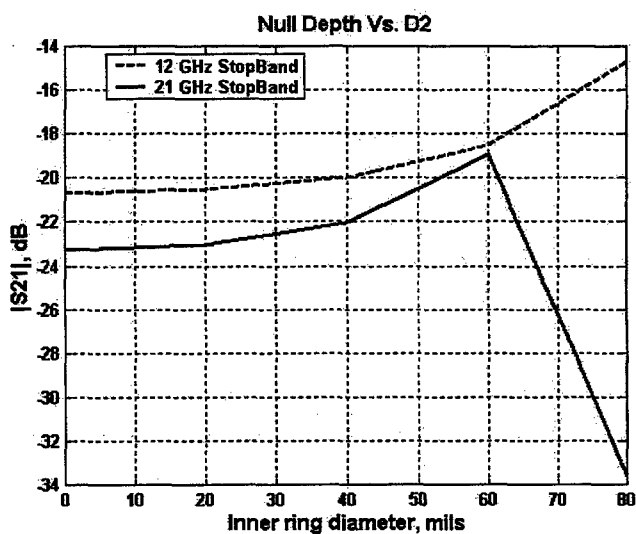


Figure 3: Null depth within stopband versus inner ring diameter.

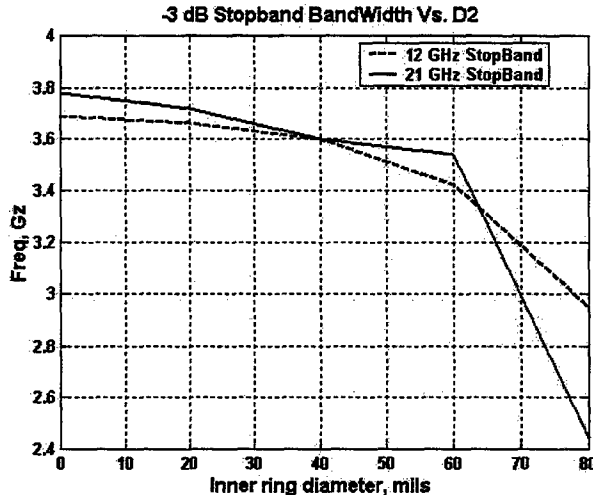


Figure 4: Bandwidth of stopband versus inner ring diameter.

IV. Coupling Analysis in a PCB

Using PBGs in a PCB stackup can lead to cross layer coupling. Pictured below is a three layer printed circuit board modeled in FDTD. The top layer is a 50Ω microstrip (25mill) overlayed on a 25mill thick RT/Duriod dielectric slab. Before inserting the PBG, the system contains a solid ground plane and behaves normally with line two being completely de-coupled from the top line. However when the PBG is present in the ground plane the new composite structure behaves as a coupled 4 port network. Figure X shows the scattering parameters for the new coupled system. The new 4 port structure exhibits PBG behavior between ports 1 and 2, while showing significant coupling within the bandgap region. This is a direct result of the reflected energy in the traditional PBG, being rerouted to the coupled line. Interducing annular rings would reduce this coupling.



Figure 5: Stackup for a simple 3 layer PCB board modeled in FDTD

V. PBG Structure as a Radiator

The radiation characteristics of the PBG structure was analyzed at it's design frequency of 12 GHz. The PBG structure can be viewed as an array of annular slots, with excitation conveniently available though the microstrip line. Typically patterns for the various annular ring dimensions are shown in figure X. The patterns are reminiscent of a series fed array, with distinct characteristics identifiable. The E-plane is assumed in the direction of propogation, and for a traveling wave mode, a linear phase and amplitude taper is expected across the E-plane. The annular slot array is fed at the center line

parallel to the direction of propagation, thus phase and amplitude symmetry exists in the H-plane. The slightly high cross polarization in the H-plane suggests the possibility of a degenerative mode existing in the annular slots.

VI. Conclusions

The use of annular rings in place of traditional circular PBG elements is thought to reduce coupling and near field intensity. In the reported systematic study the insertion of annular rings retains PBG characteristics and performance. After a threshold level of 80%, degradation in both bandwidth and null depth was found. Radiation from the annular ring PBG structure was found to have qualities similar to a series fed array of radiating slots. Future work will confirm the reduction in coupling in PCB structures due to annular rings. Future work will investigate the dual operation of annular rings as PBG's and constructive radiators.

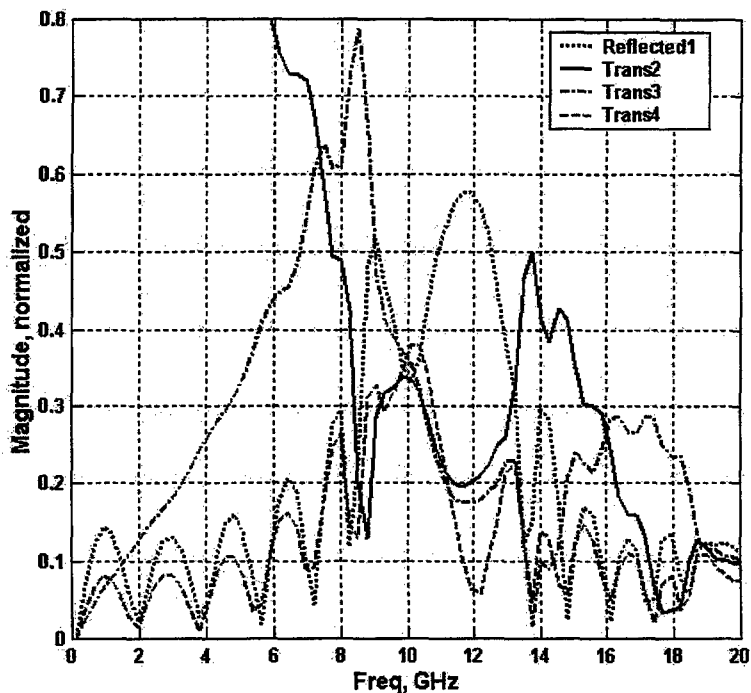


Figure 6: S parameters for 4 port nominal PBG structure.

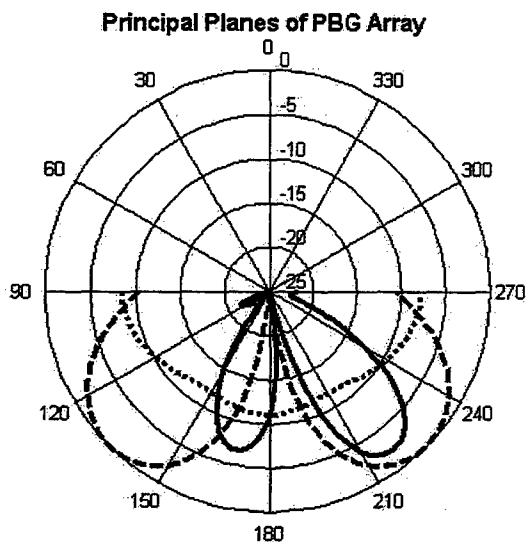


Figure 7: Principal plane patterns from PBG structure.
Solid line: E-plane Co-Pol, Dotted line: H-plane Cross-Pol, Dashed line: H-plane Co-Pol.

References

- [1] Vesna Radisic, Yonqxi Qian, Roberto Coccioli, and Tatsuo Itoh, "Novel 2-D Photonic Bandgap Structure for Microstrip Lines," *IEEE Microwave and Guided Wave Letters.*, Vol. 8, No.2, Feb. 1998.
- [2] Ian Rumsey, Todd Lammers and Melinda Piket-May, "Microstrip and Stripline Design for Novel Structures," *URSI National Radio Science meeting, Boulder Colorado, conference proceedings*, 1999.
- [3] Eli Yablonovitch and dan Sievenpiper, D-Tutorial "High Impedance Electromagnetic Surfaces," *URSI International Radio Science meeting Toronto Canada, Conference notes and Proceedings* 1999.
- [4] J. D. Joannopoulos, R. D. Meade, J. N. Minn, "Photonic Crystals," (Princeton University Press, 1995).

Fast Electromagnetic Analysis Using the Asymptotic Waveform Evaluation Method

Dan Jiao and Jian-Ming Jin

Center for Computational Electromagnetics
Department of Electrical and Computer Engineering
University of Illinois at Urbana-Champaign
Urbana, Illinois 61801-2991

Abstract

This paper describes the application of the asymptotic waveform evaluation (AWE) method to a variety of electromagnetic problems for a fast frequency-sweep analysis. These problems include (1) scattering by a perfectly electric conducting (PEC) body, (2) radiation of wire antennas on a PEC body, (3) scattering by a dispersive dielectric body, and (4) scattering and radiation of conformal cavity-backed microstrip patch antennas. It is shown that the use of AWE can speed up the analysis by more than an order of magnitude.

1 Introduction

Many electromagnetic applications require the calculation of the frequency response of a device over a wide frequency band rather than at one or a few isolated frequency points. For example, for radar target recognition, one has to compute the radar cross section (RCS) of a target over a wide frequency band to generate the range profiles and synthetic-aperture-radar (SAR) images. For analysis of antennas especially the wide-band antennas, one has to calculate the input impedance at many frequency points. Such calculations can be very time consuming when a traditional frequency-domain numerical method is used because a set of algebraic equations must be solved repeatedly at many frequency points. The number of algebraic equations is proportional to the electrical size of the problem and can be large for most applications. Therefore, there is an urgent need to find approximate solution techniques that can efficiently simulate a frequency response over a frequency band.

One such technique is the method of asymptotic waveform evaluation (AWE) [1], which was originally developed for high-speed circuit analysis. In AWE, the transfer function of a circuit is expanded into a series, and the circuit model is then approximated with a lower-order transfer function by moment matching. The AWE has recently been applied to the finite-element and finite-difference analysis of electromagnetic problems [2-9]. In these applications, the implementation of AWE is straightforward since the resultant matrix equation has a simple dependence on frequency.

For electromagnetic scattering and radiation by conducting and dielectric objects, a very useful solution technique is the method of moments (MoM) that solves a surface integral equation (SIE) for the electric current on the surface of an object. This method is advantageous because (i) it limits the unknown current on the surface of an object and (ii) it satisfies the radiation condition via the Green's function. However, the method results in a dense matrix that is computationally expensive to generate and invert. Since this matrix depends on frequency in a complex manner, one has to repeat the calculations at each frequency to obtain the solution over a band of frequencies.

In this paper, we describe the application of the AWE method to a variety of electromagnetic problems for a fast frequency-sweep analysis. These problems include (1) scattering by a perfectly electric conducting (PEC) body, (2) radiation of wire antennas on a PEC body, (3) scattering by a dispersive dielectric body, and (4) scattering and radiation of conformal cavity-backed microstrip patch antennas. All of these problems are formulated in terms of a SIE or its combination with the finite element method (FEM).

2 The AWE Method

Given an electromagnetic problem, its numerical analysis usually results in a matrix equation in the following form:

$$A(k)x(k) = y(k) \quad (1)$$

where A is a square matrix, x is an unknown vector, y is a known vector associated with the source or excitation, and k is the wavenumber related to frequency. Since the matrix A depends on frequency, it must be generated and solved repeatedly at each individual frequency in order to obtain a solution over a frequency band. This can be time consuming especially for problems whose response varies drastically with frequency. In this work, we alleviate this difficulty using the AWE method.

In accordance with the AWE method, to obtain the solution of (1) over a wide frequency band, we expand $x(k)$ into a Taylor series

$$x(k) = \sum_{n=0}^Q m_n (k - k_0)^n \quad (2)$$

where k_0 is the expansion point. Substituting this into (1), expanding the impedance matrix $A(k)$ and the excitation vector $y(k)$ into a Taylor series, and finally matching the coefficients of the equal powers of $k - k_0$ on both sides yield the recursive relation for the moment vectors:

$$m_0 = A^{(-1)}(k_0)y(k_0) \quad (3)$$

$$m_n = A^{(-1)}(k_0) \left[\frac{y^{(n)}(k_0)}{n!} - \sum_{i=1}^n \frac{A^{(i)}(k_0)m_{n-i}}{i!} \right] \quad (4)$$

$n \geq 1$

where $A^{(-1)}$ denotes the inverse of A , $A^{(i)}$ denotes the i -th derivative of A , and likewise $y^{(n)}$ denotes the n -th derivative of y .

The Taylor expansion has a limited bandwidth. To obtain a wider bandwidth, we represent $x(k)$ with a better behaved rational Padé function:

$$x(k) = \frac{\sum_{i=0}^L a_i (k - k_0)^i}{1 + \sum_{j=1}^M b_j (k - k_0)^j} \quad (5)$$

where $L + M = Q$. The unknown coefficients a_i and b_j can be calculated by substituting (2) into (5), multiplying (5) with the denominator of the Padé expansion, and matching the coefficients of the equal powers of $k - k_0$. This leads to the matrix equation

$$\begin{bmatrix} m_L & m_{L-1} & m_{L-2} & \cdots & m_{L-M+1} \\ m_{L+1} & m_L & m_{L-1} & \cdots & m_{L-M+2} \\ m_{L+2} & m_{L+1} & m_L & \cdots & m_{L-M+3} \\ \vdots & \vdots & \vdots & \ddots & \vdots \\ m_{L+M-1} & m_{L+M-2} & m_{L+M-3} & \cdots & m_L \end{bmatrix}$$

$$\times \begin{bmatrix} b_1 \\ b_2 \\ b_3 \\ \vdots \\ b_M \end{bmatrix} = - \begin{bmatrix} m_{L+1} \\ m_{L+2} \\ m_{L+3} \\ \vdots \\ m_{L+M} \end{bmatrix} \quad (6)$$

which can be solved for b_j . Once b_j are obtained, the unknown coefficients a_i can then be calculated as

$$a_i = \sum_{j=0}^i b_j m_{i-j} \quad 0 \leq i \leq L. \quad (7)$$

Clearly, in the procedure described above the impedance matrix $A(k)$ is inverted only once, which is the main reason for the efficiency of the AWE method. In the case that one expansion point is not sufficient to cover the desired frequency band, one can use multipole expansion points, which can be selected automatically using a simple binary search algorithm [3].

3 Applications

The AWE method described has been applied to a number of electromagnetic problems. A brief description of each problem is given below.

3.1 Scattering by a PEC body

The scattering by a PEC body can be formulated in terms of an electric field integral equation (EFIE) [10] or a magnetic field integral equation (MFIE). However, both EFIE and MFIE suffer from the problem of interior resonance, which yields erroneous solutions at certain frequencies. This problem can be overcome by combining EFIE and MFIE to form a combined field integral equation (CFIE) [11]. Our numerical simulations showed indeed that when the expansion point of AWE is close to the frequency of interior resonance, both EFIE and the MFIE can exhibit significant errors. Figure 1 shows the RCS of the 1-m long NASA almond. It takes the direct method 23220 s on a Digital Personal Workstation to calculate the RCS at 84 frequency points from 0 to 1.7 GHz. The number of unknowns varies from 1560 to 2148 during the frequency sweep. With the AWE method, it takes only 1989.3 s to calculate the RCS over the entire band using seven expansion points.

3.2 Wire antennas on a PEC body

For wire antennas on a PEC body, numerical solution can be obtained by applying EFIE to the wire antennas and CFIE to the PEC body. However, special basis functions are required in order to simulate the current flow at the junction between the wires and the PEC body. We implemented the AWE method into the MoM code described by Chao [12] and considered a configuration consisting of two loop antennas on a finite ground plane. The calculated results are combined with the measured data [13] in Fig. 2.

3.3 Scattering by a dielectric body

A formulation that is widely used for scattering by dielectric bodies is the so-called PMCHW [14], named after Poggio, Miller, Chang, Harrington, and Wu, who originally developed the formulation. In this formulation, the EFIE for the field outside the object is combined with the EFIE for the

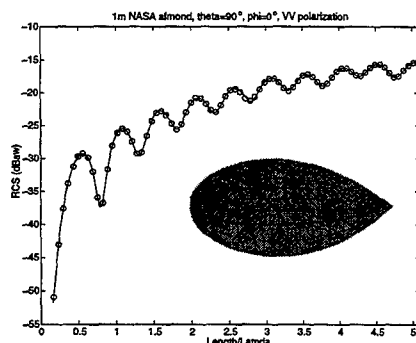


Figure 1: RCS frequency response of the 1-m long NASA almond from 0 to 1.7 GHz (VV-polarization with $\theta^{inc} = 90^\circ$ and $\phi^{inc} = 0^\circ$).

field inside the object to form a combined equation. Similarly, the MFIE for the field outside the object is combined with the MFIE for the field inside the object to form another combined equation. These two equations are then solved by the MoM. This formulation is found to be free of interior resonances and yields accurate and stable solutions. With the AWE method, we can even model dispersive dielectrics. An example is given in Fig. 3, where the backscatter RCS is displayed as a function of frequency for a dispersive dielectric sphere having a radius of 0.5 cm. The relative permittivity of the dielectric is described by the Debye model. Its real part varies from 2.56 to 2.33 and its imaginary part varies from -0.024 to -0.55 as frequency varies from 0 to 27.5 GHz. As can be seen, the numerical results agree with the exact Mie series solution very well. The AWE method speeds up the calculation by a factor of 13.

3.4 Cavity-backed microstrip patch antennas

The scattering and radiation from a cavity-backed microstrip patch antenna can be efficiently characterized using the hybrid finite-element boundary-integral (FE-BI) method [15]. The resulting matrix equation is a combination of the FEM and MoM matrix equations. Despite its complicated form, it can still be handled by the AWE method. Figure 4 shows the input impedance of a microstrip patch antenna as a function of frequency from 1 to 4 GHz. The antenna consists of a $5.0 \text{ cm} \times 3.4 \text{ cm}$ rectangular conducting patch residing on a dielectric substrate having thickness $t = 0.08770 \text{ cm}$, relative permittivity $\epsilon_r = 2.17$ and a loss tangent of 0.0015. The substrate is housed in a $7.5 \text{ cm} \times 5.1 \text{ cm}$ rectangular cavity recessed in a ground plane. The patch is excited by a current probe applied at $x_f = 1.22 \text{ cm}$ and $y_f = 0.85 \text{ cm}$. The number of unknowns used in the calculations is 1741. With a frequency increment of 0.05 GHz, it takes the direct method 4012.8 s to obtain the solution. With a 6th-order Taylor expansion ($Q = 6, L = 3, M = 3$), the AWE method produces an accurate solution with 0.01 GHz increments over the entire band in 254.2 s.

4 Conclusions

This paper described the application of the AWE method to a variety of electromagnetic problems for a fast frequency-sweep analysis, which include (1) scattering by a perfectly electric conducting (PEC) body, (2) radiation of wire antennas on a PEC body, (3) scattering by a dispersive dielectric

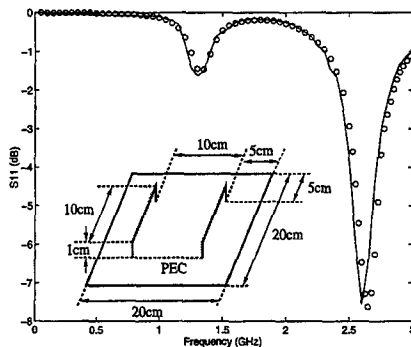


Figure 2: The S-parameter of two loop antennas on a finite ground plane (Circles: calculated. Line: measured).

body, and (4) scattering and radiation of conformal cavity-backed microstrip patch antennas. It was shown that the use of AWE can speed up the analysis by more than an order of magnitude.

Acknowledgment: This work was supported by the National Science Foundation under grant NSF ECE 94-57735 and a grant from AFOSR via the MURI Program under contract number F49620-96-1-0025.

References

- [1] L. T. Pillage and R. A. Rohrer, "Asymptotic waveform evaluation for timing analysis," *IEEE Trans. Computer-Aided Design*, vol. 9, pp. 352-366, Apr. 1990.
- [2] X. Yuan and Z. J. Cendes, "A fast method for computing the spectral response of microwave devices over a broad bandwidth," *1993 URSI Radio Science Meeting*, p. 196, Ann Arbor, MI, 1993.
- [3] M. A. Kolbehdari, M. Srinivasan, M. S. Nakhla, Q. J. Zhang, and R. Achar, "Simultaneous time and frequency domain solutions of EM problems using finite element and CFH techniques," *IEEE Trans. Microwave Theory Tech.*, vol. 44, pp. 1526-1534, Sept. 1996.
- [4] M. Li, Q. J. Zhang, and M. S. Nakhla, "Finite difference solution of EM fields by asymptotic waveform techniques," *IEE Proc.-H*, vol. 143, pp. 512-520, Dec. 1996.
- [5] J. Gong and J. L. Volakis, "AWE implementation for electromagnetic FEM analysis," *Electron. Lett.*, vol. 32, pp. 2216-2217, Nov. 1996.
- [6] S. V. Polstyanko, R. Dyczij-Edlinger, and J. F. Lee, "Fast frequency sweep technique for the efficient analysis of dielectric waveguides," *IEEE Trans. Microwave Theory Tech.*, vol. 45, pp. 1118-1126, July 1997.
- [7] J. Zhang and J. M. Jin, "Preliminary study of AWE for FEM analysis of scattering problems," *Microwave Opt. Tech. Lett.*, vol. 17, no. 1, pp. 7-12, 1998.

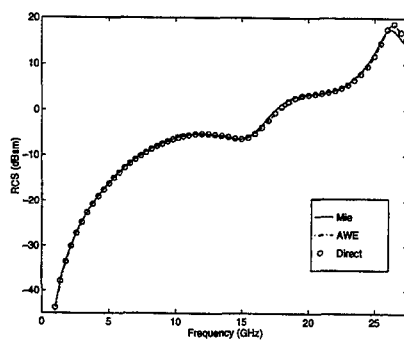


Figure 3: RCS versus frequency of a dispersive dielectric sphere having a radius of 0.5 cm.

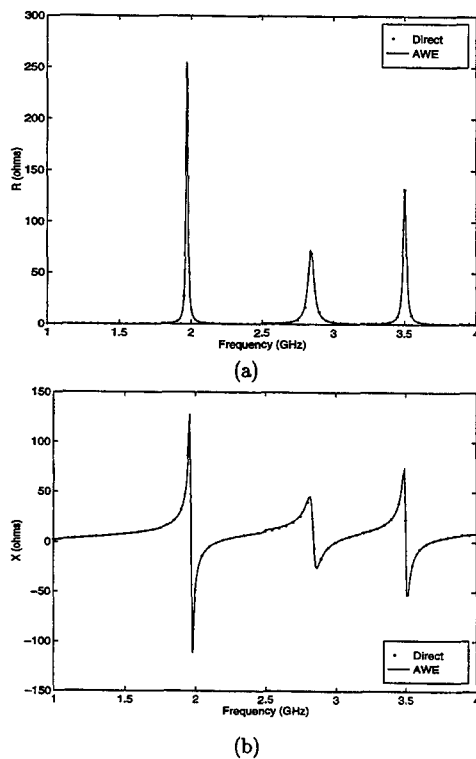


Figure 4: Input impedance versus frequency for a cavity-backed patch antenna with a probe feed. (a) Resistance. (b) Reactance.

- [8] X. M. Zhang and J. F. Lee, "Application of the AWE method with the 3-D TVFEM to model spectral responses of passive microwave components," *IEEE Trans. Microwave Theory Tech.*, vol. 46, pp. 1735-1741, Nov. 1998.
- [9] J. E. Bracken, D. K. Sun, and Z. J. Cendes, "S-domain methods for simultaneous time and frequency characterization of electromagnetic devices," *IEEE Trans. Microwave Theory Tech.*, vol. 46, pp. 1277-1290, Sept. 1998.
- [10] C. J. Reddy, M. D. Deshpande, C. R. Cockrell, and F. B. Beck, "Fast RCS computation over a frequency band using method of moments in conjunction with asymptotic waveform evaluation technique," *IEEE Trans. Antennas Propagat.*, vol. 46, pp. 1229-1233, Aug. 1998.
- [11] J. R. Mautz and R. F. Harrington, "H-field, E-field, and combined-field solutions for conducting bodies of revolution," *AEU*, vol. 32, pp. 157-164, Apr. 1978.
- [12] H. Y. Chao, "Wire and junction basis function support for the three-dimensional fast multipole method," M.S. thesis, Univ. of Illinois at Urbana-Champaign, 1998.
- [13] S. V. Georgakopoulos, C. A. Balanis, and C. B. Birtcher, "Coupling between wire antennas: analytic solution, FDTD, and measurements," *IEEE APS Int. Symp. Dig.*, vol. 1, pp. 504-507, June 1998.
- [14] J. R. Mautz and R. F. Harrington, "Electromagnetic scattering from a homogeneous material body of revolution," *AEU*, vol. 33, pp. 71-80, Feb. 1979.
- [15] J. M. Jin, *The Finite Element Method in Electromagnetics*. New York: Wiley, 1993.

**A DOMAIN-DECOMPOSITION/RECIPROCITY TECHNIQUE FOR THE ANALYSIS
OF ARBITRARILY-SHAPED MICROSTRIP ANTENNAS WITH DIELECTRIC SUBSTRATES AND
SUPERSTRATES MOUNTED ON CIRCULARLY-CYLINDRICAL PLATFORMS**

R.J. Allard, D.H. Werner, and J.S. Zmyslo
The Pennsylvania State University
Applied Research Laboratory
P.O. Box 30
State College, PA 16804

1. INTRODUCTION

Mounting microstrip patch antennas onto platforms such as circular cylinders is a practical application of conformal antenna technology. With the exception of planar structures, the circular cylinder is by far the most popular platform geometry for microstrip antennas. There are a wide range of applications for this type of antenna/platform configuration in both military and commercial sectors. Many of these applications require the use of a dielectric superstrate, which serves as a protective cover for the microstrip antenna. Much emphasis has been placed on finding accurate and efficient means for analyzing these dielectric-loaded microstrip patch antennas using a variety of different techniques.

Wong presents detailed studies in [1] of the design and operation of non-planar microstrip antennas including patches mounted on circular cylinders with both substrates and superstrates. A method for analyzing radiation characteristics of microstrip patch antennas in the Fourier domain is given in [2] including derivations of far-field radiation pattern expressions. The radiation pattern and impedance characteristics for square and circular microstrip patch antennas mounted on cylindrical platforms are also discussed in detail in [3] and [4]. In [5] the dyadic Green's functions and moment method are used to analyze cylindrical-rectangular microstrip patches with a dielectric covering, with emphasis on the impedance behavior of such antennas. A reciprocity approach using the finite-element method to model cylindrical platforms of arbitrary cross-section is employed in [6] to analyze microstrip patch antennas and arrays of microstrip patch antennas. Additional discussions regarding the impedance characteristics versus frequency for a superstrate-loaded rectangular patch antenna on a cylindrical surface are contained in [7]. Kempel presents an excellent review of the most recent advances in the modeling of conformal patch antennas in [8].

In [9] a technique for calculating far-field radiation patterns for substrate-loaded microstrip patch antennas using a reciprocity approach was introduced. This procedure was demonstrated to be both accurate and efficient for analyzing patch antennas mounted on circularly-cylindrical platforms. This paper will present an extension of this procedure, namely the inclusion of the effects of a superstrate in the far-field radiation pattern expressions for the patch antenna. The superstrate analysis procedure will be shown to be both accurate and efficient, possessing the same advantages as the substrate-only analysis presented in [9]. Two examples will be used to demonstrate the accuracy and utility of this technique for analyzing substrate- and superstrate-loaded microstrip patch antennas mounted on circularly-cylindrical platforms.

2. THEORY

The geometry being considered for this application of the reciprocity approach, as shown in Figure 1, involves a microstrip patch antenna of any arbitrary shape mounted on a dielectric-coated PEC cylinder and covered by a dielectric superstrate. In reality, this configuration would be contained within a recessed cavity in the surface of a PEC body, however since it is assumed that the dimensions of the patch antenna are sufficiently small, the effects of the cavity walls may be ignored. The radius of the PEC cylinder is denoted by a , the height of the substrate is given as b , and the height of the superstrate is c . The substrate and superstrate consist of dielectric materials with relative permittivities ϵ_{r1} and ϵ_{r2} , respectively. A reciprocity approach based on that described in [9], where patch antennas involving the presence of only a substrate were considered, is extended here to include the effects of the presence of a superstrate. This technique involves applying domain decomposition such that two separate problems of reduced size may be solved. These results are then related via the reciprocity theorem in order to calculate the resultant far-field radiation pattern. The first step in the procedure is to

solve for the current distribution on the surface of an equivalent flat patch antenna using, in this case, a Method of Moments (MoM) technique. The second step involves using an analytical technique to solve for the total electric field between two dielectric layers (i.e., the substrate and superstrate) of a coated metallic cylinder produced by an incident TEⁱ- and TMⁱ-polarized plane wave. The final step involves carrying out the required dot product between the surface current and the total electric field and integrating this result over the surface of the patch to obtain the desired E_θ and E_ϕ components of the far-zone radiation pattern.

It is convenient for this analysis to express the electromagnetic fields in terms of the Hertz vectors as [10]

$$\vec{E} = \nabla \times \vec{\nabla} \times \vec{\Pi} - j\omega\mu \vec{\nabla} \times \vec{\Pi}^* \quad (1a)$$

$$\vec{H} = j\omega\epsilon \vec{\nabla} \times \vec{\Pi} + \vec{\nabla} \times \vec{\nabla} \times \vec{\Pi}^* \quad (1b)$$

where $\vec{\Pi}$ and $\vec{\Pi}^*$ are the electric and magnetic Hertz vectors, respectively. Using the Hertz vectors and applying the reciprocity approach, the far-field radiation pattern expressions for a patch antenna mounted on a dielectric-coated PEC cylinder with a dielectric superstrate may be expressed as

$$E_\theta(r, \theta, \phi) = -j\eta_0 \frac{e^{-j\beta_0 r}}{4\pi r} \left\{ \left(\frac{\beta_0 \beta_z}{\beta_2 \beta_{\rho 2}} \right) \sum_{n=-\infty}^{\infty} (-1)^n n [b_n J_n(\beta_{\rho 2} b) + c_n Y_n(\beta_{\rho 2} b)] S_\phi(n, \theta) e^{jn\phi} \right. \\ \left. - j\beta_0 b \sum_{n=-\infty}^{\infty} (-1)^n [b_n^* J_n'(\beta_{\rho 2} b) + c_n^* Y_n'(\beta_{\rho 2} b)] S_\phi(n, \theta) e^{jn\phi} \right. \\ \left. - \left(\frac{\beta_{\rho 2}}{\beta_2} \right) \beta_0 b \sum_{n=-\infty}^{\infty} (-1)^n [b_n J_n(\beta_{\rho 2} b) + c_n Y_n(\beta_{\rho 2} b)] S_z(n, \theta) e^{jn\phi} \right\} \quad (2a)$$

$$E_\phi(r, \theta, \phi) = -j\eta_0 \frac{e^{-j\beta_0 r}}{4\pi r} \left\{ \left(\frac{\beta_0 \beta_z}{\beta_2 \beta_{\rho 2}} \right) \sum_{n=-\infty}^{\infty} (-1)^n n [p_n J_n(\beta_{\rho 2} b) + q_n Y_n(\beta_{\rho 2} b)] S_\phi(n, \theta) e^{jn\phi} \right. \\ \left. - j\beta_0 b \sum_{n=-\infty}^{\infty} (-1)^n [p_n^* J_n'(\beta_{\rho 2} b) + q_n^* Y_n'(\beta_{\rho 2} b)] S_\phi(n, \theta) e^{jn\phi} \right. \\ \left. - \left(\frac{\beta_{\rho 2}}{\beta_2} \right) \beta_0 b \sum_{n=-\infty}^{\infty} (-1)^n [p_n J_n(\beta_{\rho 2} b) + q_n Y_n(\beta_{\rho 2} b)] S_z(n, \theta) e^{jn\phi} \right\} \quad (2b)$$

where $b = a + h$ is the radius from the center of the PEC cylinder to the surface of the substrate. The infinite summations given in (2a) and (2b) may be truncated according to the convergence condition $N = 2\beta_0 a$, where N is the total number of terms that must be used to guarantee convergence of the expressions [2]. The parameters S_ϕ and S_z are surface integrals which depend on the patch current distribution given by [9]

$$S_\phi(n, \theta) = \iint_{S'} J_\phi(\phi', z') e^{-jn\phi'} e^{j\beta_z z'} d\phi' dz' \quad (3a)$$

$$S_z(n, \theta) = \iint_{S'} J_z(\phi', z') e^{-jn\phi'} e^{j\beta_z z'} d\phi' dz' \quad (3b)$$

where S' is the area of the arbitrarily-shaped conformal patch. The coefficients b_n, b_n^*, c_n and c_n^* in the TM_z case and p_n, p_n^*, q_n and q_n^* in the TE_z case are found using the matrix equations

$$\begin{bmatrix} b_n \\ b_n^* \\ c_n \\ c_n^* \end{bmatrix} = \begin{bmatrix} a_{11} & a_{12} & a_{13} & a_{14} \\ a_{21} & a_{11} & a_{23} & a_{13} \\ a_{31} & a_{32} & a_{33} & a_{34} \\ a_{41} & a_{31} & a_{43} & a_{33} \end{bmatrix}^{-1} \begin{bmatrix} 0 \\ 0 \\ 0 \\ y_4 \end{bmatrix} \quad (4a)$$

$$\begin{bmatrix} p_n \\ p_n^* \\ q_n \\ q_n^* \end{bmatrix} = \begin{bmatrix} a_{11} & a_{12} & a_{13} & a_{14} \\ a_{21} & a_{11} & a_{23} & a_{13} \\ a_{31} & a_{32} & a_{33} & a_{34} \\ a_{41} & a_{31} & a_{43} & a_{33} \end{bmatrix}^{-1} \begin{bmatrix} 0 \\ 0 \\ y_3 \\ 0 \end{bmatrix} \quad (4b)$$

respectively. The elements of the matrix and vector used in (4a) and (4b) to determine the required coefficients are

$$\begin{aligned} a_{11} &= \frac{n\beta_z \beta_0^2 [\varepsilon_{r1} - \varepsilon_{r2}]}{\beta_2 b \beta_{\rho 2} \beta_{\rho 1}^2} J_n(\beta_{\rho 2} b) & a_{12} &= j \left[\frac{\beta_{\rho 2} F_4}{\beta_{\rho 1} F_3} J_n(\beta_{\rho 2} b) - J_n'(\beta_{\rho 2} b) \right] \\ a_{13} &= \frac{n\beta_z \beta_0^2 [\varepsilon_{r1} - \varepsilon_{r2}]}{\beta_2 b \beta_{\rho 2} \beta_{\rho 1}^2} Y_n(\beta_{\rho 2} b) & a_{14} &= j \left[\frac{\beta_{\rho 2} F_4}{\beta_{\rho 1} F_3} Y_n(\beta_{\rho 2} b) - Y_n'(\beta_{\rho 2} b) \right] \\ a_{21} &= -j \left[\frac{\varepsilon_{r1}}{\varepsilon_{r2}} \frac{\beta_{\rho 2} F_2}{\beta_{\rho 1} F_1} J_n(\beta_{\rho 2} b) - J_n'(\beta_{\rho 2} b) \right] & a_{23} &= -j \left[\frac{\varepsilon_{r1}}{\varepsilon_{r2}} \frac{\beta_{\rho 2} F_2}{\beta_{\rho 1} F_1} Y_n(\beta_{\rho 2} b) - Y_n'(\beta_{\rho 2} b) \right] \\ a_{31} &= \frac{n\beta_z \beta_0^2 [\varepsilon_{r2} - 1]}{\beta_2 c \beta_{\rho 2} \beta_{\rho}^2} J_n(\beta_{\rho 2} c) & a_{32} &= -j \left[\frac{\beta_{\rho 2} H_n^{(2)'}(\beta_{\rho c})}{\beta_{\rho} H_n^{(2)}(\beta_{\rho c})} J_n(\beta_{\rho 2} c) - J_n'(\beta_{\rho 2} c) \right] \\ a_{33} &= \frac{n\beta_z \beta_0^2 [\varepsilon_{r2} - 1]}{\beta_2 c \beta_{\rho 2} \beta_{\rho}^2} Y_n(\beta_{\rho 2} c) & a_{34} &= -j \left[\frac{\beta_{\rho 2} H_n^{(2)'}(\beta_{\rho c})}{\beta_{\rho} H_n^{(2)}(\beta_{\rho c})} Y_n(\beta_{\rho 2} c) - Y_n'(\beta_{\rho 2} c) \right] \\ a_{41} &= j \left[\frac{1}{\varepsilon_{r2}} \frac{\beta_{\rho 2} H_n^{(2)'}(\beta_{\rho c})}{\beta_{\rho} H_n^{(2)}(\beta_{\rho c})} J_n(\beta_{\rho 2} c) - J_n'(\beta_{\rho 2} c) \right] & a_{43} &= j \left[\frac{1}{\varepsilon_{r2}} \frac{\beta_{\rho 2} H_n^{(2)'}(\beta_{\rho c})}{\beta_{\rho} H_n^{(2)}(\beta_{\rho c})} Y_n(\beta_{\rho 2} c) - Y_n'(\beta_{\rho 2} c) \right] \\ y_3 &= -\frac{2\sqrt{\varepsilon_{r2}} (j)^{-n}}{\pi \beta_{\rho c}} \frac{1}{H_n^{(2)}(\beta_{\rho c})} & y_4 &= \frac{2(j)^{-n}}{\pi \sqrt{\varepsilon_{r2}} \beta_{\rho c}} \frac{1}{H_n^{(2)}(\beta_{\rho c})} \end{aligned}$$

where $c = a + h + t$ is the radius from the center of the PEC cylinder to the surface of the superstrate, and F_1, F_2, F_3 , and F_4 are parameters defined as

$$\begin{aligned} F_1 &= J_n(\beta_{\rho 1} b) - \frac{J_n(\beta_{\rho 1} a)}{Y_n(\beta_{\rho 1} a)} Y_n(\beta_{\rho 1} b) & F_2 &= J_n'(\beta_{\rho 1} b) - \frac{J_n'(\beta_{\rho 1} a)}{Y_n(\beta_{\rho 1} a)} Y_n'(\beta_{\rho 1} b) \\ F_3 &= J_n(\beta_{\rho 1} b) - \frac{J_n'(\beta_{\rho 1} a)}{Y_n'(\beta_{\rho 1} a)} Y_n(\beta_{\rho 1} b) & F_4 &= J_n'(\beta_{\rho 1} b) - \frac{J_n'(\beta_{\rho 1} a)}{Y_n'(\beta_{\rho 1} a)} Y_n'(\beta_{\rho 1} b) \end{aligned}$$

The wave-number definitions used in the above expressions are defined as

$$\begin{array}{lll} \beta_1 = \beta_0 \sqrt{\epsilon_{r1}} & \beta_z = \beta_0 \cos \theta & \beta_{\rho 1} = \beta_0 \sqrt{\epsilon_{r1} - \cos^2 \theta} \\ \beta_2 = \beta_0 \sqrt{\epsilon_{r2}} & \beta_\phi = \beta_0 \sin \theta & \beta_{\rho 2} = \beta_0 \sqrt{\epsilon_{r2} - \cos^2 \theta} \end{array}$$

The procedure described here for calculating the far-field radiation patterns of a substrate- and superstrate-loaded microstrip patch antenna on a circularly-cylindrical platform has the advantage that it can be used in conjunction with MoM, FEM, or FDTD analysis techniques. The use of the reciprocity approach has allowed exact analytical expressions for the radiation patterns to be determined which can be easily and efficiently evaluated for any arbitrarily shaped microstrip patch antenna.

3. RESULTS

Two examples will now be presented to demonstrate the abilities of the reciprocity approach for analyzing substrate- and superstrate-loaded microstrip patch antennas. The first example is a comparison of the far-field patterns for two different cases. The first is that of a patch mounted on a circularly-cylindrical platform with only a substrate coating made of Duroid ($\epsilon_{r1} = 2.33$), while the second involves the same geometry but with a superstrate covering added (the patch in both cases is rectangular in shape). Since the relative permittivity of the superstrate dielectric has been chosen to be $\epsilon_{r2} = 1$ (air), this case geometry is equivalent, electrically speaking, to the case with only the substrate. The PEC cylinder has radius $a = 0.5\lambda$, the thickness of the substrate is $h = 0.05\lambda$ and the thickness of the superstrate is $t = 0.05\lambda$. The patch is fed using a microstrip feed-line with unity voltage excitation. The far-field radiation pattern produced using the superstrate reciprocity expressions and the substrate reciprocity analysis should therefore be identical. Figures 2a and 2b show comparisons between the substrate-only and substrate/superstrate axial ($\phi = 0^\circ$) and azimuthal ($\theta = 90^\circ$) gain patterns, respectively. The patterns produced when the air superstrate is included, indicated by circles on the plot, are indeed identical to those produced when the substrate-only analysis is used, represented by the solid line on the plots. This verifies the validity of the expressions derived to compute the far-field radiation pattern for a patch antenna with a superstrate covering.

Figure 3 shows the geometry for the second example which is an elliptical patch mounted on a circularly-cylindrical platform with a dielectric substrate made from Duroid ($\epsilon_{r1} = 2.33$) and a dielectric superstrate also consisting of Duroid ($\epsilon_{r2} = 2.33$). The patch has the dimensions 10 mm for the semi-major axis and 7.5 mm for the semi-minor axis, with PEC cylinder radius $a = 0.5\lambda$, substrate thickness $h = 0.1\lambda$ and superstrate thickness $t = 0.1\lambda$. The patch is fed using a probe feed with unity voltage excitation. Figures 4a and 4b show plots of the J_z and J_ϕ current distributions over the surface of the elliptical patch, respectively, produced using a MoM code for analysis of microstrip patch antennas. These plots clearly show the location of the probe attachment and the expected behavior of the current components along normal and tangential edges. Application of the reciprocity approach for the inclusion of superstrates leads to the far-field E_θ and E_ϕ radiation patterns shown in Figures 5a and 5b, respectively. These patterns agree with expected results, and once again verify the accuracy of the expressions derived using reciprocity for microstrip patches with both substrates and superstrates included.

4. CONCLUSIONS

The reciprocity approach first introduced in [9] for analyzing microstrip patch antennas on circularly-cylindrical platforms with substrate loading has been successfully extended to include superstrate loading as well. By setting the relative permittivity of the superstrate to that of air, the validity of the superstrate analysis was confirmed through a comparison with the results produced using the substrate-only expressions for the far-field radiation pattern of a rectangular microstrip patch antenna previously derived in [9]. Finally, the ability to analyze arbitrary geometries including superstrates of any relative permittivity were also demonstrated using an elliptical patch antenna with a superstrate consisting of Duroid ($\epsilon_{r2} = 2.33$).

REFERENCES

- [1] Wong, K.L., *Design of Nonplanar Microstrip Antennas and Transmission Lines*, John Wiley and Sons, Inc., 372 pp., 1999.
- [2] Ashkenazy, J., S. Shtrikman, and D. Treves, "Electric Surface Current Model for the Analysis of Microstrip Antennas on Cylindrical Bodies", *IEEE Transactions on Antennas and Propagation*, Vol. 33, No. 3, pp. 295 - 300, 1985.

- [3] Luk, K.M., K.F. Lee, and J.S. Dahele, "Analysis of the Cylindrical-Rectangular Patch Antenna", *IEEE Transactions on Antennas and Propagation*, Vol. 37, No. 2, pp. 143 – 147, 1989.
- [4] Luk, K.M., and K.F. Lee, "Characteristics of Cylindrical-Circular Patch Antenna", *IEEE Transactions on Antennas and Propagation*, Vol. 38, No. 7, pp. 1119 – 1123, 1990.
- [5] Silva, F.C., S.B.A. Fonseca, A.J.M. Soares, and A.J. Giarola, "Analysis of Microstrip Antennas on Circular-Cylindrical Substrates with a Dielectric Overlay", *IEEE Transactions on Antennas and Propagation*, Vol. 39, No. 9, pp. 1398 – 1404, 1991.
- [6] Jin, Jian-Ming, J.A. Berrie, R. Kipp, and Shung-Wu Lee, "Calculation of Radiation Patterns of Microstrip Antennas on Cylindrical Bodies of Arbitrary Cross Section", *IEEE Transactions on Antennas and Propagation*, Vol. 45, No. 1, pp. 126 – 132, 1997.
- [7] Ke, S.Y., and K.L. Wong, "Input Impedance of a Probe-Fed Superstrate-Loaded Cylindrical-Rectangular Microstrip Antenna", *Microwave and Optical Technology Letters*, Vol. 7, No. 5, pp. 232-236, 1994.
- [8] Kempel, L. C., "Advances in Modeling Conformal Antennas on Cylinders", *1999 URSI Digest*, p. 343, 1999.
- [9] Werner, D.H., G.D. Mouyis, and R. Mittra, "A Reciprocity Approach for Determining Radiation Patterns of Patch Antennas on Circularly-Cylindrical Platforms", *15th Annual Review of Progress in Applied Computational Electromagnetics*, Vol. 1, pp. 508 - 515, 1999.
- [10] Stratton, J.A., *Electromagnetic Theory*, McGraw-Hill, New York, 1941.

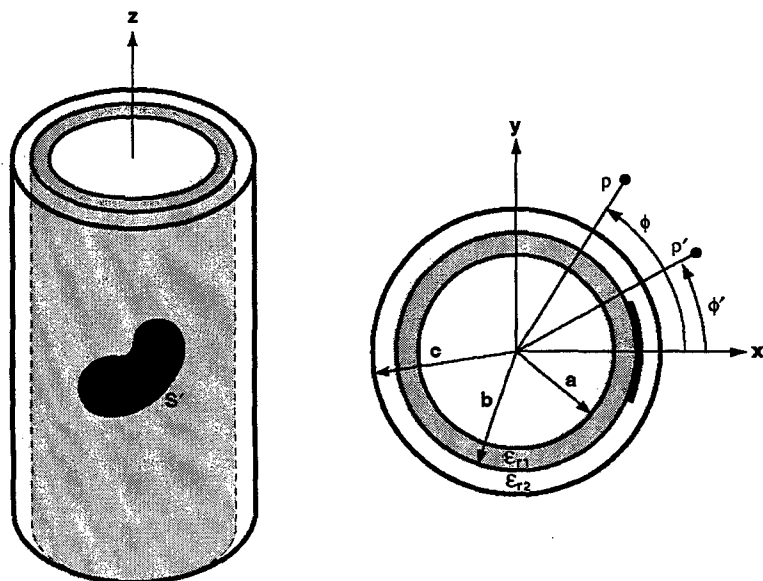


Figure 1: Arbitrarily-shaped cylindrical patch geometry with both substrate and superstrate included

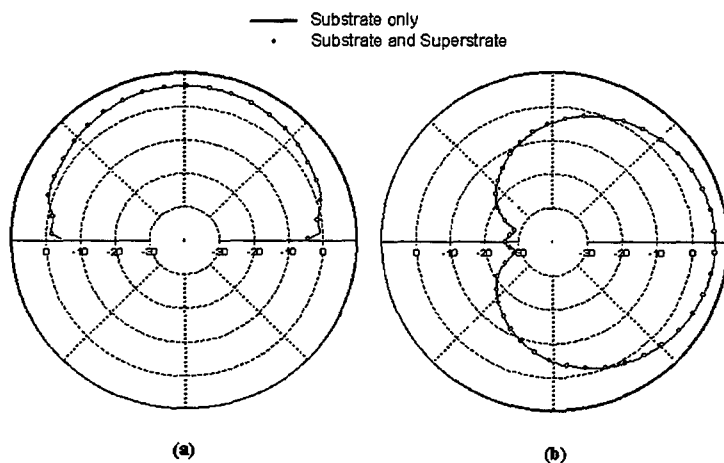


Figure 2: Gain pattern comparison for substrate-only and superstrate cases in (a) an axial plane ($\phi = 0^\circ$ and $0^\circ \leq \theta \leq 180^\circ$) and (b) the azimuthal plane ($\theta = 90^\circ$ and $0^\circ \leq \phi \leq 360^\circ$)

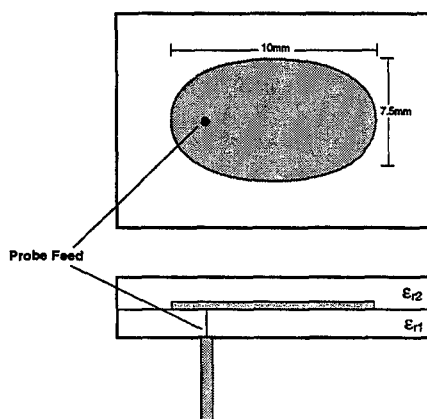
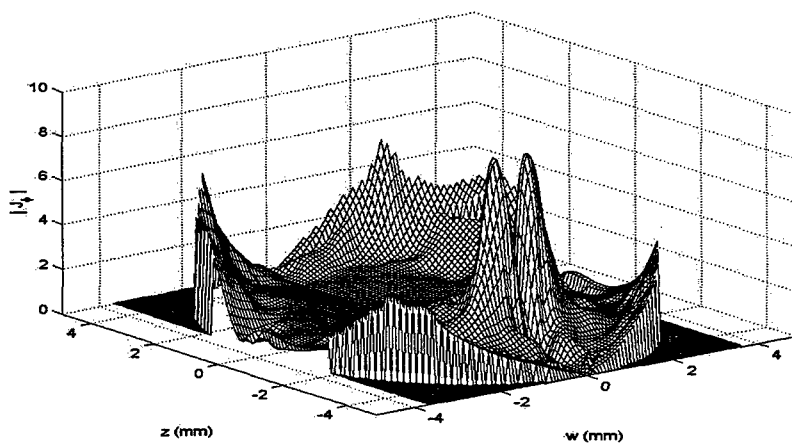
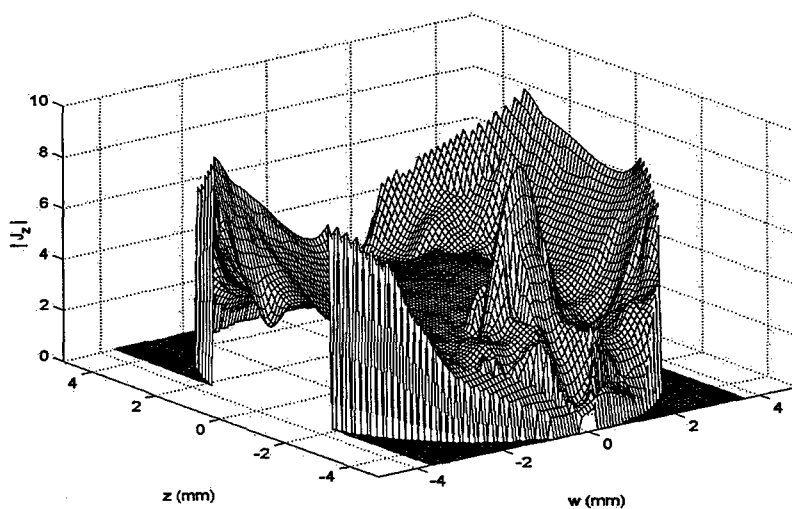


Figure 3: Geometry for probe-fed elliptical patch case with Duroid substrate and Duroid superstrate ($\epsilon_{r1} = \epsilon_{r2} = 2.33$)

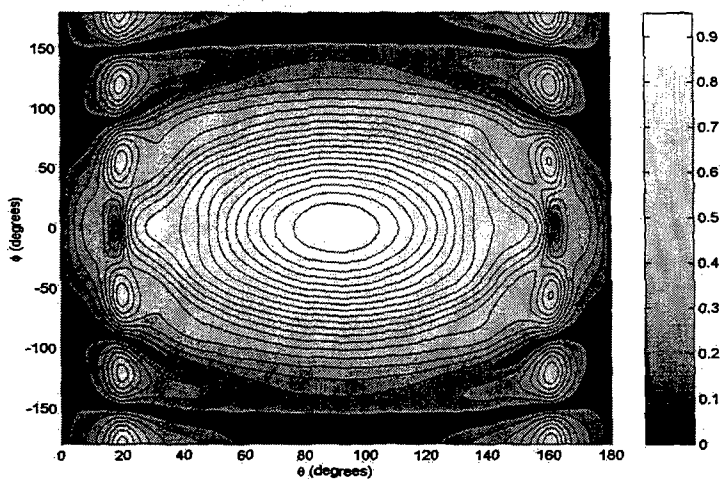


(a)

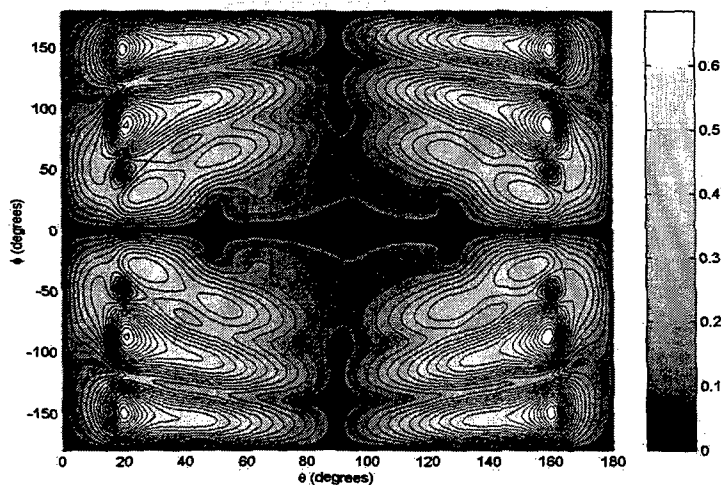


(b)

Figure 4: Surface plots of J_ϕ and J_z for an elliptical patch antenna with Duroid Substrate ($\epsilon_{r1} = 2.33$) and Duroid Superstrate ($\epsilon_{r2} = 2.33$)



(a)



(b)

Figure 5: Surface plots of (a) E_θ and (b) E_ϕ for an elliptical patch antenna with Duroid Substrate ($\epsilon_{r1} = 2.33$) and Duroid Superstrate ($\epsilon_{r2} = 2.33$)

A New FDTD Scheme to Model Chiral Media

A. Akyurtlu, D. H. Werner, and K. Aydin
Department of Electrical Engineering
Pennsylvania State University
University Park, PA 16802

I. Introduction

Bi-anisotropic materials have attracted considerable attention in recent years because of their unique properties in affecting the behavior of electromagnetic fields. Within these materials, two separate mechanisms take place. Bi-isotropy describes the coupling between the electric and magnetic materials. Anisotropy refers to the direction dependent behaviors of the electromagnetic fields. These mechanisms make the modeling of such materials in the time domain using conventional approaches extremely complicated and cumbersome. For instance, many of these schemes are unstable and none have been successfully generalized to include dispersive bi-isotropic materials. A novel and robust numerical scheme will be developed in this paper to model bi-isotropic materials in the time domain, based on the FDTD method. The main advantage of this new scheme is its inherent simplicity, which will easily allow the modeling of dispersive bi-isotropic behavior. This simple approach can also be extended to the modeling of bi-anisotropic materials in FDTD.

Previous attempts have been made in the area of modeling chiral or bi-isotropic media [1], [2]. Hunsberger, [1], was able to successfully model a chiral slab in 1-D, using a hybrid FDTD method (i.e. a combination of an implicit -- using a recursive technique-- and an explicit scheme). However, one of the main drawbacks of this scheme is the complexity of the formulation since the fields are coupled and the values at a particular cell depend on the values at neighboring cells. This is a consequence of the spatial dispersion arising from the direct implementation of chiral material constitutive equations. The implementation of this scheme for modeling dispersive bi-isotropic or bi-anisotropic materials would be extremely difficult. Another successful attempt at modeling electromagnetic propagation in bi-isotropic media using FDTD was made by Garcia et al. [2]. Although their method is less complicated than that of [1], the expressions for the field values contain additional terms that need to be obtained through approximations. For example, the electric field expression contains not only the curl of the magnetic field, but also another magnetic field term, as well as the time derivative of the magnetic field. Although both of these schemes have provided very important insights into the area of modeling bi-isotropic and bi-anisotropic media using the FDTD method, they are more complicated than the scheme proposed herein and thus make it more difficult to model more interesting aspects of bi-isotropic and bi-anisotropic materials. This paper details the main ideas behind a newly-developed scheme to model bi-isotropic materials using the FDTD method. The co- and cross-polarized transmission coefficients obtained from this scheme are compared with their analytical counterparts for validation purposes.

II. Analysis Method

This section will discuss the essential concepts behind the new FDTD technique to model a chiral medium, which is a subset of the more general bi-isotropic (BI) medium. The main idea behind this scheme is based on decomposing the electric and magnetic fields in the medium into the wavefields \mathbf{E}_+ , \mathbf{E}_- , \mathbf{H}_+ , \mathbf{H}_- , as shown in (1). These wavefields can be thought of as circularly polarized waves, where the "+" represents a right-hand circularly polarized wave and the "-" represents a left-hand circularly polarized wave [3].

$$\begin{aligned}\mathbf{E} &= \mathbf{E}_+ + \mathbf{E}_- \\ \mathbf{H} &= \mathbf{H}_+ + \mathbf{H}_-\end{aligned}\quad (1)$$

Each of the two wavefields, \mathbf{E}_+ , \mathbf{H}_+ and \mathbf{E}_- , \mathbf{H}_- sees the BI medium as an equivalent isotropic medium with respective medium parameters ϵ_+ , μ_+ and ϵ_- , μ_- [3]. The effective permittivity and permeability are expressed as:

$$\begin{aligned}\mu_{\pm} &= \mu(\cos\theta \pm \kappa_r)e^{\mp j\theta} \\ \epsilon_{\pm} &= \epsilon(\cos\theta \pm \kappa_r)e^{\pm j\theta} \\ \cos\theta &= \sqrt{1 - \chi_r^2}\end{aligned}\quad (2)$$

where χ_r is the normalized Tellegen parameter (i.e., $\chi_r = \chi/n$ and $n = \sqrt{\mu\epsilon/\mu_0\epsilon_0}$) and κ_r the normalized chirality parameter (i.e., $\kappa_r = \kappa/n$) [3]. The Tellegen parameter may also be expressed as $\chi_r = \sin\theta$, which relates χ_r to the angle θ . The two sets of wavefields are also independent and do not couple in a homogenous BI medium. This indicates that Maxwell's equations in a sourceless medium split into two independent sets and the resulting wavefields individually satisfy the following relationships:

$$\begin{aligned}\nabla \times \mathbf{E}_+ &= -j\omega\mu_+\mathbf{H}_+ \\ \nabla \times \mathbf{E}_- &= -j\omega\mu_-\mathbf{H}_- \\ \nabla \times \mathbf{H}_+ &= j\omega\epsilon_+\mathbf{E}_+ \\ \nabla \times \mathbf{H}_- &= j\omega\epsilon_-\mathbf{E}_-\end{aligned}\quad (3)$$

At this point we make the observation that these equations can be discretized and incorporated easily into a standard FDTD formulation. In summary, the electric and magnetic fields can be uncoupled into the \pm wavefields which satisfy the Maxwell's equations in the corresponding isotropic " \pm " medium using the equivalent material parameters, ϵ_{\pm} , μ_{\pm} .

III. Approach to the FDTD Formulation

Suppose we consider the simple 1-D chiral slab surrounded by free space that is illustrated in Figure 1. This problem was selected because it has a known analytical solution that can be used for validating the proposed FDTD scheme.

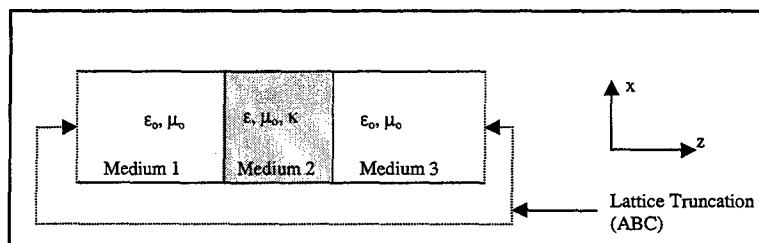


Figure 1. The modeled chiral slab surrounded by free space.

A total/scattered field formulation is used to model the electromagnetic propagation through a chiral slab for normal incidence [4]. Mur's finite-difference scheme for the absorbing boundary condition [5] was used to truncate the computational domain. As stated in Section II, the electric and magnetic fields are decomposed into their respective wavefield components, \mathbf{E}_\pm , \mathbf{H}_\pm . In a chiral medium, both co- and cross- polarized waves are supported. For this example, the direction of propagation is along the z-axis and x- and y- polarized electrical and magnetic fields exist throughout the computational domain. In the FDTD scheme proposed herein, the x-component of the electric field is composed of E_{x+} and E_{x-} and the y-component of the electric field is composed of E_{y+} and E_{y-} . The form of the excitation field used in the formulation is given by:

$$\mathbf{E} = E e^{-jkz} \left(\hat{\mathbf{u}}_x \cos(\kappa, kz) - \hat{\mathbf{u}}_y \sin(\kappa, kz) \right) \quad (4)$$

Substituting the appropriate expressions for $\hat{\mathbf{u}}_x$ and $\hat{\mathbf{u}}_y$ in terms of the circularly polarized unit vectors, $\hat{\mathbf{u}}_+$ and $\hat{\mathbf{u}}_-$ (where + refers to right-handed and - refers to left-handed circular polarization),

$$\hat{\mathbf{u}}_x = \frac{1}{\sqrt{2}} \left(\hat{\mathbf{u}}_+ + \hat{\mathbf{u}}_- \right) \quad \hat{\mathbf{u}}_y = \frac{j}{\sqrt{2}} \left(\hat{\mathbf{u}}_+ - \hat{\mathbf{u}}_- \right) \quad (5)$$

leads to the following expression:

$$\mathbf{E} = \hat{\mathbf{u}}_+ \frac{E}{\sqrt{2}} e^{-jk_z z} + \hat{\mathbf{u}}_- \frac{E}{\sqrt{2}} e^{-jk_z z} \quad (6)$$

The two complex circularly polarized unit vectors in (5) and (6) are defined by:

$$\begin{aligned}\hat{\mathbf{u}}_+ &= \frac{1}{\sqrt{2}} \begin{pmatrix} \hat{\mathbf{u}}_x - j\hat{\mathbf{u}}_y \\ \hat{\mathbf{u}}_x + j\hat{\mathbf{u}}_y \end{pmatrix} \\ \hat{\mathbf{u}}_- &= \frac{1}{\sqrt{2}} \begin{pmatrix} \hat{\mathbf{u}}_x + j\hat{\mathbf{u}}_y \\ \hat{\mathbf{u}}_x - j\hat{\mathbf{u}}_y \end{pmatrix}\end{aligned}\quad (7)$$

The x_{\pm} and y_{\pm} components of the field can now be specified as follows:

$$\begin{aligned}E_{x+} &= \frac{1}{\sqrt{2}} \frac{E}{\sqrt{2}} e^{-jk_z z} & E_{x-} &= \frac{1}{\sqrt{2}} \frac{E}{\sqrt{2}} e^{-jk_z z} \\ E_{y+} &= \frac{-j}{\sqrt{2}} \frac{E}{\sqrt{2}} e^{-jk_z z} & E_{y-} &= \frac{j}{\sqrt{2}} \frac{E}{\sqrt{2}} e^{-jk_z z}\end{aligned}\quad (8)$$

where the two wavenumbers, k_{\pm} , are defined as:

$$k_{\pm} = k(\cos\theta \pm \kappa_r) \quad (9)$$

Since the Tellegen parameter is assumed to be zero for this example,

$$\begin{aligned}\chi_r &= \sin\theta = 0 \rightarrow \theta = 0^\circ \\ k_{\pm} &= k(1 \pm \kappa_r)\end{aligned}\quad (10)$$

the wavefield components given in (8) can be written as:

$$\begin{aligned}E_{x+} &= \frac{E}{2} e^{-jk_z z} [\cos(\kappa_r k_z) - j \sin(\kappa_r k_z)] & E_{x-} &= \frac{E}{2} e^{-jk_z z} [\cos(\kappa_r k_z) + j \sin(\kappa_r k_z)] \\ E_{y+} &= \frac{-jE}{2} e^{-jk_z z} [\cos(\kappa_r k_z) - j \sin(\kappa_r k_z)] & E_{y-} &= \frac{jE}{2} e^{-jk_z z} [\cos(\kappa_r k_z) + j \sin(\kappa_r k_z)]\end{aligned}\quad (11)$$

The expressions for E_x and E_y may now be derived from (11):

$$\begin{aligned}E_x &= E_{x+} + E_{x-} = E e^{-jk_z z} \cos(\kappa_r k_z) \\ E_y &= E_{y+} + E_{y-} = -E e^{-jk_z z} \sin(\kappa_r k_z)\end{aligned}\quad (12)$$

which are in agreement with (4). The next step is to incorporate these incident fields into the FDTD formulation. The time-dependent form of E_{x+} can be derived as follows:

$$\begin{aligned}
E_{x+}(z, t) &= \text{Re} \left[E_{x+}^i(z) e^{j\omega t} \right] \\
E_{x+}(z, t) &= \text{Re} \left[e^{j\omega t} \frac{E}{2} e^{-j(kz + \kappa, kz)} \right] \\
E_{x+}(z, t) &= \text{Re} \left[\frac{E}{2} e^{j(\omega t - kz - \kappa, kz)} \right] \\
E_{x+}(z, t) &= \frac{E}{2} \cos(\omega t - kz - \kappa, kz)
\end{aligned} \tag{13}$$

A similar procedure can be followed for the remaining three components which yields

$$\begin{aligned}
E_{x-}(z, t) &= \frac{E}{2} \cos(\omega t - kz + \kappa, kz) \\
E_{y+}(z, t) &= \frac{E}{2} \sin(\omega t - kz - \kappa, kz) \\
E_{y-}(z, t) &= -\frac{E}{2} \sin(\omega t - kz + \kappa, kz)
\end{aligned} \tag{14}$$

The term, E , in the incident field expressions represents the electric field amplitude and can be specified as any functional form. For the specific example considered here, a Gaussian pulse plane wave was used to represent this amplitude factor.

The wavefields in free space follow the conventional FDTD equations, and are summed appropriately to provide the values for E_x and E_y . The modified equations for the fields propagating in the chiral slab are derived and discretized for the FDTD method in the following way:

$$\begin{aligned}
\nabla \times \mathbf{H}_{\pm} &= j\omega \epsilon_{\pm} \mathbf{E}_{\pm} \\
\nabla \times \mathbf{H}_{\pm} &= \epsilon_{\pm} \frac{\partial}{\partial t} \mathbf{E}_{\pm} \\
\nabla \times \mathbf{H}_{\pm} &= \left(\epsilon \pm j \frac{\xi}{\eta} e^{\pm j\theta} \right) \frac{\partial}{\partial t} \mathbf{E}_{\pm} \\
\xi &= (\chi_r - j\kappa_r) \sqrt{\mu_o \mu_r \epsilon_o \epsilon_r} = (\chi_r - j\kappa_r) \sqrt{\mu \epsilon} \\
\chi_r = 0 &\Rightarrow \nabla \times \mathbf{H}_{\pm} = \left(\epsilon \pm j \frac{j}{\eta} (0 - j\kappa_r) \sqrt{\mu \epsilon} \right) \frac{\partial}{\partial t} \mathbf{E}_{\pm} \\
\nabla \times \mathbf{H}_{\pm} &= \epsilon (1 \pm \kappa_r) \frac{\partial}{\partial t} \mathbf{E}_{\pm}
\end{aligned} \tag{15}$$

Discretizing this equation results in:

$$\begin{aligned}\mathbf{E}_{\pm}^{n+1} &= \mathbf{E}_{\pm}^n + \left(\frac{\Delta t}{\varepsilon(1 \pm \kappa_r) \Delta z} \right) (\mathbf{H}_{\pm}^{n+1/2}(i) - \mathbf{H}_{\pm}^{n+1/2}(i-1)) \\ \mathbf{E}^{n+1} &= \mathbf{E}_+^{n+1} + \mathbf{E}_-^{n+1}\end{aligned}\quad (16)$$

A similar procedure is used for deriving the discretized equations for the magnetic fields by starting with

$$\begin{aligned}\nabla \times \mathbf{E}_{\pm} &= -j\omega\mu_{\pm} \mathbf{H}_{\pm} \\ \nabla \times \mathbf{E}_{\pm} &= -\mu_{\pm} \frac{\partial}{\partial t} \mathbf{H}_{\pm} \\ \nabla \times \mathbf{E}_{\pm} &= -(\mu \mp j\zeta\eta e^{\mp j\theta}) \frac{\partial}{\partial t} \mathbf{H}_{\pm} \\ \zeta &= (\chi_r + j\kappa_r) \sqrt{\mu_o \mu_r \varepsilon_o \varepsilon_r} = (\chi_r + j\kappa_r) \sqrt{\mu\varepsilon} \\ \chi_r = 0 &\Rightarrow \nabla \times \mathbf{E}_{\pm} = -(\mu \mp j\eta(0 + j\kappa_r) \sqrt{\mu\varepsilon}) \frac{\partial}{\partial t} \mathbf{H}_{\pm} \\ \nabla \times \mathbf{E}_{\pm} &= -\mu(1 \pm \kappa_r) \frac{\partial}{\partial t} \mathbf{H}_{\pm}\end{aligned}\quad (17)$$

The discretized form of this equation is:

$$\begin{aligned}\mathbf{H}_{\pm}^{n+1/2} &= \mathbf{H}_{\pm}^{n-1/2} - \left(\frac{\Delta t}{\mu(1 \pm \kappa_r) \Delta z} \right) (\mathbf{E}_{\pm}^n(i+1) - \mathbf{E}_{\pm}^n(i)) \\ \mathbf{H}^{n+1/2} &= \mathbf{H}_+^{n+1/2} + \mathbf{H}_-^{n+1/2}\end{aligned}\quad (18)$$

When the wavefields are propagating in free space, governed by (15) – (18), the ε and μ , become ε_o and μ_o , and the chirality parameter κ_r goes to zero.

IV. Results

Once the time domain values for the electric and magnetic fields are obtained, they are transformed into the frequency domain using the Fast Fourier Transform. Then, the co- and cross-polarized transmission coefficients, at one cell beyond the slab, are calculated and compared with the analytical results, as shown in Figure 2.

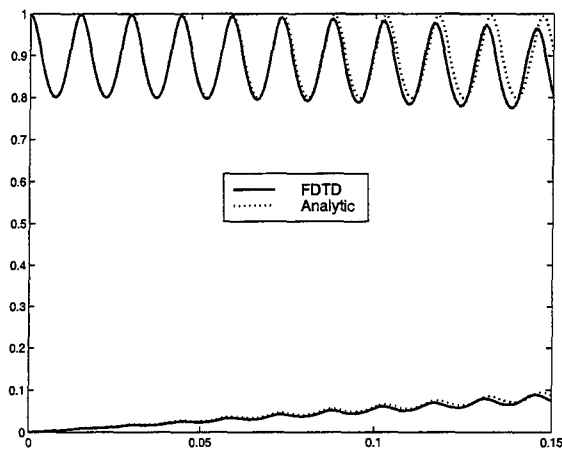


Figure 2. The frequency spectrum of the magnitude of the co- and cross-polarized transmission coefficients compared with the analytical results for $\kappa_r = 0.003$.

When κ_r is set to zero in the program, we expect the cross-polarized transmission coefficient to become zero, since the cross-polarized wave, E_y , also goes to zero. The co-polarized transmission coefficient should produce the same results as that for a dielectric slab. Figure 3 shows the co- and cross-polarized transmission coefficients with their analytical counterparts for $\kappa_r = 0.0$.

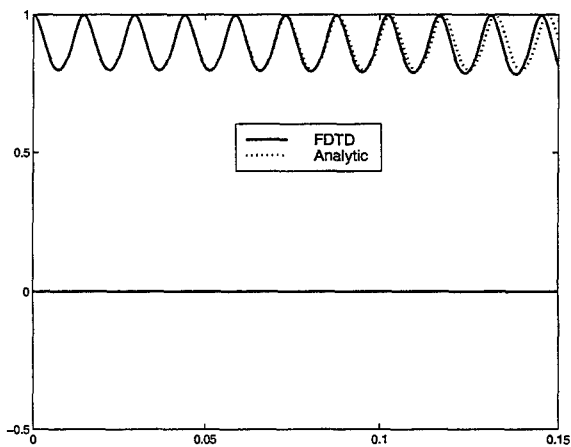


Figure 3. The frequency spectrum of the magnitude of the co- and cross-polarized transmission coefficients compared with the analytical results for $\kappa_r = 0$.

There is a deviation in the FDTD-calculated transmission coefficients from the analytical results as the frequency increases and this can be attributed to the numerical dispersion errors inherent in the FDTD method [6]. This type of behavior is typical in FDTD. The deviation can also be seen in Figure 3, which is essentially the transmission coefficient for a dielectric slab. The frequency spectrum is cut off at 0.15 GHz, which corresponds to a cell size equivalent to $1/20^{\text{th}}$ of the shortest wavelength of interest. More accurate results may be obtained for finer cell size. Schemes, such as material averaging, have been studied to improve these results (for cell sizes at $1/20^{\text{th}}$ of a wavelength) and some alternative schemes are presently being considered. The modeling of dispersive chiral materials and bi-anisotropic materials are also currently under investigation by the authors.

V. References

- [1] Hunsberger, F., "Extension of the Finite-Difference Time-Domain Method to Gyrotropic Media", Ph.D. Dissertation, Department of Electrical Engineering, Pennsylvania State University, University Park, PA, May, 1991.
- [2] Garcia, S. G., I. V. Perez, R. Martin and B. Olmedo, "Extension of Berenger's PML for Bi-Isotropic Media," *IEEE Microwave and Guided Wave Letters*, vol. 8, no. 9, pp. 297-299, 1998.
- [3] Lindell I. V., A. H. Sihvola, S. A. Tretyakov, and A. J. Viitanen, *Electromagnetic Waves in Chiral and Bi-Isotropic Media*, Artech House, Boston, 1994.
- [4] Taflove, A. and K. R. Umashankar, "The Finite-Difference Time-Domain (FD-TD) Method for Electromagnetic Scattering and Interaction Problems," *Journal of Electromagnetic Waves and Applications*, vol. 1, no. 3, pp. 243-267, 1987.
- [5] Mur, G., "Absorbing Boundary Conditions for the Finite-Difference Approximation of the Time Domain Electromagnetic Field Equations," *IEEE Transactions on Electromagnetic Compatibility*, vol. 23, pp. 377-382, 1981.
- [6] Taflove, A., *Computational Electromagnetics*, Artech House, Boston, 1995.

T-Matrix Computer Code Applied to Electromagnetic Field Penetration in Magnetic Resonance Imaging

Rafael R Canales¹, Luis F Fonseca², Fredy R Zypman³
rcanales@rrpac.upr.clu.edu¹, lfonseca@rrpac.upr.clu.edu²,
f_zypman@cuhae.upr.clu.edu³
University of Puerto Rico

Abstract

T-Matrix Theory solves the scattering problem by multilayered objects. Typical applications of T-Matrix algorithms have been limited to homogeneous spheres and ellipsoids. In this paper we generalize the T-Matrix code so that it can handle non-homogeneous scatterers. One such object consists of a small ellipsoid completely embedded inside a larger one, and with different dielectric constant than the former. This configuration is of interest to obtain more realistic information regarding field distribution and heat deposition in the human body under radio-frequency fields used in Magnetic Resonance Imaging (MRI) clinical routines. It could mimic a large object, such as the liver, inside the abdomen, or a tumor growth inside the brain. Our application of T-Matrix in MRI is novel. Typically, T-Matrix has been used to study scattering of visible radiation by nanometric particles. Since the dimensions of the scatterers (nanoparticles-human organs) and the wavelengths (nanometers-meters) scale both by about a factor of 10^9 , we realized the possibility of applying this algorithm to the human body radiation. We show here that this hypothesis turned out to be true. Moreover, beyond standard algorithms, we have implemented a module to calculate internal fields inside the scatterers.

I. Introduction

The T-Matrix or Extended Boundary Condition theory was developed in 1969 by P.C. Waterman^{1,2} for the description of acoustic and electromagnetic scattering from a single homogeneous scatterer. Peterson and Ström³ extended the range of applicability of the method to scatterers consisting of a collection of homogeneous layers each of which has constant electric and magnetic properties.

Although this theory proposes a method to solve the problem of electromagnetic scattering of a general monochromatic wave by objects of arbitrary shape, applications have been limited to the scattering of single ellipsoids or clusters. This is due to the fact that in actual implementations of the algorithm as computer code, the evaluation of general surface differentials becomes prohibitively time consuming.

T-Matrix expresses the fields as multipolar vector expansions. It fully takes into account phase-

retardation effects, which are critical in the cases where the size of the scatterers is of the order of the wavelength in the medium.

The scattered and internal fields are expressed in terms of the incident field. Each of those fields is expanded in terms of a vector spherical basis which, in turn, are solutions to the Helmholtz Equation.

$$\nabla \times \nabla \times \mathbf{E} - k^2 \mathbf{E} = 0 \quad (1)$$

The surface currents at the interfaces of the scatterers are used to link the expansion coefficients of the various fields by means of non-homogeneous, linear equations. In particular, internal field coefficients are expressed in terms of linear combinations of incident and scattered field coefficients. That linear combination contains information of surface topology, electromagnetic properties and the basis functions.

The surface topology enters through an integral of surface differentials. It is in this calculation

where T-Matrix has the most stringent limitations. On one hand, numerical evaluation of surface differentials is computationally expensive. In addition, analytical expressions of surface differentials, which speed up the computer code, can only be accomplished in the most simple situations.^{2,4,5}

In this work, we have added the possibility to deal with non-homogenous ellipsoidal objects made up of non-concentric layers. In that configuration (Fig I), an inner object is centered at the origin. An outer object, completely covering the inner one is located such that its center lays along the z axis.

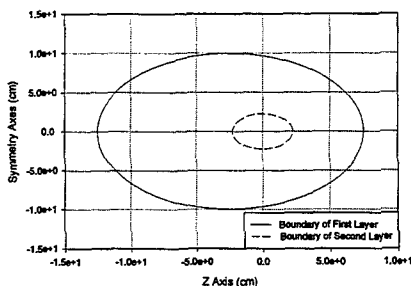


Figure I

Our interest is to represent a non-homogeneous organ to visualize the radio frequency electromagnetic field (EMRF) profiles, specific absorption rates (SAR) for configurations relevant to magnetic resonance imaging (MRI) as used in clinical settings.

With this T-Matrix code we obtain the EMRF and SAR for a variety of shapes and compositions at various frequencies. Knowledge of EMRF is critical to reliably assess image reconstruction algorithms. SAR, on the other hand, is proportional to the power deposited in the tissue, and is important to gauge the safety of radiation.

In what follows we demonstrate the portability of the code to different computer architectures and operating systems, and benchmark the program by logging the various execution times.

II. Theoretical Background

T-Matrix considers three kinds of fields: incident, scattered, and internal. In our specific application the expansion of the scattered field is in spherical Hankel functions of the first kind (non-

regular). The incident and the inner layer internal field, are expressed in term of spherical Bessel functions of the first kind (regular). The internal field in the region inside the outer layer (but outside the inner) is a combination of the regular and non-regular solutions. The expansion coefficients are stored in the so called Q-Matrices³.

We generalize the T-Matrix code beyond relating incident and scattered waves fields allowing for the possibility to evaluate internal fields. This turns out to be important for our applications in MRI since the image is strongly dependent on the internal fields. In the past this issue was somewhat less important since in the problem of scattering of light by nanoparticles, the knowledge of the internal fields was more a matter of curiosity than a relevant issue for applications.

The main aim of our program is to obtain the expansion coefficients of the fields in all the regions in terms of the coefficients of the incident field.

At the heart of the computer code are the Q-Matrices, which contain geometrical and electrical information as well as frequency. The speed of the program depends on the dimensions of the Q-Matrices (some of which need to be inverted). These dimensions are a quadratic function of the multipolar order, as shown in Table I.

Table I

Order	Dimension
1	6
2	16
3	30
4	48
5	70
6	96
7	126
8	160
9	198
10	240
11	286
12	336
13	390

Our program uses four matrices in addition to the four Q-Matrices. The former represents the smaller set needed to store linear combinations of the Q-Matrices and their inverses, which are needed to relate any set of field coefficients to the incident ones.

At the beginning of the program and its subroutines all the arrays are defined, and space is allocated in random access memory. In the poorer computer architectures, convergence is achieved only after more than eleven hours. Therefore it is of utmost importance to optimize computer resources. One way we do that is by saving the coefficients in the diagonal of the intermediate matrices.

The program also needs two kinds of arrays of dimension 3 x multipolar order which contain the expansion coefficients in terms of the basis set, of the incident, scattered, and internal fields.

In addition to the possibility to calculate internal fields in a two-layer scatterer, we also contribute a new application that allows the code to deal with more general geometries. We changed the integration subroutine, INTERARXXXX, so that it can handle a scattering objects with ellipsoidal outer boundaries. Where the XXXX mean the combination in pair of the basis expansion (regular, non-regular). In particular, we improved the code by calculating the surface differentials referred to a generic point, not necessarily the center of the ellipsoid. In doing that, we had in mind the need to tackle problems in which the internal layers where not concentric with the outer surface.

III. Algorithm and Program Code

The program code was written in Fortran 77 with 47 subroutines and 10 functions. But the backbone is composed of the functions that calculate the Hankel and Bessel functions; within the subroutines we have three that carry most of the weight of the computational problem. Figure II shows the main code flow that includes the most important subroutines. The subroutine MATRIZ calls the intermediate integration subroutine called ROMARXXXX and ROMALXXXX first and second layer respectively. Those call INTEARXXXX and INTEALXXXX respectively, which in turn evaluate the integrals for a given geometry for the construction of Q-Matrices. CLUST performs the proper algebra manipulation which, includes inversion with Q-Matrices to obtain the coefficients of internal fields. In CAMPO we use the coefficients coming from CLUST and call of VECTOR, VECPSI, VCRPSI subroutines that calculate the expansion coefficients of the incident wave, non-regular basis and regular basis respectively, when we put all this information together the result is the internal field for each layer.

For the implementation of the new geometry we made some changes in the integration subroutine. Specifically in INTEARXXXX we needed to redefine a new radial coordinate as function of center-to-center displacement in addition to the other parameters that we consider earlier such as a semi-axes and the azimuthal angle. Those do not depend on the axial angle because ours is a surface of revolution. Figure I shows a configuration with the external layer shifted away from origin.

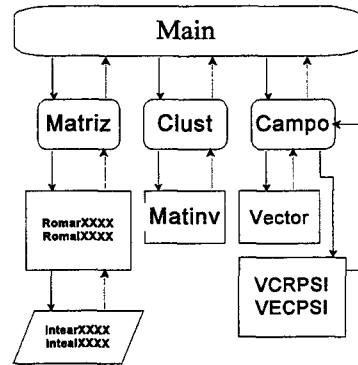


Figure II
Main code flow

IV. Program Testing

The code was tested in the electrostatic limit under well established conditions consisting of a dielectric sphere with the incident plane wave, as shown in standard textbooks⁶. The field inside the sphere is given by equation.

$$E^i = E^o \frac{3}{(\epsilon + 2)} \quad (2)$$

Where E^o is the incident electric field and ϵ is the permittivity of the dielectric sphere. In our case of relative permittivity 60 we calculate the internal field calculated by (2) and with the T-Matrix code. They agree within 10⁻⁵ %, showing the robustness of our code.

V. Results of Simulation

In this section we present results for the electric field and SAR along the symmetry axis of the system. We consider the large ellipsoid to have $\epsilon = 46.25 \sigma = 1.85$ S/m to mimic gray-white matter⁷⁻⁹. The small ellipsoid simulates a tumor with $\epsilon = 60 \sigma = 1$ S/m¹⁰. Figures III-VI shows the magnitude of the electric fields as well as their derivative to enhance the borders. Generally the field decreases as the wave penetrates the system. At 700MHz we see an enhancement of the field at the center of the small ellipsoid. This is due to a resonant cavity effect. The inset shows the lower and upper limit of the coordinates of the small ellipsoid.

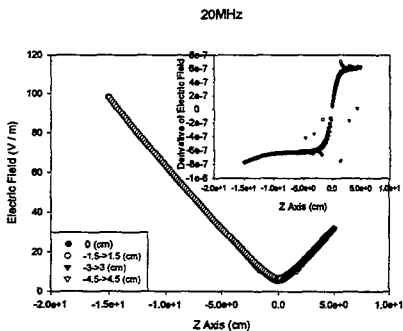


Figure III

Magnitude of electric field along the symmetry axis at 20MHz. The inset shows the result of a derivative filter to enhance the boundaries.

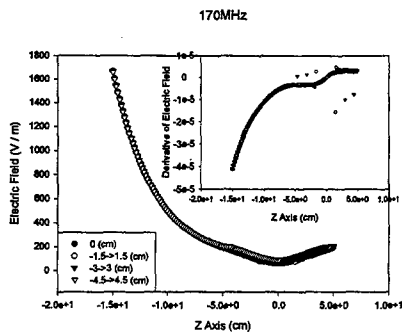


Figure V

Magnitude of electric field along the symmetry axis at 170MHz. The inset shows the result of a derivative filter to enhance the boundaries.

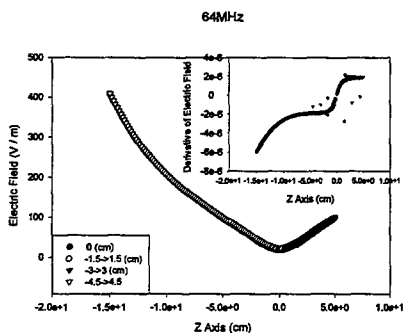


Figure IV

Magnitude of electric field along the symmetry axis at 64MHz. The inset shows the result of a derivative filter to enhance the boundaries.

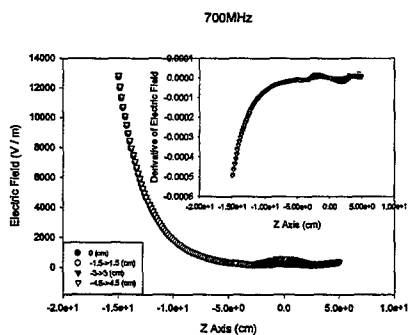


Figure VI

Magnitude of electric field along the symmetry axis at 700MHz. The inset shows the result of a derivative filter to enhance the boundaries. There is a resonant peak at the center of the small ellipsoid.

In the next four figures we plot the SAR along the Z axis. As expected the heat deposition drops as a function of depth. In addition the total heat deposition is a quadratic function of the frequency.

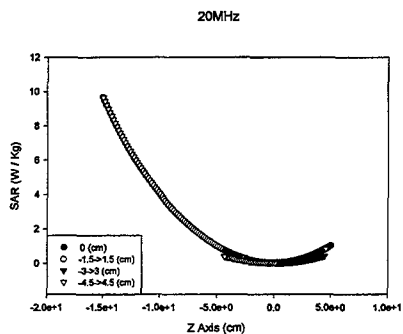


Figure VII

SAR along the symmetry axis at 20MHz. Most of the heat deposition is in the incoming region of the E & M field. As the field moves into the scatterer, conductivity reduces its magnitude.

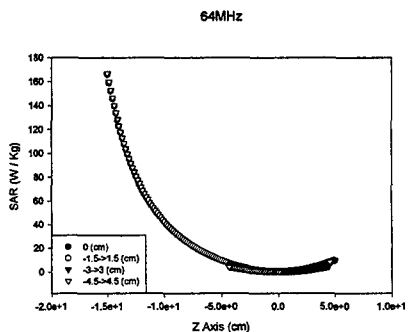


Figure VIII

SAR along the symmetry axis at 64MHz. Most of the heat deposition is in the incoming region of the E & M

field. As the field moves into the scatterer, conductivity reduces its magnitude.

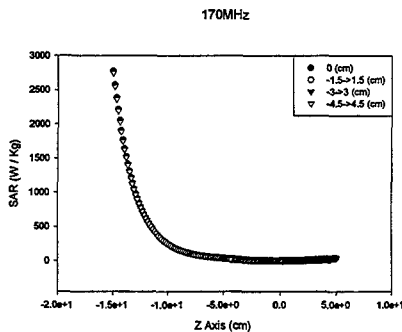


Figure IX

SAR along the symmetry axis at 170MHz. Most of the heat deposition is in the incoming region of the E & M field. As the field moves into the scatterer, conductivity reduces its magnitude.

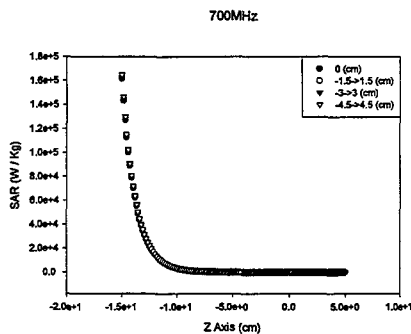


Figure X

SAR along the symmetry axis at 700MHz. Most of the heat deposition is in the incoming region of the E & M field. As the field moves into the scatterer, conductivity reduces its magnitude. One can see that SAR is a quadratic function of the frequency.

VI. Code Performance and Portability

In this section we show, that this T-Matrix code in Fortran 77 has the ability to run under different computers and resources, and has the portability to work with various operating systems. Execution time varies strongly from one system to the next. We shown in figure XI the six systems tested.

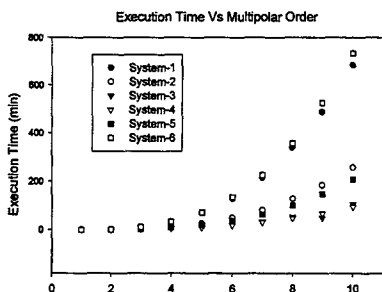


Figure XI

Run time versus multipolar order for various systems. In the increasing order: Pentium-90MHz 64MB of RAM, Pentium-200MHz 64MB of RAM, PentiumII-400MHz 128MB of RAM the systems before has Windows98, PentiumII-450MHz 500MB of RAM with Windows NT V4.0, UltraSparc-1 128MB RAM with Sun OS 5.5, SparcStation-10 32MB RAM with Sun OS 5.4.

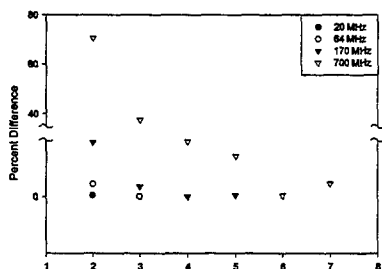


Figure XII

Convergence of the algorithm at various frequencies. Even at 700MHz the fields are reliable considering 6 multipolar orders.

VII.

Conclusions

We have described improvements to the T-Matrix computer code. These improvements allow for the evaluation of electromagnetics fields scattered by objects made up of elliptical non-concentric layers. In addition, the code now can calculate internal fields. This is a new important improvement, relevant for situation in which the size of the object allows for internal measurements. Finally we have extended the traditional use of T-Matrix from the nanometers wave lengths to the meter size scales. We found the method useful in MRI applications, in particular in the detection of soft tissue inside the human body.

VIII.

Future Work

We are setting up more realistic configurations of the human body to make full use of the versatility of this enhanced T-Matrix code. Concretely we are aiming at studying the fields with arbitrary and irregulars shapes like brain, lung, kidney and other.

IX.

Acknowledgment

This work has been supported by NIH grants GM08216-16 and CA77796-01.

X.

References

- [1] P.C. Waterman, *New Formulation Of Acoustic Scattering*, J. Acoustical Soc. Am., V45, N6, 1417,(1969).
- [2] P.C. Waterman, *Symmetry, Unitary, and Geometry in Electromagnetic Scattering*, Phys. Rev.D3, V4 N4, 835 (1971).
- [3] B. Peterson, S. Ström, *T-Matrix formulation of electromagnetic scattering from multilayered scatterers*, Phys. Rev. D, V10 N8, 2670 (1974).
- [4] W. Vargas, L. Cruz, L. Fonseca and M. Gomez, *Local fields around cluster of rotated spheroids using a T-Matrix approach*, Applied Optics 32, 2164 (1993).
- [5] B. Peterson, S. Ström, *T-Matrix for electromagnetic scattering from arbitrary number of scatterers and representations of E(3)*, Phys. Rev. D, V8 N10, 3661 (1973).
- [6] J. D. Jackson, *Classical Electrodynamics*, Second Edition, Wiley, 151.

- [7] C. Gabriel, S. Gabriel and E. Corthout, *The dielectric properties of biological tissues: I. Literature survey*, Phys. Med. Biol. 41, 2231-2249 (1996).
- [8] S. Gabriel R.W. Lau and C. Gabriel, *The dielectric properties of biological tissues: II. Measurements in the frequency range 10 Hz to 20 GHz*, Phys. Med. Biol. 41, 2251-2269 (1996).
- [9] S. Gabriel R.W. Lau and C. Gabriel, *The dielectric properties of biological tissues: III. Parametric models for the dielectric spectrum of tissues*, Phys. Med. Biol. 41, 2271-2293 (1996).
- [10] S. C. Hagness and J. E. Bridges, *Three-Dimensional FDTD Analysis of a Pulsed Microwave Confocal System for Breast Cancer Detection: Design of an Antenna-Array Element*, IEEE Trans. on Antennas Propagation, Vol. 47, N 5, 783 (1999).

SESSION 5

**INTERACTIVE
POSTER SESSION**

Characteristics of Silicon Photoconductivity under Near-Infrared Illumination

Preston P. Young, *University of Texas at Arlington Department of Electrical Engineering*

Robert Magnusson, *University of Texas at Arlington Department of Electrical Engineering*

Tim R. Holzheimer, *Raytheon Systems Company Aircraft Integration Systems*

Abstract:

Efficient illumination of semiconductor photonic elements can be accomplished through the use of high-power semiconductor laser diodes. The objectives of this research are to determine and characterize the photo-conductive characteristics of high-resistivity silicon for use in modeling and fabrication of photonic structures. This study provides guidelines for the optimum choice of laser diode output wavelength and power requirements. Measured data includes silicon photoconductivity as functions of wavelength, and incident power density for illuminating wavelengths between 810 and 1000nm.

Experimental Setup / Procedure:

The wafers for this series of experiments were fabricated by float-zone processing to provide high-resistivity ($\sim 8000 \Omega\text{-cm}$), and minority carrier lifetimes $> 1\text{msec}$. The wafer surfaces were passivated with varying thicknesses of native SiO_2 . Several samples of high resistivity silicon and one sample of GaAs were prepared by applying aluminum ohmic contacts to the ends of cleaved bars. Sample sizes ranged from approximately 2.5mm to 8mm in length by 2.5mm to 4mm in width. Nominal wafer thicknesses were 450 μm .

The individual samples were mounted between two copper contacts tinned with indium solder. The samples were held under approximately 3oz of spring compression applied between the contacts. A 0.005" K-type thermocouple probe was epoxied to the backside of each sample with thermally conductive epoxy. The mounted sample was then placed in front of the expanded beam from the Ti:sapphire laser. The experimental setup is shown in Figure 1. The beam was focused with approximately 10 degrees of convergence on the sample. A rectangular variable aperture was placed in the beam path to allow accurate illumination of only the sample area.

This setup allowed the available laser power to be most effectively utilized over a range of different sample sizes while maintaining near uniform illumination. In all cases, the sample was mounted normal to the laser source with the entire sample and both junctions illuminated as uniformly as possible. It is estimated that the incident illumination was uniform within 10%-15% over the sample surface and contacts. The effects of the thermocouple epoxy on the backside of the wafer were assumed to be negligible for measurements at wavelengths where the sample becomes transparent. The sample was biased with a regulated dc power supply and monitored with a series micro-ammeter and parallel voltmeter.

Measurements were obtained by setting a specific output wavelength at the Ti:sapphire laser (measured with the monochromator). The argon pump power was then varied to obtain Ti:sapphire

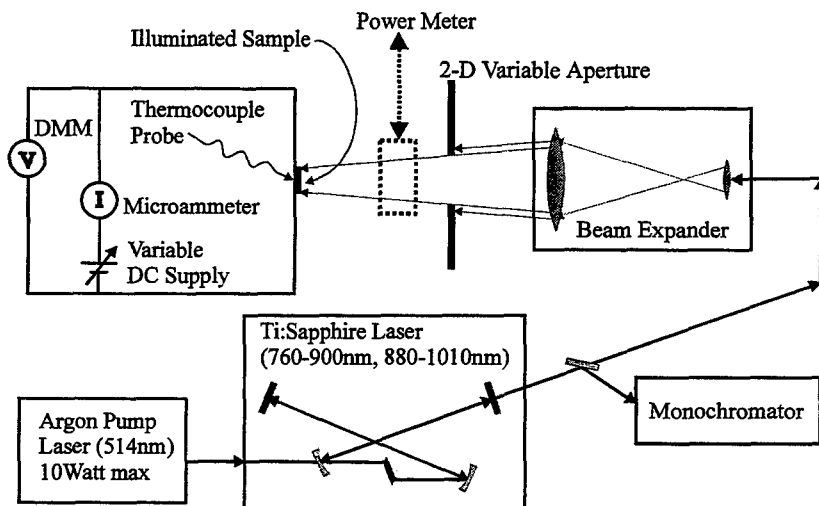


Figure 1) Schematic of Experimental Setup for Photoconductivity Measurements

output power levels allowing 3 or more incident power level measurements for a given wavelength setting. The measurements for wavelengths between 810nm and 900nm were completed with one set of mirrors (set B2); and the measurements between 900nm and 1000nm required reconfiguring the Ti:sapphire laser with an alternate mirror set (B3). The peak laser power occurred at ~820nm for mirror set B2 and at ~890nm for mirror set B3. The gain response of the Ti:sapphire crystal is highest near 800nm. This effectively reduced the available incident power density for increasing wavelength measurements.

Experimental Results:

Initially, bulk wafer reflectivity and transmission measurements were performed for each type of wafer material. These reflectivity and transmission measurements were then used to normalize the incident power density at the respective sample. Accordingly, the given values for incident power density represent the power transmitted into the wafer thus negating the effect or absence of any antireflection layers. It was observed that for nominal sample thicknesses of 450 μ m, the silicon became measurably transmissive at wavelengths above approximately 950nm. In all cases, the peak power density measurement was obtained at the maximum laser output power for each wavelength. The peak measured photon flux densities for this research ranged between approximately $2 \times 10^{18}/\text{cm}^2\text{-sec}$ and $3 \times 10^{19}/\text{cm}^2\text{-sec}$. The samples exhibited a maximum temperature rise of less than 10C at the highest incident power densities.

For these experiments, the applied DC bias was sufficiently large ($>10^5$ V/cm) so that both the electron and hole drift velocities could be assumed to be at the room temperature saturation level of approximately 10^7 cm/sec. The data obtained for the measured samples exhibited very little general dependence on the bias voltage level. This confirms that most excess photocarriers were swept out of the samples before carrier diffusion effects became significant. The measured sample current therefore

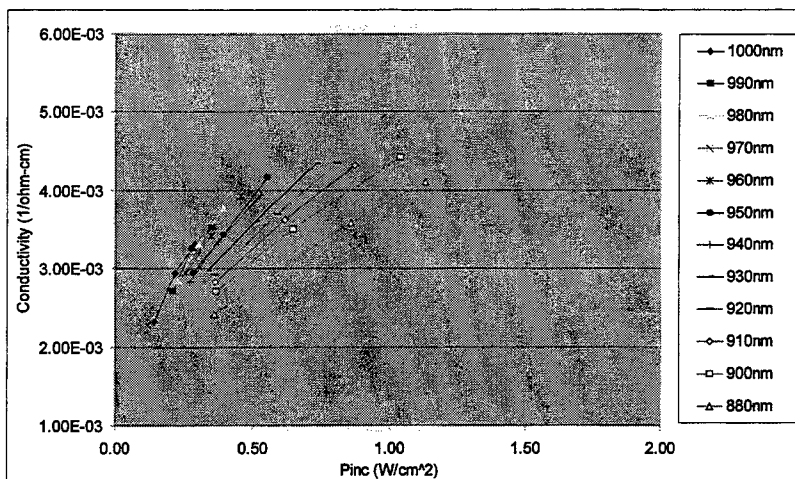


Figure 2) Graph of Sample Conductivity ($1/\text{ohm-cm}$) versus Absorbed Power Density (W/cm^2) for Mirror Set B2

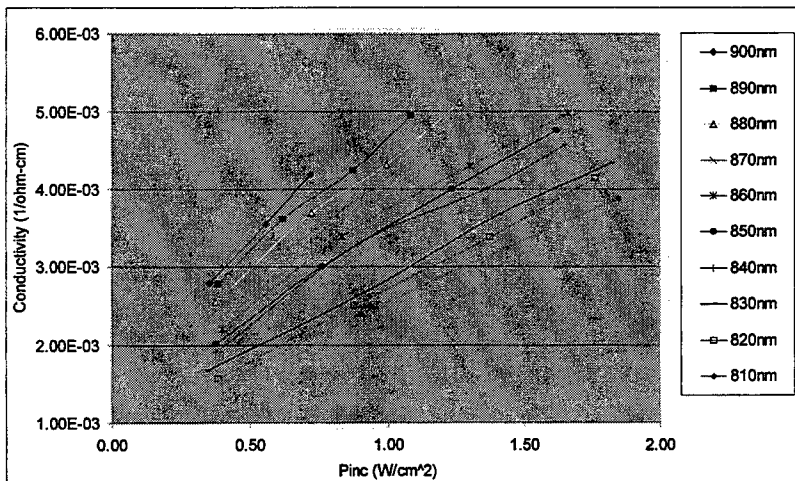


Figure 3) Graph of Sample Conductivity ($1/\text{ohm-cm}$) versus Absorbed Power Density (W/cm^2) for Mirror Set B3

provided an indication of the total number of photocarriers generated by a given incident photon flux density. This current was then used to determine the overall sample conductivity.

Samples were initially measured with the Ti:sapphire laser mirror set B2 (810nm – 900nm). The laser was then reconfigured with mirror set B3 (880nm – 1000nm) and the measurements were repeated. The mounting and unmounting of the various samples resulted in some minor discontinuity between measured results for any given sample between the two wavelength ranges. Typical measured curves for sample photoconductivity are shown in Figures 2 and 3. In each case, the results show an increase in photoconductivity with increasing wavelength and increasing power.

The results for each case also indicate that the increase in photoconductivity is a near-linear function of incident power density for any given wavelength. The results generally show that for a given absorbed power density, the photoconductivity increases steadily with wavelength until approximately 950nm. Above 950nm, the increase in photoconductivity with wavelength appears to saturate toward some maximum wavelength value. This saturation effect corresponds to the wafer reflectivity measurements where the substrate transmission becomes significant for wavelengths above 950nm.

The curves for Figures 2 and 3 are typical of the general trends for the other samples. One additional observed trend was that grouping of the conductivity curves occurs near the extremes of the short and long wavelength ranges. This effect was most pronounced for samples which had no surface passivation layers, but was slightly evident in the typical curves of Figures 2 and 3. These effects can be attributed to the silicon absorption, carrier concentration, free carrier absorption, and surface recombination characteristics. These effects are discussed in greater detail in the following section.

Experimental Analysis:

The measured data illustrates several characteristics of bulk silicon which can be used to quantify the behavior of high resistivity silicon under high power illumination. One general feature of the data is the dependence of the photoconductivity on the incident power density. Although the output power of the Ti:sapphire laser limited the amount of high power data obtained at the long wavelengths, the slopes of the long wavelength curves generally began decreasing at the highest measured power densities.

For all measured silicon samples, the values and the slopes of the photoconductivity curves at a given incident power density are generally greatest for the longest wavelengths. The slopes appear to saturate at the longest wavelengths indicating that there is a limit on the overall quantum efficiency of the carrier generation process. This effect indicates that the carrier generation process is also dependent on the carrier concentration. Each of these effects are expected characteristics of the carrier generation – recombination process as illustrated in the following discussion.

Carrier statistics dictate that for a given bulk semiconductor under steady state illumination, the majority of the filled states accumulate near the edges of the band gap. It follows that additional carriers are most easily generated by high-energy short wavelength illumination rather than with long wavelength illumination approaching that of the semiconductor energy bandgap. The measured results however indicate that photocarriers are most efficiently generated at long wavelengths for a given photon flux density. The reduced sample conductivity for short wavelength illumination can be attributed to concentration-dependent carrier recombination processes.

A primary factor in the generation of photocarriers in silicon by high power illumination is the optical absorption depth as a function of wavelength. A typical value of 50/cm [2] for the optical absorption coefficient is used for the following analysis. Figure 4 shows a typical plot of normalized intensity as a function of wafer depth for 800nm, 900nm, and 1000nm. This curve illustrates several important features. For wavelengths approaching 1000nm, approximately 10% of the incident light is transmitted through the wafer. The absorption depth for 99.9% of the incident 1000nm illumination is

nearly 1mm. This result places an upper limit on the illumination wavelength for total absorption within a given wafer thickness. In practical applications, a high reflectivity coating could be applied to the backside of the substrate to allow total absorption within the wafer.

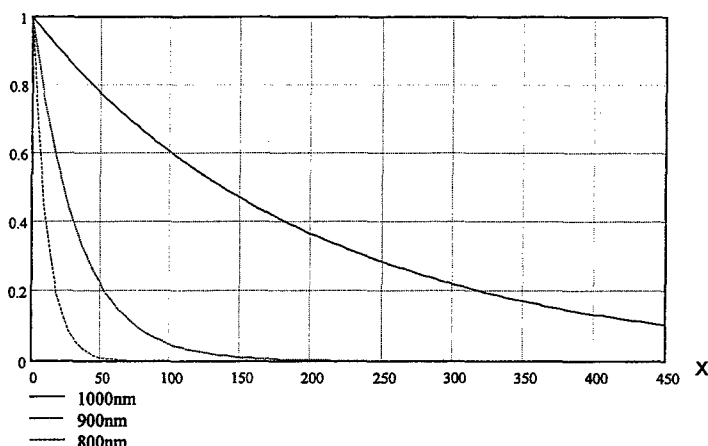


Figure 4) Graph of Normalized Intensity versus Silicon Wafer Depth (μm) for Increasing Wavelength

The curves of Figure 4 also illustrate that the incident light is absorbed very near the surface for all wavelengths below approximately 900nm. For the 800nm illumination, 99.9% of the incident light is absorbed within approximately $50\mu\text{m}$. For 900nm illumination, the total absorption depth is approximately $150\mu\text{m}$. Only a finite total number of carriers per unit area can be generated for a given incident photon flux density. The actual number of carriers is based on the total energy delivered to the sample and the quantum efficiency of the generation-recombination process.

The increased absorption of silicon with short wavelength illumination implies that all photocarriers are generated near the wafer surface. This further implies that carrier densities near the surface for short wavelength illumination will be >10 times larger than the carrier concentrations produced by long wavelength illumination. Although the short wavelength illumination produces a high localized carrier concentration, the overall sample conductivity is lower than that of long wavelength illumination. Long wavelength illumination produces a lower but more uniform carrier concentration throughout the bulk of the wafer.

Assuming that the total number of carriers generated is directly proportional to the incident photon flux (constant quantum efficiency), the total number of carriers removed from the sample is greater for long wavelength illumination. This indicates that the increased carrier concentration for short wavelength illumination enhances deleterious effects on the photoconductivity of the bulk silicon wafer. These carrier-concentration dependent effects include Auger recombination, surface recombination, free carrier absorption, and the reduction in carrier mobility as functions of carrier density and temperature.

Previous research and analysis [3, 4] indicates that the maximum practical carrier concentration for silicon is 10^{17} - $10^{18}/\text{cm}^3$. Reference [4] details each of the deleterious effects and provides order of

magnitude estimates of the dominant recombination and free carrier absorption mechanisms. Free carrier absorption significantly reduces the quantum efficiency at carrier concentrations above $10^{18}/\text{cm}^3$. Auger recombination effectively reduces the recombination lifetime in the high concentration regions thus limiting the diffusion length of the excess carriers. Additionally, the concentration-dependent carrier mobility limits the maximum illuminated conductivity for carrier densities above $10^{18}/\text{cm}^3$.

For high resistivity silicon, the electron and hole mobilities remain approximately constant for carrier concentrations below approximately $10^{16}/\text{cm}^3$ with the total mobility being reduced by approximately 80% at carrier densities of approaching $10^{18}/\text{cm}^3$. This implies that for any given photocarrier concentration above $10^{17}/\text{cm}^3$, the excess carriers cause a reduction of carrier mobility that begins to offset the increase in conductivity due to increased carrier concentration. Additional effects that may become significant for short wavelength illumination are excess localized heating of the silicon surface due to high absorption, and surface recombination due to high carrier concentrations near the wafer surface.

The effect of carrier diffusion has been largely neglected in this research and analysis due to the bias voltage applied to the samples during photoconductivity measurements. Nevertheless, for photogenerated carriers with no applied bias, ambipolar diffusion plays a significant role in determination of the steady-state carrier concentrations throughout the wafer. The ambipolar diffusion characteristics are functions of carrier concentration, lifetime, and carrier mobility. For typical specified carrier lifetimes ($>1\text{msec}$ for high resistivity silicon), the resulting ambipolar diffusion lengths can approach several centimeters per second. From this standpoint, any excess carrier concentration generated within an unbiased wafer can diffuse completely across a $500\mu\text{m}$ wafer thickness in approximately 1msec .

For high power illumination and generation of large carrier concentrations, the Auger recombination lifetimes and lengths are much shorter than intrinsic carrier lifetimes and diffusion lengths. The net effect is the reduction of local excess carrier concentrations ($>10^{18}/\text{cm}^3$) primarily by Auger recombination effects until ambipolar diffusion and Shockley-Read-Hall recombination ($<10^{17}/\text{cm}^3$) become the dominant carrier reduction mechanisms. The effects of Auger recombination and free carrier absorption effectively present a practical upper limit on the efficient generation of photocarriers.

The applied DC bias voltage allowed carrier diffusion effects to be neglected for the measured photoconductivity analysis. The diffusion effects must be considered for unbiased photocarrier generation. The presence of diffusion effects would allow a reduction in the total energy requirements for generation of the required photocarrier density and photoconductivity. Again, the best efficiency would be obtained by using a pulsed laser source with the longest wavelength chosen to allow total absorption within the wafer. The pulse repetition rate or source duty cycle could then be varied to balance the optimum generated photocarrier density with the carrier concentration-dependent absorption and recombination losses.

A semi-insulating GaAs sample was included in this study to present a simple comparison to the photoconductivity characteristics of silicon. The GaAs sample exhibited photoconductivity values similar to the silicon values except with very little wavelength dependence. This result is expected because the absorption coefficient for GaAs is typically much higher (except within a few nanometers from the bandgap wavelength) than that of silicon. Additionally, the carrier lifetimes for GaAs are several orders of magnitude shorter than for high resistivity silicon. This fact indicates that pulsed laser photocarrier generation (utilizing photocarrier diffusion) would be less efficient for GaAs when compared to silicon under the same operating conditions.

Summary / Conclusions:

The experimental results show a general trend of increasing photoconductivity with increasing wavelength for any given incident power density. The results also indicate that the rate of increasing photoconductivity with incident power density begins to roll off at high incident power densities for any given wavelength. These trends suggest that for any given incident power density, the sample is made most conductive by illumination with wavelengths approaching the longest wavelength for total absorption within the specific substrate thickness.

The measured results indicate that the average photoconductivity for short wavelength illumination is less than that obtained for the same incident photon flux density obtained for a long wavelength source. This effect is a result of carrier-concentration dependent recombination and absorption mechanisms. Long wavelength illumination up to the wafer thickness limit provides a lower but more homogeneous carrier concentration throughout the wafer. The more-uniform generation of carriers minimizes the localized loss mechanisms present for high carrier concentrations.

Assuming a constant carrier generation (quantum) efficiency, under biased sample conditions, the total number of carriers removed from the sample is greater for long wavelength illumination. Minimization of the carrier reduction effects allows generation of a greater total number of carriers within the total wafer volume. This result verifies previous analysis that predicts a maximum practical photocarrier concentration of 10^{17} - $10^{18}/\text{cm}^3$ for efficient photocarrier generation.

For practical implementation of silicon photonic structures, once the wafer thickness and illuminating wavelength are selected, appropriate passivation, reflection, and antireflection coatings should be applied. These coatings should be applied so that all exposed silicon surfaces are passivated. For unbiased operation, the required photoconductivity can best be obtained from a pulsed source with optimized output power and pulse duration. The use of a long wavelength pulsed source allows the highest carrier generation efficiency while minimizing device heating and the deleterious recombination and absorption losses.

In summary, the results suggest that unbiased photonic structures fabricated from high resistivity silicon would be best illuminated with long wavelength (approaching $1\mu\text{m}$) radiation to maximize the absorption volume for typical wafers with $450\mu\text{m}$ thickness. For illuminated sample thicknesses less than $450\mu\text{m}$, the operating wavelength should be reduced to allow total absorption within the wafer thickness. Alternately, for any given total sample conductivity under shorter wavelength illumination, an increased incident photon flux density will be required to maintain that conductivity (due to increased carrier reduction effects), resulting in reduced overall quantum efficiency and increased device heating.

References:

- [1] D.E. Aspnes, "Optical functions of intrinsic Si: Table of refractive index, extinction coefficient, and absorption coefficient versus energy (0 to 400 eV)" in Properties of Silicon. London: INSPEC, The Institution of Electrical Engineers, 1988, pp. 72-79.
- [2] R.F. Pierret, Semiconductor Device Fundamentals, Reading, MA: Addison-Wesely, 1996.
- [3] W.C. Nunnally, "Photoconductive power switches: a review" in IEEE Fifth Pulsed Power Conference. Crystal City, VA: IEEE, 1985, pp. 225-231.
- [4] R.N. Edwards, "Selectively Conducting Apertures in Photoconductive Silicon", University of Texas at Arlington Ph.D. Dissertation, August 1996, pp. 15-39.
- [5] C.M. Wolfe, N. Holonyak Jr., and G.E. Stillman, Physical Properties of Semiconductors, Englewood Cliffs, NJ: Prentice-Hall, 1989, pp. 236-274.

- [6] M. Willander and V. Grivickas, "Diffusion and Mobility of Photogenerated Carriers in Undoped Si" in Properties of Silicon. London: INSPEC, The Institution of Electrical Engineers, 1988, pp. 200-201.

Acknowledgements:

The author offers thanks to Dr. Kambiz Alavi, and Sorin Tibuleac for valuable support and insightful discussion over the course of this project.

Characteristics of Fractal Antennas

Haruo Kawakami, Yasushi Ojio, Yasushi Iizuka,
Satoshi Kogiso and Gentai Sato

Antenna Giken Co., Ltd., Laboratory

4-72 Miyagayato, Omiya-shi, Saitama Pref., 330-0011 JAPAN

E-mail: hkawa@mail.raidway.ne.jp

Fax: 81-48-684-4144

1. Introduction

In globe and conical type of the traditional Euclidean geometry, in 1970's, mathematician Benoit B. Mandelbrot of France could not express the form of cloud and mountain in the nature, and not integer but geometry shown by the fractal (it had the fraction) dimension were initiated.

The similar figure also breaks it according to some rules for the multiple. That time, it is called fractal figure^[1] the results to of develop to the large-scale figure.

A realization of the device with wide-band frequency characteristics can be expected, when this figure was observed in electromagnetism like, in order to superimpose the characteristics, which the similar figure produces in frequency characteristics, which the figure as a basis gives. Especially, until now electromagnetism research on the fractal is energetically advanced in antenna and field of the microwave, and the broadband antenna using Gasket^[2] and tree curves, Koch curve^{[3],[4]} of the Sierpinski, etc. has already been reported.

This paper is described here, because impedance characteristic and radiation pattern characteristics of basic characteristic of the Koch curve were examined.

2. Antenna Shape

Figure 1(a)-(f) is the structure of the dipole antenna described in the Koch

curve. This structure carried out the calculation in the shape from stage 0 (basis) to stage 3 at the dimension as half-wave length and full-wave length. However, the radius of this antenna element was made to be the conductor, which was enough thinner than the wavelength.

3. Characteristics

Figure 2(a)-(c) are impedance characteristic in changing the shape in the

structure of figure 1. It is proven to consist of stage 0 with stage 1, stage 2, stage 3 and wide-band characteristics are shown as well as the impedance characteristic. Figure 3(a)(b) are gain characteristic in changing in the structure of figure 1(e) for origin symmetric and X-axis symmetric. From this fact, it was proven that using this element as a basis got the antenna of wide-band characteristics.

4. Conclusion

This paper examined impedance characteristic and radiation pattern characteristics of basic characteristic of the Koch curve. As a result of

examining characteristics of the dipole antenna, impedance, radiation pattern characteristics, wide-band characteristics were obtained, and it was proven they would be enough usable using such element as a wide-band antenna in future. The structure of which better characteristics are obtained will be considered.

Reference:

- [1] J.L.Vehel,et.al.: "Fractals in Engineering", Springer(1997).
- [2] C.Puente,et.al.: "Sierpinski gasket", Electronics Letters,32,1(Jan.1996).
- [3] X.Yang,et.al.: "Fractal Antenna Elements and Arrays", Applied Microwave & Wireless,11,5(May 1999).
- [4] N. Cohen: "Exploring a Fractal Dipole", ACES Newsletter, 13, 2, pp.23-27, 1998.

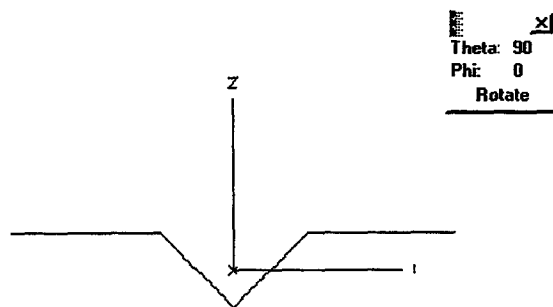


Fig.1 (a) Fractal Element Antennas of Stage 1.

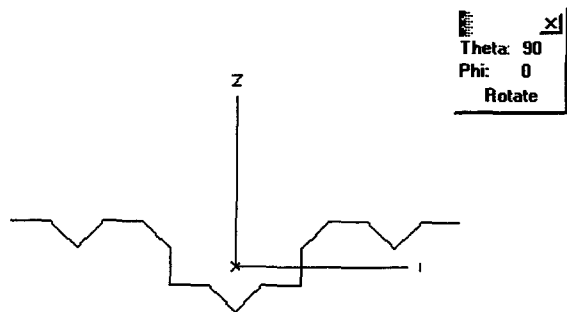


Fig.1 (b) Fractal Element Antennas of Stage 2.

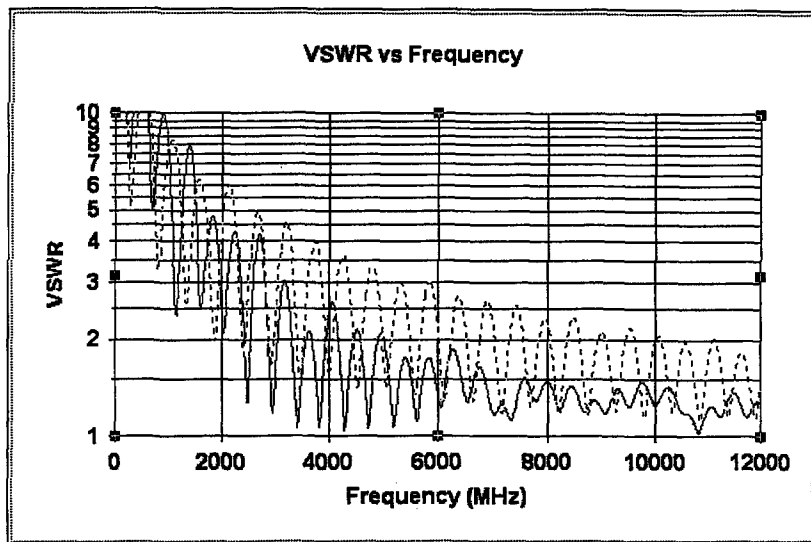


Fig.2(a) VSWR Characteristics of Fractal Element Antennas of Stage 1 and Stage 2 of Fig.1(a) and (b) ($Z_0=300\Omega$).

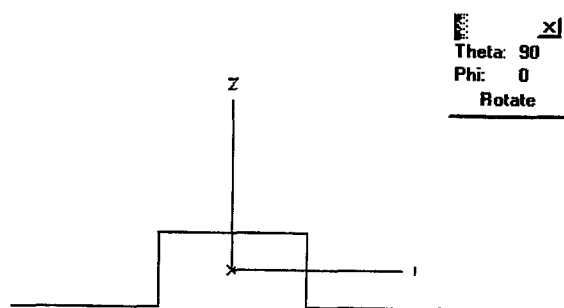


Fig.1 (c) Fractal Element Antennas of Stage 1.

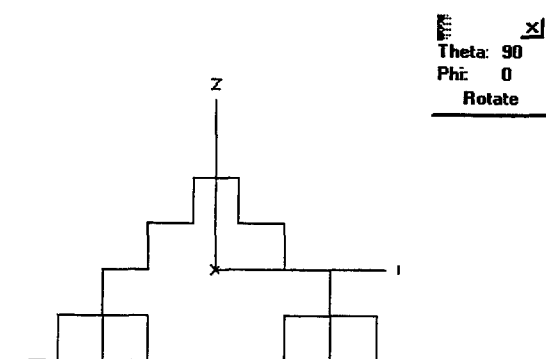


Fig.1 (d) Fractal Element Antennas of Stage 2.

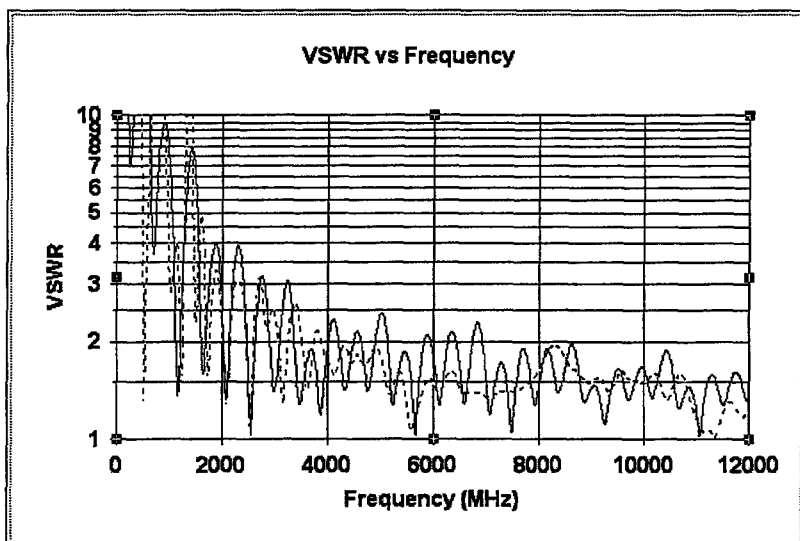


Fig.2(b) VSWR Characteristics of Fractal Element Antennas of Stage 1 and Stage 2 of Fig.1(c) and 1(d)($Z_0=300\Omega$).

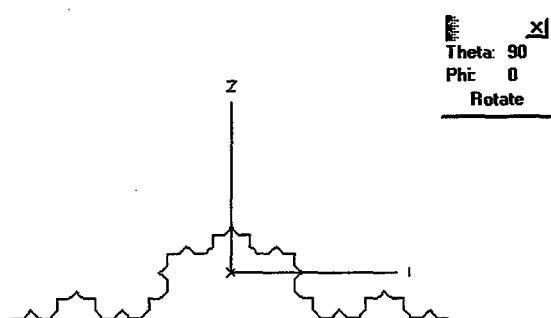


Fig.1 (e) Fractal Element Antennas of Stage 3.

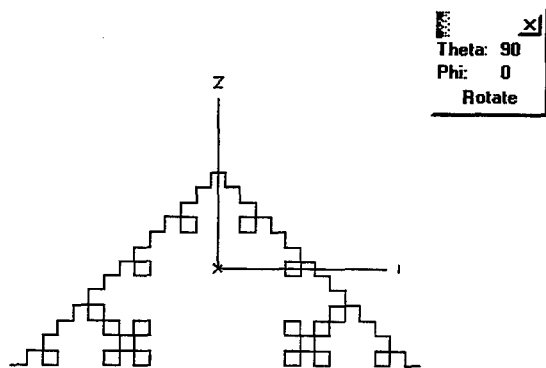


Fig.1 (f) Fractal Element Antennas of Stage 3.

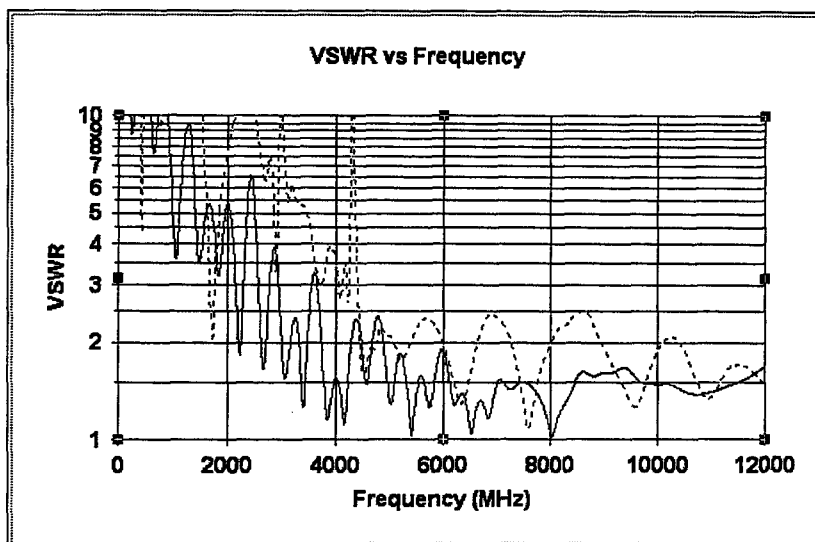


Fig.2(c) VSWR Characteristics of Fractal Element Antennas of Stage 3 of Fig.1(e) and 1(f) ($Z_0=300\Omega$).

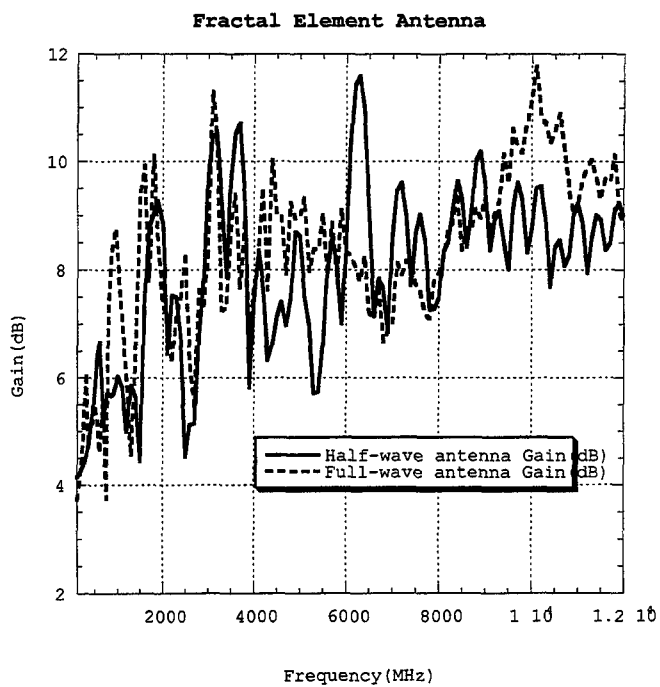


Fig. □(a) □ Characteristics of Gain for FEA

Fractal Element Antenna of Fig.1(e)
for origin symmetric and X-axis symmetric

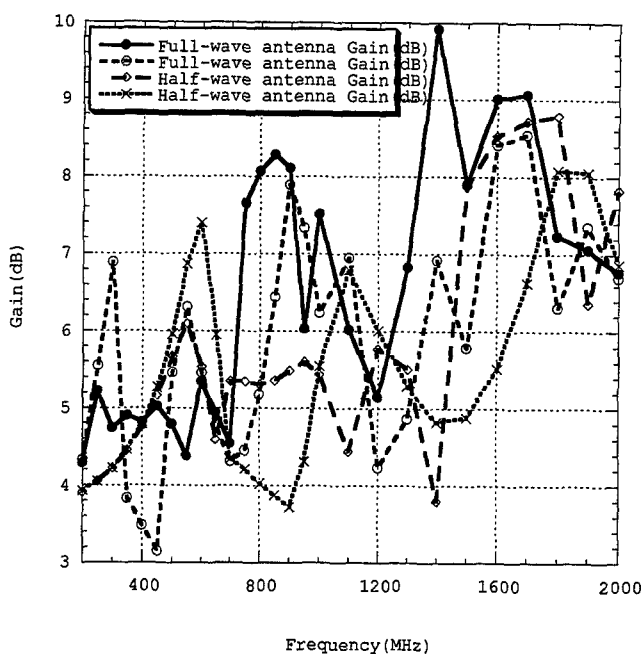


Fig.□(b)□Characteristics of Gain for FEA

Feigenbaum Encryption of Computer Codes

by

R. M. Bevensee

BOMA ENTERPRISES

P.O. Box 812 Alamo, CA, 94507-0812 USA. email: rmbevensee@cs.com

1. Summary

The Feigenbaum- or F-sequence of numbers $\{x_n\}$ is generated by the incredibly simple prescription $x_{n+1} = Fx_n(1 - x_n)$ for $n \geq 0$, starting with the private keys x_0 , $0 < x_0 < 1$, and F , the Feigenbaum parameter, in the range $0 < F \leq 4$. Effective coding demands that F be close to 4 ($x_0 \neq 0.5$ if $F = 4$). This process is used to encrypt a message sequence of symbols $\{S_n\}$ from an alphabet $\{A_m\}$, with an astronomically small chance of decoding by an intruder-attacker if the number of significant digits in x_0 and F is reasonably large (≥ 10).

Section 2 describes some of the properties of the F-sequence. Section 3 outlines the method of encryption and of decoding and explains why an initial short sequence of the encrypted message might be successfully decoded with nearly correct values of x_0 and F . Section 4, Fig. 1, presents a representative example of a short message comprised of symbols from a 56-member alphabet, and how the decoded message is corrupted for various values of x_0 and F .

In Section 4 we also introduce the private integer key K to confuse an attacker's decoding of an initial string of a coded message with very small errors in x_0 and/or in F . Case 3) of Table 1 illustrates this.

Section 5 shows an example of encrypting the opening portion of our Fortran code with this encryption process for $K = 0$.

Section 6 describes double F-sequence encryptions, using a double pair of x_0 and F keys. There is no single pair of these keys an attacker can use to decode successfully such an encrypted message. The reason is clarified in the Appendix, Section 9.

Section 7 compares F-sequence with Public-key encryption, and Section 8 outlines F-sequence communication between two persons.

2. Properties of the F-sequence

For $0 < F \leq 3$ the process terminates; for $3 < F \leq 4$ it is periodic, in the sense that it cycles between a number of stable values which depend on the value of F . For $3 < F \approx 3.45$ the process cycles between two values, then the number of values abruptly jumps to 4 until F reaches ≈ 3.545 , at which the number of values doubles again to 8, and so on, until the number of levels is infinity at $F=4$. At $F=4$ the process is chaotic: each x_n would *never repeat* if an infinite number of digits were retained.

If F_m is the value of F at which the process would cycle between m values the approach of F_m to 4 as m approaches infinity is as

$$(4 - F_m) \xrightarrow{m \rightarrow \infty} \frac{A}{(4.6692\dots)^m}, \quad (1)$$

where A depends on the process and 4.6692... is the universal Feigenbaum constant which appears in the description of many chaotic processes. This property embodied in (1) does not play a role in our considerations of coding and decoding.

The backward generation of x_n from x_{n+1} yields two values:

$$x_n = \frac{1}{2} [1 \pm \sqrt{1 - 4x_{n+1}/F}], \quad (2)$$

with $4x_{n+1}/F < 1$ because $Fx_n(1 - x_n) < 1$. Because of this backward branching an attacker would not start with an incorrect value of x_{n+1} and try to compute far back in the $\{x_n\}$ -sequence, hoping to reach a correct x (assuming he had the correct F).

We have not been able to describe analytically how initial errors in x_0 and F propagate with increasing n , thereby corrupting a decoded message. Section 4 will suggest how the corruption proceeds in several examples.

3. The Method of Encryption and of Decoding

Table 1 shows four columns. The left one lists the message symbols $S_1, S_2, \dots, S_n, \dots, S_N$. The next column lists the alphabet of members $A_1, A_2, \dots, A_k, \dots, A_m, \dots, A_M$. The first message symbol S_1 is A_k , so it is beside the k th alphabet member. The second message symbol is indicated as A_m , and so on.

x_1 , the first member of the F-sequence, determines integer T_1 in the range 1 to M as

$$T_i = [Mx_i] \quad (3)$$

for $i=1$, the brackets denoting the rounded-down integer value. Here we show $S_1 = A_k$ and $k + T_1 = \kappa \leq M$, so $\kappa \leq M$ lies in the next alphabet column in the *upper* A-column. The first coded symbol C_1 is A_κ .

x_2 , generated next, determines T_2 as above. Since message symbol $S_2 = A_m$ and $M + T_2 > M$ we show μ in the *lower* A-column. μ is found as $\mu = T_2 - (M - m)$, and the second coded symbol C_2 is A_μ .

And so the process continues, until the last message symbol S_N is coded by x_N and X_N into C_N .

Decoding proceeds in reverse: $C_1 = A_\kappa$ translates to $A_k = S_1$ by T_1 , etc.

Table 1
Encryption and Decoding Between Message Sequence $\{S_i\}$ and Coded Sequence $\{C_j\}$

The first message symbol, S_1 is alphabet member A_k , which is coded by integer T_1 into A_κ , which is coded symbol C_1 . Similarly, $S_2 = A_m$ is coded by T_2 into A_μ , which becomes coded symbol C_2 . Decoding proceeds in reverse from the $\{x_i\}$ generated from x_0 and F: $C_1 = A_\kappa$ in the table is translated by T_1 back to $A_k = S_1$, etc.

Message Symbol S	Alphabet A	Alphabet A	Coded Symbol C
S_N	1	1	.
.	2	2	.
.	.	.	.
S_n	.	.	.
.	.	.	C_N
$S_1 =$	k	.	.
.	.	.	.
.	.	.	.
$S_2 =$	m	κ	$= C_1$
.	.	.	.
.	<u>M</u>	<u>M</u>	.
		1	.
		2	.
		.	C_n
		μ	$= C_2$
		.	.
		<u>M</u>	.

Observe in (3) that a range of x_i -values will yield the same T_i . This implies that an attacker starting the F-process with nearly correct values of x_i and F might generate correct T_i for an initial short sequence of coded symbols $\{C_i\}$. These would enable him to decode this initial sequence correctly, until the initial errors in x_0 and F generated sufficient errors in the T_i as to render the decoding meaningless. Sec. 4 will present examples of this and introduce the additional private key K to subvert it.

4. An Example of a Short Message and its Decoded Corruption for Very Small Errors in x_0 and/or F

Fig. 1 lists a 2-line message composed of symbols from the alphabet of 52 capital and small letters, comma, period, space, and \. It begins with 10 periods to confuse an attacker. Coding with $x_0=X_0=.50$ to ten decimal places, $F=FEI=3.95$ to eleven significant digits, and $K=0$ (to be used below), we obtain, for the NSYM=140 message symbols, the two coded lines beginning with "AIF". Notice the coding does not suggest the initial "nonsense" string.

The remainder of the figure shows four cases of decoding. In case 1) the correct values of X_0 , FEI, and K recover the message. The block of seven lines of zeros indicates that each decoded symbol is the same as the message symbol in the Alphabet table. In case 2) we code with X_0 low by 10^{-10} and FEI correct, with $K=0$. The initial decoding is correct up to the 49th message symbol, beyond which the errors grow. The 50th numeral in the block is "1", meaning the message symbol is 1 below the decoded symbol in the alphabet table. We have not shown the case of $X_0=.5000000001$ and FEI correct, $K=0$: that decoding is entirely correct. Cases exist for which nearly correct values of X_0 , FEI, and K will yield partially or entirely correct decoding.

To overcome this tendency we introduce in case 3) the private numerical key K. Its purpose is to create an entirely incomprehensible decoded message even if the three keys are very close to their correct values. The decoded message shown is qualitatively the same as the message coded instead for $K=10$ and decoded for $K=0$. K can be used in either of two ways. It can advance the F-sequence to x_{K+1} before beginning the coding. This will prevent an attacker from starting the decoding with nearly correct x_0 and F and generating an initially correct short string, as in cases 2) and 4) of Fig. 1. Or K can be used to start the decoding with x_1 but indicate an initial K message symbols as a "nonsense" string.

In the first use of K an attacker would have to start with very accurate values of x_{K+1} and F. This x is conceptually no more difficult to deduce than x_0 , which indicates the need for an initial "nonsense" string. For the second use of K an attacker could bypass an initial "nonsense" sequence and start decoding further into the message sequence, but he too would require very accurate values of X_0 and FEI, with $K=0$.

Case 4) in Fig. 1 is for $X_0=.50$ to ten places and FEI in error by 10^{-10} , $K=0$, illustrates correct decoding for 31 symbols, after which the difference between the alphabet index of each message symbol and the corresponding decoded symbol starts to vary unpredictably—as shown in the block of seven lines below the partially decoded message.

It is important for sender and receiver to code and decode with the same long keys: if the value of X_0 and/or FEI is rounded off, such as 3.9500000000 to 3.95, a different decoded message could result!

5. Encryption and Decoding of the Initial Portion of Our Fortran Source Code

We show in Fig. 2 the initial portion of our Fortran source code for F-sequence encryption and decoding. The arbitrarily selected values of $X_0=.6528...$ and $FEI=3.9874...$ encrypted the 2552-symbol message of 80 symbols per line. (The encrypted message is not shown.) The message decoded with X_0 in error by 10^{-10} and the correct FEI, for $K=0$, shows the first 39 symbols are decoded correctly, as indicated by the first 39 symbols in the integer table. Each integer shows the separation of message symbol and decoded symbol in the Alphabet column of Table 1.

This integer table is truncated to nearly 84 lines, for brevity. Observe that an occasional short sequence is decoded correctly. For example, the sequence of five zeros in line 17 of that table shows that "gene" in line 5 of the Fortran-code message is decoded correctly, as is "NUMC" ten symbols beyond. Also, there is a string of six symbols decoded correctly: The " " sequence in the DATA C/-line of the Fortran code.

CODING:

.....Now is the TIME for all good MEN and WOMEN to educate themselves about political issues in order to vote intelligently next year.\\

```
X0= .5000000000    FEI= 3.9500000000    K= 0
      NSYM= 140
```

AifzHd,DSHcwGwMhMYPLGKJQZDlRV,ZhaDhzyWmJKKbJvgJbxvwObkUEsiwppgoyVLrnxdVR,doYiY
+CdCrnuTFzoLp,DrAvYnyfJZDvVFSnvoefwVcrFcm k KxAvKaLxFUJFuX

DECODING:

1) X0= .5000000000 FEI= 3.9500000000 K= 0
.....Now is the TIME for all good MEN and WOMEN to educate themselves about
political issues in order to vote intelligently next year.\\

[illegible]

2) X0= .4999999999 FEI= 3.9500000000 K= 0
.....Now is the TIME for all good MEN and WOLDRy.Js,GnO Z,\rosCh\ RnZaelm,h
HdbvIssffZBVSDUDNKFcbXlaBgso,gpoPgaedDtBRXToozHOFGu HVVoLacl

[illegible]

3) X0= .5000000000 FEE= 3.9500000000 K= 10
DnQG DOIYYTkoYbdsOSEU,seP gloHrAMmXnf\Hxfp,oaELLVbzlygtdftfkDyDpvIb\.\Ldx.YWfKa
djgxOorGUWAXGer.YyQMZd.wchtn\yppRhXTWZqzNOBZSOflaMlw\gPHLcef

51	16	38	48	1	51	40	46	30	30	-32	30	32	29	7	15	35	31	15	26
33	-33	-36	-18	-11	0	-1	3	4	-17	37	25	4	-6	17	1	-2	-2	5	1
-45	-18	38	-26	-1	3	52	11	3	-9	-23	-38	16	21	8	34	1	-2	1	-3
-10	42	-20	50	4	-14	22	11	-11	-24	-18	36	1	-5	-1	2	5	9	36	19
12	5	5	-15	31	-6	-15	20	17	44	34	21	38	42	-13	-10	29	-16	23	41
15	14	-25	-18	37	20	0	1	-2	-3	-1	4	13	20	11	20	23	5	5	12
-5	16	29	14	27	21	19	45	13	18	12	-3	-2	8	15	25	32	26	25	24

```
4) X0= .5000000000      FEI= 3.9500000001      K=      0
.....Now is the TIME for ajiEaWPAbrzXbljxmrlTxsqkHVBh..WuR,Pay DyaHgLS\wnw
wUmdskilOYpJfGhXyNEdPTvHdlxayV\PgbggzuzAptH.HmUBstBPJ,jTHit
```

[illegible]

Fig. 1. Coding and Decoding of a 140-symbol message (NSYM=140). The message string was coded with the values of X0, F01, and K indicated, and the incomprehensible string below NSYM=140 resulted. Four cases of decoding with various values of X0, F, and K are shown. The 7-line block of integers below each decoded message indicates the distance in the alphabet of each decoded symbol from its message symbol.

219

6. Double F-Sequence Coding

To confuse completely an attacker a sender could encrypt his message with one F-sequence and then encrypt the unintelligible result with a second sequence in one operation, using a different keyset. An attacker would not know if he decoded correctly the received message because correct decoding would reveal an unintelligible message. He could not use one set of keys to decode his received message and reveal the original message. The Appendix explains why this is so.

7. Comparison of the Efforts Required for Public-key and F-sequence Decoding

A public key encryption scheme requires the solution of a purely *mathematical* problem, such as factoring a large number into its produce of two primes, with no requirement for evaluating a decoded message for *content*. F-sequence decoding requires not only trial of an astronomical number of key combinations but also *subjective* evaluation of each decoded sequence for meaning. This latter requirement is very time-consuming and cannot be satisfied by a simple, efficient computer program.

Assuming single-sequence encryption, ten significant digits to the right of the decimal point, and $3.9 < F < 4$, we have $\approx 10^{19}$ possible combinations of x_0 and F ($K=0$). If each decoding requires 10^{-3} sec. for evaluation and there are $\approx 3 \times 10^7$ sec/year, an attacker would require $\approx 10^8$ years to explore all the combinations!

8. Secure F-sequence Communication Between Two Persons

Assume that Alice and Bob exchange F-sequence encrypted messages. Alice sends Bob a message encrypted with her keys, which Bob initially knows. She continues to use these keys until she wishes to change them, she includes the new key set in a message encoded with the old set. Bob always knows the keyset to use to decode her next message.

Likewise, Bob sends Alice messages encrypted with his initial key set, which she knows, and she checks each of his decoded messages for a change in his keyset—to be used to decode his subsequent messages.

If an attacker succeeded in "cracking" one of her messages he could continue to do so by monitoring any change in her keyset. However, the knowledge would not enable him to decipher Bob's messages. Bob would have to avoid revealing his keyset to the attacker if he requests them in a message apparently from Alice.

9. Appendix. Recovery of an Original Message in Double Encryption

Assume the sender encrypts his entire message, first with the keys x_0 and F , then with the keys x'_0 and F' . An attacker enters the final encrypted message at a point n and tries to decode and obtain the subsequent original message. Here we shall change the subscript " n " to " 1 " for simplicity.

The first encryption encoded the n th symbol in the message by $x_1 = Fx_0(1 - x_0)$ and the second encryption encoded the new n th symbol by $x'_1 = F'x'_0(1 - x'_0)$. Assuming the attacker was so clever as to deduce $x'_1 = F'x'_0(1 - x'_0)$ and $[Mx'_1] = [Mx'_1] + [Mx_1]$, he could deduce the correct message symbol according to (3).

However, he could not continue this process to generate correct $[Mx'_2]$, $[Mx'_3]$, ... and recover successive symbols of the original message. The reason is that the double encryption was done with *four* variables— x_0 , F , x'_0 , and F' , whereas the attacker has only x'_0 and F'' at his disposal. He cannot continue to generate original message symbols with so few parameters.

Extension of SuperNEC to calculate Characteristic Modes

Thomas Abbott

Department of Electrical Engineering
University of the Witwatersrand
Wits 2050
South Africa
Tel/Fax: +27-11-646-3764
email: tabbott@iee.org

1. Abstract

The Method of Moments code SuperNEC has been modified to find characteristic modes from the impedance matrix. The effect of asymmetry of the matrix on the accuracy and convergence of the characteristic mode currents was investigated. Good results were obtained on a straight wire, but those for complex structures were highly dependant on the numerical methods used, and did not converge with fine segmentation. These results are considered inaccurate, and further work on the implementation is required. The completed program will be used to design a dual-mode NVIS and low-angle HF antenna.

2. Introduction

Goals

The objectives of this study are to extend the SuperNEC engine to allow calculation of characteristic mode currents and verify the calculation method. The program can then be used to design a "smart" wire HF antenna with multiple patterns selected by switched loading, for NVIS as well as long-range applications.

Background

The theory of characteristic modes has been used successfully for a while to analyse the scattering and radiation properties of conducting bodies [2] [3]. The theory has been developed by Garbacz [4] to allow modes to be defined on conducting bodies of arbitrary shape.

Characteristic modes are defined as an orthogonal set of currents on the conducting body that, when weighted correctly, define the currents on the body due to any particular excitation. Harrington and Mautz in [2] show that for small objects only a few modes are needed to completely characterise the currents on the object, and hence the far fields due to the currents.

In [3] they show how the characteristic mode currents on an arbitrary wire object can be found by taking

eigenvectors of the Method-of-Moments (MOM) impedance matrix.

Calculation of Characteristic Modes

The currents on a structure due to a particular excitation can be found by solving the matrix equation for a set of currents that renders the tangential electric field zero on all but the excited wire segments (equation 1). This is the conventional MOM solution for the currents.

$$[Z]I = [E] \quad (1)$$

$[Z]$ is the impedance matrix, where Z_{ij} is the electric field induced on segment i due to a test current on segment j .

In a similar way, the eigenvectors of the impedance matrix yield solutions for current that satisfy the same condition, but are independent of excitation. The matrix equation can be written as that for general eigenvectors, as in equation 2, or in a form in which the currents may be seen more directly, as in equation 3 [1], where I_n is the n^{th} mode current vector, $[Z] = [R + jX]$ and I is the identity matrix.

$$(Z - I\lambda_n)I_n = 0 \quad (2)$$

$$[X]I_n = \lambda_n[R]I_n \quad (3)$$

The significance of the characteristic mode currents found from a particular eigenvector can be found from the associated eigenvalues.

$$S_n = \left| \frac{1}{(1 + j\lambda_n)} \right| \quad (4)$$

The significances are normalised and expressed in dB down on the first mode significance.

It should be noted that the actual magnitude of the currents found has no bearing on the significance of the mode, since if I is an eigenvector of $[Z]$ then so is kI , where k is a scalar. The reported magnitude is simply a result of the eigenvector normalisation performed by the algorithm used.

Practical Calculation

According to Austin and Murray [1] the eigenvectors only represent the characteristic mode currents if the impedance matrix $[Z]$ is symmetrical. This requires the use of a Galerkin Moment Method in the generation of the matrix, the method used in the MiniNEC code. Harrington and Mautz [3] relax this condition to some extent, saying that is sufficient to average the off-diagonal elements of a matrix obtained by another method, to achieve symmetry, before the eigenvectors are found. SuperNEC uses pulse basis functions to compute the impedance matrix, and it would be advantageous to be able to calculate characteristic modes directly from this.

3. Extensions to SuperNEC

SuperNEC is an object-orientated C++ Method-of-Moments program, with the basic theory the same as that of NEC2. It has a comprehensive MATLAB interface for creating structures and viewing the results of simulations. This is an ideal platform for experimentation with electromagnetic calculations, as it is easily modified and extended. The program offers a choice of basis functions for representing currents on the wire segments: the standard NEC2 basis function of sine, cosine and constant currents, or a pulse basis function [5].

The SuperNEC engine was modified to calculate the eigenvectors and eigenvalues of the impedance matrix. The actual eigenvector/eigenvalue calculation is done by the public domain package LAPACK. The requested characteristic mode currents are sorted by significance and written to the output file.

The currents on the structure are found from the eigenvectors, and these currents can then be used to solve for radiation patterns or near fields in the normal way. Currently, if the modified SuperNEC is asked to find radiation patterns or near fields, it finds them for each of the requested modes.

4. Investigations

Several structures were simulated in order to confirm the validity of the code, the numerical methods used, and the effects of errors introduced by the single-precision variables used throughout SuperNEC.

Matrix Asymmetry

The asymmetry of the MOM impedance matrix generated by different methods was investigated. Here the matrix has been found for a straight wire, with equal segment lengths. The asymmetry plotted was calculated with equation 5.

$$Asym = \log_{10} \left(\frac{\left| \frac{1}{2} \left(\frac{Z_{ij}}{Z_{ji}} + \frac{Z_{ji}}{Z_{ij}} \right) \right|}{\left| \frac{1}{2} \left(\frac{Z_{ij}}{Z_{ji}} - \frac{Z_{ji}}{Z_{ij}} \right) \right|} \right) \quad (5)$$

The asymmetry in the impedance matrix generated by the full-expansion SuperNEC is shown in Figure 1. There are significant differences between off-diagonal elements.

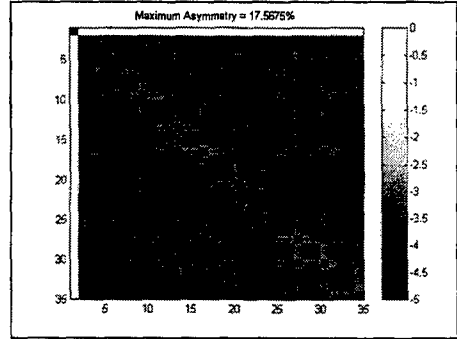


Figure 1 - Matrix asymmetry for full basis functions

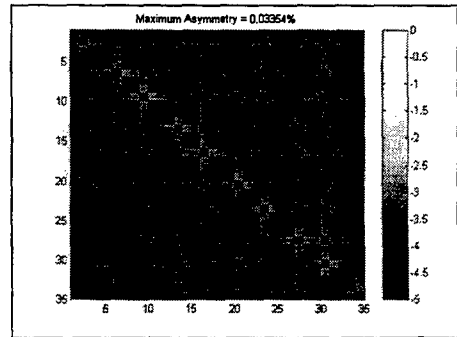


Figure 2 - Matrix asymmetry with pulse basis functions

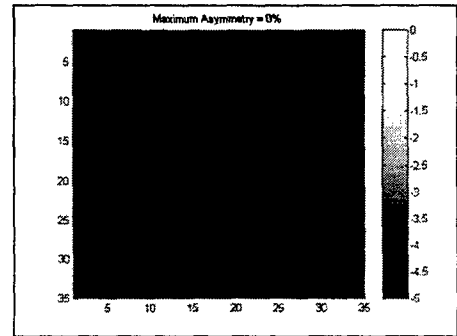


Figure 3 - Matrix asymmetry using Galerkin method

Figure 2 shows the matrix generated with pulse basis functions. This matrix is asymmetrical only to the order of the numerical precision used.

When the problem is solved in MATLAB using a Galerkin method the matrix is completely symmetrical.

Effect of Averaging

While a perfectly symmetrical matrix is desirable for finding characteristic modes, it will be advantageous to know the nature of the error introduced by simply taking eigenvectors of the asymmetrical matrix.

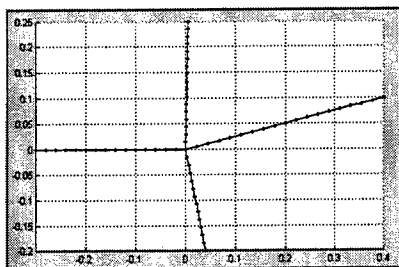


Figure 4 - Wire cross (63 segments)

The graphs below show the currents for several modes, on the irregular planar wire cross in Figure 4. The impedance matrix was calculated using the full basis functions in SuperNEC. The solid line is the current found from the matrix after averaging the off-diagonal elements, and the broken line is the current found from the original matrix before averaging. The two dotted lines are the currents that result if the matrix is made symmetrical by copying the upper triangle over onto the lower triangle, or vice-versa

A small problem with sorting the modes is that if the significance of a mode varies slightly between calculation methods, it can move several places up or down in the sort. Thus the first mode currents in Figure 6 are actually sorted as mode 3. They are placed as mode 1 to allow comparison to the currents in Figure 5.

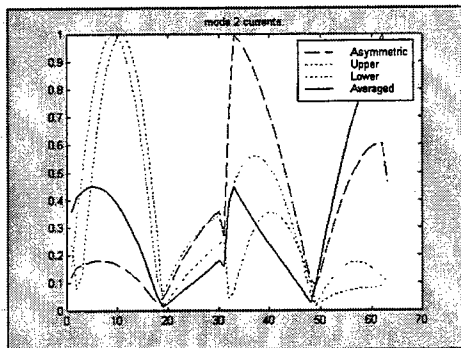
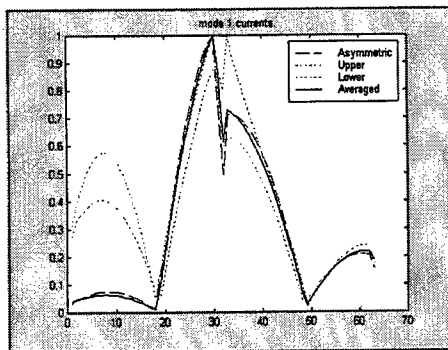


Figure 5 - Mode 1 and 2 currents, full basis functions.

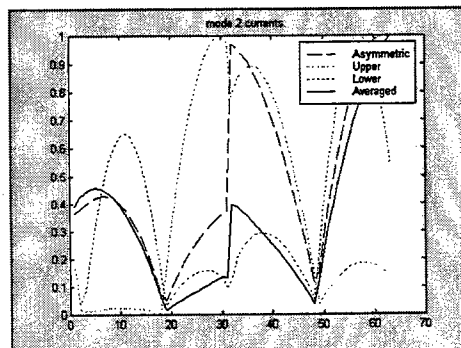
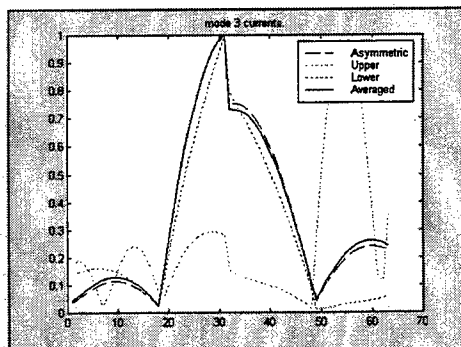


Figure 6 - Mode 1 and 2 currents, pulse basis functions.

These results show that the asymmetry of the matrix, whether generated with the pulse or full basis functions, is significant and cannot be ignored. It is also not certain that the currents found after averaging the matrix are any more

accurate than those found from the asymmetrical matrix, as there is no clear accurate answer to compare them to.

Effect of using different basis functions

Tests were conducted on various wire models to determine the effect of using the different basis functions available in SuperNEC. The number of segments was also varied, to allow the convergence of the results to be observed.

Three models were tested using the different basis functions:

1. A single wire

This is the simplest possible structure for testing. While it has no multiple-wire junctions, it has the advantage that it can be simulated easily in MATLAB, for comparison to the SuperNEC results. It is also advantageous that the characteristic mode currents are intuitively clear. The single wire is 0.6λ long, and 0.001λ thick. It was divided into 19, 35, 69 and 99 segments, for the various tests, giving segment lengths of $1/30$, $1/60$, $1/115$ and $1/165\lambda$. The shortest segments have a 1:6 radius to length ratio.

2. An asymmetrical wire cross (Figure 4)

The wires in the cross all lie in the same plane, but they are all different lengths, and are not orthogonal. The junction in the centre introduces some asymmetries into the impedance matrix when using the full SuperNEC expansion, because of the current continuity boundary conditions. The wire cross was simulated with 30, 60 and 131 segments, with segment lengths of between $1/22\lambda$ and $1/135\lambda$, and hence radius to length ratios of 1:45 to 1:7.

3. An irregular tetrahedron (Figure 7)

The tetrahedron is the final structure that was used to test the characteristic modes solutions from SuperNEC.

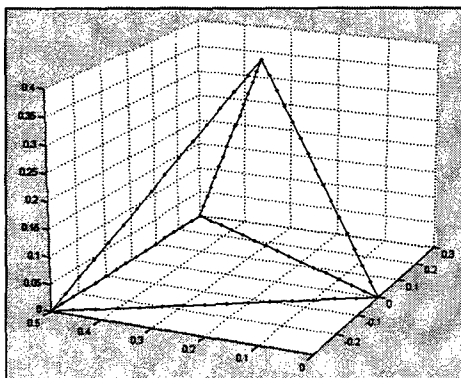


Figure 7 - asymmetrical tetrahedron (90 segments)

This structure has unequal side lengths, multiple-wire junctions and is non-planar. The tetrahedron structure is modelled using 90, 150 and 354 segments, and the segment lengths range from $1/25\lambda$ to $1/125\lambda$, and radius to length ratios range from 1:40 to 1:8.

The following graphs show the significance of the characteristic mode currents on the three structures, using different numbers of segments.

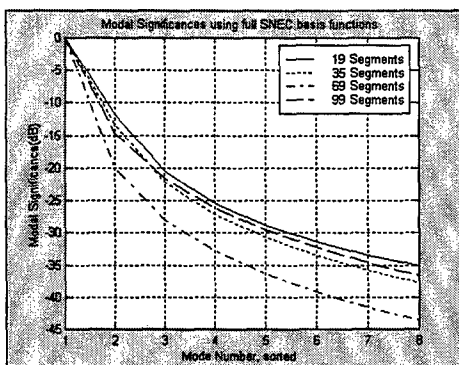


Figure 8 - Effect of number of segments, single wire.

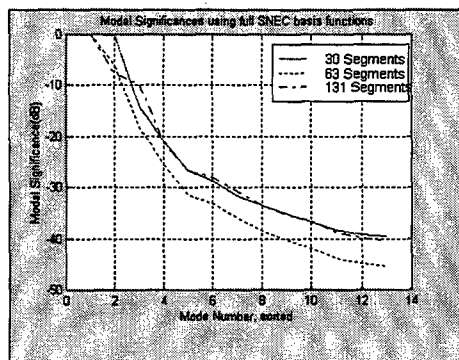


Figure 9 - Effect of number of segments, wire cross.

The results in Figure 8 - Figure 10 show a lack of convergence of the mode significance for large numbers of segments. It is possible that there is some convergence at lower numbers of segments, and that the large numbers of segments allow numerical errors to become significant, but this has not been clearly established.

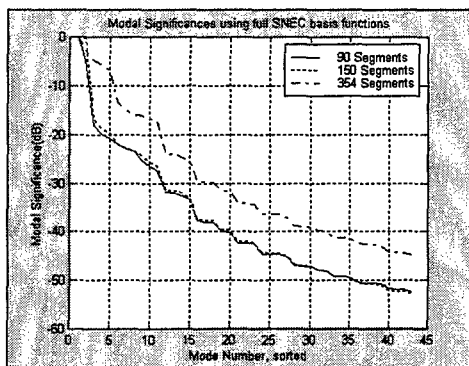


Figure 10 - Effect of number of segments, tetrahedron.

5. Conclusions

Modifying SuperNEC

The SuperNEC engine has been successfully modified to provide the eigenvectors and eigenvalues, and find mode significances, currents, near fields and radiation patterns from these. The MATLAB interface has not been modified, but the solutions can be loaded, analysed and plotted with it. Further analysis can be undertaken using task-specific MATLAB programs.

Further modifications

Several modifications to SuperNEC still need to be implemented:

- The input power to the structure should only be fixed at 1W when finding a characteristic modes solution. This will allow the version of SuperNEC to be used fully for both conventional and characteristic modes solutions.
- When calculating the radiation pattern, either the maximum or the average gain of the antenna should be normalised when finding a characteristic modes solution. The present version generally produces very low maximum values of gain (-10 to -70dB), as the small currents on the antenna do not radiate the 1W that it is assumed to be drawing from the source.
- It is proposed that a Galerkin method be added to the SuperNEC code to allow direct comparison of results on complex structures. A command-line switch or control card can be added to instruct SuperNEC that this method is to be used.

Numerical Accuracy

The calculation of eigenvectors and eigenvalues is a numerical process that is very sensitive to rounding errors.

It is not certain how significant the numerical errors in the above calculations are. Further investigation is required to determine at what level of asymmetry the results become unusable.

Once a Galerkin method has been implemented in SuperNEC, the basis functions can be compared for accuracy, and a workable method chosen.

The mode significances do not show convergence as the number of segments is increased. Some experimentation is needed to establish structure segmentation guidelines for characteristic modes solutions.

Antenna design

Characteristic modes are a useful tool in the analysis and synthesis of antennas, allowing a more intuitive approach to design than other methods involving iteration and optimising algorithms.

In [1], Austin and Murray use characteristic mode analysis of a structure to maximise vertical radiation from a vehicle antenna for NVIS communication. It is hoped to use a similar technique to generate a wire antenna for HF NVIS as well as low-angle communication. The antenna should be fed from a single port, and the dominant mode and hence radiation pattern changed by switching of loads and/or shorts.

6. Acknowledgements

The assistance of Dr Nitch in modifying the SuperNEC code is gratefully acknowledged.

7. References

1. Brian A Austin, Kevin P Murray, "The Application of Characteristic Mode Techniques to Vehicle-Mounted NVIS Antennas." *IEEE Antennas and Propagation Magazine* Vol. 40, No. 1, February 1998.
2. Roger F Harrington, Joseph R Mautz, "Theory of Characteristic Modes for Conducting Bodies." *IEEE Transactions on Antennas and Propagation*, Vol. AP-19, No. 5, September 1971.
3. Roger F Harrington, Joseph R Mautz, "Computation of Characteristic Modes for Conducting Bodies." *IEEE Transactions on Antennas and Propagation*, Vol. AP-19, No. 5, September 1971.
4. Duixian Liu, Robert J Garbacz, David M Pozar, "Antenna Synthesis and Optimisation Using Generalised Characteristic Modes." *IEEE Transactions on Antennas and Propagation*. Vol. 38, No. 6, June 1990.
5. Derek Nitch, "SuperNEC MOM-UTD Hybrid Technical Reference Manual." October 1996.

Review of Basic 3-D Geometry Considerations for Intelligent CEM Pre-Processor Applications

by

Kurt V. Sunderland
ANDRO Consulting Services
Beeches Technical Campus
Bldg. 2, Suite 1, Rte. 26N, Turin Road
Rome, NY 13440
sungod@borg.com

Abstract

An important application of an intelligent computer modeling and simulation pre-processor for computational electromagnetics (CEM) involves the validation of complex system geometries. This paper describes some solid analytical geometry concepts and algorithms that are being coded for developing expert system packages, such as ICEMES and E³EXPERT. The goal of this paper is to describe the synergy between the CEM engineer and the computer programmer or mathematician in developing software at the front end of rule-based pre-processor applications, and to explain how fundamental geometry concepts are being made part of new knowledge-based CEM modeling tools.

Introduction

Computational codes, graphical user interfaces, traditional as well as intelligent computer modeling and simulation pre-processors, and even 3-D video games are proliferating and are being realized on affordable personal computers that provide the necessary power and speed. Modern constructs allow newer ways to view problems and solutions. As a result, working through geometric spatial relationships has become more relevant than ever. At first glance, the simple solution of the distance between two points being

$$d = \sqrt{(x_2 - x_1)^2 + (y_2 - y_1)^2 + (z_2 - z_1)^2}$$

appears straightforward enough. However, real world validation complicates matters quickly. Still, many solutions can be reached using concepts from solid analytical geometry of undergraduate third semester calculus and from linear algebra. Even more advanced concepts, such as those involving Bezier curves, NURBs, and meshes, are not as out of reach to the typical software engineer as might be expected. As a side note, when writing programming code, *ceteris paribus*, simpler is better. Even though efficiency is crucial for real time movement on the screen, readability and extendibility are often more important for engineering simulation modeling.

Objects include points, lines, planes, circles, disks, cylinders, cones, spheres, and a myriad of shapes. With the move from the textbooks to the real world, it soon becomes obvious that shapes do not come in ideal forms all the time, nor are they always conveniently oriented along the coordinates' axes. More often than not, they are line segments, not lines; flat plates, not infinite planes; ellipses,

not circles or disks; non right, non circular cylinders with finite length and end caps not parallel to each other, and so forth.

This paper describes a few basic solid analytical geometry considerations that are being embodied at the front end of knowledge-based tools for CEM, in particular, the Intelligent Computational Electromagnetics Expert System (ICEMES) pre-processor [1, 2] and the Electromagnetic Environment Effects Expert Processor with Embedded Reasoning Tasker (E³EXPERT) [3]. Both of these tools incorporate modeling and simulation rules which are used to assess the integrity of CEM models that have been built a priori and/or newly-generated models which should be validated as a function of changing frequency, desired model fidelity, physics and CEM code. In general, these considerations involve integrity checks for individual object definitions, inter-object connectivity or intersection, and other basic CEM modeling aspects for surfaces in the presence of electromagnetic radiators.

Theory and Implementation

To begin, let us review simple problems in two dimensions, move up to simple problems in three dimensions, and build up tools one step at a time. A good place to begin is to find the intersection of two polygons in the xy-plane. This algorithm can be built upon the work of Prasad [4]. The plan is to go around each side of each polygon searching for intersection. This is done by comparing signs to see if both endpoints of one line segment lie on the same side of the other line segment, and vice versa.

Once reacquainted with the topic, one goes to 3-D space. At first, the literature reads differently from what one would expect. Explicit equations often will not suffice, where implicit equations and parametric equations will work. Implicit equations can better describe non-functions, such as circles. Parametric equations, where the variables themselves are functions of another variable, will draw out a graph in alternative ways and provide access to vector-valued functions. One thing to observe is that points are position vectors. Thus, finding the distance between two points involves subtracting the two position vectors, then solving for the square root of the dot product of this difference with itself. A dot product is a scalar defined as

$$U \cdot V = (u_1 v_1 + u_2 v_2 + u_3 v_3).$$

Before the engineering software developer can find the intersection of two polygons in 3-D space, he may start with making smaller algorithms for point to line segment and for line segment to line segment. A line segment AB is expressed parametrically by taking one endpoint A as the starting position vector for a reference; then subtracting the two endpoints (positions vectors) B-A for the directional vector with a scalar for length element of [0,1] resulting in

$$L(t) = A + Vt.$$

Hence, endpoint B = A + V. To find the minimum distance between a point P and a line segment AB and determine the point where this occurs on the segment: subtract the beginning endpoint A from the point P and project it onto the line segment. The projection is

$$(((P - A) \bullet V) / \|V\|^2) V.$$

$\|V\|^2$ is $V \bullet V$. If $((P - A) \bullet V)$ is greater than $V \bullet V$, then $t > 1$ and the closest point on line segment AB is B. If $((P - A) \bullet V)$ is less than zero, then $t < 0$ and the closest point on line segment AB is A. If t is an element of $[0,1]$, then the closest point is $A + (((P - A) \bullet V) / \|V\|^2) V$, and the minimum distance between the point and the line segment is the length between point P and this closest point.

Goldman [5] offers a concise solution for the intersection between two lines. The lines are expressed as

$$L_1(t) = P_1 + V_1 t \quad \text{and} \quad L_2(s) = P_2 + V_2 s.$$

Setting the two equations equal and solving for t results in

$$t = \text{Det}\{(P_2 - P_1), V_2, V_1 \times V_2\} / \|V_1 \times V_2\|^2$$

or

$$t = ((V_1 \times V_2) \bullet ((P_2 - P_1) \times V_2)) / \|V_1 \times V_2\|^2.$$

Similarly,

$$s = \text{Det}\{(P_2 - P_1), V_1, V_1 \times V_2\} / \|V_1 \times V_2\|^2$$

or

$$s = ((V_1 \times V_2) \bullet ((P_2 - P_1) \times V_1)) / \|V_1 \times V_2\|^2.$$

To review, a cross product is a vector defined as

$$A \times B = (a_y \cdot b_z - a_z \cdot b_y, a_z \cdot b_x - a_x \cdot b_z, a_x \cdot b_y - a_y \cdot b_x).$$

If the denominator is zero, then the lines are parallel. If the lines do not intersect then s and t are the parameters of the closest points on the lines. For line segments, if $t < 0$, then set $t = 0$; and if $t > 1$, then set $t = 1$; and similarly, for s .

Eberly [6] attacks the problem by creating a squared-distance quadratic function in s and t . He continues by working with the discriminant and using calculus to minimize the function over $[0,1]^2$.

Next, developing a method to determine whether a point and a finite plate intersect will be useful. The cross product of two distinct vectors is a nontrivial vector that is normal to both of the original vectors. A plane is defined by its normal and by its offset from the origin. For example, given a polygon, the question is asked if it is flat. Triangles are always flat, but a polygon with more sides can often be bent, which would warrant breaking up the polygon into smaller flat parts or adjusting the coordinates of suspect vertices. To determine flatness: take the cross product of each two consecutive sides, average these normals, and if any one normal is off from the average by more than some tolerance, return an error or a warning (unless multiple-order curved surfaces are allowable). By

normalizing the normals (i.e., ensuring unit length), one can find if a normal is off by using the following expression for unit vectors:

$$\cos \theta = U \bullet V.$$

The plane equation in standard form is

$$a(x-x_1)+b(y-y_1)+c(z-z_1) = 0,$$

where (a, b, c) is the normal vector and (x₁, y₁, z₁) is a point on the plane. In general form, it becomes

$$ax+by+cz+d=0,$$

with

$$d = -(ax_1+by_1+cz_1).$$

The next step is to plug a point into the plane equation. If zero (or some tolerance of zero), then the point is on the infinite plane. To determine if this coplanar point lies on the finite plate, first take a point within the finite plate. A point that could possibly be used is the segment connecting the midpoints of two consecutive sides, which form an angle less than 180 degrees. Connect this interior point with the point in question, and perform a line to line check around the sides. If there is intersection, then the coplanar point is off the plate.

After that, the next method is to define the spatial relationship between a line segment and the finite plate. A parametric form of a line equation is

$$x_L = x_1 + (x_2 - x_1)t, \quad y_L = y_1 + (y_2 - y_1)t, \quad z_L = z_1 + (z_2 - z_1)t$$

or

$$x_L = x_1 + it, \quad y_L = y_1 + jt, \quad z_L = z_1 + kt,$$

where t is an element of the Reals, and (i, j, k) is the directional vector. Substitute the line equation into the general plane equation and solve for t. This yields

$$t = e/f,$$

where

$$e = -((a \cdot x_1) + (b \cdot y_1) + (c \cdot z_1) + d) \quad \text{and} \quad f = (a \cdot i + b \cdot j + c \cdot k).$$

If f equals zero, then the line is parallel to the plane, and generally there is no intersection. If e also equals zero, then the infinite plane contains the line. To find out if the line segment intersects the finite plate, the line segment to line segment method around the sides of the plate is used. If necessary, the point to plate method is used with the endpoints of the line segment, as both endpoints may be on

the interior of the plate. If f is nonzero, then the intersection is a point. The point to plate and point to line segment methods are then used to see if this point of intersection is indeed on the line segment and the finite plate. To find out if two polygons in 3-D-space are connected, use line segment to finite plate looping around the sides of one polygon to the finite plane of the other polygon and vice versa.

Another example of an algorithm is finding the distance between a point P and an ellipse in 3-D space. In this case, an ellipse is an irregular hollow circle. There is a major radius and a minor radius of different lengths. The center C of the ellipse though not necessarily at the world origin, can be thought of as being the local origin. The cross product of the two radii defines the plane of the ellipse. The radii should be orthogonal to each other. Finding a location on the ellipse can be achieved parametrically for θ element of $[0, 2\pi]$ with

$$\cos \theta (r_{\text{major}} \text{ vector}) + \sin \theta (r_{\text{minor}} \text{ vector}).$$

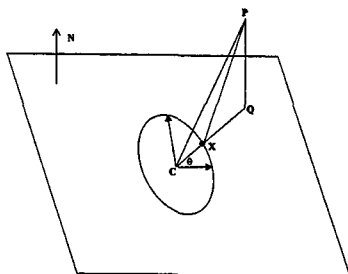


Figure 1. Distance from Point to Ellipse

In Figure 1, the projection $(P - C)$ onto the plane is $(Q - C)$, which is $(P - C) - \|P - Q\| N$, where N is the plane's normal of unit length and $\|P - Q\|$ is $N \cdot (P - C)$. By finding the angle θ between r_{major} and $(Q - C)$ with the equation

$$\cos \theta = (r_{\text{major}} \cdot (Q - C)) / (\|r_{\text{major}}\| \|Q - C\|)$$

one can use the parametric equation to find the point X where $Q - C$ intersects the ellipse. If point P hovers right above the center C within some tolerance, then the distance between the point and the ellipse is

$$d = \sqrt{\| \text{radius} \|^2 + \|P - C\|^2}$$

where radius is the shorter of the two radii. Otherwise, take the length of the vector $(P - C) - (X - C)$, and the minimum distance between a point to an ellipse is determined.

These basic tools or methods can be employed to discern geometrical relationships with more complex objects, such as elliptical cylinders and cones. A cylinder is an ellipse extended along an orientation vector, which might not be the same as the normal vector. One starts by culling down possibilities on a case by case basis. Determining the distance between an object and the cylinder's orientation axis relative to radius' length is a good start. Checking if an endpoint lies above, below, or in between the two end caps' planes is also a useful test. A cone can be considered as a cylinder whose radius changes linearly with the distance along the orientation vector. Interpolation will meet this task, even for frusta.

Conclusion

The realms of CEM engineering and Computer Aided Graphic Design continue to merge as the power and speed of PC's grow rapidly and new paradigms emerge. One of the aims of this paper has been to provide insight to the CEM engineer in working with the graphic designer of computer simulation applications. Several basic validating algorithms of 3-D-space geometries have been demonstrated using concepts from undergraduate calculus and elementary linear algebra. The methods and tools described above only scratch the surface. These have been extended to more complex objects and modeling scenarios, and are being implemented in more rigorous fashion within tools like ICEMES and E³EXPERT in an attempt to sufficiently capture and automate CEM model integrity testing and validation reasoning using knowledge-based, expert system techniques. Updates on the progress of this research and development will be the subject of future ACES publications.

Further recommended reading on this subject includes *Graphic Gems*, which conveniently provides example code in C language and is an ongoing series. Foley *et al.* [7] sets a standard in the graphics field and gives among other things a good coverage of transformations and parametric cubic curves. Rockwood and Chambers [8] teaches the reader about Bezier curves and surfaces. They also give an interactive electronic book that is helpful. Their book moves right along at a senior undergraduate/beginning graduate level. It is suggested that the reader may wish to review Larson *et al.* [9] for calculus and Kolman [10] for linear algebra.

References

- [1] A. L. Drozd, T. W. Blocher, et al., "Illustrating the Application of Expert Systems to Computational Electromagnetics Modeling and Simulation", In *Conference Proceedings of the 14th Annual Review of Progress in Applied Computational Electromagnetics* (Monterey, CA, Mar. 16-20), 1998, pp. 36-41.
- [2] A. L. Drozd and T. W. Blocher, "Heuristics-Based Computational Electromagnetics: A State-of-the-Art Technique for End-to-End EMC Modeling and Analysis of Large, Complex Structures", In *Conference Proceedings of the 1998 IEEE International Symposium on Electromagnetic Compatibility* (Denver, CO, Aug. 23-28 August), 1998, pp. 1144-1149.

- [3] A. L. Drozd, A. J. Pesta, et al., "Application and Demonstration of a Knowledge-Based Approach to Interference Rejection for EMC", In *Conference Proceedings of the 1998 IEEE International Symposium on Electromagnetic Compatibility* (Denver, CO, Aug. 23-28), 1998, pp. 537-542.
- [4] Mukesh Prasad, "Intersection of Line Segments", *Graphic Gems II*, Academic Press, San Diego, CA, 1991, pp. 7-9.
- [5] R. Goldman, "Intersection of Two Lines in Three-Space", *Graphic Gems*, Academic Press, San Diego, CA 1990, p. 304.
- [6] D. Eberly, "Distance between Two Line Segments in 3-D", available through the Internet: <http://www.eberly@Magic-software.com>
- [7] J. D. Foley, A. van Dam, S. K. Feiner and J. F. Hughes, *Computer Graphics: Principles and Practice*, 2nd ed., Addison-Wesley, New York, 1990.
- [8] A. Rockwood and P. Chambers, *Interactive Curves and Surfaces*, Morgan Kaufmann, San Francisco, 1996.
- [9] R. E. Larson, R. P. Hostetler, and B. H. Edwards, *Calculus with Analytic Geometry*, 5th ed., D. C. Heath and Company, Lexington, Massachusetts, 1994.
- [10] B. Kolman, *Elementary Linear Algebra*, 2nd ed., Macmillan Publishers, New York, 1977.

MODELLING OF LOADED WIRE CONDUCTOR ABOVE PERFECTLY CONDUCTING GROUND BY USING 3D TLM METHOD

Nebojša S. Dončovi¹, Bratislav D. Milovanović¹, Vladica M. Trenkić²

¹Faculty of Electronic Engineering, University of Niš, Yugoslavia, E-mail: [doncov, bata]@elfak.ni.ac.yu

²Kimberley Communications Consultants Ltd., Nottingham, U.K., E-mail: vlada@kccuk.com

Abstract - In this paper, coupling between electromagnetic field of dipole antenna and loaded thin wire structures is modelled by using the transmission-line modelling (TLM) method. Two basic integrated 3-D TLM solutions of wire modelling are presented and compared for the appropriate example. Two models, for describing connection of a resistive load at the wire ends to perfectly conducting ground are proposed and verified. Calculated results are presented in a frequency domain and compared with the results obtained by using miniNEC simulator.

INTRODUCTION

In many problems in applied electromagnetics it is necessary to simulate coupling between electromagnetic field and wires. Examples are in electromagnetic compatibility (EMC), in antennas and in microwave design. Focusing in particular on the electromagnetic compatibility problems, the main difficulty as far as numerical modelling is concerned is that it is normally inefficient to describe in detail the geometrical features of wires in a mesh which is normally configured to model propagation in a large space, e.g. free-space, room, or equipment cabinet. The problem is particularly acute when differential numerical methods, such as transmission-line modelling (TLM) method and finite-difference time-domain (FD-TD) method, are used in modelling.

Two basic approaches for treating wires in TLM have evolved: the so-called separated [1,2,3] and integrated solutions [4,5,6,7,8]. In the separated solutions, the wires are treated separately from the rest of the problem, allowing for field coupling to the wire by introducing equivalent sources derived from knowledge of the incident fields in the vicinity of the wire. Separated solutions for TLM are simple and can deal easily with both single and multi-wire problems. However, they have obvious limitation that any electromagnetic interaction of the wires with the rest of the modelled structures must be negligible small. So, it is only one-way coupling from the electromagnetic field to the wires that is effectively modelled by separated solutions which is, clearly, inadequate for EMC problems.

The simplest integrated solutions in TLM are those where wires are modelled by using short-circuit nodes or shorted link-lines adjacent to the wire surface. In that way wires are explicitly included in the model, hence the model is consistent and two-way coupling is simulated. However, computational resource limitations and geometrical disparity between whole modelled space and core of the EMC problem, means that the wire is usually modelled by no more than a single node cross-section on a rectangular Cartesian mesh. This results in a rather crude "rectangular shape" model of the wire. More sophisticated integrated solution (TLM wire node), which can allow for accurate modelling of wires with a considerably smaller diameter than the node size, uses special wire networks embedded between [4] or within nodes [5,6,7,8] to model signal propagation along the wire, while allowing for interaction with the electromagnetic field. In order to accomplish this task, the wire network is formed by using additional link and stub lines. The ability to model very fine wires without excessive computational costs makes the wire node increasingly popular in TLM simulations.

In this paper, for the example of resonant frequency calculation of dipole antenna in free space, advantage of TLM wire node in relation to first integrated wire solutions is shown. After that, wire conductor above perfectly conducting ground, excited by dipole antenna (Fig.1), is modelled by using TLM wire node. In order to verify the obtained TLM

results, for the case of unloaded wire conductor ($R_1 = R_2 = \infty$), the same structure is analysed by using miniNEC, a simulator based on the method of moments.

In EMC problems, beside geometrical features of the wire, it is necessary to model exactly lossy terminations of the wire [8,9]. In this paper, for the example of loaded wire conductor in the field of dipole antenna (Fig.1) and by using TLM wire node, two possible models for describing connection of a resistive load at the wire ends to perfectly conducting ground are considered. Calculated results for the current induced at the one end of wire conductor are shown in the frequency domain and compared with those obtained by running miniNEC simulator.

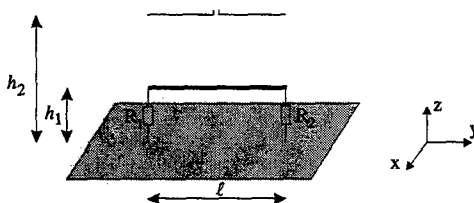


Fig.1 Loaded wire conductor above perfectly conducting ground in the field of dipole antenna

THEORETICAL BACKGROUND

The simplest integrated TLM solutions describe wire by using short-circuit nodes (Fig.2a) or shorted link-lines adjacent to the wire surface (Fig.2b) [1]. In the first case, wire presence in the mesh is included by modifying the scattering matrix in the following way:

$${}_nV^r = -{}_nV^i \quad (1)$$

where ${}_nV^i$ and ${}_nV^r$ are vectors of incident and reflected voltages, respectively, on appropriate TLM link-lines at time-step n . The scattering matrix for the short-circuit node is diagonal with elements equal to -1.

In the second case, the connection matrix is modified in the following way:

$${}_{n+1}V^i = {}_nV^r. \quad (2)$$

In both cases, the wire is usually modelled by no more than a single cross-section, which causes shift of the resonance by (5+10) % to lower frequencies, a problem that is referred to as "resonance error" [7].

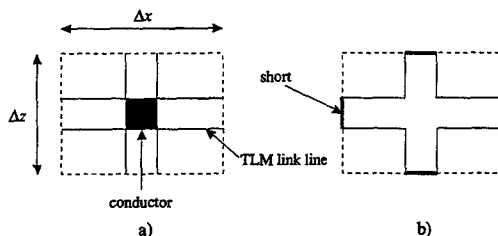


Fig.2 Cross-section of the wire running in y direction, modelled by:
a) short-circuit TLM node, b) shorted TLM link-lines

In TLM wire node [6,7], wire structures are considered as new elements that increase the capacitance and inductance of the medium in which they are placed. Thus, an appropriate wire network needs to be interposed over the existing TLM network to model the required deficit of electromagnetic parameters of the medium. In order to achieve consistency with the rest of the TLM model, it is most suitable to form wire networks by using TLM link and stub lines (Fig.3) with characteristic impedances, denoted as Z_{wy} and Z_{wzy} , respectively.

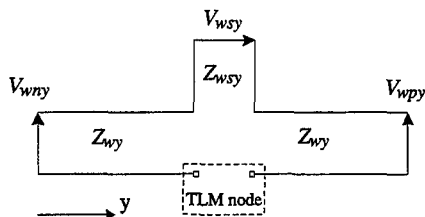


Fig.3 Wire network

An interface between the wire network and the rest of TLM network must be devised to simulate coupling between the electromagnetic field and the wire. In order to model wire junction and bends, wire network segments pass through the centre of the TLM node (Fig.4). In that case, coupling between the field and wire coincides with the scattering event in the node which makes the scattering matrix calculation, for the nodes containing a segment of wire network, more complex. Because of that, a simple and elegant approach is developed [6], which solves interfacing between arbitrary complex wire network and arbitrary complex TLM nodes without a modification of the scattering procedure.

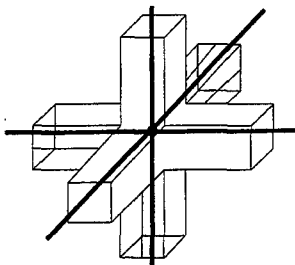


Fig.4 Wire network segments embedded within the TLM node

RESISTIVE LOAD TERMINATION

In TLM method, resistive load at the end of the wire can be treated in two ways [8,9]. In the first case, lossy termination is shifted to the centre of the last wire segment, causing changes in scattering procedure of the wire node. Also, resistive load can be defined exactly at the wire end, and in that case, a Thevenin equivalent circuit is used to determine the required reflection coefficient (Fig.5). A resistor R has been used to connect the minimum end of wire to a nearby ground or metal. The required reflection coefficient ρ for this wire termination is given by:

$$\rho = \frac{R - Z_{wy}}{R + Z_{wy}} \quad (3)$$

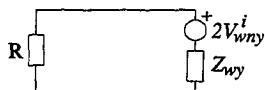


Fig.5. Lossy termination for minimum end of wire

Depending of its location, load termination connects wire to basis of fictitious cylinder in points a and b (Fig.6). Fictitious cylinder represents capacitance and inductance of wire per unit length and approximately is modelled by the single column of TLM cells through which is passes. Its diameter is the effective diameter of a column of metal filled TLM cells, which is unfortunately, different for capacitance and inductance and is obtained empirically [9]. Connection between fictitious cylinder and wire is realised only if they are on equal potential, i.e. if appropriate TLM ports are shorted.

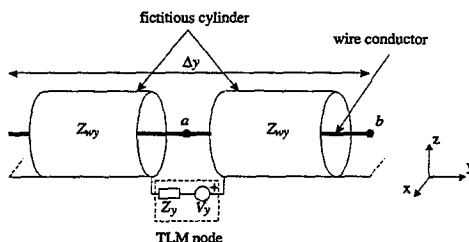


Fig.6 Fictitious cylinder

For describing connection of a resistive load at the wire ends to perfectly conducting ground, two possible models are proposed in this paper. First model is based on using short lines on appropriate face of the last TLM wire nodes (Fig.7a), while second model, beside straight wire segments, uses bent-wire segments [9] at the ends of the wire (Fig.7b). In both models, resistive load should be located in point a (R included by calculating the reflection coefficient from Eq. (3)) or b (R included in the scattering matrix calculation).

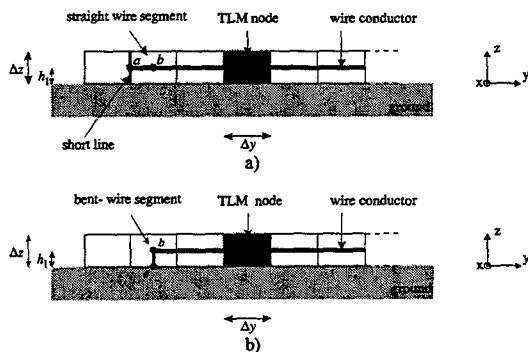


Fig.7 Models of describing connection of a resistive load at the wire ends to perfectly conducting ground

NUMERICAL ANALYSIS

Advantage of TLM wire node in relation to first integrated wire solutions is shown for the example of resonant frequencies calculation of dipole antenna, length $\ell=1$ m, in free space. At first, dipole antenna is modelled by using shorted link-lines adjacent to the wire surface with a single node cross-section on a rectangular Cartesian mesh. Dipole antenna is excited by impulse magnetic field along a closed path c surrounding the wire, based on Ampere's law:

$$\oint_c \vec{H} d\vec{l} = I. \quad (4)$$

Axial component of electromagnetic field of dipole antenna, for the case of uniform TLM mesh ($\Delta x = \Delta y = \Delta z = 4.76$ cm), is shown in Fig.8. Two resonances, which can be noticed, are far away from theoretical resonant frequencies for thin dipole antenna: 150 MHz and 450 MHz. This great deviation between calculated and theoretical results can be explained with a rather crude "rectangular shape" model of the wire.

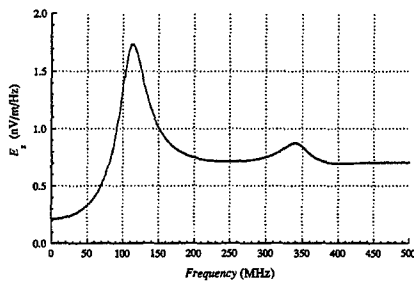


Fig.8 Resonant frequencies of dipole antenna in free space, modelled by using shorted TLM link-lines

At the same time, dipole antenna is modelled by using TLM wire node. It is used uniform TLM mesh with $35 \times 35 \times 50$ nodes and dimensions of node $\Delta x = \Delta y = \Delta z = 4.76$ cm. Radius of dipole antenna is $r=5$ mm. At the centre of dipole antenna, it is applied, as an excitation, voltage source $V_{source}=1$ V with 50-Ohm impedance to reduce the sharpness of the resonances. Fig.9 shows the current magnitude at the centre of dipole antenna.

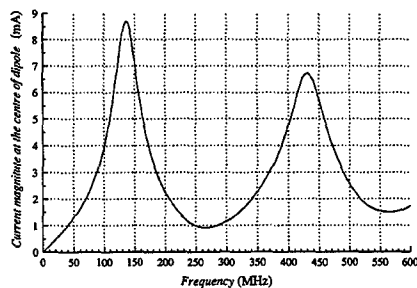


Fig.9 Resonant frequencies of dipole antenna in free space, modelled by using TLM wire node

As it can be seen from Fig.9, calculated TLM results are much closer to theoretical resonant frequencies, even the same TLM node dimensions are used as in the previous case.

After that, unloaded wire conductor (Fig.1, $R_1 = R_2 = \infty$), length $\ell=1$ m and radius $r=2.5$ mm, above perfectly conducting ground ($h_1=2.4$ cm), in the field of dipole antenna ($h_2=52.4$ cm), is modelled by using TLM wire node. For the TLM simulation, it is used non-uniform mesh with $35 \times 75 \times 50$ nodes. Resolution of the TLM mesh is increased in the space between wire conductor and dipole antenna. Magnitude of induced current at the centre of wire conductor, and current distribution along wire conductor at resonant frequency $f=440$ MHz, obtained by using TLM wire node (solid line) and miniNEC simulator (dotted line) are shown in Figs.10 and 11, respectively. To reduce the sharpness of the resonances, 50-Ohm impedance is placed at the centre of wire conductor.

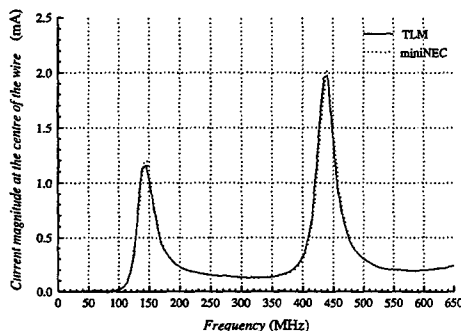


Fig.10 Magnitude of induced current at the centre of the unloaded wire conductor, obtained by using: TLM wire node (solid line) and miniNEC simulator (dotted line)

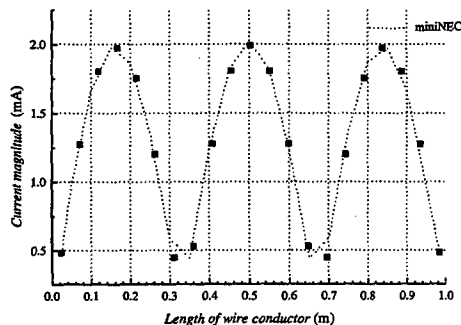


Fig.11 Current distribution along unloaded wire conductor at $f=440$ MHz, obtained by using: TLM wire node (■) and miniNEC simulator (dotted line)

It can be noticed excellent agreement between TLM results and results obtained by running miniNEC simulator, which indicates good TLM modelling of wire conductor above perfectly conducting ground.

For the example of wire conductor with same dimensions, terminated at both ends with $R_1 = R_2 = 100 \text{ Ohm}$, two proposed models, for describing connection of a resistive load at the wire ends to perfectly conducting ground, are verified. Magnitude of induced current at the one end of loaded wire conductor in the frequency domain, obtained by applying the proposed models and miniNEC simulator, is shown in Figs. 12 and 13, respectively. As it can be seen, both models give good results in comparison with miniNEC results and could be used for resonant frequency prediction of loaded wire conductor. However, it should be noticed that the first model gives better results at lower frequencies, while the second model better describes the modelled connection at higher frequencies. Also, model decision strongly depends on type and geometrical features of the termination and wire structures [8].

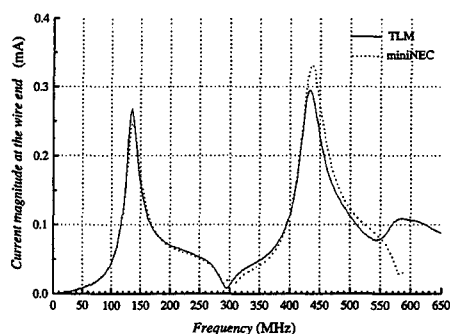


Fig.12 Magnitude of induced current at the wire end, obtained by using the first model (Fig.7a)

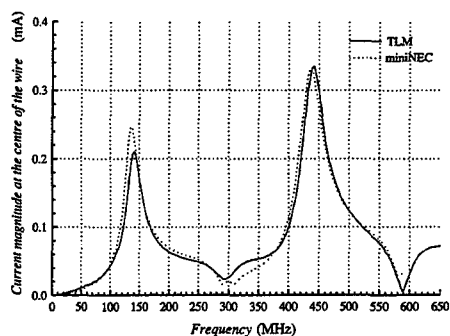


Fig.13 Magnitude of induced current at the wire end, obtained by using the second model (Fig.7b)

CONCLUSION

In this paper, two current integrated TLM solutions of couple modelling between electromagnetic field and wire structures are presented. For the appropriate example, the advantage of TLM wire node in relation to the first integrated wire solutions is shown. The key feature of the presented wire node is its ability to model very fine wires on the otherwise coarse mesh, making it adequate for the large modelling space encountered in the EMC problems. With some recent

developments (integrated multiconductor TLM model), TLM method can now be used to model very complicated wire structures, without generating excessive demand for computing resources.

For the first time, two TLM models, for describing connection of a resistive load at the wire ends to perfectly conducting ground are proposed and verified in this paper. The results obtained with these models are found to be in very good agreement with the Method of Moments model. In this paper, we have assumed that only resistive loads (i.e. no capacitors or inductors) are used for the termination. A further generalisation of proposed models is possible for termination modelling by arbitrary lumped circuits.

REFERENCES

- [1] C.Christopoulos, *The Transmission-Line Modelling Method*, Series on Electromagnetic Wave Theory, IEEE/OUP, 1995.
- [2] J.G.Herring, *The Developments in The Transmission Line Modelling Method for Electromagnetic Compatibility Studies*, Ph.D. Thesis, University of Nottingham, 1993.
- [3] B.Milovanović, N.Dončov, S.Tomovska, *TLM Modelling of Field-to-Wire Coupling*, Proceedings of the 6th Telecommunications Forum TELFOR'98, Beograd, Yugoslavia, pp.513-516, 1998.
- [4] A.Wlodarczyk, D.P.Johns, *New Wire Interface for Graded 3-D TLM*, Electronic Letters, Vol. 28, No.8, pp.728-729, 1992.
- [5] J.A.Porti, J.A.Morente, M.Khalladi, A.Gallego, *Comparison of Thin-Wire Models for TLM Method*, Electronic Letters, Vol.28, No.20, pp.1910-1911, 1992.
- [6] V.Trenkić, C.Christopoulos, *An Efficient Implementation of Wire Nodes in TLM*, Proceedings of the 2nd International Workshop on TLM Modelling- Theory and Applications, Munich, Germany, pp.60-67, 1997.
- [7] V.Trenkić, A.J.Wlodarczyk, R.A.Scaramuzza, *Modelling of Coupling between Transient Electromagnetic Field and Complex Wire Structures*, International Journal of Numerical Modelling: Electronic Networks, Devices and Fields, 1999.
- [8] B.Milovanović, N.Dončov, V.Trenkić, *TLM Modelling of Loaded Two-Wire Line in the Field of Dipole Antenna*, Proceedings of the 4th International IEEE MTT AP & ComSoc Conference TELSIS'99, Niš, Yugoslavia, pp.202-205, 1999.
- [9] R.Scaramuzza, *Wire Node for TLM simulation*, Tech.Rep.KCC524: Issue 1, Kimberley Communications Consultants Ltd., 1997.

Evanescent tunneling and quantile motion of electromagnetic waves in wave guides of varying cross section

E. Gjonaj

Technische Universität Darmstadt, FB 18 Elektrotechnik und Informationstechnik, Fachgebiet Theorie Elektromagnetischer Felder, Schlossgartenstr. 8, D-64289 Darmstadt, Germany. E-mail: gjonaj@temf.tu-darmstadt.de

Abstract—We discuss applications of the quantile concept of trajectories and velocities of electromagnetic waves propagating in wave guides of varying cross section. Quantile motion is a general description for the transport properties of measurable conserved quantities in quantum mechanics as well as in classical electrodynamics. Here, we show that the quantile motion of electromagnetic energy in a wave guide is the direct result of an electromagnetic signal measurement. Thus, the quantile velocity corresponds to the electromagnetic signal velocity also in the evanescent tunneling regime, in the presence of barriers and inhomogeneities in the medium of propagation. We show that this signal velocity is always smaller than the speed of light in vacuum. Using numerical examples we demonstrate how typical wave phenomena can be described in terms of quantile motion.

I. INTRODUCTION

In recent years the tunneling of an evanescent electromagnetic pulse in a wave guide with a cross section reduced over part of its longitudinal extension has been studied. In a series of microwave experiments [1–3] the electromagnetic signal velocity was identified with the velocity of the maximum of the pulse crossing over the wave guide. This assumption led to the prediction of superluminal signal velocities in the evanescent tunneling regime. The same assumption was also adopted from Chiao et al. in similar tunneling experiments with thin dielectric barriers [4].

The concept of quantile motion has already been used for the calculation of tunneling times in the quantum mechanical tunneling [5]. In this paper we extend this concept to describe the motion electromagnetic waves through barriers and inhomogeneities in the medium of propagation. The aim of this paper is the calculation of tunneling times, i.e., the time an electromagnetic wave spends in a barrier region as well as the times it takes for the wave to be transmitted through and reflected by the barrier, respectively. The magnitude of the electromagnetic tunneling times is of considerable importance for several imaging techniques [6] and semiconductor device models [7]. From the theoretical point of view, the calculation of tunneling times is strongly related to the causality of signal propagation, i.e., to the question of superluminal velocities in the evanescent tunneling regime.

In our quantile model the arrival times of the electromagnetic signal are measured by means of physical

detectors located on both sides of the barrier. A physical detector always needs a certain amount of energy to signalize a change of its state, therefore we use the quantile velocity of a density obtained by way of normalizing the electromagnetic energy density of the pulse to unity [5]. Depending on the sensitivity of the detector, quantile trajectories are obtained, from which tunneling times and velocities are derived.

In the following a numerical simulation of the microwave experiments with wave packets in wave guides with varying cross section is carried through and the quantile trajectories of tunneling wave packets are calculated numerically. It is shown rigorously that the quantile velocity is not superluminal. A short discussion of the quantile motion in dispersive and absorptive media is presented.

II. STATIONARY WAVES IN WAVE GUIDES OF VARYING CROSS SECTIONS

We shall consider a wave guide of rectangular cross section and perfectly conducting walls, extending in the longitudinal z direction from $-\infty$ to $+\infty$. The simplest construction allowing for an interpretation in terms of tunneling for an electromagnetic signal propagating in the wave guide is obtained by assuming a narrowing of the cross section, e.g., in the transverse x direction extending to the left of the origin for $z > 0$ as shown in Fig. 1.

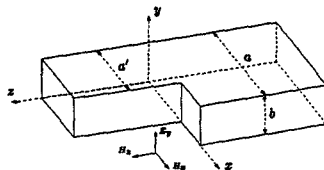


FIG. 1. Geometry of a wave guide with a one-sided reduction of the cross section at origin extending to infinity.

For the sake of simplicity we shall consider only the propagation of TE -waves of the type H_{n0} . Such a situation can be realized indeed if we choose a constant height of the wave guide (given by b in Fig. 1) small enough for all waves of the type H_{nm} with $m \geq 1$ to be everywhere evanescent. Thus, the stationary electromagnetic field in the wave guide reduces to the three field components, E_y ,

H_x , and H_z , each depending on x and z . One of the field components can be considered as independent, e.g., E_y , whereas the other two follow from the Maxwell equation $i\omega\mu\mu_0\mathbf{H} = \nabla \times \mathbf{E}$, where ω is the frequency of the wave and $\mu = 1$ is the magnetic permeability of vacuum.

The solution for the stationary electric field component E_y fulfilling the Helmholtz wave equation with the appropriate boundary conditions is a superposition of modes

$$E_y^{n0}(x, z) = \begin{cases} \sin\left(\frac{n\pi x}{a}\right)e^{\pm i\kappa_n z}, & z < 0, \\ \sin\left(\frac{n\pi x}{a'}\right)e^{\pm i\kappa'_n z}, & z > 0, \end{cases} \quad (1)$$

where we denote $\kappa_n = \sqrt{(\omega/c)^2 - (n\pi/a)^2}$ and $\kappa'_n = \sqrt{(\omega/c)^2 - (n\pi/a')^2}$ the discrete wave numbers associated with the two regions of the wave guide.

Considering a given mode H_{m0} as the incoming wave incident from the right ($z < 0$) we are led to the solution ansatz

$$E_y(x, z) = \begin{cases} \sin\left(\frac{m\pi x}{a}\right)e^{i\kappa_m z} + \sum_{n=1}^{\infty} \mathcal{A}_n^R \sin\left(\frac{n\pi x}{a}\right)e^{-i\kappa_n z} \\ \sum_{n=1}^{\infty} \mathcal{A}_n^T \sin\left(\frac{n\pi x}{a'}\right)e^{i\kappa'_n z} \end{cases} \quad (2)$$

in the regions $z < 0$ and $z > 0$, respectively. Here, \mathcal{A}_n^R and \mathcal{A}_n^T are the (complex) amplitudes of the reflected and transmitted modes. Since an infinite number of different modes is needed in order to fulfill the boundary conditions at $z = 0$, the type of the outgoing wave never coincides with that of the incident one.

Requiring continuity for the electric field component E_y and for the transverse magnetic field component H_x at the wave guide aperture at $z = 0$, we obtain after a short calculation the integral equation

$$\int_0^{a'} dx' K(x, x') \epsilon(x') = \kappa_m \sin\left(\frac{m\pi x}{a}\right), \quad 0 \leq x \leq a, \quad (3)$$

with the value of the electric field strength at the aperture, $\epsilon(x) = E_y(x, z = 0)$, as unknown function. The kernel $K(x, x')$ is given by the series

$$K(x, x') = \sum_{n=1}^{\infty} \left[\frac{\kappa_n}{a} \sin\left(\frac{n\pi x}{a}\right) \sin\left(\frac{n\pi x'}{a}\right) + \frac{\kappa'_n}{a'} \sin\left(\frac{n\pi x}{a'}\right) \sin\left(\frac{n\pi x'}{a'}\right) \right], \quad (4)$$

which diverges throughout the integration region. In order to determine the reflection and transmission amplitudes \mathcal{A}_n^R and \mathcal{A}_n^T one has to expand the solution $\epsilon(x)$ of the integral equation (3) into the normal mode solutions in the respective wave guide regions.

The integral equation (3) is generally not solvable in closed form and the field $\epsilon(x)$ has to be determined numerically. We can, however, try to find approximate expressions for \mathcal{A}_n^R and \mathcal{A}_n^T by using the alternative representation of the integral equation (3) as a system of linear equations for the coefficients $\mathcal{A}_n^{(2)}$,

$$\sum_{n=1}^{\infty} \left[\delta_{nk} + \frac{4}{aa'\kappa'_k} T_{nk} \right] \mathcal{A}_n^{(2)} = \frac{4\kappa_m}{a'\kappa'_k} \Lambda_{mk}, \quad (5)$$

where $T_{nk} = \sum_{l=1}^{\infty} \kappa_l \Lambda_{ln} \Lambda_{lk}$ and

$$\Lambda_{mk} = (-1)^k \frac{a'k}{\pi} \frac{\sin(m\pi a'/a)}{(ma'/a)^2 - k^2}. \quad (6)$$

Under certain conditions discussed below we can assume the transition matrix T to be nearly diagonal and write its elements as

$$T_{nk} = \kappa'_k \left(\frac{a'}{2}\right)^2 (\delta_{nk} + m_{nk}). \quad (7)$$

Here, m is a complex matrix with elements fulfilling $|m_{nk}| \ll 1$. The solution of (5) follows then from the expansion of the corresponding inverse matrix into a fast converging Neumann series

$$\mathcal{A}_n^{(2)} = \frac{4\kappa_m}{a'} \left(\frac{a}{a'}\right) \sum_{k=1}^{\infty} \left[1 - \left(\frac{a'}{a+a'}\right)m + \dots \right]_{nk} \frac{\Lambda_{mk}}{\kappa'_k}.$$

Neglecting all the terms but the leading one in the above expansion, we obtain the coefficients

$$\mathcal{A}_n^{(2)} = (-1)^n \left(\frac{a}{a+a'}\right) \frac{4n\kappa_m}{\pi\kappa'_n} \frac{\sin(m\pi a'/a)}{(ma'/a)^2 - n^2}, \quad (8)$$

implying at $z = 0$, e.g., a transverse magnetic field component H_x given by

$$H_x(x, 0) = -\left(\frac{2a}{a+a'}\right) \frac{\kappa_m}{\omega\mu\mu_0} \sin\left(\frac{m\pi x}{a}\right). \quad (9)$$

Equation (9) predicts an increase in the magnitude of the transverse magnetic field component H_x at $z = 0$ (which is expected for this wave guide configuration), but the shape of the field there still coincides with that of the incident mode H_{m0} . Thus, the approximation leading to (8) seems appropriate in the limiting case of geometric optics, i.e., if the wave length is short compared to the cross sections a and a' of the wave guide. In the case of an evanescent wave for $z > 0$, however, more terms in the above expansion are needed for the boundary conditions at $z = 0$ to be fulfilled. Therefore, a numerical solution of equation (3) is used in what follows.

We now turn to a more complicated geometry for the wave guide involving two boundary conditions at $z = 0$ and $z = L$, where L is the length of a symmetrically placed barrier as shown in Fig. 2.

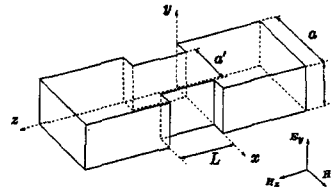


FIG. 2. Geometry of a wave guide with a symmetric reduction of the cross section between $z = 0$ and $z = L$.

Numerical simulations of the stationary field components in the wave guide are shown in Fig. 3 and Fig. 4. The continuity of the transverse field components at the wave guide aperture as well as the magnetic field singularities at the narrowing edges are shown in Fig. 3. Figure 4 is a spectral diagram with reflection and transmission coefficients (in the regions $z < 0$ and $z > L$, respectively) of the incident mode and of the next higher mode.

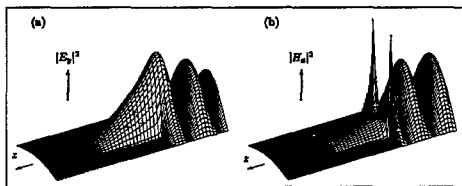


FIG. 3. Stationary fields in evanescent tunneling. The wave guide dimensions are $a = 1$ cm, $a' = 0.4$ cm, and $L = 1$ cm (see Fig. 2). The incoming wave incident from the right is the H_{10} mode of frequency $\omega = 21$ GHz.

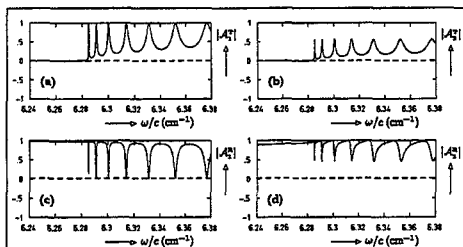


FIG. 4. Spectral diagram with the transmission and reflection coefficients of the first two modes H_{10} and H_{20} , where H_{10} is the incident mode. The wave guide dimensions are $a = 1$ cm, $a' = 0.5$ cm, and $L = 1$ cm (see Fig. 2).

Because of the magnetic field singularities, in a real experiment the local maxima of the magnetic field strength would always be located in the vicinity of the wave guide edges. A measurement of the field maxima would, therefore, give no information on the velocity of a tunneling electromagnetic signal. If, instead, we refer to the electromagnetic energy density in the wave guide we can avoid dealing with singularities by recalling that the singularities of the energy density are integrable. Poynting's theorem in our case reads

$$\frac{\partial w_{em}(x, z, t)}{\partial t} + \frac{\partial s_x(x, z, t)}{\partial x} + \frac{\partial s_z(x, z, t)}{\partial z} = 0, \quad (10)$$

where w_{em} is the two-dimensional energy density and s_x and s_z are the components of the Poynting vector. Integrating (10) over the transverse direction x the second term in (10) vanishes and we obtain

$$\frac{\partial}{\partial t} \mathcal{W}(z, t) + \frac{\partial}{\partial z} \mathcal{S}_z(z, t) = 0, \quad (11)$$

where $\mathcal{W}(z, t)$ and $\mathcal{S}_z(z, t)$ are now the one-dimensional energy and current densities in the longitudinal direction z . These quantities are free of singularities and fulfill the one-dimensional continuity equation (11). Therefore, it is appropriate to consider the energy density $\mathcal{W}(z, t)$ instead of the electric and magnetic field strengths in order to investigate the tunneling properties of electromagnetic signals in wave guides.

Returning to the stationary fields, we may use (11) to obtain unitarity relations between the reflection and transmission coefficients of the modes \mathcal{A}_n^R and \mathcal{A}_n^T . We find the time-averaged longitudinal current

$$\tilde{S}_z(z) = -\frac{1}{2} \text{Re} \int dx E_y(x, z) H_z^*(x, z) \quad (12)$$

to be a constant along the wave guide. Comparing the expressions for $\tilde{S}_z(z)$ in the reflection and transmission region we obtain the unitarity relation

$$\sum_{n=1}^{n_c} \frac{\kappa_n}{\kappa_m} |\mathcal{A}_n^R|^2 + \frac{a'}{a} \sum_{n=1}^{n'_c} \frac{\kappa'_n}{\kappa_m} |\mathcal{A}_n^T|^2 = 1, \quad (13)$$

where H_{m0} is the incident mode, H_{n_c0} and $H_{n'_c0}$ are the cut-off-modes in the reflection and transmission region, respectively. The appearance in (13) of the upper limits n_c and n'_c in the summation index n is a consequence of time averaging the current density $\mathcal{S}_z(z)$. Thus, equation (13) does not imply, that only propagating modes $n \leq n_c$ ($n \leq n'_c$) are responsible for the energy transport through the barrier. Energy transfer over the barrier occurs in the time-harmonic case also through the evanescent modes making possible the so-called electromagnetic tunneling.

III. TUNNELING OF WAVE PACKETS. COMPARISON WITH EXPERIMENTS

In the following we construct tunneling wave packets in the wave guide as a superposition of the stationary solutions found above. For such a superposition to be a propagating, incoming wave in the region to the right of the barrier ($z < 0$) it must not contain wave components below the cut-off-frequency ω_c (evanescent components) in this region. Therefore we use, e.g., for the electric field component E_y the expression

$$E_y(x, z, t) = \int_{\omega_c}^{\infty} d\omega f(\omega) E_{ys}(x, z; \omega) e^{-i\omega t}, \quad (14)$$

where $f(\omega)$ is the spectral distribution of frequencies normalized in the interval (ω_c, ∞) and E_{ys} is the stationary electric field component.

In Fig. 5–Fig. 7 numerical simulations with Gaussian-like wave packets in the wave guide are shown. The spectral distribution $f(\omega)$ in this case is given by

$$f(\omega) = \frac{1}{\tilde{N}} \frac{\Theta(\omega - \omega_c)}{(\sqrt{2\pi}\sigma_\omega)^{1/2}} \exp\left(-\frac{(\omega - \omega_0)^2}{4\sigma_\omega^2}\right), \quad (15)$$

where \tilde{N} is a normalization factor, ω_0 is the mean frequency and σ_ω is the spectral width of the wave packet.

Figure 5 demonstrates the tunneling process through a symmetrically placed barrier in the wave guide for an incident mode of the type H_{10} . The wave guide dimensions are $a = 1$ cm, $a' = 0.5$ cm, and $L = 5$ cm. The incident Gaussian wave packet is centered about $\omega_0 = 30$ GHz with spectral width $\sigma_\omega = 1.5$ GHz. Most of the frequencies of the spectrum (15) are taken above the cut-off frequency ω'_c of the barrier region $L > z > 0$.

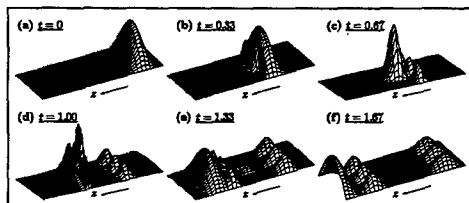


FIG. 5. Time development of a tunneling Gaussian wave packet. The electric field strength $|E_y|^2$ is shown. Times are given in picoseconds.

In Fig. 6 the resonant tunneling of a Gaussian wave packet is shown. The wave guide dimensions are the same as in Fig. 4. The spectral function of the incoming wave packet centered at $\omega_0 = 18.97$ GHz with $\sigma_\omega = 0.015$ GHz extends over more than one resonance (see also Fig. 4) leading to multiple reflections of the wave packet at the barrier walls.

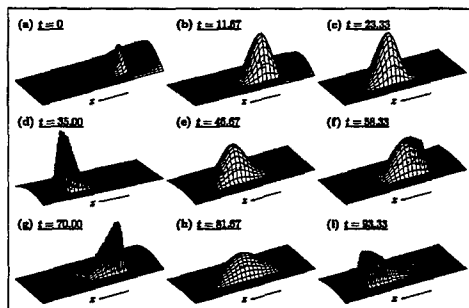


FIG. 6. Time development of a tunneling Gaussian wave packet in resonant tunneling. The electric field strength $|E_y|^2$ is shown. Times are given in picoseconds.

In Fig. 7 we compute the longitudinal energy density

$\mathcal{W}(z, t)$ in the time domain at a fixed position z behind the barrier and for different barrier lengths L . The dimensions of the symmetric wave guide are $a = 1$ cm and $a' = 0.5$ cm. The incident wave packet is of the type H_{10} with frequencies centered about $\omega_0 = 15$ GHz and a spectral width of $\sigma_\omega = 0.6$ GHz. The wave packet is chosen such that tunneling takes place mainly in the evanescent regime. Under this condition we observe that the maximum of the wave packet can appear behind the barrier earlier than when moving in the free space with the vacuum speed of light c . This behavior becomes more obvious for large L as the transmission rate decreases significantly.

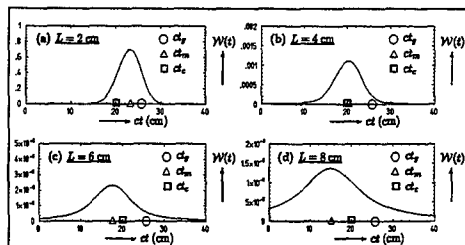


FIG. 7. Longitudinal energy density $\mathcal{W}(z, t)$ of an incident Gaussian wave packet in the time domain at a fixed position behind the barrier, $\Delta z = 20$ cm away from the position of the center of the wave packet at $t = 0$. The box, the triangle, and the circle correspond to the arrival times of the pulse maximum in vacuum, in a wave guide without barrier, and in the wave guide with a barrier of length L , respectively. For long barriers the tunneling of the pulse maximum becomes superluminal (case (c) and (d)).

As another example we consider the tunneling of Kaiser-Bessel wave packets [8] with a limited and discrete frequency spectrum in a given interval $[\omega_-, \omega_+]$. The Kaiser-Bessel-window is given by

$$f(n) = \frac{I_0 \left[\pi \alpha \sqrt{1 - (2n/N)^2} \right]}{I_0(\pi \alpha)}, \quad 0 \leq |n| \leq \frac{N}{2}, \quad (16)$$

where α is the parameter characterizing the width of the distribution and N is the number of the stationary-wave components with frequencies $\omega_n = \omega_- + (n + N/2)(\omega_+ - \omega_-)/N$ for $n = -N/2, \dots, -1, 0, 1, \dots, N/2$. The distribution (16) ensures optimal wave packet localization in the time domain and was also used in the microwave experiments [1]. In Fig. 8 we compute the tunneling time of the maximum of a Kaiser-Bessel wave packet between the beginning and end of the barrier as a function of the barrier length L . We consider wave packets tunneling in the propagating and evanescent regime and compare in the respective case the tunneling velocity of the maximum with the group velocity in the wave guide and the velocity of light in vacuum c . In both cases the incoming

wave packet is a superposition of $N = 800$ frequencies in the interval $51.52 \text{ GHz} \leq \omega \leq 57.81 \text{ GHz}$ with the spectral distribution (16) for $\alpha = 1$. The wave guide dimensions are $a = 22.86 \text{ mm}$, $a' = 18 \text{ mm}$ in the propagating case and $a = 22.86 \text{ mm}$, $a' = 15.8 \text{ mm}$ in the evanescent case, respectively. In the evanescent case the same tunneling situation as in [1] is computed. Here, we observe the tunneling velocity of the maximum of the wave packet for long barriers to be independent of the barrier length L . This behavior corresponds to the Hartman effect which is well-known from the quantum-mechanical tunneling [9,10]. Thus, evanescent tunneling of the maximum becomes highly superluminal. In the example of Fig. 8 we obtain a transmission time $\tau_T \approx 127.78 \text{ ps}$ at a barrier length $L = 100 \text{ mm}$ for the maximum of the wave packet. The corresponding transmission velocity is $v_T = L/\tau_T \approx 2.8c$ in very good agreement with the experimental result given in [1].

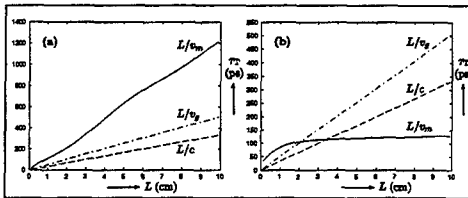


FIG. 8. The transmission time of the pulse maximum (solid line), the "transmission time" for the free motion in vacuum (dashed line) and in the wave guide without barrier (broken line) for a Kaiser-Bessel wave packet are plotted as functions of the barrier length L . (a) Non-evanescent tunneling. (b) Evanescent tunneling.

IV. QUANTILE MOTION AND CAUSALITY OF ELECTROMAGNETIC SIGNAL PROPAGATION.

We measure the arrival time of a signal with a detector placed at the fixed position z_P . We assume that the region in which the energy of an electromagnetic pulse is essentially different from zero is initially far away from the position z_P of the detector. The detection of the electromagnetic signal requires the deposition of a certain amount W of energy in the detector to cause a change of its state indicating the arrival of the signal. This is equivalent to the condition

$$\int_{z_P}^{\infty} dz \mathcal{W}(z, t) = W \quad (17)$$

on the time t of arrival of the signal. Repeated measurements at different positions z_{P1}, z_{P2}, \dots yield arrival times t_1, t_2, \dots corresponding to these positions. They are discrete points on a trajectory $z_P = z_P(t)$, which is found by requiring the condition

$$\int_{z_P(t)}^{\infty} dz \mathcal{W}(z, t) = W \quad (18)$$

to hold at all times t . If we denote by W_0 the total energy contained in the pulse then $P = W/W_0$ is the fraction of energy needed for detection and $q(z, t) = \mathcal{W}(z, t)/W_0$ is the normalized energy density. Equation (18) can be put into the form

$$\int_{z_P(t)}^{\infty} dz q(z, t) = P, \quad 0 < P < 1. \quad (19)$$

We define the quantity $z_P = z_P(t)$ as the quantile trajectory of the electromagnetic signal [5]. It depends on the fraction P , and thus on the sensitivity $W = PW_0$ of the detector. The corresponding quantile signal velocity is then given by

$$v_P(t) = \frac{dz_P(t)}{dt}. \quad (20)$$

Examples of quantile trajectories for tunneling Gaussian signals in wave guides of varying cross section are given in Fig. 9. It shows that the presence of a barrier in the wave guide may only lead to a slower signal propagation at any given time t and for every detector sensitivity P . Thus, no quantile signal velocity larger than the speed of light in vacuum c is possible. Especially, in the strong evanescent tunneling regime (see Fig. 9b) the tunneling velocity is much smaller than c , and, as physically expected, most of the trajectories turn back to the reflection region.

The behavior of the quantile trajectories for different P values reflects several properties of the tunneling process. In Fig. 9a the reflected and transmitted quantile trajectories split into trajectory bunches propagating with different velocities in the wave guide. They correspond to the electromagnetic modes produced in the tunneling as described in the previous section. This coincidence between the behavior of quantile trajectories and typical wave phenomena in tunneling can be observed also in the case of resonant tunneling (see Fig. 9c and Fig. 9d).

The causality of quantile motion can be demonstrated explicitly, for instance, in the case of tunneling TE -waves. Using the definition (18) and the continuity relation (11) we derive the quantile velocity (18),

$$v_P(t) = \frac{dz_P(t)}{dt} = \frac{\mathcal{S}[z_P(t), t]}{\mathcal{W}[z_P(t), t]}. \quad (21)$$

The modulus of the velocity field characterizing the differential equation (21) is

$$|v(z, t)| = \frac{2c \left| \sum_{n=1}^{\infty} \text{Re}[cE_y^n] \text{Re}[H_z^n] \right|}{\left| \sum_{n=1}^{\infty} \text{Re}[cE_y^n]^2 + \text{Re}[H_z^n]^2 + \text{Re}[H_x^n]^2 \right|} \leq c.$$

Thus, $v_q(t)$ never exceeds the vacuum speed of light c , i.e., the signal propagation described by the quantile trajectory is causal. This result is a general property of the

quantile motion and holds independently of the type of the tunneling wave.

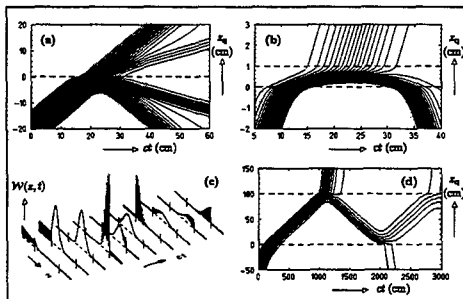


FIG. 9. Examples of quantile trajectories. (a) Evanescent tunneling with short barrier. Trajectories for $0.05 \leq P \leq 0.95$ in steps of $\Delta P = 0.02$ are shown. The wave guide dimensions are $a = 1$ cm, $a' = 0.3$ cm, and $L = 0.1$ cm. The incident Gaussian wave packet has $\omega_0 = 30$ GHz and $\sigma_\omega = 0.3$ GHz. (b) Evanescent tunneling with long barrier. The barrier length is $L = 1$ cm. The incident wave packet has $\omega_0 = 22.5$ GHz and $\sigma_\omega = 0.3$ GHz. Trajectories for $10^{-3} \leq P \leq 2.5 \times 10^{-2}$ in steps of $\Delta P = 5 \times 10^{-4}$ are computed. (c), (d) Energy distribution and quantile trajectories in resonant tunneling.

V. NOTE ON THE QUANTILE MOTION IN DISPERSIVE AND ABSORPTIVE MEDIA

It has been known for a long time that electromagnetic signal propagation in the spectral region of a dispersive medium characterized by anomalous dispersion and strong absorption leads to superluminal phase and group velocity [11–13]. Even though the shape of the propagating signal may be substantially deformed in comparison to the shape of the incoming wave, a propagation velocity has been considered which coincides with the velocity of one of the pulse maxima. Then, the velocity obtained this way is again superluminal. This result was recently confirmed by the experiments with dielectric layers at Berkeley [4] and by the experiments with photonic barriers in wave guides [14] in Cologne. However, if one considers instead of the pulse maxima the energy transport in the medium of propagation no superluminal velocities occur.

We may apply the concept of quantile motion also for the wave propagation in dispersive media. Sufficient condition for this is the existence of a measurable quantity with a positive spatial density (see [5]). Since the total energy in the medium is conserved, its density fulfills a continuity equation similar to (10). Thus, quantile trajectories for the total energy in a dispersive and absorptive medium may be easily defined in complete analogy

to the above description for the (conserved) electromagnetic energy in wave guides. The application of quantile motion for the electromagnetic signal propagation in dispersive media has been carried through in [15]. In all cases it has been shown that the quantile velocities for the signal remain below the vacuum speed of light c . An argument analogous to the one used in this paper shows rigorously that the quantile velocity in the oscillator model of dispersive and absorptive media is always smaller than the vacuum speed of light. This and related results will be presented in a forthcoming publication.

VI. CONCLUSIONS

The concept of quantile motion has been applied to the propagation of electromagnetic waves in wave guides of varying cross section and in dispersive and absorptive media. It has been shown that the signal velocity measured with a detector of finite sensitivity never becomes superluminal. In the context of electromagnetic wave propagation the quantile velocity is a generalization to finite sensitivity detectors of Sommerfeld's concept [11], who described the front velocity as the speed of a signal measured by a detector of infinite sensitivity.

- [1] A. Enders, G. Nimtz, *J. Phys. I France* 2, 1693 (1992).
- [2] A. Enders, G. Nimtz, *J. Phys. I France* 2, 1089 (1993).
- [3] A. Enders, G. Nimtz, H. Spieker, *J. Phys. I France* 4, 565 (1994).
- [4] A.M. Steinberg, R.Y. Chiao, *Phys. Rev. A* 49, 2071 (1994).
- [5] A.M. Steinberg, *Ann. Phys. (Leipzig)* 7-8, (1998).
- [6] S. Brandt, H. D. Dahmen, E. Gjonaj, T. Stroh, *Phys. Lett. A* 249, 265 (1998).
- [7] A.A. Lucas, *J. Vac. Sci. Technol. A* 6, 461 (1988).
- [8] P. Gueret, *Electronic Properties of Multilayers and Low-Dimensional Semiconductor*, ed. by J.M. Chamberlain, L. Eaves, J.C. Portal, 317, (Plenum, N. Y. 1990).
- [9] F.J. Harris, *Proc. IEEE Vol. 66 No. 1*, 51 (1978).
- [10] T.E. Hartman, *J. Appl. Phys.* 33, 3427 (1962).
- [11] E.H. Hauge and J.A. Støvneng, *Rev. Mod. Phys.* 61, 917 (1989).
- [12] A. Sommerfeld, *Phys. Zeitschr.* 8, 841 (1907).
- [13] A. Sommerfeld, *Ann. der Phys.* 44, 177 (1914).
- [14] L. Brillouin, *Wave Propagation and Group Velocity*, Academic Press N.Y., (1960).
- [15] G. Nimtz, H. Spieker, H.M. Brodowsky, *J. Phys. I France* 4, 1379-1382 (1994).
- [16] W. Heitmann, G. Nimtz, *Ann. Phys. (Leipzig)* 7-8, (1998).
- [17] E. Gjonaj, *Quantilbewegung und Kausalität*, Ph.D. Thesis, University of Siegen, Germany, (1998).

A Modal Approach for the Calculation of Scattering Parameters in Lossfree and Lossy Structures Using the FI-Technique

Rolf Schuhmann, Peter Hammes, Stefan Setzer, Bernd Trapp, Thomas Weiland

Darmstadt University of Technology
FG Theorie Elektromagnetischer Felder, Schlossgartenstr.8, 64289 Darmstadt, Germany
schuhmann@temf.tu-darmstadt.de

ABSTRACT

In this paper we present a new approach for the calculation of scattering parameters of microwave devices based on the discretization with the Finite Integration (FI)-Technique. The macroscopic properties of such devices are extracted from field solutions, which are calculated from a superposition of the eigenvectors of the associated system matrix. As the evaluation of the scattering parameters for different frequencies can be performed in a numerically cheap postprocessing step, the solution of the eigenvalue problem turns out to be the main task of the simulation procedure. Therefore several numerical algorithms for the solution of the real or complex eigenproblem emerging from lossfree or lossy problems, respectively, are applied.

INTRODUCTION

The usage of modal approaches is a well-known and very general technique, which can be applied to the solution of both continuous and discrete field problems. The underlying discretization method we use in this paper is the Finite Integration (FI)-Technique [1,2,3], which could be substituted by a wide range of similar methods leading to large algebraic matrix equations characterizing the electromagnetic behavior of the structure to be simulated. As our special interest is in the calculation of scattering parameters, however, some special properties of the FI-Technique are utilized, resulting in a highly efficient and accurate extraction of waveguide mode related data from the field solutions.

Basing on a dual grid doublet $\{\vec{G}, \vec{G}^*\}$ the FI-Technique supplies a consistent transformation of Maxwell's Equations into a set of matrix equations:

$$\begin{aligned} \vec{C}\vec{e} &= -\frac{d}{dt}\vec{\hat{b}} \longleftrightarrow \text{curl } \vec{E} = -\frac{\partial}{\partial t}\vec{B} \\ \vec{C}\vec{h} &= \frac{d}{dt}\vec{\hat{a}} + \vec{j} \longleftrightarrow \text{curl } \vec{B} = \frac{\partial}{\partial t}\vec{D} + \vec{J} \\ \vec{S}\vec{\hat{b}} &= 0 \longleftrightarrow \text{div } \vec{B} = 0 \\ \vec{S}\vec{\hat{a}} &= \vec{q} \longleftrightarrow \text{div } \vec{D} = q \end{aligned} \quad (1)$$

$$\begin{aligned} \vec{\hat{a}} &= \vec{M}_\epsilon \vec{e} \longleftrightarrow \vec{D} = \epsilon \vec{E} \\ \vec{\hat{b}} &= \vec{M}_\mu \vec{h} \longleftrightarrow \vec{B} = \mu \vec{H} \\ \vec{\hat{j}} &= \vec{j}_s + \vec{M}_\sigma \vec{e} \longleftrightarrow \vec{J} = \vec{J}_s + \sigma \vec{E} \end{aligned} \quad (2)$$

The discrete vectors $\underline{\mathbf{e}}$ and $\underline{\mathbf{h}}$ are the electric grid voltages and magnetic grid fluxes, defined on the edges and facets of the primary grid G , respectively, and the vectors $\underline{\mathbf{d}}$, $\underline{\mathbf{h}}$ and $\underline{\mathbf{j}}$ are the electric grid fluxes, the magnetic grid voltages and the electric grid currents, defined on facets and edges of the dual grid \tilde{G} . The matrices \mathbf{C} and $\tilde{\mathbf{C}}$ are the discrete curl-operators for the primary and the dual grid (with $\tilde{\mathbf{C}} = \mathbf{C}^T$); \mathbf{S} and $\tilde{\mathbf{S}}$ are the discrete div-operators ("source"). The discrete vectors are related to each other by the material matrices in (2), which can be established in diagonal form for so-called "dual orthogonal grid" (DOG)-systems. For more details on the method cf. [2].

An important issue in the analysis and design of microwave components is the computation of macroscopic quantities, such as the amplitudes of incoming and reflected waves at the ports and the associated scattering parameters. Fig.1 shows the notation of these quantities for a two-port system, where one *port* is defined as one propagating mode in one of the waveguide lines connected to the structure.

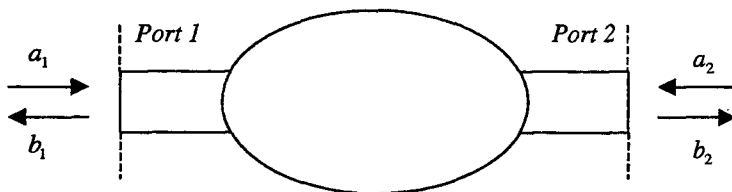


Fig.1: Microwave structure with two waveguide ports. For each port (each waveguide mode) the wave amplitudes of incoming (a_1, a_2) and outgoing (b_1, b_2) waves are to be calculated.

The desired scattering matrix $\underline{\mathbf{S}}(\omega)$ is then defined by

$$\begin{pmatrix} \underline{b}_1 \\ \underline{b}_2 \end{pmatrix} = \underline{\mathbf{S}} \begin{pmatrix} \underline{a}_1 \\ \underline{a}_2 \end{pmatrix}, \quad \underline{\mathbf{S}} = \begin{pmatrix} \underline{S}_{11} & \underline{S}_{12} \\ \underline{S}_{21} & \underline{S}_{22} \end{pmatrix}, \quad (3)$$

where the a_i and b_i are the amplitudes of incoming and outgoing waves, respectively (the underline denoting complex quantities).

To deal with such quantities within a full-wave simulation technique like the FI-Technique, the knowledge of the field patterns of the waveguide modes in the port planes is mandatory. This requires the solution of a "two-dimensional" (related to the number of spatial dimensions) algebraic eigenvalue problem,

$$\mathbf{A}_{2D}(\omega) \underline{\mathbf{e}}_{i,trans} = k_i^2 \underline{\mathbf{e}}_{i,trans}, \quad (4)$$

to determine the transversal electric fields $\underline{\mathbf{e}}_{i,trans}$ and the propagation constants k_i of at least the fundamental mode in each of the waveguides. The system matrix $\mathbf{A}_{2D}(\omega)$ of this equation is real and non-symmetric for lossfree ports. Further, for homogeneous ports the eigenvectors $\underline{\mathbf{e}}_{i,trans}$ in (4) do not depend on the frequency [1].

An important property of the FI-Technique is, that the *discrete* solutions of this eigenvalue problem fulfill the orthogonality properties of continuous waveguide modes [4,5]

$$\langle mode_i, mode_j \rangle = \mathbf{e}_{i,trans}^T \mathbf{K} \mathbf{h}_{j,trans} = \delta_{ij} \longleftrightarrow \int_A (\vec{E} \times \vec{H}) \cdot d\vec{A} = \delta_{ij}, \quad (5)$$

where \mathbf{K} is a matrix operator modeling the cross-product of the transversal mode fields. This enables an *exact* (up to the level of numerical noise) extraction of the wave amplitudes of any field solution in the discrete space and can be utilized for several highly accurate techniques for the computation of scattering parameters.

CALCULATION OF S-PARAMETERS IN TIME AND FREQUENCY DOMAIN

Applying the FI-Technique in *time domain* on a cartesian grid using the leap-frog time iteration scheme, we obtain the same update equations for the electric and magnetic field vectors as in the well-known FDTD algorithm [2,4,6]. The orthogonality property of the waveguide modes mentioned above can then be applied to establish a special absorbing boundary condition for waveguides: The fields are decomposed at the boundary planes of the computational grid using (5), and each mode can be treated separately using its previously calculated propagating constant k_i . This procedure not only minimizes spurious reflections at the boundary planes, but also leads to a time series of wave amplitudes $a_i(n \cdot \Delta t)$ and $b_i(n \cdot \Delta t)$, which can easily be transformed in the frequency domain using a Discrete Fourier Transform (DFT). If one (and only one) of the ports is excited by a given wave amplitude $a_1(n \cdot \Delta t)$, one column of the S-parameter matrix can be calculated from each simulation run.

In many cases this highly efficient time domain approach is superior to frequency domain methods, as no algebraic solver has to be applied and broadband results can be obtained by a single simulation run. However, in some cases it suffers from the high number of time steps to be performed, especially when the structure includes sharp resonance peaks (leading to long settling times), or if fine geometric details have to be resolved by the mesh (leading to a small time-step width due to the Courant-criterion).

Alternatively, the same boundary operator can be included in a *frequency domain* approach. The governing equation there is the inhomogeneous discrete curl-curl-equation [7]

$$(\mathbf{C}^T \mathbf{M}_\mu^{-1} \mathbf{C} + i\omega \mathbf{M}_\sigma - \omega^2 \mathbf{M}_\epsilon) \vec{e} = -i\omega \vec{J}_s \longleftrightarrow \text{curl } \mu^{-1} \text{curl} + i\omega \sigma - \omega^2 \epsilon \vec{E} = -i\omega \vec{J}_s. \quad (6)$$

The implementation of the absorbing boundary condition causes the system matrix of this formulation to become non-symmetric and complex and to have complex eigenvalues due to the energy flow through the port planes [8]. This makes the solution of the system much more expensive, and there are only some rare cases, where this approach can compete with time domain calculations, even if modern solvers and preconditioning techniques are applied.

To stick to real-valued systems at least for lossfree structures, also closed (PEC or PMC) boundary conditions can be applied in the frequency domain [9]. After calculating a field solution, again the wave amplitudes can be extracted, but now all incoming wave amplitudes $a_i(\omega)$ are unequal to zero.

To calculate the $n \times n$ -S-matrix (with $n=2$ for the two-port system in Fig.1) therefore n linear independent field solutions from different excitation terms in (6) are required. These excitations are somehow arbitrary; a good choice is to calculate the equivalent surface currents at the port planes from the modal fields (the solutions of the two-dimensional eigenvalue problem) at these ports. If the calcula-

tion domain contains materials with dielectric or finite-conductivity losses, again the system matrix becomes complex, which considerably increases the computation time.

The main disadvantage of both of the frequency domain approaches is, that the scattering parameters at only one frequency point are obtained from one computation run. To obtain S-parameter curves for a given frequency range, therefore a series of linear system of equations has to be solved.

MODAL APPROACH

The modal approach introduced in the following chapter does not have this disadvantage, but allows the efficient calculation of scattering parameters over a certain frequency range. A similar approach for a Finite Element discretization has already proposed by Brauer and Lizalek in [10]. An alternative formulation basing on the impedance matrix of multi-port systems was presented in [11].

The starting point is again the discrete curl-curl-equation

$$\mathbf{A}_{3D} \mathbf{e} - \omega^2 \mathbf{M}_\epsilon \mathbf{e} = -i\omega \mathbf{j}_s. \quad (7)$$

Its system matrix $\mathbf{A}_{3D} = \mathbf{C}^T \mathbf{M}_\mu^{-1} \mathbf{C}$ (for lossfree structures) is also the system matrix of the (three-dimensional) eigenvalue problem for cavities:

$$\mathbf{C}^T \mathbf{M}_\mu^{-1} \mathbf{C} \mathbf{e}_j = \omega_j^2 \mathbf{M}_\epsilon \mathbf{e}_j. \quad (8)$$

The solutions of (8) are the eigenfrequencies ω_j and the associated eigenmodes \mathbf{e}_j , which fulfill the orthogonality relation

$$\mathbf{e}_i^T \mathbf{M}_\epsilon \mathbf{e}_j = \delta_{ij}. \quad (9)$$

In the modal approach the solution of the inhomogeneous problem (6) is expressed as a superposition of a number p of these eigenmodes:

$$\mathbf{e} = \sum_{j=1}^p \alpha_j \mathbf{e}_j, \quad (10)$$

where the unknowns are now the scalar, in general complex, coefficients α_j . Inserting (10) in (7) we get

$$\sum_{j=1}^p \alpha_j (\omega_j^2 - \omega^2) \mathbf{M}_\epsilon \mathbf{e}_j = -i\omega \mathbf{j}_s. \quad (11)$$

Multiplying this equation by \mathbf{e}_k^T finally leads to an explicit formula for these coefficients:

$$\alpha_k = \frac{-i\omega}{\omega_k^2 - \omega^2} \mathbf{e}_k^T \mathbf{j}_s. \quad (12)$$

Once the eigensolutions of (8) have been calculated, this formula can be easily evaluated for arbitrary frequencies ω . From the frequency dependence in (12) it can be expected, that the main influence on the field solution comes from eigensolutions with $\omega_k \approx \omega$. In practice, usually some 10 to 40 modes with eigenfrequencies in or near the desired frequency range are sufficient for accurate solutions.

The main computational cost of this approach is due to the calculation of p solutions of the three-dimensional eigenvalue problem (8). For lossfree structures, (8) can easily be transformed in a symmetric, real-valued eigenproblem $\mathbf{A} \mathbf{x} = \omega^2 \mathbf{x}$, which can be efficiently solved by modern algebraic

algorithms. In our implementation we use a simultaneous subspace method [12], which is part of the EM-software package MAFIA [3].

If conductivity losses have to be considered (via a nonzero matrix \mathbf{M}_σ), the same procedure leads to a linear system of dimension $p \times p$ for the coefficients $\underline{\alpha}_k$:

$$\frac{\omega_k^2 - \omega^2}{-i\omega} \cdot \underline{\alpha}_k - \sum_{j=1}^p ((\underline{\epsilon}_k^T \mathbf{M}_\sigma \underline{\epsilon}_j) \cdot \underline{\alpha}_j) = \underline{\epsilon}_k^T \underline{j}_s, \quad (13)$$

which has to be solved at each frequency point. As the order p of the field expansion in (10) is usually a low number, the efficiency of the method is only slightly decreased.

However, this formula with a finite number p of eigenmodes only leads to accurate results, if the fields in the structure are mainly determined by those eigenvectors, which can exist in both the lossy and the lossfree model. In other words, having $\mathbf{M}_\sigma \neq 0$, the frequency dependence expressed in (13) does not provide a clear criterion, which eigensolutions of the lossfree problem (8) should be considered in the expansion, as the system's off-diagonal entries (the sum-terms) do not depend on the eigenfrequencies ω_k .

As an alternative especially for structures with higher losses, the eigenmodes of the complex eigenvalue problem

$$\mathbf{C}^T \mathbf{M}_\mu^{-1} \mathbf{C} \underline{\epsilon}_j = \underline{\omega}_j^2 \underline{\mathbf{M}}_\epsilon \underline{\epsilon}_j, \quad \underline{\mathbf{M}}_\epsilon = \mathbf{M}_\epsilon + \frac{1}{i\omega_0} \mathbf{M}_\sigma \quad (14)$$

can be applied. To stick to a linear formulation, the complex permittivity matrix $\underline{\mathbf{M}}_\epsilon$ is approximated by an evaluation at one frequency ω_0 in the middle of the desired frequency range. Note, that for DOG-systems this matrix is diagonal and can be easily inverted. The eigenvalue problem can then be transformed into a standard problem with a symmetric, complex (but not Hermitian) system matrix

$$\underline{\mathbf{A}}_{3D} = \underline{\mathbf{M}}_\epsilon^{-1/2} \mathbf{C}^T \mathbf{M}_\mu^{-1} \mathbf{C} \underline{\mathbf{M}}_\epsilon^{-1/2}. \quad (15)$$

This approach again leads to the explicit formula (12), but now the eigenvectors $\underline{\epsilon}_j$ as well as the eigenfrequencies $\underline{\omega}_j$ have to be calculated from the complex formulation in equations (14,15).

To solve this complex eigenproblem, two different algorithms are applied: The first one is a generalization of the subspace iteration method mentioned above, using an accelerating technique with complex Chebyshev polynomials [13]. For problems with small losses, a whole set of eigensolutions can be calculated within one iteration cycle. The main disadvantages of this algorithm are, that an estimation of the spectrum of the system matrix in the complex plane has to be performed, and that the numerical cost is increased for higher losses.

As a second algorithm therefore the Jacobi-Davidson algorithm proposed by Sleijpen et al. [14] is applied. It allows the successive calculation of those eigensolutions with eigenvalues nearest to a so-called 'target-value' in the complex plane. Previous investigations of this method in the context of eigenvalue problems with the FI-technique [15] have shown, that its convergence speed does not depend as strong on the loss factors in the structure as with the simultaneous subspace method. However, for large problems (with matrix dimensions above 10^5) sometimes a breakdown of the convergence can be observed due to a loss of some orthogonality properties in calculations with finite accuracy. This problem can be solved by a multiple re-orthogonalization of the iteration vectors.

EXAMPLE

As an example, the scattering parameters of the so-called 'comblne'-filter in Fig.2 are calculated. To get a validation of the modal approach above, the results from a time domain calculation using exactly the same grid model serve as a reference for the reflection and the transmission coefficients.

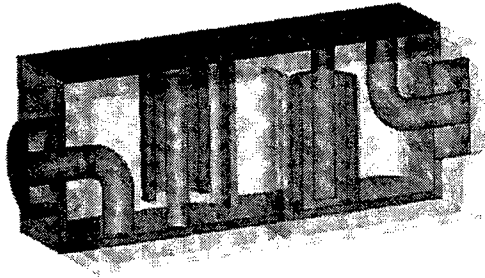


Fig.2: Comblne filter driven by two coaxial waveguide ports.

The frequency curves in Fig.3 show a small passband with steep slopes (note the small frequency range) and a middle frequency of about 1.67 GHz. This leads to long settling times in the time domain calculation.

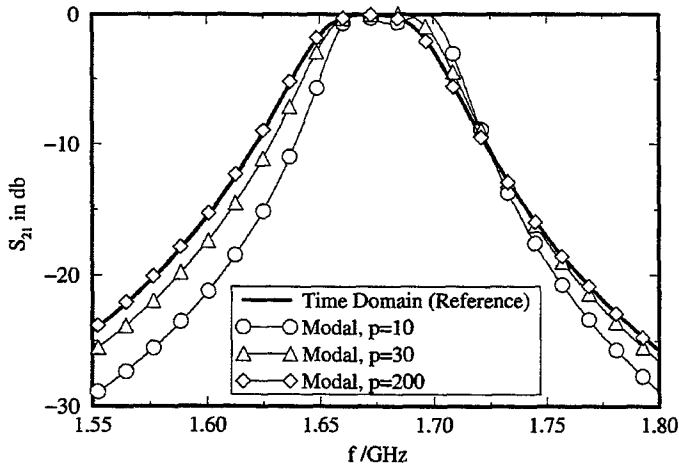


Fig.3: Transmission coefficient S_{21} in the comblne filter. Results from a time domain calculation (reference) and from the modal approach using 10, 30, 200 eigenmodes, respectively.

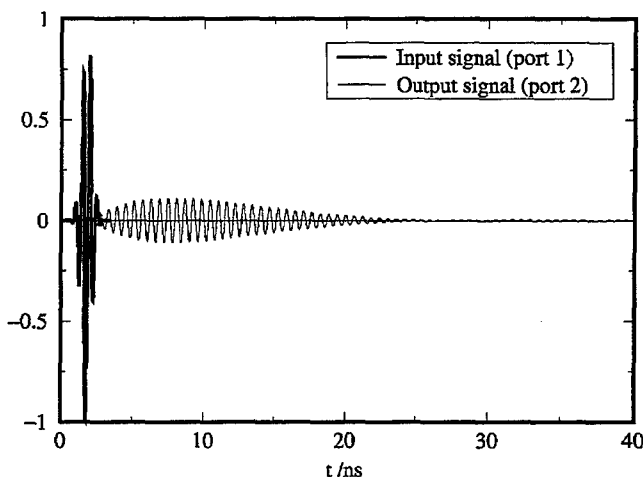


Fig.4: Input and output signal in the time domain simulation of the combine filter. The steepness of the slopes leads to long settling times.

The modal approach already leads to qualitatively good results for a expansion with only $p=10$ modes with eigenfrequencies between 1.6 GHz and 8.1 GHz. Using $p=30$ eigenmodes (eigenfrequencies up to 17 GHz) the results agree very well with the reference, and the calculation with $p=200$ modes has nearly perfectly converged. The calculation times, including mesh generation and matrix calculation, behave like 1 : 5.9% : 7.3% : 55% (time domain, modal approach with 10, 30, 200 modes).

An example including lossy materials using the complex eigenvalue solvers will be given in the conference presentation.

CONCLUSION

The modal approach is an efficient method for the calculation of scattering parameters. The main numerical cost is due to the solution of the three-dimensional eigenproblem of the closed structure, whereas for the final extraction of the S-parameters only an explicit formula or a small linear system has to be evaluated at each frequency point. Therefore efficient and robust eigenvalue solvers have to be available, especially for the complex formulation arising from lossy structures. A promising algorithm is the Jacobi-Davidson method, which has been slightly modified for the application to large problems. Further investigations will focus on validation and error estimation techniques, especially in the field of structures with small losses, where two variants of the basic approach can be applied.

REFERENCES

- [1] T.Weiland: 'A Numerical Method for the Solution of the Eigenvalue Problem of Longitudinally

Homogeneous Waveguides', *Electron. Commun. (AEÜ)*, Vol. 31, p. 308, 1977.

- [2] T.Weiland: 'Time Domain Electromagnetic Field Computation with Finite Difference Methods', *International Journal of Numerical Modelling: Electronic Networks, Devices and Fields*, Vol. 9, pp. 295-319, 1996.
- [3] MAFIA Userguide, The MAFIA Collaboration, CST GmbH, Lauteschlägerstr. 38, 64289 Darmstadt, Germany, 1997.
- [4] M.Dohlus: 'Ein Beitrag zur numerischen Berechnung elektromagnetischer Felder im Zeitbereich', Ph.D.-Thesis, Darmstadt University of Technology, 1992.
- [5] R.Schuhmann: 'Die Nichtorthogonale Finite-Integrations-Methode zur Simulation elektromagnetischer Felder', Ph.D.-Thesis, Darmstadt University of Technology, 1999.
- [6] K.S.Yee: 'Numerical Solution of Initial Boundary Value Problems Involving Maxwell's Equations in Isotropic Media', *IEEE Transactions on Antennas and Propagation*, Vol. 17, S. 585-589, 1966.
- [7] P.Hahne, T.Weiland: '3D Eddy Current Computation in the Frequency Domain Regarding the Displacement Current', *Transactions on Magnetics*, Vol. 28, No. 2, pp. 1801-1804, 1992.
- [8] R.Schuhmann, M.Clemens, P.Thoma, T.Weiland: 'Frequency and Time Domain Computations of S-Parameters Using the Finite Integration Technique'. *Proceedings of the 12th ACES Conference, Monterey*, pp.1295-1302, 1996.
- [9] A.Christ, H.Hartnagel, 'Three-Dimensional Finite-Difference Method for the Analysis of Microwave-Device Embedding', *IEEE Transactions on Microwave Theory and Technique*, Vol. 35, No. 8, pp. 688-696, August 1987.
- [10] J.R.Brauer, G.C.Lizalek: 'Microwave Filter Analysis Using a New 3-D Finite-Element Modal Frequency Method', *IEEE Transactions on Microwave Theory and Techniques*, Vol. 45, No. 5, pp. 810-818, 1997.
- [11] M.Dohlus, R.Schuhmann, T.Weiland: 'Calculation of Frequency Domain Parameters Using 3D Eigensolutions', *International Journal of Numerical Modelling: Electronic Networks, Devices and Fields, Special Issue*, Vol. 12, pp. 41-68, 1999.
- [12] M.Timm, D.Schmitt, R.Schuhmann, T.Weiland: 'Simultaneous Computation of Higher Eigenmodes in Lossfree Waveguides and Cavities', *IEEE Transactions on Magnetics*, Vol. 34, No. 5, pp. 3240-3243, 1998.
- [13] D.Schmitt, R.Schuhmann, T.Weiland: 'The Complex Subspace Iteration for the Computation of Eigenmodes in Lossy Cavities', *International Journal of Numerical Modelling: Electronic Networks, Devices and Fields*, Vol. 8, pp. 385-398, 1995.
- [14] G.Sleijpen, H.van der Vorst: 'A Jacobi-Davidson Iteration Method for Linear Eigenvalue Problems', *SIAM J. Matrix Anal. Appl.* 17, pp. 401-425, 1995.
- [15] S.Setzer, T.Weiland: 'Computing Eigenmodes in Highly Lossy Accelerating Structures', *Proceedings of the XIX International LINAC Conference, Chicalgo, Illinois, USA*, 1998.

A Modular Technique for the Calculation of Wave Guide Structures

by

Johannes Borkes,

Institute for Mobile Satellite Communication Techniques, Kamp-Lintfort/Germany

Adalbert Beyer and Oliver Pertz

Department of Electrical Engineering, Duisburg University/Germany

Tel. +492033791055, Fax +492033793218, Email Pertz@uni-duisburg.de

Abstract: In this paper a generalized method is presented for the description of the propagation properties wave guide structures. Starting with the procedure, at first the boundary value problem will be formulated. Thereafter, the solution of the above problem will be performed. Being able to consider material losses and anisotropic behavior of materials, and even secondary order effects like metallization thickness, this method allows a realistic description of these structures. The treatment of fields is carried out by means of a modified mode matching technique thus accelerating the numerical procedure. Several examples prove the applicability of the method.

1 Introduction

The characteristics of the shielded planar and quasi-planar wave guides can only be computed from the total transverse structure, since the circuit components influence each other increasingly because of the dense integration and the enhanced frequency beyond 100 GHz. The analysis of shielded wave guides is usually computed by Finite Element Methods (FEM) [1,2] or Finite Difference Methods (FDM) [3,4], the Method of Lines (MoL) [5], the Spectral Domain approach (SDA) [6,7], the Transmission Line Matrix Method (TLM) [8,9], or the Mode Matching Technique (MMT) using orthogonal series [10-12]. These methods proved their efficiency in many, single-computed or special classes of structures.

In this work the mode matching technique is used, in which the continuity conditions between the adjacent regions are fulfilled. The boundary conditions on the shielding and on the inner metallizations will be enforced. From the resulting equation system the properties and the field solutions of the structure can be deduced. It was applied successfully to the computation of the propagation properties of micro-strip transmission lines, strip-lines, image-lines, fin-lines and coplanar lines as well. In contrary to several different other methods, the finite metallization thicknesses can easily be computed by including additional regions. But in this regard the method presented here has also further advantages; i.e. it is not necessary to know any special basis functions, like for instance in the spectral domain method.

2 Theory

In most of the practically relevant cases the shielding and the inner metallization of the cross-section of a shielded planar or a quasi-planar structure are composed by regions perpendicular to each other. For this reason the transverse structure can almost always be subdivided into single rectangular subregions. As an example, Fig. 1 shows one possible elementary subregion named "I".

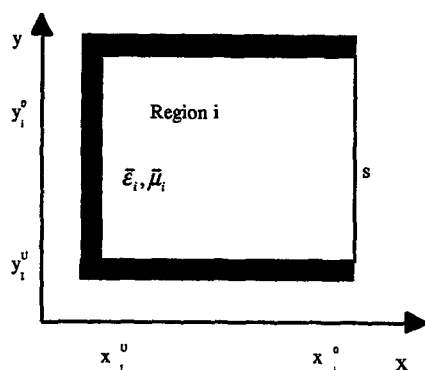


Fig. 1: The subregion i of a cross-section of the wave guide structure under study.

The coordinates x, y are situated in the transverse plane. The wave propagating in positive z -direction is described by $\exp(-j(\omega t - k_z z))$ for all field components. Under such conditions the region can be described by a data collection

$$P_o = \{G_i, M_i; i=1(1)N\} \quad (1)$$

with

$$G_i = \{(x_i^u, y_i^u), (x_i^o, y_i^o)\} \text{ and } M_i = \{\bar{\epsilon}_i, \bar{\mu}_i\}, \quad (2)$$

where G_i and M_i is the data-set of the geometric description of subregion i , M_i is the data-set of the material properties of subregion i and N is the number of the rectangular, homogenous filled subregions.

When analyzing the description of the structure it is possible to conclude from the geometric neighborhood to the electric one and thus also to the necessary matching conditions. An exception is the case of infinitely thin metallization. Here the electric neighborhood must be replaced by the statement of the regions divided by the metallization. From this analysis an expanded description of the problem is obtained

$$P_o = \{P_i; i=1(1)N\}, \quad (3)$$

$$P_i = \{G_i, M_i, S_i\}, \quad (4)$$

$$A = \{A_m; m=1(1)M\}, \quad (5)$$

$$A_m = \{i_m, K_m, s_m\}. \quad (6)$$

the set S_i contains those parts of the boundary of region i that must be matched to the neighboring subregions.

An elementary subregion S_i in Fig. 1 consisting of three electric walls ($K \rightarrow \infty$) and one open surface is described uniquely by means of a data collection

$$P_i^s = \{G_i, M_i, s\} \quad (7)$$

with G_i and M_i as in equation (2) the collection of the geometrical description in terms of two opposite edge co-ordinates of the rectangular region and the collection of material data respectively denoting the open side and the field solution for the elementary region. It should be mentioned, however that there are three further elementary regions additionally, which can be obtained by rotating that in Fig. 1. The cross-section of the transverse structure is composed by uni-, bi-, trilaterally, or

completely open subregions which are superimposed. The description of composed regions results from the combination of the descriptions of the possible four elementary regions

$$P_i = \bigcup_s P_i^s = \bigcup_s \{G_i, M_i, s\} = \{G_i, M_i, S_i\}. \quad (8)$$

Here the index collection S_i contains the open sides of the composed region. The electric and magnetic fields of the subregions are obtained by superimposing the fields of the elementary subregions

$$\vec{E}_i = \sum_{s \in S_i} \vec{E}_i^s \quad \text{and} \quad \vec{H}_i = \sum_{s \in S_i} \vec{H}_i^s. \quad (9)$$

For the electromagnetic field at one side $t \in S_i$ of a composed subarea with the normal unity vector \vec{n}_t , the following conditions will be valid

$$(\vec{E}_i \times \vec{n}_t)_t = \left(\left(\sum_{s \in S_i} \vec{E}_i^s \right) \times \vec{n}_t \right)_t = (\vec{E}_i^t \times \vec{n}_t)_t, \quad (10)$$

$$(\vec{H}_i \times \vec{n}_t)_t = \left(\left(\sum_{s \in S_i} \vec{H}_i^s \right) \times \vec{n}_t \right)_t = \sum_{s \in S_i} (\vec{H}_i^s \times \vec{n}_t)_t. \quad (11)$$

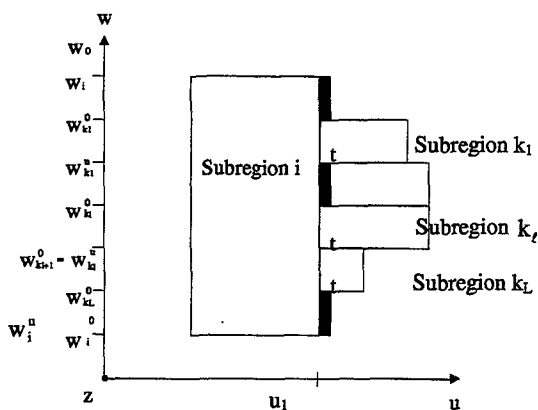
Hence it follows that in matching at the side t of a rectangular subregion to another subregion only the field expressions of the elementary subregion t is of interest for the electrical field strength, whereas for the magnetic field strength all elementary field expressions of a region must be taken into consideration.

The matching of the electric and the magnetic field strength is realized by using an orthogonal series for the field strength components tangential to the area of interest. In Figure 2 an exemplary transversal mode matching situation is presented. Here w, z are the coordinates tangential to the interface u_1 between the areas $(i_m, i_k, \ell = 1(1)L_m)$ and u the co-ordinate normal to the area's interface, respectively. In the further course of the section the index i_m is left out for legibility. The matching conditions according to Figure 2 are

$$(E_z, E_w)_s = \begin{cases} (E_{z_{k_1}}, E_{w_{k_1}})_t & w_{k_1}^u \leq w \leq w_{k_1}^o \\ (E_{z_{k_1}}, E_{w_u})_t & w_{k_1}^u \leq w \leq w_{k_1}^o \\ (E_{z_{k_L}}, E_{w_{k_L}})_t & w_{k_L}^u \leq w \leq w_{k_L}^o \end{cases} \quad (12)$$

$$w_i^u \leq w \leq w_i^o$$

$$(H_w, H_z)_s = (H_{w_u}, H_{z_{k_1}})_t \quad w_{k_1}^u \leq w \leq w_{k_1}^o \quad \text{for } \ell = 1(1)L. \quad (13)$$



Hereby the electrical field in subregions $K_i, i = 1(1)L$ is developed following the eigenfunctions of the electrical field strength of subregion i . The magnetic field strength in subregion i is developed according to the eigenfunctions of the magnetic field strength from subregion K_i . This kind of counter wise development of orthogonal series is necessary to fulfill the boundary conditions of the electric and magnetic field strength on any possible existing metallizations lying in the matching interface.

Considering equations (10) and (11) we obtain by the help of the vectorial field expressions

$$\tilde{D}e_{ii}^{ss} \tilde{C}_i^s = \sum_{\ell=1}^L \tilde{D}e_{ik_\ell}^{ss} \tilde{C}_{k_\ell}^s, \quad \sum_{r \in S_{k_\ell}} \tilde{D}h_{kk_\ell}^{rr} \tilde{C}_{k_\ell}^r = \sum_{r \in S_j} \tilde{D}h_{k_\ell k_\ell}^{rr} \tilde{C}_i^r \quad \text{for } \ell = 1(1)L. \quad (14)$$

Hereby the field amplitudes of an elementary field expression have been combined to

$$\bar{C}_i^s = \begin{bmatrix} C_{i,1,1}^s \\ \vdots \\ C_{i,1,N^s-1}^s \\ C_{i,2,0}^s \\ \vdots \\ C_{i,2,N^s-1}^s \end{bmatrix}. \quad (15)$$

Now, this system consisting of $L+1$ equations together with the equations obtained by the other matching conditions at interfaces can be inserted into the system matrix leading to a homogenous matrix equation

$$\vec{s}(k) \cdot \vec{c} = 0. \quad (16)$$

By evaluating $\det(\tilde{S}(k_z)) = 0$ the values k_{zi} of this equation corresponding to the propagation constants of the eigenmodes can be obtained. From this, with the help of equation (16), the field amplitudes \tilde{C}_i can be determined.

Structures with finite dimensions in a closed shielding have a countable infinite number of eigenvalues k_{zi} . With increasing frequency and growing dimensions of the shielding the solution spectrum of the modes becomes gradually denser. To set up the system matrix the equations have to be ordered and numbered. For the interface matching we get L_m equations from the magnetic field and one equation for the electrical field matching, thus

$$M_o = \sum_{m=1}^M (L_m + 1) = M + \sum_{m=1}^M L_m \quad (17)$$

equations for all matching conditions can be obtained. These equations are inserted into the system matrix. The position of the coupling matrices results on the one hand from the matching number m and on the other hand from the numbers i and k of the subregions, and from the term of the elementary field expressions. The column address of the coupling matrices follows from the truncation indices N_i^s , $s \in S_i$, of the single subregions of the structure. The number of the field amplitudes \tilde{C} and thus the dimension of the system matrix N_{oo} for the whole structure results from

$$N_{oo} = \sum_{i=1}^N \sum_{s \in S_i} (2N_i^s - 1). \quad (18)$$

Normally the system matrix is sparse, for special cases a band matrix can be obtained, but this is not valid generally. With growing number of subregions, the number of the elements in the system matrix is of $O(N^2)$. Furthermore, the calculation of the system matrix determinant is of $O(N^3)$. This yields the necessity of reducing the dimension carried out by inserting all the equations for the electrical field matching into the equations of the magnetic field matching. Hereby the matrix dimension is reduced to

$$N_r = N_{oo} - \sum_{m=1}^M (2N_{im}^s - 1) \quad (19)$$

If all principal boundary conditions are fulfilled the metallization boundaries share at most two subregions in a matching condition, and the system matrix can at least be halved.

It should still be supplemented that the electromagnetic field for all four elementary regions by using the Hertzian potentials can be obtained. For the electric field strength components by leaving out the factor $e^{j(\omega t + k_z z)}$ as mentioned above the following expression is valid:

$$E_x^s = \sum_j (-k_{xj}^s d_1 C_{1j}^s + k_{xj}^s C_{2j}^s) \cos(k_{xj}^s \cdot (x - x_o^s)) \sin(k_{y_j}^s \cdot (y - y_o^s)) \quad (20)$$

$$E_y^s = \sum_j (-k_{yj}^s d_1 C_{1j}^s + k_{yj}^s C_{2j}^s) \sin(k_{xj}^s \cdot (x - x_o^s)) \cos(k_{y_j}^s \cdot (y - y_o^s)), \quad (21)$$

$$E_z^s = \sum_j d_2 C_{1j}^s \sin(k_{xj}^s \cdot (x - x_o^s)) \sin(k_{y_j}^s \cdot (y - y_o^s)), \quad (22)$$

with

$$d_1 = k_z / (\omega \epsilon_o \epsilon_r), d_2 = (k_o^2 \epsilon_r \mu_r - k_z^2) / (j \omega \epsilon_o \epsilon_r), \text{ and } k_o^2 = \omega^2 \mu_o \epsilon_o. \quad (23)$$

The magnetic field can simply be obtained by substituting sines by cosines and vice versa, and the abbreviations $-d_1$ and d_2 in (23) in equation (20)-(22) are to replace by d_3 and d_4 respectively

$$d_3 = k_z / (\omega \mu_o \mu_r), \quad d_4 = (k_o^2 \epsilon_r \mu_r - k_z^2) / (j \omega \mu_o \mu_r). \quad (24)$$

3. Results

The applicability of the method presented here is shown on several aspects of a microstrip transmission line. The partitions of the cross-section have been chosen according to Fig. 3, which must be judged under following different criteria. Here the speed of the convergence, the regularity of the convergence and the numerical stability of the partition procedure are of special importance.

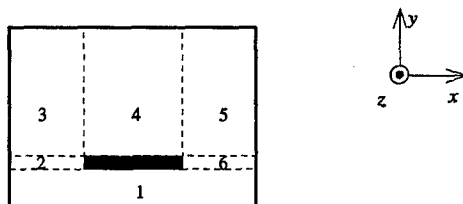


Fig. 3: Partitions of a symmetrical microstrip transmission line cross-section (Shielding $22.86 \text{ mm} \times 10.16 \text{ mm}$, substrate height 1.58 mm , metallization thickness $17.5 \mu\text{m}$, metallization width 4.6 mm , $\epsilon_r = 2.33$).

The fulfillment of the continuity conditions between the different subregions is achieved by the development of orthogonal series of the electrical and magnetic field strength components tangential to the matching interface. Inherently this procedure fulfills the continuity conditions at the mean root-square error minimum.

Fig. 4 shows the normalized matching field strengths E_x and H_x of a microstrip transmission line in the section plane between substrate and air region.

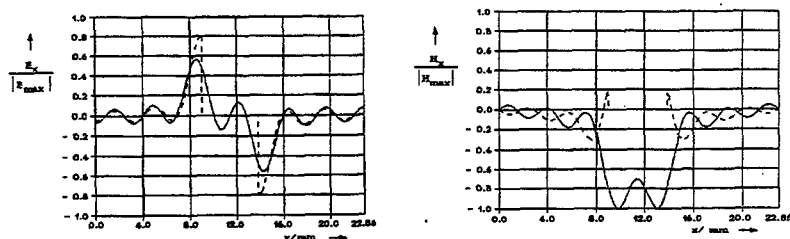


Fig. 4: Tangential electrical and magnetic field strengths at the boundary between substrate and metallization of a microstrip transmission line (a) normalized electric field strength, (b) normalized magnetic field strength.

The dashed curve presents the field strength in the air region, the solid one the field strength in the substrate region. Obviously, the continuity condition for the field strength is very well fulfilled in the air regions, because of the truncation indices chosen proportionally to the width aspect ratio. In the area of metallization the boundary conditions $(E_x, E_z) = 0$ can only be adapted badly. The approximation of the singularities of the field strengths at the corners is problematic, too. These can only be approximated by a time-consuming procedure.

Finally, in figures 5a), b) and c) the field distribution in a cross-section at any time for the quasi-TEM-wave of the structure after Fig. 3 is presented.

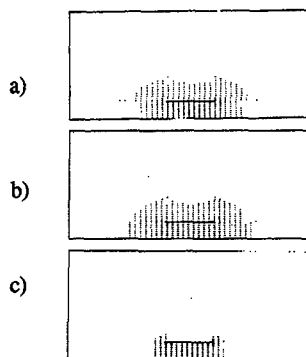


Fig. 5: Quasi-TEM-wave at $f = 10$ GHz; $\epsilon_r = 2.33$, $\epsilon_{eff} = 2.042$. a) Transverse electrical field strength, b) Transverse magnetic field strength, c) Longitudinal component of the Poynting vector.

This strip-controlled wave type carries its total active power below the strip in the substrate. The name quasi-TEM wave describes the fact that the longitudinal field strength components in contrast to the transverse components can be neglected.

4. Conclusion

The numerical results for a microstrip line presented in this paper show the applicability of the described technique for a special partition. The description of the transverse structure allows to take into an account also secondary effect like the influence of finite metallization thickness and mounting grooves and even the effects of anisotropic substrates with diagonal permeability and permittivity tensors. Furthermore, this technique can be used for transmission lines, which are able to divide the transverse structure into rectangular, homogeneous subregions.

5. References

- 1 Silvester, P.: A general high-order finite-element waveguide analysis program. *IEEE-Transactions on Microwave Theory and Techniques*, Vol. MTT-17, No. 4, April 1969, pp. 204-210.
- 2 Newman, H.S. and Krowne, C.M.: analysis of ferrite circulators by 2-D Finite-Element and recursive Green's function techniques. *IEEE-Transactions on Microwave Theory and Techniques*, Vol. MTT-46, No. 2, February 1998, pp. 167-177.
- 3 Gwarek, W.K.: analysis of an arbitrary-shaped planar circuit – A time domain approach. *IEEE-Transactions on Microwave Theory and Techniques*, Vol. MTT-33, No. 10, October 1985, pp. 1067-1072.
- 4 Wang, Y. and Ling, H.: Multimode parameter extraction for multiconductor transmission lines via single-pass FDTD and signal-processing techniques. *IEEE-Transactions on Microwave Theory and Techniques*, Vol. MTT-46, No. 1, January 1998, pp. 89-96.
- 5 Pregla, R.: Analysis of planar microwave structures on magnetized ferrite substrate. *Archiv für Elektronische Übertragungstechnik. IEEE-Transactions on Microwave Theory and Techniques*, Vol. MTT-40, 1986, pp. 270-274.

- 6 Itoh, T.: Spectral domain immittance approach for dispersion characteristics of generalized printed transmission lines. *IEEE-Transactions on Microwave Theory and Techniques*, Vol. MTT-28, No. 7, July 1980, pp. 733-736.
- 7 Cano, G., Medina, F., and Horno, M.: On the efficient implementation of SDA for boxed strip-like and slot-like structures. *IEEE-Transactions on Microwave Theory and Techniques*, Vol. MTT-46, No. 11, November 1998, pp. 1801-1806.
- 8 Hoefer, W.J.R.: The transmission-line matrix method-theory and application. *IEEE-Transactions on Microwave Theory and Techniques*, Vol. MTT-33, No. 10, October 1985, pp. 882-893.
- 9 Mueller, U. and Beyer, A.: Nonlinear simulations in time domain methods. *International Journal of Microwave and Millimeter-Wave Computer-Aided Engineering*, Vol. 5, No. 3, 1995, pp. 139-148.
- 10 Kühn, E.: A mode-matching method for solving field problems in waveguide and resonator circuits. *AEÜ, Band 27*, 1973, pp. 511-518.
- 11 Beyer, A.: Analysis of the characteristics of an earthed finline. *IEEE-Transactions on Microwave Theory and Techniques*, Vol. MTT-29, No. 7, July 1981, pp. 676-680.
- 12 Shih, Y.C., Itoh, T. and Bui, L.Q.: Computer-aided design of millimeter-wave E-plane filters. *IEEE-Transactions on Microwave Theory and Techniques*, Vol. MTT-31, No. 2, February 1983, pp. 135-141.
- 13 Balaji, V. and Vahldieck, R.: Mode-matching analysis of circular ridged waveguide discontinuities. *IEEE-Transactions on Microwave Theory and Techniques*, Vol. MTT-46, No. 2, February 1998, pp. 191-195.

WAVE PROPAGATION THROUGH 2D CLUSTERS OF COUPLED CYLINDRICAL RESONATORS.

Ross A. Speciale

polytope@msn.com

ABSTRACT

Numerical simulations of the complex vector fields of electromagnetic traveling waves, guided through 2D clusters of tightly coupled cylindrical resonators, have been performed using *Fortran* codes originally developed for the analysis and design of charged particle accelerators. The interpolated, high-resolution field maps obtained have been visualized by using the interactive graphic capabilities of *Matlab*. Further, the advanced numerical processing capabilities of *Matlab* have also been used to compute the complex weights of expansions in orthogonal eigenfunctions that closely approximate the field values obtained, while satisfying the boundary conditions.

1. The Symmetries of Six-Port Resonators.

Cylindrical microwave cavity resonators, that have six ports symmetrically-located around the outer wall, exhibit C_{6v} rotation symmetry about the cavity axis, and reflection symmetries about six axial planes.

The coupling ports of such resonators are spaced by 60° in relative azimuth around the cavity axis, so that the resonators simultaneously exhibit axial rotation symmetry with a 60° azimuth period, and reflection symmetries with respect to two sets of three axial planes each. The three symmetry-planes of a first set are spaced by 120° in relative azimuth, each of the planes running through the centers of opposite ports. The three symmetry-planes of the second set are located halfway in azimuth between the symmetry-planes of the first set, and bisect the 60° azimuth angles between adjacent ports of the resonator (Figure 1).

2. Hexagonal Clusters.

Any cylindrical resonator that simultaneously exhibits the above described symmetries may be *directly* coupled to six other physically identical cylindrical resonators that physically surround it, the six outer resonators having mutually-parallel axes, and all six axes being parallel to the axis of the single central resonator.

Further, being the axes of the six outer resonators equidistant from the axis of the central resonator, the traces of those axes on any orthogonal plane are at the corners of a symmetrically-located regular hexagon (Figure 2).

Such direct mutual coupling of C_{6v} -symmetric six-port cylindrical cavity resonators may be extended infinitely in all directions, thus creating a two-dimensional, periodic microwave wave-guiding structure that exhibits the same geometrical periodicity along the three directions running through the 180° -opposite ports of each resonator.

This type of microwave wave-guiding structure is a doubly-periodic, electrically-large network composed of identical unit-cells in the form of directly-coupled six-port cylindrical microwave cavity resonators, ordered in an hexagonal lattice. The network resembles thus a honeycomb with intercommunicating cylindrical cells (Figure 3).

Hexagonal clusters of directly-coupled microwave resonators, having axis-to-axis spacing in the order of a half free-space wavelength, may be used as slow-wave guiding structures that convey electromagnetic waves through hundreds of identical resonators over distances covering a large number of wavelengths.

The wave propagation takes place through the direct electromagnetic coupling between the internal fields of each resonator and that of the six immediately-adjacent resonators, by way of the common-wall coupling ports.

3. Multiple Wave-Sets.

Further, such hexagonal clusters of directly-coupled six-port resonators may be used to simultaneously guide multiple sets of mutually-synchronous slow waves, each set being generated by a different group of mutually-coherent sources connected to the cluster in some arbitrary distribution, and with each source in any given group having quite arbitrary relative amplitude and phase with respect all the other.

Clearly, *different sets* of slow waves may simultaneously propagate in any number of *different directions* within the two dimensions of the cluster, by coupling from each resonator to the six immediately adjacent resonators.

The simultaneous propagation of multiple wave-sets in many different arbitrary directions establishes total two-way connectivity everywhere throughout the cluster, so that any two arbitrarily-selected resonators of the cluster are (directly or indirectly) coupled through numerous *multiple signal-paths*.

The internal wave-field distributions inside the resonators of a cluster, due to multiple simultaneous guided-wave sets are then generated by the *linear superposition* of the individual wave-fields of all the wave sets. The total internal field inside the resonators of the cluster may be then expressed as a *linear combinations* of the individual wave-fields, with complex weights representing the relative amplitudes and phases of the various component fields.

4. Wide Band Transmission.

Recent research results prove that by designing the coupling ports of the resonators in a cluster as common-wall resonant irises, with each iris resonating on the *same frequency* as *all* the cavity-resonators, *wide-band* wave-transmission is attained through the whole cluster, with typical relative bandwidth in the order of 25-30 % [1].

Obvious iris-size constraints due to the small electrical size of *fundamental-mode* resonators, and to the relatively large number of irises in each resonator, may be easily circumvented by using either *dumb-bell shaped* irises or *dielectric-filled* irises (Figure 4).

5. Clustered Arrays.

Wide-band clusters of C_{6V} symmetric six-port resonators aligned in hexagonal lattices are presently being investigated for possible applicability as *signal-distribution* circuits in electronically-steered, "*Clustered*" phased arrays. The use of such clusters as signal-distribution circuits within the feed-networks of phased arrays would vastly reduce the number of the amplitude- and phase-controlled sources required in transmission for performing electronic beam steering. The reduction in the number of sources becomes possible because each of the aperture distributions required for steering the array beam in any of the specified directions may then be generated by *linear superposition* of the partial aperture fields individually-generated by the sources used [2, 3].

The aperture distributions that correspond to the specified radiation patterns of a steered array and to the different beam-pointing directions, may then be synthesized as *linear combinations* with *complex weights* of the individual aperture fields contributions of all the controlled sources used. All the sources can simultaneously contribute to such linear combination, provided the two-way connectivity of the signal-distribution circuit makes possible for each source to simultaneously feed all the array elements and for each element to be simultaneously fed by all the sources. The total two-way connectivity of clusters makes this synergism possible, so that a *predetermined minimum number* of mutually-coherent, optimally-located sources can synchronously generate any of the required aperture distributions by *linear superposition* of partial fields.

6. Numerical Field Analysis.

This paper reviews the results of 2D numerical electromagnetic analysis work, performed on typical six-port unit-cell resonators and on small clusters, to generate graphic displays of the internal complex traveling-wave fields that propagate through either: a) a single cylindrical, six-port microwave cavity resonator (Figure 1); or b) an electrically-small hexagonal cluster (Figure 2).

The ultimate objective of the performed numerical field analysis is to determine the functional dependence of the properties of the two dimensional slow-wave-propagation through an hexagonal cluster from the detailed *common geometry* of all its mutually-identical resonators. The propagation properties of the waves guided through a cluster clearly only depend on the common geometry of all its resonators, each resonator being a *unit-cell* of the cluster.

The slow-wave propagation properties are fundamentally characterized by the dependence of: 1) the wave *phase-velocity*, and 2) the *wave-impedance* from: a) the wave *frequency* (dispersion), and b) the specific *azimuth* angle of the *direction of wave propagation* through the cluster, relative to the *planes* of reflection *symmetry* (anisotropy). The wave-direction azimuth angle is defined in the common median plane of all the coupling ports.

7. From Unit-Cells to Cluster Waves.

Results obtained in previous extensive network-analysis studies [5-8] express the functional dependence of the propagation properties of waves guided through an hexagonal cluster of directly-coupled resonators, from the electrical parameter matrices of a *single* unit-cell, such as the Z , Y , $ABCD$ or S matrix.

The objective of the numerical field analyses performed is then to *mathematically express* the quantitative correlation between any realistic unit-cell geometry, as specified by a minimum number of dimensional parameters, and the corresponding electrical network-parameter matrices, being these either Z , Y , $ABCD$ or S parameters.

Such mathematical expressions would make possible the direct computation of the required electrical network-parameters of a six-port resonator from its geometrical dimensions, the dimensions that specify the unit-cell size and shape. The propagation properties of the cluster waves could then be computed from the unit-cell electrical parameters by using the previous network analysis results [5-8].

This effort aims therefore at generating a sufficiently accurate *electrical model* of a six-port cylindrical resonator, a model that expresses the unit-cell electrical performance in terms of its Z , Y , $ABCD$ or S parameter matrices, cast as functions of the unit-cell physical size and shape. The C_{6V} rotation- and reflection-symmetries and the implied *reciprocity* of the unit-cell resonators substantially simplify the task by reducing the order of each network-parameters matrix, from $6 \times 6 = 36$ entries to *only two* different values. The two different values may for instance be given by the Z_{11} and Z_{12} entries of the 6×6 impedance matrix Z , or the Y_{11} and Y_{12} entries of the 6×6 admittance matrix Y , as both these matrices are at the same time *symmetric* and *circulant*.

8. The Poisson/Superfish Programs.

The numerical 2D electromagnetic analysis work here reported has been performed by using some of the particle accelerator programs known as the *Poisson/Superfish* codes of the Los Alamos National Laboratory.

Nine different *Matlab* post-processing programs were also generated to perform various data manipulations and graphic visualizations of the numerical field data obtained.

The functionality of the *Poisson/Superfish* programs used has been reviewed in a previous paper [4].

Specific emphasis was given there to the program *CFISH* that performs the 2D analysis of the *complex vector fields of traveling waves*. Extensive documentation covering all the *Poisson/Superfish* codes, and executable codes that run under Windows 95/98 /NT 4.0 are *freely* available for downloading from two *ftp-servers* of the Los Alamos Accelerator Code Group (LAACG) [9].

The set of 2D EM field-analysis codes, known as *Poisson/Superfish*, has been developed and progressively improved by the Los Alamos Laboratory Accelerator Codes Group (LAACG), and it is primarily intended for application to particle accelerator design [9, 10]. Various components of that set are nevertheless sufficiently general to be applicable in the analysis of communication antennas and phased arrays.

Field analyses performed by the *CFISH* program in 2D Cartesian coordinates can only solve for *transverse-electric* modes. For the analysis of *transverse-magnetic* modes this limitation may however be circumvented by solving for the *conjugate field* where the computed H_z component represents the physical E_z field to within a known scaling factor. Notwithstanding these limitations the program is very useful and its price is hard to beat.

While the *FISH* code only computes local field amplitudes, and is mainly used for searching and identifying the modes of resonant structures, the *CFISH* code actually computes the local *real* and *imaginary* components of complex vector fields, and can therefore map *traveling-wave* propagation processes in *non-resonant* systems.

The RF field solver *FISH* accepts, as inputs, Cartesian x and y coordinates specifying the location of a single point-source. The RF field solver *CFISH*, however, can even accept the locations, amplitude- and phase-settings of *multiple RF* sources ($n \leq 5$). These can either be point-sources or line-sources.

In particular, the *CFISH* program can analyze the complex EM fields generated, at any specified fixed frequency, by multiple RF line-sources ($n \leq 5$), each line-source having different amplitude- and phase-settings.

The *CFISH* program provides thus the capability of simulating the simultaneous propagation of *multiple sets* of traveling waves, in all possible directions, through two-dimensional wave-guiding structures.

9. Medium Parameters and Boundary Conditions.

Further, using the *CFISH* program, different regions of the field-domain can be geometrically outlined and electrically specified by selectively assigning the local values of the real and imaginary parts of the permittivity ϵ' and ϵ'' , and those of the permeability μ' and μ'' , thus simulating *complex media* and *absorbing boundaries*.

Either *Dirichlet* or *Neuman* boundary conditions can be assigned to selected external or internal field-interfaces, in both the *FISH* and *CFISH* EM field solver programs. *Conjugate* field solutions are obtained by appropriately *switching* the boundary condition types (*Dirichlet* \leftrightarrow *Neuman*).

All the numerous *FORTRAN 77* programs in the *Poisson/Superfish* set have already been ported, from their original *UNIX* and/or *CRAY* environment, to high-end PC-Work Stations running Windows 95 or Windows NT.

10. Post-Processing and Graphic Displays with *Matlab* .

Nine *Matlab* programs have been written to perform a number of different post-processing operations upon the numerical field data generated by the *Poisson/Superfish* codes. Smooth input field data are obtained that cover rectangular regions of user-specified size and location in Cartesian coordinates. These input field data are generated by the *Fortran* program *SF7* through localized interpolation of the mesh-node values with harmonic polynomials.

Table I summarizes the capabilities and functionality of the nine *Matlab* post-processing programs used.

The nine programs read the files of interpolated values of the real and imaginary parts of the H_z , E_x and E_y field-components and the corresponding x and y location-coordinates. These are the components of the numerically-computed *transverse-electric* field, that is the *conjugate* of the actual *transverse-magnetic* physical field.

The input data to *Matlab* cover (in all but the case of program *twoport.m*) only the *top half* of the total field domain, in order to reduce by a factor two the mesh size and the computation time. Those input data are then first used to fill the top-half rows of a larger rectangular matrix, and then used to fill the remaining rows with a mirror-image of the top rows. A complete representation of the field through the whole analysis domain is thus obtained.

Three of the nine *Matlab* programs directly plot the input *real* and *imaginary* parts of the field values in the form of 3D displays, of *contour* plots and of longitudinal *cuts*. Four other *Matlab* programs first combine the real and imaginary parts into complex field values and compute then the field *magnitudes* and *phases* as the complex absolute values and respectively the arguments thereof. The field magnitudes and phases are then similarly visualized in 3D, *contour* and longitudinal *cuts*.

The *Matlab* program *cvpolar.m* first converts the complex x and y field components to polar R and Φ components, and generates then the corresponding graphic displays. The nine *Matlab* post-processing programs listed in *Table I* generate a total of 187 different types of graphic presentation of the numerically-computed fields.

The programs *cvfields.m* and *cvpolar.m* display the cavity resonator fields on a 2×2 inch square region centered on the resonator axis, with a 2D resolution of 120×120 steps, with a total of 14,641 field values each.

The *Matlab* program *points.m* was used to verify the Cartesian coordinates of the junctions between straight- and arc-shaped boundary segments in the single six-port unit-cell cylindrical resonator geometry.

11. Field-Pattern Examples.

The figures 5-11 show seven examples of the field displays generated by the nine *Matlab* post-processing programs. *Figure 5* generated with the *halfs1xp.m* program shows the pattern of the *imaginary part* of the z -axis magnetic field H_z , on a 8×7.2 inch domain covering the whole single six-port resonator structure of *Figure 1*, on a 100×120 point grid. The input wave is clearly shown propagating down the left-hand waveguide and filling the resonator cavity before entering the other five passive waveguides.

The waves emerging from the resonator are clearly shown to be quite heavily attenuated soon after entering the impedance-matched absorbing regions at the end of the five passive waveguides. *Figure 6* shows a contour display of the same field pattern of *Figure 5*. Similarly, *Figure 7* generated by the *cvfields.m* program shows the pattern of the *magnitude* of the z -axis magnetic field H_z on a 2×2 inch square region centered on the resonator axis, with a 2D resolution of 120×120 steps, and *Figure 8* shows a contour display of the same field pattern of the previous *Figure 7*. Further, *Figure 9* shows a longitudinal cut of the phase of the H_z field along the common axes of the left-hand and right-hand waveguides through the cavity resonator region, with dashed vertical lines marking the positions of its input and output ports. Finally, the *Figures 10* and *11* show contour plots of the magnitudes of the *radial* and *azimuth* components E_r and E_ϕ of the total *transverse electric* field.

Longitudinal cuts through various phase patterns show the *electrical length* of the cylindrical resonator, between the left-hand input port and the right-hand output port, to be approximately 220° or slightly over half wave.

12. Expansions in Orthogonal Functions.

The dimensionality of any numerical representation of the internal complex vector fields of slow waves guided through a six-port resonator is however always too large to be directly usable in any practical model.

Even a minimally-acceptable numerical 2D field-representation, on a 121×121 Cartesian-coordinate grid centered on the cavity axis, includes $121^2 = 14,641$ field points. Each point is the location of 3 complex vector-field components each having a real and an imaginary part, for a total of $6 \times 14,641 = 87,846$ values.

A set of field values that large is obviously quite impractical as a basis for any model. Fortunately the field values obtained numerically are not mutually independent, but satisfy Maxwell's equation as elegantly expressed by either the *E*-field or *H*-field *curl-curl* equations.

Further, those equations admit mathematically-complete sets of mutually-orthogonal eigenfunctions, that may be used to approximate the numerically computed fields with the partial sums of eigenfunction expansions, each sum being completely defined by the values of a *finite number* of complex expansion coefficients.

The mutual orthogonality of the eigenfunctions in each set provides the possibility of independently computing the complex coefficient of each term in any given expansion, by a procedure similar to that used for the computation of Fourier coefficients. That procedure is based on evaluating the *inner product* of each candidate eigenfunction with one of the numerically-computed field patterns.

A complication is here however introduced by the numerically-computed fields being given in *numerical form* rather than as closed-form expressions of functions of two variables. This demands the numerical evaluation of the inner products of two complex functions of two variables (the Cartesian *x* and *y* coordinates), one of the two function being defined by a relatively large *2D numerical table*, a numerical *matrix* defined on a Cartesian grid.

Such evaluation must be obtained by performing a *double numerical integration* or *quadrature* with two nested loops (an *inner loop* and an *outer loop*), while saving the computed intermediate values in *global variables* for carry-over from one loop to the other. Both loops may execute a numerical procedure based on established quadrature formulas such as *Newton-Coates*, *Gauss* or *Gauss-Kronrod*.

The use of truncated modal expansions for the representation of the numerically-computed complex fields very substantially reduces the dimensionality of the field representations, as only a relatively small number of complex expansion coefficients is required to fully describe the given field to within a specified tolerance. Further, the field represented by the expansion is automatically divergence-free, and is an exact solution of Maxwell's equations that may approximate the given numerically computed field to any desired tolerance, while at the same time rigorously satisfying the imposed boundary conditions.

Expansions in cylindrical *Hankel* functions with appropriate *K_r* values, heuristically selected to *match* the graphically-displayed *radial field dependence* within a resonator, and with appropriate order *n* selected to match the graphically-displayed *angular periodicity*, clearly are the most appropriate choice for approximating the numerically-computed, azimuth-periodic *2D* internal complex vector-fields of slow waves propagating through a six-port cylindrical cavity resonator or through a small cluster.

The expressions of these cylindrical orthogonal functions are given by:

$$\psi_{nK_r} = H_n^{(1,2)}(K_r, r) e^{in\varphi} = [J_n(K_r, r) \pm iY_n(K_r, r)] e^{in\varphi}$$

These functions must then be *numerically evaluated* on the *same Cartesian grids* as the numerically-simulated complex field pattern $\mathcal{F}(x, y)$ to be expanded, prior to *numerically evaluating* the corresponding expansion coefficients. These numerical evaluations may be performed by substituting :

$$r = \sqrt{(x - x_0)^2 + (y - y_0)^2} \quad \text{and} \quad \varphi = \text{atan } 2[(y - y_0), (x - x_0)]$$

where (x_0, y_0) is the *origin* for the *Hankel* function, that may (or possibly may not?) be coincident with the center of the cavity resonator. The normalized complex expansion coefficients are then expressed by:

$$c_{nK_r} = \frac{1}{\|\psi_{nK_r}\|} \int_{x_{\min}}^{x_{\max}} \int_{y_{\min}}^{y_{\max}} \psi_{nK_r}(x, y) \mathcal{F}(x, y) dy dx$$

The fields obtained by exciting a cavity resonator or a cluster through only one of its input/output waveguides, with a single microwave source, obviously have reflection symmetry with respect to the input waveguide axis.

REFERENCES.

- [1] Speciale R. A. , "Mathematical Representation of Multiport Resonator Test Data," Proceedings of the 13th Annual Review of Progress in Applied Computational Electromagnetics, Vol. 1, pages 516-532, Monterey, California, March 17-21, 1997.
- [2] Speciale R. A. , "Wave Propagation on Two Dimensional Slow-Wave Structures with Hexagonal Lattice," Proceedings of the 13th Annual Review of Progress in Applied Computational Electromagnetics, Vol. 2, pages 1015-1028, Monterey, California, March 17-21, 1997.
- [3] Speciale R. A. , US Patent No. 5,512,906 Awarded April 30, 1996 (Accessible at :
http://patent.womplex.ibm.com/details?patent_number=5512906, and at :
http://patent.womplex.ibm.com/cgi-bin/db2www.cmd/v3/claims.d2w.../report?patent_number=5512906.
- [4] Speciale R. A. , " Computation of Clustered Phased Array EM Fields Using Particle Accelerator Codes," Proceedings of the 15th Annual Review of Progress in Applied Computational Electromagnetics, pages 72-85, Monterey, California, March 15-20, 1999.
- [5] Speciale R. A. , "Advanced Design of Phased Array Beam-Forming Networks," *IEEE Antenna and Propagation Magazine*, Vol. 38 , No. 4 , pp. 22-34, August 1996.
- [6] Speciale R. A. , "Synthesis of Phased Array Aperture Distributions," Paper submitted on January 11, 1997 for publication in the *IEEE Antenna and Propagation Magazine*, currently being edited to conform to reviewer's suggestions (a preliminary 85-page version of the manuscript is available and copy thereof may be requested from the author).
- [7] Speciale R. A. , "Symmetry Analysis of Large Two Dimensional Clusters of Coupled Cavity Resonators," Proceedings of the 1993 *IEEE Antenna and Propagation Society International Symposium*, Vol. 3, pages 1258-1261, Ann Arbor, Michigan, June 28-July 2, 1993.
- [8] Speciale R. A. , " Wave Propagation on Two-Level Twin-Stacked-Honeycomb Structures," Proceedings of the 13th Annual Review of Progress in Applied Computational Electromagnetics, Vol. 2, pages 1029-1035, Monterey, California, March 17-21, 1997.
- [9] Billen J. H. and Young L. M. , "*Poisson/Superfish*," Software System Documentation, Report LA-UR-96-1834 (Revised August 28, 1997), Los Alamos National Laboratory, Los Alamos, New Mexico.
- [10] Cooper R. K. et al. , "Electromagnetic Design Codes Maintained on the MFE Network by the LAACG," Proceedings of the 5th Annual Review of Progress in Applied Computational Electromagnetics, Monterey, California, March 20-24, 1989, pages 9-21.



Matlab Post-Processing Programs

File Name	Interpolated Region	Interpolation Grid	Displayed Region	Display Resolution	No. of Figures	Display Param.	Plot Types	Displayed Fields
<i>sp1ttr3.m</i>	28.636 × 4.318 cm	100 × 20	28.636 × 8.636 cm	100 × 40	21	Real & Imaginary	3D, Cont. & Cuts	E_x E_y H_z
<i>points.m</i>	-	-	8.0 × 7.2 inch	-	3	Cartesian Coordinates of the Fixed Boundary Points of the Half Sixport		
<i>twoport.m</i>	8.0 × 1.5625 inch	100 × 40	8.0 × 1.5625 inch	100 × 40	21	Real & Imaginary	3D, Cont. & Cuts	E_x E_y H_z
<i>halfsixp.m</i>	8.0 × 3.6 inch	100 × 60	8.0 × 7.2 inch	100 × 120	21	Real & Imaginary	3D, Cont. & Cuts	E_x E_y H_z
<i>halfcavt.m</i>	8.0 × 3.6 inch	100 × 60	2.0 × 2.0 inch	25 × 120	21	Real & Imaginary	3D, Cont. & Cuts	E_x E_y H_z
<i>spfields.m</i>	8.0 × 3.6 inch	100 × 60	8.0 × 7.2 inch	100 × 120	25	Mag & Phase	3D, Cont. & Cuts	E_x E_y H_z
<i>spflds2.m</i>	8.0 × 3.6 inch	100 × 60	8.0 × 7.2 inch	100 × 120	25	Mag & Phase	3D, Cont. & Cuts	E_x E_y H_z
<i>cvfields.m</i>	2.0 × 2.0 inch	120 × 60	2.0 × 2.0 inch	120 × 120	25	Mag & Phase	3D, Cont. & Cuts	E_x E_y H_z
<i>cvpolar.m</i>	2.0 × 2.0 inch	120 × 60	2.0 × 2.0 inch	120 × 120	25	Mag & Phase	3D, Cont. & Cuts	E_r E_ϕ H_z

Table I - Capabilities of the nine *MATLAB* Post-Processing Programs used to generate a total of 187 Graphic Displays of the Internal Fields of the Six-Port Unit-Cell.

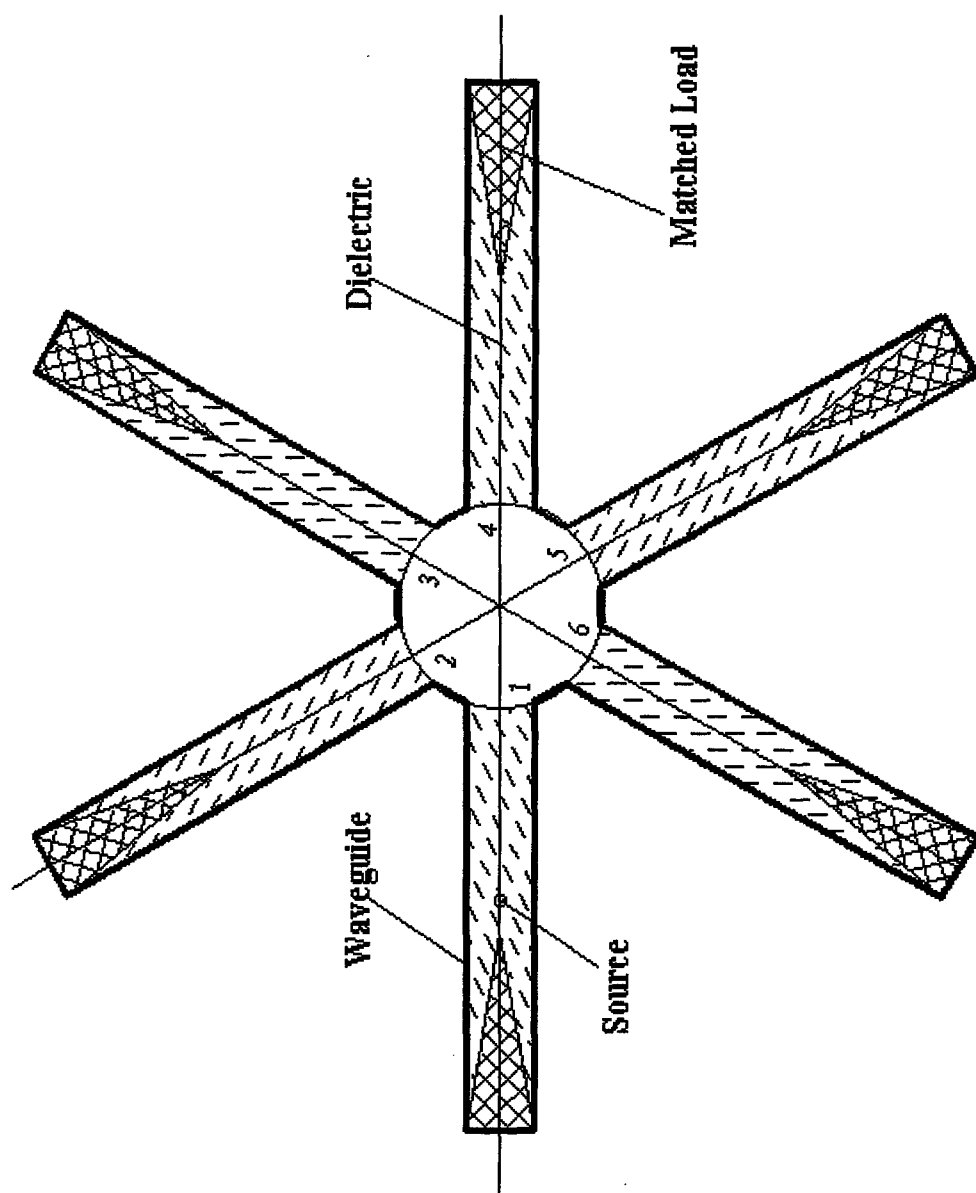


Figure 1 - Six-Port Cylindrical Cavity Resonator with C-6v Rotation/Reflection Symmetry.

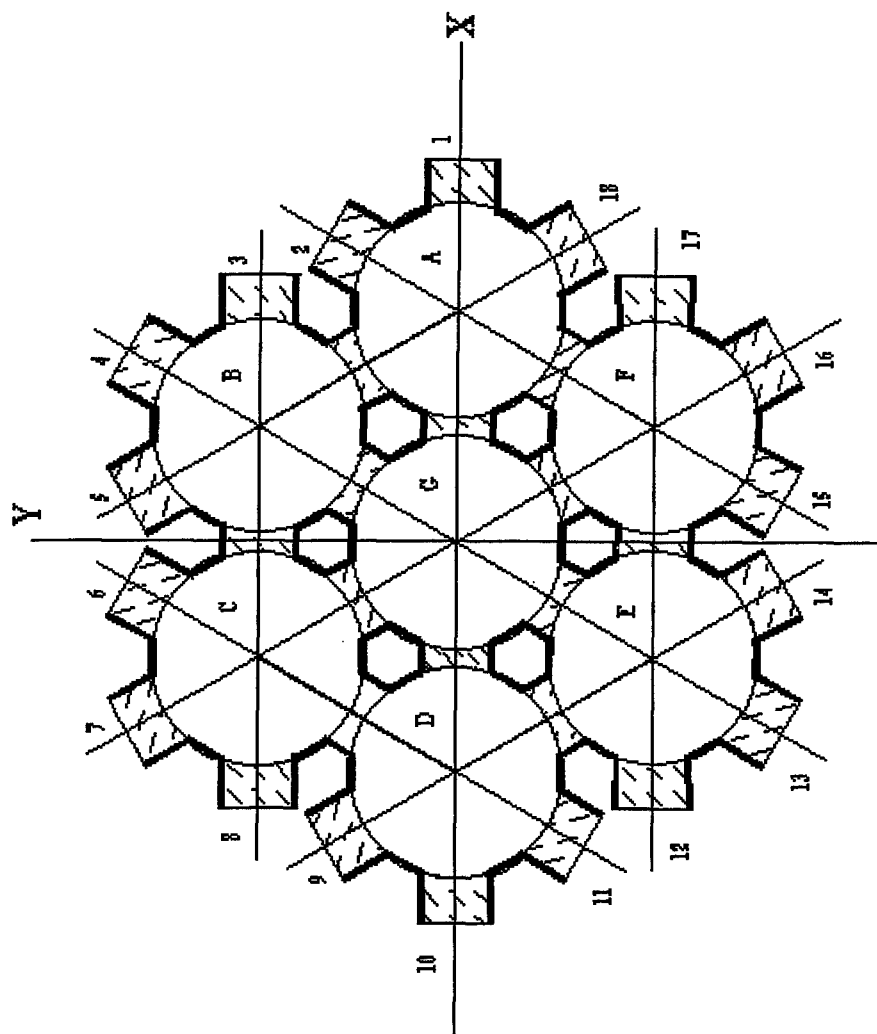


Figure 2 - Hexagonal Cluster of Resonant-Iris-Coupled Cylindrical Cavity Resonators.

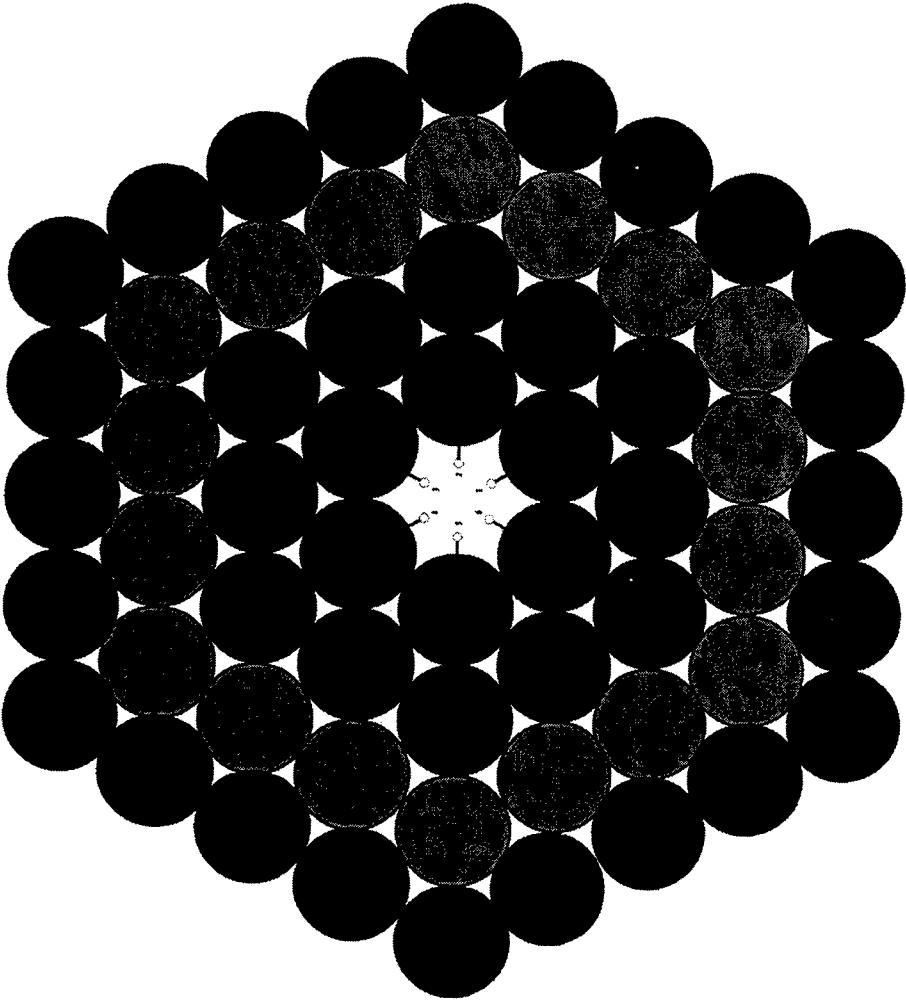
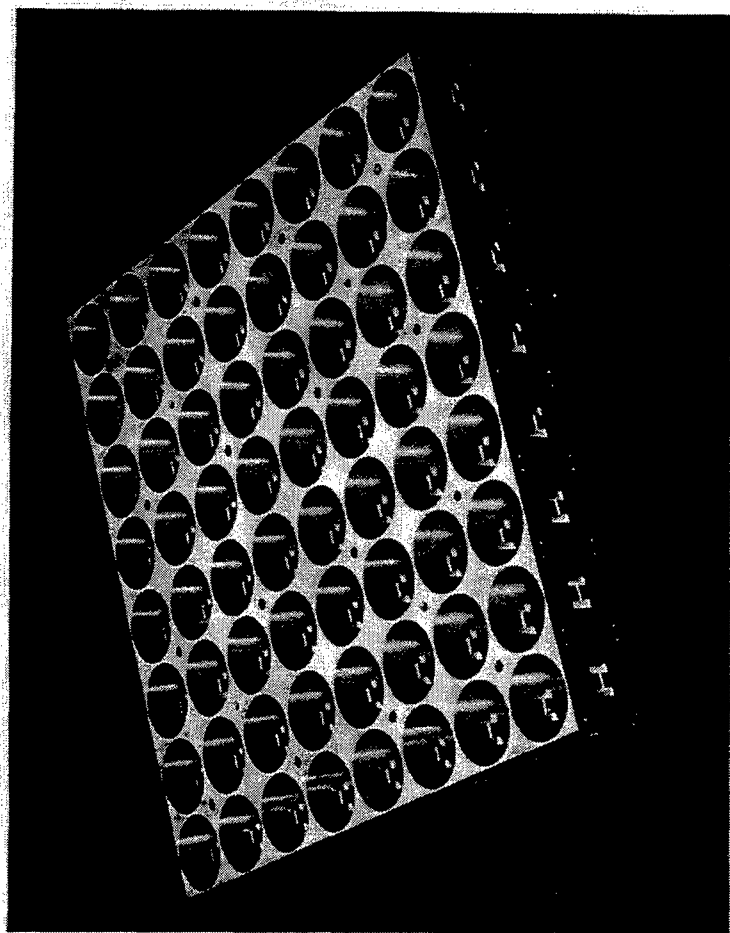


Figure 3 - Hexagonal Cluster of Coupled Cylindrical Cavity Resonators.



**Figure 4 - An 8×8 Cluster of Cylindrical TM_{010} Cavity Resonators
Coupled through Resonant Dumbbell-Shaped Irises.**

FIGURE 5 - 3D PLOT OF THE IMAGINARY Z-AXIS MAGNETIC FIELD COMPONENT

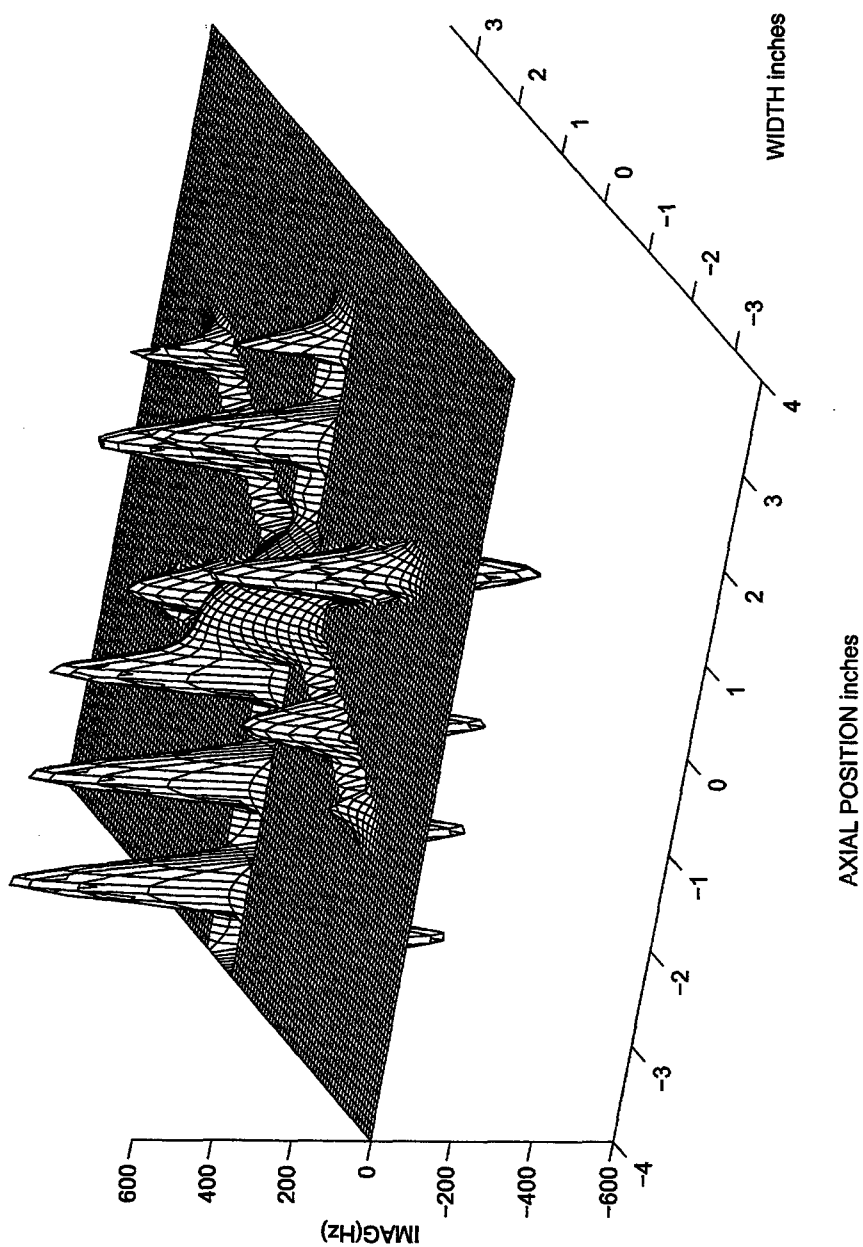


FIGURE 6 -- CONTOUR PLOT OF THE IMAGINARY Z-AXIS MAGNETIC FIELD COMPONENT

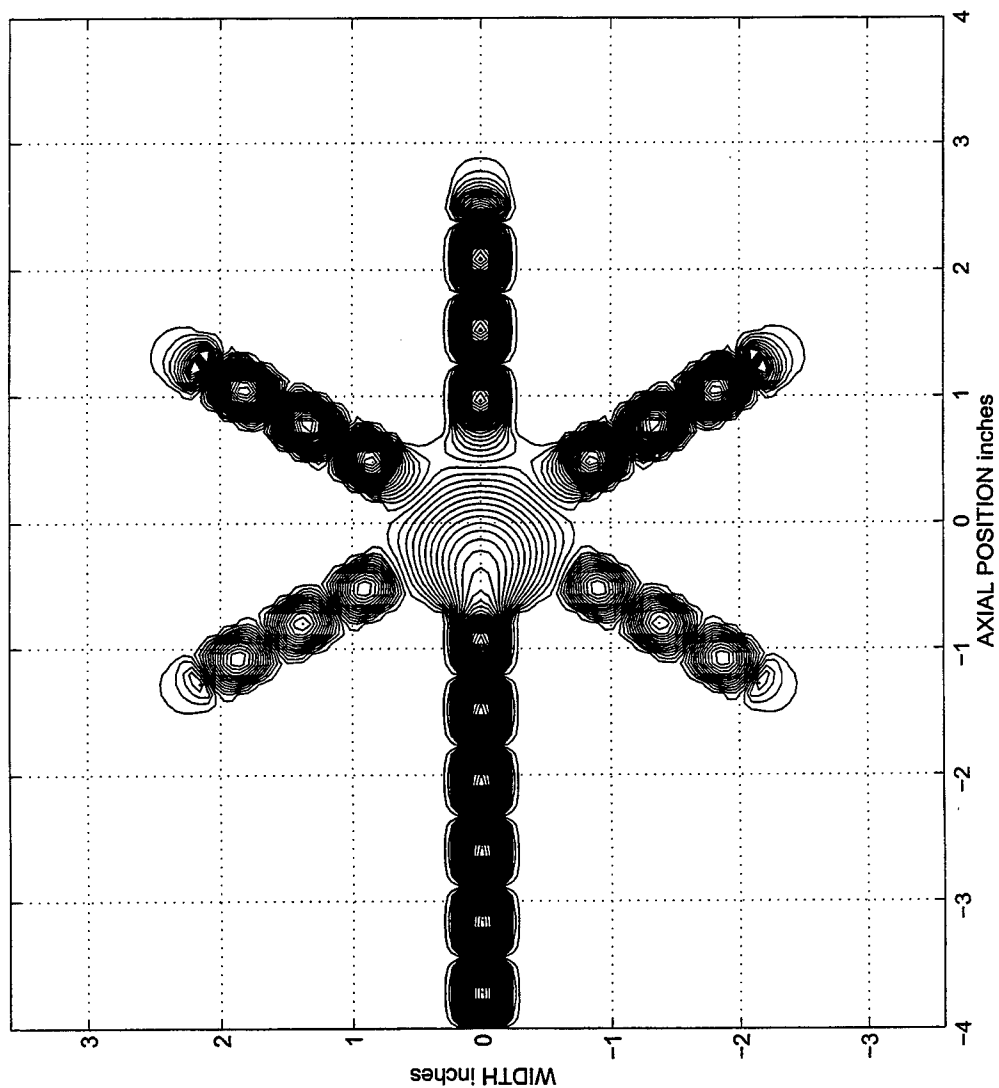


FIGURE 7 - AMPLITUDE OF THE Z-AXIS MAGNETIC FIELD IN THE RESONATOR REGION

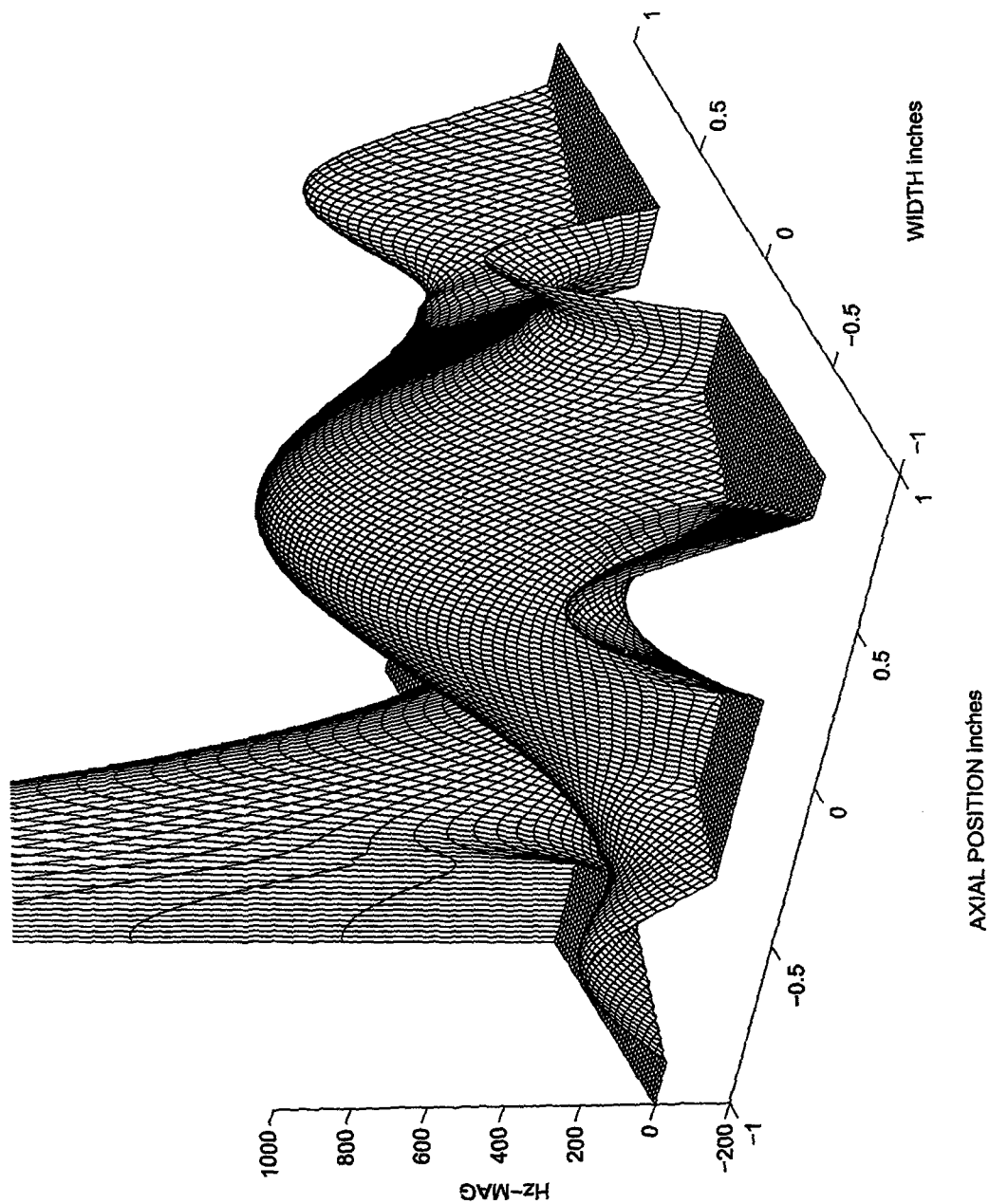


FIGURE 8 - CONTOUR PLOT OF THE AMPLITUDE OF THE Hz-FIELD IN THE RESONATOR REGION

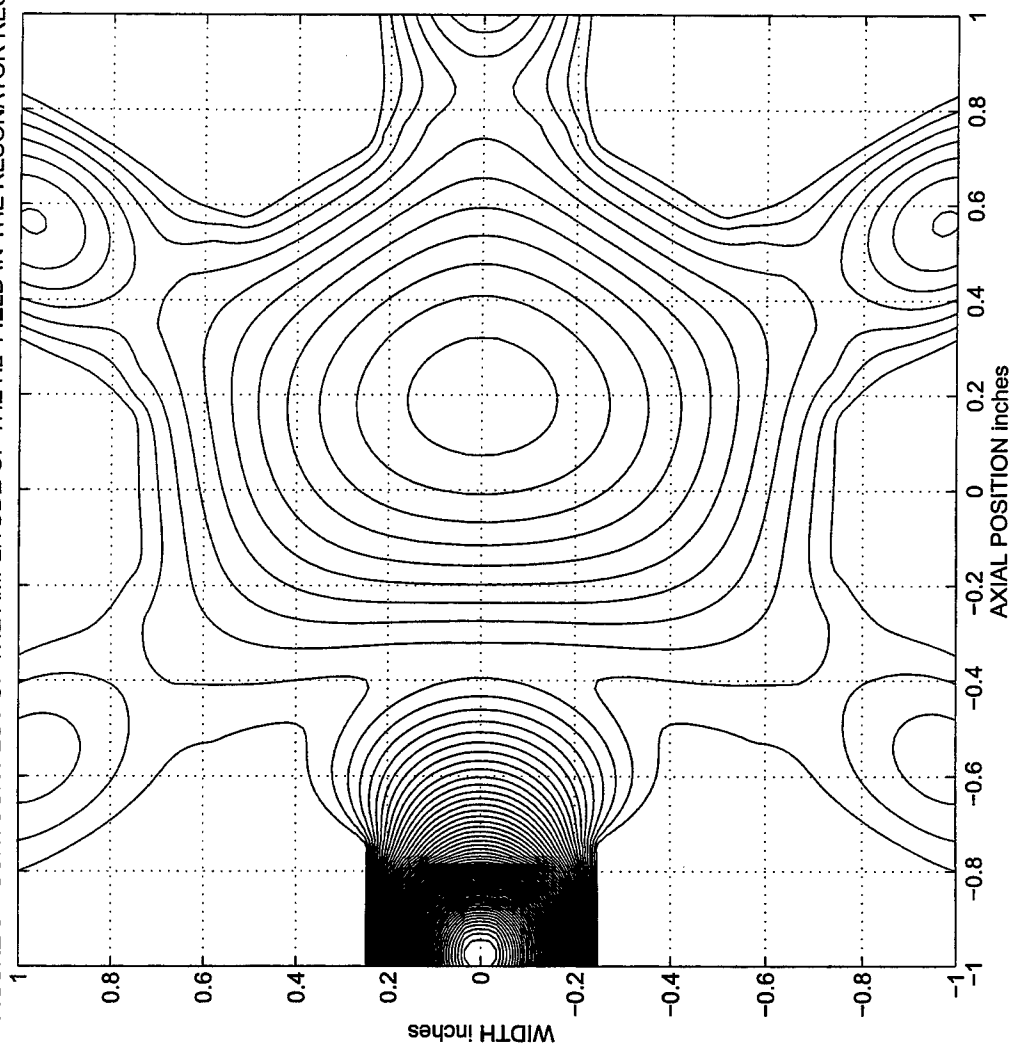


FIGURE 9 - PLOT OF THE PHASE OF THE Hz FIELD COMPONENT

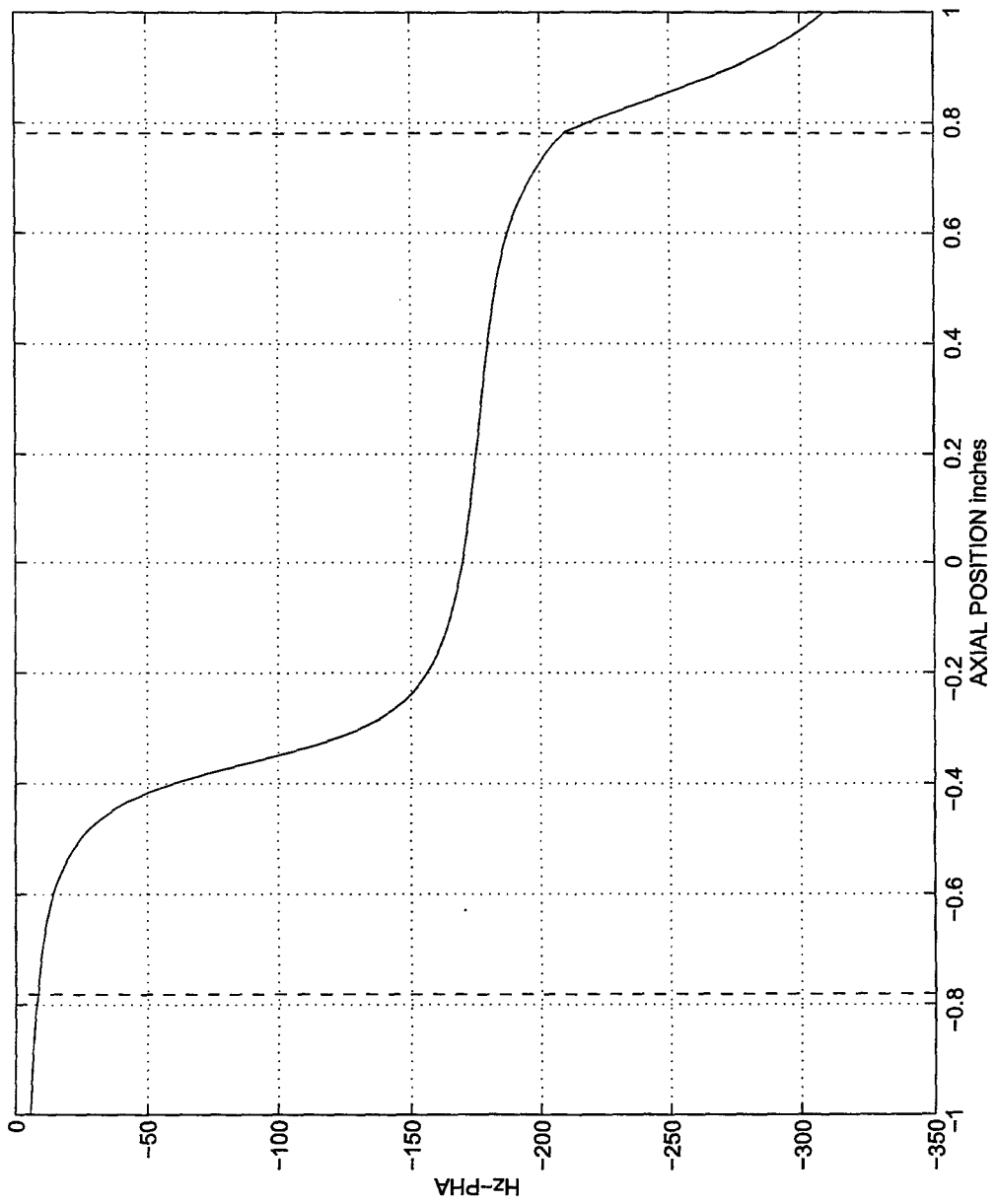


FIGURE 10 - CONTOUR PLOT OF THE AMPLITUDE OF THE RADIAL ELECTRIC FIELD COMPONENT

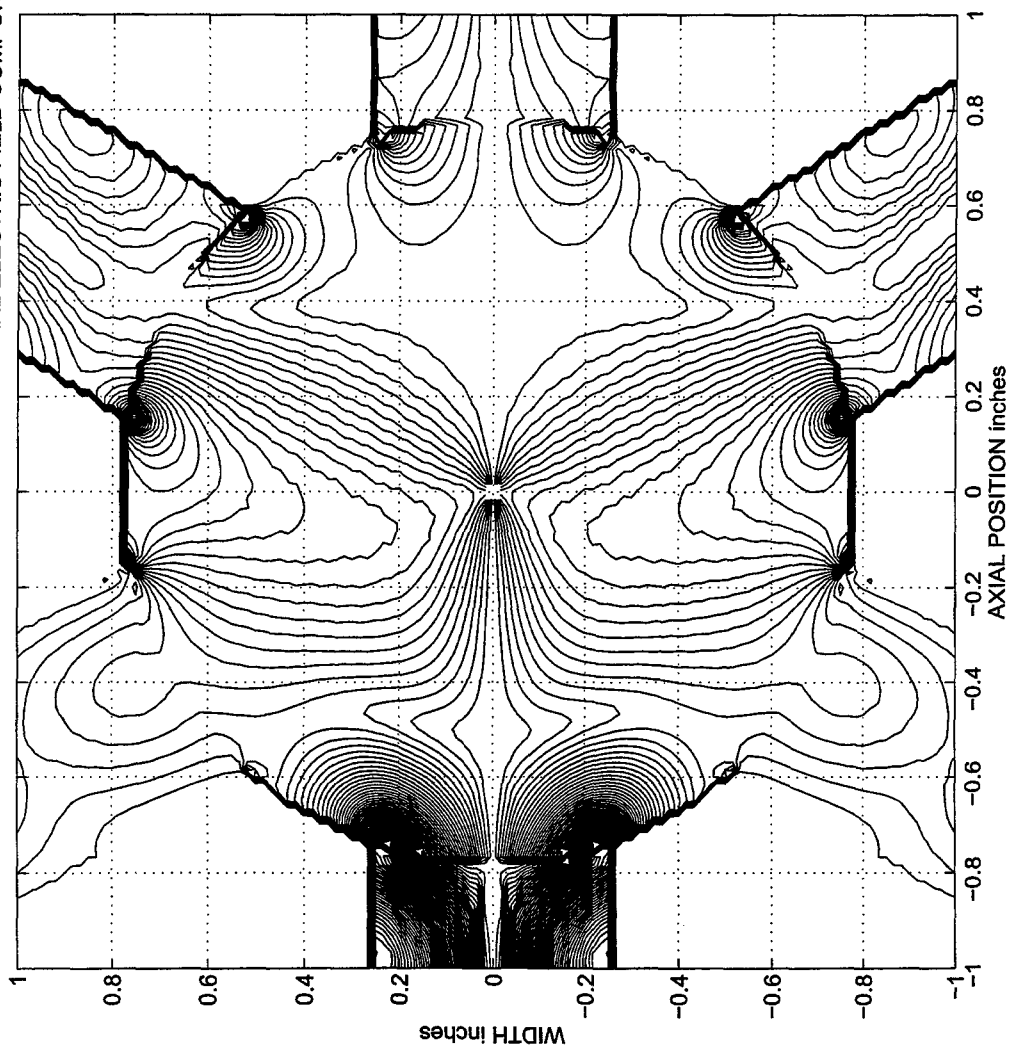
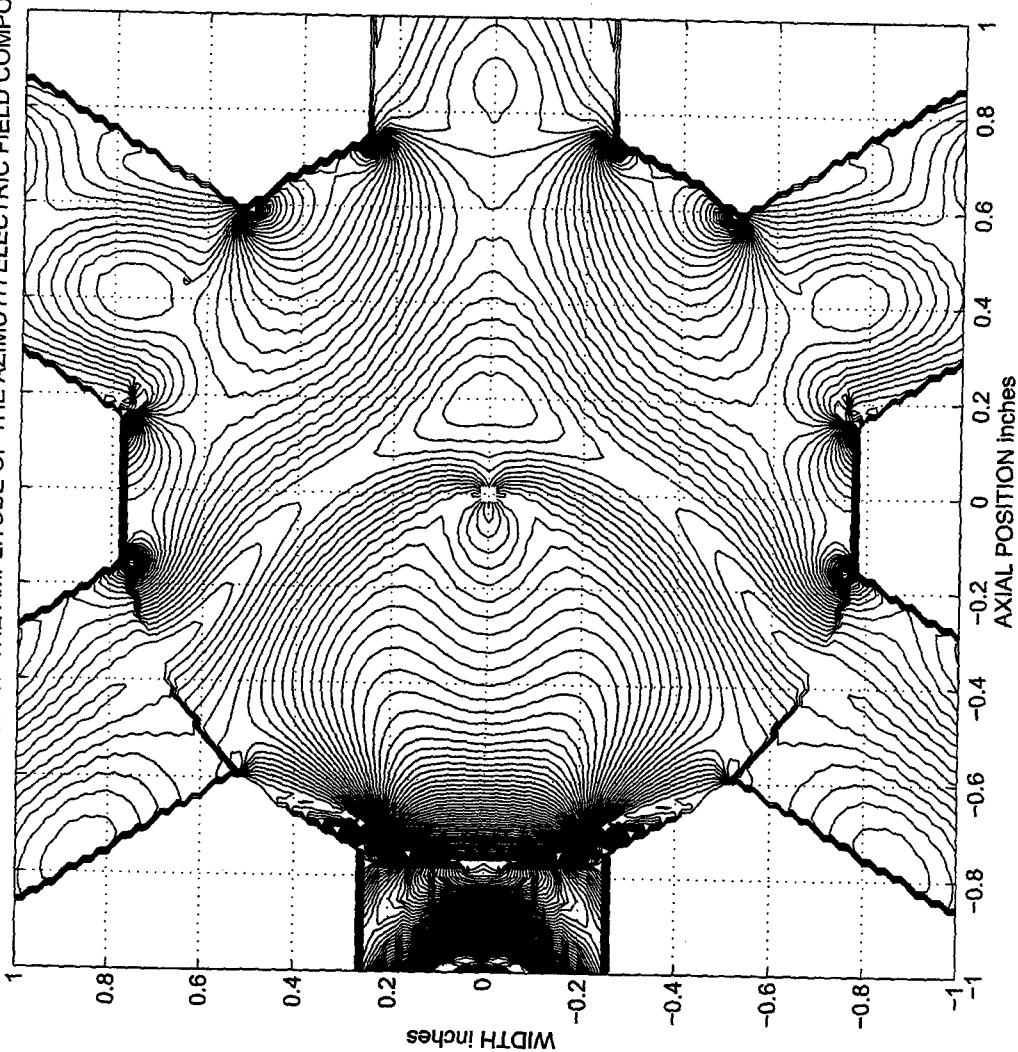


FIGURE 11 - CONTOUR PLOT OF THE AMPLITUDE OF THE AZIMUTH ELECTRIC FIELD COMPONENT



Design Software for Cylindrical Helix Antennas

M. Slater
MLAR Consulting
Montreal
Mike_sl@bigfoot.com

C.W. Trueman
Concordia University
Montreal
Trueman@ece.concordia.ca

Abstract-This paper provides a software tool for designing a cylindrical helix to meet a performance specification. The helix has circumference C , pitch angle α , and number of turns N . It operates over an infinite ground plane. The performance specification consists of a minimum gain value, a 3 dB beamwidth, a maximum value for the axial ratio, all of which must all be maintained over a specified bandwidth. The helix radius is chosen to make the helix circumference equal to the wavelength at the center of the band. The design objective is to define the pitch angle and the number of turns. The Helix Design software identifies "solutions" or regions in the pitch-turns plane that satisfy the specification over the desired bandwidth. This interactive design tool permits the user to start the process by working at the center frequency with a "loose" specification, obtaining a large "solution" region, then gradually tightening the specification, causing the solution regions in the pitch-turns plane to become smaller. Adding a frequency bandwidth narrows the solution space further. Too tight a specification or too wide a bandwidth leads to no solutions and so the design cannot be realized with a cylindrical helix. The Helix Design Software should help engineers to rapidly focus on the pitch and number of turns that can realize a particular performance specification.

1 Introduction

Kraus [1] describes the performance of an axial-mode helix antenna and provides graphs and formulas helpful in helix antenna design. King and Wong [2] did extensive measurements of helix performance that yielded design curves and graphs. Lee, Wong and Larm [3] as well as Emerson [4] suggested improvements to the Kraus model of helix performance, especially for longer helices. There are some software tools for helix analysis on the Internet [5,6]. These tools require the antenna designer to specify the helix circumference, pitch angle and number of turns, and then compute the corresponding performance results: gain, beamwidth and axial ratio as a function of frequency. This paper provides a helix design software tool called "Helix Design" that accepts the desired performance specification, gain, beamwidth, axial ratio and bandwidth, and determines the possible designs that can realize this performance.

The "Helix Design" software uses a database of helix performance data created by modeling the helix[7] using the well-known "Numerical Electromagnetics Code"(NEC)[8]. Helices of various radii, pitches and numbers of turns were analyzed over a range of

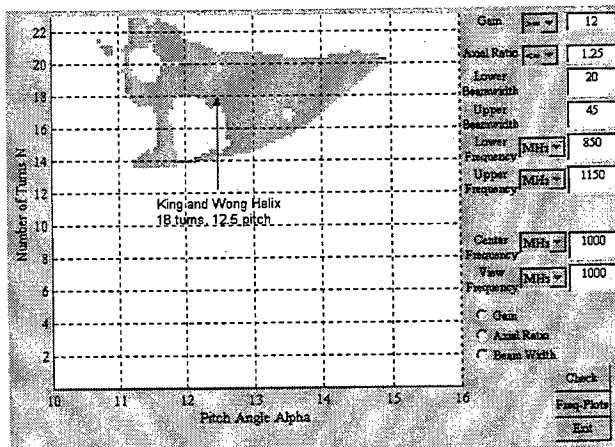


Figure 1 The Design Window.

frequencies and the gain, axial ratio, and beamwidth were tabulated. Helices from 2 to 22 turns with pitch angles varying from 10 to 16 degrees were examined from 850 to 1200 MHz. The design software uses frequency scaling and linear interpolation to determine the performance of any helix design within the range of the database.

2 The Helix Design Software

The Helix Design software incorporates a MATLAB engine but runs as a stand-alone program. It presents the user with the "Design Window" shown in Fig. 1. With this window we can define the performance specifications and bandwidth, and then identify the possible designs for the helix.

2.1 Performance Specification

The "performance specification" consists of the desired gain, axial ratio and beamwidth over a specified bandwidth. The user specifies the frequency bandwidth, from frequency f_{\min} to frequency f_{\max} . For most designs, the gain must be greater than G_{\min} over the specified bandwidth. The axial ratio must be less than AR_{\max} over the bandwidth. The beamwidth is defined as the number of degrees between the 3 dB points in the main lobe. The user can specify a minimum beamwidth, BMW_{\min} , and a maximum beamwidth, BMW_{\max} , such that the beamwidth must lie in the range $BMW_{\min} \leq BMW \leq BMW_{\max}$. The gain, axial ratio and beamwidth must be maintained over the whole frequency range from f_{\min} to f_{\max} . The helix design defines the physical characteristics of the helix: the number of turns N , the pitch angle α , and the circumference C of the helix. With these values we can actually build the helix.

The "center frequency" f_{cen} is defined to be the frequency where the circumference of the helix, C , is equal to one wavelength. The user chooses the center frequency relative to the minimum and maximum frequency f_{\min} and f_{\max} . Usually the arithmetic mean is chosen as the center frequency, although the user is free to choose any value within the bandwidth.

2.2 The Design Window

The user starts the program, which displays the Design Window shown in Fig. 1. The user enters the desired performance specification in the appropriate fields: gain, axial ratio, lower and upper beamwidth limits, and the desired frequency range, including the user's choice of center frequency. The window shows the pitch-turns plane with the pitch on the horizontal axis and the number of turns on the vertical. Selecting the "Check" button at the lower right corner sets the program to work identifying the "solution space": the regions in the pitch-turns plane where the helix meets the desired performance specification over the whole bandwidth.

For example, suppose we want a minimum gain of 12 dB, a maximum

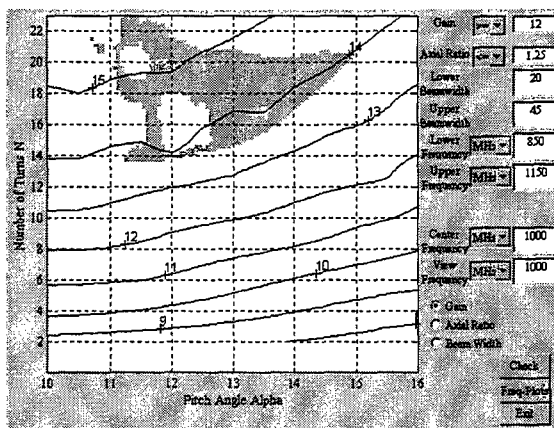


Figure 2 Gain contours at 1000 MHz.

axial ratio of 1.25, a beamwidth between 20 and 45 degrees, and a bandwidth from 850 to 1150 MHz. In Ref. [2], a helix of 18 turns and pitch angle 12.5 degrees realizes this performance specification. In the design window in Fig. 1 we select the center frequency as 1000 MHz and then click the "Check" button at the lower right. The program identifies the shaded "solution space" shown in Fig. 1 as all possible designs for the helix that meet the performance specification. Fig. 1 shows an extensive region, which includes 18 turns and 12.5 degrees pitch. Many other combinations of turns and pitch realize the specification as well.

2.3 Contour Maps: Gain, Axial Ratio and Beamwidth

The Design Window makes available contours of gain, axial ratio and beamwidth at specific frequencies. The user enters a frequency in the "view frequency" field, and then selects gain, axial ratio or beamwidth by clicking one of the buttons at the lower right. Fig. 2 shows the gain contours at the center frequency of 1000 MHz. At this frequency the gain is well above the minimum of 12 dB in the specification. Fig. 3 shows the axial ratio contours at 1000 MHz. The axial ratio at this frequency is also well below the maximum of 1.25 for all the highlighted regions. Selecting "Beam Width" gets a similar contour map for the beamwidth at this frequency.

The Helix Design software permits more than one set of contours to be displayed at one time. This is illustrated in Fig. 4 where we see contours of both gain and beamwidth, at 1000 MHz. The highlighted regions show that the beamwidth at this frequency is within the specified range. The figure indicates that, at least at this one frequency, we could have a gain of almost 15 dB, with a narrow beamwidth of roughly 25 degrees.

2.4 Exploring the Limiting Factors

The Helix Design software can give us insight into which of the performance specifications has the most impact in narrowing the solution space of possible helix designs. Set the "view frequency" to either the lowest or the highest frequency in the band, and look at the contours for gain, for axial ratio and for beamwidth. Thus in our example, using a the view frequency of 850 MHz, and displaying the gain, as in Fig. 5, shows that the shaded region touches the 12 dB gain contour. If we were to relax the gain requirement at 850 MHz we would have a larger solution space of possible designs for the helix. We can use the design

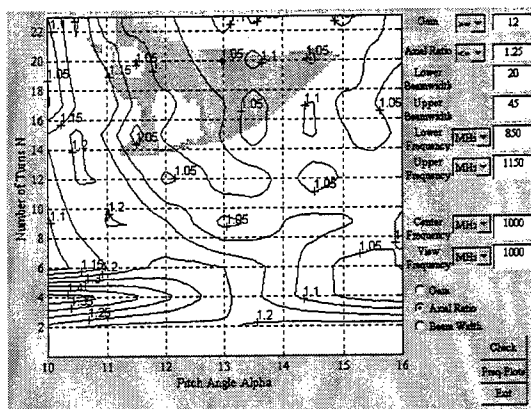


Figure 3 Axial Ratio Contours at 1000 MHz

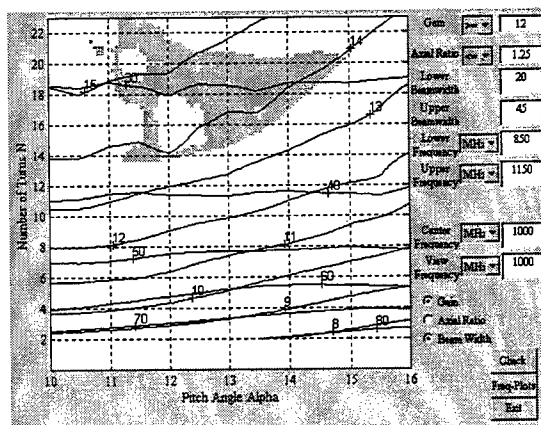


Figure 4 Gain and beamwidth contours at 1000 MHz.

window to explore the possibilities for helix performance for a given application. Thus if we start with the lower and upper frequencies set equal to the center frequency, and enter the desired gain, axial ratio and beamwidth, and click the "Check" button, we determine whether the desired performance is possible at the center frequency. A large "solution space" is often obtained at this stage. Widening the bandwidth narrows the solution space. We can use the "view frequency" and contour-mapping capabilities to identify which of the performance specifications is responsible for the narrowing. Sometimes we can refine the performance specification by making appropriate tradeoffs.

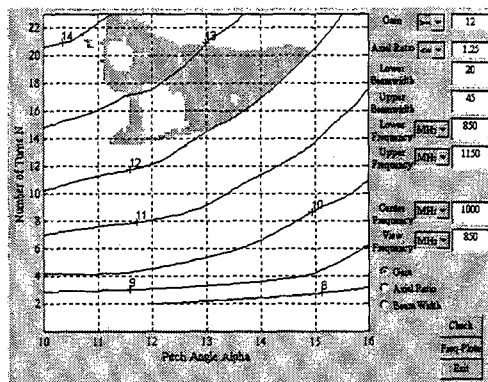


Figure 5 Gain contour at 850 MHz.

2.5 Frequency Plot Window

The user can examine the performance of the helix as a function of frequency using the "frequency plot" window. Choose a design for the helix, namely values for the pitch angle α and the number of turns N from the highlighted regions in Fig. 1, and then select the "Freq-Plots" button at the lower right, to see the window of Fig. 6. Enter the design values in the "pitch angle" and "number of turns" fields. For example, we can use the King and Wong design of 12.5 degrees pitch and 18 turns. The program then graphs the gain, axial ratio and the beamwidth over the specified bandwidth, as shown in Fig. 6. The results correspond very well with those presented by King and Wong[2]. However, Fig. 1 indicates that many other helix designs can realize the desired performance. For example, we could choose a helix with fewer turns. From the solution space in Fig. 1 we see that a helix of 14 turns and a pitch angle of 11.5 degrees would achieve the same performance specification. The frequency plot window for this design is shown in Figure 7. The shorter helix, with 14 instead of 18 turns, may be desirable because it is lighter and smaller. However, comparing the performance in Figs. 6 and 7 shows that the shorter helix has a poorer axial ratio above about 1050 MHz. Note that the axial ratio still meets the performance specification. The choice of 14 or 18 turns depends on whether the engineer wishes to tighten the axial ratio specification, or whether it is more important to use the smaller antenna.

3 Conclusions

The Helix Design Software tool provides an alternative approach to designing helices. The classical approach has been to iteratively design a helix according to the guidelines developed by Kraus or King and Wong, and then examine the performance. The

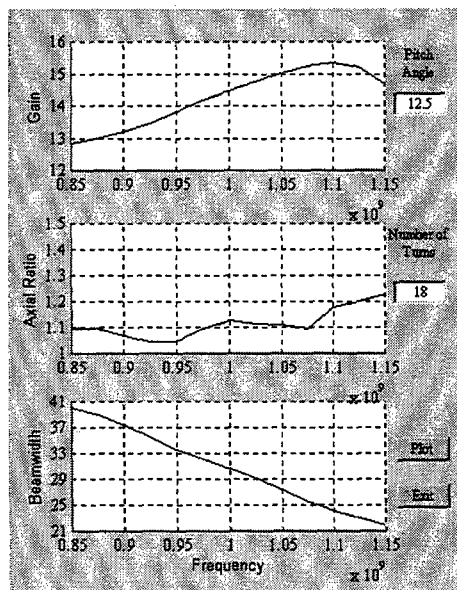


Figure 6 Frequency response with 18 turns and a 12.5 degree pitch.

Helix Design Software permits us to specify the desired performance and then identify all possible combinations of pitch angle and number of turns for a cylindrical helix that meet the specification. The program can then be used to identify the limiting factors in the performance specification. We can choose a design that meets our performance specification and also meets other criteria such as minimize the size or weight. The Helix Design Software permits us to explore whether we could meet a more stringent performance specification over the given bandwidth.

4 References

1. Kraus, J.D., Antennas, 2nd edition, McGraw-Hill, 1988.
2. King, H.E., and Wong, J.L., "Characteristics of 1 to 8 Wavelength Uniform Helical Antennas", IEEE Trans. On Antennas and Propagation, Vol. AP-28, No. 2, pp. 291-296, March 1980.
3. Lee, K.F., Wong, P.F., and Larm, K.F., "Theory of the Frequency Responses of Uniform and Quasi-Tapered Helical Antennas", IEEE Trans. On Antennas and Propagation, Vol. AP-30, pp. 1017-1021, 1982.
4. Emerson, D.T., "The Gain of Axial Mode Helix Antenna: A Numerical Modeling Study", <http://www.tuc.nrao.edu/~demerson/helixgain/helix.htm>, 1994.
5. Cronin, J., Helical-O-Matic.N2VNO, jdc@cci.com.
6. Granholm, H., Helix v2.0.
7. Trueman, C. W., Sultan, N., Kubina, S.J., Pellerin, T., "Software for Modeling Helix Antennas with NEC and Validation by Measurement", 12th Annual Conference Proceedings of the Applied Computational Electromagnetics Society (ACES), Vol. II, pp. 703-710, 1996.
8. Burke, G.J., "Numerical Electromagnetics Code NEC-4 Method of Moments", Lawrence Livermore National Laboratory, Report No. UCRL-MA-109338, Jan. 1992.

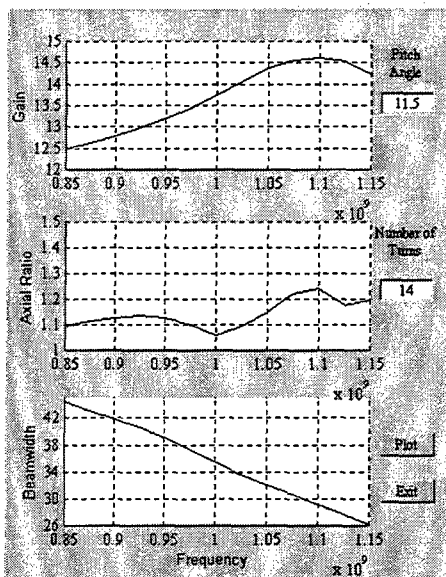


Figure 7 Frequency response with 14 turns and a 11.5 degree pitch.

THE ANALYSIS OF A CENTER-FED HELICAL MICROSTRIP ANTENNA MOUNTED ON A DIELECTRIC-COATED CIRCULAR CYLINDER USING THE RECIPROCITY THEROEM

R.A. Martin and D.H. Werner
The Pennsylvania State University
Applied Research Laboratory
PO Box 30
State College, PA 16804-0030

1. Introduction

The use of conformal antennas has become of great interest in recent years and several books and technical reports have been written discussing various aspects of their analysis and design [1-6]. A direct analytical approach for determining radiation patterns of microstrip antennas mounted on dielectric-coated metallic cylinders has been developed in [7]. More recently, an approach that exploits the Reciprocity Theorem has been used to find expressions for the radiated fields of an arbitrarily-shaped microstrip antenna mounted on a circularly-cylindrical platform [8]. One of the main advantages of this technique is that it does not require the tedious evaluation of complicated layered media Green's functions for curved geometries in the evaluation of the far-zone fields.

The propagation and radiation characteristics of the tape helix with a conducting core and dielectric substrate have been investigated in [9, 10]. In particular, an equation was derived in [9, 10] that describes the dispersion characteristics of the tape helix. The circuit and radiation characteristics of a helical antenna of square cross-section with a dielectric core have been studied in [11]. The analysis techniques developed in [9-11] either assume that the helix is infinite in extent or is being end-fed. In this paper, we consider a center-fed helical microstrip antenna of finite length. The reciprocity approach, originally introduced in [8], will be applied here in order to conveniently derive expressions for the far-zone radiation patterns of this helical microstrip structure.

2. Theoretical Development

A. The Reciprocity Theorem

In order to find equations for the far-field radiation patterns of an arbitrarily shaped microstrip patch, a procedure invoking the Reciprocity Theorem is used. Suppose we consider the system shown in Figure 1

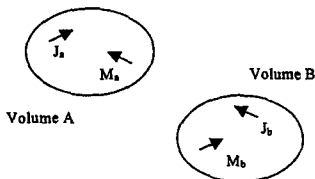


Figure 1: Reciprocity Theorem

By using Maxwell's equations and assuming no magnetic sources, $\vec{M}_a = \vec{M}_b = 0$, it can be shown that

$$\iiint_{V_a} \vec{E}_a \cdot \vec{J}_b dV = \iiint_{V_b} \vec{E}_b \cdot \vec{J}_a dV \quad (1)$$

If a further assumption is made that source "a" is an infinitesimal dipole located at some point (x_0, y_0, z_0) , then (1) may be expressed in the following way:

$$\vec{E}_b(x_0, y_0, z_0) \cdot \hat{u} = \frac{1}{h} \iiint_{V_b} \vec{E}_a \cdot \vec{J}_b dV' \quad (2)$$

Finally, by assuming that source "b" is an arbitrarily shaped microstrip patch mounted on the surface of a dielectric-coated PEC cylinder, we arrive at the following result:

$$\vec{E}_b(x_0, y_0, z_0) \cdot \hat{u} = \frac{1}{\Pi} \iint_{S_b} \vec{E}_a \cdot \vec{J}_{S_b} dS' \quad (3)$$

where S_b represents the surface area of an arbitrarily-shaped patch and \vec{J}_{S_b} is the corresponding current density on the surface of the patch. The integration of the dot product of the known field \vec{E}_a at the surface of a dielectric-coated cylinder (evaluated in the absence of the patch) and the antenna surface current will provide the required far-field radiation patterns of the patch antenna.

B. Far-Field Expressions

The geometry for the problem of interest is shown in Figure 2. The cylinder has an inner radius of a and an outer radius of b . The dielectric coating has a relative permittivity of ϵ_r and a thickness of $h=b-a$. This type of microstrip antenna configuration is becoming increasingly popular due to its conformal nature and unique radiation characteristics.

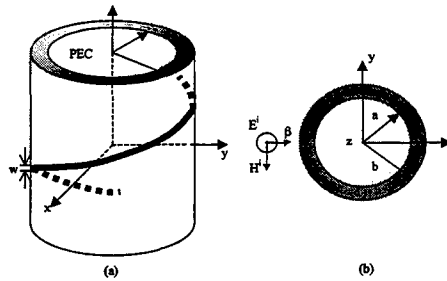


Figure 2: Geometry (a) and Top View (b) for TM^z Case

If the assumption is made that the width of the microstrip helix is small compared to a wavelength, then the current will be essentially constant over the width. Therefore, a good approximation for the current distribution on a center-fed helix will be

$$\vec{J}_s(l') = \frac{I_0}{w} \sin \left[\beta_1 \left(\frac{L}{2} - |l'| \right) \right] \hat{u}_s \quad (4)$$

where L represents the total length of the wire strip, l' is the arclength measured along the strip, and \hat{u}_s is the unit vector directed along the length of the helix. Since the helical microstrip antenna is mounted on a cylindrical platform, the surface current can be divided into the following components:

$$\vec{J}_s(l') = J_\phi(l') \hat{u}_\phi + J_z(l') \hat{u}_z \quad (5)$$

Next, the incident electric fields are grouped into two cases: namely the TM^z and TE^z . Using (3) in conjunction with these two cases leads to the expressions for the theta and phi components of the far-field radiation pattern given by

$$E_\theta(r, \theta, \phi) = -\frac{b}{\Pi} \iint_{S'} \vec{E}_i^{TM} \cdot \vec{J}_s d\phi' dz' \quad (6)$$

$$E_\phi(r, \theta, \phi) = -\frac{b}{\Pi} \iint_{S'} \vec{E}_i^{TE} \cdot \vec{J}_s d\phi' dz'$$

The modal expressions for the fields \vec{E}_i^{TM} and \vec{E}_i^{TE} can be obtained by solving the scattering problem for a plane wave obliquely incident on a dielectric-coated PEC circular cylinder. Substituting these field expansions into (6) and integrating the results term-by-term yields

$$E_\theta(r, \theta, \phi) = -j\eta_0 \frac{e^{-j\beta_0 r}}{4\pi r} \left\{ \frac{\beta_z}{\beta_\rho b} \sum_{n=-\infty}^{\infty} n(-1)^n [j^{-n} J_n(\beta_\rho b) + a_n H_n^{(2)}(\beta_\rho b)] S_\phi(n, \beta_z) e^{jn\phi} \right. \\ \left. - j\beta_0 \sum_{n=-\infty}^{\infty} a_n^* (-1)^n H_n^{(2)'}(\beta_\rho b) S_\phi(n, \beta_z) e^{jn\phi} \right. \\ \left. - \beta_0 \sin \theta \sum_{n=-\infty}^{\infty} (-1)^n [j^{-n} J_n(\beta_\rho b) + a_n H_n^{(2)}(\beta_\rho b)] S_z(n, \beta_z) e^{jn\phi} \right\} \quad (7)$$

$$E_\phi(r, \theta, \phi) = -j\eta_0 \frac{e^{-j\beta_0 r}}{4\pi r} \left\{ \frac{\beta_z}{\beta_\rho b} \sum_{n=-\infty}^{\infty} b_n^* (-1)^n n H_n^{(2)}(\beta_\rho b) S_\phi(n, \beta_z) e^{jn\phi} \right. \\ \left. - j\beta_0 \sum_{n=-\infty}^{\infty} (-1)^n [j^{-n} J_n(\beta_\rho b) + b_n^* H_n^{(2)'}(\beta_\rho b)] S_\phi(n, \beta_z) e^{jn\phi} \right. \\ \left. - \beta_0 \sin \theta \sum_{n=-\infty}^{\infty} b_n (-1)^n H_n^{(2)}(\beta_\rho b) S_z(n, \beta_z) e^{jn\phi} \right\} \quad (8)$$

where

$$S_\phi(n, \beta_z) = b \iint_{S'} J_\phi(z', \phi') e^{-jn\phi'} e^{j\beta_z z'} d\phi' dz' \quad (9)$$

$$S_z(n, \beta_z) = b \iint_{S'} J_z(z', \phi') e^{-jn\phi'} e^{j\beta_z z'} d\phi' dz' \quad (10)$$

Expressions for the coefficients a_n , a_n^* , b_n , and b_n^* may be found in [9].

3. The Center-Fed Helix

The final step in solving for the radiated fields involves finding the closed-form expressions for the integrals given in (9) and (10). In order to simplify the form of these integrals, it is convenient to define the angle of the microstrip with respect to the azimuthal plane as

$$\psi = \arctan\left(\frac{d}{b}\right) \quad (11)$$

where the parameter d is the pitch of the helix. At this point, we introduce the following change of variables:

$$z' = l' \sin \psi + w' \cos \psi \quad (12)$$

$$\phi' = \frac{1}{b} [l' \cos \psi - w' \sin \psi] \quad (13)$$

in order to transform the integrals given in (9) and (10) into the more convenient form

$$S_\phi(n, \beta_z) = \frac{b}{\sqrt{b^2 + d^2}} \int_{-\frac{L}{2}}^{\frac{L}{2}} \int_{-\frac{w}{2}}^{\frac{w}{2}} J_\phi(l') e^{-jn \frac{l'}{b} \cos \psi} e^{jn \frac{w'}{b} \sin \psi} e^{j\beta_z l' \sin \psi} e^{j\beta_z w' \cos \psi} dw' dl' \quad (14)$$

$$S_z(n, \beta_z) = \frac{d}{\sqrt{b^2 + d^2}} \int_{-\frac{L}{2}}^{\frac{L}{2}} \int_{-\frac{w}{2}}^{\frac{w}{2}} J_z(l') e^{-jn \frac{l'}{b} \cos \psi} e^{jn \frac{w'}{b} \sin \psi} e^{j\beta_z l' \sin \psi} e^{j\beta_z w' \cos \psi} dw' dl' \quad (15)$$

These equations show that the ϕ - and z -components of the current density are related by a constant. In other words,

$$J_z(l') = \left(\frac{d}{b}\right) J_\phi(l') \quad (16)$$

$$S_z(n, \beta_z) = \left(\frac{d}{b}\right) S_\phi(n, \beta_z) \quad (17)$$

Substituting the expression for $\bar{J}_z(l')$ defined in (4) into (14) and evaluating the required integrals leads to the following closed-form result:

$$S_\phi(n, \beta_z) = \frac{I_0 b}{\sqrt{b^2 + d^2}} \operatorname{sinc} \left[\frac{w}{2} v \right] \begin{cases} F_1(t, u) & , u^2 \neq t^2 \\ F_2(t, u) & , u^2 = t^2 \end{cases} \quad (18)$$

where

$$F_1(t, u) = 8 \sin \left[\frac{L}{4} (t + u) \right] \sin \left[\frac{L}{4} (t - u) \right] \left[\frac{t}{t^2 - u^2} \right] \quad (19)$$

$$F_2(t, u) = \frac{L}{2} \sin \left[\frac{L}{2} t \right] \quad (20)$$

$$t = \beta_1 \quad (21)$$

$$u = \frac{n \cos \psi - \beta_z b \sin \psi}{b} \quad (22)$$

$$v = \frac{n \sin \psi + \beta_z b \cos \psi}{b} \quad (23)$$

Similarly, it can be shown that

$$S_z(n, \beta_z) = \frac{I_0 d}{\sqrt{b^2 + d^2}} \operatorname{sinc} \left[\frac{w}{2} v \right] \begin{cases} F_1(t, u) & , u^2 \neq t^2 \\ F_2(t, u) & , u^2 = t^2 \end{cases} \quad (24)$$

4. Degenerate Cases

Here we consider two important degenerate cases of the helical microstrip antenna that represent the two extremes of the helical geometry - zero-pitch ($d = 0$) and infinite-pitch ($d = \infty$). By limiting the length of the helix to one-half wavelength ($L = \lambda/2$) and by also increasing the width of the helix to one-half wavelength ($w = \lambda/2$), the degenerate helix resembles an azimuthal and an axial half-wave cylindrical-rectangular microstrip patch antenna for $d = 0$ and $d = \infty$, respectively. Equations for the far-field radiation patterns of these antennas have been derived in [8]. Comparing previous results with the analytical expressions derived here for the helix will act as a verification of the proposed reciprocity approach.

A. Zero-Pitch Half-Wavelength Helix

A helix of zero-pitch ($d = 0$) and the assumption of the current distribution in (4) implies that the current on the helix is ϕ -directed. This also implies that (24) will be equal to zero. For simplicity, we will assume that the dielectric has a relative permittivity of unity. Finally, by considering only the azimuthal plane ($\theta = 90^\circ$), the equation for the far-field radiation pattern greatly simplifies to

$$E_\phi(r, \theta = 90^\circ, \phi) = -\eta_0 \beta_0 \frac{e^{-j\beta_0 r}}{4\pi r} \sum_{n=-\infty}^{\infty} (-1)^n \left[j^{-n} J'_n(\beta_0 b) + b_n^* H_n^{(2)'}(\beta_0 b) \right] S_\phi(n, 0) e^{jn\phi} \quad (25)$$

where

$$S_\phi(n, 0) = I_0 \begin{cases} F_1(t, u) & , u^2 \neq t^2 \\ F_2(t, u) & , u^2 = t^2 \end{cases} \quad (26)$$

$$F_1(t, u) = 4 \cos \left[\frac{L}{2} u \right] \left[\frac{t}{t^2 - u^2} \right] = 4 \cos \left[\frac{n\lambda}{4b} \right] \left[\frac{\beta_0}{\beta_0^2 - \left(\frac{n}{b} \right)^2} \right] \quad (27)$$

$$F_2(t, u) = \frac{L}{2} = \frac{\lambda}{4} \quad (28)$$

A computer code to calculate the far zone electric fields of a half-wave patch antenna was developed for [8]. This code was modified to accommodate the geometry specified above. For comparison purposes, a cylinder with a radius of one-half wavelength and a dielectric thickness of one-twentieth of a wavelength was considered. The results of this comparison are found in Figure 3.

B. Infinite-Pitch Half-Wavelength Helix

The infinite-pitch helix represents a half-wave axial cylindrical-rectangular microstrip patch antenna. This case will have only a z-directed current on the helix. Therefore, applying the same simplifications as used in the previous case, the far-field radiation pattern may be expressed as:

$$E_\theta(r, \theta = 90^\circ, \phi) = j\eta_0\beta_0 \frac{e^{-j\beta_0 r}}{4\pi r} \sum_{n=-\infty}^{\infty} (-1)^n [j^{-n} J_n(\beta_0 b) + a_n H_n^{(2)}(\beta_0 b)] S_z(n, 0) e^{jn\phi} \quad (29)$$

where

$$S_z(n, 0) = \frac{4I_0}{\beta_0} \text{sinc} \left[\frac{wn}{2b} \right] \quad (30)$$

A comparison of the results for this geometry are plotted in Figure 4.

5. Examples and Results

A Method of Moments (MoM) computer code was used to model different cases of the center-fed helical antenna mounted on a cylindrical platform. The variations between the cases examined were in the pitch of the helix. The radius, dielectric constant and thickness of the substrate material, and number of turns were kept constant. The results from the MoM code were then compared to the analytical results obtained above. The following table is a guide to the cases examined for this paper.

Name	Radius of PEC	Dielectric Thickness	Pitch	Number of Turns
Case 1	$0.125 \lambda_0$	$0.05 \lambda_0$	$0.5 \lambda_0$	One Turn
Case 2	$0.125 \lambda_0$	$0.05 \lambda_0$	$2\pi b \lambda_0$	One Turn

The dimensions of the helix were relative to the free-space wavelength at 10 GHz. Comparisons of the results for the two cases considered in the above table are found in Figures 5 and 6, respectively.

Mutual coupling effects have been neglected in the exact analytical technique presented in this paper. In cases of low pitch, the current on consecutive turns of the helix will deviate somewhat from the ideal due to the effects of mutual coupling. Examining consecutive cases of increasing pitch, it was determined that if the pitch of the helix is such that the spacing between consecutive turns is on the order of a half-wavelength or greater, then the effects of coupling are minimal.

Future work on this project includes the addition of a superstrate to the geometry. Also, the case of multiple helices is of interest. The analysis presented in this paper may be easily extended to include bifilar and quadrifilar helices.

References

- [1] Hansen, R.C., ed., *Conformal Antenna Array Design Handbook*, Dept. of the Navy, Air Systems Command, AD A110091, Sept 1981.
- [2] Mailloux, R.J., *Phased Array Antenna Handbook*, Artech House, Inc., Norwood, MA, 1994.
- [3] Zurcher, J.F., Gardiol, F.E., *Broadband Patch Antennas*, Artech House, Inc., Norwood, MA, 1995.
- [4] Pozar, D.M., Schaubert, D.H., eds., *Microstrip Antennas: The Analysis and Design of Microstrip Antennas and Arrays*, IEEE Press, New York, 1995.
- [5] Sainati, R.A., *CAD of Microstrip Antennas for Wireless Applications*, Artech House, Inc., Norwood, MA, 1996.
- [6] Wong, K.L., *Design of Nonplanar Microstrip Antennas and Transmission Lines*, John Wiley & Sons, Inc., New York, 1999.
- [7] Ashkenazy, J., Shtrikman, S., Treves, D., "Electrical Surface Current Model for the Analysis of Microstrip Antennas on Cylindrical Bodies," *IEEE Trans. Antennas Propagat.*, Vol. AP-33, No. 3, pp. 295-300, March 1985.
- [8] Werner, D.H., Martin, R.A., Mittra, R., Zmyslo, J.S., "A Reciprocity Approach for Calculating Radiation Patterns of Arbitrarily Shaped Microstrip Antennas Mounted on Circularly-Cylindrical Platforms", Submitted for publication in *IEEE Trans. Antennas Propagat.*, Aug. 1999.
- [9] Mittra, R., "Wave Propagation on Helices," *IEEE Trans. Antennas Propagat.*, Vol. AP-11, No. 9, pp. 585-586, 1963.
- [10] Peterson, A.F., Greene, B.S., and Mittra, R., "Propagation and Radiation Characteristics of the Tape Helix with a Conducting Core and Dielectric Substrate," *IEEE Trans. Antennas Propagat.*, Vol. 38, No. 4, pp. 578-583, April 1990.
- [11] Casey, J.P., and Bansal, R., "Square Helical Antenna with a Dielectric Core", *IEEE Trans. Antennas Propagat.*, Vol. 30, No. 4, pp. 429-436, Nov. 1988.

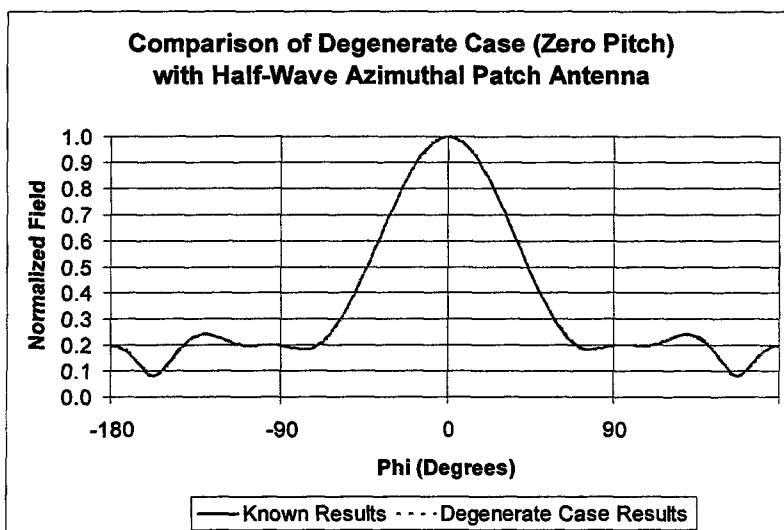


Figure 3 – Comparison of Far Fields for the Degenerate Case of a Half-Wave, Zero-Pitch Helical Antenna with the Known Results for a Half-Wave Azimuthal Cylindrical-Rectangular Microstrip Patch

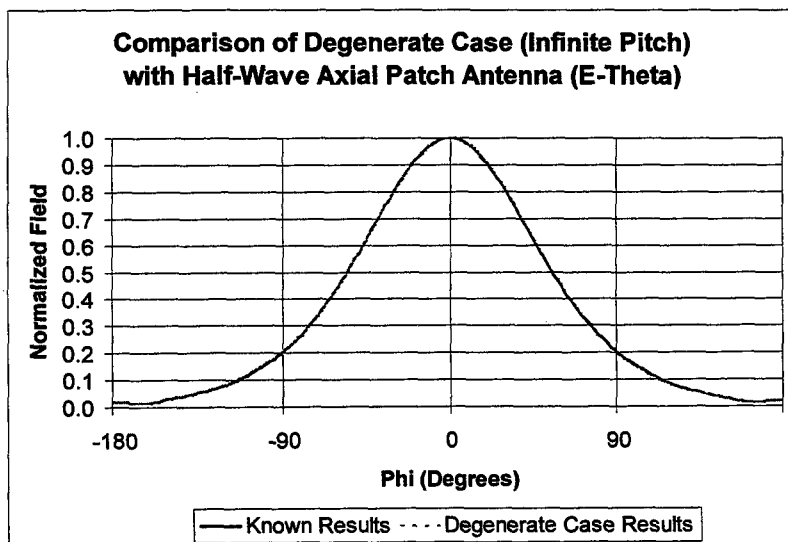


Figure 4 – Comparison of Far Fields for the Degenerate Case of a Half-Wave, Infinite-Pitch Helical Antenna with the Known Results for a Half-Wave Axial Cylindrical-Rectangular Microstrip Patch

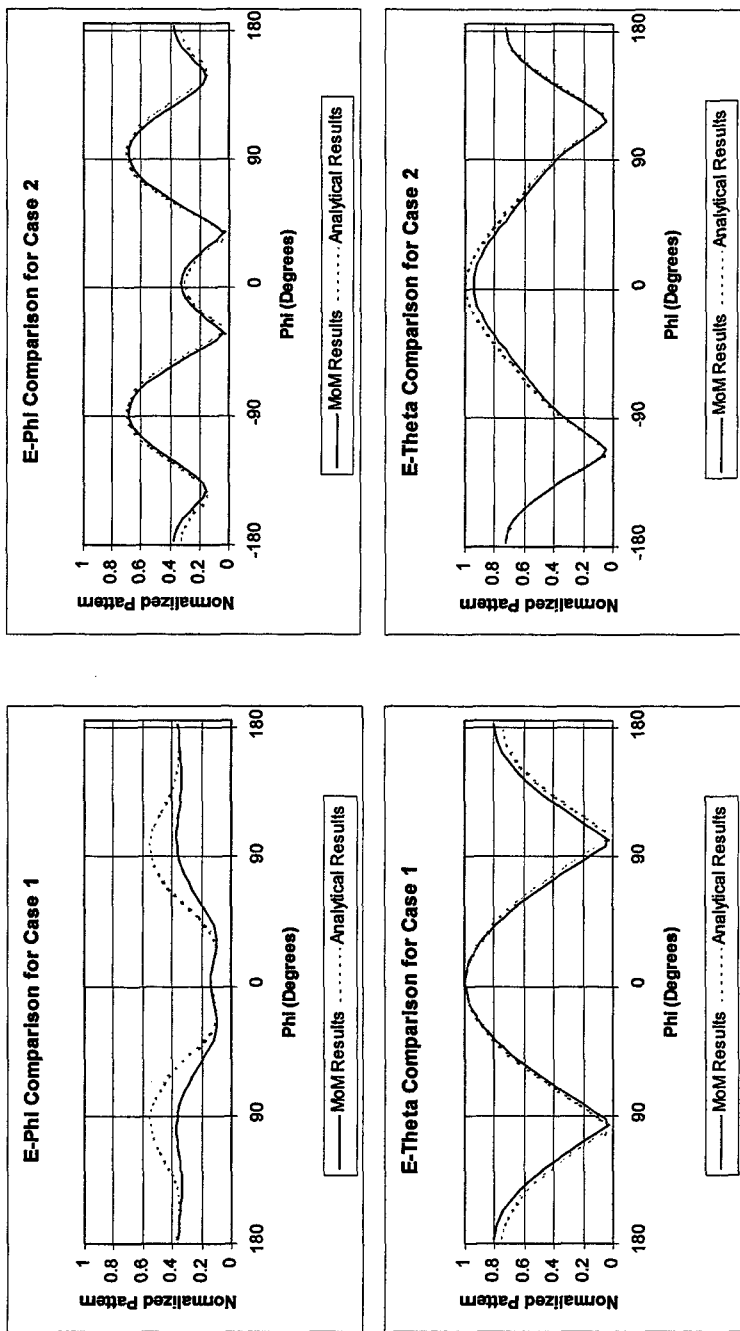


Figure 6 – Far Field Comparison Between MoM Code Results and Analytical Results for Case 2

Figure 5 – Far Field Comparison Between MoM Code Results and Analytical Results for Case 1

NEAR TO FAR FIELD TRANSFORMATION FOR A FDTD BOR WITH PML ABC AND SUB-GRID CAPABILITY

Vicente Rodriguez-Pereyra¹, Atef Z. Elsherbeni², and Charles E. Smith²

¹Department of Electrical Engineering and Computer Science, Texas A&M University-Kingsville
Kingsville, TX 78363 e-mail: vicente.rodriguez@tamuk.edu

²Department of Electrical Engineering, The University of Mississippi
University, MS 38677 e-mail: atef@olemiss.edu

Abstract - Various types of antennas and transmission media for electromagnetic waves (coax cable, waveguides, etc) exhibit symmetry around an axis of rotation and hence are called bodies of revolution. By analytically extracting the known periodic behavior of the fields in the azimuth, the fields everywhere may be found by solving Maxwell's equations in a single two dimension plane. Although the use of BOR approach with the finite difference time domain (FDTD) technique has already been reported, this paper presents a frequency domain near to far field transformation and a finer sub-grid model to the FDTD-BOR algorithm with PML absorbing boundaries. The developed algorithm produced good agreement with published data and is being used for the analysis and design of new types of axi-symmetric antennas for personal wireless communications.

INTRODUCTION

A large number of structures in the field of electromagnetics are symmetric around an axis of rotation. Among them are transmission media, (coaxial cables and cylindrical waveguides), antennas (wire dipoles, circular microstrip patches, cylindrical dielectric resonator antennas), etc. There are also structures that have this rotational symmetry, on to which it is desirable to mount certain electromagnetic device, for example, the fuselage of an aircraft or missile. Since the rotational behavior of the fields around this type of structure is known, it is possible to extract this behavior analytically, and then solve Maxwell's equations in a single 2D plane. This body of revolution (BOR) approach has been applied to several numerical methods in electromagnetics, including the method of moments (MOM) and the finite difference time domain (FDTD).

In this paper, the FDTD BOR PML algorithm used in [1-3] is modified. A near to far field transformation is incorporated into the FDTD BOR algorithm. The near to far field transformation routines compute the far field radiation pattern for structures in free space with or without an infinite ground plane. A sub-grid capability is also added to the code, which allows to model certain types of feeds that are usually small in relation to the antenna being fed. Coaxial probe feeds for microstrip patches and waveguide feeds on conical horns are examples of feeds that can be analyzed by this sub-grid approach. The finer sub-grid can also be used to model thin wires at the axis. Numerical results based on the developed algorithm agree with previously published data obtained using other techniques.

THE FDTD BOR PML TECHNIQUE

The FDTD BOR PML technique is derived from Maxwell's curl equations, following the derivation shown in [1-3] updating equations. As an example the updating equation for E_r component is given by

$$E_r^{n+1}(i,j) = \left(\frac{1 - \frac{\sigma_r^* \Delta t}{2\epsilon_0 \epsilon_r}}{1 + \frac{\sigma_r^* \Delta t}{2\epsilon_0 \epsilon_r}} \right) E_r^n(i,j) - \left(\frac{\frac{\Delta t}{\epsilon_0 \epsilon_r}}{1 + \frac{\sigma_r^* \Delta t}{2\epsilon_0 \epsilon_r}} \right) \times \left[\left(\frac{H_\phi^{n+\frac{1}{2}}(i,j) - H_\phi^{n+\frac{1}{2}}(i,j-1)}{\Delta z} \right) - \frac{m H_z^{n+\frac{1}{2}}(i,j)}{(i)\Delta r} \right] \quad (1)$$

The other updating equations have a similar form. The singularity at the axis is handled in the manner explained in [1-3]. These updating equations are used in the computational domain (CD). Surrounding the CD an absorbing boundary condition (ABC) is created; which surrounds the CD on all sides, except for the axis of rotation side. The derivation of the PML updating equations follows the same steps as the derivation for the CD FDTD-BOR algorithm. The complete derivation is presented in [1,3]. The E_r component of the updating PML equation is presented here for illustration purposes:

$$E_z^{n+1}(ij) = - \left(\frac{\sigma_z^* \Delta t - 2\epsilon}{\sigma_z^* \Delta t + 2\epsilon} \right) E_z^n(ij) + \left(\frac{2\Delta t}{\sigma_z^* \Delta t + 2\epsilon} \right) \times \frac{1}{\Delta z} \left(H_{\phi z}^{n+\frac{1}{2}}(ij) - H_{\phi z}^{n+\frac{1}{2}}(ij-1) + H_{\phi r}^{n+\frac{1}{2}}(ij) - H_{\phi r}^{n+\frac{1}{2}}(ij-1) \right) \quad (2)$$

The profile of the magnetic and electric conductivities in the PML region is obtained by using the approach presented in [4]. The losses increase from zero at the PML-CD boundary to a maximum value following a parabolic profile.

THE NEAR TO FAR FIELD TRANSFORMATION

In electromagnetic problems information about the far field is often required. Computational resources would not allow us to increase the FDTD mesh to include the far field region. A near to far field (NF-FF) transformation is used instead. The near to far field transformation procedure may be performed following two different paths [5]. One method calls for the transformation in the time domain. The second method is to compute the near field currents in the time domain followed by a Fourier transform to get the currents as a function of frequency, and then the radiation from these currents produces the far field information as a function of frequency. The NF-FF transformation described here uses the second method. The currents are computed at discrete frequencies using the discrete Fourier transform (DFT) as the time loop is being executed. Once the surface currents are obtained at these discrete frequencies the far field may be computed at any angle of observation at these discrete frequencies. This approach is very well suited to compute the bi-static radiation patterns, for the selected frequencies.

a) Computing the Surface Currents.

The NF-FF is based on the equivalence principle. An imaginary closed surface is defined which surrounds the geometry being solved. The fields inside this imaginary closed surface are assumed to be zero while outside the surface the correct fields remain. At the imaginary surface a set of magnetic and electric currents exists to account for the discontinuity of the field. These electric J_s and magnetic M_s surface currents are computed using the following equations:

$$\vec{J}_s = \hat{n} \times H^{\text{ext}}, \quad \vec{M}_s = -\hat{n} \times E^{\text{ext}} \quad (3)$$

The surface currents in the equation above will be computed on a surface that surrounds the object under study. In cylindrical coordinates the ideal surface will be a circular cylinder. Since we are using a BOR approach, the cylinder is reduced to three straight line segments that generate the cylinder, as shown in Fig. 1. One of these segments has the normal vector $\hat{n} = \hat{a}_r$, this surface will be identified as the outer side. The other two segments have $\hat{n} = \hat{a}_z$ or $\hat{n} = -\hat{a}_z$; these surfaces will be known as the top and bottom sides, respectively. Figure 1, shows which currents are present on each of the segments that generate the imaginary closed surface. On each segment a total of four different currents are present. There are two electric surface current components and two magnetic surface current components. Also the top segment and the bottom segment have the same currents. On the outer side the only currents present are J_z , J_ϕ , M_z , and M_ϕ . These currents are computed using (3). When applying (3) to compute J_z , J_ϕ , M_z , and M_ϕ , we obtain

$$J_z \hat{a}_z = H_\phi \hat{a}_z, \quad J_\phi \hat{a}_\phi = -H_z \hat{a}_\phi, \quad M_z \hat{a}_z = -E_\phi \hat{a}_z, \quad M_\phi \hat{a}_\phi = E_z \hat{a}_\phi \quad (4)$$

The current elements are located at the center of the side of the cell that touches the imaginary surface. Because of the positioning of the fields in the FDTD BOR mesh [1-3], locating the surface currents at the center of the side of a cell implies that some averaging has to be performed to find the value of a given field at the location of the surface current. Figure 2 shows which magnetic field components are averaged to find the value of the magnetic field at the point where a surface electric current is computed. The top and bottom sides are computed in the same way. The surface currents present on the top and bottom sides are J_z , J_ϕ , M_z , and M_ϕ . The only difference between the top and bottom sides is a factor of -1. This factor comes from the normal vectors to these sides pointing in opposite directions. Hence, when applying (3) to compute J_z , J_ϕ , M_z , and M_ϕ , it yields

$$J_r \hat{a}_r = (Fn) \times (-H_\phi) \hat{a}_r, \quad J_\phi \hat{a}_\phi = (Fn) H_r \hat{a}_\phi, \quad M_r \hat{a}_r = (Fn) E_\phi \hat{a}_r, \quad M_\phi \hat{a}_\phi = (Fn) \times (-E_r) \hat{a}_\phi \quad (5)$$

where Fn is 1 for the top side and -1 for the bottom side.

The surface currents are computed every time step and the results is added to a discrete Fourier transform (DFT) sum as

$$G(f) = \sum_{n=0}^{N_t} g(n\Delta t) e^{j2\pi f(n-1)\Delta t} \quad (6)$$

where N_t is the number of time steps in the FDTD simulation and f is the frequency of interest.

b) Computing the Far Field.

To compute the far field, the auxiliary vectors N and L are computed in cylindrical coordinates the θ and φ components of the auxiliary vectors are presented in [6]. Figure 3 shows the angles and vectors used in the near to far field transformation. The three sides that form the imaginary surface are integrated separately and the results from each one is added to obtain the far field at a given angle of observation. The θ component of the auxiliary vector N on the top side is studied to illustrate the derivation. Starting with

$$N_\theta^{top} = \int_{r'=0}^{r'=a} \int_{\phi'=0}^{\phi'=2\pi} [J_r \cos\theta \cos(\phi - \phi') + J_\phi \cos\theta \sin(\phi - \phi')] \times e^{-jmk\phi'} e^{jk(r' \sin\theta \cos(\phi - \phi'))} e^{jk(z' \cos\theta)} r' d\phi' dr' \quad (7)$$

Notice that the term $e^{-jmk\phi'}$ has been introduced to take into account the periodic behavior of the currents in the azimuth. If the terms in (7) are rearranged and letting $\beta = kr' \sin\theta$ the following is obtained:

$$N_\theta^{top} = \cos\theta \int_0^a e^{jk(z' \cos\theta)} r' \left[J_r \int_0^{2\pi} \cos(\phi - \phi') e^{-jmk\phi'} e^{j\beta \cos(\phi - \phi')} d\phi' + J_\phi \int_0^{2\pi} \sin(\phi - \phi') e^{-jmk\phi'} e^{j\beta \cos(\phi - \phi')} d\phi' \right] dr' \quad (8)$$

Considering the term

$$\int_{\phi'=0}^{\phi'=2\pi} \cos(\phi - \phi') e^{-jmk\phi'} e^{j\beta \cos(\phi - \phi')} d\phi' \quad (9)$$

and multiplying (9) by $e^{jm\varphi} e^{-jmk\varphi}$ the following equation is obtained:

$$e^{-jmk\varphi} \int_{\phi'=0}^{\phi'=2\pi} \cos(\phi - \phi') e^{jm(\phi - \phi')} e^{j\beta \cos(\phi - \phi')} d\phi' \quad (10)$$

By expanding the cosine in terms of exponential functions yields and, if $\alpha' = -(\varphi - \varphi')$ is assumed and a change of variable is

performed, (10) becomes

$$e^{-jm\phi} \left[\frac{1}{2} \int_{\alpha'=\pi-\phi}^{\alpha'=2\pi-\phi} e^{j[-(m+1)\alpha']} e^{j\beta \cos \alpha'} d\alpha' + \frac{1}{2} \int_{\alpha'=\pi-\phi}^{\alpha'=2\pi-\phi} e^{j[-(m-1)\alpha']} e^{j\beta \cos \alpha'} d\alpha' \right] \quad (11)$$

The integrands in (11) are periodic with period 2π . The following Bessel function integral [6]

$$J_m(\beta) = \frac{j^{-m}}{2\pi} \int_{\alpha=0}^{\alpha=2\pi} e^{jm\alpha} e^{j\beta \cos \alpha} d\alpha \quad (12)$$

is then used to simplify (11) to

$$\pi e^{-jm\phi} \left[\frac{(-1)^{(m+1)}}{j^{(m+1)}} J_{m+1}(\beta) + \frac{(-1)^{(m-1)}}{j^{(m-1)}} J_{m-1}(\beta) \right] \quad (13)$$

Based on (13), equation (8) can be re-written as

$$N_{\theta}^{top} = \cos \theta \int_{r'=0}^{r'=a} e^{jk(r' \cos \theta)} r' \times \left[J_r \pi e^{-jm\phi} \left[\frac{(-1)^{(m+1)}}{j^{(m+1)}} J_{m+1}(\beta) + \frac{(-1)^{(m-1)}}{j^{(m-1)}} J_{m-1}(\beta) \right] + J_{\phi} \int_0^{2\pi} \sin(\phi - \phi') e^{-jm\phi'} e^{j\beta \cos(\phi - \phi')} d\phi' \right] dr' \quad (14)$$

Consider now the term

$$\int_{\phi'=0}^{\phi'=2\pi} \sin(\phi - \phi') e^{-jm\phi'} e^{jk(r' \sin \theta \cos(\phi - \phi'))} d\phi' \quad (15)$$

then, following a similar approach as shown for the cosine term, it can be shown that (15) yields

$$-\pi e^{-jm\phi} \left[\frac{(-1)^{(m-1)}}{j^{(m)}} J_{m-1}(\beta) - \frac{(-1)^{(m+1)}}{j^{(m+2)}} J_{m+1}(\beta) \right] \quad (16)$$

Hence, equation (14) becomes

$$N_{\theta}^{top} = \cos \theta \int_{r'=0}^{r'=a} e^{jk(r' \cos \theta)} r' \times \left[J_r \pi e^{-jm\phi} \left[\frac{(-1)^{(m+1)}}{j^{(m+1)}} J_{m+1}(kr' \sin \theta) + \frac{(-1)^{(m-1)}}{j^{(m-1)}} J_{m-1}(kr' \sin \theta) \right] \right. \\ \left. + J_{\phi} (-\pi e^{-jm\phi}) \left[\frac{(-1)^{(m-1)}}{j^{(m)}} J_{m-1}(kr' \sin \theta) - \frac{(-1)^{(m+1)}}{j^{(m+2)}} J_{m+1}(kr' \sin \theta) \right] \right] dr' \quad (17)$$

The equations for the other components of the auxiliary vectors for each of the segments that define the imaginary surface are derived using the same procedure. The auxiliary vectors are then used to compute the far field as shown in [6].

c) *Computing the far field in the presence of a ground plane.*

Large numbers of antennas radiate in the presence of a large (mathematically infinite) ground plane. In such cases, the currents are computed in the same manner that was described above. When defining the imaginary surface for antennas in the presence of a ground plane the lower segment must touch the ground plane. The currents computed on the lower segment are not used when computing the far field. Image theory is then used to get rid of the infinite ground plane. When a current contribution is added the contribution of its image is added as well.

FINER SUB-GRID FOR FDTD-BOR-PML.

The coaxial line is a common transmission media used to feed antennas. The BOR can easily model a coaxial line. In most cases the coaxial feed is connected to the antenna through a ground plane as shown in Figure 4. By setting FDTD cells close to the axis as perfect electric conductor (PEC) and nearby cells as PEC, a coaxial line is easily modeled. These coaxial probes are relatively small when compared with the antenna being fed. Figure 5 shows that by using a finer grid around a portion of the axis of the rotational symmetry and a coarser grid in the rest of the domain a good model of a small coaxial feed may be defined without having to use a fine grid mesh in the entire computational domain. This approach of using two different grids has been used by Maloney, et al. [7]. A similar approach is used here to model a coaxial feed accurately. As in [7] only one time step will be used in the whole computational domain. If the Courant condition is satisfied for the finer grid, it is automatically satisfied for the coarser grid. In each of the grids, the CD-FDTD-BOR equations that were derived in [1-3] hold. Special equations must be derived for the boundaries between the fine and coarse grids.

a) *Derivation of the Equations at the boundary between grids.*

Figure 5 shows a FDTD BOR mesh with a model of a coaxial line using a finer grid. The ratio between the coarse grid and the finer grid is given by: $N_{ratio} = \Delta z / \Delta z^f = \Delta r / \Delta r^f$, where the superscript f indicates the finer grid quantities. The sub-grid is accomplished by defining two meshes with different $\Delta \xi$ s. Inside these meshes the same FDTD-BOR equations are used. The finer mesh is defined to be located inside the coarser mesh. A boundary is defined inside the coarser mesh where it meets the finer mesh, as shown in Fig. 6.

b) *Derivation of the Equations at the Top Boundary.*

Figure 6 shows cells on the top boundary between the fine and coarse meshes. The top boundary is used to illustrate how the update equations for the fields at the boundary between grids are derived. The boundary fields belong to the fine grid. For a given cell on the top boundary, the H_ϕ , H_r fields on the coarse grid need fields located in the fine grid to be updated. For the H_ϕ ($i, Jtop$), the CD-FDTD-BOR updating equation derived in [1-3] for updating the field is modified to take into account the need for fine grid fields to update the H_ϕ field component. The following equation is used for H_ϕ close to the top boundary.

$$H_\phi^{n+1/2}(i, Jtop) = C_{h\phi h} H_\phi^{n-1/2}(i, Jtop) - C_{h\phi e} \left[\left(\frac{E_r^n(i, Jtop+1) - E_r^f}{\Delta z} \right) - \left(\frac{E_z^n(i+1, Jtop) - E_z^n(i, Jtop)}{\Delta r} \right) \right] \quad (18)$$

where $C_{h\phi e}$ and $C_{h\phi h}$ are coefficients related to the electric and magnetic properties of the media at the location of the cell as presented in [1,3]. Also

$$E_r^f = \frac{1}{N_{ratio}} \sum_{k=0}^{N_{ratio}-1} E_r^n(i^f + k, n\tau^f) \quad (19)$$

and by studying the relation between the indices of both the fine and coarse grids, we obtain

$$i^f = \frac{N_{ratio}}{2} + [N_{ratio}(i-1)] + .5 \quad (20)$$

At the top boundary the following components are found: E_ϕ , E_r , and H_r . Of these components only the ones that are tangential

to the boundary need special equations. Hence only E_ϕ and E_z require special equations.

Figure 6 shows that to compute these fields at their locations on the fine mesh a field located at the coarse mesh is needed at a position where the field has not been defined. Three point interpolation is used to find the values of the fields at points in between the locations where the fields are defined in the coarse mesh. The CD-FDTD BOR equation derived in [1-3] for the E_ϕ component is also used to update the E_ϕ in the fine grid. At the boundary, to update E_ϕ , H_r from the coarse grid is needed. The H_r component from the coarse grid is computed using a three point interpolation of the neighboring H_r components on the coarse grid. Introducing these changes to CD-FDTD-BOR the following equation is derived to take care of the E_ϕ on the top boundary.

$$E_\phi^{n+1}(i^f, nz^f) = C_{\phi\phi}^f E_\phi^n(i^f, nz^f) + C_{\phi H}^f \left[\left(\frac{H_r^c - H_r^{n+\frac{1}{2}}(i^f, nz^f - 1)}{\Delta z/2 + \Delta z^f/2} \right) - \left(\frac{H_z^{n+\frac{1}{2}}(i^f, nz^f) - H_z^{n+\frac{1}{2}}(i^f - 1, nz^f)}{\Delta r^f} \right) \right] \quad (21)$$

where H_r^c is given by a three point interpolation of the neighboring H_r as shown in [3].

Following a similar procedure it is possible to derive the updating equations for the fine grid components tangent to the boundary and for the coarse grid component close to the boundary at the other segments of the boundary.

NUMERICAL RESULTS

a) Analysis of a circular loop of half wavelength radius.

Figure 7 shows the far field for a loop, the loop is modeled by setting the E_ϕ component at a distance from the axis that corresponds to a half wavelength of the frequency at which the far field is computed. For the case shown, $\Delta r = \Delta z = 3.7037\text{mm}$ and the far field computed at 500MHz. By locating the source at a cell with index $i=81$, a loop of radius $\lambda/2$ is generated. The numerical results agree with those reported in [6].

b) Analysis of a Hertzian dipole 2λ above an infinite ground plane

Figure 8 shows the geometry for a Hertzian dipole two wavelengths above a ground plane. The Hertzian is modeled by forcing a waveform to the E_z component of the field located 2λ above the ground plane close to the axis. The pattern shown in Fig. 8 is a very good match when compared with the results shown in [6] for the same geometry.

c) Analysis of a monopole on a finite circular ground plane.

The structure analyzed in [8] is studied in this section. The geometry is a 0.224λ long monopole of radius 0.003λ as shown in Fig. 9. To accurately model the monopole, Δr of the uniform grid model must be equal to twice the radius of the monopole. Therefore at 1GHz, Δr should be equal to 0.18cm. With this Δr , the ground plane must be 500 cells. However, with the subgrid model, with $N_{\text{ratio}}=3$, the fine grid region can have $\Delta r^f=0.18\text{cm}$ while Δr for the coarse grid region becomes 0.54cm which reduces the number of cells required to simulate the ground plane to 166 cells. The other parameters of the simulation are : $\Delta z = \Delta r^f$, and $\Delta z = \Delta r$; $nz=30$, and $n=170$; $J_{\text{bot}}=5$, $J_{\text{top}}=25$, $J_{\text{out}}=4$. The geometry is executed for 8000 time steps. The structure is excited by assigning a Blackman-Harris waveform [1,3] to the $E_x(1,1)$ field component with $N_{\text{half}}=50 \Delta t$ and $t_0 = 60 \Delta t$. The far field pattern obtained is in good agreement with both the measured and the theoretical results reported in [8].

CONCLUSIONS

A body of revolution FDTD is developed to analyze the near and far field parameters of antennas and other microwave structures such as open and closed cavities [1-3]. The introduction of the sub-grid procedure produced significant reduction of needed computer resources required to simulate such structures with small feeds of thin wires at the axis of rotation. All the capabilities introduced in this developed algorithm make it a desirable tool for the analysis of rotationally symmetric antennas.

REFERENCES

- [1] V. Rodriguez-Pereyra, A. Z. Elsherbeni, and C. E. Smith "A Body of Revolution Finite Difference Time Domain Method with Perfectly Matched Layer Absorbing Boundary" *Progress in Electromagnetic Research (PIER)*, vol. 24, pp. 257-277, 1999.
- [2] V. Rodriguez-Pereyra "Development of a Finite Difference Time Domain Algorithm for Body of Revolution Structures Including a Perfectly Matched Layers Absorbing Boundary Condition" *Ph.D. Dissertation*, Department of Electrical Engineering, University of Mississippi, Aug. 1990.

- [3] V. Rodriguez-Pereyra, A. Z. Elsherbeni, C. E. Smith "Electromagnetic Analysis of Axi-Symmetric Structures", *IEEE southeastcon '99*, Lexington, Kentucky, March 1999.
- [4] J-P. Berenger, "A Perfectly Matched Layer for the Absorption of Electromagnetic Waves", *J. of Comp. Physics*. No.114, pp.185-200, 1994.
- [5] A. Taflovie, *Computational Electrodynamics: the finite-difference time-domain method*. Norwood, MA: Artech House, 1995.
- [6] C. Balanis, *Antenna Theory: Analysis and Design*. New York, NY: Wiley, 1997.
- [7] J. G. Maloney, G. S. Smith, and W. R. Scott, jr. "Accurate Computation of the Radiation from Simple Antennas Using the Finite-Difference Time-Domain Method", *IEEE Trans. Antennas and Prop.*, Vol.38, No.7, pp. 1059-1068, July 1994.
- [8] K. H. Awadalla and T. S. M. MacLean, "Monopole Antenna at Center of Circular Ground Plane: Input Impedance and Radiation Pattern", *IEEE Trans. Antennas and Prop.*, Vol. 27, No. 2, pp.151-153, March 1979.

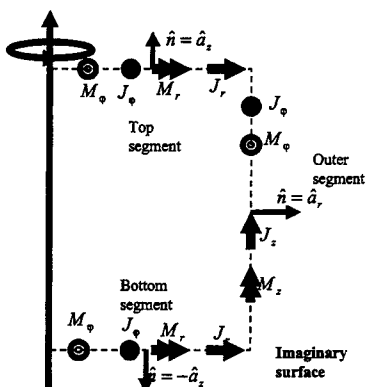


Fig. 1. The Imaginary surface and the 3 segments, showing the currents and normal vectors.

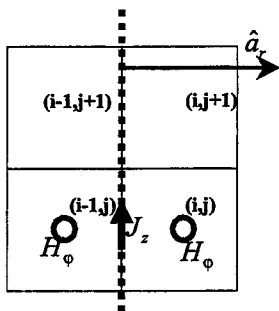


Fig. 2. Computation of an electric surface current on the outer segment.

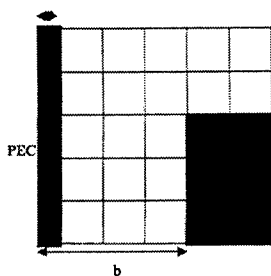


Fig. 4. A FDTD-BOR Model for a coaxial probe.

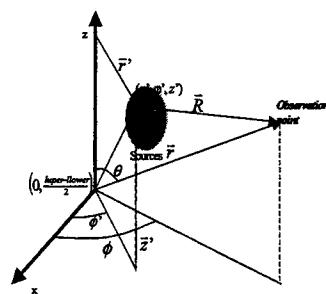


Fig. 3. Vectors and angles for the near to far field transformation.

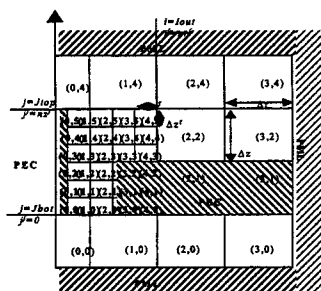


Fig. 5. FDTD-BOR Sub-Grid model for a coaxial probe.

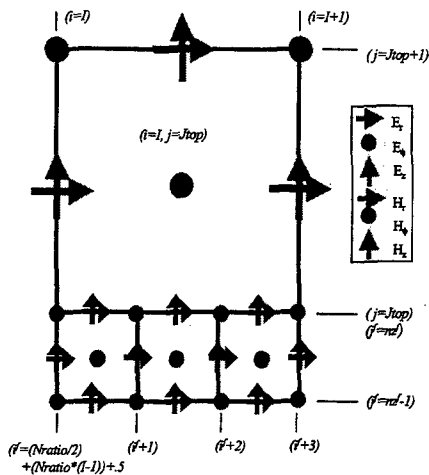


Fig. 6. The grid and sub-grid top boundary.

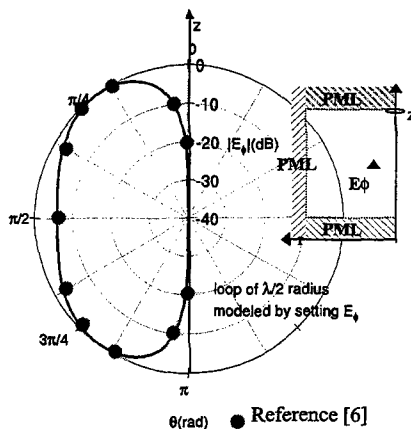


Fig. 7. Radiation pattern of a loop of radius half wavelength in free space.

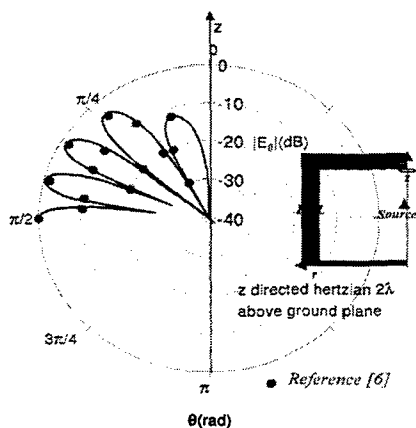


Fig. 8. A Hertzian z directed dipole two wavelengths above an infinite ground plane

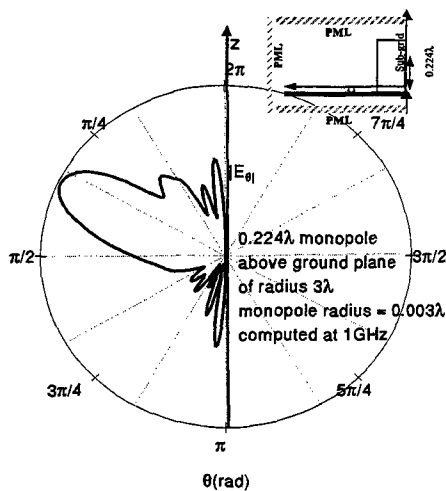


Fig. 9. Radiation pattern for a monopole on a finite ground plane.

SORRY! PAPER WAS PULLED

SORRY! PAPER WAS PULLED

SORRY! PAPER WAS PULLED

SORRY! PAPER WAS PULLED

SORRY! PAPER WAS PULLED

PLENARY SESSION II

Tom Cwik

Design on Computer—A Coming of Age

Tom Cwik
MS 168-522
Jet Propulsion Laboratory
Pasadena CA 91109
cwik@jpl.nasa.gov

One key purpose of computer simulation is to focus and limit the number of laboratory experiments needed in the design process. Whether building a multi-million dollar jet fighter or a dipole array, an accurate model that predicts key performance parameters is considered essential for reducing cost and meeting design specifications. The software should ideally provide high fidelity, near real-time simulation results, as well as an interface to the design engineer that is relatively simple and is tailored to the problem space being considered. This software will encompass the physical and engineering properties of the device or system being built, the mathematical methods appropriate for analysis, sophisticated algorithm developments, exploitation of the computer architecture being used, and appropriate visualization and graphical interfaces. The software is also ideally priced to sell, easy to maintain and has a minimal learning curve for users.

Though we are clearly far from reaching these goals, electromagnetic design on computer has evolved rapidly over the last three decades and continues to advance in a range of areas. Not ten years ago, there were only a handful of commercial simulation codes available, and these dominantly used text input and output, with the designer sometimes painstakingly entering the antenna, scatterer or waveguide geometry. Many times the software was incomplete, requiring external libraries for special functions or linear system solution. Similarly, the number of textbooks in the area of computational electromagnetics was small, consisting mainly of specialized books for specific applications or algorithms. Currently, the number of commercial self-contained simulation software suites is growing both in breadth and sophistication with different vendors even competing in well-defined component design areas. And in the bookstore, the number of relevant textbooks has greatly multiplied with most having the described software freely available.

This talk will examine the state-of-the-art in computational electromagnetics, grouping the field into advances in 1) components or system design and related electromagnetic algorithms, 2) available computer hardware and architecture and 3) integrated design environments including optimization methods. Initially an evaluation of each area will be presented with specific items that require further research and development following. The application to antenna design, microdevice analysis, multi-disciplinary design and optimization as well as other areas will be presented.

SESSION 6

**COMPUTATIONAL
BIO-ELECTROMAGNETICS**

Chairs: Ray Luebbers and Susan Hagness

Numerical Investigation of Two Confocal Microwave Imaging Systems for Breast Tumor Detection

Susan C. Hagness¹, Xu Li¹, Elise C. Fear², and Maria A. Stuchly²

¹ Department of Electrical and Computer Engineering, University of Wisconsin
1415 Engineering Drive, Madison, WI 53706
hagness@engr.wisc.edu, xli@students.wisc.edu

² Department of Electrical and Computer Engineering, University of Victoria
P.O. Box 3055 STN CSC, Victoria BC V8W 3P6
efear@engr.UVic.CA, mstuchly@engr.UVic.CA

1 Introduction

Timely diagnosis of small breast tumors, especially those less than 10 mm in diameter, leads to the most effective treatment and highest survival rates. X-ray mammography, which exposes women to ionizing radiation, is the most effective imaging method for detecting non-palpable early-stage breast cancer. However, despite significant progress in improving mammographic technique, persisting limitations result in a relatively high number of false negatives and false positives [1,2]. Thus, techniques that image other physical tissue properties are under investigation [3,4].

Breast cancer screening approaches using non-ionizing microwave technology represent an alternative modality that could complement existing methods while mitigating several of the disadvantages. We are currently investigating confocal microwave imaging based on the principles of ultrawideband backscatter radar techniques and confocal optical microscopy [5-8]. The physical basis for this system is the significant contrast in the dielectric properties of normal breast tissue and malignant tumors suggested by limited amounts of published data at microwave frequencies [9-11]. Pulsed confocal microwave imaging would exploit these differences for the purpose of tumor detection.

The design concept is to synthetically focus a low-power pulsed microwave signal at a focal point in the breast and efficiently collect any backscattered energy. The intensity of the backscattered signal increases dramatically when the focused transmitted signal encounters a malignant tumor, due to the large dielectric contrast between the tumor and adjacent normal breast tissue. The focus is achieved synthetically through the use of an electronically scanned antenna array together with signal processing techniques. One antenna transmits an ultrashort pulse into the breast and the backscattered returns are recorded at the same antenna. This is repeated sequentially for each antenna in the array. As a post-processing step, the backscattered waveforms are time-shifted and added to create a synthetic focus. The position of the focus is scanned throughout the breast by adjusting the assumed distribution of time shifts of the stored backscatter waveforms. If a scattering object, such as a malignant tumor, exists at the focal point, the waveforms add coherently. If scattering objects exist elsewhere, the waveforms add incoherently. In this manner, tumor backscatter signals are enhanced while clutter signals are minimized. Systematic scanning of the synthetic focus from point to point within the breast creates a three-dimensional microwave image.

2 System Configurations

The finite-difference time-domain (FDTD) method is used to simulate the operation of a confocal microwave imaging antenna array. Here, we consider two possible system configurations:

System #1. The patient lies in a supine position while a planar two-dimensional (2-D) antenna array is placed in contact with the naturally flattened breast. A low-loss matched liquid may be used to fill gaps between the breast and the antenna array. This configuration is illustrated in Figure 1a.

System #2. The patient lies prone on a supporting table with the breasts extending through openings in the table surface. An antenna array is placed at a constant distance around the naturally pendulous breast immersed in a low-loss matched liquid. Translating the array vertically allows for scans of different cross sections through the breast. This configuration is illustrated in Figure 1b.

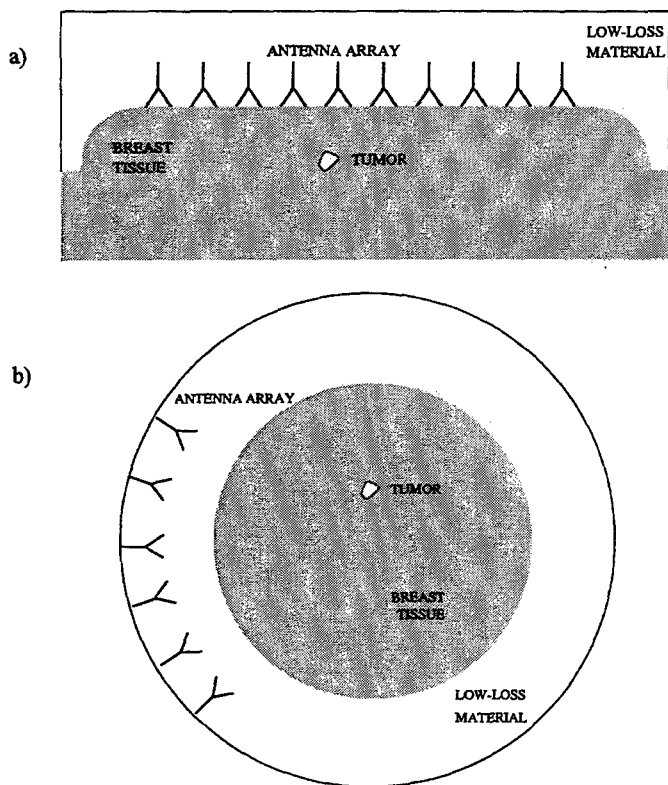


Figure 1. Schematics of two pulsed confocal microwave imaging systems. a) System #1: side view of a planar 2-D antenna array. b) System #2: bottom view of a circular antenna array.

3 FDTD Models

Tumor detection algorithms for system #1 have been explored using 2-D FDTD simulations. The microwave sensor is modeled as a 17-element 1-D monopole antenna array spanning 8 cm, placed at the surface of the breast. The breast model includes a 1-mm-thick skin layer ($\epsilon_r = 36$ and $\sigma = 4$ S/m at 6 GHz [12-14]). To simulate the heterogeneity of normal breast tissue, we have introduced $\pm 10\%$ random fluctuations of ϵ_r and σ over observable distance scales of 0.5 cm; this range represents an upper bound on the data variability reported by both Joines *et al* [11] and Chaudhary *et al* [9]. A 0.5-cm-diameter tumor is embedded in a slab of normal breast tissue at a depth of 3.0 cm directly below the center of the antenna array. The estimated baseline dielectric properties at 6 GHz in our models are as follows: $\epsilon_r = 9$ and $\sigma = 0.4$ S/m for normal breast tissue and $\epsilon_r = 50$ and $\sigma = 7$ S/m for malignant tumors. Since we are using ultrawideband pulses (for example, a differentiated Gaussian with an amplitude spectrum peak at 6 GHz and spectral content extending to 20 GHz), the dispersive properties of breast tissue need to be considered. Variations in ϵ_r and σ over the frequency band of interest (100 MHz to 20 GHz) have been modeled using single-pole Debye dispersion equations as given by Foster and Schwan [15]:

$$\epsilon_r(f) = \epsilon_\infty - \frac{j\sigma_s}{2\pi f \epsilon_0} + \frac{\epsilon_s - \epsilon_\infty}{1 + j(f/f_p)}$$

with parameters chosen to curve fit the published data on breast tissue up to 1 GHz and the four-pole Cole-Cole models published by Gabriel [12-14] for muscle and fatty tissue. The dielectric properties above 1-3 GHz represent extrapolated and estimated values resulting from these Debye and Cole-Cole curve-fitting procedures of data measured at lower frequencies.

Tumor detection algorithms for system #2 have been investigated using 3-D FDTD simulations. Here, the microwave sensor is modeled as a 8-element resistively loaded Wu-King dipole [16] antenna array. The antennas are placed at a constant distance of 3 cm from the skin, along an arc spanning approximately 60 degrees. The breast is modeled as a 10-cm-diameter cylinder of homogeneous breast tissue ($\epsilon_r = 9$ and $\sigma = 0.4$ S/m) with a 2-mm-thick skin layer ($\epsilon_r = 36$ and $\sigma = 4$ S/m). In these simulations, the dispersive and heterogeneous properties have not yet been incorporated. A 0.5-cm-diameter tumor ($\epsilon_r = 50$ and $\sigma = 4$ S/m) is embedded in the cylindrical breast model at a depth of 1.25 cm, centered spatially with respect to the antenna array. The breast cylinder and the antenna array are immersed in a low-loss liquid matched to the dielectric constant of normal breast tissue ($\epsilon_r = 9$ and $\sigma = 0$ S/m).

In both sets of simulations, the transmitted by each antenna is a differentiated Gaussian pulse:

$$V(t) = V_0 \cdot (t - t_0) \cdot e^{-(t-t_0)^2/\tau^2}$$

where $\tau = 40$ ps and $t_0 = 4\tau$ for system #1, and $\tau = 62.5$ ps and $t_0 = 4\tau$ for system #2. The resulting signals have a temporal duration (full-width at half-maximum) of 110 ps and 170 ps, respectively. The grid boundaries are terminated with perfectly matched layer absorbing boundary conditions [17].

4 Tumor Detection Algorithms

We have developed preliminary image formation algorithms for tumor detection, and have tested them on FDTD-computed backscatter data from the breast models associated with each of the two microwave imaging systems.

System Configuration #1

Here, the microwave sensor is comprised of a linear array of $M = 17$ antennas. A simulated scan involves exciting each antenna one at a time with a short pulse and measuring the backscattered response at the same antenna element. This process is repeated for each element of the array, resulting in M received backscattered waveforms, each containing a total of N time-sampling points.

Step 1. A preliminary scan of a "breast phantom" (the FDTD model with homogeneous breast tissue and no tumor) is performed to obtain M FDTD-computed calibration waveforms. Then, the scan of the "patient" (the FDTD model with the breast tissue heterogeneity and tumor present) is performed. The recorded FDTD-computed backscattered waveforms from the patient scan are calibrated by subtracting the previously obtained calibration waveforms. Thus, the resulting M signals contain only the backscatter from the tumor and the heterogeneous breast tissue. The skin backscatter and incident signal, both of which appear early-on in time, are removed through the calibration process.

Step 2. The overall data set from the microwave sensor is in the form of an $M \times N$ integer array A where $A(m, n)$ is the n th data point in the m th received waveform. The appropriate time shift, $t_m(x, y)$, needed for the coherent-addition process is given by $2d_m(x, y)/v$, where $d_m(x, y)$ is the one-way distance from the m th transmit/receive antenna element to the focal point at coordinates (x, y) and v is the average velocity of propagation in breast. For the m th waveform, the discrete-time shift index is $\tau_m = t_m / \Delta t$, where Δt is the time interval between the time-sampling data points. The differentiated Gaussian signal is zero at its center point; thus, $A(m, \tau_m) = 0$. In order to obtain a non-zero sum in Step 3, each received backscattered waveform is integrated over time as follows:

$$B(m, \tau) = \int A(m, \tau') d\tau'$$

This is equivalent to the backscattered waveform that would be received if each antenna transmitted a baseband Gaussian pulse, rather than a differentiated Gaussian pulse.

Step 3. The 2-D image is created by time-shifting and summing data points from each received waveform for each synthetic focal point in the breast. The resulting sum for a specific synthetic focal point is given by

$$I(x, y) = \left(\sum_m B(m, \tau_m) \right)^2.$$

The synthetic focal point (x, y) is scanned throughout the region of interest in increments of 0.125 cm. Each summed value is converted to a gray scale pixel at (x, y) using an appropriate mapping function. A sample result is shown in Figure 2.

Step 3. The modified M signals are cross-correlated with the antenna impulse response from Step 1, in order to enhance the tumor returns. Finally, the time delays are applied to M signals in a manner similar to that described above for System Configuration #1. The synthetic focal point is scanned throughout the region of interest in increments of 0.25 cm. For each synthetic focal point, the delayed signals from each antenna are summed and averaged over a time window corresponding to 0.25 cm. The envelope of the final data set is displayed, as shown in Figure 3.

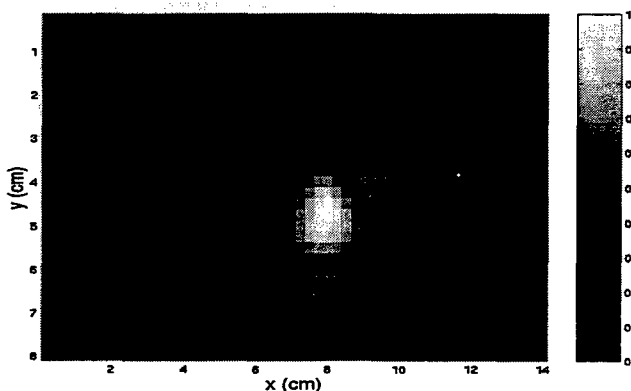


Figure 3. A microwave breast image reconstructed from the processed backscattered waveforms computed for system #2. The peak response in the reconstructed image occurs at $x=8$ cm, $y=4.5$ cm. This corresponds directly to the location of the 0.5-cm-diameter malignant tumor in the FDTD model.

5 Conclusions

The use of focused ultrashort microwave pulses in confocal microwave imaging enhances the detection resolution, reduces the problem of background clutter, and permits simple, robust signal processing to be applied to the problem of breast cancer detection. The simple signal processing techniques, demonstrated here through the use of FDTD simulations, overcome the limitations faced by conventional microwave tomographic approaches [18-20], where there remain key unresolved problems in imaging high-contrast internal structures and avoiding extremely long computation times as well as vulnerability to small experimental uncertainties and noise.

6 References

- [1] J. G. Elmore, M. B. Barton, V. M. Mocer, S. Polk, P. J. Arena, and S. W. Fletcher, "Ten-year risk of false positive screening mammograms and clinical breast examinations," *New Engl. J. Med.*, 338(16):1089-1096, 1998.
- [2] F. M. Hall, J. M. Storella, D. Z. Silverstone, and G. Wyshak, "Nonpalpable breast lesions: recommendation for biopsy based on suspicion of carcinoma at mammography," *Radiology*, 167:353-358, 1988.
- [3] M. Sabel and H. Aichinger, "Recent developments in breast imaging," *Phys. Med. Biol.*, 41:315-368, 1996.

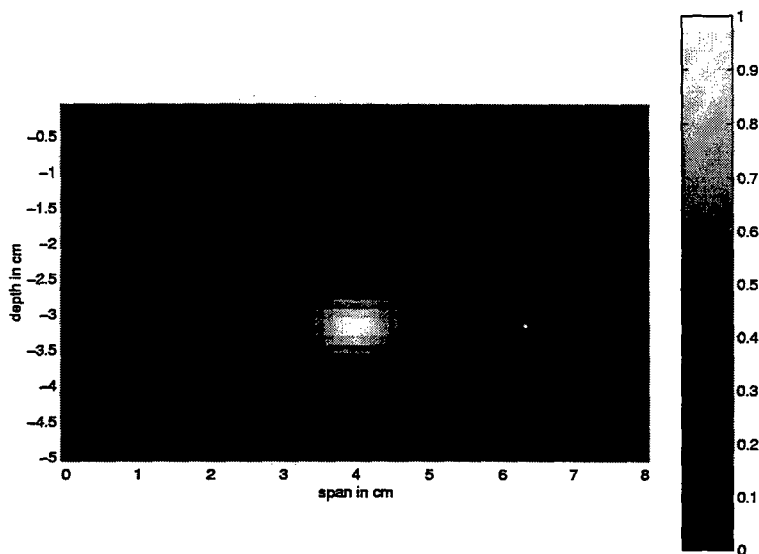


Figure 2. A microwave breast image reconstructed from the processed backscattered waveforms computed for system #1. The peak response in the reconstructed image occurs at a depth of 3 cm below the skin surface, centered at below the 8-cm-wide antenna array. This is precisely the location of the 0.5-cm-diameter malignant tumor in the FDTD model.

System Configuration #2

Here, the microwave sensor is comprised of an arc of $M = 8$ antennas. As in system #1, scanning is performed by sequential pulsing of each array element.

Step 1. A preliminary simulation is performed to obtain the antenna impulse response in a low-loss fat-like medium. This FDTD model consists of a single Wu-King dipole embedded in a homogeneous fatty tissue phantom. Then, the scan of the "patient" (the FDTD model with the homogeneous breast tissue, skin, and tumor present) is performed. The recorded FDTD-computed backscattered waveforms from the patient scan are calibrated by subtracting the previously obtained antenna-response calibration waveform. The resulting M signals are dominated by the backscatter from the skin, which tends to obscure the tumor response.

Step 2. A backscattered waveform is computed for a solid cylinder of skin (a "skin phantom") similar in size to the breast cylinder. Two time-shifted, scaled, and summed versions of the skin-phantom waveform provide an adequate approximation to the skin backscatter present in the patient-scan data set. This approximate signal representing the backscatter from the skin is subtracted from each of the M signals, greatly reducing the effect of the skin in subsequent image formation and tumor detection.

- [4] S. H. Heywang-Kobrunner, "Nonmammographic breast imaging techniques," *Current Opinion in Radiology*, 4:146-154, 1992.
- [5] S. C. Hagness, A. Taflove, and J. E. Bridges, "Two-dimensional FDTD analysis of a pulsed microwave confocal system for breast cancer detection: Fixed-focus and antenna-array sensors," *IEEE Trans. Biomed. Eng.*, 45:1470-1479, Dec. 1998.
- [6] S. C. Hagness, A. Taflove, and J. E. Bridges, "Wideband ultralow reverberation antenna for biological sensing," *Electron. Lett.*, 33(19):1594-1595, 1997.
- [7] S. C. Hagness, A. Taflove, and J. E. Bridges, "Three-dimensional FDTD analysis of a pulsed microwave confocal system for breast cancer detection: Design of an antenna-array element," *IEEE Trans. Antennas Propagat.*, 47:783-791, May 1999.
- [8] E. Fear and M. A. Stuchly, "Microwave system for breast tumor detection," *Microwave and Guided Wave Letters*, vol. 9, Nov. 1999.
- [9] S. S. Chaudhary, R. K. Mishra, A. Swarup, and J. M. Thomas, "Dielectric properties of normal and malignant human breast tissues at radiowave and microwave frequencies," *Indian J. Biochem. and Biophys.*, 21:76-79, February 1984.
- [10] A. J. Surowiec, S. S. Stuchly, J. R. Barr, and A. Swarup, "Dielectric properties of breast carcinoma and the surrounding tissues," *IEEE Trans. Biomed. Eng.*, 35:257-263, April 1988.
- [11] W. T. Joines, Y. Z. Dhenxing, and R. L. Jirtle, "The measured electrical properties of normal and malignant human tissues from 50 to 900 MHz," *Med. Phys.*, 21:547-550, April 1994.
- [12] C. Gabriel, S. Gabriel, and E. Corthout, "The dielectric properties of biological tissues: I. Literature survey," *Phys. Med. Biol.*, 41(11):2231-2249, November 1996.
- [13] S. Gabriel, R. W. Lau, and C. Gabriel, "The dielectric properties of biological tissues: II. Measurements on the frequency range 10 Hz to 20 GHz," *Phys. Med. Biol.*, 41(11):2251-2269, November 1996.
- [14] S. Gabriel, R. W. Lau, and C. Gabriel, "The dielectric properties of biological tissues: III. Parametric models for the dielectric spectrum of tissues," *Phys. Med. Biol.*, 41(11):2271-2293, November 1996.
- [15] K. R. Foster and H. P. Schwan, "Dielectric properties of tissues and biological materials: a critical review," *Critical Reviews for Biomedical Engineering*, 17:25-104, 1989.
- [16] T. T. Wu and R. W. P. King, "The cylindrical antenna with nonreflective resistive loading," *IEEE Trans. Antennas Propagat.*, 13:369-373, May 1965 (and correction by L.C. Shen and R.W.P. King, 13:998, Nov. 1965).
- [17] J. P. Berenger, "A perfectly matched layer for the absorption of electromagnetic waves," *Journal of Computational Physics*, 144:185-200, 1994.
- [18] A. Franchois, A. Joisel, C. Pichot, and J. Ch. Bolomey, "Quantitative microwave imaging with a 2.45-GHz planar microwave camera," *IEEE Trans. Medical Imaging*, 17:550-561, Aug. 1998.
- [19] P.M. Meaney, K.D. Paulsen, J.T. Chang, M.W. Fanning and A. Hartov, "Nonactive antenna compensation for fixed-array microwave imaging: Part II - imaging results," *IEEE Trans. Med. Imag.*, 18:508-518, June 1999.
- [20] S. Y. Semenov, A. E. Bulyshev, A. E. Souvorov, R. H. Svenson, Y. E. Sizov, V. Y. Borisov, V. G. Posukh, I. M. Kozlov, A. G. Nazarov, and G. P. Tatsis, "Microwave tomography: Theoretical and experimental investigation of the iteration reconstruction algorithm," *IEEE Trans. Microwave Theory Tech.*, 46:133-141, Feb. 1998.

FDTD Studies on SAR in Biological Cells Exposed to 837 and 1900 MHz in a TEM Cell. A.W. Guy, Professor Emeritus, University of Washington, 18122 60th PL NE, Kenmore, WA 98028, (425) 486-6439, benc@seanet.com

This paper describes a theoretical analysis of a TEM cell exposure system used for *in vitro* studies of the effect of cellular telephone (CT) and Personal Communication System (PCS) electromagnetic (EM) fields on living cells. This type of TEM cell was chosen since the cross sectional aspect ratio between the width and height provided a more uniform field and efficient energy coupling to cell flasks than that of the more conventional devices. Also incorporated in the design but not discussed in this paper was a very stable environmental control system suitable for maintaining a very constant temperature, essential for *in vitro* exposure studies. An earlier analysis of a truncated and less realistic version of this model and the associated dosimetry was previously described by the author, (Guy, et al., 1999). Commercially available XFDTD version 5.05 finite-difference-time-domain (FDTD) software was used to carry out the analysis.

The mesh size of the FDTD space containing the TEM cell model shown in Figure 1A was 1 mm, with dimensions of 157x101x587 voxels in the x, y and z directions corresponding to a total volume of 9.3 million cells. The x, y and z axes corresponded to the directions across the widest dimension from left to right, the narrowest dimension from left to right and the longest dimension from bottom to top, respectively in Figure 1A. A feed voltage of 1 volt in series with 50 ohms was inserted between the 1 cell wide air gap between the bottom end of the septum and the closed end of the tapered outside shell of the TEM cell. A 50-ohm termination resistance was inserted in the gap at the upper end of the TEM cell model. Figure 1B illustrates the 0.333-mm local meshed FDTD model (external local mesh not shown) of the Falcon #2050 14-ml test tube chosen for the *in vitro* studies. For the studies the flasks contained a 10-ml of solution of one of three possible cell groups; suspended blood cells, lymphoma cells, or salmonella cells. For brevity only the blood cells are discussed in this paper. Figure 1B shows the individual voxels and the meniscus at the surface of the solution. Though the meniscus can have considerable influence on the SAR in exposed cells within and near it, for this case its influence probably was negligible since all of the cells were centrifuged down to the lowest 1/3-ml volume of the flask before they were exposed.

For the CT exposures, the vessels were exposed in two groups of three tubes, with a group placed on each side of the septum of the TEM cell as shown in Figure 2 for the xz plane view. The figure illustrates the configuration of the flask group in the 234x72x321 1/3mm local (dark) mesh contained within the 157x101x587 1 mm main (light) mesh. Before calculating the SAR in the flasks exposed at CT and PCS frequencies, FDTD calculations were done to determine the electric (E) and magnetic field (H) uniformity within the TEM cell. The E and H fields at 837 MHz were found to be very uniform for the empty TEM cell in the regions where the flasks would be placed. A maximum E field strength of 270 V/m and H field strength of 0.716 A/m were calculated in the exposure volume for an input power of 1 watt to the TEM cell and the calculated input impedance of 50.1-j0.311 ohms. The calculated electric and magnetic fields at 1900 MHz were less uniform than the former and had maximum strengths of 440 V/m and 0.987 respectively in the empty space normally occupied by the cell preparations. The calculated input impedance for this case was 48.3-j1.31 ohms.

Figure 3 illustrates the gray scale graphical results of the SAR calculations for one of the two identical arrays of tubes exposed to 1 watt at 837 MHz, each containing 10-ml of suspended human blood cells. The exposure field vectors and the SAR distribution are shown for each principal cross-section in the vertical direction and horizontal cross sections near the bottom, middle and the top of the tube. The highest SAR occurring at the periphery of the cross-sectional plane shown in the E-K plane at the right side of the figure is due to eddy currents flowing around the periphery of the tube, induced by the magnetic field vector perpendicular to the plane. The magnitude of the SAR at the center of the tube is more than 12 dB less than at the sides. The low SAR at the center, corresponding to the darker areas of the H-K cross section at the left of the figure, is due to the weak coupling of the electric field, perpendicular to the long axis of the tube. The region of brighter areas in the H-K section at the bottom of the tubes is due to the eddy currents induced by the magnetic field flowing across the bottom in a horizontal direction. As indicated by the statistics and histogram in Figure 4A (large standard deviation, large ratio between peak and average SAR and the peak of the histogram shifted

well to the left of the normal distribution), any suspended cells are subjected to a very wide range of SAR values for these exposure conditions. It had been suggested by biologists doing research with the preparations that if the cells were centrifuged down to the bottom 1/3-ml of liquid in the tube they may be restricted to and exposed to the more uniform SAR seen in the distribution pattern for that region. Figure 4B illustrates the statistics and histogram for the SAR distributions in the bottom 1/3-ml of liquid in the tube. There appears to be marked improvement in the uniformity of the SAR distribution, closely matching a normal curve. Figure 5 illustrates the gray scale graphical results of the SAR calculations for one of the two identical arrays of exposed tubes exposed to the PCS frequency of 1.9 GHz, each containing 10-ml of suspended human blood cells. It can be seen that the calculated SAR distribution is in some ways similar but in other ways different from that obtained for the 837 MHz exposures. The circulating eddy current phenomenon is still apparent from the E-K and E-H plane views of gray scale plots. The SAR distribution in the H-K plane contains bands of low SAR due to the interference patterns set up by the higher order modes in the TEM cell. It can be seen, as expected, that the magnitude of the SAR is increased by nearly an order of magnitude due to the increased field strength from constructive multimode interference and the increased coupling at the higher frequency. As for the case of the 837 MHz exposures, the statistics and histogram in Figure 6A (large standard deviation, large ratio between peak and average SAR and the peak of the histogram shifted well to the left of the normal distribution), for any suspended cells would be subjected to a very wide range of SAR values for these exposure conditions. However for the cells centrifuged down to the lower 1/3 ml of solution, the 1.9 GHz exposure results in about the same uniformity as obtained with the 837 MHz exposure as can be seen from the histogram in Figure 6B.

CONCLUSIONS

A FDTD TEM cell model has been formulated and used to calculate the SAR distribution patterns in cell suspensions exposed to 837 MHz and 1.9 GHz electromagnetic fields. Regardless whether exposures are from a single dominant TEM mode or to multiple modes the results provide quantitative dosimetry support for *in vitro* cellular studies relating to the assessment of the safety of cellular telephones and PCS in terms of human health effects. The results provide guidance as to the best location for the placement of the cells in the exposed solution and for the setting of input power levels to the TEM cell exposure system.

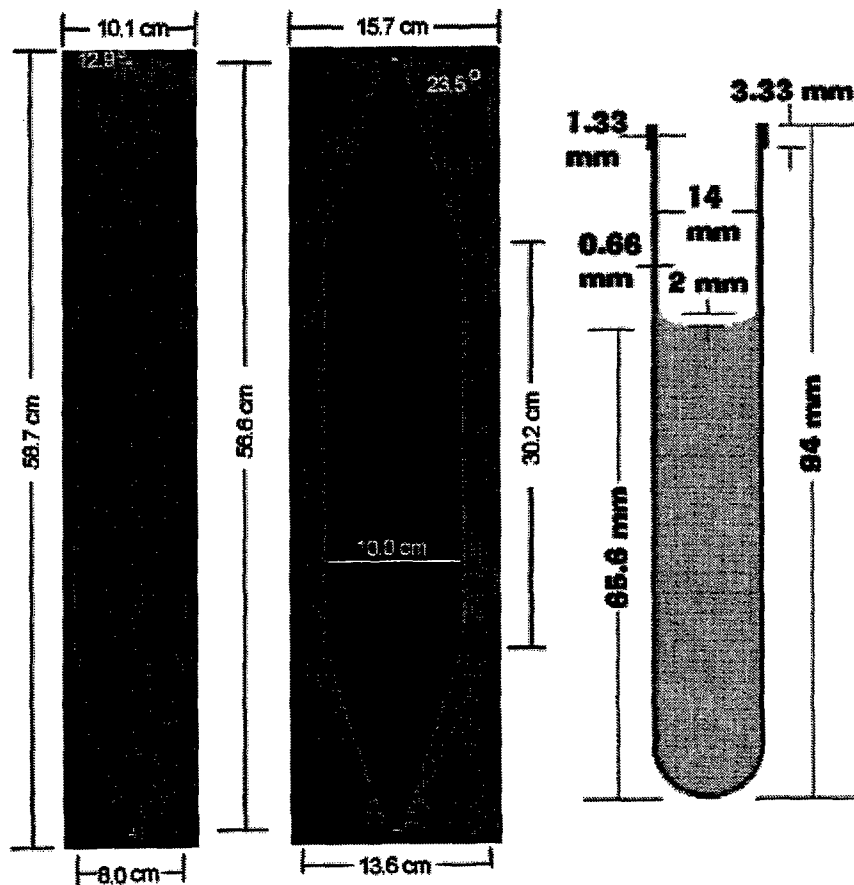
REFERENCE

Guy AW, Chou CK, McDougall JA, 1999, A quarter century of *in vitro* research: A new look at exposure methods, Bioelectromagnetics 20: 21-39, Supplement 4, Special issue honoring the retirement of C. Durney

ACKNOWLEDGEMENT

The author thanks Wireless Technology Research, LLB. For their support of this reported research.

XFDTD TEM CELL MODEL 157x101x587 1mm VOXELS



A. 1-mm main grid model

B. 0.333 mm local grid model

Figure 1. XFDTD models of TEM cell and test tube used for *in vitro* studies.

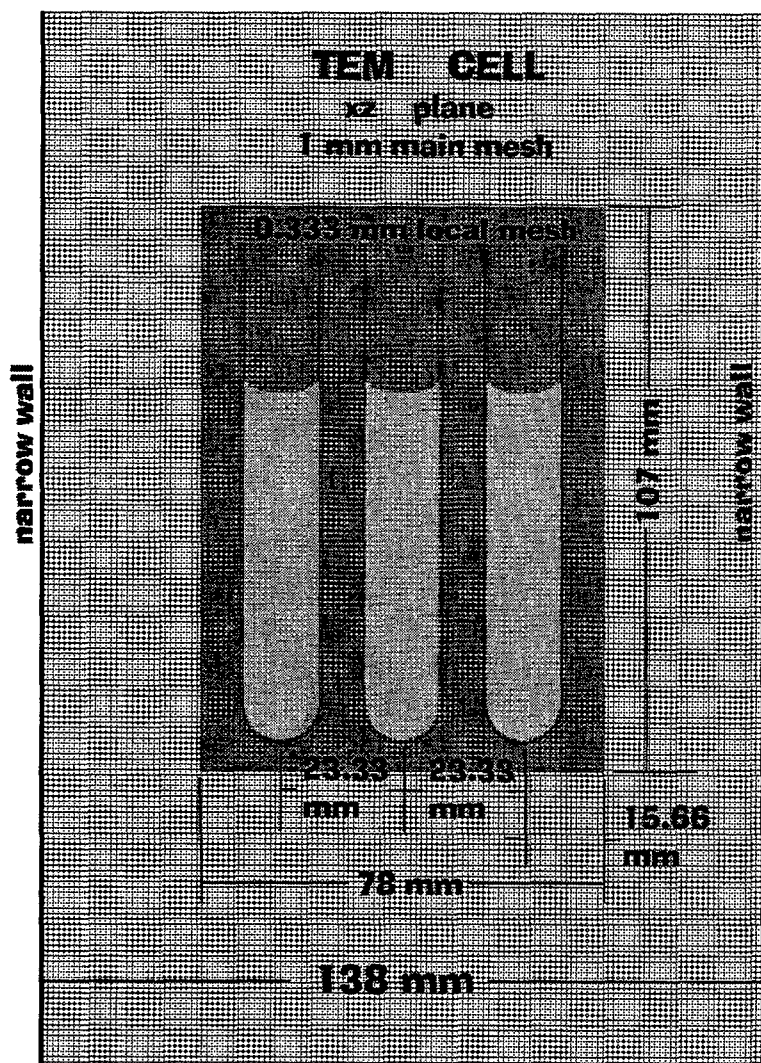


Figure 2. Position of 234x72x321 0.333 mm cell test tube local meshes (each side of septum) in plane parallel to septum of TEM cell.

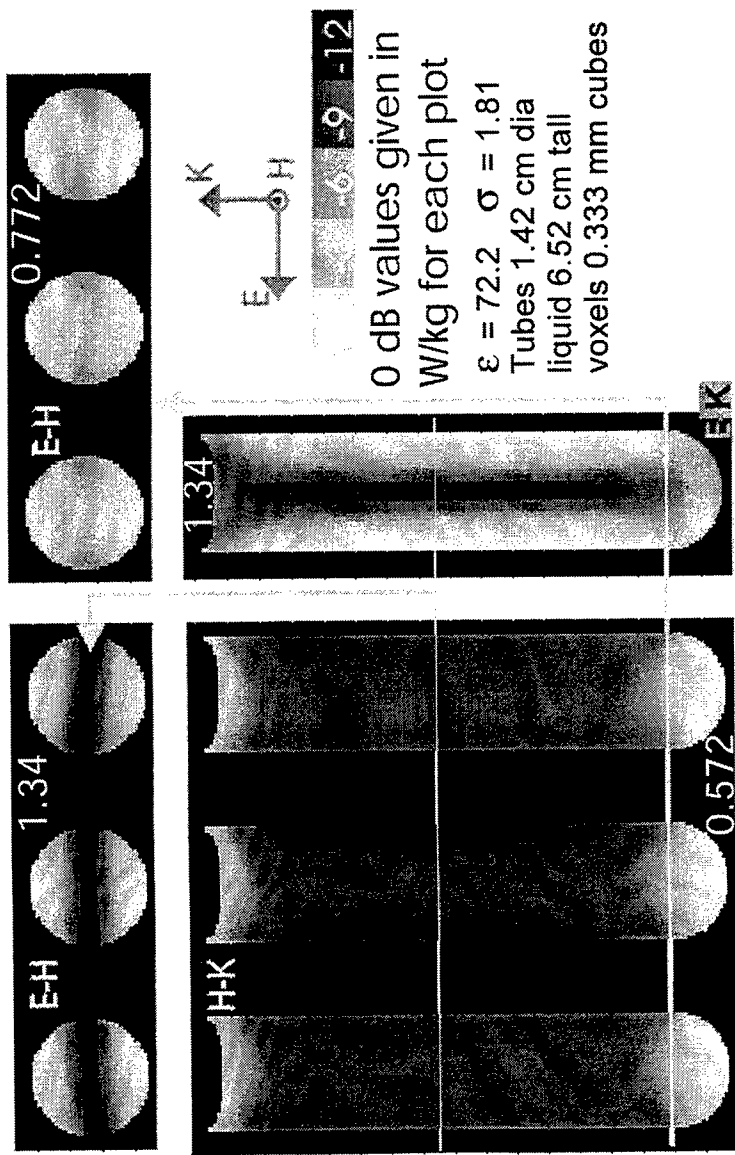
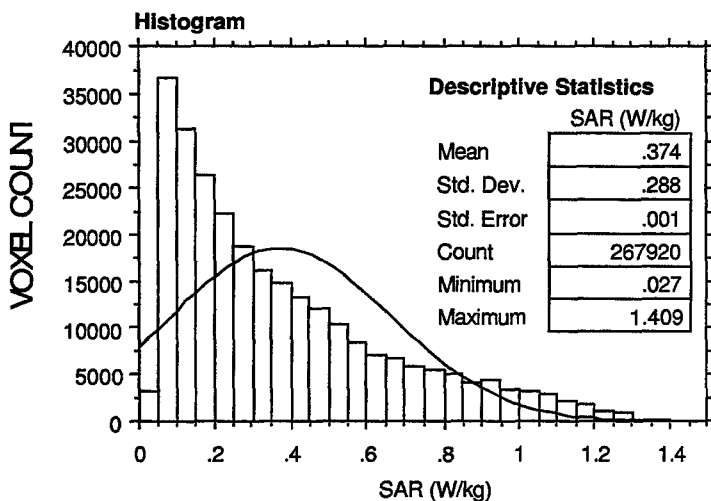
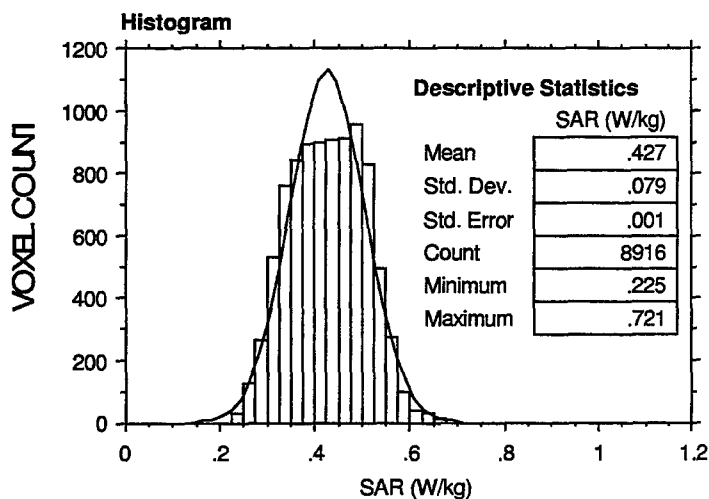


Figure 3. Calculated SAR distribution in TEM cell model in 3 of group of 6 vessels, each containing 10 ml of blood cell medium exposed to 837 MHz in TEM cell with 1.0 Watt input power.



A. Entire 10 ml Volume



B. Bottom 1/3 ml of Volume

Figure 4. Histograms of calculated SAR distribution in TEM cell model of suspended human blood cells in 10 ml solution with normal comparison in of first of a group of 3 tubes exposed in TEM cell at 837 MHz, 1.0 watt input.

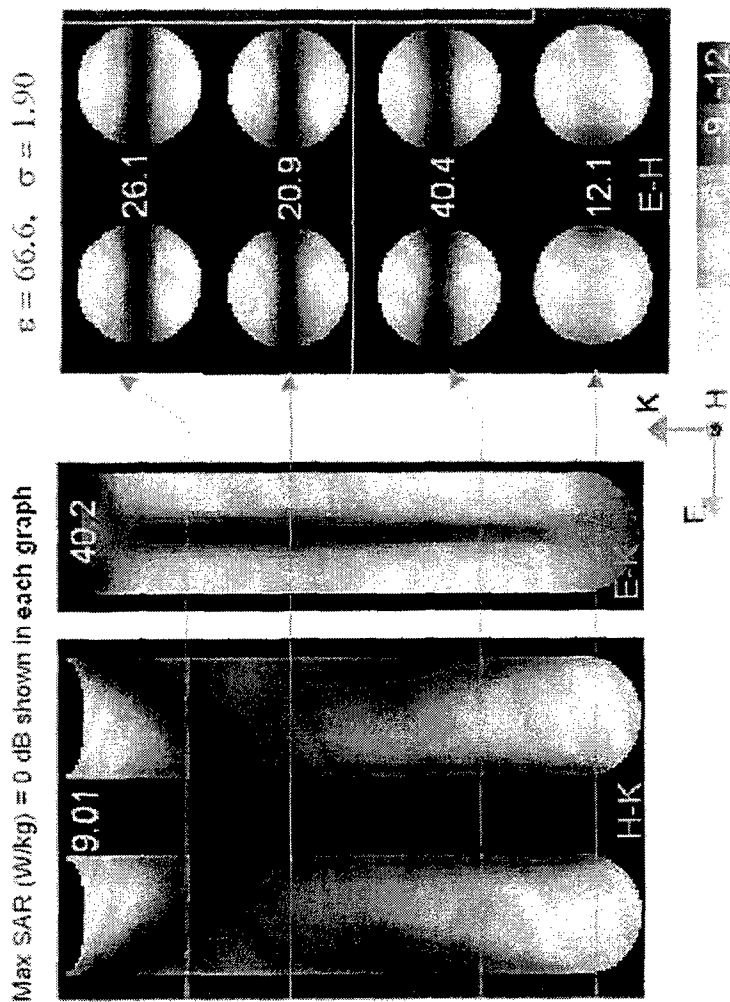
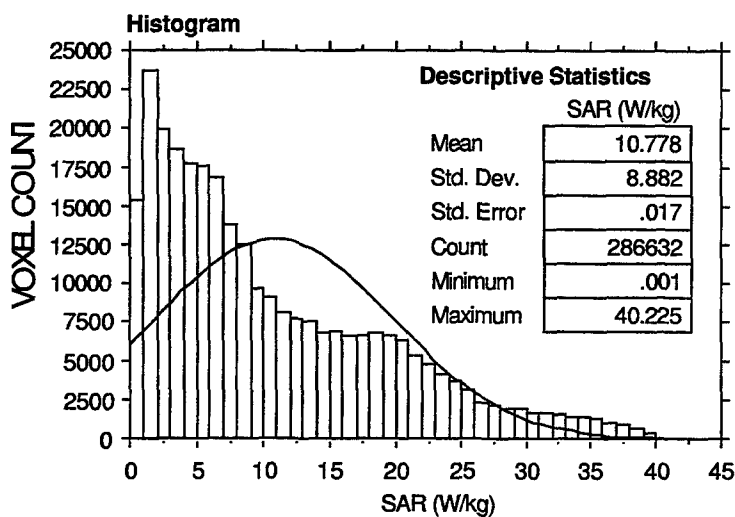
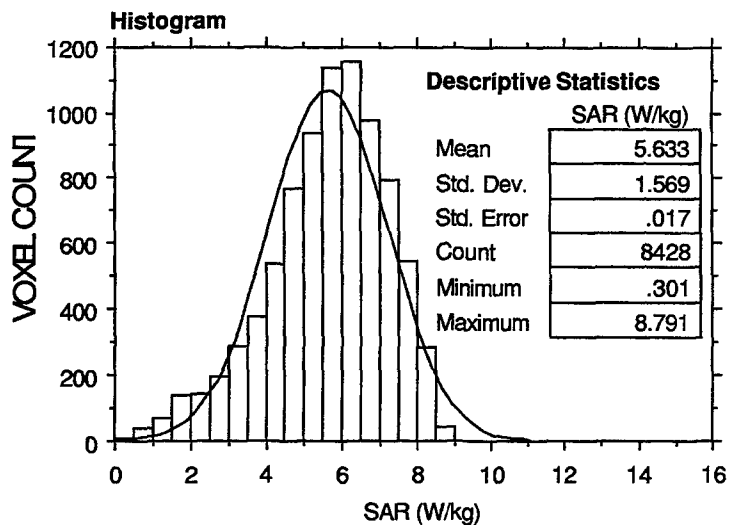


Figure 5. XFDTD derived SAR distribution in 2 of a group of 4 Falcon #2056, 14 ml test tubes, each containing human blood cells in 10 ml of medium exposed to 1.9 GHz in TEM cell with 1 watt input.



A. Entire 10 ml Volume



B. Bottom 1/3 ml of Volume

Figure 6. Histograms of calculated SAR distribution in suspended human blood cells in 10 ml solution with normal comparison in one of the group of 4 tubes exposed in TEM cell at 1.9 GHz, 1.0 watt input.

Modelling of Personnel Electromagnetic Radiation Hazards Deliberations of a Novice

Alan Nott, BEE, CEng, MIEE
Senior Electromagnetics and Software Engineer
Army Engineering Agency (AEA)
Department of Defence, Australia.
email: alan.nott@aea.sptcomd.defence.gov.au

Abstract:

This paper discusses some of the work commencing at the Australian Army's Army Engineering Agency in relation to Finite Difference Time Domain and Finite Element Method modelling of personnel hazards of electromagnetic radiation. It discusses the nature of various models, and some of the problems encountered in their creation from the point of view of the comparative novice. Some examples of current work are presented.

Background:

The undesirable effects of electromagnetic radiation on the human body can be a cause for concern, particularly where levels are sufficiently high to cause permanent damage. Different exposure levels produce different responses. High levels can cause burns, blindness and development of cataracts and tumours. Lower levels produce more subtle effects including headaches and other discomfort, behavioral changes, short-term memory loss, as well as possible stimulation of changes at the cellular and DNA levels, and these may provide a trigger for the eventual development of tumours. At low levels, however, factors other than the exposure levels can also have an important influence. These include the frequency, modulation and orientation of the field, the exposure regime, the latency period, as well as the predisposition of the individual to tumour development. At sufficiently low field levels tumor development may be slow or not occur at all. The question then arises as to what levels of radiation can be considered as globally 'safe'. And indeed, what is the meaning of 'safe'.

Tumour development is most commonly attributed to the heating effects of electromagnetic radiation, and there is a tendency to assume that physiological effects do not occur where the localised temperature rise is less than 1°C. From this basis a temperature rise of 0.1°C is generally considered to be 'safe'. Specific Absorption Rate (SAR) is the measure of energy deposited in the tissue, generally specified in Watt/kg. Temperature rise is a function of the SAR and the ability of the body to cool the tissue. However, as both quantities are difficult to measure directly, Standards generally give electric and magnetic fields which are estimated to produce the SAR levels (and hence tissue temperature rise), and it is these derived fields that are generally measured in personnel radiation hazard (personnel RADHAZ) assessments. Reference 1 is the Australian Standard for personnel RADHAZ. As with other Standards, this was based largely on the World Health Organisation document of Reference 2.

However, as field strengths change rapidly in the close proximity of antennas, and in confined spaces, as well as being disturbed by the measurement process itself, reliable measurements are often difficult or impossible. For cellular phone assessments, SAR estimations have been made using a partial mannequin filled with material which electromagnetically and thermally mimic human tissue over the frequency range of interest. The SAR is then inferred from temperature rise, measured directly by thermal instrumentation embedded in strategic locations such as the eyes, which are particularly sensitive to electromagnetic radiation. This sensitivity arises from both the electromagnetic parameters of the eyes, and the relative lack of cooling available from blood circulation.

While much work has been done on the cellular phone, little, if any assessments address the Manpack radio such as those in common use with the Australian Army. The most significant radios are an HF set (2 to 30 MHz) with a nominal power of 20 Watt, and a VHF set (30 to 88 MHz) with a nominal power of 10 Watt. While the output power of both these transmitters can be set at a range of different nominal levels, there is a need to determine the settings that can be used which do not exceed 'safe' levels specified in the appropriate Standards.

Some work has been done on the Manpack configuration involving the measurement of fields generated by the radio in isolation or above a ground plane. Because of a range of measurement uncertainties, approved

practices require that measurements be taken at distances less than 10cm from the antenna. However it can be shown that the antenna itself is not the only source of radiation. Considerable field levels arise from the case itself which is capacitively coupled to the back of the wearer, and who 'stands in' for the other half of a dipole antenna, albeit somewhat unbalanced.

Other Manpack configurations to be investigated include a range of stances (standing, sitting, prone). As the anatomical model represents the standing position, the manipulations of this data to the range of other stances will prove to be an interesting mathematical challenge. One possible solution is to adapt the fully articulated body provided with 3D Studio® (Figure 1) to determine the orientations of the slices of the body in the different stances.

In addition to the Manpack personnel RADHAZ assessments a range of vehicle installations, principally the Perentie (Land Rover) 4 X 4, and two armored personnel carrier (APC) configurations. These installations typically have up to 100-Watt nominal power over the HF and VHF bands. The Commander's hatch of one APC being within 18 inches of an HF whip is of particular concern. There are also some interesting perturbations of HF near fields in Perentie installations, arising from resonances of the canopy support and roll bar structures.

Modelling methods:

Two methods are potential candidates for personnel RADHAZ investigations – the Finite Difference Time Domain (FDTD) and Finite Element Method (FEM). Although models for each technique contain essentially the same data, the representation of it is quite different. The FDTD model consists of uniform cubes, each assigned with the appropriate (averaged) ϵ_r , σ , and density. The FEM model consists of three-dimensional solids conforming to the shapes of the various body entities, and again assigned the appropriate parameters. Both modelling techniques require a 'white-space' around the model as well as an absorbing or non-reflecting outer boundary, and both of these add to the total model size. Depictions of these model structures are shown in Figures 2 and 3.

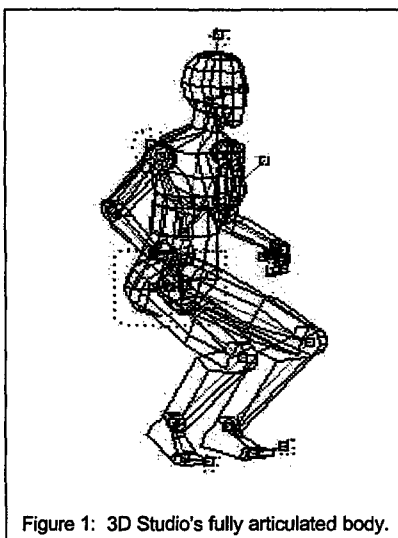


Figure 1: 3D Studio's fully articulated body.

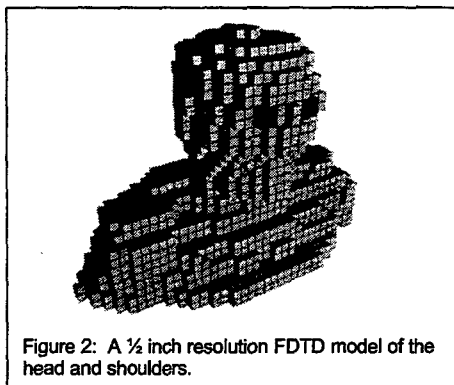


Figure 2: A 1/2 inch resolution FDTD model of the head and shoulders.

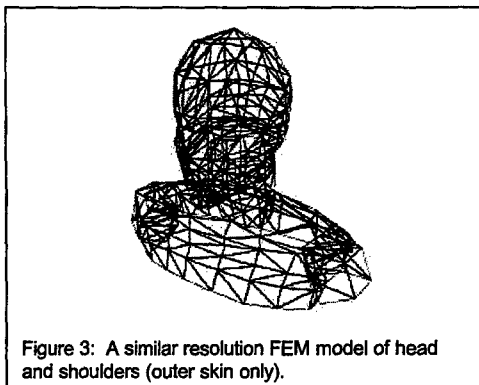


Figure 3: A similar resolution FEM model of head and shoulders (outer skin only).

®3D Studio is a registered trademark of Autodesk Inc.

Whatever modelling technique is used, detailed anatomical data on the human body is needed. For this reason an anatomically based model was obtained from Dr Om Gandhi of the University of Utah. This data is supported by programs, which allow construction of varying resolution FDTD models. The raw data for this model consists of a file containing a series of $\frac{1}{4}$ inch resolution horizontal 'slices' taken at strategic levels over the height of the body. This data was derived from the anatomical drawings in Eycleshymer and Schoemaker's "A Cross-Section Anatomy", first published in 1911 (Reference 3). This epic work contains 113 cross-sections, which were created by hand-tracing body slices on glass plates, and then retracing them on drawing paper from which lithographic plates were made. Each illustration is liberally annotated in the Language of Science – which is, of course, Latin. One such cross-section is shown at Figure 4.

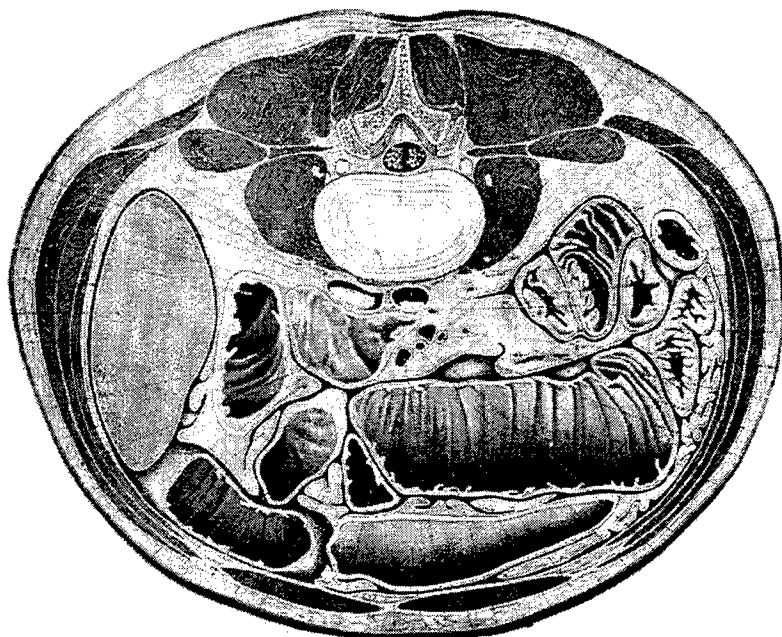


Figure 4: A typical cross-section taken just below the region of the stomach, and passing through Arcus vertebrae lumbalis III which can be clearly seen at the top centre. (Annotation has been removed)

Each $\frac{1}{4}$ " X $\frac{1}{4}$ " cell of a slice has been extracted from such a drawing and assigned a specific tissue type, thus implying electromagnetic parameters and density. The model uses a total of 14 different tissue types - viz.: muscle, fat/bone, blood, intestine, cartilage, liver, kidney, pancreas, spleen, lung, heart, brain/CSF/nerve, skin and eye. Using interpolation techniques, this data, together with a table of electromagnetic parameters (dielectric constant and conductivity - ϵ_r and σ) for the frequency of interest, code has been written to construct a Finite Difference Time Domain model of the body. The density data allows SAR (in Watt/kg) to be calculated from the power deposited in the tissue on a cell-by-cell basis.

Cell size considerations for FDTD models:

Conventional wisdom (Reference 4) is that the cell size should probably be a maximum of 0.1 wavelengths. A larger cell size could approach the Nyquist sampling limit of $\Delta x = \lambda/2$ and significant aliasing of signal components may result. Too small a cell size may lead to rounding errors, requiring increased mathematical precision to overcome. The upper frequency of interest is 88 MHz, and $\lambda/10$ is 0.34m, or 13.5 inches. Another restraint on the cell size of the body is that it be able to resolve, for example, the power deposited in the eye. This implies that a cell size of the order of $\frac{1}{2}$ inch is appropriate to this task. Such a model is under creation at AEA.

FDTD model considerations:

For the $\frac{1}{2}$ inch resolution FDTD model, the body tissues require about 15,000 cells. The box enclosing the body model (bounding box) has 130,000 cells. Adding a minimum of white space around this doubles the number. The addition of the Manpack radio fitted with a 3m whip brings the total up to 900,000 cells.

The bounding box for an armoured personnel carrier such as the M577, complete with a standard radio equipment fit has dimensions of 2.5 X 6.3 X 4.8 metre, requiring just over 37 million cells. Adding white space and an absorbing boundary would raise this number to almost 100 million cells. Most of these cells represent the air in the model space, either in the hull or around it. A problem of this size is not trivial, and is in the domain of mainframe computers, rather than the most enthusiastic desktop. Increasing the cell size to $\lambda/10$ would reduce the 100 million cells to about 60000 cells for the M577, and the body model would degenerate to about 5 cells. It may be possible to run the majority of the M577 model at $\lambda/10$ or a little finer cell size, and the model of the man at sufficiently high resolution that separate organs can be reasonably represented. It remains to be seen whether this can be done in a single model with graded cell size, or will require two separate models, the finer resolution man model being driven by the fields computed with the coarser M577 model.

While FDTD models of structures such as the body and M577 are not particularly complex to construct once the geometrical data is obtained, running the models can require very significant computing resources. What is needed is a method of representing the solids involved using element sizes commensurate with the resolution required in any particular region. While this may be possible with adaptations of standard FDTD techniques, it is inherent in the finite element method.

FEM model considerations:

FEM models generally consist of tetrahedra rather than the cubic cells used with FDTD. Within reason they can be irregular – ie of different sizes and aspect ratios. This allows resolution optimisation to be applied, with smaller tetrahedra where it is needed and larger elsewhere. FEM models can be made to conform to arbitrary shaped objects, rather than representing curved surfaces with a staircased boundary as with the cube-based structure of FDTD models. As the vertices of the model are not at regular locations, the FEM method does carry the overhead of storage of vertex locations. However, the benefits of varying element size and more efficient problem description may outweigh this overhead.

AEA obtained the Ansoft FEM package "HFSS" (Reference 5), and set about to devise efficient ways of model creation. Although models may contain 2D elements for sources, thin wires and other objects, the major elements of most models are solids. These are known as ACIS models as defined in the SAT file format (Reference 6). ACIS is an object-oriented three-dimensional geometric modelling engine, and provides a transportable format for solid models.

HFSS comes with a 3D Modeller which allows rapid creation of simple structures. It also allows input of solids from AutoCAD® and other CAD packages using the SAT format. It also allows inputting of polylines and 3D faces using the DXF (Drawing eXchange Format) files. Unfortunately HFSS discards all the 'Z' data in DXF files and each entity has to be manually repositioned in the 3D Modeller. AEA already has a large number of detailed vehicle and other models which can be output in .DXF format, and the inability to import them into HFSS is a cause of concern. Although a 3D Face model and the required solid model may have identical topology (a series of vertices in space connected to form a closed structure), AutoCAD does not provide any means of converting a closed entity of 3D faces to the corresponding solid. While it may be possible to write a translator to ACIS format, as it is a particularly complex format, other methods of geometry transfer should be investigated first.

®AutoCAD is a registered trademark of Autodesk Inc.

Another interesting feature of the 3D Modeller is its Macro capability. Macros can be written either during 3D Modelling sessions, or by external processes. By writing a DXF to the Macro translator, it should be possible to overcome this shortcoming of HFSS. The 3D Modeller also has the ability to create a solid from a series of 3D Faces by using the "CONNECT" command.

Thus the following methods are available for creation of solid models for HFSS:

1. Create the solid model manually in HFSS.
2. Create the solid model in AutoCAD and import it as a .SAT file.
3. Output existing AutoCAD 3D Face models as .DXF files, create a Macro from the .DXF file and run it, then connect the resultant faces in the 3D Modeller to form the solid.
4. A combination of the above.

Vehicle models, the hull/body solids, which are topologically simple could be created either with methods 1 or 2. Details of radio installations etc where they already exist in AutoCAD, could then be merged using method 3.

Because of the complexity of the shapes of the various organs and the body itself, creation of body models presents some interesting challenges. One possible method using Version 14 of AutoCAD, involves using cross-section images from Reference 3.

These images can be displayed on a layer in AutoCAD, and polylines traced around the perimeters of entities of interest. The polylines can then be read into HFSS using Method 3 above, and the cross-sections for each entity connected to form a solid using the 3D Modeller "CONNECT" command..

So that the complexity of the resultant solid is not excessive, care needs to be taken to limit the number of vertices of the polylines, and indeed the number of defining slices. To that end some work has been done in developing an optimisation process that selects vertex locations to give the minimum error for a given number of vertices. This process creates new vertex locations based on truncated Fourier transform series derived from the original vertex locations.

The real world:

In the absence of non-linear effects, antenna gain is independent of the radiated power and any nominal drive level can be assumed for modelling purposes. However, when computing field levels and related quantities, the drive level data forms an essential part of the model, either during modelling or post-processing. Enquiries as to what power is radiated by a particular installation normally result in the quotation of the nominal power output. Leaving aside the effects of modulation, the power radiated is seldom what is 'dialed up'. This is particularly so with electrically short radiators such as vehicle whips operating at a few MHz.

To model the real world, measurements need to be taken to characterise the outputs of the various transmitter configurations across their frequency range. These measurements should be performed in conjunction with a series of near-field measurements which can be used to validate the model. As the VHF equipment has a 50 ohm cable to the antenna base, through-line monitoring can readily establish transmitter output power levels. Losses in the antenna tuning unit and the whip itself should be small but are not easily measured. The HF equipment has an open wire feeder to the whip antenna. As this is far from a 50 ohm system, through-line techniques are not applicable and current thinking is to determine transmitter output power in terms of measured antenna impedance and base voltage or current.

Once validated models have been developed, they can be used as a basis for development of procedures so that the accepted safe levels of exposure are not exceeded. Model data will also be valuable for ordnance RADHAZ assessments and as an input to propagation analysis studies.

A simple body model, comprising a solid conforming to the skin shape and filled with an 'average body' material has been used in some initial work to investigate the use of the FEM package. This body has been used to display fields in a Manpack configuration (Figure 5) as well as with an M577 armoured personnel carrier, fitted with a single HF radio (Figure 6). The same model has also been used to investigate body currents induced by a shark repellent device worn by divers and which couples high energy electric pulses into the water (Figure 7). Another area of investigation is the enhancing effects of metal framed spectacles on the field levels around the eyes (Figure 8).

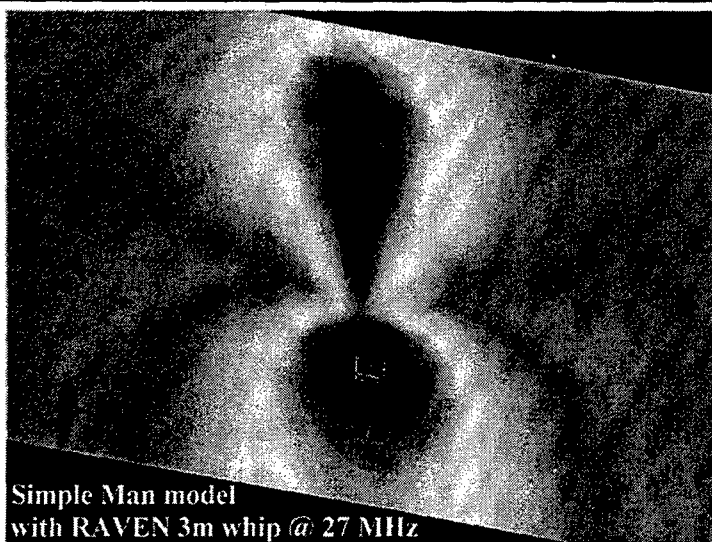


Figure 5: Fields around a Manpack configuration. Note the high fields centered on the case of the radio itself.

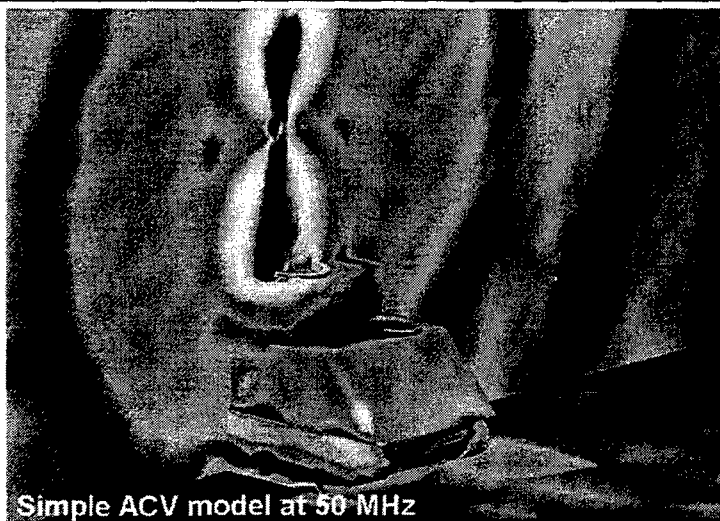


Figure 6: A VHF installation on an M577 showing fields on a cut plane passing near the whip, and surface currents on the hull and ground.

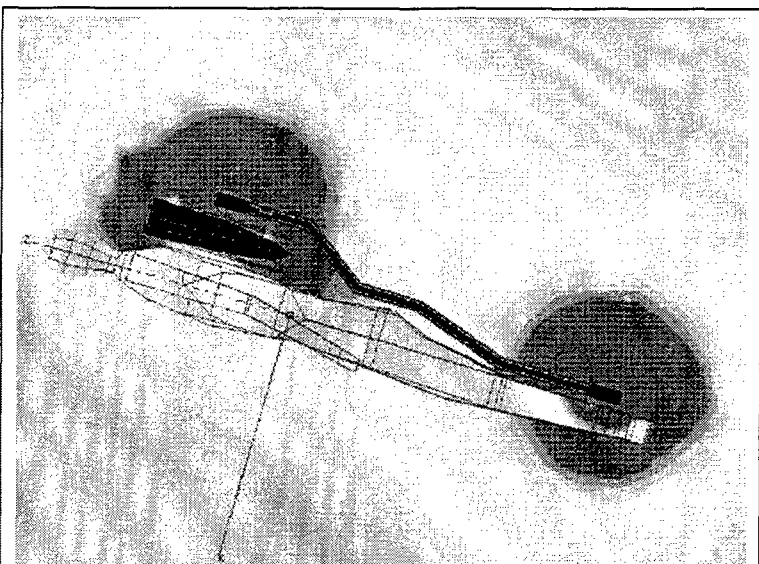


Figure 7: Fields around diver wearing shark repelling device. This model was used to assess the levels of body currents induced in the diver.

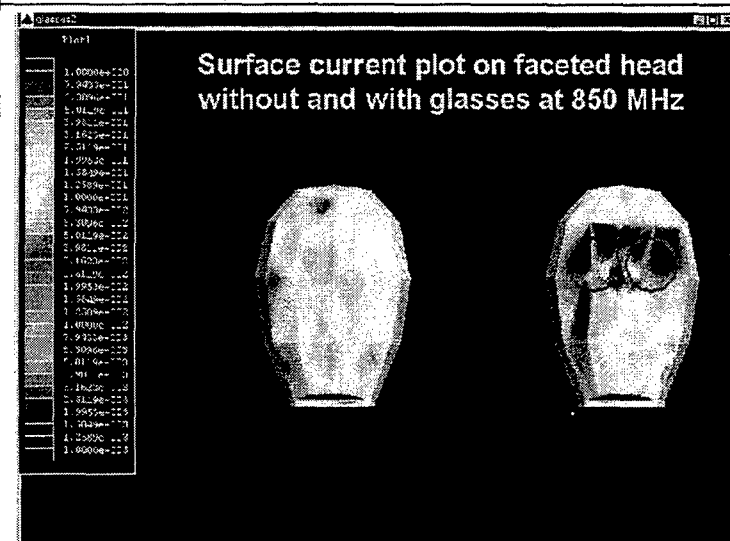


Figure 8: Surface currents on a simple model of a head showing the effects of metal-rimmed glasses.

Conclusions:

This paper describes some of the work done by AEA to assess personnel hazards of electromagnetic fields. Both FDTD and FEM modelling strategies have potential to address these personnel RADHAZ issues. Which technique is appropriate is a function of the model size, which depends on the model complexity and the detail required. FDTD models could address Manpack configurations. For larger models incorporating vehicle installations, FEM models might provide the only solution because of model size. A hybrid approach may exist using FEM to model the larger structure containing an 'average' body, and FDTD for the body model, with boundary conditions imposed from the FEM model.

The nature of body models for both Finite Difference Time Domain and the Finite Element Method has been described. Some of the difficulties in creating such models has been discussed, in particular the creation of models in different stances. This may involve the use of an articulated body model to modify the positions and orientations of body slices from which both the FDTD and FEM models are derived.

Models for personnel RADHAZ assessments also need to include accurate representations of the radiating sources, including the vehicles in which they are installed. The inability to readily convert the existing 3D Face models into the corresponding solid (ACIS) models compatible with the FEM modeller is a cause of concern.

Work is also needed to characterise the actual power radiated from radio installations for their different power settings and configurations before the corresponding models can be considered to represent the real world.

References:

- [1] Standards Australia / Standards New Zealand: "Interim Australian/New Zealand Standard "Radiofrequency fields – Part 1: Maximum exposure levels – 3 kHz to 300 GHz". AS/NZS 2772.1(Int):1998.
- [2] World Health Organisation (WHO): "Environmental health criteria 137: Electromagnetic Fields 300 Hz to 300 GHz (1993)".
- [3] Albert C. Eyedshymer and Daniel M. Schoemaker: "A Cross-section Anatomy". Appelton-Century-Crofts 1970.
- [4] Karl J. Kunz and Raymond J. Luebbers: "The Finite Difference Time Domain Method for Electromagnetics: CRC Press 1993. ISBN 0-8493-8657-8
- [5] Ansoft Corporation, Pittsburg, PA. "High Frequency Structure Simulator (HFSS) Version 6" 1999.
- [6] Spacial Technology Inc :SAT File Format" www.spatial.com/support/publications/satfile.htm

Modeling Interference Between Very Low Frequency Electromagnetic Fields and Implanted Cardiac Pacemakers

Trevor W. Dawson and Maria A. Stuchly
Dept. Elec. & Comp. Eng., University of Victoria
PO Box 3055 Stn CSC Victoria BC Canada V8W 3P6

Abstract

The possibility of low-frequency (e.g., 60-Hz and harmonics) external electric or magnetic fields interfering with the normal operation of an implanted cardiac pacemaker is a topic of great practical significance. An external electric field induces a capacitive current associated with a conservative electric field in the body interior. This can interfere with pacemaker operation due to resulting voltage differences induced either between the pacemaker case and electrodes, or between pairs of electrodes. An applied magnetic field permeates the body, serving as a volume source with an associated nonconservative internal electric field. The pacemaker case, leads and electrodes form portions of closed conducting paths which are completed via the conducting tissues of the body. Inductive effects involving such paths must properly be accounted for.

The advent of anatomically derived high-resolution (millimeter-scale) conductivity models of the human body, coupled with efficient computational schemes, permits the practical estimation of such effects using numerical modeling. Both electric and magnetic source effects can be incorporated into the efficient Scalar Potential Finite Difference modeling scheme. Additionally, some published experimental work on pacemaker interference involves contact electrodes on the body surface to emulate external electric field excitation. Such sources can also readily be incorporated into the numerical modeling scheme. The numerical modeling then additionally provides a means of quantifying the differences between induction by an external electric field and by contact electrodes.

This paper presents computed data for cardiac pacemaker interference, based on a 3.6-mm-resolution conductivity model of the human body, under excitation by an external electric field and by several electrode source configurations involving the feet and either the head or shoulders. The extension to interference by magnetic sources is also indicated.

1 Introduction

Problems involving low frequency induction in (electrically small) conductors can be solved using Stevenson's method, in which the full electromagnetic field is evaluated sequentially from power series in frequency. This method has the advantage of isolating contributions due to electric and magnetic source fields. In the present application, only the zeroth (static) and first-order terms are of practical interest.

A low-frequency external electric field induces a time-harmonic surface charge distribution on the body, which cancels the static internal field in the body. The internal electric field is then first order in frequency and conservative. It is associated with a capacitive current flow in the body, with current flow lines terminating on surface charges. It might be anticipated that this induction mode can interfere with pacemaker operation as a result of voltage differences induced either between the pacemaker case and electrodes, or between pairs of electrodes.

Conversely, an applied magnetic field permeates the body without perturbation. It acts as an applied electromotive forces distributed throughout the volume, and gives rise to a nonconservative internal electric field and an associated current system consisting of closed loops. The pacemaker case, leads and electrodes can form parts of closed conducting paths which are completed via the conducting tissues of the body. Inductive effects involving such paths must properly be accounted for. In particular, pacemaker interference due to extraneous voltages induced directly on the pacemaker leads might be expected.

In fact, the susceptibility of cardiac pacemakers to electromagnetic interference (EMI) by external electric and magnetic fields is well known. Moreover, some pacemaker models may be particularly sensitive to 50- or 60-Hz fields, such as those associated with power transmission systems. These frequencies are particularly problematic to filter out, since they overlap the natural *QRS* wave spectrum [1, 2]. The quantification of such effects is therefore of practical significance, particularly for considering any occupational exposure limitations for power utility workers with implanted pacemakers. It should be noted that, in contrast to the case of exposure to magnetic fields, electric field effects can be eliminated by the use of a protective suit.

Known instances of pacemaker EMI due to strong 50- to 60-Hz electric fields arise both from clinical reports and from laboratory studies. The latter are particularly useful, since their controlled nature enables quantification of the relationship between the source strength, the short circuit current (current from the body to ground), and the nature of any resulting interference.

Reported laboratory studies have involved either exposure of human subjects to known 50-Hz uniform electric fields, or simulation of an external field by contact current injection electrodes on the shoulders and soles of the feet. The first type of exposure is somewhat difficult to control accurately, but indicates that the interference threshold depends on the pacemaker type and manufacturer, the lead configurations, as well as body characteristics and posture. Unipolar pacemakers have a much lower induced body current susceptibility threshold than bipolar units. The relationship between electric field strength and body characteristics and short circuit current is indicated by extensive published data [3]. Conversely, the contact electrode source method permits accurate control over the short circuit current. Here, current injection electrodes were placed on the shoulders and soles of the feet of volunteers with pacemakers [4, 5].

Current can be injected either symmetrically or asymmetrically to various combinations of the shoulder and foot electrodes, and the various pacemaker interference thresholds determined. These results are particularly useful for relating interference thresholds to short circuit current. However, the detailed relationship between the two experimental source mechanisms is somewhat problematic [6].

The recent development of millimeter-scale anatomically-based electromagnetic models of the human body, together with progress in computational electromagnetics, makes numerical modeling a viable and flexible alternative method for assessing pacemaker EMI. Both electric and magnetic source field effects can be incorporated into the efficient Scalar Potential Finite Difference (SPFD) modeling scheme (which is the numerical realization of Stevenson's method) and its hybridization with the quasistatic finite difference time domain (QS-FDTD) method. The SPFD method also readily admits contact electrode sources. Consequently, the result is a scheme for the accurate assessment of the relationship between contact electrode sources and uniform external electric fields.

Electric fields induced in various tissues, based on heterogeneous human body models exposed to 50- or 60-Hz uniform electric fields, have been computed by various research groups [7, 8, 9]. In the research presented here, we use a high-resolution (cubic voxels with 3.6-mm edges) model of the human body, modified to include a pacemaker, together with previously developed and verified computational methods [10].

2 Methods

2.1 Body Models

The body models are based on magnetic resonance imaging (MRI) [11] and are described in detail elsewhere [9]. The calculations involve low- and high-resolution models, comprising cubic voxels with 7.2-mm or 3.6-mm edges aligned with the Cartesian axes oriented so that the *x*-, *y*- and *z*-axes run from left-to-right, back-to-front, and foot-to-head, respectively. The body models comprise some 90 separate materials. Of these, 81 are associated with actual tissues, and the remainder with various air cavities, body waste materials and the pacemaker pulse generator. Each voxel is assigned a conductivity value, based on the most recently available measurements, corresponding to its dominant tissue type. The various tissues form a total of 33 distinct groups ("organs") for final dosimetric analysis. The high resolution is sufficient for resolution of all major body components, as well as some of the smaller organs and tissues. Care has been taken to maintain electrical continuity of bone, muscle, blood vessels

and skin. As an indication of the magnitude of the computational problem, the high (low) resolution model comprises 1630710 (203073) conducting voxels.

2.2 Pacemaker Model

A metallic box representing a pacemaker pulse generator was digitally inserted in the left pectoral subcutaneous fat layer of the models, consistent with an approximate clinical placement. The central image of Figure 1 shows

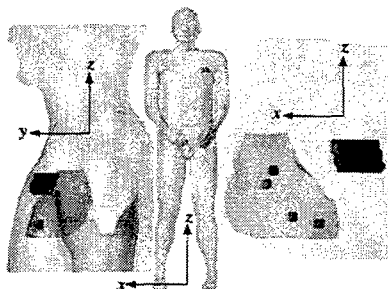


Figure 1: Views of the body model exterior (center), and left and front views of portions of the body model. The pacemaker pulse generator is represented by a dark box and the electrodes by sets of two for the atrial (upper) and ventricular placement (lower) in the heart.

a semitransparent view of the body surface and the underlying pacemaker pulse generator (case) and pacing electrodes. Other tissues are omitted, so that the true heterogeneity of the model is obscured.

For cases involving electric excitation (external field or contact electrode sources), the induced internal field can be described by a scalar potential (voltage) field. The character (diameter and resistivity) of the pacemaker leads, combined with absence of directly induced voltages along them in the absence of magnetic excitation, allows them to be neglected. The assessment of EMI effects for electric fields is therefore reduced to the problem of determining the ambient voltage differences between various combinations of pacemaker electrodes and/or the pulse generator. It is then necessary only to specify the electrode placement within the model heart corresponding to the pacemaker lead type (unipolar, bipolar). The required voltage differences may be extracted from the computed whole-body data at the post-processing stage. To this end, six points were selected. Two were on the pacemaker pulse generator, at its lowest and highest points relative to the z-axis. In addition, two atrial and two ventricular electrode sites were selected. The first and third images of Figure 1 respectively depict close-up views of portions of the model thorax, emphasizing the heart and pacemaker pulse generator, and indicating the selected pacemaker electrode locations. As is evident in the leftmost image, the atrial and ventricular electrode pairs for these computations each lie in a common y plane. The third image shows the atrial electrodes to be separated by two voxels horizontally and 4 voxels vertically for a 1.61-cm separation. The ventricular electrodes are separated by 8 voxels horizontally and 2 voxels vertically, for a 2.97-cm separation.

For scenarios involving magnetic excitation, the possibility of induction along the pacemaker leads must additionally be accounted for. To this end, the lead paths must be specified within each modeling scenario. In practice, the leads are approximated in a staircased manner conformal with the voxel edges. The current induced along each insulated lead appears as an extra unknown in the modeling, and constrains the ambient induced current pattern in the surrounding tissues. The return current paths between pacemaker electrodes and pulse generator are closed by way of the body volume conductivity distribution.

2.3 Source Scenarios

At the time of writing, results were available only for the two electric source mechanisms. One configuration involves a uniform external electric field directed vertically from head to foot, with the upright body model in electrical contact with a ground plane over the soles of both feet.

The remaining configurations involve excitation by contact electrodes placed on the body exterior. Five electrode sites were chosen, one on the top of the head, and one on each shoulder and sole of each foot. The latter four sites permit a comparison with previously published pacemaker EMI experimental data [5]. Using these electrodes, four current injection scenarios were specified. Two approximately symmetric scenarios involved current injection via the head electrode or both shoulder electrodes, and extraction via the soles of both feet. Current injection via one shoulder and extraction via the opposite foot yields two asymmetric scenarios.

All data are normalized to a 0.1-mA (100- μ A) short-circuit current, to facilitate comparisons within this work, as well as with previously published data.

2.4 Computational Methods

2.4.1 External Electric Field - Hybrid Modeling

An applied external electric field is significantly perturbed by the presence of the conducting body, and this perturbation must be accounted for in the modeling. This can be handled in a relatively efficient manner for the low resolution model using a quasistatic FDTD code [12]. However, the FDTD code involves full vector field computations, and hardware resources available for this work limit its applicability to the low-resolution model.

The quasistatic problem can also be formulated using Stevenson's method [13, 14]. This is a frequency-domain method, so that a common time-factor $e^{+j\omega t}$ is assumed and suppressed throughout, where $\omega = 2\pi f$, and f (=60 Hz) is the frequency used in the modeling. The advantage is that the complete electromagnetic field can be synthesized from solutions to a series of scalar potential problems. Thus, full use of this scheme would involve solution of an external potential problem. In practice, however, internal computations on the high resolution model can be accomplished using a hybrid method combining the existing QS-FDTD code with a Scalar Potential Finite Difference Method. Here, the internal electric field can be derived from a scalar potential field, $V(\mathbf{r}) \equiv -j\omega\psi(\mathbf{r})$, according to

$$\mathbf{E}(\mathbf{r}) = -j\omega\nabla\psi(\mathbf{r}). \quad (1)$$

The frequency-independent modified potential is governed by the differential equation

$$\nabla \cdot [\sigma(\mathbf{r}) \nabla\psi(\mathbf{r})] = 0 \quad (2)$$

inside the body, (which is a statement of current conservation, $\nabla \cdot \mathbf{J}(\mathbf{r}) = 0$), subject to the boundary condition

$$\sigma(\mathbf{r}) \hat{\mathbf{n}} \cdot \nabla\psi(\mathbf{r}) = -\rho_{s0}(\mathbf{r}) \quad (3)$$

at the body surface. Here $\rho_{s0}(\mathbf{r})$ is the static limit of the surface charge density induced on the body by the external electric field.

In the hybrid method, the QS-FDTD method is used to compute the surface charge density on the low-resolution model. This is then interpolated onto the high-resolution one, and the SPFD code used to solve the resulting scalar problem (2,3).

On a related note, the quasistatic FDTD code does not directly lead to the induced voltage distribution, which is the primary quantity of interest in modeling pacemaker EMI by electric fields. In principle, the required voltage information can be computed from the vector electric field by integration. In practice, use of the hybrid code without interpolation provides a simple method for accomplishing this task with existing tested computational tools.

2.4.2 Contact Electrodes - SPFD Modeling

In modeling current injection source, both sources and internal fields are of zeroth-order. The appropriate differential equation and boundary conditions are based on the representation

$$\mathbf{E}(\mathbf{r}) = -\nabla V(\mathbf{r}). \quad (4)$$

of the internal electric field in terms of a standard potential field. This is to satisfy the differential equation

$$\nabla \cdot [\sigma(\mathbf{r}) \nabla V(\mathbf{r})] = 0, \quad (5)$$

subject to the boundary condition

$$\sigma(\mathbf{r}) \hat{\mathbf{n}} \cdot \nabla \psi(\mathbf{r}) = -\hat{\mathbf{n}} \cdot \mathbf{J}_0^e(\mathbf{r}) \quad (6)$$

at the body surface, where $\mathbf{J}_0^e(\mathbf{r})$ is the static limit of the injected current density at any contact electrodes. This boundary value problem can be solved directly on the high resolution model using the SPFD method.

2.4.3 External Magnetic Field - SPFD Modeling

Excitation involving external magnetic fields can also be handled directly by the SPFD code. In this case, the internal electric field has the (nonconservative) representation

$$\mathbf{E}(\mathbf{r}) = -j\omega \{ \mathbf{A}_0(\mathbf{r}) + \nabla \psi(\mathbf{r}) \}, \quad (7)$$

where $\mathbf{A}_0(\mathbf{r})$ is a vector potential for the static limit of the applied magnetic field. Conservation of internal current density requires the scalar potential to satisfy the differential equation

$$\nabla \cdot [\sigma(\mathbf{r}) \nabla \psi(\mathbf{r})] = -\nabla \cdot [\sigma(\mathbf{r}) \mathbf{A}_0(\mathbf{r})] \quad (8)$$

subject to the boundary condition of tangential current flow at the surface.

Equation (7) shows how the applied magnetic field is manifested as a distributed voltage source. The effect of this contribution on the pacemaker leads must be accounted for in the modeling. Since each lead is insulated, the associated current is separately conserved, except at the terminations at the electrodes and pacemaker case. The requirement of continuity of tangential electric fields imposes a constraint between the local electric field inside the lead and the adjacent field in the body tissue, along the length of the lead. The mathematical specification is completed by imposing a requirement of total current conservation in the neighbourhood of each lead termination.

3 Results and Discussion

The external field excitation runs employed a nominal 60-Hz, 1-kV m⁻¹ (rms) uniform external electric field. This produced short-circuit currents of 18.7 μ A and 17.4 μ A in the high and low resolution models, respectively. Consequently, the desired 100- μ A current corresponds to a 60-Hz uniform external electric field strength of 5.36 kV/m and 5.75 kV/m in the respective cases. The difference (about 7%) in short circuit current between the two resolutions arises mainly from fine-scale geometrical differences in the body surfaces and the attendant difficulties in the charge interpolation process. The better resolution of the body internal structure also contributes to a lesser degree.

Figure 2 depicts the potential distribution over a central *x-z* cross-section of the body for the three "symmetric" electric source configurations. The leftmost panel corresponds to a uniform external electric field directed from head to foot, while the central and right panels respectively correspond to current injection via a single electrode at the top of the head and via both shoulders. All three cases are normalized to a total short-circuit current of 100 μ A through the soles of both feet. Each lines represent the intersection of one member of a set of uniformly spaced equipotential surfaces with the vertical plane. These are superimposed on a greyscale representation of the same potential distribution, with values indicated on the associated color legend.

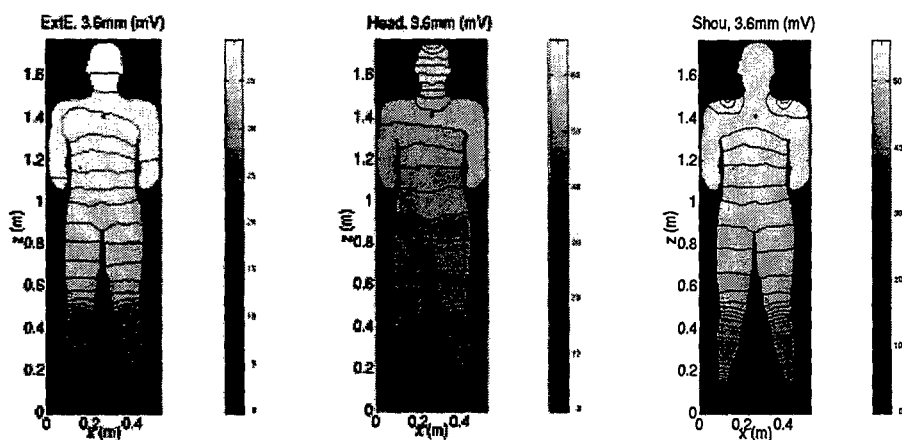


Figure 2: Lines of equipotential in a vertical side-to-side cross section for the three symmetric electric excitations.

Table 1: Bipolar electrode electric potential differences (mV).

Values (mV)	Pac(r)	Ven(m)	Ven(r)	Atr(m)	Atr(r)
ExtE	3.372	2.817	2.929	3.170	3.115
Head	3.790	3.031	3.227	3.658	3.559
Shou	4.199	3.342	3.499	3.853	3.773
AsyL	4.694	3.503	3.586	3.912	3.820
AsyR	3.703	3.182	3.411	3.794	3.725

Table 1 indicates the computed voltages for the five source scenarios, based on a common 100- μ A short-circuit current. The first column indicated the source mechanism, with "ExtE" denoting the external field case. The rows "AsyL" and "AsyR" respectively correspond to asymmetric current injection via the left or right shoulders and extraction to ground via the opposite foot. The second column pertains to a reference point on the pacemaker case. Since this case is metallic, it should be an equipotential surface. However, in numerical modeling using a general-purpose code, it is necessary to assign a large but finite conductivity value to it. This value was chosen to be $\sigma = 100$ S/m, for a contrast of over 30 relative to the highest conductivity in the remainder of the body model components. It was observed that the resulting voltage variations over the pacemaker case were less than about 0.05% for all excitations. The remaining columns indicate the computed voltages at the main "(m)" and reference "(r)" ventricular ("Ven") and atrial ("Atr") electrode sites.

In the bipolar case, the relevant indicator is the magnitude of the voltage difference across each electrode pair. This information can be discerned from Table 1, and is presented in Table 2. For the bipolar ventricular electrode, the values range from a minimum of 0.084 mV for the "AsyL" electrode configuration to a maximum of 0.196 mV for the "Head" electrode configuration. The analogous values for the bipolar atrial electrode range from 0.056 mV for the unscaled external electric field configuration to a maximum of 0.099 mV for the "Head" electrode configuration.

Table 2: Bipolar electrode electric potential differences (mV).

Values (mV)	Ventricular	Atrial
ExtE	0.112	0.056
Head	0.196	0.099
Shou	0.157	0.080
AsyL	0.084	0.093
AsyR	0.229	0.068

Similarly, the appropriate indicator for EMI in the unipolar arrangement is the potential difference induced between a pacemaker electrode and the case. These values may again be obtained from Table 1, and are presented in Table 3. Current injection via the left shoulder ("AsyL") leads to the highest potential differences for all four

Table 3: Bipolar electrode electric potential differences (mV).

Values (mV)	Ven(m)	Ven(r)	Atr(m)	Atr(r)
ExtE	0.555	0.443	0.201	0.257
Head	0.759	0.563	0.132	0.231
Shou	0.856	0.700	0.346	0.426
AsyL	1.192	1.108	0.782	0.875
AsyR	0.521	0.291	0.091	0.023

points. Conversely, injection via the right shoulder ("AsyR") leads to the lowest potential differences for all four points. This can be explained by the current flowing mostly through the upper right torso and the center left heart location. The remaining cases are intermediate.

4 Conclusions

These results demonstrate that available computational schemes, hardware, and human body models are suitable for realistic assessment of the possibility of cardiac pacemaker interference by applied external electric and magnetic fields. Moreover, numerical modeling also provides a convenient method for comparing and contrasting different source mechanisms. In particular, the differences between excitation by external electric fields and systems of contact electrodes can be quantified. The latter method is both simpler to implement experimentally and to solve numerically, and provides a practical and convenient means for simulating the effects of an external electric field. Greater correspondence between electrode sources and external fields could be obtained by using more electrodes and applying appropriate source current weighting factors.

Acknowledgment

This research was supported by EPRI Contract No. WO 2966-14. The authors also thank Mr. K. Caputa (U. of Victoria) for his contribution to this work.

References

- [1] W. Irnich. Interference in pacemakers. *P.A.C.E.*, 7:1021-1048, 1984.

- [2] D. M. Beams. Pacemaker sense amplifiers. In J. G. Webster, editor, *Design of Cardiac Pacemakers*, pages 207–211. IEEE Press, New York, 1993.
- [3] D. W. Deno and L. E. Zaffanelli. Field effects of overhead transmission lines and stations. In *Transmission Line Reference Book: 345 kV and Above, Second Edition*, pages 365–379. EPRI, Palo Alto, CA, 1982.
- [4] P. S. Astridge, G. C. Kaye, S. Whitworth, P. Kelly, A. J. Camm, and E. J. Perrins. The response of implanted dual chamber pacemakers to 50 hz extraneous electrical interference. *P.A.C.E.*, 16:1966–1974, 1993.
- [5] G. C. Kaye, G. S. Butrous, A. Allen, S. J. Meldrum, J. C. Male, and A. J. Camm. The effect of 50 hz external electrical interference on implanted cardiac pacemakers. *P.A.C.E.*, 11:999–1008, 1988.
- [6] A. Sastre. Susceptibility of implanted pacemakers and defibrillators to interference by power-frequency electric and magnetic fields. Technical report, EPRI, Palo Alto, CA, August 1997.
- [7] P. Baraton, J. Cahouet, and B. Hutzler. Three-dimensional computation of the electric fields induced in a human body by magnetic fields. Technical Report 93NV00013 (ISSN 1161-0573), Electricité de France, EDF-DER, Service IPN, Département SID, 1 Avenue du Général-de-Gaulle, 92141 Clamart Cedex, May 1993.
- [8] C. M. Furse and O. P. Gandhi. Calculation of electric fields and currents induced in a millimeter-resolution human model at 60 Hz using the FDTD method. *Bioelectromagnetics*, 19:293–299, 1998.
- [9] Trevor W. Dawson, Kris Caputa, and Maria A. Stuchly. High-resolution organ dosimetry for human exposure to low-frequency electric fields. *IEEE Trans. Power Delivery*, 13(2):366–373, April 1998.
- [10] Trevor W. Dawson, Jan De Moerloose, and Maria A. Stuchly. Hybrid finite-difference method for high-resolution modelling of low-frequency electric induction in humans. *J. Comp. Phys.*, 136(2):640–653, September 15th 1997.
- [11] I. G. Zubal, C. R. Harrell, E. O. Smith, Z. Rattner, G. R. Gindi, and P. H. Hoffer. Computerized three dimensional segmented human anatomy. *Phys. Med. Biol.*, 21:299–302, 1994.
- [12] Jan De Moerloose, Trevor W. Dawson, and Maria A. Stuchly. Application of finite difference time domain algorithm to quasi-static field analysis. *Radio Science*, 32(2):329–342, March-April 1997.
- [13] J. Van Bladel. *Electromagnetic Fields*. Hemisphere Publishing Corporation, Washington D.C., revised printing edition, 1985.
- [14] J. S. Asvestas and R. E. Kleinman. Low-frequency scattering by perfectly conducting obstacles. *J. Math. Phys.*, 12(5):795–811, May 1971.

Using Computational Electromagnetics to solve an Occupational Health & Safety Incident

**Timothy Priest, Kevin Goldsmith
and Dean DuRieu**

Air Operations Division
Defence Science and Technology Organisation
Department of Defence, Australia
Timothy.priest@dsto.defence.gov.au

1. Abstract

An incident occurred on an Australian submarine whereby waveguide flange mounting bolts became loose, allowing the unpressurised waveguide to leak EM energy. The problem was discovered when the submarine's crew noticed a bright arc from the vicinity of the waveguide joint. The waveguide was subsequently repaired at sea, without measuring or estimating the gap in the guide. The crew were concerned about their exposure to EM radiation and asked for a study of the possible exposure to be conducted. The Defence Science and Technology Organisation (DSTO) was contacted and asked to undertake the study.

This paper discusses the process by which an estimate of the crew exposure was determined. The process involved using FD (finite difference) code to estimate the leakage as a function of the width of a slot in the waveguide and measurement of the reverberation characteristics of the submarine chamber. The FE code was used to estimate the power leaked into the chamber for a given slot width. The measurements were then used to establish the relationship between the power transmitted into the chamber and field strength in the chamber. The field strength was then compared to the current National Standard exposure limits.

2. Introduction

In December 1998, DSTO was asked by DAO (defence acquisition organisation) to investigate an EMI/C issue on-board an Australian submarine [1]. Two adjoining flanges on a waveguide had inadvertently become loose while at sea. The fault was first recognised when a crewmember noticed a "flash" from the waveguide; at which time it was noted that several of the waveguide's connecting bolts were loose. The waveguide was subsequently fixed while the vessel was still at sea [2], making it impossible to determine the actual "separation" of the waveguide flanges at the time of the incident.

To further complicate matters, standard measurement methods were deemed to be neither appropriate nor accurate for testing on-board a closed metallic vessel such as a submarine. At the frequencies of interest, the chamber was expected to act as a resonant cavity and mode-stirred techniques were needed to make measurements of the peak electric field experienced in the chamber [3]. This approach was necessary since the measuring equipment may otherwise be located on a nodal point (point of minimum field) of the resonant cavity, at an anti-nodal point (point of maximum field), or anywhere in between; normal measurement techniques would therefore give uncertain, and possibly misleading, results. The resonant nature of the submarine chamber also meant that the nature of the electric field inside the chamber was modified in such a way as to make calculation of an effective antenna gain (of the leaking waveguide) impractical.

1. The unknown size of the waveguide gap, and the reverberant nature of the chamber, meant testing for possible over-exposure to RF radiation required a two-stage approach:

1. The resonant properties of the submarine cavity had to be measured in order to determine the maximum leakage power that would exceed Australian Standard 2772.1, both for long-term and single-dose exposure levels [4] in the given environment.
2. Computational analysis of the waveguide structure (where the leak occurred) so that the minimum waveguide "separation" needed to exceed the maximum leakage power (as determined in the first stage) could be found.

3. Theory

3.1. Reverberant cavities

A reverberant chamber is defined as any chamber that will support standing (or near-standing) -wave modes within it. Any closed metallic cavity that has electromagnetic energy of sufficiently high frequency injected into it will exhibit reverberant characteristics, in which standing waves are established in the cavity. These modes are formed and maintained according to the boundary conditions set by the source of EM energy and the cavity geometry. For a perfectly conducting rectangular enclosure with dimensions a , b , and d , the electric field at any point in three-space is given by [5]

$$E_{k,l,m} = E_0 \sin\left(\frac{k\pi x}{a}\right) \sin\left(\frac{l\pi y}{b}\right) \sin\left(\frac{m\pi z}{d}\right) \quad (1)$$

where x , y , and z are the cartesian position coordinates, E_0 is the electric field amplitude and k , l , and m are integers, no two of which may be zero at the same time.

3.2. Mode-tuning of resonant cavities

The use of mode-tuning in reverberant chambers was first proposed in 1968 [6]. In mode-tuning the modes present in a resonant cavity are changed by varying the boundary conditions of the chamber. Chamber boundary conditions are usually changed using a mechanical tuning-device, which should have dimensions that are comparable to at least one of the dimensions of the reverberant chamber [7]. Preferably, the tuner should also be asymmetric in all three dimensions. This helps to ensure independent data is obtained over the complete revolution of the tuner.

The time-averaged characteristics of the field are taken over a complete iteration of the changing boundary conditions. If enough modes are present in the cavity for effective "tuning" to occur, the standard deviation (SD) and the expected (average) value of the sample space will be the same, and hence the normalised standard deviation (NSD) will be unity. On the other hand, if there are insufficient modes in the cavity to be effectively "tuned", the NSD will be less than unity. Correct operation of a "tuned" resonant cavity also requires the peak-to-average ratio to be approximately [8]

$$\frac{[P_{rec}]}{\langle P_{rec} \rangle} \cong \left\{ 0.577 + \ln(N) + \frac{1}{2N} \right\} \quad (2)$$

where N is the number of independent samples, $[P_{rec}]$ is the maximum power that should be observed for the N samples and $\langle P_{rec} \rangle$ is the expected (average) value of received power for the N independent samples.

While the chamber under investigation in this study was not rectangular (the submarine cross-section being circular and the chamber being a section of this circle), the rectangular analysis will suffice as an order of magnitude calculation. A complete analysis of circular waveguide resonators can be found in advanced electromagnetics texts [9]. Assuming the chamber has dimensions similar to that of a $10 \times 6 \times 3$ m rectangular enclosure, the lowest order mode sustainable by the chamber is 29.2MHz. The total number of possible modes at

1GHz is in excess of 50×10^3 , far greater than the number of modes needed for effective mode-tuning [3].

3.3. The quality factor (Q) of a chamber

An important measure of a reverberant chamber is the quality factor (Q), since it is a good indicator as to the ability of a chamber to support standing waves (modes). The Q of a chamber is defined as 2π times the ratio of the time-averaged energy stored in the cavity to the energy loss per cycle. For a resonant cavity, the Q can be written as [3]

$$Q = \frac{16\pi^2 V \langle P_{rec} \rangle}{\lambda^3 P_t} = \frac{16\pi^2 V}{\lambda^3 L_{ins}} \quad (3)$$

where V is the chamber volume, P_t is the power transmitted into the chamber and L_{ins} is the linearised insertion loss. The Q of a chamber is influenced by a number of factors including, but not limited to: internal geometry, the ratio of the volume of the chamber to its surface area, the skin-depth (δ) of the chamber's bounding walls, and the presence of any absorbing materials (including personnel) inside the chamber. Although a finite chamber Q is desirable, due to the Lorentzian widening of the modal structure from energy losses, if the Q of a chamber falls too far, the chamber will no longer support resonant modes, and mode-tuning will not be possible.

The average received power $\langle P_{rec} \rangle$ in a reverberation chamber is given by

$$\langle P_{rec} \rangle = \frac{1 E_o^2 \lambda^2}{2 4\pi\eta} \quad (4)$$

where E_o^2 is the mean-squared value of the electric field and η is the impedance of free space. Combining Equations 3 and 4 and rearranging gives

$$P_t = \frac{2\pi V E_o^2}{\lambda Q \eta} \quad (5)$$

which gives the transmitted power needed to achieve a given mean-squared electric field.

4. Experimental and Computational

4.1. Submarine chamber measurements

The experimental arrangement used for testing the submarine chamber is shown in Figure 1. The signal from the tracking generator was fed into a pre-amplifier before being split by a directional coupler. The main signal from the directional coupler was then sent directly to the transmit (Tx) antenna. The -10dB output from the directional coupler was monitored using a power meter, as shown in Figure 1(a).

The Tx antenna was positioned in the middle of the submarine chamber facing the mode-tuner. The Rx antenna was placed on the opposite side of the chamber, facing obliquely towards a wall and positioned such that it was obscured from the Tx antenna by the mode-tuner. The signal from the Rx antenna was then fed directly to the spectrum analyser. The data acquisition and control system was controlled using a custom Labview program and the data was logged directly to disk for analysis.

The mode-tuner used in the testing, is shown in Figure 1(b). The mode-tuner was designed and constructed to meet assembly time, space and ingress/egress constraints on the submarine. The mode-tuner had to be easy to (dis)assemble, light and self-powered, while still having similar dimensions to the chamber in at least two dimensions when assembled. The DSTO-designed tuner was found to be adequate only in the height dimension as it was constrained by submarine equipment in the radial dimension.

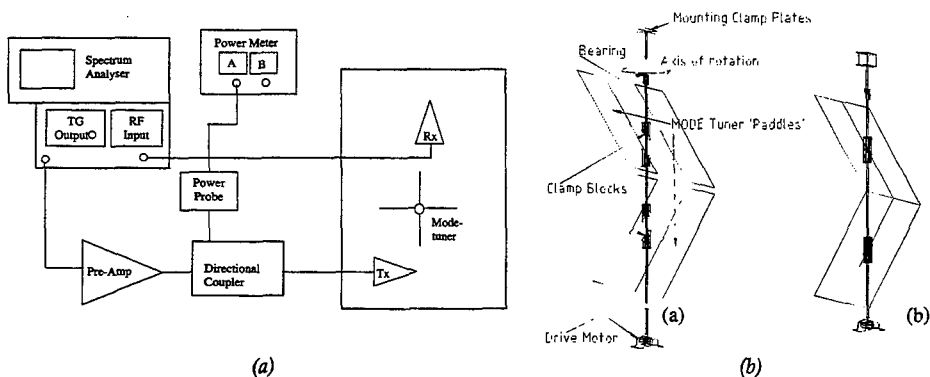


Figure 1: (a) Experimental arrangement used to acquire the data on-board the submarine.
 (b) The mode-tuning element used for "tuning" the modes in the submarine chamber throughout the experiment.

RF measurements of the chamber were made for several different frequencies around the operational frequency of the waveguide. This was done so as to accommodate for the tolerances and drift in the transmitter operating frequency. For the measurements the mode-tuner was set to rotate while transmitting on the Tx antenna at the frequency of interest. The spectrum analyser tracking-generator setting was adjusted until the limit of linearity in the pre-amplifier was reached over one complete revolution of the mode-tuner. The forward and received power for a complete mode-tuner rotation were then measured and logged to disk for analysis.

For the frequency at which the waveguide normally operates the following procedure was also carried out: the Rx antenna direction was changed and the procedure repeated for the new antenna direction, after which the entrance door was opened and the procedure repeated again for both orientations (facing the door and 90° to it) of the Rx antenna. Finally, four personnel went into the chamber and the procedure given above was repeated in order to observe what effect further loading the chamber had on the Q. This procedure was necessary, as the state of the entrance door and the number of personnel loading the chamber at the time of failure was not accurately known.

4.2. Computational analysis

As stated earlier, the faulty radar waveguide was repaired while at sea with no documented evidence as to the actual state of the waveguide at the time the fault was noticed. As a result, in order to identify the likelihood for personnel over-exposure, an estimate of the size of the waveguide-gap needed for the field to exceed the Australian standard was required. There were several ways in which this could be achieved:

1. A large section of the waveguide could be removed from the submarine and reassembled in the DSTO's reverberant chamber. The total leakage power from the guide, as a function of waveguide separation, could then be measured accurately.
2. The waveguide section that failed could be modelled using appropriate computational electromagnetic modelling (CEM). Different gap sizes would then be modelled in the waveguide section to ascertain the leakage power as a function of gap size.

3. The problem could be studied analytically, with appropriate estimations, assuming the waveguide gap acted as a simple slot antenna.

The second approach has the advantage of being relatively fast to model and evaluate. However, the CEM approach should be regarded as a *first-cut* solution only, since this approach will allow only an estimate of the expected power leakage as a function of gap size. Accurate determination of the leakage power using CEM would require detailed analysis and modelling of the waveguide; at which stage the time required would be comparable to testing the actual guide as per approach 1. The third approach could also have been used to obtain an estimate of the leakage power. However, the accuracy of this method suffers greatly from the finite conductivity of the waveguide and the finite size of the waveguide "sheet" on which the slot resides [10] and as a result this method was not seriously considered.

Given that there was no information available on the waveguide gap-size at the time of failure, it was decided that CEM modelling should initially be utilised. If the CEM method then showed a high likelihood for over-exposure (or even borderline exposure) to personnel, the first approach above would then be implemented to obtain accurate data of the leakage power from the waveguide as a function of gap size.

The CEM code used to model the waveguide was GEMACS (General Electromagnetic model for the Analysis of Complex Systems) [11]. One of the features of GEMACS is the ability to model interior/exterior problems in one model and link them at the interior/exterior interface(s). For the CEM model of the waveguide, a hybrid solution technique was used: FD (Finite Difference) modelling was used for the internal waveguide problem, while the external problem was modelled using a hybrid GTD/MOM (Geometric Theory of Diffraction/ Method Of Moments) approach. This approach allowed precise control over the internal excitation of the waveguide while keeping the processing time for the problem within acceptable limits.

The FD approach used for modelling the interior problem requires that a grid (or step) size be chosen for the structure under investigation. This grid size determines the resolution (accuracy) with which the model is calculated. However, smaller grid sizes also increase the program execution time in a non-linear manner so that care must be taken when choosing a grid size so that computational time does not become unworkably large. In the present case the internal waveguide problem was modelled using a grid of the same size as the smallest gap that would be modelled in the waveguide. Ideally, the grid size should be substantially smaller than the gap in the waveguide. However, the increased processing time of this change would be intolerable.

Another problem with modelling the waveguide was the shape of the opening (gap) in the waveguide. As can be seen from Figure 2(a) and (b), the actual gap in the waveguide was wedge-shaped. However, modelling a wedge shape for this problem would require using very small grid sizes, even for crude models of the wedge. Such a small FD grid size becomes computationally prohibitive because of the increased processing time. Since the model of the waveguide was taken to be a "first-cut", it was decided to forego modelling the sides of the waveguide gap and use the much simpler model shown in Figure 2(c).

As previously stated, the external problem was modelled using a hybrid MOM/GTD computational model. For this particular waveguide problem only a simple MOM/GTD model was needed, since we were only interested in the total power leaked into the far-field by the waveguide gap and not the interactions of the waveguide with exterior surfaces. The total power leaking from the waveguide gap was verified in two ways: by integrating over the sphere of solid angle and by measuring the power before and after the gap in the waveguide. The two powers were then compared to provide a rationality check.

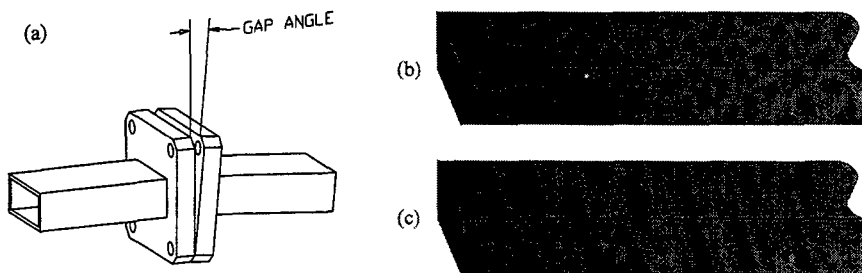


Figure 2: (a) Diagram of the waveguide assembly to be modelled, showing the expected "wedge" shape of the gap that would have occurred in the failed waveguide junction.
 (b) Model of the waveguide.
 (c) Simplified model of the waveguide used in the current analysis.

One of the problems with modelling the waveguide in isolation was that the waveguide model had to be terminated at both ends in a way that would reflect the physical reality of the waveguide's internal field while ensuring that no spurious RF emissions occurred. The requirement for preservation of the internal waveguide field was met by exciting the waveguide with a probe source set $\approx \frac{1}{4}\lambda$ from one end of the waveguide. The gap in the waveguide was then positioned a number of wavelengths from the source, to ensure that any higher-order modes excited by the source were attenuated significantly before reaching the gap in the waveguide.

The two ends of the waveguide were enclosed using conductive plates, with the far end of the waveguide also being terminated with a resistive load to absorb incident energy from the waveguide. A load with the correct admittance was needed to terminate the waveguide at this end otherwise the modelled waveguide would act as a waveguide resonator; the internal field of such a configuration would clearly not match the real-world characteristics of the waveguide being modelled. The leakage power for a number of gap sizes was then found, allowing the minimum gap-size needed to exceed the OH&S standard to be found.

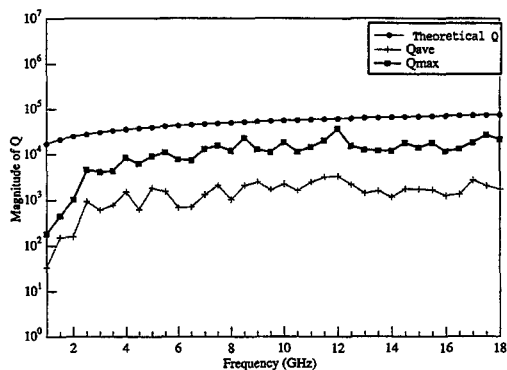


Figure 3: Comparison of the measured and theoretical Q for the chamber. The theoretical chamber calculations assume a rectangular cavity. Similar calculations on a circular cross-section resonator yield similar results. Both the average chamber Q (Q_{ave}) and the maximum chamber Q (Q_{max}) are shown above.

5. Results

5.1. Submarine cavity measurements

Figure 3 compares the measured Q for the chamber to the theoretical Q for a similar sized rectangular chamber. Two relative measures of Q have been taken in Figure 3. Q_{ave} gives the average Q for the chamber, while Q_{max} gives the maximum measured Q for the chamber. While both measures of Q for the submarine chamber are considerably lower than the theoretical Q across the entire frequency range it is not unexpected; the chamber contained a substantial surface area of absorbent material, such as seating, work-stations and unshielded wiring which increase the surface-area to volume ratio and losses in the chamber. In the calculations below the value Q_{ave} is used for measuring the average exposure levels while Q_{max} is used to calculate the peak exposure levels.

5.2. Calculation of Exposure Levels

The occupational exposure limit for long-term RF exposure is (from Equation 5)

$$\langle P_t \rangle = \frac{2\pi V E_o^2}{\lambda Q_{ave} \eta}$$

Using the value for Q_{ave} for the waveguide operational frequency, the average transmitted power $\langle P_t \rangle$ needed to exceed the long-term exposure levels was found to be 288W.

Figure 4(a) shows the calculated average power output from the waveguide (where the duty cycle of the transmitter has also been factored in) using the CEM modelling described in the text. Comparing the value calculated above with Figure 4(a) shows that the long-term exposure level was not exceeded for any reasonable gap size in the waveguide.

The maximum permissible occupational exposure limit is (from Equation 5)

$$|P_t| = \frac{2\pi V E_o^2}{\lambda Q_{max} \eta} \quad (6)$$

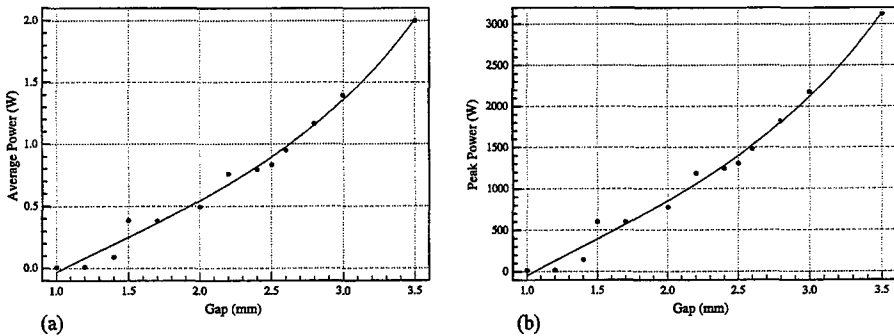


Figure 4: Calculated average (a) and peak (b) power from the leaking waveguide as a function of "gap" size. The average power here includes the duty cycle of the RF waveguide. The solid lines are a guide to the eye only.

Using the value for Q_{\max} for the waveguide operational frequency, the peak transmitted power $|P_t|$ needed to exceed the safe peak-exposure level was found to be 38.7kW. Again, comparing this value with Figure 4(b), which shows the calculated peak power output from the waveguide, shows that the peak-exposure level was not exceeded for any reasonable gap size in the waveguide.

6. Conclusions

Well established CEM techniques have been used to study and solve an OH&S issue on-board an Australian submarine, obviating the need to conduct full-scale experimental tests. The CEM modelling approach was not only more cost effective but also resulted in greatly reduced turn-around time when compared to the alternatives; the results of the modelling were known within one week. It is interesting to note that, even with fast workstations and modern CEM techniques, even relatively simple problems, such as this leaking waveguide can become computationally complex, and time-prohibitive, very quickly.

This OH&S problem originated from a simple question: "Has the crew been over-exposed?" The solution of this problem is example of using several techniques (usually quite diverse) to solve a complicated problem. Firstly, reverberation chamber measurement techniques were required to characterize to a submarine chamber. Then, since the waveguide had already been fixed, CEM techniques were required to model the waveguide and obtain a reasonable measure of the expected power leaked from the faulty waveguide.

This combination of techniques has resulted in a qualitative rather than quantitative answer to the original question; the level of exposure to personnel on-board the submarine due to the leaking waveguide was substantially less (>10dB) than the levels permitted under the Australian standard [3] for both average and peak-level exposure.

7. References

1. Goldsmith, K.R. and A. Horobin, *Teleconference*. 1998.
2. Priest, T.S., *Discussion with crewmembers of "Dechaineux"*. 1999.
3. Hill, D.A., *Electromagnetic Theory of Reverberation Chambers*. 1998, NIST: Boulder, Colorado.
4. 2772.1(Int), A.N., *Part 1: Maximum exposure levels-3kHz to 300GHz*, in *Radiofrequency fields*. 1998.
5. Sadiku, M.N.O., *Elements of Electromagnetics*. 1989, Orlando: Saunders.
6. Mendez, H.A. *A new approach to electromagnetic field-strength measurements in shielded enclosures*. in *Western Electronic Show and Convention*. 1968. Los Angeles, CA: Wescon Technical Papers.
7. Crawford, M.L. and G.H. Koepke, *Design, Evaluation and Use of a Reverberation Chamber for Performing Electro Magnetic Susceptibility/Vulnerability Measurements*. 1986, Electromagnetic Fields Division, National Institute of Standards and Technology.
8. Koepke, G.H. and J.M. Ladbury. *New electric field expressions for EMC testing in a reverberation chamber*. in *17th DASC*. 1998. Bellevue, Washington.
9. Jackson, J.D., *Classical Electrodynamics*. second ed. 1975, New York: Wiley.
10. Kraus, J.D., *Antennas*. 2nd ed. 1988: McGraw-Hill.
11. Coffey, E., L., N. Coffey, W., and D. Kadlec, L., *GEMACS sourcebook*. April 1988, Rome Air Development Centre: Albuquerque.

Analysis of Permanent Magnet Type of MRI Taking Account of Hysteresis and Eddy Current and Experimental Verification

Norio Takahashi, Siti Zubaidah and Takeshi Kayano
Department of Electrical and Electronic Engineering
Okayama University, Okayama 700-8530, Japan
e-mail: {norio, siti, kayano}@eplab.elec.okayama-u.ac.jp

Koji Miyata and Ken Ohashi
Magnetic Materials R&D Center
Shin-Etsu Chemical Co. Ltd., Takefu 915-0802, Japan
e-mail: {s03224,s05215}@sec.shinetsu.co.jp

Abstract - A modeling technique of minor loop using typical hysteresis loops is shown. The effect of the direction of current of gradient coil on the residual flux density is investigated, and the behavior of minor loops in the pole piece of a permanent magnet type of MRI is also examined. The calculated results are compared with measured ones. It is shown that the useful information can be obtained by 3-D axis-symmetric analysis.

I. INTRODUCTION

As the permanent magnet type of MRI [1] contains pole pieces and yokes which are made of steel, the minor loop on the initial curve of pole pieces due to the pulse excitation and the eddy current induced in the steel affect the magnetic characteristics of permanent magnet assembly [2], [3]. In order to improve the imaging quality of MRI, the behaviour of residual flux on pole piece should be examined in detail.

In this paper, the nonlinear iteration method for the analysis considering minor loop is discussed, and also the modeling technique of minor loop using typical major hysteresis loops is shown. The behavior of magnetic characteristics of permanent magnet assembly is examined considering hysteresis and eddy current. The experimental verification is also shown.

II. ANALYZED MODEL

Fig. 1 shows a permanent magnet assembly for MRI device. The yoke is composed of two plates (530mm), other two circular plates (ϕ 330mm) and four columns which are made of steel. The permanent magnet has a hole (ϕ 60mm). Although the actual assembly is three-dimensional having four columns, it is simplified to an axis-symmetric one to reduce the CPU time and memory requirements. The yoke and pole piece are made of steel (SS400), and its conductivity is 7.51×10^6 S/m. The residual magnetization of Nd-Fe-B magnet is 1.21 T. The gradient coil having 15 turns is located on the surface of the pole piece.

Fig. 2 shows a pulse current series in the gradient coil. The flux density B in this model is produced by the permanent magnet and the gradient coil. Therefore, working points in the pole pieces are located on the initial magnetization curve and on the minor loop.

III. METHOD OF ANALYSIS

A. Choice of B - H curve in Newton-Raphson Iteration

The choice of minor loop in the Newton-Raphson nonlinear iteration (NR method) is carried out as follows:

- (a) Let us assume that B and H at a step is located at the point a on the initial magnetization curve ① shown in Fig. 3. If the obtained flux density $B_1^{(k)}$ of the k -th iteration at the instant t

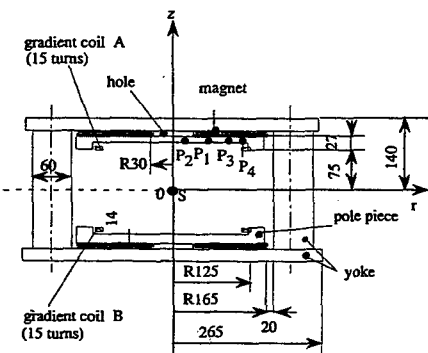
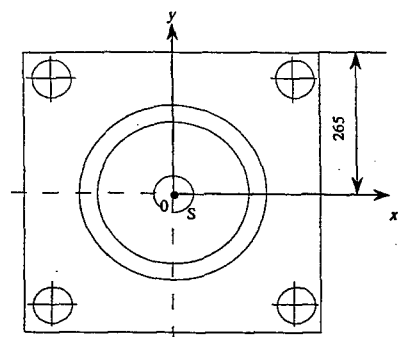
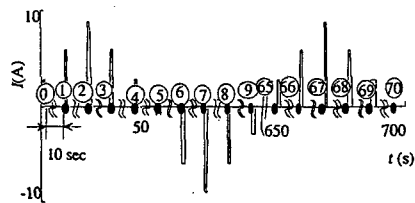
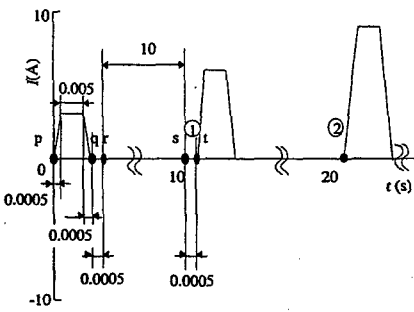


Fig. 1 Permanent magnet type of MRI.



(a) pulse series



(b) enlarged pulse series

Fig. 2 Pulse current series in a gradient coil.

is larger than $B_1^{(t-\Delta t)(k)}$ at the instant $t-\Delta t$, the operating point of B and H exists on the initial magnetization curve ①.

- If the flux density $B_1^{(k)}$ is reduced ($B_1^{(k)} < B_1^{(t-\Delta t)(k)}$), the operating point of B and H moves on the upper minor loop ② as shown in Fig. 3. In Fig. 3, the case when the operating point is reached to the point $b(B_1^{(3)})$ after three NR iterations ($B_1^{(1)} > B_1^{(2)} > B_1^{(3)}$) is shown.
- When the flux density $B_1^{(k)}$ at the k -th step ($k > 3$) of NR method is larger than $B_1^{(1)}$, $B_1^{(k)}$ moves on the lower minor loop ③ shown in Fig. 3. In the NR iteration, the operating point moves on loop ③ when B is reduced, the operating point moves on loop ③ when B is increased.
- If the operating point is located at the point h on the lower loop in Fig. 3, the operating point moves on small upper minor loop ④ and upper hysteresis loop ⑤ when B is reduced, and the operating point moves on loop ③ when B is increased.

B. Modeling of Minor Loop

The upper and lower minor loops can be determined as follows:

1) *Upper minor loop*: The upper minor loop ② is represented by the upper hysteresis loop shown in Fig. 4, which is approximated by a cubic spline function. Typical hysteresis loops

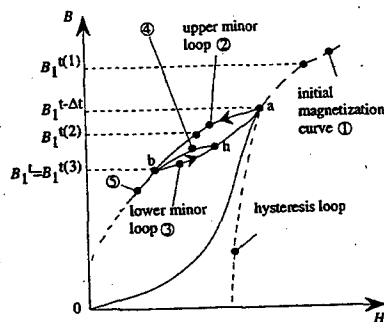


Fig. 3. Minor Loop.

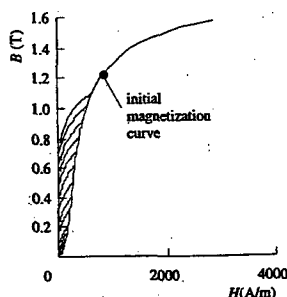


Fig. 4. Measured upper hysteresis loops (steel).

are measured using a permeameter [4]. The specimen is steel 'SS400' and the dimension is $10 \times 50 \times 300$ mm. The upper hysteresis loop used is interpolated by the measured loops which are stored. The small upper minor loop ④ which was denoted in Section III.A.(d) can be obtained from the lower minor loop b-h in the same way that the lower minor loop ③ is obtained from the upper minor loop ② as shown in the following Section III.B.2.

2) *Lower minor loop*: The lower minor loop ③ is obtained from the upper minor loop ②, assuming that the lower loop is symmetric with the upper one with respect to the middle point of the line a-b.

IV. RESULTS AND DISCUSSION

A. Behaviour of B and H

Fig. 5 shows the operating point of B and H at various points $P_1 \sim P_4$ on the pole piece shown in Fig. 1(b). The direction of current of gradient coil A is assumed as the same with that of gradient coil B in order to reduce the analyzed region to 1/4. The minor loop is taken into account only in the pole piece, because there was no remarkable difference if the minor loop is taken into account in the yoke adjacent to the pole piece. The flux densities at the instants ①, ②, ..., (the instant when there is no current in the gradient coil) shown in Fig. 2 are denoted by the white circles. The figure suggests that the operating point of B and H at respective positions in the pole piece is moved to the different minor loops due to the difference of flux density. Moreover, the residual flux density (corresponding to the value denoted by the white circle in Fig. 5) changes with time when the eddy current flows in the pole piece. On the contrary, it almost does not change with time when there is no eddy current.

B. Effect of Direction of Current

The effect of the direction of currents in gradient coils A and B is examined. Fig. 6 shows the change of the z-component B_z of flux density with time at the middle point S(0,0) in the space shown in Fig. 1. The flux densities at the instants ①, ②, ..., when the current becomes equal to zero and the transient phenomenon of current is finished, are plotted. The flux density with eddy current is smaller than that without eddy current due to the opposing magnetic field produced by the eddy current. The figure suggests that the change of B_z at the instant $I = 0$ in the case of same direction (the direction of current in gradient coil A is the same with that in gradient coil B) is larger than that in the case of different direction.

The change ΔB_z of residual flux density at the point S(0,0) in the gap is examined. ΔB_z

corresponds to the output of the probe coil of MRI. ΔB_z is given by

$$\Delta B_z = B_{zi} - B_{z0} \quad (1)$$

where B_{z0} is the flux density at the instant $t=0$ ($I=0A$). B_{zi} is the flux density at the instant $t=i$ ($I=0A$) shown in Fig. 2. If there is no eddy current and no minor loop in the pole piece, ΔB_z is always equal to zero, because B_z does not change with time.

Fig. 7 shows the change ΔB_z of residual flux density with time. The loop of ΔB_z at same direction is larger than that at opposite direction.

C. 3-D Analysis

3-D finite element analysis using hexahedral elements is carried out for the static case with no excitation. Fig. 8 shows the flux distribution. Table 1 shows the comparison among the z-components of flux density obtained by 3-D axis-symmetric and 3-D analyses and measured flux density. Only the result of static analysis is compared, because the CPU time for 3-D analysis in 2695 steps like the case of Fig. 6 is not practical.

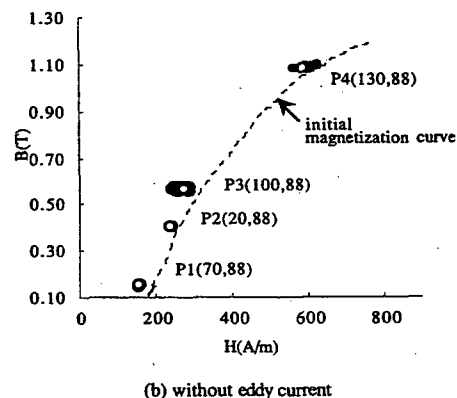
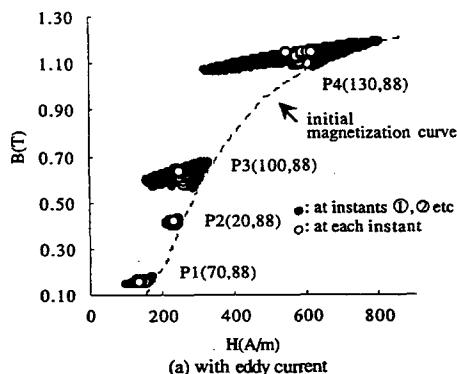


Fig.5 B and H on minor loop (same direction).

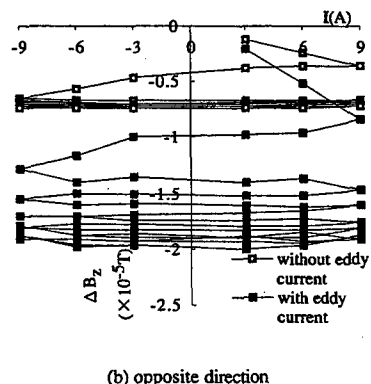
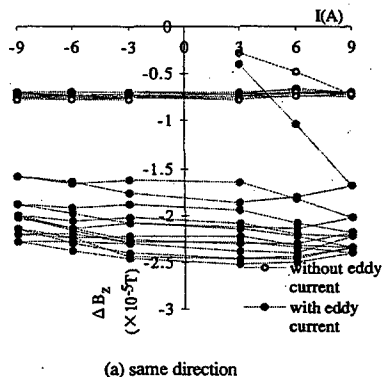


Fig.7 Change of residual flux density.

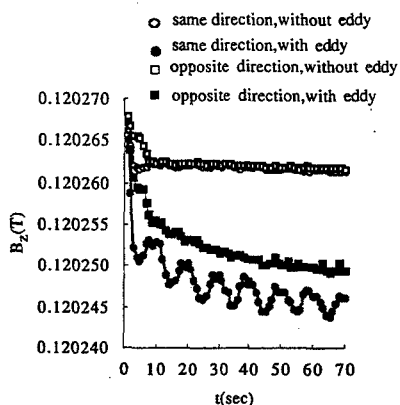


Fig.6 Flux densities at instants ①, ② etc
(point S in gap).

Table 1 Comparison of flux density

	$B_z(T)$	$\epsilon_B(\%)$
Axi-symmetric	0.1138335	5.1
3-D	0.1081378	0.14
Measured	0.1082945	—

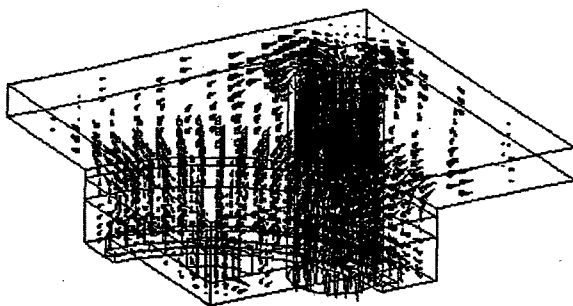


Fig.8 Flux distribution.

V. EXPERIMENT

The flux density at the point S(0,0) is measured using an NMR type sensor. In this case, the current of gradient coil is the same direction. Figs.9 and 10 show the comparison between the calculated B_z and ΔB_z (3-D axi-symmetric analysis) and measured one. The behavior of B_z is similar to the measured one.

VI. CONCLUSIONS

The obtained results can be summarized as follows:

- (1) The modeling of minor loop by interpolating typical major hysteresis loops is effective for the analysis of the behavior of B and H in permanent magnet type MRI.
- (2) The 3-D axi-symmetric analysis can be applicable to the study of the behavior of the magnetic characteristics, because the tendency of the calculated result is similar to the measured one.

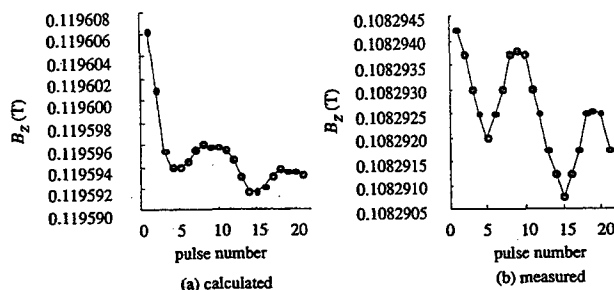


Fig. 9 Change of flux density (point S, same direction).

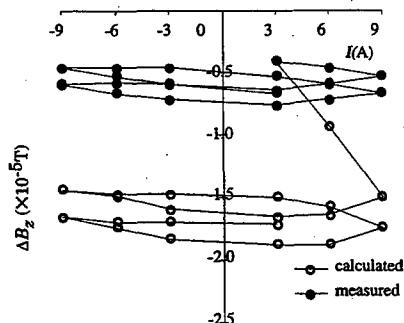


Fig.10 Comparison between calculated and measured ΔB_z (point S, same direction).

REFERENCES

- [1] T.Miyamoto, H.Sakurai, H.Takabayashi and M.Aoki, "A development of a permanent magnet assembly for MRI devices using Nd-Fe-B material", *IEEE Trans. Magn.*, vol.25, no.5, pp.3907-3909, Sept. 1989.
- [2] K.Miyata, K.Ohashi, N.Takahashi and H.Ukita, "Analysis of magnetic characteristics of permanent magnet assembly for MRI devices taking account of hysteresis and eddy current", *IEEE Trans. Magn.*, vol.34, no.5, pp.3356-3359, 1998.
- [3] N.Takahashi, T.Kayano, K.Miyata and K.Ohashi, "Effect of minor loop on magnetic characteristics of permanent magnet type of MRI," *IEEE Trans.Magn.*, vol. 35, no.3, pp.1893-1896, 1999.
- [4] IEC, "Method of measurement of the d.c. magnetic properties of solid steels in a closed magnetic circuit", 404-4 TC68 WG2 N63, Sept., 1991.

SESSION 7

**VIRTUAL REALITY
IN REAL-WORLD
APPLICATIONS**

Chairs: Stan Kubina and Dennis DeCarlo

A Virtual Radiation Pattern Range and Its Uses C-130/Hercules HF Notch Antenna

Stanley J. Kubina, Christopher W. Trueman and David Gaudine
EMC Laboratory, Concordia University
Montreal, Canada
Doc@emc2.concordia.ca

Abstract:

The elements of a Computational Virtual Radiation Pattern Range are described in its application to the modeling of the HF Notch Antenna on the C-130/HERCULES aircraft. The simulation results had been validated by comparisons with results from a physical scale-model pattern and impedance range. Special advantages of the virtual range are described particularly with regard ease of generation of performance data and insights into the excitation of resonant aircraft modes. In addition, the simulation of antenna performance for aircraft operation at various heights above ground is readily available.

INTRODUCTION

The C-130/HERCULES is a transportation workhorse in the air fleets of many countries. Lockheed Martin have the C-130(J) as a modernized variant of the aircraft. It is a four-engine high wing STOL aircraft with distinctly large wings, large vertical stabilizer and a swept tail-cone profile as shown in Figure 1. Here the C-130 is shown landing in Darwin, Australia as part of the East Timor mission. This aircraft has been modelled at the EMC Laboratory for NAWCAD in its C-130/TACAMO configuration [1] of five wire antennas extending from the fuselage to the vertical stabilizer. For general uses the aircraft had been equipped with two similar HF wire antennas extending from the forward fuselage to the vertical stabilizer, barely visible in Fig.1. In modernizations of the avionics suite, the Canadian DND CC-130/Hercules includes a small deep, flush-mounted, HF dorsal notch antenna at the base of the vertical stabilizer. This is also the HF antenna now on the C-130(J) aircraft. The detail is shown in the wire-grid model of Figure 2.

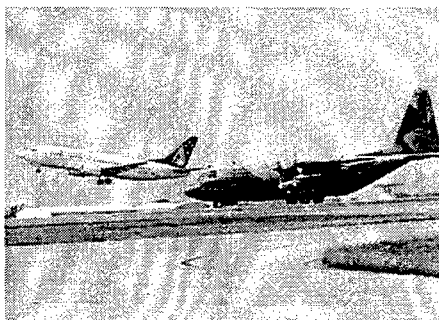


Fig.1 – Canadian C-130 landing in Darwin

The HF radio plays an important part in global communications scenarios encountered by the Canadian CC-130 fleet of aircraft. Its importance is emphasized by the installation of an HF Near Vertical Ionospheric Sounding Capability. Thus it is important to have the necessary technical data to be able to predict or analyze the performance of this important communications system.

The performance of HF Communications Systems had been systematized by Military Specification MIL-A-9080¹ in the early 1950's. It is based on extensive research carried out at the Stanford Research

¹ MIL-A-9080, "Antenna, Liaison Communication Equipment", General Specification for Design of, Feb. 1954.

Institute in that era [2]. The core of this specification is the concept of a singular numerical quantification of performance at each frequency based on the evaluation of all the component factors, power transfer and radiation distribution, that dictate this performance for any communications mode. The details are elaborated later in this paper. A physical calibrated scale-model radiation pattern range is the measurement facility that provides the requisite radiation pattern data. Larger scale models, mounted on non-metallic supports and carefully isolated impedance meters are used to obtain the impedance data.

A Virtual Radiation Pattern Range, based on computer simulation, must achieve the necessary electromagnetic equivalence of the antenna and the aircraft structure to provide the same detailed information as the physical ranges. It must also be calibrated or validated by the best available tools in any given application.

ELEMENTS OF A VIRTUAL RADIATION PATTERN RANGE

The origin of the electromagnetic scale-modeling art dates back to the work of Dr. George Sinclair [3] at Ohio State. Scale models are made as precisely as possible from stable materials, and where necessary coated with conductive materials to emulate perfectly conducting surfaces. The models are hollowed out to have self-contained transmitters or detectors to provide the requisite emulation of free-space conditions. The scale used is determined by several considerations including the pattern range, the frequency used and often the type of antenna that is being modeled. A scale model of the antenna must also be constructed and verified.

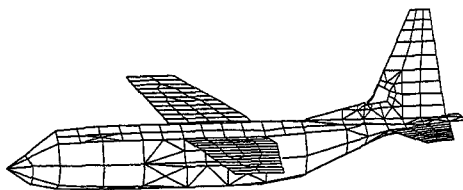
An electromagnetic computational engine, be it Moment Method, FDTD or any other, requires the counterpart of the scale model, i.e. a discretized computer model, whose characteristics are suited to that particular simulation engine. This paper describes results obtained primarily with the NEC4 [4] computer code using a wire-grid model.

Creating the Wire-Grid Model

The C-130/Hercules wire-grid model was carefully meshed to replicate the outer dimensions and contours of the aircraft. Although this process can now be CAD-based - from CATIA files into our

model generation software (DIDEC), the base model developed for NAWCAD was created by digitizing available aircraft drawings. It was subsequently modified to increase the segmentation density only in selected regions to keep the segment count low, and in the vertical stabilizer to include the notch antenna detail. The electromagnetic equivalence of the model was maintained by judicious use of the MESHES, FNDRAD software coupled to verification by CHECK [5]. The 933-segment model is shown in Figure 2.

Figure 2 - 933 Segment C-130 Model: HF Notch



CHECK verifies for geometrical errors and against the known guidelines for NEC model creation. The segment lengths are selected to be $\lambda/10$ in the middle of the 2-30MHz HF frequency band. The finer segmentation near critical regions is targeted to be $\lambda/20$ in length. The reliability of this practice has been established by validation in the extensive experimental and computational data set provided by Mishra et al. [6].

The CHECK program can produce various useful statistics that characterize the wire-grid model that it is asked to analyze. One of these, a histogram of normalized segment lengths vs. frequency is shown in Figure 3. The extent of the finer segmentation detail is shown in the skewed distribution favoring the

smaller segments. This also represents the compromise made to keep the segment count as low as possible.

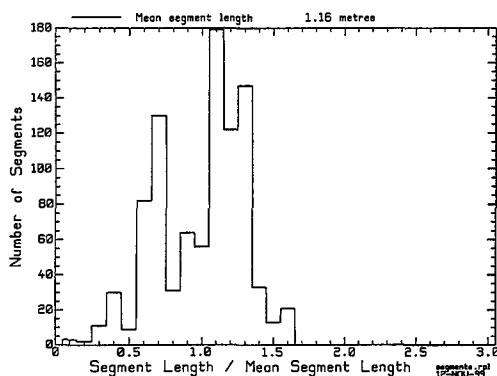


Figure 3 – Histogram of Normalized Segments vs. Freq.: C-130

element at the lower base of the notch that represents the lead from the antenna coupler.

Executing the Final Computer Model

Experience at the EMC Laboratory has shown that it is prudent to carry out a High Resolution Spectral Sweep of the model with the selected computational engine over the frequency range of interest. In the 2-30MHz range, this sweep is carried out at 0.1MHz increments. Such a sweep is the equivalent of a stepped-frequency sweep of sources and receivers on a physical modeling range.

The High Resolution Spectral Sweep is carried out in a batch execution file. Each of the runs, however, is with an input file that specifies the requisite number of conical radiation pattern cuts. These correspond to those normally carried out on a pattern range in order to accurately determine the reference isotropic signal level and to carry out the required radiation pattern integrations to calculate the communications mode performance parameters for each frequency.

The NEC output file at each frequency is 'stripped' to the essential elements that are required for all the subsequent processing and displays of the output. Thus data on the input geometry is stored together with real and imaginary parts of the segment currents, the real and imaginary values of impedance and the amplitudes of both components of the electric field intensity for each conical cut. In addition the requisite radiation pattern integration to derive the isotropic level is carried out by a routine called ISOLEV and the value is stored in the complete solution file for each frequency.

It should be noted that the current on the excitation segment that is used to calculate the antenna driving impedance at each frequency provides the counterpart of the impedance data from physical measurements. However the currents on each wire segment that result from the NEC solution are an extra bonus over the data available from a physical range. As will be seen later, the current distributions on the airframe at each frequency produce exceptional insights into resonance behavior that are not readily available in physical measurements.

Impedance of the HF Notch vs. Frequency

A parameter extraction utility is available to extract and to plot the impedance data vs. frequency. Normally, with projects such as this, this would only be done for 2-30MHz. However, as the runs were being initiated, it was found that a Lockheed Martin development report was available² that contained impedance and radiation pattern information from scale model measurements. The design of the antenna was such as to place its impedance crossover frequency at approximately 35MHz. Thus the frequency sweep was extended to 40MHz to adequately cover this important highlight. The plot of antenna impedance is shown in Figure 4. Thus encouraging validation of this feature is obtained from this report prepared some 17 years ago! Company clearance to present a more direct comparison could not be arranged in time for this paper. Hence only general references and comments shall be made in order to respect the Lockheed Martin restrictions.

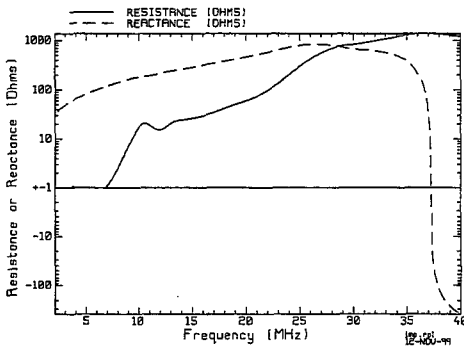


Fig. 4 - Computed HF Notch Antenna Impedance 2-40MHz

The significance of the interesting humps and nulls is that they represent the augmentation of the radiation resistance of the antenna by the resonant modes of the airframe.

It can be seen that because these computations are for a perfectly conducting structure and because the antenna is small in terms of wavelength, the resistance values are small at the lower end of the band.

A higher resolution plot for 2-30 MHz is shown in Figure 5. This now shows the additional interesting detail below 7 MHz.

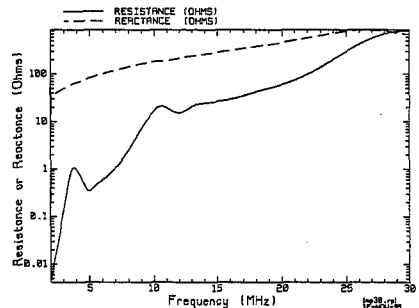


Fig. 5- Computed Impedance HF Notch 2-30 MHz

² P. M. Burdell, "C-130 H.F. Notch Antenna Design and Development", LG82ER0036, March 1982, Lockheed-Georgia Company.

These features have an interesting correlation with the radiation patterns and the performance parameters of the antenna. Thus our Virtual Range has already produced credible impedance data. When such information is available simultaneously with an experimental measurement program, the productivity of both is augmented considerably.

Calibrated Principal Plane patterns represent the basic data that are usually presented for aircraft antennas. Because of aircraft attitude changes, it is also desirable to know at least a limited number of conical pattern cuts. In order to establish the isotropic level in measurement programs, these latter must be measured in any case. Calibrated patterns are essential for range computations. Some of these are presented later in this paper. But because HF antennas operate over four octaves, the radiation pattern changes are so extensive that it is difficult to discriminate between the performance of different antennas. It is for these reasons that specific HF Performance Parameters were derived which are directly related to performance in the dominant communications modes. In this paper these are presented first, followed by some typical radiation patterns. Physical scale-model range pattern data must also be processed similarly to provide these performance values.

Radiation Pattern Efficiency

The referenced MIL-A-9080 specification presents the concept of a total HF Antenna System Efficiency at each frequency. It is the product of the main factors associated with power transfer and pattern shape:

- Radiation Pattern Efficiency;
- Antenna Efficiency;
- Coupler Efficiency;
- Transmission Line Efficiency.

The Radiation Pattern Efficiency is defined as the radiation of the total power radiated in a 'useful sector' to the total power radiated. The 'useful sector' is the cone $\pm 30^\circ$ around the azimuth plane that had been found to be most dominant for long range ionospheric communications.

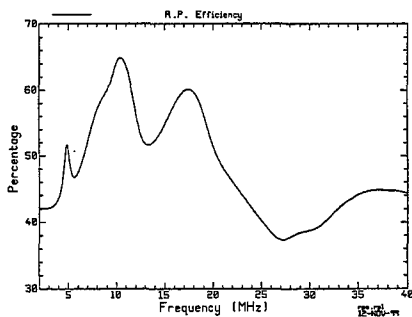


Fig. 6 - RPE vs. Frequency - HF Notch

The Radiation Pattern Efficiency, or η_s , is automatically calculated by the ISOLEV software routine and added to the solution file. It is shown in Figure 6. There are several aspects of this plot that are useful to consider. From operational aspects, it can be seen that the radiation pattern efficiency is low at low frequencies and at those beyond 20 MHz. We would expect that in these regions, the patterns will show a lot of energy being radiated towards the zenith rather than the horizon.

At the same time, the three distinct peaks identify frequency regions where there is a considerable change of patterns with frequency. Closer scrutiny shows that these peaks are related to

the highlights, peaks and dips, in the radiation resistance curve. An examination of the $\%E_0$, or percent vertical polarization plot will show similar detail.

Plots of $\%E_0$ vs. Frequency

For over-the-horizon ground wave propagation vertical polarization is required. To measure the performance for this mode, the $\%E_0$ & sub- $\%E_0$ parameters are computed. The latter is the % of vertical polarized radiation in the 'useful sector'. These ratios are shown plotted in Figures 7.

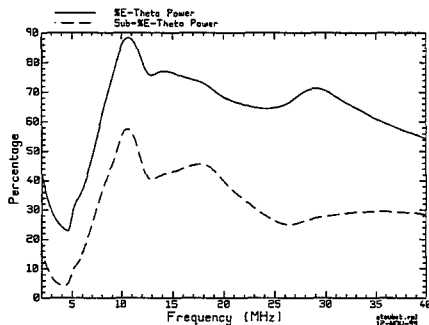


Fig. 7 - $\%E_0$ & Sub- $\%E_0$ vs. Frequency - HF Notch

A comparison of the highlights of these plots with the impedance and radiation pattern efficiency plots produces revealing insights. The dominant feature is the high amount of vertical polarization near 10MHz. This aircraft has a huge vertical stabilizer. It is obvious that the antenna excites an aircraft mode that involves a path with the vertical stabilizer. At the same time, the null near 5MHz implies that the RP efficiency peak is due to an increase in radiation of a horizontal polarization component. Noting the differences between the two plots of this figure reveals dominant features about the pattern shapes at these frequencies. Consideration of such detail paves

the way for more meaningful examination of the radiation patterns themselves.

The other performance parameter is that related to Nap-of-Earth communications performance.

Nap-of-Earth Communications Performance Parameter

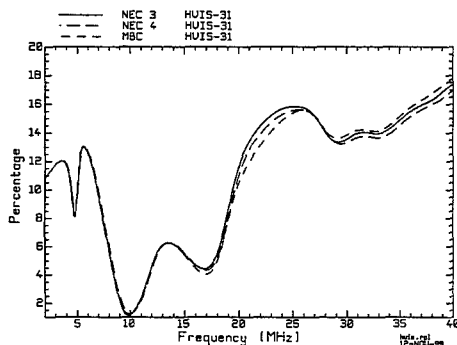


Fig. 8 HVIS Parameter vs. Frequency - HF Notch

For helicopters and low-flying aircraft over rough terrain, it has been found that a near-vertical angle of incidence propagation mode using the ionosphere can provide over-the-horizon communications when ground wave losses are too high. The parameter that has been established to evaluate radiation pattern distributions is the relative amount of power in the angle $\pm 30^\circ$ about the zenith. In the EMC Laboratory software this is labeled as the HVIS Parameter. A plot of this parameter with frequency is shown in Fig. 8. This figure shows values for three different codes that were tested. Once more the correlation of the highlights with the preceding plots

above should be made. Of particular interest operationally, is the very low value of this parameter around 10 MHz.

RADIATION PATTERN AND AIRCRAFT COUPLING INSIGHTS

These validated Virtual Range results allow the ready examination of the radiation pattern variations with frequency for range calculations at specific frequencies. One could proceed to examine the entire band - relative simplicity of the low frequency patterns, whose shape is usually determined by the antenna itself, to the complexity and rapid change at the higher frequencies. In this paper we merely provide a sampling to expose principal plane detail from instantaneous access to the output data base.

An especially important feature of the Virtual Computational Pattern Range is the ability to compute the entire data base at various aircraft heights above ground. An example had been provided in previous work on helicopters [7].

An example of principal plane radiation patterns at 11.20 MHz is shown in Figure 9. Note the isotropic reference level and the relative amplitude and detail for both polarizations. Such detail allows us to understand the performance parameter plots in the preceding figures. Finally it is often useful to present the radiation patterns in a three-dimensional format. A typical plot is shown in Figure 10 for 4.7 MHz. Although the reference values to calibrate these patterns are listed, this presentation is useful mainly in providing the volumetric appreciation of antenna coverage. In this particular case it also shows a relative complexity due to the excitation of aircraft resonance modes at this lower frequency because of the aircraft size.

The coupling of the antenna to the aircraft and the excitation of specific aircraft resonance modes is best illustrated by a color version of the TDPAT display shown in Figure 10 as it is swept in frequency. In this display the wire grid model itself is color-coded to display the amplitude (or phase) of the segment currents, while the volumetric pattern is shown alongside. Such a frequency sweep in movie-like format shall be a part of the oral presentation. It will show the symmetric and anti-symmetric modes [8] showing up in the intensification of selected paths along the aircraft fuselage.

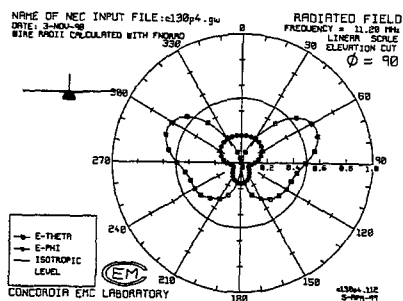
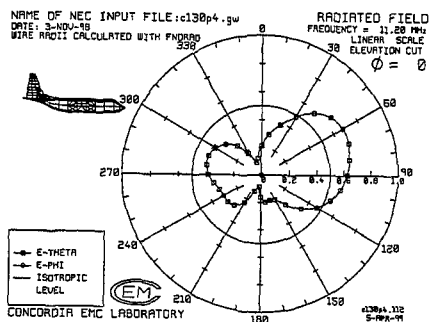
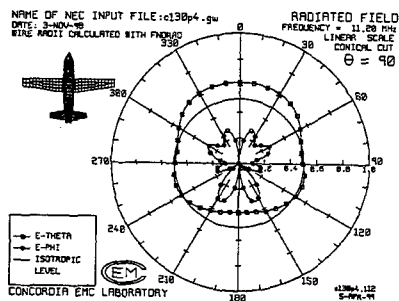
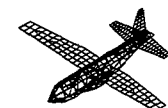
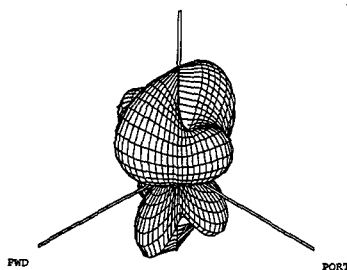


Figure 9 – Principal Plane Radiation Patterns:
 HF Notch Antenna – 11.20 MHz

NAME OF NEC INPUT FILE: c130p4.gw
 DATE: 3-NOV-98
 THE WIRE RADII IN THIS FILE WERE CALCULATED WITH TOP



TOP VIEW
 QUADRANT NO. 1
 MINIMUM THETA 0
 MAXIMUM THETA 180
 MAX FIELD STRENGTH
 AT THIS FREQUENCY
 0.545E-01 V/M
 MAX VALUE PLOTTED
 0.437E-01 V/M
 ISOTROPIC LEVEL
 0.418E-01 V/M
 SOLUTION FILE:
 C130P4.47



E-THETA
 AT
 4.7 MHz
 LINEAR
 SCALE

CONCORDIA EMC LABORATORY

1/21/99

Figure 10 – TDPAT Display – HF
 Notch Antenna : 4.7 MHz

CONCLUDING COMMENTS

A Virtual Radiation Pattern Range has been created by an integrated system for computational model creation, computational engine execution, data base consolidation and multi-dimensional display of the results. In its application to the C-130/HERCULES HF Notch Antenna, it has been possible to validate it by reference to previous physical scale-model results that had been produced some 17 years ago!

An exceptionally useful feature is the possibility of obtaining operationally useful radiation pattern and performance information for aircraft communication scenarios involving variations of height above ground. In addition, current distribution displays provide insights into antenna operation that could not be produced on physical pattern ranges without resort to deliberate and complex current probing instrumentation.

Acknowledgments

The computational modeling of the C-130/HERCULES HF Notch Antenna had been commissioned by Mr. Harvey Tremblay, DTA 3-5 of the Canadian Department of Defence. His support and encouragement are gratefully acknowledged. Scrupulous generation of the data for this paper had been the work of research assistants Miss Tuyet Nguyen and Mr. Khamnoi Soukchaseum of the EMC Laboratory.

References

- [1] Q.C. Luu, S. J. Kubina, C. W. Trueman and D. DeCarlo, "High resolution spectral analysis of HF coupling modes on the EC-130 aircraft", Proceedings of the 9th Annual Review in ACEM, ACES, Monterey CA, March 1993.
- [2] J. V. N. Granger and J. T. Bolljahn, "Aircraft Antennas". Proc. I.R.E., pp.932-938, May 1955.
- [3] G. Sinclair, E. C. Jordan and E. W. Vaughan, "Measurements of Aircraft Antenna Patterns Using Models", Proc. I.R.E., Vol. 35, pp. 1451-1462, December 1947.
- [4] G. J. Burke and A. J. Poggio, "Numerical Electromagnetics Code- Method of Moments, Part III: User's Guide", Tech. Doc. 116, NESC ELEX 3041, July 1977, etc.
- [5] C. W. Trueman and S. J. Kubina, "Verifying wire-grid model integrity with program "CHECK", ACES Journal, Vol.5, No.2, pp.17-42, Winter 1990.
- [6] C. L. Larose, S. R. Mishra and C. W. Trueman, "Measured RCS polar contour maps for code validation", ACES Journal, Vol. 11, No.3, November 1996.
- [7] S. J. Kubina, "Measurement and computer simulation of antennas on ships and aircraft for results of operational reliability", Proc. AGARD Lecture Series No. 165, October 1989.
- [8] Q. C. Luu, "Numerical techniques for the study of HF coupling modes on large aircraft", M. A. Sc. Thesis, ECE Dept., Concordia University, May 1994.

HF TOWEL-BAR ANTENNA LOCATION STUDY ABOARD AN H-3 SIKORSKY HELICOPTER

Saad N. Tabet[†], Carl D. Myers[‡], and Dennis DeCarlo[†]

Naval Air Warfare Center – Aircraft Division

RF Sensors Branch – Code 4.5.5.5

Building 2187, Unit #5

48110 Shaw Road

Patuxent River, MD 20670-1906

TabetS@navair.navy.mil[†]

MyersCD@navair.navy.mil[‡]

DecarloD@navair.navy.mil[†]

Phone: (301) 342-0042[†]/(301) 342-9175[‡]/(301) 342-9152[†]

FAX: (301) 342-0121[†]/(301) 342-9185^{‡†}

Abstract

A towel-bar antenna and its mounting locations are investigated aboard an H-3 Sikorsky helicopter, in the 2 to 30 MHz High Frequency (HF) range. This HF antenna is mounted on the port aft tail area of the helicopter fuselage.

The HF antenna is modeled and analyzed using the Numerical Electromagnetics Code-Method of Moments (NEC-MoM). The radiation patterns (RPs) at three frequencies of operation of the HF antenna are also measured in a tapered anechoic chamber using an eighth-scale rotorless metallic helicopter model.

The complete NEC-MoM modeling and analysis effort of the HF antenna is carried out on a full helicopter model (including the main and side rotors). Moreover, three more cases are also considered at frequencies matching the measured ones, and with the helicopter rotorless. The three measured and computed cases are compared for modeling accuracy, thus justifying the complete set of NEC-MoM models analyzed.

The results from the complete set of NEC-MoM models are used to determine the optimal length, standoff heights, and positions of the feed and termination points of the antenna. Based on the comparisons of those results, a recommendation is made as to which configuration best serves the mission of this HF antenna aboard the H-3 helicopter.

1. General Description: The antenna considered in this study is a "towel-bar" type HF antenna mounted aboard an H-3 Sikorsky helicopter. An illustration of the helicopter and the HF antenna mounted on it are shown in Fig. 1.

The antenna conductors are made of highly conductive steel tubing 1-inch in diameter. The antenna is attached to the fuselage via dielectric standoffs, used to hold the antenna in place with respect to the fuselage and provide electrical isolation from the fuselage. The antenna has several sections attached together by head masts at the standoff locations. The standoffs provide capacitive coupling between the antenna and the fuselage.

The HF antenna was modeled using wire-grid modeling and NEC-MoM, developed at Lawrence Livermore National Laboratories [1]. A set of user interface software from the EMC Laboratory at Concordia University [2] was used for the creation, visualization and analysis efforts of the HF antenna models.

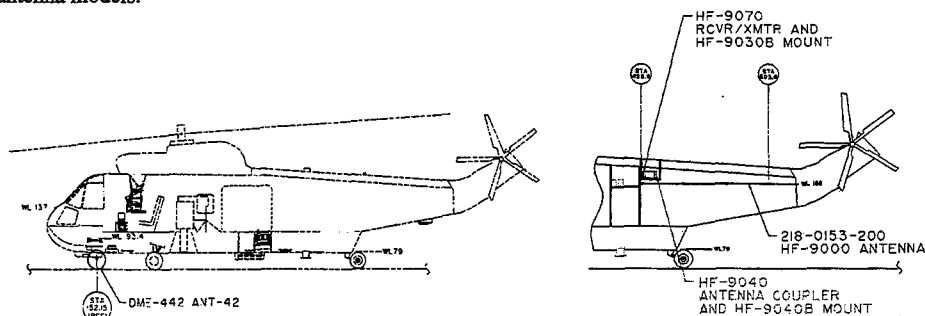


Fig. 1. Illustrations of a Sikorsky H-3 Helicopter and the HF Towel-Bar Antenna.

Furthermore, antenna performance on full size aircraft can be duplicated via scale models, if the dimensions and electromagnetics properties are scaled appropriately. The predominant factors are the dimensions, frequencies of operation, capacitance of standoffs, and conductivity. The full size dimensions are divided by the scale factor; frequency and conductivity are multiplied by the scale factor. Conductivity losses usually have very minor effects on the operation of most antennas. In general, slight discrepancies in scaling will usually affect the impedance properties more significantly than the radiation properties. Scale model radiation properties are usually considered to be highly accurate.

2. NEC-MoM Model: A dense wire-grid NEC-MoM model, developed by Concordia University, was used in the modeling and analysis of the HF antenna. The wire-grid model is shown in Fig. 2, and was based on the "equal-area" technique of wire-grid modeling. In this technique, the radii of the wire segments used were chosen in such a way that unfolding and flattening the segments generated approximately covered grids.

The NEC-MoM model contained more than 1390 wire segments, for every configuration under study. Table 1 summarizes the entire set of configurations considered during this study. For each case in Table 1, except for the cases in the last three rows, the HF antenna was modeled and studied in the 2 to 30 MHz frequency range, in increments of 0.1 MHz. The 0.1 MHz increments in frequency were used to identify every peculiar behavior in the frequency response of the antenna.

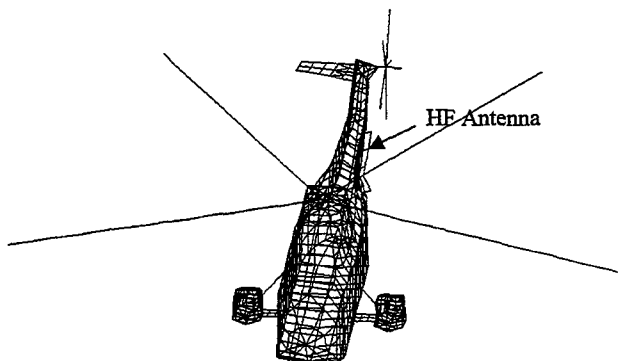


Fig. 2. NEC-MoM Model of H-3 Sikorsky Helicopter with HF Towel-Bar Antenna.

The last three rows in Table 1 were cases compiled with the helicopter's main and side rotors' blades removed, to match the eighth-scale model used in the measurements. Then the shorted 145-inch antenna was studied at 12.5, 16.9, and 30.0 MHz (same frequencies as the measured ones, after they are scaled back).

Table 1. HF Antenna Configurations Studied.

Antenna Termination	Length (in)	FS Location Feed, Termination	WL Location	Standoff (in)	Frequency Range (MHz)	Frequency Incr. (MHz)	Rotors Positions	Rotors Rotation
Shorted	145	460, 604	155	8	2 to 30	0.1	flat	no rotation
Shorted	145	460, 604	155	10	2 to 30	0.1	flat	no rotation
Shorted	145	460, 604	155	12	2 to 30	0.1	flat	no rotation
Shorted	145	460, 604	155	10	2 to 30	0.1	4 deg.	no rotation
Shorted	145	460, 604	155	10	2 to 30	0.1	4 deg.	36 deg. Rotation
Shorted	98	460, 559	155	10	2 to 30	0.1	flat	no rotation
Shorted	194	407, 604	155	10	2 to 30	0.1	flat	no rotation
Shorted	145	460, 604	110	10	2 to 30	0.1	flat	no rotation
Shorted	145	483, 345	155	10	2 to 30	0.1	4 deg.	no rotation
Shorted	194	436, 240	167	10	2 to 30	0.1	flat	no rotation
Opened w/o capacitor	145	460, 604	155	10	2 to 30	0.1	flat	no rotation
Opened w/ capacitor	145	460, 604	155	10	2 to 30	0.1	flat	no rotation
Shorted	145	460, 604	155	10	12.5	None	flat	no rotation
Shorted	145	460, 604	155	10	16.9	None	flat	no rotation
Shorted	145	460, 604	155	10	30	None	flat	no rotation

Vertical and horizontal polarization RPs were computed at every frequency of study. Pitch and roll cuts (in 5-degree increments) were computed. Conical cuts (in 5-degree increments) were also computed at each of the following elevation angles: 0, 13, 17, 21, 25, 31, 37, 45, 53, 60, 66, 72, 78, 84, 90, 96, 102, 108, 114, 120, 127, 135, 143, 155, and 180 degrees. The angles where the elevation and conical cuts were computed are specific angles used in the Concordia University computer modules to calculate HF range critical antenna parameters, and are based on empirical in-flight measurements. These software modules were used to calculate the following critical antenna parameters:

- Input impedance
- Isotropic level
- Percentage E_θ (% E_θ), defined as the percentage of the total radiated power contained in the E_θ component
- Sub-percentage E_θ (sub-% E_θ), defined as the percentage of the total radiated power contained in the E_θ component in a conical sector extending from 30 degrees above to 30 degrees below the horizon
- Radiation pattern efficiency (RPE), defined as the percentage of the total radiated power contained in a conical sector extending from 30 degrees above to 30 degrees below the horizon
- Near Vertical Incidence Skywave (NVIS, sometimes referred to as HVIS where H stands for high frequency), defined as the percentage of the total radiated power contained in a spherical sector extending down to 30 degrees from zenith. NVIS is most commonly used between 2 and 10 MHz, due to high losses (atmospheric and other) at higher frequencies.

The Concordia University software modules were also used to generate polar and rectangular 2-D contour plots and three-dimensional (3-D) RPs. Moreover, current distribution on the entire helicopter was computed, at every frequency of analysis.

For the three rotorless helicopter cases of the HF antenna analyzed at 12.5, 16.9, and 30.0 MHz, the elevation and conical cuts were computed at 2-degree increments. This was done to achieve better detail in the RPs thus allowing for a better comparison to the eighth-scale model measured RPs.

3. Eighth-Scale Model: An eighth-scale physical model of the helicopter and the HF antenna, shown in Fig. 3, was used to conduct the scale model measurements. The model was constructed of wood and covered with copper sheets. The copper sheet seams were soldered and some areas were covered with aluminum tape to provide a smooth conductive surface. The actual driveshaft cover of the helicopter is composed of a dielectric composite material. However, wood was used to simulate the driveshaft in the eighth-scale model. The inside was hollowed out and a threaded rod was inserted to duplicate the real driveshaft. The cover was overlaid with gray duct tape to provide a better visual appearance. No rotor blades were installed on the model for these measurements.

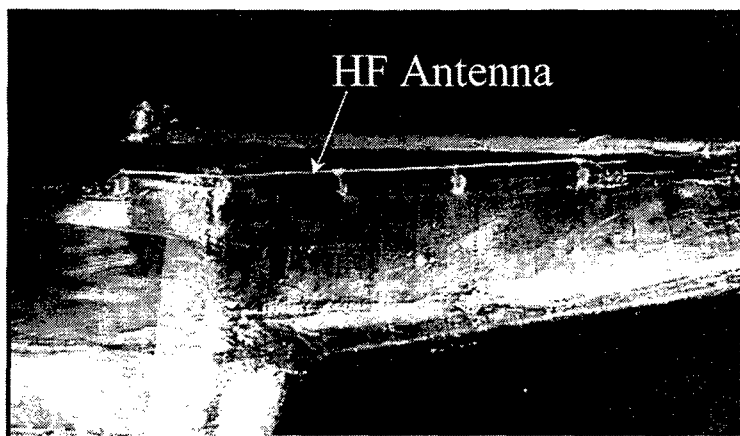


Fig. 3. Eighth-Scale Model of HF Towel-Bar Antenna and Helicopter.

The HF antenna was simply scaled to one-eighth of its physical dimensions, as shown in Fig. 3. The HF RPs were measured at three frequencies: 12.5, 16.9, and 30.0 MHz, and for both vertical and horizontal polarizations. Conical cuts, from 10 degrees below the horizon all the way up to zenith (in 10-degree increments), were measured. In addition, pitch and roll RPs were measured. Fig. 4 describes the aircraft coordinate system used for both, measured and computed RP data.

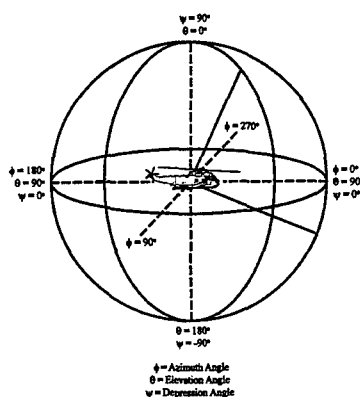


Fig. 4. Aircraft Coordinate System.

The measurements were performed at the FARM (Facilities for Antenna and RCS Measurements), NAWCAD, Patuxent River, MD. The facility used was a pyramidal anechoic chamber measuring 25-ft x 25-ft x 90-ft. The measurements set up is shown in Fig. 5.

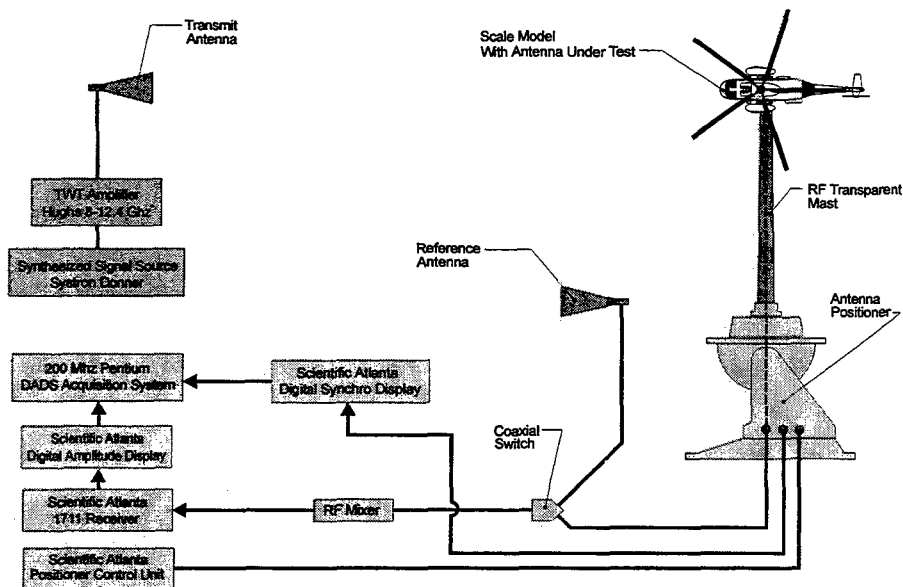


Fig. 5. Eighth-Scale Model Measurement Setup for the HF Antenna Aboard an H-3 Helicopter.

3. Results: Due to the enormous amounts of data generated in the effort, only a few samples of the results will be displayed and discussed in this paper. Overlays of measured and computed azimuth RPs at 12.5, 16.9, and 30.0 MHz, on a rotorless helicopter model, are shown in Figs. 6, 7, and 8, respectively. The horizontal polarization patterns showed very good agreement with the measured ones. However, there were some discrepancies between the vertical polarization patterns, especially in Fig. 7. Revisiting the measured data of this case showed that the measured data suffered from inaccurate recordings (receiver dropout) in portions of the first and fourth quadrants. Hence, only a comparison of the second and third quadrants was valid. Also, it is important to note that the antenna exhibits more dominant horizontal polarization than vertical, mainly at the lower end of the HF range. In general, the good agreement between the measured and computed RPs provided good confidence in the remaining computed results, where measurements were not available for comparison purposes.

A comparison of the study cases with different standoff lengths, shown in Table 1, showed that the antenna's performance was not significantly affected by the standoff lengths used. However, 8-inch standoffs do not provide a good enough electrical separation and/or isolation at the lower frequencies, while 12-inch standoffs are more vulnerable to vibrations and other mechanical problems that could arise from using longer standoffs. Hence, the decision was made to go with 10-inch standoffs for the majority of the HF antenna study.

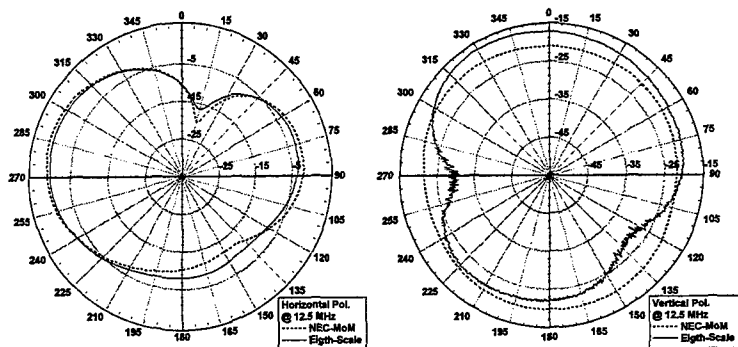


Fig. 6. Computed Versus Measured Radiation Patterns at 12.5 MHz.

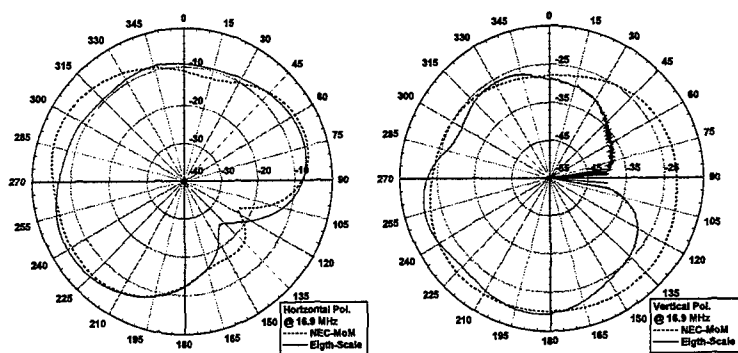


Fig. 7. Computed Versus Measured Radiation Patterns at 16.9 MHz.

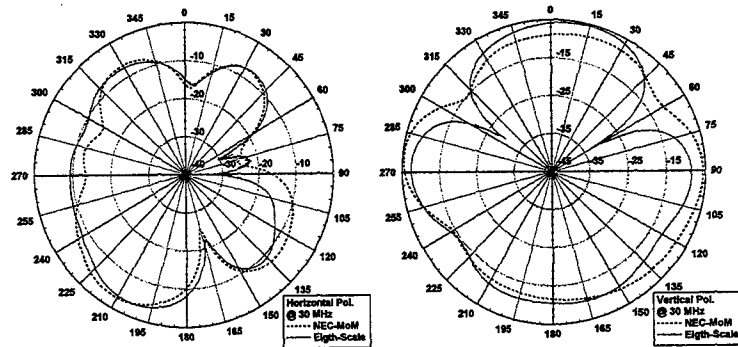


Fig. 8. Computed Versus Measured Radiation Patterns at 30.0 MHz.

Comparing the antenna input resistance (R_{in}) and input reactance (X_{in}) results for the 98-inch, 145-inch, and the 194-inch cases (see Fig. 9) showed that the length of the antenna had a significant effect on the location of the resonance frequency, as well as, the peak resistance and reactance values at resonance. This information along with the remainder of the antenna parameters were used, in conjunction with the mechanical constraints, to select the best antenna configuration for the helicopter.

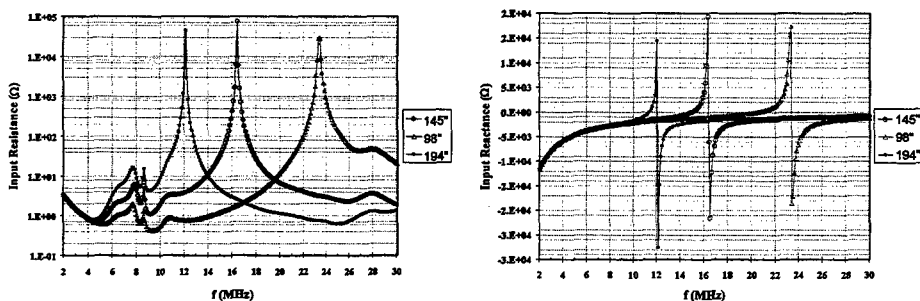


Fig. 9. Input Resistance and Reactance Comparisons for Different Lengths of the HF Antenna.

4. Conclusions: The close agreement between the measured and computed RPs shown in Figs. 6, 7, and 8, shows that both methods (computational modeling and scale model measurements) work hand-in-hand in providing good confidence in the achieved results. The complete set of computed data, for all of the pertinent antenna parameters, provides significant insight into the operation of the HF antenna. All factors considered, the 145-inch shorted towel-bar with 10-inch standoffs (fed at FS 459.8 and shorted at FS 603.8) is the recommended location for placing the HF antenna system.

5. References:

- [1] G.J. Burke and A.J. Poggio, "Numerical Electromagnetics Code – Method of Moments, Part I: Program Description-Theory, and Part III: User's Guide," Technical Document 116, Lawrence Livermore Laboratory, Naval Electronics Systems Command (NAVELEX 3041), January 1981.
- [2] S.J. Kubina and C.W. Trueman, "The EMC Laboratory Integrated Software System for Model Creation, Visualization and Analysis," Report No. TN-EMC-93-06, Rev. 2, Concordia University EMC Laboratory, October 1995.

Improving Model Confidence through Metamorphosis

Capt. D.R. Munn, Royal Military College of Canada

e-mail: munn-d@rmc.ca

Dr. C.W. Trueman, Concordia University

e-mail: trueman@ece.concordia.ca

Abstract

The confidence in radiation patterns from a complex wire-grid model can be improved by "morphing" complex model from a simple shape with a known radiation pattern. The case of the Cormorant helicopter morphed from a cylinder is presented. By starting with a $\frac{1}{4}\lambda$ monopole antenna on a cylinder of resonant length and slowly morphing it into the Cormorant helicopter, a sequence of radiation patterns is generated that demonstrate a continuously changing shape which provides a link between the first and last radiation pattern.

Introduction

When a wire-grid model of an aircraft such as the Cormorant helicopter, Fig. 1, is constructed in accordance with the "modeling guidelines" of Ref. [1] and verified for integrity using the "CHECK" guidelines [2], then we have a high degree of confidence that the radiation patterns computed using the model will be correct. But if the model is to be used to design a new HF antenna configuration, then the cost of an error may be very high. Then further confidence in the computer model can be gained by traditional "model validation", that is, by comparing the predicted radiation patterns with full-scale or scale-model measurements. Agreement with measurements is hard proof that the model correctly predicts the performance. Then the computer model can be used to study the performance changes due to modifications in the antenna geometry, or relocation of the antenna, or with a different antenna. Thus, once a model is "validated" for a given antenna geometry it is common to accept the results computed with that model for a somewhat different antenna geometry as also being valid. Once we have confidence in the original model, we will also have confidence in a "nearby" model, that is a model which differs by small changes from the original.

In the absence of measured data for the Cormorant model, it has been necessary to explore other methods for establishing confidence in the model beyond the fundamental level of satisfying the guidelines of Refs. [1] and [2]. The "model morphing" method described in this paper is akin to proof by induction in mathematics. If the starting point is true and we can derive result $i+1$ from result i , then result $i+1$ must be true. We start with a geometry that has been validated against measured data. Then we argue that the normal practice in computer modeling is to accept as valid results that are computed with a model that differs only by small changes from a previous model that we accepted as valid. This method of building confidence is thus based on the extrapolation of a validated result. We will transform or "morph" the initial model into the final helicopter configuration.

Goldhirsh validated the monopole on cylinder geometry against measurements in Refs. [3] and [4] and his results can be used to provide a traditional validation of the wire-grid model of the cylinder with the monopole. The idea is then to transform or "morph" the antenna and cylinder geometry in a series of small steps. At each step the wire-grid model satisfies the guidelines of Refs. [1] and [2] and so we have basic confidence in the model. By progressing through many small changes we can achieve the morphing of a monopole and cylinder into a triline antenna and helicopter. First, the monopole is transformed into the triline antenna in small steps, and then the cylinder is evolved into the helicopter. At each step, it is expected that the radiation patterns will depend in a continuous fashion upon the antenna and model geometry; and if the geometrical change is small the patterns for the next shape will be close to those of the previous one. As we progress through many shapes, the radiation patterns undergo a gradual metamorphosis or fluid change into those of the triline antenna on the helicopter. Observing the changes in the radiation patterns and antenna performance at each step lends significant insight into the relation of features in the radiation patterns to features of the helicopter geometry.

Another point of view is an analogy with the calculus of variations. If you know the exact solution to a problem and you make a small change to the problem then you expect the solution to the "perturbed" problem to be almost the same as the solution to the original problem. The results vary continuously with the input. Any large change in the radiation pattern that results from a small change in the model would be an indication that the model is no longer valid, that is, something has gone amiss in deriving the model. If we perturb the geometry in a series of small changes, and continue to satisfy the NEC modelling guidelines [1, 2] at each step then we expect to have the same degree of confidence in the model after the small change as in the model before the small change.

The Monopole and Cylinder Geometry

The first step in this method of validation is to reproduce Goldhirsh's results using a cylinder that is representative of the helicopter. Goldhirsh's experiments were carried out using cylinders and antennas that were measured in

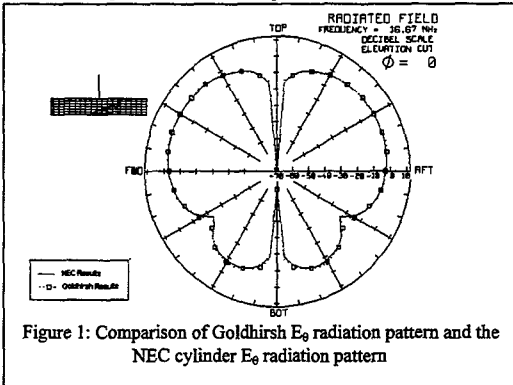


Figure 1: Comparison of Goldhirsh E_θ radiation pattern and the NEC cylinder E_θ radiation pattern

wavelengths and were relative to each other (i.e. a cylinder of length λ , an antenna of length $\lambda/4$ and the resonant frequency). Therefore it is possible to use a cylinder with the same overall dimensions as the helicopter as long as the antenna size and frequency used have the same relationship to the cylinder as those in Goldhirsh's work. To that end, a cylinder with a length of 18m and a radius of 1.5m was chosen. This cylinder would enclose the entire helicopter excluding the engines, rotors, spars and the horizontal and vertical stabilizers. The resonant frequency for this cylinder is 16.667 MHz and the length of the $\lambda/4$ monopole is 4.5m. The wire grid model of the cylinder and antenna was constructed following the wire-grid modeling guidelines[1] and its integrity was confirmed as in Ref. [2]. Figure 1 shows E_θ radiation pattern in the xz plane with Goldhirsh's computed pattern. The two patterns agree well and this "validation" of the wire-grid model is the starting point for our morphing process.

From Monopole to Tranline Antenna

The first step in the morphing process is the change from a monopole antenna at the top of the cylinder into the tranline antenna at a position corresponding to its location on the helicopter. The monopole is bent at 0.3 m above its base, equal to the length of the standoff of the tranline antenna. The monopole is gradually bent through 90 degrees to become parallel to the cylinder surface. This rotation is done in small increments to allow for a smooth transition of the radiation pattern as shown in Figures 2 and 3.

Next the bent monopole is rotated around the cylinder until it reaches the same waterline as the helicopter antenna, as shown in figures 4, 5 and 6. Again this is done in a sequence of small steps and we note that the radiation pattern changes smoothly as we progress from one step to the next. The next step is to move the bent monopole until the connection point to the cylinder is at the same station as the helicopter antenna, as shown in figure 7. Then the straight wire antenna is bent and lengthened into the same shape as the tranline antenna, figures 8 and 9. The forward and aft portions of the antenna remain parallel to the longitudinal axis of the cylinder. The forward section remains fixed in position as the aft section is displaced upward. The two remained joined by a diagonal wire. The morphed antenna can be seen in detail in the upper left corner of the figure.

We now have an antenna in the proper location and of the proper shape. But the tranline is shorted to the helicopter at its aft end. Simply shorting the end of our bent wire to the cylinder would introduce a discontinuous change, violating our continuity assumption that if small changes are made in the geometry then small changes result in the patterns. To connect the end of the antenna to the cylinder without introducing a discontinuity, we add a wire segment attaching the end of the antenna to the cylinder, loaded with a very high resistance, making it an open circuit. Then we gradually reduce the value of the resistance to zero, resulting in the pattern variations shown in figures 10 to 13. This allowed for a smooth transition from an open-circuit tranline antenna to a short-circuit tranline antenna.

Evolution of the Radiation Patterns

Figure 2 and those following show the cylinder model beside the $\phi=0$ elevation radiation pattern, displaying E_θ and E_ϕ . The front of the cylinder is in the lower left corner and the orientation of the radiation pattern is as it is labeled. The source at the base of the monopole is one volt at 16.667 MHz. All of these figures are individual frames to a movie sequence that demonstrates the metamorphosis of the model from cylinder to helicopter, and the corresponding changes in the radiation patterns.

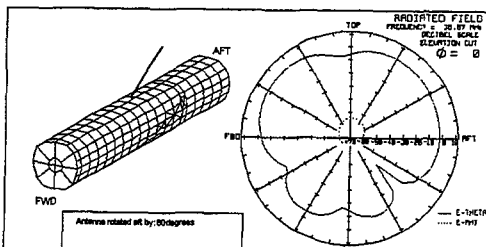


Figure 2: Radiation pattern for the cylinder model with the antenna rotated aft by 60°.

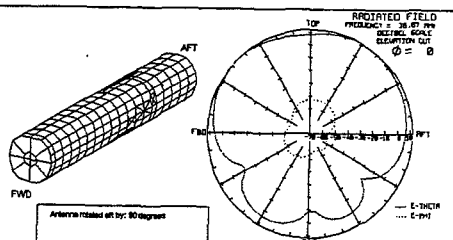


Figure 3: Radiation pattern for the cylinder model with the antenna rotated aft by 90°.

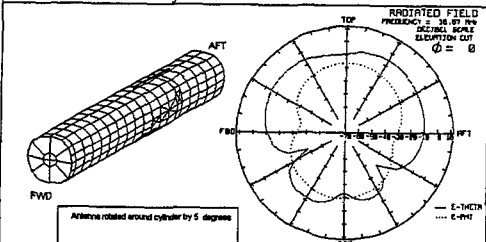


Figure 4: Radiation pattern for the antenna rotated around the cylinder by 5°.

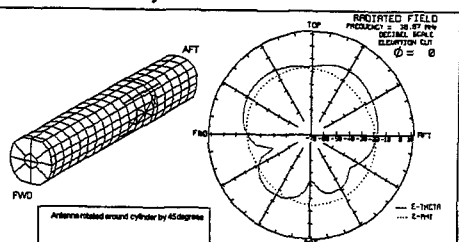


Figure 5: Radiation Pattern for the antenna rotated around the cylinder by 45°.

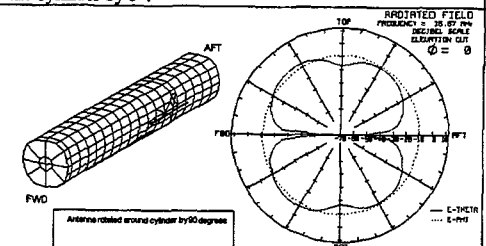


Figure 6: Radiation pattern for the antenna rotated around the cylinder by 90°.

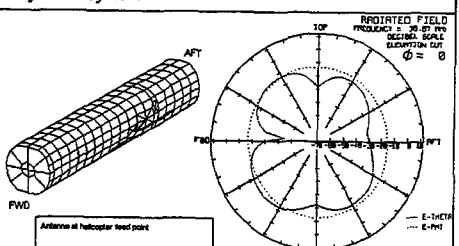


Figure 7: Radiation pattern when the antenna is located at the helicopter feed point.

Figure 2 shows the radiation pattern for the antenna rotated aft by 60°. The E_θ radiation pattern shows that the nulls in the lower quadrants have rotated clockwise a further 5° and the aft null has increased from -25 dB to -40 dB. Figure 3 shows the radiation pattern when the antenna is parallel to the longitudinal axis of the cylinder. The clockwise rotation of the pattern is the same as it was in figure 2 and the lower aft null has once again decreased. The most significant change is that the overall strength of the field has increased by approximately 10 dB for both E_θ and E_ϕ . This sequence indicates that the major increases in the field strength occur when the antenna angle is between 86° and 90°.

Figure 4 shows the radiation pattern generated when the antenna is rotated around the longitudinal axis of the cylinder by 5°. The E_θ pattern remains unchanged, but the E_ϕ pattern is increased by approximately 40 dB. Figure 5 shows the radiation pattern for the antenna rotated 45° around the cylinder. The lobe in the lower aft quadrant of the E_θ radiation pattern has decreased in size by approximately 4 dB and the null in the forward lower quadrant has rotated clockwise by approximately 5°. The E_ϕ radiation pattern is becoming more omni-directional as the nulls in figure 4 have

disappeared. Figure 6 shows the radiation pattern for the antenna rotated around the cylinder by 90° . The E_θ pattern now has the basic figure eight shape with the antenna lying along the FWD/AFT axis. The E_ϕ radiation pattern is now omnidirectional suggesting that the vertical feed segment of the antenna most heavily influences it.

Figure 7 shows the radiation pattern generated when the feed point of the antenna is aligned with the co-ordinates on the cylinder that represent the feed point on the helicopter. The E_ϕ radiation pattern is still basically omnidirectional while the aft null on the E_θ radiation pattern has decreased by 25 dB. From this point on in the morphing process, the feed point of the antenna remains fixed in position, and the shape is evolved into the helicopter trailing antenna.

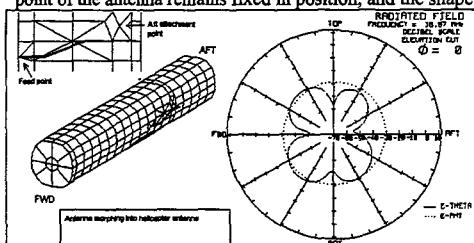


Figure 8: Radiation Patterns for the antenna half way through metamorphosis.

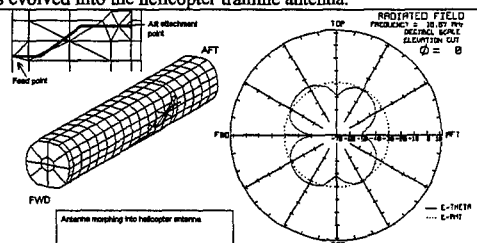


Figure 9: Radiation patterns for the open-circuit helicopter antenna.

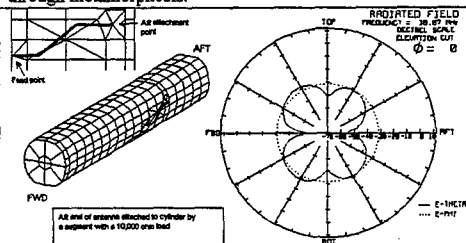


Figure 10: Radiation patterns for the helicopter antenna with a 10,000-ohm termination load

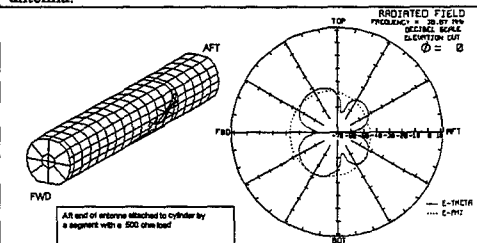


Figure 11: Radiation patterns for the helicopter antenna with a 500-ohm termination load

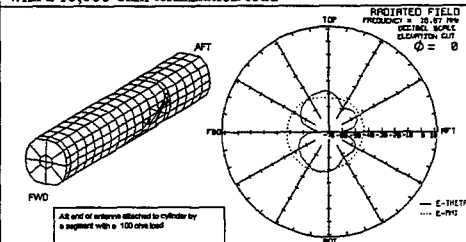


Figure 12: Radiation patterns for the helicopter antenna with a 100-ohm termination load

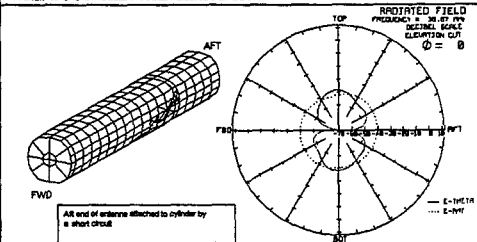


Figure 13: Radiation patterns for the helicopter antenna terminated with a short-circuit

Figure 8 shows the radiation pattern from the antenna that is half way through the morphing process. The only change in the radiation patterns is the increase in the aft null in the E_θ pattern by approximately 10 dB. Figure 9 shows the radiation pattern for the morphed antenna with the aft end as an open-circuit. The E_ϕ radiation pattern remains virtually unchanged and the E_θ pattern has a slight overall increase of approximately 3 dB. Figure 10 shows the radiation pattern

generated when the open circuited antenna is terminated to the cylinder with a 10,000-ohm resistive load. The final length of the antenna is 3.06 m including the termination. The purpose of this load is to mimic the open circuit condition of figure 9. As can be seen by the radiation pattern in figure 10 this is successful. Both the E_θ and E_ϕ radiation patterns maintain their shape with only a slight decrease in strength of approximately 2 dB.

The final step in this morphing process is to decrease the resistive load until a short-circuit state is achieved. Figure 11 shows the radiation pattern for the antenna with a 500-ohm termination load. The aft lobes of the E_θ radiation pattern decrease more than the forward lobes by approximately 5dB. The aft side of the E_ϕ pattern continues to flatten with a decrease of approximately 9 dB compared to the 1 dB decrease at the forward side. Figure 12 shows the radiation pattern for the antenna with a 100-ohm termination load. The upper and lower nulls in the E_θ radiation pattern have begun to disappear and the rear lobes have now decreased significantly. The overall size of the E_θ pattern has decreased. The E_ϕ curve has now begun to flatten at the top and bottom and the forward side has decreased in size. Figure 13 shows the radiation patterns for the antenna terminated in a short-circuit. The E_θ radiation pattern has become essentially a two lobe structure with only a hint of the upper and lower nulls remaining and they are shifted well into the aft quadrants. The E_ϕ radiation pattern has returned to an almost omni-directional shape with a slight flattening occurring in the upper forward quadrant. This sequence when viewed in movie format with all of the intermediate frames, shows that the greatest change in the radiation patterns occurs as the termination load approaches zero.

Morphing Guidelines

This section will develop a helicopter geometry constructed of simple geometric shapes such as cylinders, cones, and cubes. Such "simplified models" have been used to predict helicopter antenna patterns by other computational methods such as Transmission Line Method (TLM) or Finite Difference Time Domain (FDTD) which use simple geometric shapes in their model building. We will make small changes in the geometry of the cylinder, progressively altering its shape towards that of the simplified helicopter, while monitoring the radiation pattern. This is done respecting the "morphing guidelines" of Table 1. These guidelines were developed by experimentation with various simple models in order to ensure that the morphing process will provide insight into the radiation patterns and frequency dependence of the tranline antenna. Maintaining the major dimensions ensures that the resonant frequencies of the cylinder, the intermediate structures, and the helicopter are related. The second guideline recommends adding the rotors to the structure early in the process as they control the basic resonant behavior of the helicopter. The third points out that focusing attention on one part of the structure at a time allows changes in the patterns to be directly associated with changes in that part of the structure. The forth is the basic concept of "morphing". Changing the flat end of the cylinder into the rounded nose of the helicopter must be done gradually as a series of small changes. Guideline 5 recommends against any changes in the wire grid in the region not being morphed. In particular, since a change in the wire-grid topology in the region of the antenna can change the antenna patterns, it is best to maintain the grid topology unchanged except in the area where the "morphing" is taking place. Guideline 6 suggests that the order in which changes are made to the model should not be decided a priori. That is we should not insist that first the nose be altered, then the tail, then the base of the antenna, and so forth. Rather, at a given stage in the morphing process it may be useful to explore changing say either the nose or the tail, and following the change that is most insightful.

Table 1: Morphing Guidelines

1. Determine the major dimensions of the structure and maintain them throughout.
2. Add major geometrical structures associated with resonance first.
3. Add one new geometric structure at a time.
4. Build larger features in stages.
5. Maintain the same wire-grid representation in critical areas throughout the morphing.
6. Do not commit to pursuing one path of model development.

Following these straightforward guidelines maintains the integrity of the process and allows for the best observation of model validation at every step.

Morphing The Cylinder Into The Helicopter

Early experimentation revealed that both the main and tail rotors have significant effects on the antenna performance and because these effects are easily recognized, they can be used as landmarks to evaluate changes. The guidelines advise adding the major geometrical structures that might be associated with resonance first. For the helicopter these are the rotors. First we will add the tail and the tail rotors, and then the main rotor.

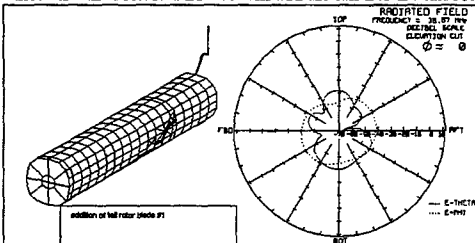


Figure 14 Radiation Pattern for model with one tail rotor blade

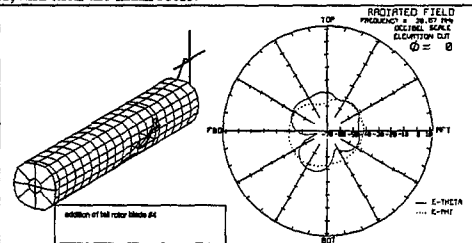


Figure 15: Radiation Pattern for model with four tail rotor blades

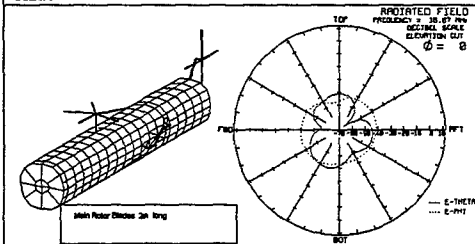


Figure 16: Radiation Pattern for model with 2 m main rotor blades

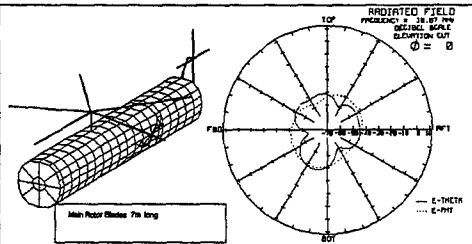


Figure 17: Radiation Pattern for model with 7m main rotor blades

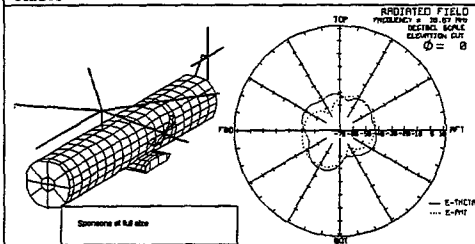


Figure 18: Radiation Pattern for model with sponsons added

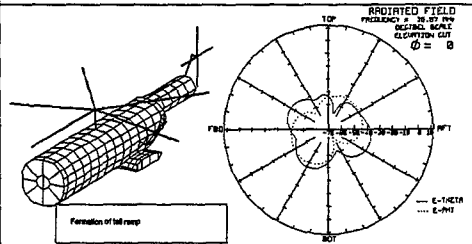


Figure 19: Radiation Pattern for the model with the rear ramp added

Figure 14 shows the radiation pattern for the model with the top, vertical tail rotor blade in place. This addition generates a significant change in the radiation pattern especially in the upper forward quadrant. Fig. 15 has all four tail rotor blades. Figure 16 shows the radiation pattern when the main rotor blades are added at a length of 2 m. The radiation pattern shows significant changes with the most notable being the near disappearance of the null in the bottom aft quadrant, the null in the forward lower quadrant has moved into the top forward quadrant and the maximum in the upper aft quadrant has changed into a sharp null. Fig. 17 shows the pattern with full size main rotor blades. The radiation pattern retains the three-lobe pattern that began when the rotor blades were 2 m long in figure 16 although the depth of the nulls have changed and the pattern has undergone a counterclockwise rotation.

The next step in this model development is the addition of the sponsons located on either side of the cylinder with the port sponson located 0.4 m below the antenna feedpoint. The radiation pattern for the full sponsons is shown in figure

18. The radiation pattern is the result of gradual changes in the field caused by a gradual growth in the size of the sponson. The pattern still maintains the three-lobe structure encountered earlier. However the nulls are decreasing which results in an overall tendency to a omni-directional field.

In accordance with morphing guideline 3, it has taken the construction of 18 simplified models to morph the cylinder into the model shown in figure 18.

To replicate the helicopter's tail pylon, the aft 5-m of the cylinder is reduced in diameter from 3 m to 1.66 m. The top of the tail cylinder is maintained at the same height as the main cylinder. Figure 19 is the radiation pattern for the two-cylinder model with the rear ramp. The effect of the tail cylinder on the radiation pattern is to increase the nulls in the top and bottom aft quadrants. The subtle changes that occur in the current distribution include a reduction in the current on the starboard aft main rotor blade and an increase in current on the tail rotor blades.

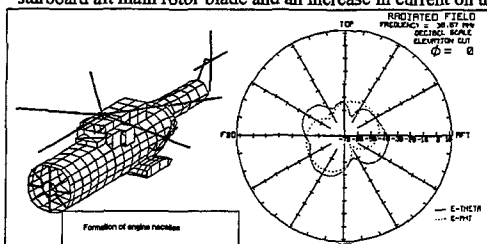


Figure 20: Radiation Pattern for the model with engine nacelles added

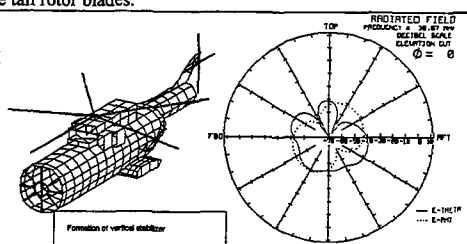


Figure 21: Radiation Pattern for the model with the addition of the vertical stabilizer

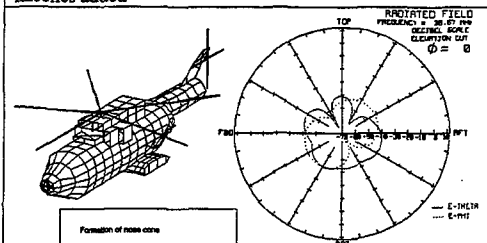


Figure 22: Radiation Pattern for the model with conical nose section added

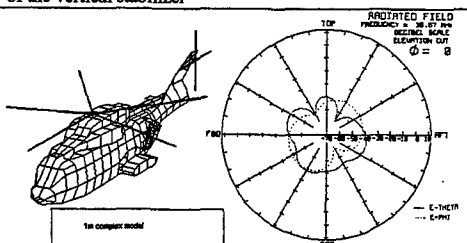


Figure 23: Radiation pattern for 1m complex helicopter model

The addition of the engine nacelles has a minor influence on the radiation pattern at this particular frequency. Figure 20 shows the radiation pattern for the model with the simplified engine nacelles added. These nacelles were built up using rectangles to replicate the general shape of the more complex model. This began by creating the large cube on the centerline that represents the center engine and growing it to full size. The two side cubes representing the port and starboard engines were then grown so that the whole process took the creation of seven simplified models to complete the metamorphosis.

Figure 21 shows the radiation pattern for the model with the creation of the vertical tail stabilizer from the tail rotor support. The radiation pattern shows significant changes especially the increased nulls located at $\pm 30^\circ$ from the top and the disappearance of the null in the bottom aft quadrant.

Figure 22 shows the radiation pattern for the model with the forward 2.5 m of the main cylinder replaced by a conical nose. This was done by successively "sharpening" the front of the cylinder until nose resembled a truncated cone. In accordance with guideline 3 this process took three simple models to complete the metamorphosis. At this frequency the change has little effect on the radiation pattern or current distribution.

This completes the morphing of the cylinder into the simplified helicopter model. The entire process required the construction of 132 different wire-grid models however by complying with the morphing guidelines and building on each successive model, this is a fairly routine task. Fig. 23 shows the radiation patterns of the actual helicopter model for comparison with those of the simplified model of Fig. 22.

Conclusion

This paper has presented a method for increasing our confidence in a wire grid model and gaining insight into the radiation patterns of the antenna. We start with a simple, well validated structure, namely a monopole on a cylinder. We gradually change the geometry, or "morph", the monopole shape and location into that of the helicopter's tranline antenna. Then we morph the cylinder shape into the helicopter. A set of guidelines for the morphing process has been given.

Since we expect the radiation patterns to depend in a continuous manner on the antenna and helicopter geometry, each small change in the geometry introduces a similar small change in the patterns and antenna performance. This paper has explored the evolution of the patterns at one frequency, 16.67 MHz. A companion paper[ref] shows how the antenna performance over the 2 to 30 MHz band changes as we morph the cylinder into the helicopter.

References

- [1] C.W. Trueman and S.J. Kubina, "Fields of Complex Surfaces Using Wire Grid Modeling", IEEE Transactions on Magnetism, Vol.27, No.5, September 1991
- [2] C.W. Trueman and S.J. Kubina, "Verifying Wire-Grid Model Integrity with Program CHECK". ACES Journal Vol.5, No. 2, Winter 1990
- [3] J. Goldhirsh, D.L. Knepp, R.J. Doviak, "Radiation from a Dipole Near a Conducting Cylinder of Finite Length", IEEE Transactions. on EMC, Vol. EMC 12, No. 3 pp. 96-105 August 1970.
- [4] J. Goldhirsh, D.L. Knepp, R.J. Doviak, R. Unks, "Radiation from a Short Dipole or Monopole Near a Thick Conducting Cylinder of Resonant Length" IEEE Transactions. on Antennas. and Propagation. Vol. AP-19 pp. 279-282 March 1971.

MODEL MORPHING FOR INSIGHT INTO THE HF ASSESSMENT PARAMETERS

Capt. D.R. Munn, Royal Military College of Canada

e-mail: munn-d@rmc.ca

Dr. C.W. Trueman, Concordia University

e-mail: trueman@ece.concordia.ca

Abstract

The graph of HF assessment parameters from complex models such as helicopters can be difficult to analyze especially when resonant features are generated by more than one part of the structure. This difficulty can be alleviated by "morphing" the model from a simple structure into a complex one while observing the graph of the assessment parameter. Starting with a tranline antenna in free space and slowly morphing through numerous stages of increasing complexity to the Cormorant helicopter model generates assessment parameter graphs that become the frames of a movie. Observing this movie provides insight into the generation of the various features that show up in the assessment parameters.

Introduction

The purpose of this paper is to apply the morphing process introduced by Munn[1] to provide insight into the behavior of a helicopter's HF antenna as a function of frequency. Granger's "percent E-theta" ($\%E_\theta$) assessment parameter [2] defined as ratio of the power radiated into the E_θ field component to the total power radiated. Graphing $\%E_\theta$ as a function of frequency displays the effectiveness of the antenna for HF communication. $\%E_\theta$ vs. frequency often reveals the resonant behavior of the helicopter or other airframe[3]. In this paper, we will show that as the model evolves during the morphing process, we can associate specific airframe resonances with features of the aircraft such as the main rotor.

In this paper the metamorphosis begins with the transmission line antenna and its image in the aircraft skin isolated in free space, and ends with a 1-metre wire-grid model of the full Cormorant helicopter. All of the models used in this paper adhere to the modeling guidelines introduced in Ref. [1] and conform to the integrity checks described in Ref. [4].

Tranline Alone

Figure 1 shows the tranline antenna, with its image in the aircraft skin explicitly represented with wires. The image wires are located the same distance behind the aircraft skin as the distance of the antenna wires in front of the skin. We see that $\%E_\theta$ curve rises steadily from 2 and 30 MHz. The loop path would be a full wavelength at ... MHz, at which the antenna has its first resonance. In the HF band the antenna is well below resonance. Only about 28% of the field is radiated into the E_θ polarization as the primarily-horizontal loop radiates E_θ primarily. The fraction of the power radiated into E_θ increases with frequency.

Tranline on the Cylinder

The next step in the morphing process is to introduce a cylinder representing the fuselage of the helicopter. We start with the tranline antenna centered on a cylinder of radius 1.5 m and length 11.5 m.

The $\%E_\theta$ vs. frequency curve is not greatly different for the antenna on the cylinder than isolated (with its image) in free space. In Fig. 2 the value of $\%E_\theta$ at 2 MHz is about the same at about 9% as in Fig. 1, but around 10 MHz we see a distinct plateau. We increase the length of the "nose" of the cylinder until the cylinder is 18 m long, representing the helicopter's length. This cylinder can enclose the entire helicopter excluding the engines, rotors, sponsons and the horizontal and vertical stabilizers, and has the tranline antenna positioned as it is on the helicopter. As the cylinder's length increases, the curve of Fig. 2 gradually changes into that of Fig. 3, in which there are two distinct plateaus, one that is a continuation of the 10 MHz plateau from Fig. 2 and a second plateau above 22 MHz. This suggests that the position of the antenna in relation to the ends of the cylinder defines the frequency bands where the antenna performance is best. This also suggests that given the freedom to position the tranline antenna anywhere on the helicopter, the antenna engineer could control the frequency range where $\%E_\theta$ is optimized.

Adding the Tail Rotor Blades

The next stage in the simple model development is the addition of the tail rotor. Fig. 4 shows that the changes brought about by adding a support wire representing the vertical stabilizer and the top blade of the tail rotor are quire small. This support wire is not a part of the final model but only provides a means of attachment for the tail rotor to ensure that the morphing guideline regarding distance from feed point to the center of the tail rotor is met. This support itself does not have a significant effect on $\%E_\theta$, because it stands a quarter-wave tall at 55 MHz. But when the top, vertical tail rotor blade is added as in Fig. 4, the leading edge of the high frequency plateau is shifted down in frequency to approximately 20 MHz. This has the effect of broadening the plateau and increasing the slope preceding it. This can be explained by the fact that the distance from the tip of the blade to the base of the tail rotor support is 3.76m which is equal to a quarter wavelength at 19.94 MHz. The resonance of this vertical wire structure strongly affects the fraction of the power radiated into E_θ .

The addition of the remaining tail rotor blades, Fig. 5, has the effect of decreasing the $\%E_\theta$ between 18 and 22 MHz. The current on the support wire is now split among the four rotor blades, two of which are horizontal, and primarily radiate E_ϕ , so the fraction of the power radiated into E_θ is reduced.

Main Rotor Blades

The next step in the morphing process is the addition of the main rotor blade. We begin with the main rotor drive shaft. This addition, much like the tail rotor support wire, has no visible effect on $\%E_\theta$. Its short length makes this wire resonant at frequencies much higher than the HF range. But as we "grow" the five main rotor blades, the resonant frequency comes down into the HF range and has a major effect on the frequency dependence of $\%E_\theta$.

Figures 6, 7 and 8 show the $\%E_\theta$ for increasing lengths of main rotor blade. With 1 m blades, the main rotor introduces a resonance around 22 MHz, which is quite broad, shown in Fig. 6. With 2 m blades, Fig. 7, the resonant frequency has come down to about 14.5 MHz and is narrower. The frequency of the peak is that at which the path length from the base of the rotor shaft to the tip of the rotor blade is a quarter of the wavelength. The shaft carries a large current which splits up into five parts at the center of the rotor. The large current on the vertical shaft radiates E_θ effectively. Fig. 8 shows the $\%E_\theta$ curve with full-length rotor blades. The frequency dependence is now quite

complex. There is a tall, narrow resonance peak at about 7 MHz, followed by a doublet feature with a peak at about 8 MHz and a sharp trough at about 10 MHz. The path from the tip of a rotor blade to the tip of another is a half-wavelength at 9.55 MHz; this may be associated with the doublet feature.

Adding The Sponsons

The sponsons were added to the cylinder in three stages. At the first step the sponsons protrude 0.15 m beyond the side of the cylinder; at the second, 0.5m; and at the third step 0.775 m beyond the cylinder, as shown in Figure 9. The $\%E_\theta$ curve shows the most significant effect of the sponsons is the development of a peak at 16 MHz. Other investigations, doing the morphing in a different sequence, suggest that this peak is created through interaction of the sponsons with the tail rotor. There are lesser effects of the sponsons on $\%E_\theta$ such as a slight increase below 10 MHz and slight decrease around 26.5 MHz. Increasing the size of the sponsons has the effect of increasing the size of the maximum at 16 MHz and slightly lowering the $\%E_\theta$ above 24 MHz.

The Rear Ramp and Tail

Figure 10 shows the effect of changing the aft section of the cylinder to model the rear ramp and tail of the helicopter more precisely. The effect this modification is to increase the height of the peak located between 15 and 20 MHz. A secondary effect is the slight increase in $\%E_\theta$ at all frequencies above 11 MHz. In general making a structure thinner increases the magnitude of resonance effects but tends to decrease the bandwidth.

The Engine Nacelles

The next stage of the model development is the build up of the engine nacelles. The Cormorant helicopter has three engines, one aligned along the centerline and one angled out to each side. Explicitly modeling the engine nacelles shortens the rotor shaft from 1.3 m to 0.3 m, replacing a 1 m thin wire with the box representing the nacelles. This has a dramatic effect on the current flow in this part of the structure and in turn on the fraction of the field radiated into E_θ . Figure 11 shows the $\%E_\theta$ curve for the fully developed engine nacelles. This has the effect of shifting the sharp maximum associated with the main rotor blades up in frequency to 9 MHz and decreasing its height. It also changes the doublet first seen in Fig. 8. There is now a small maximum at 11 MHz. The higher frequency behavior is changed as well, with a new, broad maximum at 25 MHz.

The Vertical Stabilizer

The vertical support wire for the tail rotor is expanded in Figure 12 into a representation of the surfaces of the vertical stabilizer. This modification has the effect of broadening and shifting the maximum from 17 MHz to 18 MHz, which now envelops the maximum located at 25 MHz. This reaffirms the concept mentioned earlier that the large maximum, which first appeared with the sponsons, is a product of interaction between the sponsons and the tail rotor.

Tapering the Nose

Figure 13 shows the model with the front 2.5 m tapered. This represents the portion of the main cylinder that comprises the cockpit on the helicopter. The rotor maximum on the $\%E_\theta$ curve has shifted up in frequency to 9.6 MHz and has increased to 60.75 %. The minimum next to it has decreased to 30 % and the maximum at 10.2 MHz has increased to 35 %. The maximum at 12 MHz is

decreased to 30.8%.

The significant effect on $\%E_\theta$ by the tapering of the nose has been the frequency shift and increase in magnitude of the rotor maximum. Inspection of the current distribution for the models involved reveal that the path length for current flow along the centerline wire on top of the forward portion of the cylinder is decreased, which has the effect of raising the frequency.

The Complete Cormorant Model

Figure 14 shows the $\%E_\theta$ curve for the Cormorant helicopter modelled with a 1m wire-grid. The frequency dependence of $\%E_\theta$ for the wire-grid model of the actual helicopter shape is remarkably close to that of the cone-cylinder-box model in Fig. 13. All the main features of the curve are present in the simplified model.

Conclusion

In Ref. [1] we examined the radiation pattern of the tranline antenna at one frequency, as the cylinder model was evolved into the helicopter. In this paper, we have looked at the frequency dependence of the fraction of the power that the tranline radiates into E_θ as the cylinder is morphed into the helicopter. In the oral presentation, a movie will be shown, illustrating the smooth changes in the $\%E_\theta$ curve as features are gradually added to morph the cylinder into the helicopter. Figs. 1 to 14 are individual frames from the movie.

The morphing process is useful in clearly associating certain features of the frequency dependence with geometrical features of the helicopter. The most obvious is the sharp resonance at about 9 MHz, associated with a quarter-wave path from the base of the rotor shaft to the tip of the blade. Less obvious is the broad peak at about 18 MHz, which is associated with a path including the sponsons, the aft fuselage and the tail rotor.

References

- [1] [1] D.R. Munn and C.W. Trueman, "Improving Model Confidence Through Metamorphosis", ACES 2000.
- [2] J.V. Granger; *System Considerations in Aircraft Antenna Design*; I.R.E. Transactions on Airborne Electronics, Vol. AE-1, pp1-12, December 1951
- [3] [2] S.J. Kubina, C.W. Trueman, Q. Luu and D. Gaudine, "Visualization Aids for Effective Aircraft Antenna Simulations" Proceedings ACES, Monterey CA, March 1998.
- [4] C.W. Trueman and S.J. Kubina, "Verifying Wire-Grid Model Integrity with Program CHECK". ACES Journal Vol.5, No. 2, Winter 1990

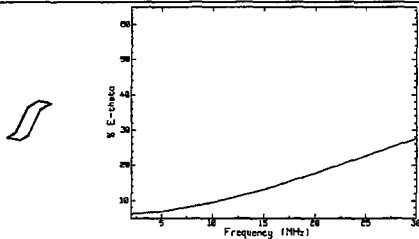


Figure 1 % E_θ of the tranline antenna in free space.

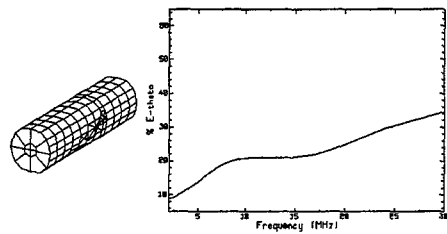


Figure 2 % E_θ for the antenna on an 11.5 m cylinder.

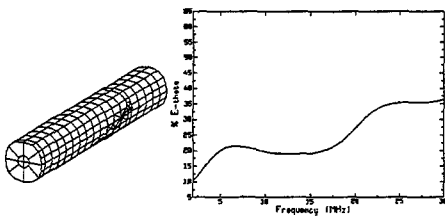


Figure 3 % E_θ for antenna and 18 m cylinder.

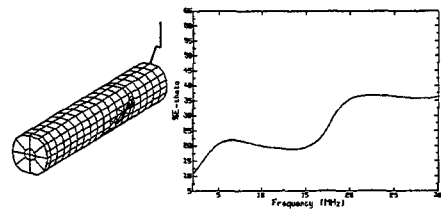


Figure 4: % E_θ of model with one tail rotor blade.

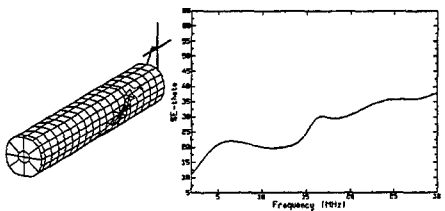


Figure 5 % E_θ of model with four tail rotor blades.

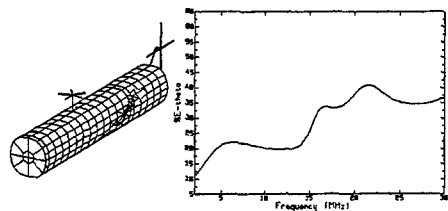


Figure 6 % E_θ for model with 1m main rotor blades.

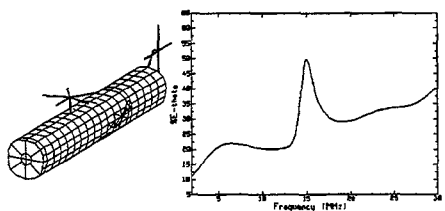


Figure 7 % E_θ for model with 2m main rotor blades.

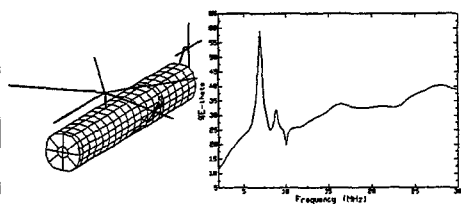


Figure 8 % E_θ with 7.85 m, full length main rotor blades.

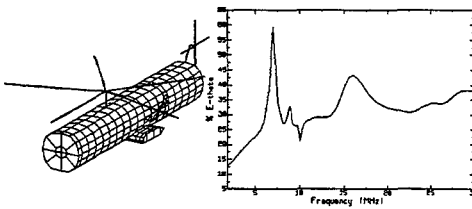


Figure 9 % E_θ for model with 0.775m sponsons

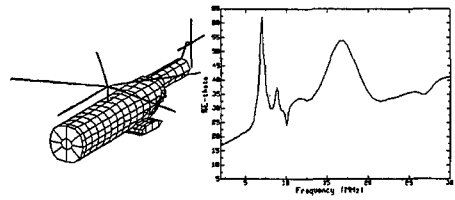


Figure 10 % E_θ for model with rear ramp fully developed.

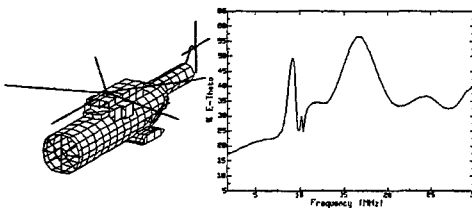


Figure 11 % E_θ for model with full engine nacelles.

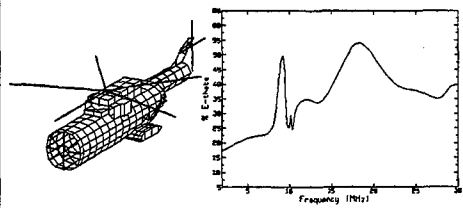


Figure 12: % E_θ for the model with the vertical stabilizer added.

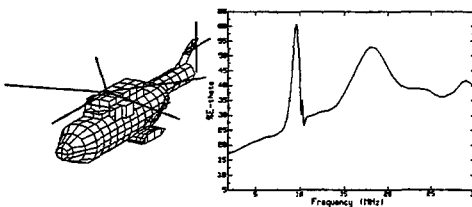


Figure 13 % E_θ for the model with the front 2.5m tapered

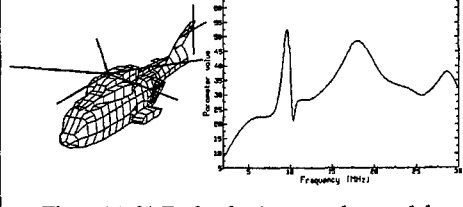


Figure 14 % E_θ for the 1m complex model

3D Modeling of Complex Helicopter Structures: Predictions and Measurements *

Anastasis C. Polycarpou, Dong-Ho Han, Stavros V. Georgakopoulos
and Constantine A. Balanis

Tel: (480) 965-3909, Fax: (480) 965-8325, E-mail: balanis@asu.edu
Department of Electrical Engineering, Telecommunications Research Center
Arizona State University, Tempe, AZ 85287-7206

I. Introduction

With the most recent advances in wireless communications, helicopters have become carriers of several transmitting and receiving antennas which constantly exchange information with other aircraft, satellites and ground stations. In many cases, air-to-ground communication occurs when the helicopter is flying at low altitudes over forest areas and rough terrain. Therefore, the gain of the transmitting or receiving signal may be severely reduced. In other cases, voice communication may be adversely affected by the rotation of the rotors since rotor rotation often generates a Doppler effect which impairs the spectrum of the voice signal. Another challenge in helicopter electromagnetics is the design of efficient and practical high-frequency (HF) antennas, as well as other types of antennas including those operating within the very-high-frequency (VHF) and ultra-high-frequency (UHF) bands. A few examples of helicopter antennas include towel-bar loops and inverted L's, blades, tilted whips, slots and microstrip patches. The towel-bar antennas are mainly used at HF frequencies for *beyond line-of-side* (BLOS) voice communications, primarily using the *near-vertical-incidence skywave* (NVIS) mode. The latter utilizes the properties of the ionosphere at low frequencies (2-10 MHz) to direct the signal over mountains at distances up to 300 km. For VHF communications, whips and blades are the antenna types often used. For UHF communications, such as satellite and GPS (global positioning system), microstrip patch and slot antennas are the most suitable. Some of the reasons include low profile, lightweight, small size and conformability. Designing, analyzing and optimizing radiation characteristics of antennas mounted on a structurally complex helicopter airframe are challenging tasks. The electrical length, shape and position of the antenna on the airframe strongly affect its radiation characteristics and performance.

Electromagnetic analysis of helicopter antennas mandates computationally efficient and accurate numerical methods. Numerical efficiency is extremely important because of the enormous size of the computational domain. In this paper, three well-known numerical methods were used to analyze primarily HF and VHF antennas on two different helicopters. These methods include the finite-difference time-domain (FDTD) method, the finite element method (FEM) and the method of moments (MoM), specifically the *NEC* code. Numerical predictions are compared with measurements performed in the electromagnetic anechoic chamber (EMAC) of Arizona State University (ASU).

*This work was sponsored by the Advanced Helicopter Electromagnetics Industrial Associates Program and NASA Grand NAG-1-1082.

II. HF Towel-Bar Antennas

In this section, the radiation characteristics of HF antennas mounted on a 10:1 scaled helicopter (NASA model) and a full-scale helicopter (Apache) are examined using the FDTD method, the FEM, the NEC [1] and measurements. Self/mutual impedances and radiation patterns are computed for frequencies within the HF band.

A. Nasa Scale Helicopter Model

Analysis of HF towel-bar antennas is performed on the NASA scale helicopter model shown in Figure 1. This figure shows two HF wire loops mounted on the tail boom of the NASA helicopter, which is approximately a 10:1 scale model of the full-length helicopter. The HF loops are also scaled down by a factor of 10 whereas the HF frequency band is scaled up by the same factor. In other words, the HF characteristics of these two loops must be computed in a frequency band between 30 and 300 MHz instead of 3 and 30 MHz. This scaling in frequency is valid provided the material properties of the helicopter are lossless.

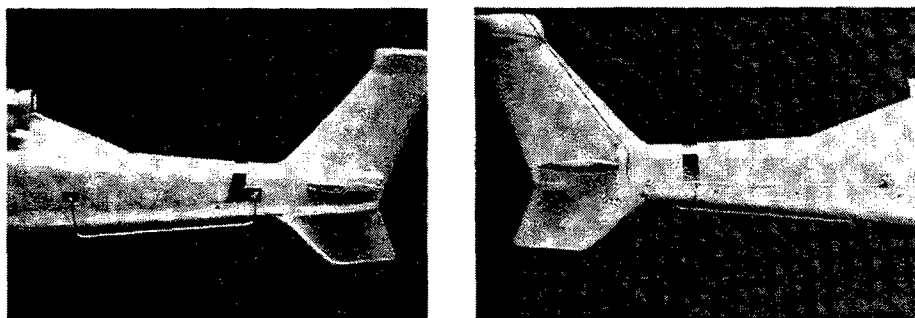


Figure 1: Two sideviews of the 14-ft and 24-ft scaled towel-bar antennas mounted on the tail boom of the NASA scale helicopter model.

The photograph on the left illustrates the 14-ft scaled towel-bar antenna mounted on the port side of the helicopter, whereas the photograph on the right illustrates the 24-ft scaled towel-bar antenna mounted on the starboard side of the helicopter. The 24-ft scaled towel-bar antenna extends all the way to the tip of the vertical stabilizer. Initially, the rotor blades of the helicopter were not included in the simulation. The analysis of the two HF loops on the helicopter was performed using the FDTD, the FEM and the NEC. The aim of this analysis was to compute self and mutual impedances as well as the S-parameters of the two-antenna system.

Using the FDTD, the cell size was 10 mm and the computational space was $82 \times 186 \times 58$ cells. Voltage sources with internal resistors were used at the input terminals of the antennas to reduce the total number of time steps required. Internal resistors are utilized when the antennas are highly resonant since the transient currents often decay very slowly as a function of time. The total number of time steps used was 7,000. Using the FEM, an unstructured grid composed of linear tetrahedral elements was used to model the helicopter and the surrounding free space. A total number of 214,677 tetrahedrons and 290,150 unknowns were used to model the geometry. The number of non-zero entries in the FEM matrix was 4.6 million whereas the average edge length of the mesh was 50 mm. Using the NEC, a wire grid was used to discretize the helicopter and the two HF antennas. Near the attachment

points, the grid was extremely fine in order to model better the current flow from the antennas to the helicopter frame. The average grid size was 50 mm whereas the total number of unknowns was 2,133. Note that the resulting FEM matrix is sparse whereas the resulting NEC matrix is dense.

The input impedance of the 14-ft loop was computed versus frequency using the FDTD, the FEM and the NEC. The numerical predictions, as those are compared with measurements performed in the EMAC of ASU, are shown in Figure 2 for both real and imaginary parts. Note that the frequency range of interest is scaled up by a factor of 10. The comparison among all four data sets illustrates a good agreement. The predictions by the NEC are the closest to the measurements which is attributed to a better geometry representation of the actual HF antenna. Both the FDTD and the FEM predict the parallel resonance as being shifted slightly toward lower frequencies. The reason is related to the complexity of drafting this loop antenna on the helicopter model; the overall length of the antenna model is slightly different from that of the actual element.

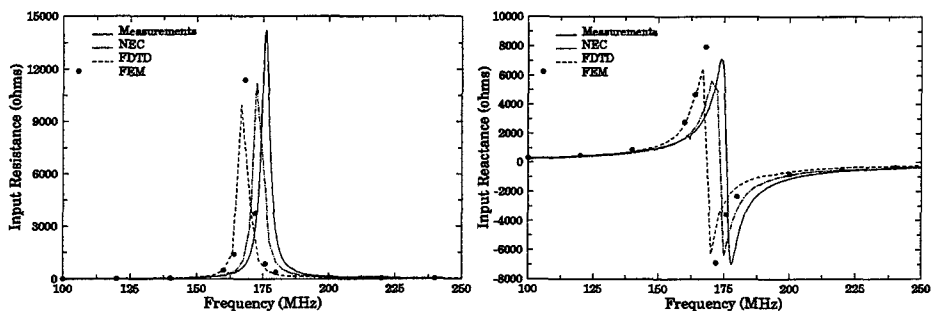


Figure 2: Input impedance of a 14-ft scaled towel-bar antenna mounted on the tail boom of the NASA scale helicopter model.

Besides input impedance, mutual coupling between two antennas is also of great significance because interference and noise can potentially destroy signal integrity and detection. The mutual coupling, S_{12} , between the 14-ft and the 24-ft antennas is calculated within the frequency range of interest using primarily the FDTD [2]. The predicted data, obtained with and without the rotors, are compared with measurements performed in the absence of the rotors. As illustrated in Figure 3, the predicted data agree fairly well with the measurements. It is interesting to point out that the mutual coupling between the two HF loops is lower than -30 dB with a local maximum near 200 MHz. Note also that the presence of the rotors might have a small effect on the mutual coupling between the two antennas especially when the total length of the blades corresponds to odd multiples of a wavelength.

B. Apache (AH-64) Helicopter

The Apache is another helicopter that we simulated. A 14-ft loop antenna and a 24-ft inverted-L antenna are shown in Figure 4 as those are mounted on the tail boom of the helicopter. In this section, only the radiation patterns for the 14-ft loop antenna will be examined. The principal gain patterns, excluding any mismatch losses, are computed using both the FEM and the FDTD. The comparisons for all three principal patterns, namely roll, pitch and yaw, are shown in Figure 5. The agreement between the two methods is excellent even though the geometry is complex. The minor discrepancies observed for the yaw planes might be attributed to the staircasing of the FDTD method, possible non-physical

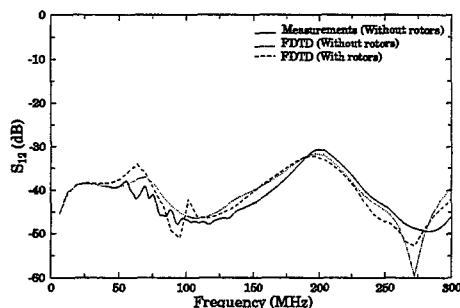


Figure 3: S_{12} between the 14-ft and 24-ft towel-bar antennas on the NASA scale helicopter model.

reflections from the absorbing boundary conditions (ABC's) in either method, or finite discretization errors. It should be emphasize here that the FDTD predictions were obtained based on a $\lambda_o/79$ cubical cell at 30 MHz, whereas the FEM predictions were obtained based on an average edge length of $\lambda_o/50$ near the fuselage and $\lambda_o/12.5$ near the ABC's.

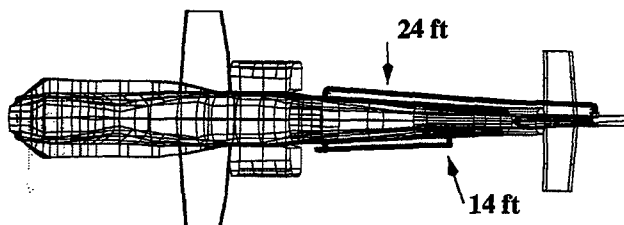


Figure 4: Towel-bar antennas on the Apache full-scale helicopter.

III. Rotor Modulation

Rotor modulation on the magnitude and phase of the radiation gain pattern of an HF antenna mounted on the tail boom of the NASA scale helicopter model is examined in this section. The helicopter, which is scaled down by a factor of 10, is shown in Figure 6 (a) with a 14-ft wire loop antenna mounted on its tail. HF antennas are often used in the *near-vertical-incidence skywave* (NVIS) mode. In this mode, the radiated pattern should exhibit a maximum toward zenith. The gain pattern along a conical contour ($\theta = 40^\circ$) is plotted in Figure 6 (b) for both vertical and horizontal polarizations. The orientation of the blades is such that one pair is aligned with the main body of the fuselage. It is quite interesting to observe that at this frequency, which is also true for all frequencies in the low HF band, one polarization complements the other. Specifically, the vertical polarization exhibits a maximum toward the nose and tail whereas a minimum occurs toward the sides of the helicopter. On the other hand, the horizontal polarization exhibits a maximum toward the sides of the helicopter whereas a minimum occurs toward the nose and tail. Therefore, the total gain is close to an omnidirectional pattern which is extremely desirable for HF communications in the NVIS mode.

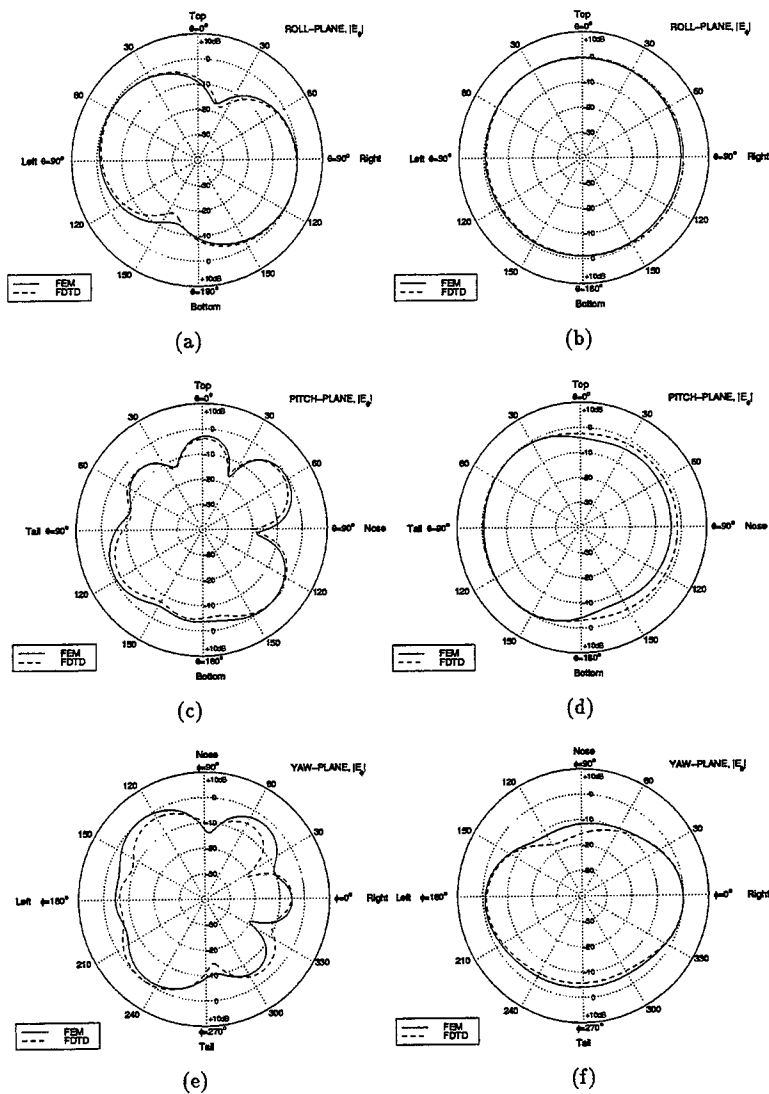


Figure 5: Gain patterns (excluding the mismatch loss) of the 14-ft towel-bar antenna on the Apache helicopter at 24.13 MHz. (a) roll plane (vertical polarization); (b) roll plane (horizontal polarization) (c) pitch plane (vertical polarization); (d) pitch plane (horizontal polarization) (e) yaw plane (vertical polarization); (f) yaw plane (horizontal polarization).

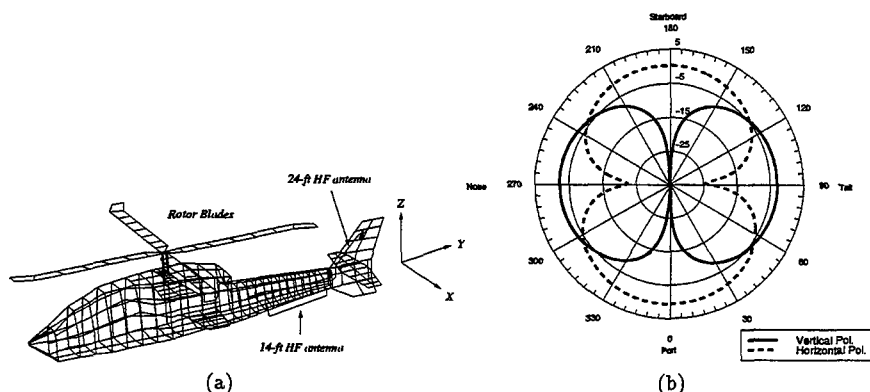


Figure 6: (a) Wire-grid model of the 10:1 scaled NASA helicopter, (b) Conical yaw-plane pattern at $\theta = 40^\circ$ and $f = 60$ MHz.

The main purpose of this investigation is to quantify the modulation on the magnitude and phase of the radiation pattern as the rotors are spinning about an axis. The level of rotor modulation on the magnitude of the vertical gain pattern is depicted versus frequency in Figure 7 (a) for the vertical polarization at an observation point specified by an elevation angle $\theta = 40^\circ$ and an azimuth angle $\phi = 90^\circ$. The maximum gain is also shown in these graphs in order to provide a point of reference. As illustrated in the graph, the rotor modulation level for frequencies below 80 MHz is very small to affect communication; however, at 90 MHz where a deep null in the vertical gain occurs, the maximum rotor modulation level is substantial (almost 20 dB). At approximately 104 MHz there is another peak for the maximum rotor modulation level; this peak is about 5 dB. The frequency it occurs corresponds to a pair of rotor blades with electrical length of half a wavelength.

A similar graph, but plotting the horizontal gain instead of the vertical gain at an azimuth angle of 0 degrees (port side) and elevation angle of 40 degrees, is shown in Figure 7 (b). Note that according to Figure 6 (b), the horizontal polarization toward the port side of the helicopter is the co-polarized component. The corresponding modulation due to the rotor blades is maintained at negligible levels for frequencies below 90 MHz. At 104 MHz, where the length of a pair of blades becomes equal to half a wavelength, the maximum modulation on the horizontal gain in the port-side direction attains values equal to 25 dB, which is a substantially larger variation compared to that of the vertical gain. In other words, in the frequency vicinity of blade resonance, meaning when the total length of a pair of blades becomes half a wavelength, the horizontal gain toward the port/starboard directions of the helicopter is more susceptible to rotor modulation than the corresponding vertical gain toward the nose/tail directions of the helicopter.

IV. Ground Effects

When helicopters fly at low altitudes, ground effects on the antenna radiation patterns should not be neglected, especially at the HF and VHF frequency bands. In this section, the effects of ground parameters on the radiation patterns of an antenna mounted on a helicopter are investigated using the FEM. The computational difficulty of the problem is simplified considerably by adopting the

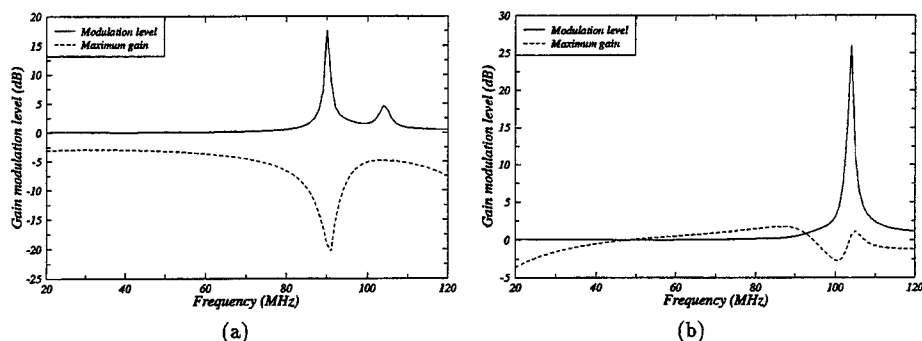


Figure 7: Maximum modulation level on the gain of the 14-ft HF loop antenna mounted on the tail boom of the NASA scale helicopter model. The observation point corresponds to an elevation angle of $\theta = 40^\circ$. (a) Vertical pol. at $\phi = 90^\circ$ (tail side), (b) Horizontal pol. at $\phi = 0^\circ$ (port side).

Equivalence principle and Norton's approximation [3]. This approach was validated for simple Hertzian dipoles located above a lossy ground [4].

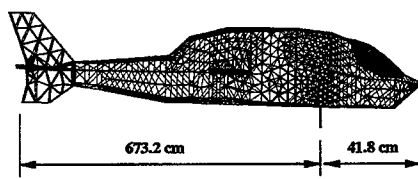


Figure 8: Discretized model of the NASA helicopter.

The ground effects on the radiation patterns of a VHF antenna mounted on the NASA scaled helicopter, whose geometry is shown in Figure 8, are investigated in this section. The VHF antenna configuration corresponds to a 12.75-cm monopole mounted on the front-bottom part of the helicopter. The height of the helicopter, measured from the ground level to the feed point of the antenna, is either $\lambda_o/4$ or $\lambda_o/2$, where λ_o is computed at a frequency of 500 MHz. As for ground specifications, two cases are examined: one with dry soil, which has $\sigma = 0.001[S/m]$ and $\epsilon_r = 3$, and another one with wet soil, which has $\sigma = 0.01[S/m]$ and $\epsilon_r = 5$. However, since the helicopter is scaled down by a factor of 10 and the frequency is scaled up by the same factor, the ground conductivity needs also to be scaled up by 10. Note that scaling the conductivity is an approximation. Therefore, according to this scaling, the conductivity of the dry soil at the scaled frequency should be 0.01 [S/m] whereas the conductivity for the wet soil should be 0.1 [S/m]. The vertically polarized pitch plane gain patterns, both in the absence and presence of the ground (dry or wet soil), are shown in Figure 9 (a) for a helicopter height of $\lambda_o/4$ at 500 MHz. Compared to the free-space pattern, it is observed that the overall gain of the pattern at most observation angles has been reduced due to reflections from the ground. The most profound reduction in gain however, occurs at zenith and near grazing angles, i.e., lower than 60° . The same type of pattern is shown in Figure 9 (b) but for a helicopter height of $\lambda_o/2$ at 500 MHz. Compared to the previous case where the height was only $\lambda_o/4$, ground effects on the pattern are now weaker; thus,

the corresponding pattern closely resembles that of the free space. Ground effects on the pattern are noticeable for observation angles mainly along zenith and grazing (lower than 75°).

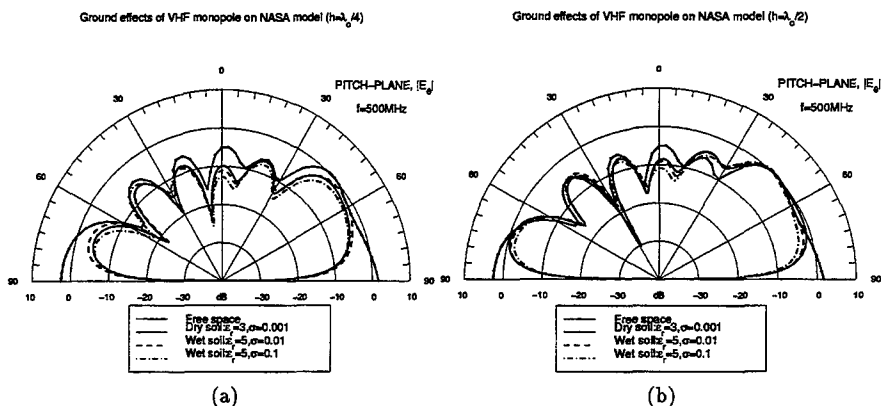


Figure 9: Ground effects on the vertically polarized pitch-plane patterns of the NASA scaled helicopter at a frequency of 500 MHz. Helicopter height is (a) $h = \lambda_0/4$, (b) $h = \lambda_0/2$.

V. Conclusions

In this paper, some major issues related with helicopter communications in the HF and VHF bands were investigated using numerical methods and measurements. These include antenna analysis, such as computation of input impedance and radiation patterns, antenna coupling, rotor modulation, and ground effects. Accurate antenna analysis is crucial in any communication system. Reduction of coupling below a given threshold is also an objective. Based on this analysis, rotor-blade rotation has a significant effect on the gain patterns of an HF towel-bar antenna especially at resonant frequencies. Although not discussed here, rotor modulation on the input resistance is also substantial [5]. It was also shown in this paper that ground may reduce the gain of a VHF helicopter antenna for elevation angles near grazing and zenith.

References

- [1] G. J. Burke and A. J. Poggio, "Numerical electromagnetics code (NEC) - method of moments," Tech. Rep. Technical Document 11, Naval Ocean Systems Center, San Diego, Calif., Jan. 1981.
- [2] S. V. Georgakopoulos, C. A. Balanis, and C. R. Birtcher, "Cosite interference between wire antennas on helicopter structures and rotor modulation effects: FDTD vs. measurements," *IEEE Trans. Electromagn. Compat.*, vol. 41, pp. 221-233, Aug. 1999.
- [3] T. Maclean and Z. Wu, *Radiowave Propagation over Ground*. London: Chapman and Hall, 1993.
- [4] J. R. Wait, "The ancient and modern history of EM ground-wave propagation," *IEEE Antennas Propagat. Magazine*, vol. 40, pp. 7-24, Oct. 1998.
- [5] A. C. Polycarpou, C. A. Balanis, and A. Stefanov, "Helicopter rotor-blade modulation of antenna radiation characteristics," *IEEE Trans. on Antennas and Propagation*, submitted.

Increasing the Productivity of NEC Analysis with Virtual Reality and 3D Laser Scanners

Kevin J. Cybert and Daniel D. Reuster
ARINC

Annapolis, MD 21401

Kcybert@arinc.com and Dreuster@arinc.com

Abstract

A new method for developing NEC wire frame models that employs a laser scanner and 3D graphic software is presented. A method for displaying NEC output data utilizing 3D graphic software and virtual reality viewers is also presented. Examples for both model development and data visualization are presented for the US Army's M-1068 and CH-47, respectively.

Wire Frame Model Generation

One of the most time consuming tasks of NEC modeling is the generation of the wire mesh models. ARINC currently uses a 3D graphics package (I-DEAS) to create wire mesh models for various numerical analysis codes. Using this graphics package allows the models to be drawn on the computer screen with a simple "point-and-click" process. The graphics package is three-dimensional, so the model can be rotated spatially to allow for easier meshing. Once the model is drawn in the graphics package, a geometric translator is used to generate an input file that can be used by NEC or GEMACS.

Inputting the basic shape of the object into the graphics package so that it can be properly meshed is still a difficult task. A volumetric representation of the object may be purchased from a commercial model house, if one is available; however, these commercial models are not generally in a form that can be directly used for the numerical modeling. Usually the commercial models are developed with ascetic appearance in mind only. For any purchased model, the accuracy of the model must be checked to verify overall size, correct components, and correct configuration. If a commercial model is not available, one has to be created from scratch using to-scale drawings. This can be a tedious and time-consuming process.

In order to obtain a more accurate surface representation for the objects which need to modeled, and to reduce the time required to create the models, ARINC is using a new laser scanner that was developed by Spatial Integrated Systems, Inc. This scanner was first used for the creation of a model for the M-1068 Command Vehicle. A good commercial model was not available nor was a complete set of drawings readily accessible. Figure 1 shows the laser scanner (black box on tripod) measuring the M-1068 vehicle.



Figure 1. M-1068 Being Laser Scanned

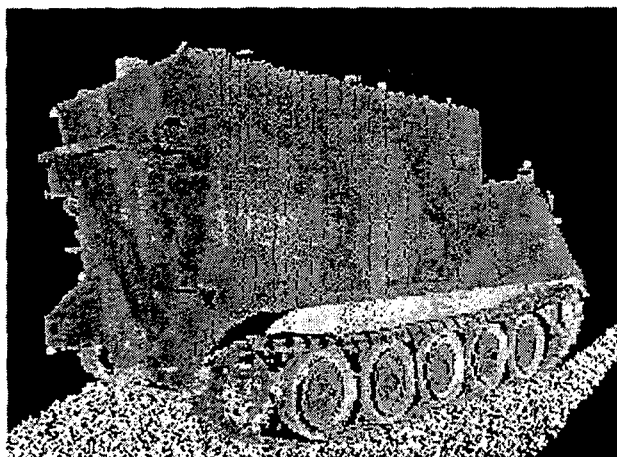


Figure 2. 2D Laser Range Image of the M-1068 from Laser Scanner

The 3D-laser scanner utilizes an artificial intelligence engine that integrates a series of 2D laser range images into a 3D virtual reality model. Figure 2 shows a 2D-laser range image for the M-1068 generated by the laser scanner. The model can be viewed using standard virtual reality technology or imported into CAD/CAM systems for engineering analysis and machining. The virtual reality image is accurate to within 1/2 inch of the dimensions of the vehicle scanned. Figure 3 shows the virtual reality image generated by the laser scanning system.

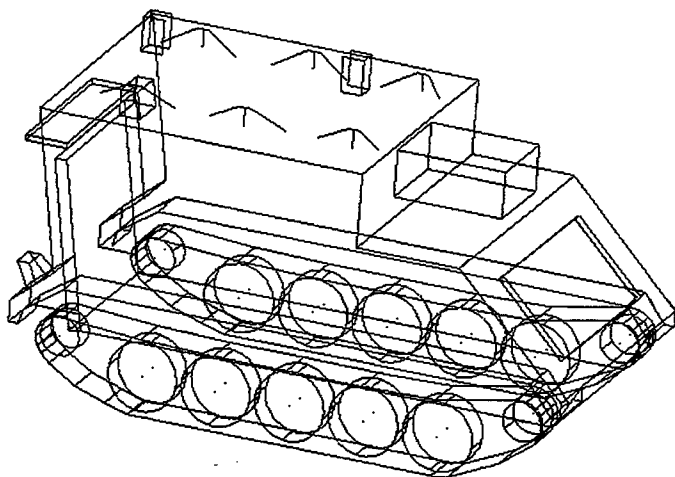


Figure 3. Virtual Reality Image of the M-1068

The virtual reality models are imported into I-DEAS for transformation into wire mesh models. By using the scanner, the wire mesh models are created from accurate representations of the vehicle. This reduces the amount of time needed to verify the accuracy and configuration of the outline model. The virtual reality model is meshed to the proper density based on the frequencies to be analyzed. Figure 4 shows the wire mesh model of the M-1068 command vehicle meshed for a frequency of 100 MHz.

The wire mesh models are used as input data for a variety of electromagnetic analysis tools, such as NEC and GEMACS. Utilizing the wire mesh models and the appropriate electromagnetic analysis tools, various radio frequency communications systems are installed, analyzed, and tested, all in virtual reality space.

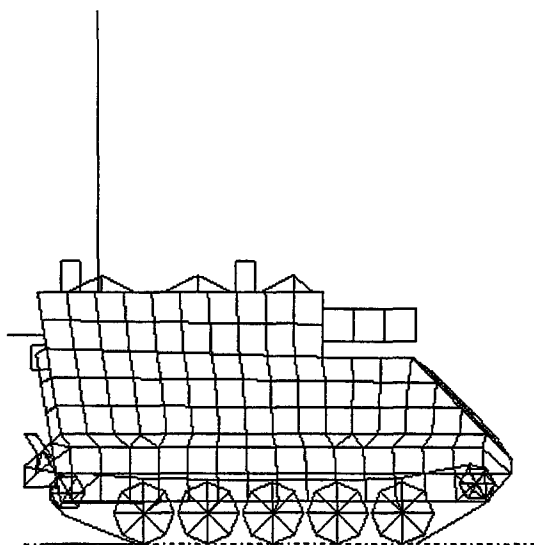


Figure 4. Wire Mesh Model of the M-1068

NEC Output Data Visualization

The US Army was experiencing dropout on its CH-47 Chinook helicopter using its HF antenna for near vertical incident skywave communications. Using this non-line-of-sight communication system, radio signals are bounced off of the upper atmosphere. ARINC was asked to help improve the near vertical incident skywave performance of the antenna. To perform this task a variety of computer modeling and visualization techniques were utilized.

The first step in the electromagnetic modeling process was to create the wire mesh model for the CH-47 and the existing antenna. The antenna was a bent towel bar antenna mounted on the left side of the helicopter. For this step, the modeling tools discussed in the previous section were utilized. Several of the antenna's performance characteristics were then studied in order to understand the antenna's overall behavior. For this type of analysis, ARINC has developed a variety of 3D virtual reality graphic interfaces that clearly depict the results of NEC and GEMACS analysis.

Figure 5 shows a computer generated radiation pattern for the existing antenna. A 3D-visualization technique was used to render the NEC analysis output and display the objects in a virtual reality viewer.

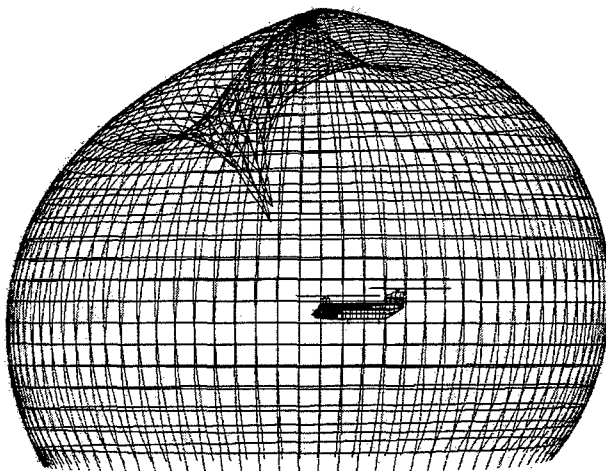


Figure 5. CH-47 HF Antenna Pattern

For near vertical incident skywave communications, the portion of the radiation pattern that is critical is from directly over the helicopter to about 40° down, and 360° about the helicopter. From Figure 5, it can be seen that there is a large null in the antenna pattern almost directly overhead. This is the area where the existing antenna was failing.

With the accuracy of the computer model thus validated, ARINC then "placed" various antenna configurations on the helicopter model in an effort to correct the problem. For the Chinook, ARINC determined the antenna that exhibited the best NVIS performance was a towel bar antenna located on the top of the fuselage. This antenna was selected after analyzing over forty alternatives.

Figure 6 shows the radiation pattern of the new towel bar antenna on top of the CH-47 helicopter. Comparing the radiation patterns of the original antenna and newly designed antenna clearly shows the improved performance of the new antenna. Not only has the large null been removed from the critical NVIS region, but the antenna gain in the NVIS region of the pattern was also improved by a factor of 100.

A newly designed antenna for the CH-47 Chinook helicopter has been placed into production and is currently being installed on the Chinook fleet.

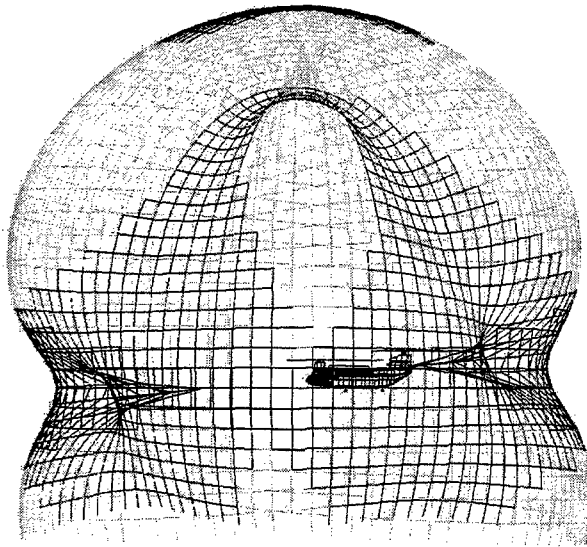


Figure 6. CH-47 Top Towel Bar Radiation Pattern

Conclusion

The process described in this paper shows how integrating laser scanners, 3D graphics packages, and virtual reality viewers into existing numerical analysis packages can lead to a successful antenna design analysis without the need for expensive prototype development. ARINC has taken the costly and risky iterative prototype development process and reduced the cost, time, and risk involved with developing new antennas.

ARINC has developed numerous wire mesh models for many different electromagnetic modeling and simulation applications and for use with various numerical analysis codes. We have performed antenna analysis and design for helicopters such as the Apache, the Blackhawk, the PaveLow, and the Kiowa Warrior; for airplanes such as the C-130 Hercules, C-2 Greyhound, Boeing 747, and EA-6BB Prowler; and for ground vehicles such as the HMMWV, the Bradley, the M1A1, and armored personnel carriers. Our efforts include near vertical incident skywave analysis, propagation and interference analysis, antenna design, and surface current and input impedance analysis. The use of laser scanners, 3D graphics packages, and virtual reality viewers greatly assists in all phases of electromagnetic analysis and design.

An interactive HTML based multimedia course on antennas

Ulrich Türk and Peter Russer

Institut für Hochfrequenztechnik, Technische Universität München
Arcisstr. 21, D-80333 Munich, Germany

tuerk@hft.ei.tum.de, <http://www.hft.e-technik.tu-muenchen.de/Lehre/MM>

Abstract

In this paper we present an interactive multimedia course on antennas for supporting education in high frequency engineering. It is mainly designed for personal use on the student's personal computer, but it can also be distributed via internet as it is based on standard internet file formats. Different media including animations and interactive 3D illustrations help students to understand the complex theory of electromagnetic fields. In many cases, computer animations of different phenomena can be changed by setting up parameters; the effects of the changes can be studied immediately.

1 Introduction

In the early 90's, educators and researchers thought of interactive books which could combine all different media types in a single document for use in education. Andries van Dam [1] had the vision of electronic books that display information in several ways of presentation and focus especially on the visual presentation of topics. Software for multimedia-based and computer-based engineering education has already been presented by several authors [3, 2, 4, 5]. These computer based-courses shift the tasks of teachers and educators from uni-directional teaching to interactive support of individual learning. Today, multimedia technology provides the ability to develop multimedia documents that realize all key ideas of multimedia, even when using average hardware. Education in engineering is a field that certainly benefits from new forms of presentation of complex topics. Especially electromagnetic engineering with its rather high-level mathematics (namely vector analysis) loses its reputation amongst students of being a difficult discipline.

Our basic idea is to develop an interactive course on phenomena of electromagnetic waves and their propagation. As a first point we demonstrate a multimedia program on antennas. In the following we describe the main concept of the course, present some technical aspects of its implementation and finally show some examples of the finished pages.

2 Concept

The goal is to create an electronic book that provides its contents in a large variety of media: text, still pictures, movies, interactive graphics and animations. Emphasis is placed on the interactive parts

of the course as those are the most attractive and also most effective elements as far as understanding is concerned. The presentation is to address both abstract as well as the visual thinking. We have determined the following requirements:

- employment of interactive elements, especially interactive animations and pictures whenever likely being of interest
- fast response time of the interactive objects
- presentation of the necessary theory combined with examples and applications
- short and clear sections
- several levels of detail when presenting topics including a starting page naming the main points of a section, hyperlinks in the section to more detailed informations, closing page with summary
- demonstrative presentation of the mathematical derivations
- a platform-independent implementation designed to run "off-line"
- sophisticated navigation support for the user.

The last item is vital for documents based on hyperlinks, as without a clear document structure the user feels quickly "lost in hyperspace". Therefore we spent quite some effort on clear and smart controls for browsing the course.

3 Technical aspects

As the development of multimedia products is both expensive and time consuming we decided to declare the portability between different platforms as one principal goal. Currently the standard internet markup language HTML is the only option for real cross-platform presentation of multimedia contents. The design of the course restricts the choice of browsers to the two mainly used browsers, Netscape Navigator and Microsoft Internet Explorer, both of version 4 or higher. These browser support CSS style sheets which are extensively used for the definition of the layout. Still pictures are supplied in GIF format, simple animations are made of a series of single pictures. More complex animations are stored in Apple Quicktime format, the interactive 3D graphics are supplied as VRML files that are displayed by specialized plug-ins. Dynamic control of the multimedia elements as well as the navigation controls are programmed with Javascript. All illustrations and animations that are based on computational calculation are created with Matlab.

As mentioned before, the use of these open standard formats offers the advantage of portability between different platforms. In addition they include the ability to realize the user interface rapidly. A drawback is the fact that it is not easy to implement or integrate extra tools, like e.g. field simulators written in Java or commercial CAE software. Unfortunately there are still many problems caused when running Java programs on different platforms. A tradeoff between the different possibilities lead to the method of precomputed data for most of the interactive illustrations and animations. Especially when exploring the effects of changing parameters on certain phenomena, the user must choose from a list of discrete values for the parameters rather than setting the parameters freely. As a compensation the user gets immediate access to the new data without having to wait for calculations to take place.

4 Structure of the course

Hyperlink-based media imply various ways to read or browse the document respectively. This demands to let the user choose his preferred way of exploring the document. We decided to offer two ways of navigation: a free mode and a guided tour mode. In the free mode the user can either follow the linear structure of the chained pages, like one would use a book starting at the beginning and following the pages, or quickly steer to certain sections using the pull-down menus. The guided tour offers a choice of the pages which give a broad and general overview about antennas. Users running the tour can store links to sections of their interest and explore them later more accurately.

Easy and fast access to the information is accomplished by presenting the topics on several levels of detail: a starting page will describe the main points of the sections with hyperlinks to different paragraphs, the pages of the section contain hyperlinks to more detailed information, e.g. derivations of formulas or additional examples and a final page summarizes the contents. In the tour mode there is - depending on the settings - a checkup for a personal feedback about the progress made. The same level of detail mechanism used in the general structure applies also to the visual elements. Normally only still pictures are shown in the document. By user action these illustrations are replaced by their time-varying or interactive versions. This strategy speeds up browsing the pages.

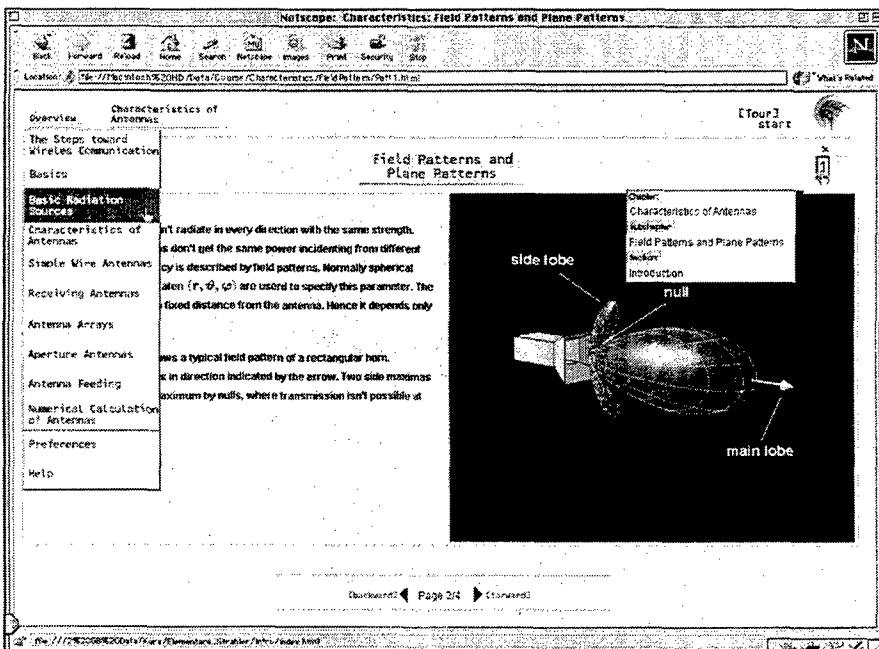


Figure 1: Basic layout of a page; on the left an opened pulldown menu, on the right an opened info box of a bookmark

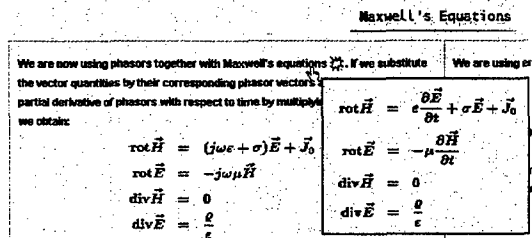


Figure 2: Pop-up box showing additional information

5 Samples of the user interface and the content

The topics treated in the course range from a short historical review of the discovery of electromagnetic waves and the first wireless transmission to a short review of fundamentals of electromagnetic theory and to the main part, antennas. Here different types of antennas are presented, starting from elementary emitters like e.g. the Hertzian dipole, presenting different forms of wire and aperture antennas together with their typical properties, treating antenna arrays and problems for feeding of antennas and ending with a section on numerical calculation of radiation fields.

The basic layout of the pages is shown in figure 1. The central area with the actual page content is

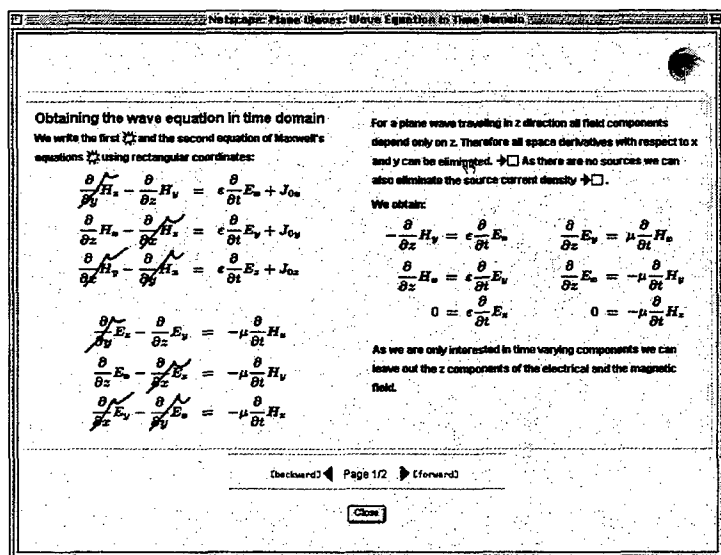


Figure 3: Derivation of plane waves in lossless medium

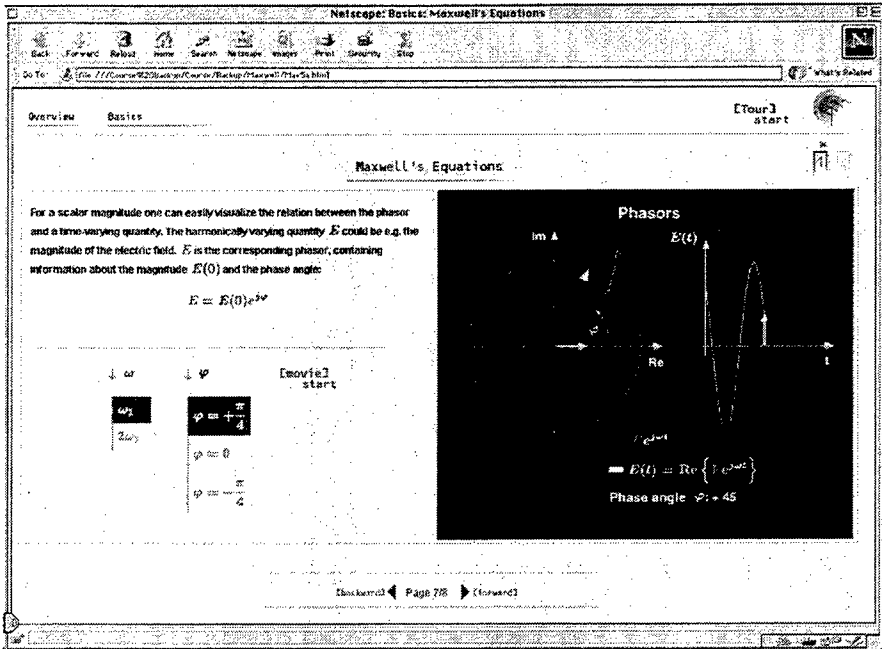


Figure 4: Interactive movies showing complex phasors; the two parameters can be set on the left side

divided into two parts. Most of the pages consist of a visual element on the right side and a descriptive part on the left side. Above and below this content area the navigation controls are located. On the upper left we can see the two pull-down menus which give quick access to the chapters and subchapter of the course. The chapter menu contains in addition a help item and access to the configuration page of the program. On the right side of the top line we find an icon to launch the tour mode and a popup search menu residing behind the logo icon. Below these two parts are two "smart" bookmark controls that will substitute the rather clumsy bookmark mechanism implemented in the browsers. A click on one of the two bookmark bins stores a link to the current page. It can be followed later on by simply clicking it again. Just pointing the mouse over the bin displays a small box containing information about the page that has been bookmarked and which content it has (see figure 1). The navigation bar on the bottom of the window provides the basic functions of browsing forward and backwards. When switched to the tour mode, additional information about the progress in the tour is shown.

Besides well-known hyperlinks the text of the pages contains also areas for activating popup infos. Figure 2 shows how the user can easily recall Maxwell's Equations and follow the further mathematical transformations. These elements are extensively used throughout the course. They give quick access to information that is crucial for the understanding and might otherwise be hidden behind phrases like "... as we can derive from formula x.y on page z ...".

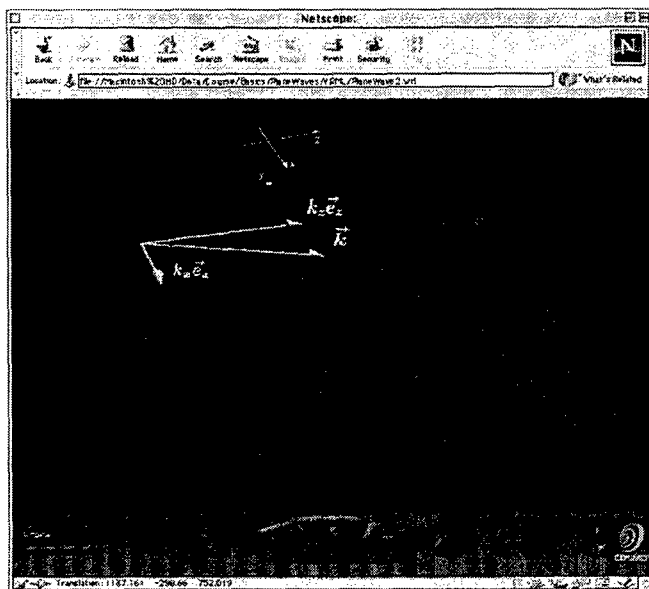


Figure 5: VRML-Animation showing a plane wave in lossy medium. The user can change his point of view while the animation is running.

To some extent, even the mathematical transformations are made interactive. Figure 3 shows an example explaining the derivation of the fields of a planar wave propagating in z -direction. A click on the corresponding area in the text crosses out all terms depending on coordinates other than z . Figure 4 shows how the user can set parameters and watch their effects in an animation.

All pictures showing spatial objects can be replaced by an interactive 3D-graphics programmed in VRML. The user can move freely around and change his point of view even while an animation is running. Some interesting prestored viewpoints can be easily recalled in order to navigate faster. In our example (figure 5), one of these viewpoints is a side view of the wave where one can clearly recognize the exponential decay of the amplitude.

6 Summary and outlook

We have presented an interactive multimedia course on antennas that can help combining abstract and imaginary concepts and thereby make learning more effective. The extensive use of 3D illustrations that can be explored by the user supports students enormously in understanding the complex theory behind high frequency engineering. In some lessons we have already presented some VRML graphics regarding antenna patterns and found that these interactive graphics helped students enormously in understanding. The vivid interest from the students' side encouraged us to use these visualization techniques more frequently.

7 Acknowledgment

We would like to thank the Bavarian State Department for supporting this research project.

References

- [1] van Dam, A., "Electronic Books and Interactive Illustrations - Transcript of a Talk" in *Interactive Learning Through Visualization*. Springer, 1992
- [2] Garner, D., "Visual EMag: A 2-D Electromagnetic Simulator for Undergraduates", *14th Annual Review of Progress in Applied Computational Electromagnetics 1998, Conference Proceedings*, pp. 581-582.
- [3] Miller, E. K., "Visualization: A Powerful Tool for Understanding Electromagnetics", *13th Annual Review of Progress in Applied Computational Electromagnetics 1997, Conference Proceedings*, pp. 2-7.
- [4] Iskander, M. F., "Multimedia- and Computer-Based Engineering Education", *Proceedings of the 29th European Microwave Conference 1999 (EuMC'99), Munich, Germany*, pp. 90-92.
- [5] Hoefer, W., "The Effective Use of Computer Modeling and Visualization in Microwave Education", *Proceedings of the 29th European Microwave Conference 1999 (EuMC'99), Munich, Germany*, pp. 86-89.

SESSION 8

EMC

Chairs: Bruce Archambeault and Jim Drewniak

Adding Imperfections to EMC FDTD Models as a Means of Increasing Accuracy

Colin E. Brench

Compaq Computer Corporation
200 Forest Street, Marlborough, MA 01752

Abstract: Those involved with the computer modeling of electromagnetic phenomena are usually looking to create the most precise and accurate models possible. There are many aids to this work that will lead to the creation of regular, aligned, and neat structures. While in some areas this is a definite advantage, to the EMC engineer, it can be the source of a surprising number of errors. Identifying these problem areas and ways to avoid them are discussed in this paper.

Introduction

EMC engineering unlike many other EM disciplines is not an exact science. By the very nature of the practical problems faced, there are always a great many unknowns, and frequently only very specific portions of a problem are modeled. Over the past ten years a number of modeling problems that seemed to have been properly solved, some even verified experimentally, have been found to be in error. The computational results were absolutely correct for each of these simulations; however, the models used were not exact representations of the problems. The perfection inherent in the creation process resulted in models much more geometrically accurate than reality. Such perfect models can be a surprisingly large source of error or, at the very least, cause vital information to be missed. These "perfect" properties are:

1. alignment to a perfect grid
2. purely polarized sources
3. symmetry
4. ideal source impedance
5. non-invasive field monitor points

All of these problems were discovered during FDTD modeling, by the author and others well experienced in EMC modeling. FDTD codes, by their broadband nature, are particularly sensitive to resonance effects. Due to the rectangular grid used to create the models, all of the elements of the FDTD model are perfectly aligned. This has a result of enhancing resonance effects and creating other problems. There is no doubt that these or similar problems could occur with different modeling techniques. Care should be taken when creating models using any numerical technique to avoid perfect or idealized properties.

Any perfect property has the potential to produce misleading results if not carefully addressed during the development of the model. Fortunately problems can be avoided by simply being aware of these properties and taking steps to add some appropriate imperfections into the model. Each of these properties are discussed together with basic examples, making it easier for the modeler to decide which of these traps might be problematic during the creation of a given model.

Perfect Grid Alignment

One consideration when preparing models of highly resonant structures for use with the FDTD technique is the large number of time steps that will be needed for the simulation to run to completion. "Snap to grid" is a great feature for creating models with no missing corners and all edges meeting at precise right angles. The downside of this particular form of perfection is that ringing of the structure is maximized as any two plates can be perfectly aligned and parallel, thus requiring an excessively large number of time steps to resolve. The ringing is enhanced by the use of Perfect Electric or Magnetic Conductors (PEC and PMC). However, the ringing is only slightly reduced by using actual values for the metal conductivity.

A means of reducing the ringing effect is to add a definite angle between the plates. In this way the energy is partially coupled out of the structure on each reflection. It has been shown that the results of a simulation using even significantly angled walls can provide substantially the same amplitude - frequency response as a perfect simulation, which was run for between two to six times as many time steps.

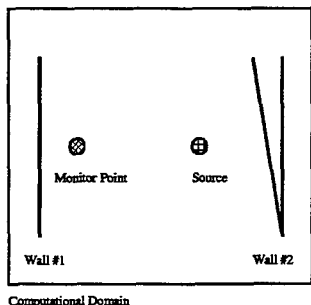


Figure 1. Simple Model

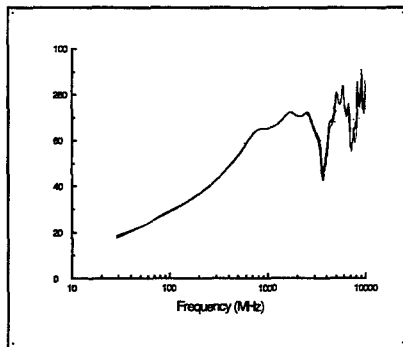


Figure 2. Frequency Response for All Cases

Figure 1 shows a simple FDTD model to illustrate this effect. The model has two parallel walls with a source and monitor point between them. This model was run initially with parallel walls and then twice more with one of the walls at different angles. As can be seen in Figure 2 the frequency response is practically identical for three wall angles, including perfectly parallel. Figures 3 and 4 show the time domain response for the parallel plate case and for the case with the steepest angle between them. Clearly the angled model converges most quickly.

To break up perfect parallelism of the model elements it is necessary to angle some plates. This requires stair step approximations to the desired line. Having the facility to generate angled plates built in to the primary CAD interface will greatly simplify this process. Physical enclosures will be manufactured with a draw angle if molded, or will bow if made from sheet metal. It is not necessary to accurately reproduce the real angles; one simply needs to provide some added imperfection to the model element alignment. An alternative to creating angled plates would be to add some asymmetric plates to form a shallow pyramid structure to eliminate the perfect parallelism.

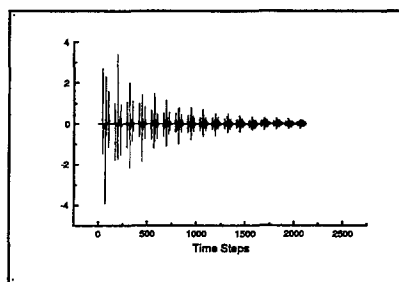


Figure 3. Parallel Wall Time Domain Response

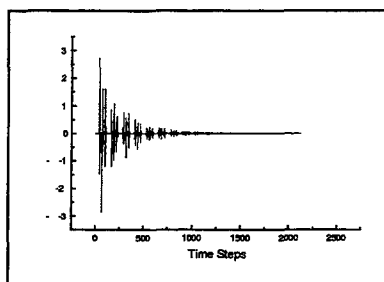


Figure 4. Angled Wall Time Domain Response

A similar situation will occur where arrays of conductors or slots are at perfect right angles. In this case there will only be minimal coupling between them, whereas in reality the imperfections in the alignments will be responsible for the coupling. It is these imperfections that the EMC engineer needs to understand. This is a more generic problem and relates to both time and frequency domain codes.

Pure Polarization

Pure polarization in FDTD models results from the same model creation process as with the perfectly aligned model elements. In the simplest models where the source is linearly polarized there is absolutely no cross-polarized component. Such pure polarization is not bad by itself; however, when it is also aligned exactly with other elements in the model, the problem becomes apparent.

As in the case for perfectly aligned model elements, when the field from the source is cross-polarized with respect to a model element, there is no coupling. For example, when a slot, in an otherwise perfect shield, is modeled with a co-polarized wire source there will be no energy coupled through that slot. It would, therefore, be possible to model an infinitely long slot and get no leakage through it. Even a small angle between the source and slot would cause the model results to at least indicate some leakage. It is the null in the response of this perfect model that can lead to problems.

An example of this occurred during the development of an EMI shield that was highly dependent upon the polarization of the source. With the lack of any cross-polarized component in the source, there was no leakage and the design appeared to work. To exacerbate this problem, experimental verification of a simplified prototype confirmed that the model worked as expected. However, once production units were available it was found not to work. The error was traced to a much stronger cross-polarized component in the real product source than was found in the prototype or in the model.

One possible means of addressing this would be to create specialized sources that are polarized diagonally across the FDTD grid. If cubical cells are used, the resulting field will have equal components in all orientations, but even if extreme cell dimensions are chosen, there will still be significant energy in each orientation. Since EMC problems are usually complex it is a safe assumption that no perfectly aligned linearly polarized field will be seen.

Symmetry

When building models of structures for EMC modeling the question of where to excite the structure must be addressed. In many instances the first point chosen will be the center or the middle of an edge. This choice can often hide possible solutions, as it will not excite all relevant modes in the structure.

Consider that many EMI test sites and compact antenna ranges are built in such a way as to break up the uniformity and symmetry of unwanted reflections. In this way the site performance is enhanced. When creating models, the same considerations apply. One way of approaching this is to simply ensure that the model is not centered in the computational domain and that the source is offset to some extent. While these will not provide a complete solution, neither will they mask effects that perfect symmetry can hide.

An example of where this symmetry problem was found was in the analysis of the radiation from VLSI device heat sinks. The first work was performed with a center feed to the heat sink. Later work looked more carefully at the details of the source and it was discovered that, depending upon the device activity, the source was significantly offset from the center. The result of this particular offset was not significantly detectable for the frequency range of interest. However, it was sufficient to make it an area of concern for future, higher speed devices.

During some experimental work to evaluate coupling in cavities with FDTD, probes were placed in the center of opposite walls. It was initially assumed that the location was not too important providing the experimental and numerical models were identical. However, the locations chosen happened to be in a null with respect to each other. These locations made correlation extremely difficult. Moving one of the probes permitted much better results.

There is no foolproof way to include a symmetry check within a code. The responsibility lies with the modeler to examine the model goals and be sure that a special case is not being created.

Ideal Source Impedance

When developing an antenna or performing circuit analysis there is no doubt that the feed or source impedance is a vital consideration. It would not be expected to get correct results without including source impedance. However, when examining physical structures it is not intuitively obvious that source impedance is an equally important factor. It is easy to take a structure modeled using FDTD and apply a simple wire current source as a means of exciting it. The source impedance is of particular importance for cases where the structure is excited directly. There are situations where this is not critical but in all these cases the source is not closely coupled to the structure.

Figure 5 shows the differences in frequency response between using a current source versus voltage source to drive a simple dipole. The dipole is two meters in length and center fed. It can be seen that there are two very different frequency responses. The voltage source is represented by the dotted line, and shows the response usually expected. The emission peak corresponds to a dipole length of approximately one half wavelength. By comparison, the solid line shows the frequency response of the same antenna driven by a current source; in this case the peak occurs at the extremely high impedance of the antenna at the full-wave resonance. It should be noted that the frequency response of the voltage driven dipole is not exactly as would be expected from a matched feed, just very much closer than that for the current source case.

Any current source can be converted into a more realistic source by the addition of a shunt resistance; similarly a voltage source can be implemented with a series resistance. The addition of reactive

components is also beneficial but much can be achieved with resistance alone. Configuring a valid source reactance correctly over the wide frequency range appropriate to an FDTD model can be difficult and probably is only warranted in special cases. A key engineering axiom is to keep everything as simple as possible.

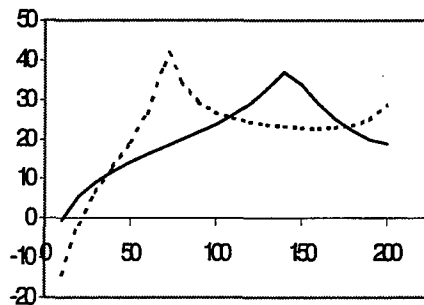


Figure 5. Frequency Response of a Dipole

Non-Invasive Field Monitor Points

FDTD permits easy access to the fields at any point within the computational domain. In general this is a very useful feature and has many uses. The ability to map field propagation and or current paths on a structure is a very powerful tool that can be used by the EMC engineer to both better understand the electromagnetic behavior and to clearly demonstrate to non EMC practitioners what is happening.

FDTD codes can include post processing to permit determination of the rf potential between conductors or the current within a conductor or array of conductors. This feature has proven extremely valuable in bridging the gap between circuit modeling and physical modeling. However, the field monitor points used may not provide the expected results unless the load impedance of the measurement is included in some manner. Without a suitable load impedance in the model, the calculated voltage will be that of the open circuit case. This problem is very similar to that associated with a perfect current or voltage source.

In a different category, there can be a problem when trying to experimentally verify the fields modeled. This is due to the absence of the probe and its cable from the model. Whilst the probe itself may be small, the effects of the cable could easily be a determining factor in the actual field pattern. This particular problem can be considered more operator error than the other items, as it should be clear that the probe and cable need to be included in the model.

Summary

All of the perfections discussed in this paper are usually considered advantageous to the modeler, permitting clear and concise models to be created and analyzed. For many EM applications, this is exactly what is wanted. However, EMC engineers, always somewhat unusual in their needs and applications, require something further to ensure that the problems solved are the ones of interest and not those from a perfect model.

The most obvious way to ensure that a model is a true representation of the problem geometry is to be very exact in reproducing every small detail of the problem. This will lead to extremely complex models. In practice, a careful balance must be maintained between creating overly complex models requiring a lot of detail, and simplified models that might be misleading. One possible way of maintaining relatively simple models is to eliminate the perfect model characteristics that cause the problems. Adding small imperfections to an FDTD model can provide a possible way to avoid errors in FDTD models without the complexity of including every small detail.

Clearly, avoiding most of these problems must be addressed on a case by case basis as the solution resides in creating models in a specific manner. However, there are some possible additions to the typical FDTD EMC tool that could help minimize the risk of falling in to some of these traps.

Adding small imperfections into a model can help ensure that the model will run with a reasonable number of time steps and ensure that no modes or cross-polarized components are missed. The issues of model symmetry and the effects of measurement probes can only be addressed by taking care in the initial creation of the model. In the final analysis all of these issues lie with the modeler understanding all the subtleties of the technique and the needs and goals for the model.

As the state of the art of EMC modeling advances it is encouraging to see excessive accuracy becoming a problem, something not familiar to EMC engineers. To be certain that some of these problems are avoided it is often necessary to run more than one model. The addition of imperfections into the FDTD model is the first attempt at providing a consistent means to solve EMC problems with a single model.

References

1. Archambeault, Ramahi, Brench, EMI/EMC Computational Modeling Handbook. Boston: Kluwer Academic Publications, 1998.
2. Colin E. Brench, "On the Development of a Low Cost, High Performance, EMI Shield", IEEE International Symposium on EMC, August 1999, pp. 65-68.
3. Brench, Colin E. and Ramahi, Omar M., "Source Selection Criteria for FDTD Models", IEEE International Symposium on EMC, August 1998, pp. 491-494.

Power Conversion Techniques for Portable EMI Sensitive Applications

Reinaldo Perez
Jet Propulsion Laboratory
California Institute of Technology

Abstract

In circuit applications that demand low noise, such as in many portable wireless devices, there is a need to optimize circuit design in power converter circuits. The path to low noise performance does not necessarily require exotic circuit techniques or the latest IC features. Conventional low noise power supply techniques are "tweaked" to improve the performance of dc/dc conversion circuits. A series of improved circuit designs are outlined such as redesigns in push-pull converters, the use of negative rail, the usage of charge pumps (also known as inductorless design), single resistance-capacitance filter, and PCB ground layout. The design techniques are explained and sample circuits are shown. Noise measurements of such re-designed circuits are performed with the improved results explained. Some final attention is paid to pitfalls occurring from using digital layout design hardware in the use of mostly analog layout methods in power conversion circuits.

SUMMARY

In applications that demand low noise such as in portable wireless devices, designers typically stay away from dc/dc converter circuits and instead linear supplies are used. However, linear supplies tend to put a toll in battery life since linear power supply are highly inefficient. In this work several options of improved design are explored

Consider First a Push-Pull Converter.

A push-pull converter (also known as a forward converter) differs from the more widely used buck, boost, or inverting converter in that its energy is never stored in the magnetic component [1]. In inductor based dc-dc converters (like the buck, boost), the inductor alternately collects the energy from the input supply and transfer it to the output. The output filter capacitor alone must support the whole load while the coil is recharging. In the proposed push pull design, the transformer does not store the energy but rather transfer it. In the proposed design of Figures 1 and 2; at any instant, one of two switches is on, and the current flows in the transformer primary and secondary windings simultaneously. The proposed design in Figures 1 and 2 are very quiet designs, specially for negative power supplies which usually exhibit a very poor rejection of noise in their negative rails. A description of the main noise reductions features of the designs in Figures 1 and 2 will be provided.

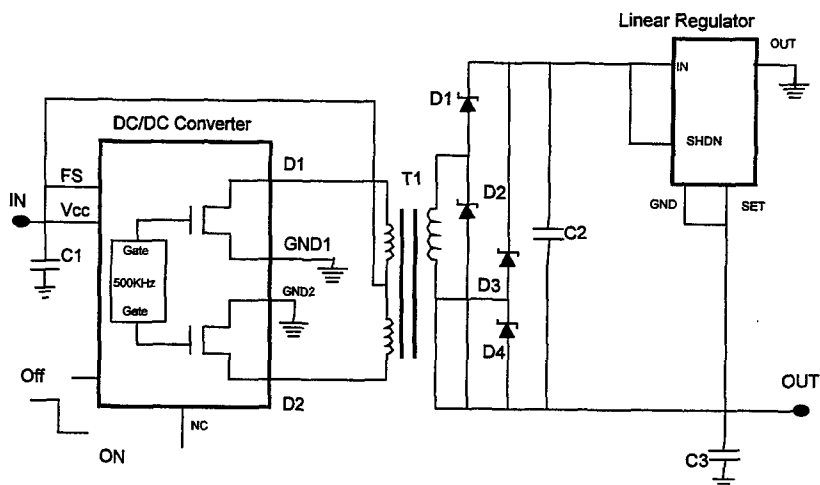


Figure 1. Forward converter design offering much quiet ripple noise environment ($< 10\text{mV p-p}$)

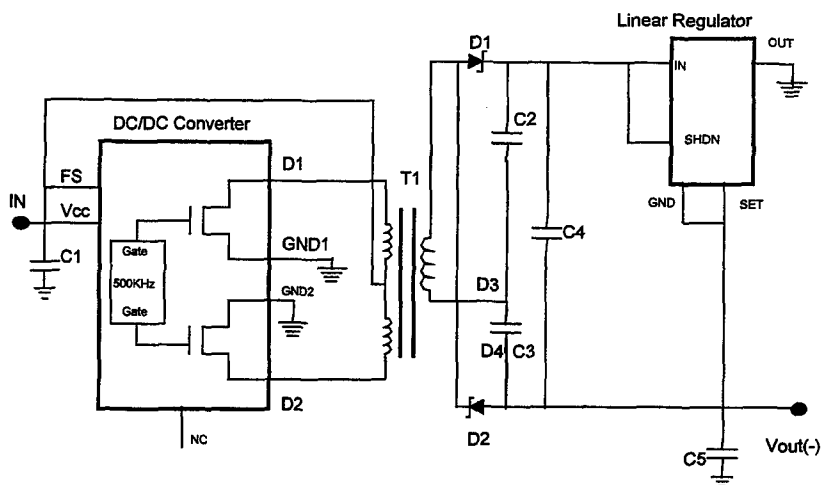


Figure 2. Low noise push-pull design connecting secondary in voltage doubling configuration

In most pre-amp applications negative power supply is needed in addition to the regular positive power supply. Filtering the positive power supply is usually sufficient, not so is the case for negative power supply rails. The designs of figures 1 and 2 are also good for

Charge Pump Designs.

418

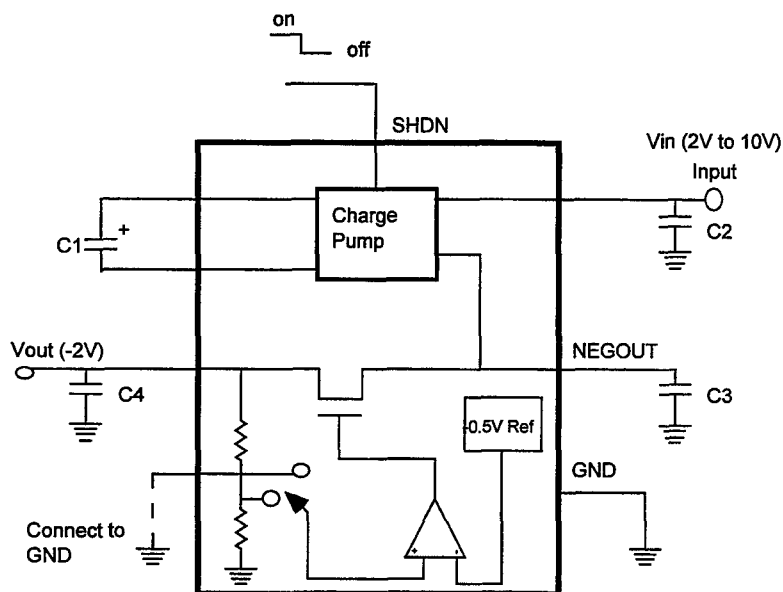


Figure 4.0 Light load application with an internal regulator within a charge pump IC.

Synchronized Design.

Filtering and shielding are the common strategies used for conducted noise suppression. An alternate design approach that can save the cost and inconvenience of these solutions is to “lock” the dc-dc converter’s operating (and noise generating) frequency to a clock source that confines the ripple and emitted spectrum to frequencies that don’t interfere with the rest of the system. This solution does not reduce the amplitude of the radiated noise, but it confines the noise spectrum to less intrusive harmonics located away from the frequencies that could hurt the performance of a device (e.g the IF frequency of a wireless device). This can be accomplished using the SYNC input of the dc-dc converter to lock the converter oscillator to an external clock source. A design implementing this type of synchronization is shown in Figure 6. The paper explains this type of synchronization circuit. Figure 7 shows a look at the spectrum with and without synchronization for the circuit in Figure 6.

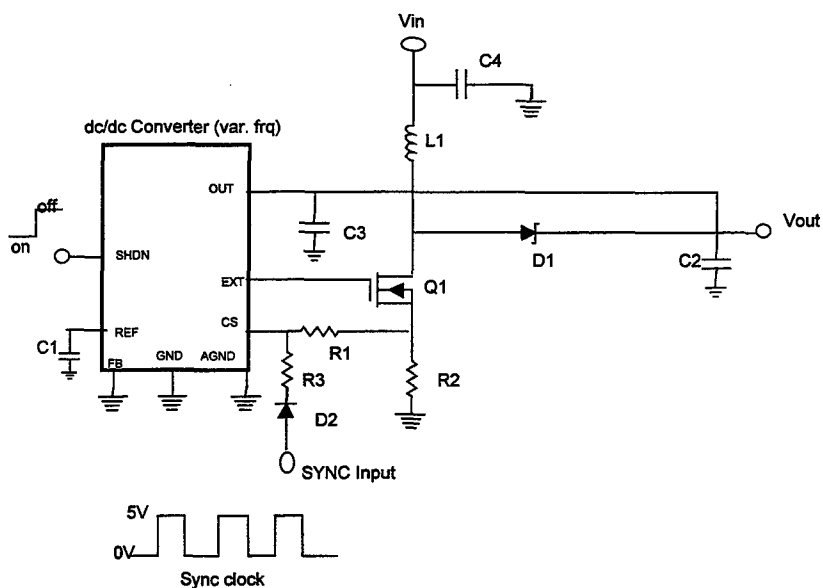


Figure 6.0 Variable frequency dc-dc converter can be synchronize through their current sense input.

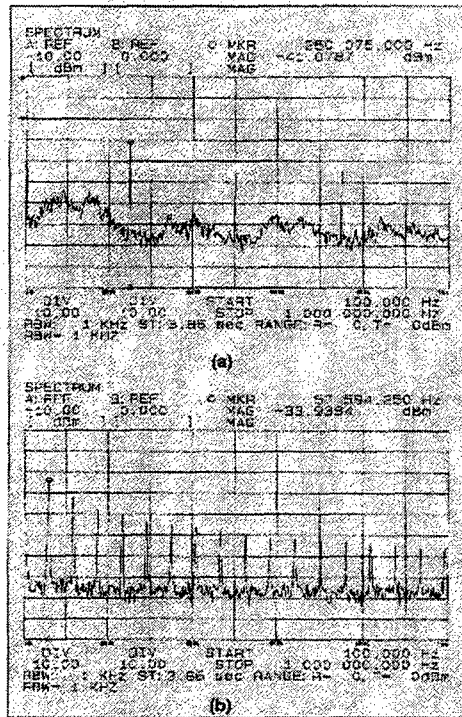


Figure 7.0 Noise spectrum plots for the circuit in figure 6 showing the benefits of synchronization: (a) without synchronization, (b) with synchronization.

Other Simple Noise Reduction Techniques.

Simple resistance RC filter: Use when the load current is low. It is the lowest cost. Feasibility of this option depends on whether it can be inserted in series with the load without a significant voltage drop in the output or a degraded load regulation. For example, at a 10 mA load, a 10 ohm resistor will drop 100 mV. A 1uF capacitor will add a 15KHz roll-off to the output. Always remember to add the filter after the circuit feedback's connection. The RC filter can also be made just to filter out the portion of the load that needs low noise, not necessarily the whole spectrum.

PCB Layout. This is the most common source of dc-dc noise problems. [3] Although the main cause of the problem is inductor fields, high dI/dt in circuit components and traces, and high dV/dt at circuit nodes can be severely aggravated by poor layout. Many poor

layout are being generated by auto route layout software intended for logic design. Of particular importance to watch are:

- a) Keep the switching nodes physically small: In conventional dc/dc converters, the nodes are where the coil, switch, and diode meet. These nodes are antennas and can radiate. The traces should be wide to carry high current and smallest as possible (lengthwise).....(more will be described in paper)
- b) In many power supply design with resistor feedback, locate feedback resistors right next to the IC feedback pin, and keep the trace area at the feedback pin minimized. The feedback pin is a high impedance node, and therefore is susceptible to noise radiate from other parts of the circuit.....(more will be described in paper).
- c) Identify the traces through which high currents are flowing and size them as wide and short as possible. In particular, pay attention to the vias through the PCB, because these are poor conductors at high currents, specially in high speed switching circuits.....(more will be discussed in paper).
- d) Ensure that low noise grounds such as those in feedback resistors, reference bypass capacitors, and the IC analog ground pins are not polluted from high currents in power ground traces. Should use a separate plane from that of power ground.....(more will be discussed in paper).
- e) Avoid cutting up the ground plane with too many long jumpers traces. This is a common problem because the ground plane and the signal plane are usually one above the other but very close to each other. Signal traces are often jumpered through the ground plane (wrong thing to do)and should instead be jumpered to through a layer other than ground.....(more will be discussed in paper)

Conclusion:

In this paper it is shown that improve design techniques are needed for addressing noise issues in dc-dc converters for portable electronic devices. Some of these design techniques have been addressed with appropriate sample circuits. It is expected that power supply designers can benefit from some of the insights in this discussions.

References:

- [1] John D. Lenk, "Simplified design of switching power supplies," EDN series for Design Engineers, B-H Publishers, 1995.
- [2] L.H. Dixon, "switching power supply topology review, Unitrode Seminar SEM 200, 1997.
- [3] Perez, R. "An study in the Proper Design of Grounding for SMPS Converters and the role of CEM," 1999 ACES Symposium, Monterey, CA, March 12-15,1999.

Using the Partial Element Equivalent Circuit (PEEC) Simulation Technique To Properly Analyze Power/Ground Plane EMI Decoupling Performance

Bruce Archambeault
IBM
Research Triangle Park, NC 27712
Barch@us.ibm.com

INTRODUCTION

Decoupling capacitors are used to provide a local source of charge for ICs requiring a significant amount of supply current in response to internal switching. If sufficient decoupling capacitors are not used, the required supply current is not available, and the device does not operate properly, and signal integrity data errors can result. In addition to the signal integrity requirement, decoupling capacitors serve as EMC filters to prevent high frequency RF signals from propagating throughout the PC board. This requires them to provide a low impedance across the frequencies of interest.

The proper number of decoupling capacitors, and the proper value of those decoupling capacitors is always a topic of debate between EMC engineers and design engineers. Some typical rules-of-thumb require a decoupling capacitor for each power pin on an IC. Other rules-of-thumb require at least one decoupling capacitor per side of physically large ICs. Still other rules-of-thumb require decoupling capacitors spread evenly over every square inch of the board. Very little real information about the optimum approach is available in the technical literature.

Traditionally, the values of the decoupling capacitors are largely based upon habit and the experience of the EMC engineer. Values of .01 μf are typically used. Often smaller capacitors are used in parallel with the main decoupling capacitor to provide a high frequency and a low frequency filtering effect. However, potential cross resonances can have a negative effect when using multiple capacitors in close proximity.

The overall result is that the design of the power plane decoupling (between a power plane and a ground reference plane) has been historically difficult to properly design or analyze. With on-board clock speeds of 400 – 800 MHz becoming common, a more rational approach must be taken to optimize the design of decoupling capacitors on the printed circuit (PC) board.

The Partial Element Equivalent Circuit (PEEC) simulation technique was first introduced 25 years ago [1]. It has mostly been used for quasi-static partial inductance calculations until recently. New developments [2] have made PEEC a full-wave tool with time domain capabilities.

Modeling and simulation is not new to EMC applications. There have been many articles in the literature using the method of Moments (MoM), the Finite-Difference Time-Domain (FDTD) technique, the Transmission Line Method (TLM) or the Finite Element method (FEM). Each of these different techniques have areas where their individual strengths make them the best choice for a particular modeling problem, and each has areas where they are not appropriate. Therefore, a tool-box strategy is necessary, where the engineer has more than one modeling technique available, allowing the use of the proper technique for the given task.

PEEC has recently become a popular alternative to some of the more traditional modeling techniques. One of its biggest advantages is the easy ability to add circuit elements into an electromagnetic simulator, making it a preferred choice for printed circuit board simulations which include lumped circuit elements, such as inductance, capacitance, and resistance. A number of examples of PEEC's usefulness in EMC modeling applications will be presented here.

DECOUPLING CAPACITOR PERFORMANCE MEASUREMENT PROCESS

Since a 'real' PC board is quite complex, it is difficult to isolate the various EMC effects to know that a particular change to the board has produced an effect that is directly traceable to that original change. Therefore, a special PC board was created to help analyze the effects of a variety of decoupling capacitor configurations.

Test Board Description

This investigation focused upon a 4-layer PC board, with the external dimensions of 10 x 12 inches. This was considered to be a typical board used in current products. Since the frequency range under investigation extended from 30 MHz to over 1 GHz, a repeatable and well controlled connection method to the test board was required. A set of 15 SMA connectors were installed across the board as shown in Figure 1. Each of the SMA connectors was surrounded by four locations for SMT decoupling capacitors as shown in the insert.

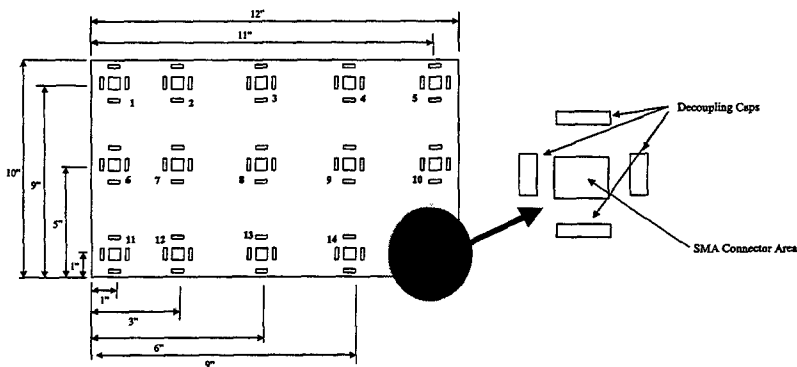


Figure 1 Test Board SMA Connector Configuration

In addition to the SMA connectors, and the surrounding decoupling capacitor sites, locations for additional SMT decoupling capacitors were located every inch on the PC Board, creating a capacitor matrix of 99 capacitors (when fully loaded).

All measurements were taken with a Network/Impedance analyzer. Both one-port and two-port measurements were used. One port measurements were impedance measurements, while the two port measurements were S_{21} ¹. Examples of each result will be provided in the following section.

Initial measurements were impedance measurements. Observing the impedance across the frequency range of 30 – 1800 MHz allowed a better understanding of the effectiveness of the natural interplane capacitance, the effects of decoupling capacitors, and board resonances. However, impedance at a given location on a PC board is not the primary concern for EMC engineers. A more important parameter for EMC engineers is the amount of 'noise'² at a remote location due to some IC source location. The remote location might be the edge of the PC board (where it was located near a seam in the metal shielded enclosure), or near a via for an I/O signal trace, which was then connected to an external connector. Therefore, the S_{21} parameter is a better indication of the decoupling configuration's performance for EMC considerations. The goal is to have as low as possible S_{21} between a potential source, and a remote location of concern.

Decoupling Capacitor Configuration Measurement Results

There was a number of different types of configurations measured, as well as the capacitor value being varied. Initial measurements focused on impedance of the board at various locations, and with different configurations of capacitors. The difference between local source decoupling, and distributed decoupling was then investigated. Finally, the number of capacitors, and various values of capacitance (both single and multiple values) were investigated.

Quantity of Distributed Decoupling Capacitors (.01uF Only)

The investigation into the number of decoupling capacitors distributed across the board used only .01uF SMT capacitors. The S_{21} 'transfer function' was measured for a variety of different port combinations, and with a variety of capacitors distributed across the board. Every effort was made to distribute the capacitors evenly across the board for all quantities of capacitors. While a number of different point-to-point measurements were made, only one is shown here as an example (Figure 2).

As can be seen in Figure 2, the more capacitors, the lower the S_{21} transfer function in the lower frequency ranges (below 200 – 400 MHz). Also, at higher frequencies, the overall envelop for the S_{21} transfer function decreased slightly (even though the resonant frequency shifted) as more capacitors were added.

The maximum number of capacitors was 99 distributed capacitors, representing one capacitor every square inch across the PC test board. Figure 3 shows a summary of all the various transfer function ports with the full (99) number of capacitors.

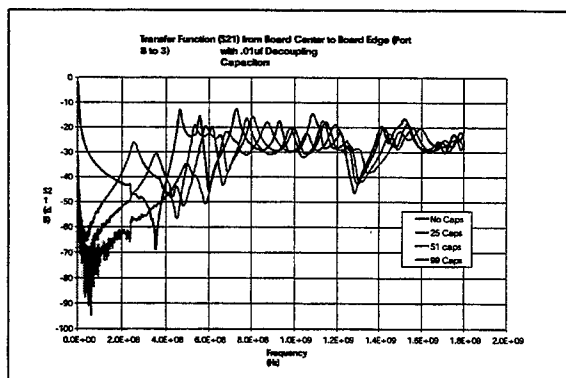
While careful measurements are a good source of information, they are tedious at best, and are often impossible. Therefore a modeling technique was desired that would allow

¹ S_{21} is a measure of the voltage at a remote location due to a source voltage.

² The noise in this case is due to the switching within the IC, and the current drawn from the power/ground plane structure to support the sudden switching.

accurate results as compared to the measured results. The PEEC technique was chosen as the best modeling technique for this problem.

Figure 2



Brief Description of PEEC

There are a number of technical articles describing the PEEC technique in detail, and those will not be repeated here. However, a very brief description will be presented.

PEEC is based on the integral equation formulation. All the structures to be modeled are divided into electrically small elements. The coupling between each element is described as an equivalent circuit shown in Figure 4. Once the matrix of equivalent circuits are developed, then a SPICE-like circuit solver is used to for the response of the system to the simulation applied to it.

Since the solution is a circuit based solution, then individual circuit elements, such as resistance, capacitance, and inductance can be easily added to any set of elements or nodes.

For these models, the equivalent series inductance of 2 nH and resistance of 50 mohms were added to account for the capacitor, via and pad inductance and resistance. This was very important, since this inductance becomes the dominant parameter at high frequencies.

Figure 3

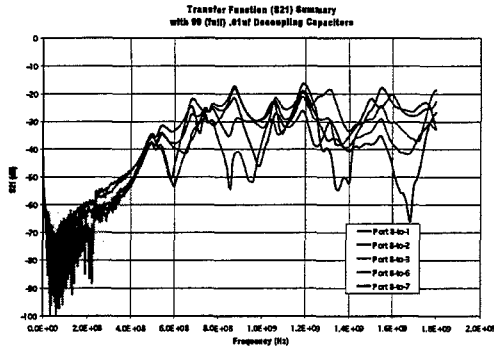
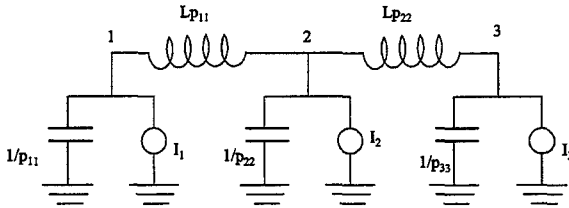


Figure 4 Basic PEEC Circuit



Modeling Results

The same real-world board was modeled using PEEC. The segments were forced to be no larger than $1/20^{\text{th}}$ of a wavelength. The ratio of signal-in to signal-out was used as the measurement goodness.

A variety of different configurations were modeled. Figure 5 shows the comparison of the modeled and measured S21 parameter for the case of 99 0.01 uF capacitors (one per square inch), and Figure 6 shows the modeled and measured comparison for the case of alternating 0.01 uF and 330 pF capacitors. In both cases the agreement was considered very good for EMC applications. The transfer function was clearly worse in the frequency range of 100-200 MHz with the combination of different values (due to cross resonances), demonstrating why this is a poor design choice.

Figure 5

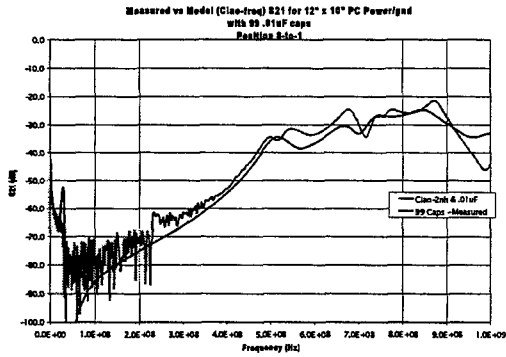
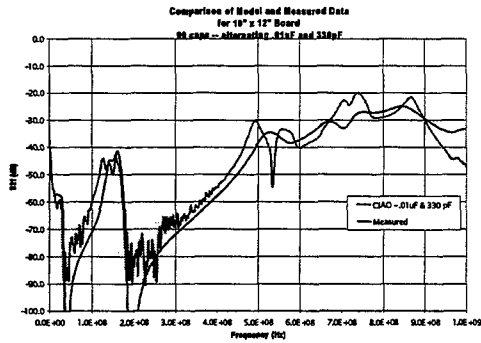


Figure 6



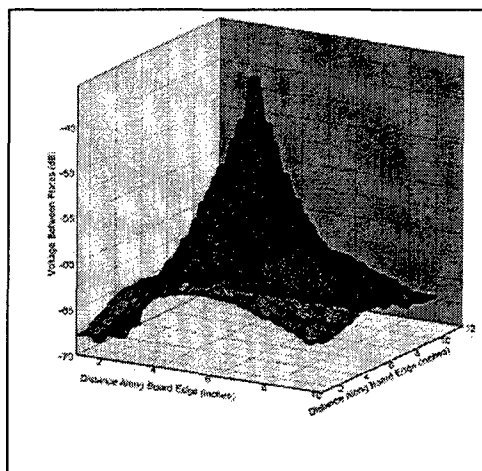
Voltage Distribution

One of the great advantages to modeling is the ability to 'see' things that is impossible to measure in the real-world laboratory. Often this gives us greater understanding about what is actually occurring, and how to optimize the design.

Figure 7 through 9 shows the voltage (between the plates) distribution at the frequencies of 100 MHz, 500 MHz, and 700 MHz, when the source is located at the center of the board, and the board is loaded with alternating 0.01 uF capacitors and 330 pF capacitors (every square inch). At lower frequencies, (before resonance effects start) the decoupling capacitors are 'working' since the voltage amplitude quickly reduces with distance from

the source. However, once the resonant frequency range is reached, the standing wave patterns between the plates show that a high level of voltage may be far from the source, and even along the edge of the board (where it can radiate outward and is a major concern to EMC engineers).

Figure 7 Voltage Distribution Between Plates @ 100 MHz



SUMMARY

A careful measurement analysis was made of various decoupling strategies. Results from this set of measurements have shown that the performance of decoupling capacitors, regardless of their values, is quite limited in frequency range. The natural inductance of the capacitor, the via and associated pads all contribute to high impedance at higher frequencies.

In addition to the measured results, it was demonstrated that PEEC can be successfully used to model this complex structure, even with many capacitors/inductors/resistors. Good agreement between measured and modeled results were shown. The modeled results can be extended beyond where the measurements are possible, and can show the voltage distribution between the plates at various frequencies. This allows even greater understanding of the limitations of the decoupling capacitor design strategy, and leads to a better design strategy.

References:

- [1] A.E. Ruehli, "Equivalent Circuit Models for Three-Dimensional Multiconductor Systems," IEEE Trans. on Microwave Theory and Techniques, Vol. MTT-22, No. 3, March 1974

[2] J. Garrett, A.E. Ruehli, C.R. Paul, "Stability Improvement of Integral Equation Models,"
Proc. IEEE Antennas Prop. Society Symposium, Montreal, Canada, July 1997

Figure 8 Voltage Distribution Between Plates @ 500 MHz

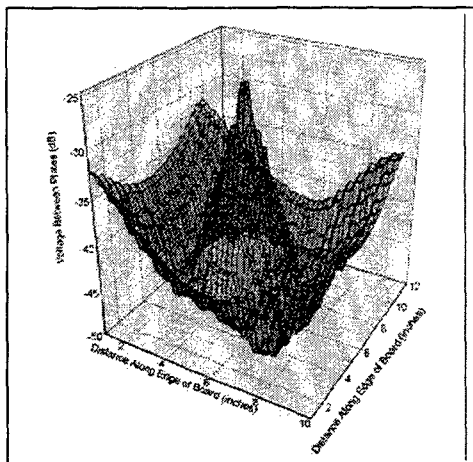
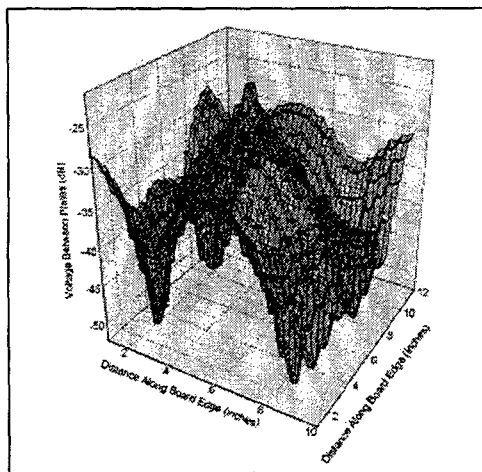


Figure 9 Voltage Distribution Between Plates @ 700 MHz



EMI Model Validation and Standard Challenge Problems

Bruce Archambeault, Ph.D.
IBM
3039 Cornwallis Road
Research Triangle Park, NC 27709
Barch@us.ibm.com

James L. Drewniak, Ph. D.
EMC Laboratory
University of Missouri-Rolla
1870 Miner Circle, 114 EECH
Rolla, MO 65409-0040
Drewniak@ece.umr.edu

Introduction

There are a number of numerical techniques available for modeling EMI problems, including various commercial software. Each of the different modeling techniques have areas where they match the problem quite well, and can provide accurate and reliable results. Also, each of the different modeling techniques have areas where they do *not* match the problem well, and can create questionable results. A potential user must be able to evaluate the various options against their style problems in order to better understand which method is most suitable, and possibly evaluate commercial software.

In addition to applying a specific modeling technique or software package to an appropriate problem, it is desirable to be able to validate the results against previous modeling efforts or measured data. While many technical papers have shown results from models, and many include measurements or other validations, the details of the models and measurements are often not sufficiently reported to allow someone to repeat the model and directly compare results.

A joint IEEE/EMC Society TC-9 Committee and the Applied Computational Electromagnetic Society (ACES) effort has resulted in a central web location for contributors to provide model and measurement data to share and compare with others. In addition to the data repository, a set of standard challenge problems have been proposed over the past few years, and they are also located at this web site.

Validation Data

A committee has been established to review all submittals to this storage location. The submittal must include sufficient detail about how the modeling was accomplished (if any), and how the measurements were conducted (if any) so that the modeling and/or experiments can be easily repeated. The results from these models and/or measurements must be clearly presented, and a simple ASCII text file with the data must be available for downloading. The submittal will be posted on the web once accepted by the review committee and will be available for downloading by interested engineers.

All submittals are expected to contain sufficient information that the user can reproduce the reported results. Model and measurement data or multiple modeling techniques (showing the same results) are preferred so that there is validation within the submittal. Engineers using this data are encouraged to provide their results as further validation of the specific model and results.

Challenge and Specific Standard Problems

The second major purpose of this web location is to provide a central location where interested researchers and engineers can download the details of the IEEE/EMC Society TC-9 Challenge and Specific Standard Modeling Problems. These problems have been designed to allow users to highlight strengths and weaknesses of various modeling techniques and tools.

The Challenge problems are difficult problems that may require an EM modeling expert. These problems include shielding problems, PC boards with long wires attached, PC boards with microstrips, system-level shielded enclosures connected to remote PC boards via long wires, and others. Many of these problems can not be solved by certain modeling techniques, or require limiting assumptions, while those same problems can be solved in a straightforward manner by other modeling techniques. Some problems may require multiple modeling stages (where the output of one model becomes the input to a second model), or hybrid modeling techniques.

These challenging problems were created specifically to highlight how certain techniques are well suited to some problems, but not well suited to other problems. Since there is no simple modeling technique that can do all the various types of modeling required by the typical EMC engineer, a variety of tools are often required.

In 1998, two challenge problems were proposed. Problem 98-01 (Figure 1) consisted of a shielded metal box with an aperture. The source was a common mode voltage between an internal motherboard-daughter card combination. A second daughter card provided partial shielding between the source and the aperture. Problem 98-02 consisted of a PC board with traces, and long wires running off the PC board. A split in the board's reference plane was included.

In 1999, four challenge problems were proposed. Problem 99-01 (Figure 3) concerned the emissions along the edge of a PC Board, due to a trace on that board. Problem 99-02 (Figure 4) was to find the difference in shielding performance of a number of different seam shapes. Problem 99-03 (Figure 5) was a system level problem, with an enclosed shielded box, and a PC board connected by a long cable. Problem 99-04 (Figure 6) was to find the crosstalk between active and passive pins in a complex high speed connector.

The Specific Standard Problems are more limited in scope, and intended to be 'simpler' to solve. They are more useful for evaluating a commercial software by a potential user, since they are more limited and can be solved by a non-expert, and in a reasonable amount of time. These problems are again selected to highlight the strengths and weaknesses of the various modeling techniques.

These Specific Standard Problems include a heatsink emissions problem, a PC board decoupling problem, a microstrip problem, and a shielding problem. The dimensions are selected so that these problems can be converted into reasonable sized models, and solved in a short amount of time. Examples of results for each of these problems are posted along with the problems, so that potential tool purchasers can compare their evaluation results to the posted results. As additional results become available, they will be added to the web location.

Summary

A central location has been developed to allow interested persons to use previous results as a source for numerical modeling validation. This site will be carefully monitored by a review committee to insure only high quality information is posted on this site.

Also available from this site will be the IEEE/EMC Society TC-9 Challenge and Specific Standard Modeling problems. The problems are specified in sufficient detail so that users can easily create models which allow direct comparison to data from other contributors, and allow evaluation of commercial software as well.

This site has been developed as a joint ACES and IEEE/EMC TC-9 effort.

Figure 1 Problem #98-01

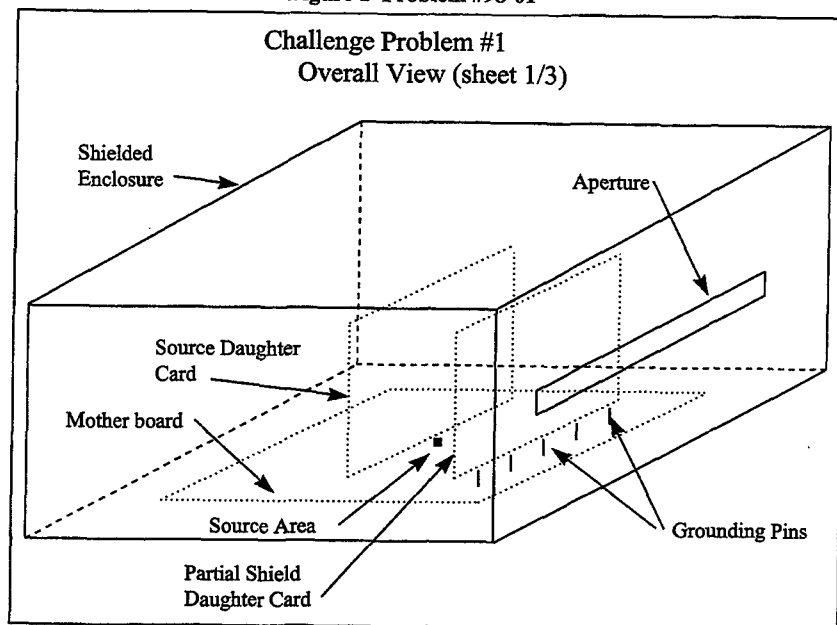


Figure 2 Problem 98-02

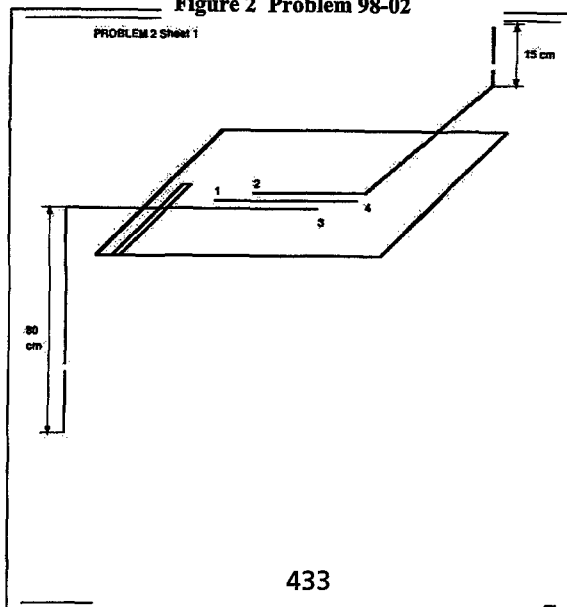


Figure 3 Problem 99-01 Emissions Along Edge of PC Board due to Trace

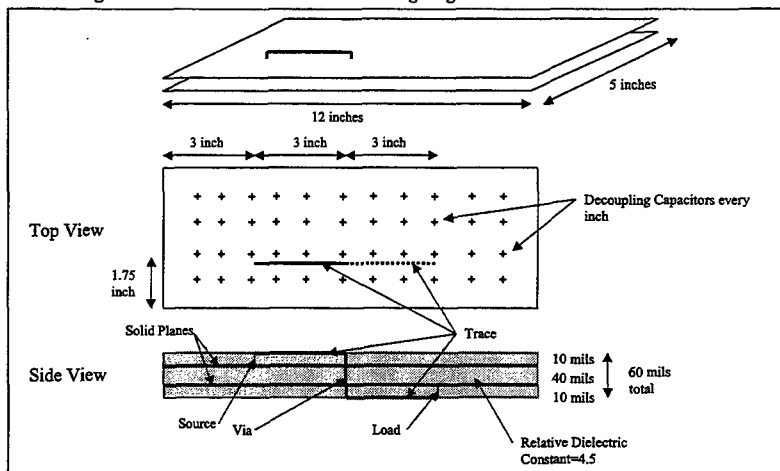


Figure 4 Problem 99-02 Shielding of Various Seam Shapes

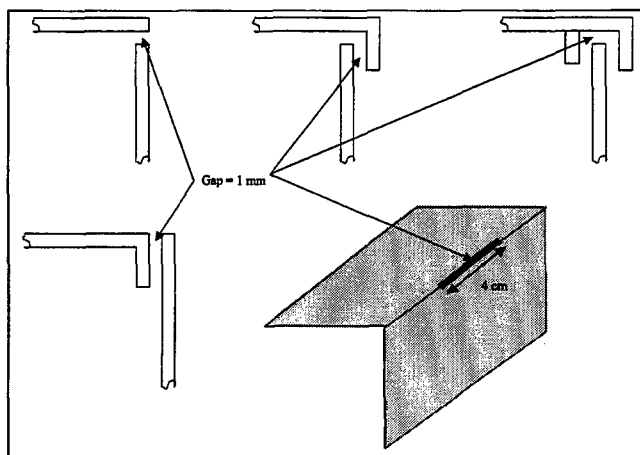


Figure 5 Problem 99-03 Emissions from a Interconnected System

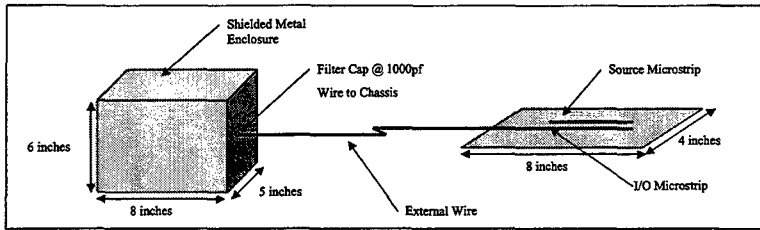
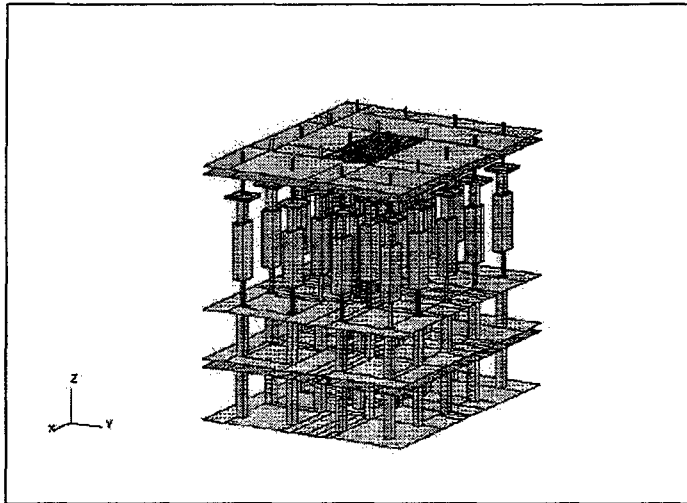


Figure 6 Problem 99-04 Crosstalk within High Speed Connector



Modeling EMI Resulting from a Signal Via Transition Through Power/Ground Layers

Wei Cui, Xiaoning Ye, Bruce Archambeault*, Doug White*, Min Li**, James L. Drewniak

Electromagnetic Compatibility Laboratory
Department of Electrical and Computer Engineering
University of Missouri-Rolla
Rolla, MO 65401

wcui@ece.UMR.edu, xiaoning@UMR.edu, drewniak@ece.UMR.edu

* IBM

Research Triangle Park, NC 27709
barch@us.ibm.com, dowwhite@us.ibm.com

Abstract

Signal transitioning through layers on vias are very common in multi-layer printed circuit board (PCB) design. For a signal via transitioning through the internal power and ground planes, the return current must switch from one reference plane to another reference plane. The discontinuity of the return current at the via excites the power and ground planes, and results in noise on the power bus that can lead to signal integrity, as well as EMI problems. Numerical methods, such as the finite-difference time-domain (FDTD), Moment of Methods (MoM), and partial element equivalent circuit (PEEC) method, were employed herein to study this problem. The modeled results are supported by measurements. In addition, a common EMI mitigation approach of adding a decoupling capacitor was investigated with the FDTD method.

I. Introduction

A signal trace that is routed on different layers is common in multi-layer PCB design due to the increasing board density. Vias are necessary for the signal current to transition to a different plane. A typical signal trace transitioning through a via on a 4-layer board is shown in Figure 1. The signal current at the via goes through the internal power and ground planes. At high frequencies, the return current has to jump from the lower reference plane to the upper reference plane. The current returns by a displacement current through the inter-plane capacitance of the power and ground planes. However, the discontinuity of the return current at the via excites the power bus, and can result in an EMI or SI problem. For a number of signal lines with via transitions, such as address lines or a data-bus, the simultaneous switching signals may result in a significant power bus noise, with potentially severe EMI or SI problems. The problem due to the signal transitioning through a via has been a concern for both signal integrity and EMC performance. Efforts have been made to mitigate this problem, such as by placing a decoupling capacitor near the via. Studies of the via interconnects have been reported, and the via parameters were extracted with the FDTD method [1]. In other signal integrity studies, the waveforms at the source and the load on the signal traces with via transitions were analyzed with the FDTD method [2]. Since numerical methods are very appropriate to model this problem, EMI resulting from the signal via transitioning through the internal power and ground planes was studied herein with FDTD, MoM, and PEEC methods. These methods had similar computational complexity in modeling this problem, and resulted in good accuracy in analyzing this problem. In addition, the mitigation strategy of placing a decoupling capacitor near the via was evaluated with FDTD method.

** M. Li was with the University of Missouri-Rolla. She is now with Lucent Technologies, Engineering Research Center, Princeton, NJ 08542, mli4@lucent.com.

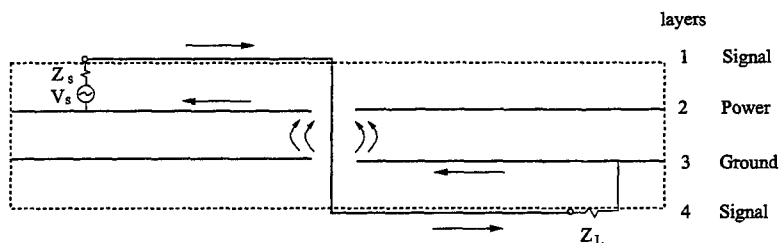
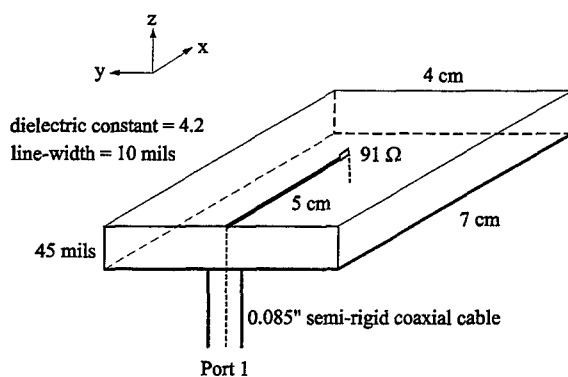


Figure 1. The signal via transitioning through the internal power and ground planes for a 4-layer PCB.

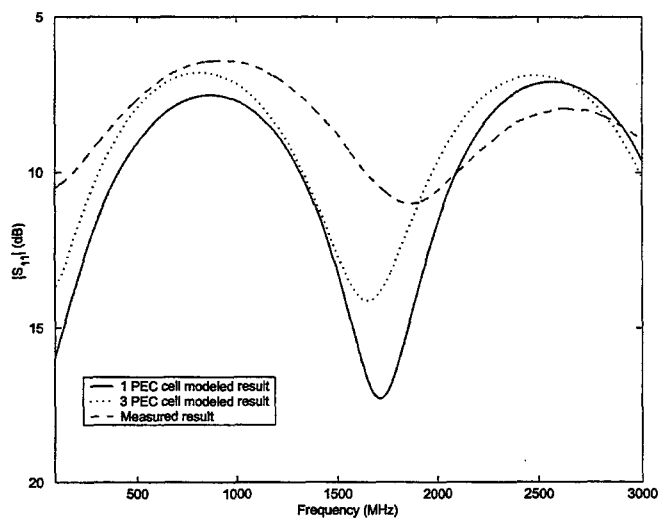
II. EMI Modeling – FDTD, PEEC, MoM

Modeling a signal trace on a PCB is essential to study the signal via transition problem. For a PCB with a configuration as shown in Figure 1, the signal trace is routed on the top and bottom planes of the PCB, and has a microstrip line structure. Since the line-width is small compared with the board dimensions, the mixed-scale problem is usually a difficulty in the FDTD modeling. With MoM and PEEC, however, this presents little difficulty. Modeling a typical microstrip line with the FDTD method was first studied herein to obtain adequate accuracy and avoid inordinately long computation times. The modeled PCB configuration is shown in Figure 2(a). There was a microstrip line on the top plane of a double-sided board. The board had a dimension of $7\text{ cm} \times 4\text{ cm}$. The line-width was 10 mils. , and the length was 5 cm . The microstrip line had a characteristic impedance of $88\ \Omega$ measured with a Tektronix 11801B TDR, and a $91\ \Omega$ resistor terminated this microstrip line. The layer thickness was 45 mils. , and the relative dielectric constant was $\epsilon_r = 3.5$. A $0.085''$ semi-rigid coaxial cable probe was connected to the PCB trace, and an HP8753D network analyzer was used for $|S_{11}|$ measurements. In the FDTD modeling, the microstrip line was first modeled as one cell of a perfect electric conductor (PEC). The cell size was $1\text{ mm} \times 0.254\text{ mm} \times 0.356\text{ mm}$, and the total cell number was 734,968. Then, as a test, the same microstrip line was modeled as three cells of PEC. For this modeling, the cell size was $0.333\text{ mm} \times 0.0847\text{ mm} \times 0.356\text{ mm}$, and the total cell number was 4,658,448. The cell size for the long edge of the board was reduced to 0.333 mm in the three-cell modeling to maintain the appropriate aspect ratio of the cell edge. There were 7 cells of white space and 7 cells of PML appended to each side of the truncated computational domain. The modeled results of $|S_{11}|$ are shown in Figure 2(b), together with the measured results. The difference between the measured results and the one-cell modeling results is less than 2 dB at most frequencies, and there is slight improvement for the three-cell modeling. Since the computation intensity increases greatly with the three-cell modeling for the problem at hand, it is suitable here to model the microstrip line with one PEC cell. The accuracy of one-cell modeling is adequate for EMC analysis in this case, especially since the microstrip line is not a significant factor in the EMI excitation. Rather, it is critical that the modeling fidelity at the via layer transition be adequate.

Modeling a signal via transitioning through the power and ground planes was studied with a 4-layer experimental board. The top view and side view of the test board are shown in Figures 3(a), and 3(b). The board had a dimension of $15\text{ cm} \times 10\text{ cm}$, and the inter-plane spacing was 45 mils. The relative dielectric constant of the board was $\epsilon_r = 3.5$. The second and third layers were used as entire power and ground planes. The signal trace on the top plane was connected to the trace on the bottom plane with a via. The signal via went through the internal power bus. The characteristic impedance of the signal trace was $88\ \Omega$, and a $91\ \Omega$ resistor on the bottom plane terminated the signal trace to the bottom side of Layer-3. Port 1 and Port 2 on the board were used to determine the $|S_{21}|$, where Port 1 was connected to the signal trace on the top plane, and Port 2 was connected to the power and ground planes as shown in Figure 3(b). There was no capacitor mounted on the pads for the present case. The via diameter of the signal transition was 20 mils. , and the $91\ \Omega$ SMT resistor was connected to Layer 3 by a wire of diameter of 20 mils.



(a)



(b)

Figure 2. The FDTD modeling of a microstrip line with one cell or three cells of PEC in width. (a) The configuration of the test board, and (b) the modeled and measured $|S_{11}|$ results.

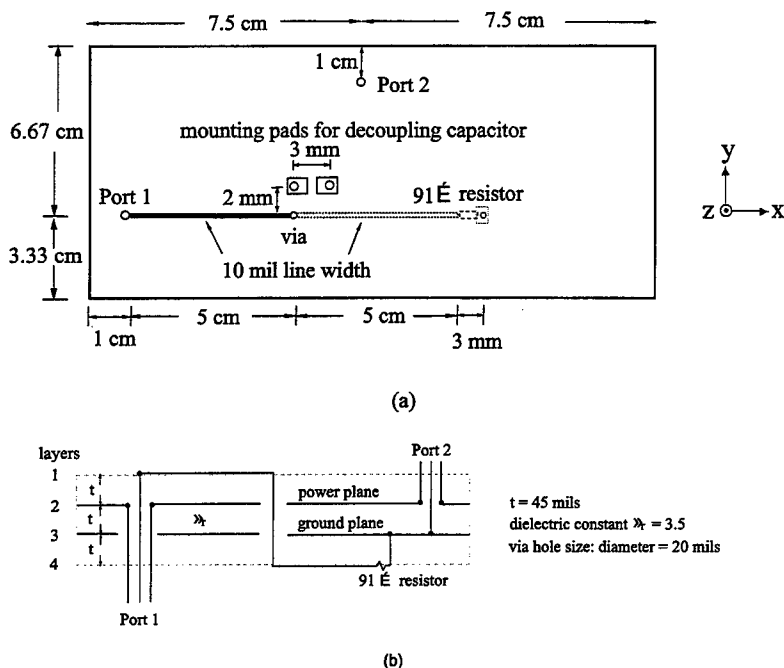


Figure 3. The configuration of the test board under study. (a) The top view, and (b) the side view.

Three numerical methods, FDTD, MoM, and PEEC methods, were employed to model the EMI resulting from the studied test board. In the FDTD modeling, the cell size was $1\text{ mm} \times 0.254\text{ mm} \times 0.356\text{ mm}$, and the total number of cells was approximately 3.4 million. The signal trace was modeled with one cell of PEC in width, and the dielectric layer between two adjacent planes was modeled with three cells. The dielectric loss was approximated by using a conductivity of $4 \times 10^{-5}\text{ S/cm}$ at all frequencies of interest. Seven cells of white space, and seven cells of PML were added to the truncated computational domain. A modulated Gaussian source with $50\text{ }\Omega$ impedance was applied at Port 1, and Port 2 was terminated with a $50\text{ }\Omega$ load. A thin-wire algorithm was used for modeling the signal via and the wires that connected the resistor to the ground plane [3]. The time step was $5.71 \times 10^{-13}\text{ sec}$, and 40,000 time steps were used to record the voltage and current time histories at Port 1 and Port 2. Approximately 60 hours of computation time was required to complete the modeling from 100 MHz – 3 GHz on a Pentium III 550 Xeon. This time could be reduced by as much as a factor of four using Prony or GPOF methods [4]. The same configuration was modeled with MoM and PEEC methods as well [5][6]. For the MoM modeling, the total number of unknowns was approximately 3000, and the patch size was on the order of $1/10\text{th}$ of the shortest wavelength. The power/ground planes and microstrip trace were modeled as conductors with zero thickness. It took 5 hours to complete the modeling from 100 MHz to 2 GHz on an IBM RS6000 workstation. In the PEEC modeling, the unknown number was 4500, and the cell size was approximately $1/12\text{th}$ of the shortest wavelength. The $|S_{21}|$ was calculated from 100 MHz to 1.4 GHz. The power/ground planes and microstrip trace were modeled with the actual thickness. It took 32 hours on a RS6000 workstation for this modeling.

The modeled results of $|S_{21}|$ with FDTD, MoM, and PEEC methods, as well as the measured results are shown in Figure 4. In general, all modeled results and measured results agree well from 100 MHz to 2 GHz. The peaks of $|S_{21}|$ at 530 MHz, 790 MHz, and 1060 MHz are corresponding to the TM_{10} , TM_{01} , and TM_{20} modes of the power bus. At high frequencies, the discrepancies of the peaks between the modeled and measured results are in part due to the dielectric loss.

Since the dielectric loss of the test board increased with frequency, and the dielectric loss in the modeling was the same at all frequencies, the measured $|S_{21}|$ was lower than the modeled results at higher resonance frequencies.

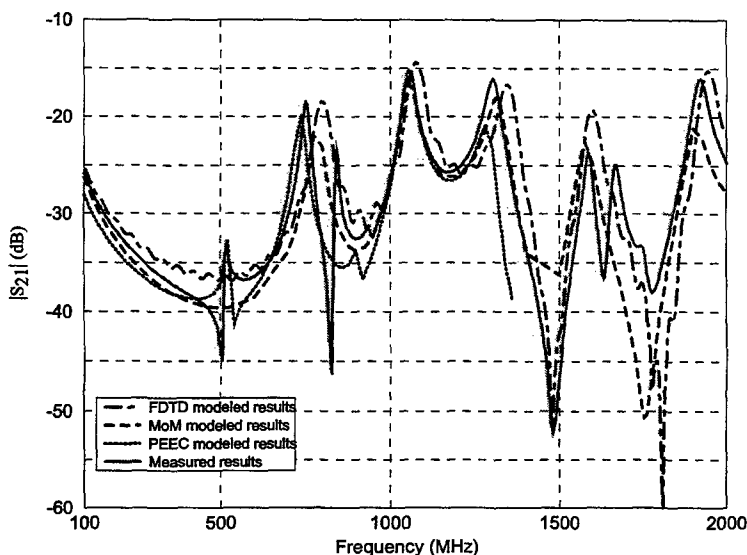


Figure 4. The measured results of $|S_{21}|$ and modeled results with FDTD, MoM, and PEEC methods.

III. Limits of EMI Mitigation Using a Decoupling Capacitor at the Transition

A decoupling capacitor placed near the via is often considered as a mitigation approach for the EMC problem due to the signal via transition. The decoupling capacitor is supposed to provide a low impedance path for the signal return current than the power bus parallel planes. However, the interconnect of a decoupling capacitor limits the effectiveness of the capacitor. At high frequencies, since the inductance of the interconnect is significant, the impedance of the power and ground planes is lower due to the inter-plane capacitance and distributed nature of the planes. The return current takes the path of the displacement current between the power and ground planes. To investigate the limits of a decoupling capacitor for mitigating the EMI problem, numerical modeling was used again to analyze the resulting EMI.

The signal via transition with a decoupling capacitor placed near the via was modeled with the FDTD method. The studied test board had a configuration identical to the test board shown in Figure 3. A $0.01 \mu\text{F}$ decoupling capacitor was placed on the top plane, and 2 mm away from the via. The connection of the capacitor to the power and ground planes is shown in Figure 5. The connecting vias of the capacitor were placed directly in the mounting pads to minimize the interconnect inductance. In the FDTD modeling, these vias were modeled with a thin-wire algorithm, and the capacitor was modeled as a lumped element with one cell. The internal resistance of the capacitor was 0.13Ω , and was also modeled with one cell in series with the capacitor. Since the board dimensions, the layer spacing, and the dielectric constant remained the same as the previous test board, the modeling details, such as cell size, cell number, and time step were identical to those used in the previous modeling. The modeled results of $|S_{21}|$, before and after the decoupling capacitor was mounted on the test board are shown in Figure 6. The modeled results were supported by the measured results, which are shown in the same figure.

The radiated fields 3-meter away from the board were also calculated from the FDTD modeling for EMI purposes. The radiated fields were normalized to a 1-mV source and are shown in Figure 7. From the results of $|S_{21}|$ and the radiated fields, it is apparent that there is little improvement when placing a decoupling capacitor near the via transition. This might be attributed to the interconnect inductance of the decoupling capacitor. The interconnect inductance was then calculated from the first resonance frequency in $|S_{21}|$. In Figure 6, while most peaks occurred at the resonance frequencies corresponding to the TM_{mn} modes of the power bus, a peak at 125 MHz was introduced when the capacitor was mounted on the board. This peak was due to the inter-plane capacitance of the power bus in resonance with the interconnect inductance of the decoupling capacitor. First, the inter-plane capacitance between the power and ground planes was estimated based on the plane area, the layer spacing, and the dielectric constant, and the approximate capacitance was 0.4 nF . Then the interconnect inductance of the decoupling capacitor was determined as approximately 4 nH . The interconnect inductance was significant in part due to the board thickness. Therefore, beyond a few hundred MHz, the decoupling capacitor had little effect in providing a low impedance path for the return current. The return current primarily used the parallel-plane path of the power/ground layer pair. The modeled $|S_{21}|$ was somewhat smaller than the measured result at 125 MHz. This discrepancy is because the test board had a smaller dielectric loss at low frequencies than used in the modeling. Also the capacitor ESR used in the modeling may have been too large.

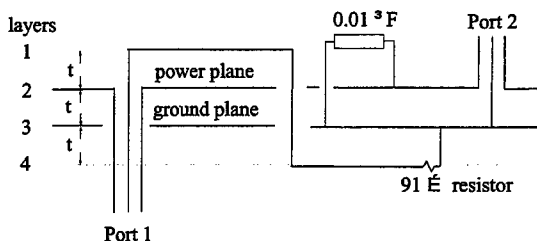


Figure 5. A $0.01\text{ }\mu\text{F}$ decoupling capacitor connected to the power bus as a potential EMI mitigation approach.

IV. Conclusions

The EMI resulting from a signal via transitioning through the internal power and ground planes can be modeled with FDTD, MoM, and PEEC methods with moderate computational intensity. The modeled results with these methods compare well with each other and measurements. Modeling a signal trace with one cell in width in FDTD modeling is adequate for EMI purposes in this study. The power bus noise and resulting EMI can be determined from numerical methods for both signal integrity and EMC purposes. In addition, using decoupling capacitors as a mitigation approach can be evaluated with numerical methods. The numerical modeling is a fast approach to estimate the resulting EMI as a function of the board geometry, such as the board thickness, the location of the decoupling capacitor, the dielectric constant and the dielectric loss. As the interconnect of the decoupling capacitor becomes significant at high frequencies, other EMI mitigation approaches must be considered. The effects of proposed EMI mitigation approaches can be readily studied with numerical methods for estimating EMI and developing design guidelines.

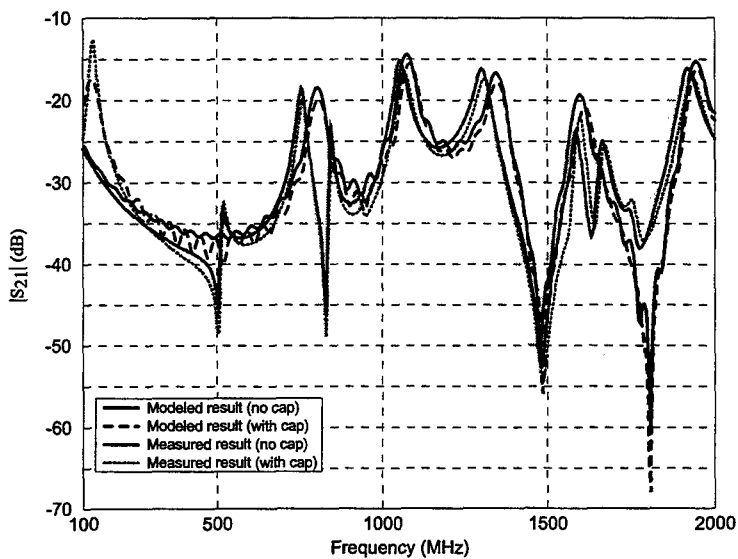


Figure 6. The modeled and measured $|S_{21}|$ of the test board with and without the decoupling capacitor.

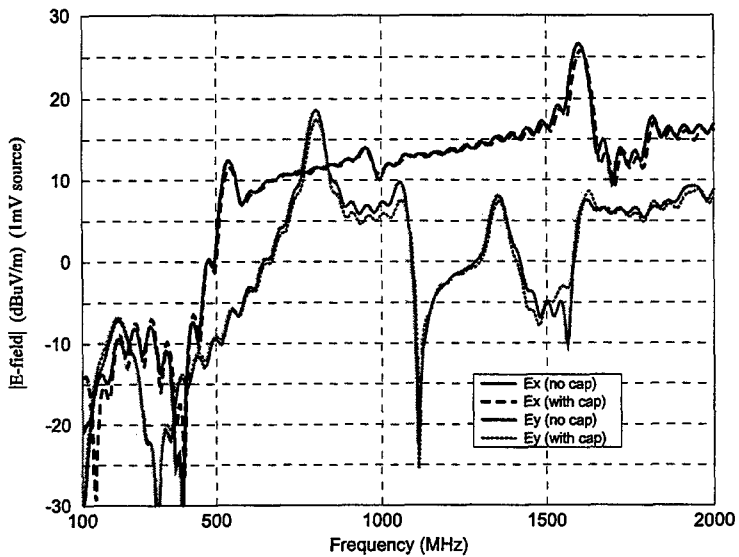


Figure 7. The modeled radiated fields for the test board with and without the decoupling capacitor.

References

- [1] C. Schuster, A. Witzig, and W. Fitchner, "Electromagnetic analysis of interconnects using the finite difference time domain methods", *Proceedings of the European Conference on Circuit Theory and Design ECCTD'99*, vol. 1, pp. 547-550, Stresa, Italy, August – September 1999.
- [2] "Effects of vias on simultaneous switching noise and capacitors placed near vias", *Application Example 7 on* <http://www.sigrity.com/ApplicationExamples/app7.pdf>.
- [3] A. Taflovie, *Computational Electrodynamics: The finite-difference time-domain method*, Norwood, MA: Artech House, Inc., 1995.
- [4] X. Luo, M. Li, and J. L. Drewniak, "Time history extrapolation for FDTD modeling of shielding enclosure designs and EMI antenna geometries", *Proc. IEEE Int. Symp. on Electrom. Comp.*, Denver, Colorado, August 1998, pp. 1172-1177.
- [5] S. Daijavad and B. Rubin, "Detailed analysis of a canonical structure in electromagnetic radiation problems", *IEEE Trans. on Electrom. Comp.*, May 1993, pp. 231-234.
- [6] A. Ruehli, "Partial element equivalent circuit (PEEC) method and its application in the frequency and time domain", *Proc. IEEE Int. Symp. on Electrom. Comp.*, Santa Clara, California, August 1996, pp.128-133.

Techniques for Optimizing FEM/MoM Codes

Y. Ji, T. H. Hubing, and H. Wang
Electromagnetic Compatibility Laboratory
Department of Electrical & Computer Engineering
University of Missouri-Rolla
Rolla, MO 65401
yji@umr.edu, hubing@umr.edu, haoh@umr.edu

Abstract - This paper presents techniques for optimizing the performance of FEM/MoM codes. The process of computing MoM matrices can be accelerated by choosing the order of Gaussian Quadrature calculations adaptively and taking advantage of the symmetric nature of the impedance (or admittance) matrix. Optimizing loop index order and buffering loop indices can significantly improve the performance of matrix operations. Unrolling techniques can be utilized to exploit the power of high-speed cache memory and reduce data access time. Preconditioning techniques can enhance the spectral properties of the FEM/MoM matrix equations and dramatically improve the convergence rate of iterative solvers.

Index Terms - Hybrid FEM/MoM, code performance, loop index order, unrolling, buffering, preconditioned iterative solvers.

I. Introduction

The hybrid FEM/MoM method combines the finite element method (FEM) and the method of moments (MoM) to model inhomogeneous unbounded problems. These two methods are coupled by enforcing field continuity on the boundary that separates the FEM and MoM regions. Figure 1 shows the structure of EMAP5, a FEM/MoM code developed at University of Missouri-Rolla [1,2]. Table 1 lists the computation time required for EMAP5 to model a sample geometry with 579 FEM unknowns and 1,155 MoM unknowns. The performance bottlenecks are computing the MoM matrices, assembling and solving the final matrix equation. The time spent on other tasks such as reading the input file and generating output is minor, thus is not listed in Table 1.

This paper presents techniques that can be used to optimize FEM/MoM codes. Section II discusses how to optimize routines. Section III describes how to optimize the computation of the MoM matrices. Section IV shows that adjusting loop-index order, buffering loop indices, and unrolling techniques can significantly improve the code efficiency. Section V presents preconditioning techniques that can greatly improve the efficiency of iterative solvers. Finally, conclusions are drawn in Section VI. Sample problems analyzed using the EMAP5 code running on a Sun workstation are used to illustrate the improvements in run time that can be expected.

II. Optimizing Routines

Numerical codes are usually composed of routines (modules, functions). The length of a routine is not only a maintenance concern, but also an efficiency concern. A very short routine is not efficient because calling a routine involves expensive context switching operations (save the status of the current routine, then load another routine). On the other hand, a long routine is not efficient if it does not fit in the code cache. Therefore, it is best to divide codes into proper-size routines. The code length of each routine should not exceed 200 lines, excluding comments and blank lines [3]. The most error-prone routines are those larger than 500 lines of code [4].

Crucial routines must be examined, re-written and carefully tested to improve code performance. In FEM/MoM codes, a large portion of computation time is spent on matrix operations. Matrix operations should be put in separate routines that are optimized for the hardware they will run on. Although many

compilers support code optimization, well-written codes can be further optimized as shown in latter sections.

III. Optimizing Computation of the MoM Matrices

The Gaussian Quadrature technique is generally used to numerically evaluate integrands over two surface patches in MoM. The choice of Gaussian Quadrature order (1-point, 3-point, or 7-point) can be determined adaptively depending on the distance between two patches. For example, suppose R_{cp} is the distance between the centroids of the triangle pair in Figure 2, and $MaxEdgeLen$ is the maximum edge length of the source (or observing) triangular patch. The following procedure can be used to adaptively determine the Gaussian Quadrature order of the source (or observing) triangular patch,

```

if ( Rcp/MaxEdgeLen > 10 )
    QuadType = 1;      /* use 1-point Gaussian Quadrature */
else if ( Rcp/MaxEdgeLen > 5 )
    QuadType = 3;      /* use 3-point Gaussian Quadrature */
else QuadType = 7;      /* use 7-point Gaussian Quadrature */

```

Furthermore, the impedance (or admittance) matrix in MoM is symmetric. Only half of the entries need to be computed.

IV. Optimizing Matrix Operations

The structure of computer memory is typically organized in a hierarchy [5] as shown in Figure 3. The higher-level media supports faster access but is more expensive. Performance data reported in this paper is measured on a Sun Ultra-II 250MHz workstation in units of MFlops (million floating-point operations per second). Figure 4 shows the code performance versus the size of problem being solved. The code performs best when data fits in the data cache. The code performance drops when data is stored in the primary cache and the first-level memory (DRAM/SDRAM). The code performance is 75% higher when data is stored in primary cache than in DRAM. In typical numerical applications, most data is stored in DRAM. The following two sub-sections present how to improve the performance of matrix operations by utilizing cache memory efficiently.

A. Optimizing inner-product operations in the complex bi-conjugate gradient method

Iterative solvers are widely used to solve large-scale matrix equations. The complex bi-conjugate gradient method (CBCG) introduced by Jacobs [6] can be used to solve the final complex matrix equation generated by FEM/MoM, which is of the form

$$[A][x]=[b] \quad (1)$$

where $[A]$ is an $N \times N$ complex matrix, and $[b]$ and $[x]$ are $N \times 1$ complex column vectors. Both $[A]$ and $[b]$ are known while $[x]$ is unknown. As Table 1 indicates, solving the final matrix equation is one of the bottlenecks of the EMAP5 code performance.

The most time-consuming portion of CBCG are the operations computing the product of $A p_k$ and $A^H p_k$, where $[A]$ is the coefficient matrix, A^H is the Hermitian of matrix A , p_k is the direction vector, and p_k is the bi-direction vector. Both of these operations involve N^2 complex number multiplications. All other operations in CBCG only require $O(N)$ complex multiplications. A natural implementation of $[C]_N = [A]_{N,N} [P]_N$ in the C programming language is shown below,

```

for ( i=0; i<N; i++)
    for ( j=0; j<N; j++)

```

$$C[i] = A[i][j] * P[j];$$

The above loop index order is defined as (i, j) . This implementation works fine. A natural implementation of $[C]_N = [A]_{N,N}^H [P]_N$ is as follows,

```
for ( i=0; i<N; i++ )
    for ( j=0; j<N; j++ )
        C[i] = Conjugate( A[j][i] ) * P[j];
```

The above implementation is inefficient because data in the C language is row-major (row-indexed). Whenever index j increases by one, the address of $A[j][i]$ will jump N address spaces. If the next $A[j][i]$ is not in the data cache, a cache miss occurs. The next $A[j][i]$ and its neighbor units (a cache block) will be swapped from DRAM into the data cache. Frequent cache misses can significantly degrade the code performance. To better utilize the data-caching feature, it is desirable to access data in a cache block continuously to reduce the number of cache misses. For the above example, the loop index can be changed from (i, j) to (j, i) (the loop body is the same) as shown below,

```
for ( j=0; j<N; j++ )
    for ( i=0; i<N; i++ )
        C[i] = Conjugate( A[j][i] ) * P[j];
```

As shown in Table 2, this change of loop index order increases the performance from 1.52 MFlops to 2.94 MFlops, (i.e. by 93%).

Buffering the loop indices i and j in registers can improve the code performance even further. The following code (in the C language) stores two integers in registers,

```
register int i, j;
```

This ensures that the loop indices i and j will not be swapped out from cache memory to DRAM. Many C compilers do not optimize codes by buffering temporary variables. Programmers must decide how to buffer variables by themselves. It can be difficult to decide how to buffer temporary variables in a large routine because computers have a limited number of registers. Therefore, crucial codes (in terms of computational cost) should be put into separate routines of proper size and tuned to optimize performance. As shown in Table 2, buffering loop indices i and j improves the code performance by 90% (from 2.94 MFlops to 5.32MFlops) without compiler optimization and 11% (from 10.42MFlops to 11.6 MFlops) with compiler optimization. Choosing the proper loop index and buffering loop indices improves the overall code performance by a factor of 2.5 without compiler optimization and 2.6 with compiler optimization.

B. Optimizing matrix multiplication

Hybrid FEM/MoM codes perform many matrix multiplications [1]. This process is numerically intensive, involving $O(N^3)$ floating point operations. Choosing the proper loop index order is critical to the code performance. For typical matrix multiplication $[A]_{N,N} = [B]_{N,N} * [C]_{N,N}$, loop index (i, j, k) refers to the following loop order,

```
for ( i=0; i<N; i++ )
    for( j=0; j<N; j++ )
        for( k=0; k<N; k++ )
            A[i][j] += B[i][k]*C[k][j];
```

Table 3 shows the code performance of all six possible combinations of loop indices. It is clear that (k, i, j) and (i, k, j) are the best loop index orders. Without compiler optimization, the best/worst performance

ratio is 1.88. With compiler optimization, the best/worst performance ratio is 5.0. This indicates that codes that are more efficient can be better optimized by compilers.

Unrolling techniques [5] can efficiently utilize cache blocks to reduce data access time. The basic idea of unrolling is to reduce the number of iterative loops, but add statements to loop bodies to do the missing iterations. For the above matrix multiplication codes, a four-way unrolling implementation is shown below,

```
for ( i=0; i<N; i++ )
  for ( k=0; k<N; k+=4 )
    for ( j=0; j<N; j++ ) {
      A[i][j] += B[i][k]*C[k][j];
      A[i][j] += B[i][k+1]*C[k+1][j];
      A[i][j] += B[i][k+2]*C[k+2][j];
      A[i][j] += B[i][k+3]*C[k+3][j];
    }
}
```

Table 4 shows the code performance improvement obtained by using this 4-way unrolling technique and buffering loop indices. The time required for matrix multiplication is reduced by 68%.

V. Preconditioned Iterative Solvers

The coefficient matrices generated by the application of hybrid FEM/MOM codes to complex geometries often have very large condition numbers. It is difficult to apply iterative solvers to these matrix equations. However, in general, a matrix equation can be transformed into another matrix equation so that the new matrix equation has the same solution as the original one, but has better spectral properties. For instance, both sides of Equation (1) can be multiplied by a square matrix P^{-1} ,

$$P^{-1}Ax = P^{-1}b \quad (2)$$

where P has the following properties,

- (1) $K(P^{-1}A) \ll K(A)$
- (2) $\det(P^{-1}A) \neq 0$
- (3) it is inexpensive to solve $Px = b$

and where $K(\bullet)$ and $\det(\bullet)$ are the condition number and the determinant of a matrix, respectively. Such a matrix P is called a *preconditioner*. This technique is called *preconditioning*. Condition (1) assures favorable spectral properties for the new linear system. Condition (2) guarantees that the new system, Equation (2), has the same non-trivial solution as Equation (1). Condition (3) is essential to ensure the efficiency of preconditioned iterative solvers. In preconditioned iterative algorithms, it is not necessary to solve P^{-1} explicitly. Instead, a linear system of the form $Px = b$ is solved at each step.

A new equation solver has been developed for EMAP5 based on the preconditioned Bi-Conjugated Gradient Stabilized method (BiCGSTAB) [2]. Two printed circuit board (PCB) problems and one scattering problem have been chosen to test the new solver. As shown in Table 5, the new solver has improved the efficiency of the matrix equation solver by a factor of 48 in Problem 1 (from 206.10 sec to 3.55 sec), by a factor of 150 in Problem 2 (from 6,037.90 sec to 40.10 sec), and by a factor of 48 in Problem 3 (from 386.77 sec to 8.10 sec). The overall improvements for the three problems are 221%, 783% and 636%, respectively. This shows that preconditioning techniques can dramatically improve the convergence rate of iterative solvers and the overall performance of FEM/MoM codes.

VI. Conclusions

This paper presents techniques for optimizing FEM/MoM codes. Numerical codes should be divided into routines of appropriate length for the sake of maintenance and performance. Crucial routines should be well tuned to the hardware they will run on. The performance bottlenecks of FEM/MoM codes are computing the MoM matrices and assembling and solving the final matrix equation. The process of computing the MoM matrices can be accelerated by using an adaptive Gaussian Quadrature technique and by taking advantage of the symmetric nature of the impedance (admittance) matrix. The performance of matrix operations can be significantly improved by optimizing loop index order and buffering loop indices. Unrolling techniques can be utilized to reduce data access time. The hybrid FEM/MoM method often generates matrix equations with very large condition numbers. It can be difficult to apply iterative solvers to these matrix equations directly. Preconditioning techniques can be used to improve the spectral properties of matrix equations and dramatically accelerate the convergence rate of iterative solvers. Together, these optimization techniques can greatly reduce the overall run time of hybrid FEM/MoM codes analyzing large problems.

References:

- [1] M. Ali, T. H. Hubing, and J. L. Drewniak, "A hybrid FEM/MoM technique for electromagnetic scattering and radiation from dielectric objects with attached wires," *IEEE Trans. on Electromagnetic Compatibility*, vol. 39, pp. 304-314, Nov. 1997.
- [2] Y. Ji, M. Ali, and T. H. Hubing, "EMC applications of the EMAP5 hybrid FEM/MoM code," *Proceedings of the IEEE 1998 International Symposium on Electromagnetic Compatibility*, vol. 1, pp. 177-181, Denver, Colorado, Aug. 1998.
- [3] S. McConnell, *Code Complete*, Washington: Microsoft Press, 1993.
- [4] C. Jones, *Programming Productivity*, New York: McGraw-Hill, 1986.
- [5] D. Loshin, *High Performance Computing Demystified*, Boston: Academic Press, 1994.
- [6] D. A. H. Jacobs, "A generalization of the conjugate gradient method to solve complex system," *IMA J. Numerical Anal.* vol. 6, pp 447-452, 1986.
- [7] R. Barrett, M. Berry, T. F. Chan, F. Demmel, J. M. Donato, J. Dongarra, V. Eijkhout, R. Pozo, C. Romine, and H. Van der Vorst, *Templates for the Solution of Linear Systems: Building Blocks for Iterative Methods*, Philadelphia: SIAM, 1994.

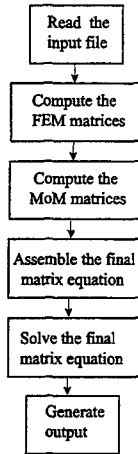


Figure 1. The EMAP5 code structure.

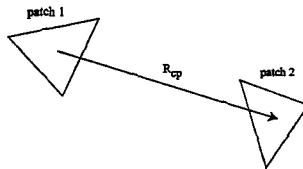


Figure 2. Center-to-center distance between two surface patches.

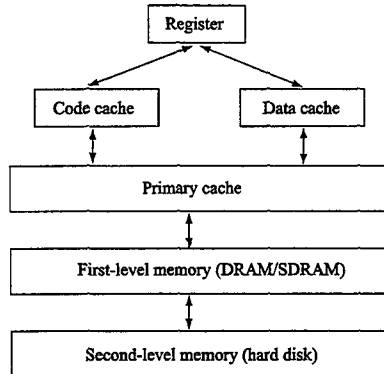


Figure 3. Memory hierarchies.

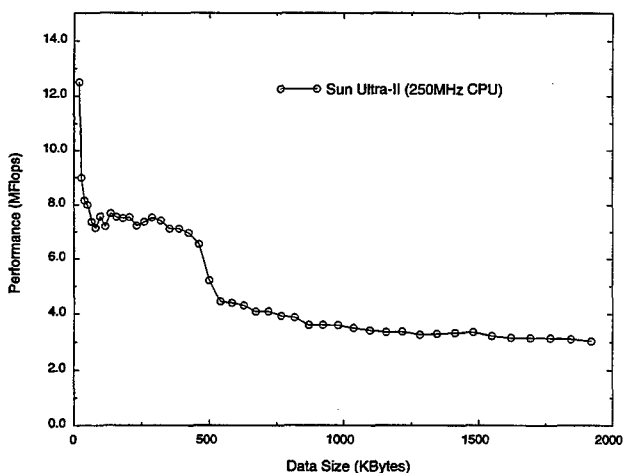


Figure 4. Code performance verses data size.

Table 1. Time required to model a problem with 579 FEM and 1,155 MoM unknowns.

Total time (min.)	Compute the FEM matrices (min.)	Compute the MoM matrices (min.)	Assemble the final matrix equation (min.)	Solve the final matrix equation (min.)
174	0.1	20	92	63

Table 2. Performance of $[C]_N = [A]_{N \times N}^H [P]_N$ versus loop index permutation when $N = 400$.

	Loop index	Use registers to buffer variables (Yes/No)	Performance (MFlops)	
			No compiler optimization	Using compiler optimization
Case 1	(i, k)	No	1.52	3.23
Case 2	(k, i)	No	2.94	10.42
Case 3	(k, i)	Yes	5.32	11.60
Improvement (best/worst)			250%	260%

Table 3. Performance of $[A]_{N,N} = [B]_{N,N} * [C]_{N,N}$ versus loop index permutation when $N=400$.

	Loop index	Performance (MFlops)	
		No compiler optimization	Using compiler optimization
Case 1	(k, j, i)	0.90	1.57
Case 2	(j, k, i)	0.95	3.64
Case 3	(j, i, k)	1.36	3.64
Case 4	(i, j, k)	1.31	3.71
Case 5	(k, i, j)	1.78	7.72
Case 6	(i, k, j)	1.79	7.72
Improvement (best/worst)		188%	500%

Table 4. Performance of $[A]_{N,N} = [B]_{N,N} * [C]_{N,N}$ using unrolling techniques when $N=400$.

	Use registers to buffer variables	Performance (MFlops)	
		No compiler optimization	Using compiler optimization
Case 1	No	1.31	3.71
Case 2	Yes	1.85	3.70
Unrolling	Yes	2.20	6.26

Table 5. Time required to solve three sample problems.

	Compute FEM and MoM matrices (sec)	Forming the final matrix equation (sec)	Original		Preconditioned		Overall improve- ment (%)
			Solving the final equation (sec)	Total (sec)	Solving the final equation (sec)	Total (sec)	
Problem 1	48.00	40.23	206.10	294.22	3.55	91.78	221%
Problem 2	287.20	438.60	6,037.90	6,763.7	40.10	765.90	783%
Problem 3	40.12	11.33	386.77	438.22	8.10	59.55	636%

Numerical Modeling of Shielding by a Wire Mesh Box

Gerald J. Burke and David J. Steich
Lawrence Livermore National Laboratory
Livermore, CA 94550
burke2@llnl.gov and steich1@llnl.gov

Introduction

The rebar mesh in concrete walls often represents a primary means for shielding the inside of a building from fields due to lightning or other sources, or for preventing unintended radiation from sources in the building. Real situations can be very complicated, with the rebar mesh embedded in concrete and involving ground, grounding structures, apertures in the walls and conductors penetrating the walls. For this paper we consider the simple case of a plane wave incident on a wire mesh box to examine the effects of mesh parameters and evaluate the accuracy of the modeling codes for this application. The modeling was done with the NEC-4 moment method code, and also a FDTD code where the mesh box was modeled with rows of conducting cells, and a FDTD code coupled to a thin-wire model [1]. We also have looked at the effects of wires penetrating the mesh, a thin gap in the mesh, unbonded junctions and excitation by nearby currents rather than a plane wave.

In the next section we will briefly describe the numerical modeling methods used. Next, results are shown for a plane wave incident on a wire mesh box. The effect of varying the wire spacing, wire radius and frequency are demonstrated. Results from moment-method and FDTD codes are compared for validation, and the shielding is also compared with the analytic results developed by Casey [2].

Numerical Modeling Methods

Results for the mesh box were obtained by running a finite difference time domain (FDTD) code and a frequency domain moment method code NEC-4 [3]. Advantages of a moment method code such as NEC for modeling the mesh box are that wires can have arbitrary radius and location, and electric and magnetic fields can be computed at arbitrary locations near the structure. Also, the low frequency response can be obtained from one or a few frequency evaluations, while a time domain solution might need to be run for a long time period in order to extract the low frequencies from a Fourier transform.

A limitation of NEC for this application is that results become inaccurate when the spacing between wires in the mesh is less than several times the wire diameter. The error due to the thin-wire approximation will be demonstrated in our results. However, the conductor spacing for most rebar will probably be such that a thin-wire model will be suitable. Another limitation of NEC for modeling the mesh box is an instability that can occur with electrically small loops. The problem is seen as an erroneous loop current that grows as the inverse of frequency due to the moment-method matrix becoming ill-conditioned. Loop currents were seen in the mesh box at low frequencies, but did not appear to have a significant effect on the field evaluated at the center of the box.

The FDTD results for the box were obtained from a code using the Yee algorithm [4] with

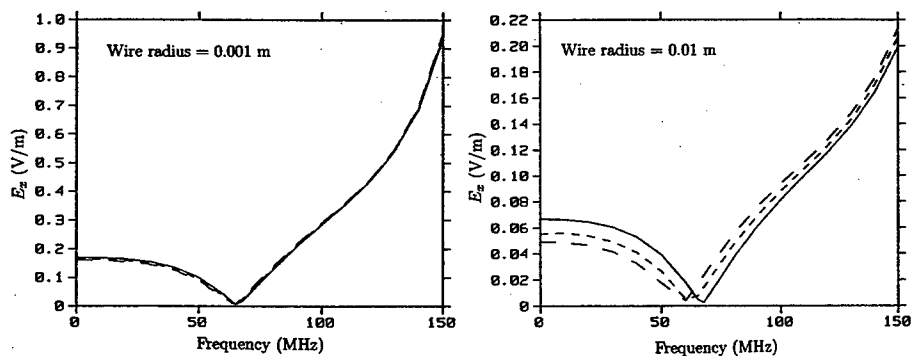


Fig. 1. Field at the center of a wire mesh box with 1 m side and five cells per side; NEC model with number of segments per mesh cell of 1 (solid), 2 (short dash) and 4 (long dash).

cubic cells and a PML absorbing boundary. It was found that a relatively thick PML region (12 cells) was needed to avoid reflections that would distort the low frequency response. The basic Yee algorithm is not well suited to modeling thin wires. A linear conductor can be represented with a string of highly conducting cells, but the diameter of the equivalent round wire is uncertain, but somewhat less than the cell width. We used this approach for modeling a mesh of thick wires where the NEC thin-wire model would not be accurate. To model wires thinner than the cell size we used the method described by Holland [1], in which transmission line differential equations representing the wire current and voltage are coupled to the equations for fields in the mesh. The box was excited with an incident plane wave having a Gaussian profile with full-width-half-max of about three times the width of the box. Shorter pulses would excite resonant modes in the box which would ring for a long time and were not of interest for the study of lightning effects. The solution was run for about 2000 time steps, and the response was then extended in time using the Generalized Pencil of Functions technique [5] until it had decayed to a very small value. The extended response was then Fourier transformed and deconvolved with the Gaussian pulse.

An error in loop currents similar to that seen in NEC was observed in the FDTD results for the mesh box. In the time domain it is manifest as a residual DC current in the loops that would flow forever after the actual response has decayed away. In a Fourier transform these DC currents would contribute an inverse frequency term at low frequencies as seen in NEC. This similarity to NEC could be expected, since the Yee algorithm expressed in integral form uses the field at the center of each edge to approximate the line integral of field around a face, similar to the point sampling in NEC.

Shielding by a Mesh Box

A box one meter on a side was chosen to study the shielding from a plane wave. Since NEC computes the scattered near field due to currents, the code had to be modified to add the incident plane wave field. The cancellation of incident and scattered fields will increase the relative error when shielding is high. The excitation in NEC was a plane wave of 1 V/m incident along the z axis with electric field in the x direction. The resulting E_x at the center of the box with 5 cells per side, and wire spacing of 0.2 m, is shown in Figure 1 for wire radii of 0.01 m and 0.001 m.

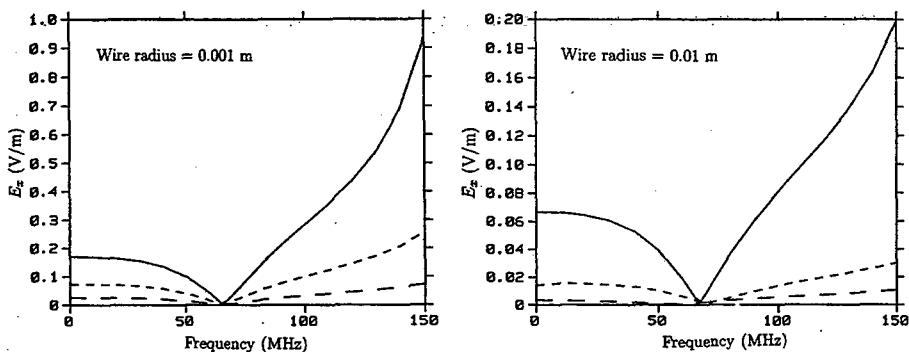


Fig. 2. NEC results for shielding by a 1 m mesh box with number of mesh cells per side of 5 (solid), 10 (short dash) and 21 (long dash).

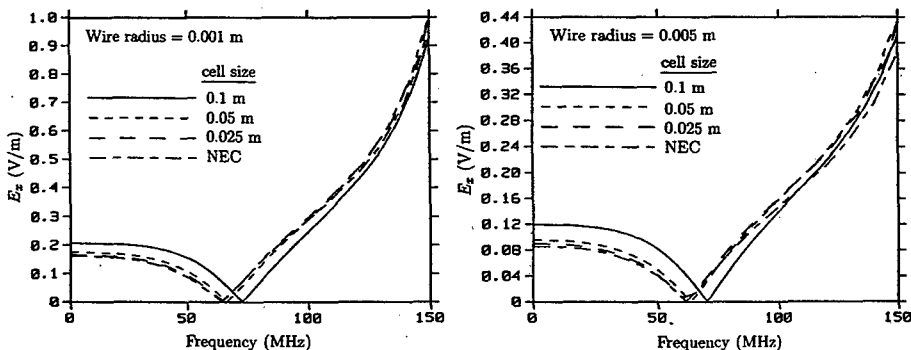


Fig. 3. FDTD solution for the field at the center of a wire mesh box with 1 m side and five mesh cells per side, using the thin-wire algorithm. The FDTD cell size was varied to test convergence.

In both cases the field is seen to remain relatively constant at low frequencies, then go into a null around 60 MHz and then begin rising as the electrical size of the mesh cells becomes larger. These NEC models were run with 1, 2 and 4 segments per side of each mesh opening (segment lengths of 0.2 m, 0.1 m and 0.05 m) to test the convergence of the solution. Convergence is good for a wire radius of 0.001 m, but more variation is seen for the 0.01 m radius due to the increased cancellation of fields. The field at the center of the 1 m box is shown in Figure 2 for 5, 10 and 21 mesh cells per side and wire radii of 0.001 m and 0.01 m. The reduced mesh size relative to the box size is seen to increase shielding, while shielding still becomes independent of mesh size relative to wavelength at low frequencies.

FDTD solutions for the same mesh box, with 1 m sides and five mesh cells per side, are shown in Figure 3. The thin-wire algorithm [1] was used to include the wires, and the FDTD cell size was varied from 0.1 m to 0.025 m to test convergence. NEC results using four segments per side of a mesh cell are included for comparison. The result for 0.1 m cells with a wire in every other

cell are not too well converged, but the models with smaller cells compare well with NEC. The 0.01 m radius results are not shown, since the thin-wire FDTD algorithm became unstable with a cell size of 0.025 m. FDTD solutions in which wires were modeled by strings of highly conducting cells are shown in Figure 4. The wire spacing was 0.2 m in each case, with a wire in every fourth cell for 0.05 m cells (equivalent radius of about 0.02 m) and a wire in every eighth cell for 0.025 m cells (equivalent radius of about 0.01 m.) These results indicate that both NEC and FDTD algorithms are capable of modeling shielding by a mesh box, although relative error in the interior fields can be expected to increase as the shielding becomes more complete with increased conductor radius or increasing number of conductors in the walls.

The null that occurs around 57 MHz in the electric field at the center of the box is a characteristic feature of all of these results. The transfer function for field can be approximated as an inductance only at frequencies well above this null. This notch was also observed in the measurements made by Nyffeler et al. [6]. Since it occurs at too low a frequency to be associated with a resonant mode, it appears that it may be the result of interference between fields entering the box through different paths. To investigate this phenomena and attempt to get a better understanding of how the field enters the box, we tried modeling the box with some faces solid and some with mesh. The FDTD code was used with wires represented as strings of conducting cells, since with this code it is easy to make selected faces solid so that they are totally impenetrable by the field. A NEC mesh model will always have some leakage, even when the wire radius a and separation d are set for the "equal area" condition $2\pi a = d$. In the results here the term "TE faces" refers to the four faces on which the incident electric field is transverse to the face normal. "TM faces" refers to the other two faces where the incident H is transverse to the normal and E is normal to the face.

The modeling results showed that for frequencies from zero through 57 MHz the field entering through TM faces was nearly in phase with the phase of the incident field outside the box, while field entering through TE faces (mainly the face that the wave was incident on) had nearly constant phase through the box in the direction of the wave propagation. The interference of these fields produced the null on a plane across the center of the box. No null was seen away from the center position. The field entering the box through TM faces was dominant at low frequencies, and remained relatively constant to about 70 MHz. The field entering through TE faces increased approximately linearly with frequency, and exceeded the field from TM faces above about 57 MHz, so the null occurs when the two modes are equal and canceling. The null was seen in cubical boxes, but not when the box dimension parallel to the incident electric field is stretched to two or more times the other dimensions.

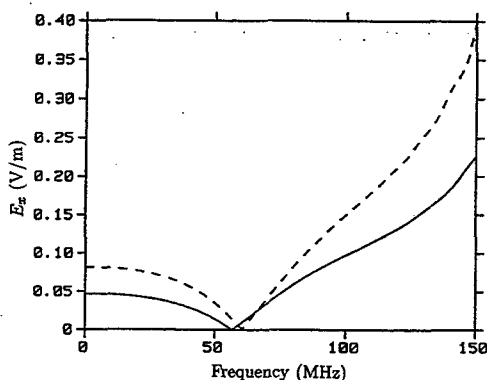


Fig. 4. FDTD solution for the field at the center of the mesh box with 1 m sides and five mesh cells per side. Wires were modeled as strings of conducting cells with a wire in every fourth cell with 0.05 m cells (solid) and in every eighth cell with 0.025 m cells (dashed).

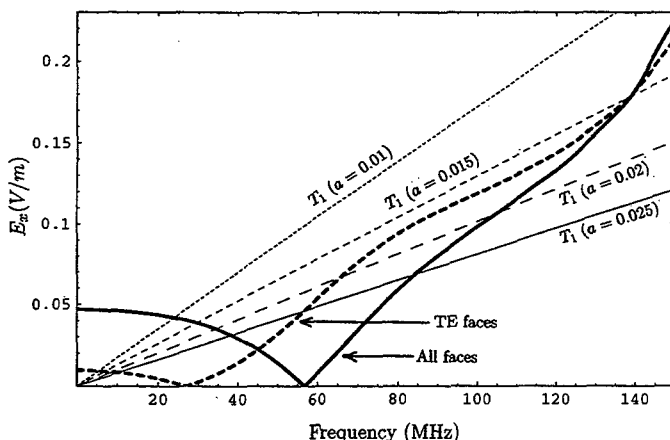


Fig. 5. Comparison of the transmission coefficient for normal incidence on an infinite mesh with the FDTD solution for a box with mesh on all sides and mesh on only the TE faces.

These numerical results were compared with analytic approximations derived by Casey [2] for the shielding by a wire mesh. Casey's results are based on a surface impedance operator derived from the space-averaged tangential electric field and space-averaged surface current density on the mesh. He applies this analysis to several cases, including a plane wave incident on an infinite mesh screen and quasistatic shielding by a mesh enclosure. For a plane wave incident normal to an infinite mesh, Casey's transmission coefficients reduce to

$$T_1 = \frac{d\mu_0\omega \log[(1 - e^{-2\pi a/d})^{-1}]}{\sqrt{(\pi\eta)^2 + [d\mu_0\omega \log[(1 - e^{-2\pi a/d})^{-1}]]^2}} \quad (1)$$

where d is the width of the square mesh cells and a is the wire radius. If the exponentials are replaced by two terms of their small argument approximation (1) reduces to

$$T_0 = \frac{d\mu_0\omega \log\left(\frac{d}{2\pi a}\right)}{\sqrt{(\pi\eta)^2 + [d\mu_0\omega \log\left(\frac{d}{2\pi a}\right)]^2}} \quad (2)$$

which is equivalent to the result derived by Lamb [7].

The transmission coefficient T_1 is compared in Figure 5 with FDTD results for the field at the center of the 1 m mesh box with 1 V/m wave incident normal to a face. In the FDTD model the wires were represented as strings of highly conducting cells with five openings per side of the box and a FDTD cell size of 0.05 m. Thus there were three free-space cells between wires, with the conductors spaced by four cells or $d = 0.2$ m. With strings of conducting cells, the radius of the equivalent round wire is somewhat uncertain but is expected to be in the range of 0.015 to 0.02 m for the 0.05 m cell size. In addition to the FDTD result for mesh on all sides of the box, Figure 5 includes the result for mesh on the four TE faces with the two TM faces solid. As expected, the result for mesh only on TE faces is in better agreement with T_1 than with

mesh on all faces. The increasing slope of the numerical results above 140 MHz is the result of the cavity resonance which occurs around 206 MHz.

Casey's transmission coefficient T_1 and the simpler form T_0 are compared in Figure 6 with the numerical solution for a plane wave normally incident on an infinite, uniform mesh with $d = 0.2$ m and frequency of 30 MHz. The numerical results are from a 2D moment method solution using the thin-wire approximation for the infinite mesh. The boundary condition was matched on the wire axis. For the "A" result the current was located on the wire surface with a displacement transverse to the direction to the evaluation point, while for the "B" result the current was numerically integrated around the wire.

The electric field was evaluated at a distance 0.5 m behind the mesh, the same distance as the center of the 1 m box. All results are in agreement when wire radius a is much less than the wire spacing d . This agreement continued to hold as frequency was reduced to below 10 KHz, which indicates that the difference between the transmission coefficient and the field in the box is not due to near field effects. As the wire radius is increased, the numerical result goes into a null at $2\pi a = d$ and then increases for larger wire radius. Since the transmitted field should go to zero when the wires touch at $2a = d$, Casey's transmission coefficient is giving a credible result, while Lamb's approximation shows the same behavior as the thin-wire numerical models. This behavior of the thin-wire approximation to over estimate the shielding in the vicinity of $2\pi a = d$ is known as the "equal area rule" and is often used when it is desired to make a mesh represent a solid surface. However, in this case it represents an error in greatly over estimating the shielding.

Casey [2] also uses the surface impedance operator to derive expressions for shielding by wire mesh enclosures. He considers infinite parallel plates, a cylinder and a sphere, but the results for electrostatic shielding involve the enclosure shape only through the surface area and volume of the enclosure. For an enclosure with volume V_e and surface area S_e his result for the ratio of electrostatic field in the shielded region to field in the absence of the shield is

$$T_e = \left(1 + \frac{V_e}{l_e S_e}\right)^{-1} \quad \text{where} \quad l_e = \frac{d}{4\pi} \log[(1 - e^{-2\pi a/d})^{-1}]. \quad (3)$$

This result is compared with numerical results for the 1 m mesh box with $d = 0.2$ m in Figure 7. The numerical values up to a radius of 0.01 m were obtained with NEC for a frequency of 10 KHz. Since the NEC result for 0.01 m radius converged slowly, as seen in Figure 1, the values for one and four segments per side of the mesh cells are plotted in Figure 7. Also, the thin-wire approximation in NEC may over estimate the shielding for thick wires, as was seen in Figure 6.

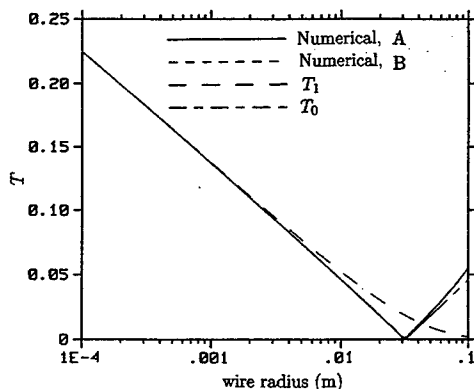


Fig. 6. Comparison of the transmission coefficients T_0 and T_1 for normal incidence on an infinite mesh with the numerical solution for an infinite screen of parallel wires with wire spacing 0.2 m and wire radius varied.

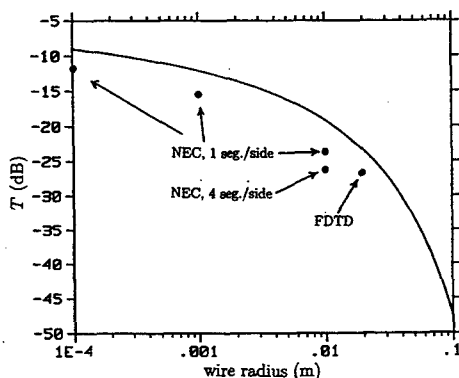


Fig. 7. Comparison of Casey's result for electrostatic shielding by an enclosure with the numerical solution for the mesh box for varying wire radius. Results for 0.01 m radius and less are from NEC and 0.02 m radius is FDTD.

The value plotted at 0.02 m radius in Figure 7 is from the FDTD code with a cell size of 0.05 m and wires modeled as strings of conducting cells. The numerical results show good agreement in trend with equation (3), although they are lower by about 3 dB. In Figure 8, NEC results for boxes with 5, 10 and 21 cells per side are compared with equation (3) for varying d and wire radii of 0.001 and 0.01 m. Again, the results agree in trend, but NEC results are about 3 dB lower than Casey's result.

Conclusion

Wire mesh cages were modeled using a thin-wire moment method code (NEC) and FDTD with either a thin wire algorithm or strings of conducting cells. All of these methods were found to be capable of giving accurate results for the shielding. When the conductor diameter was increased to about an eighth to a quarter of the conductor spacing the FDTD code with conducting cells was the preferable method, since the thin-wire moment method over estimated the shielding while the thin-wire FDTD algorithm became unstable. As the shielding became more complete due to increased conductor diameter or number of conductors the error in the scattered field solution (NEC) increased and convergence became slow due to the cancellation of fields.

The shielding of the mesh cage was found to become independent of frequency for wavelengths much greater than five times the cage size, but continued to depend on the mesh size relative to cage size down to essentially zero frequency. For wavelengths less than about $1/5$ of the cage size the field entering the cage increased roughly linearly until the cavity resonance was approached. The shielding was found to be predicted reasonably well by the plane wave transmission coefficient for higher frequencies (but below resonance). Low frequency shielding was in general agreement with Kendal Casey's result for electrostatic shielding by an enclosure, but the field in the box was about 3 dB less than Casey's result.

We also modeled mesh boxes modified with unbonded junctions, gaps and penetrating wires. An analytical result by Wait [8] showed greater shielding with unbonded junctions than with

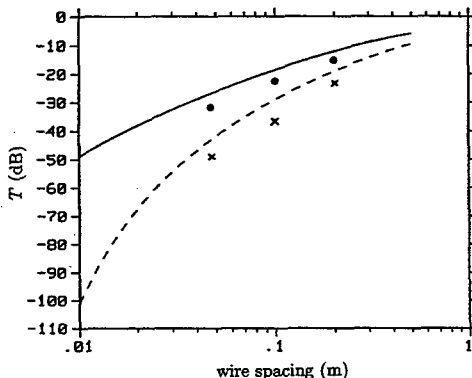


Fig. 8 Comparison of Casey's result for electrostatic shielding by an enclosure with the numerical solution for the mesh box for varying wire spacing. Solid line and dots are for a radius of 0.001 m, and dashed line and "x" are for a radius of 0.01 m.

bonded junctions for an infinite mesh. There are also measurements that support this result [9]. However, the NEC model for the box showed no difference between unbonded and bonded junctions at low frequencies. With unbonded junctions on the 1 m box a resonance occurred around 60 MHz where the field in the box was a few dB above the field of the incident wave. From about 80 to 150 MHz there was again little difference. A thin gap encircling the top of the box on three sides also had little effect on field penetration at low frequencies but introduced a resonance around 50 MHz where the field inside was over 10 dB greater than the incident field. Of course, a gap completely encircling the box allowed field to enter down to low frequency. A wire penetrating into the cage without bonding to the mesh also allowed field to enter to low frequencies: When the wire was bonded to the mesh it increased the field in the cage by a smaller amount, but resulted in a large field penetration when either the interior or exterior parts of the wire were resonant.

Results of using wires to represent the lightning current showed that it is easy to introduce artifacts associated with resonances and charge concentrations on the 'lightning' wire that are not related to the actual lightning. More thought needs to be given to the way the lightning should be represented in a more complete model.

Work performed under the auspices of the U. S. Department of Energy by the Lawrence Livermore National Laboratory under Contract W-7405-Eng-48.

References

- [1] R. Holland, "Finite-Difference Analysis of EMP Coupling to Thin Struts and Wires," *IEEE Trans. Electromagnetic Compatibility*, v. EMC-23, no. 2, May 1981.
- [2] K. F. Casey, "Electromagnetic Shielding Behavior of Wire-Mesh Screens," *IEEE Trans. on Electromagnetic Compat.*, vol. 30, no. 3, pp. 298-306, Aug. 1988.
- [3] G. J. Burke, Numerical Electromagnetics Code — NEC-4, UCRL-MA-109338, Lawrence Livermore National Laboratory, CA, January 1992.
- [4] K. S. Yee, "Numerical solution of initial boundary value problems involving Maxwell's equations in isotropic media," *IEEE Trans. Antennas Propagat.*, Vol. AP-14, pp. 302-307, May 1966.
- [5] T. K. Sarkar and O. Pereira, "Using the Matrix Pencil Method to Estimate the Parameters of a Sum of Complex Exponentials," *IEEE Antennas and Propagation Magazine*, Vol. 37, No. 1, February 1995.
- [6] M. Nyffeler, B. Braendli, B. Reusser, E. Doerr, D. V. Giri and E. R. Tomer, "On the Interaction of Electromagnetic Fields with Wire Cage Structures," *IEEE Trans. on Electromagnetic Compat.*, vol. 34, no. 4, pp. 471-477, Nov. 1992.
- [7] H. Lamb, "On the diffraction in transmission of electric waves by a metallic grating," *Proc. London Math. Soc.*, vol. 29, pp. 523-544, 1898.
- [8] J. R. Wait, "Theories of Scattering from Wire Grid and Mesh Structures," in *Electromagnetic Scattering*, P. L. Uslenghi, Ed., New York, Academic Press, 1978, pp. 253-287.
- [9] M. I. Kontrovich, V. Yu. Petrunikin, N. A. Yesepkina and M. I. Astrakhan, "The Coefficient of Reflection of a Plane Electromagnetic Wave from a Plane Wire Mesh," *Radio Engineering and Electron. Phys.*, vol. 2, pp. 222-231, 1962.

SESSION 9

PROPAGATION

Chairs: Steve Fast and Frank Ryan

A Fast Quasi Three-Dimensional Propagation Model for Urban Microcells

Joseph W. Schuster
Remcom, Inc.
State College, PA
E-mail: jws@remcom.com

Raymond J. Luebbers
Department of Electrical Engineering
The Pennsylvania State University
E-mail: RayL@psu.edu

Abstract

Many of the recently published deterministic models for predicting radio wave propagation in urban microcells combine a two-dimensional ray tracing algorithm with the geometrical theory of diffraction for evaluating the field strength. In order to reduce the computation time, these 2-D models must ignore propagation over buildings and interaction with the terrain other than reflections from a flat ground plane. But because of these restrictions these models will not be reliable in urban environments with low buildings or hilly terrain. This paper presents an approach which can be used when propagation paths over building rooftops and terrain interactions are important, but which continues to use a two-dimensional ray tracing algorithm in order to permit fast computation times.

1. Introduction

A number of papers on deterministic two-dimensional (2-D) propagation models have been published over the last five years, and some of the more recent ones include [1-3]. This type of model is intended for situations where the transmitting and receiving antennas are located close to the ground relative to the building heights, because for these situations the buildings can be approximated as being infinitely high, and the interactions with the buildings are entirely determined by the 2-D ground level perimeters, or footprints, of the buildings, and ray paths which diffract over the rooftops of buildings are assumed to be of negligible amplitude compared with rays that propagate between buildings. Although this may be good approximation in some urban areas, there are also areas where a three-dimensional model is required even for antennas at low heights due to the presence of a significant number of low buildings or to a hilly terrain. Several full three-dimensional models have also been developed [4-6], but these are usually much slower computationally and in many cases require restrictions on the building shapes and the number of interactions to keep the problem tractable.

In this paper a quasi three-dimensional model is presented which is able to predict propagation paths over low buildings and hills, but which still employs a fast 2-D ray tracing using only the footprints of the buildings. The term "three-dimensional" in the title refers to the fact that the vertical component of the paths is accounted for in the predictions and the term "quasi" refers to the fact that the vertical component is constructed analytically and not by carrying out a full 3-D ray trace. This model can predict line-of-sight (LOS), singly diffracted, and doubly diffracted paths over one or more buildings. These paths can also include reflections from the building walls, diffractions from the vertical edges and interactions with the ground, and these interactions can occur before or after the path passes over a building roof. The diffracted fields are evaluated using the UTD diffraction coefficients, modified for finite conductivity [7].

A similar approach to the one presented here is [8], but their approach differs from ours in how the 2-D ray tracing is conducted and in how the diffracted paths are constructed. Our approach also makes use of extensive storing and reuse of ray path data which allows for quickly changing antennas heights and adding new antenna sites to the analysis.

A simple example of propagation over a building rooftop by means of a single diffraction is shown in Figure 1. The path clears the left-hand side of the building but must reach the receiver by diffracting at the right-hand wall down to street level. There is also a weaker doubly diffracted path, which is not shown, that diffracts at both edges of the roof. However, if the transmitter was lowered sufficiently, the only path would be the doubly diffracted path. On the other hand, if the transmitter or receiver was raised sufficiently, a LOS path would exist in addition to the diffracted paths. These paths could not be predicted by a 2-D propagation model, but the quasi 3-D model would be applicable to all of these antenna heights. The model can also include reflections from the building walls and diffractions from the vertical edges, with these interactions occurring before or after the path passes over the rooftop of the building.

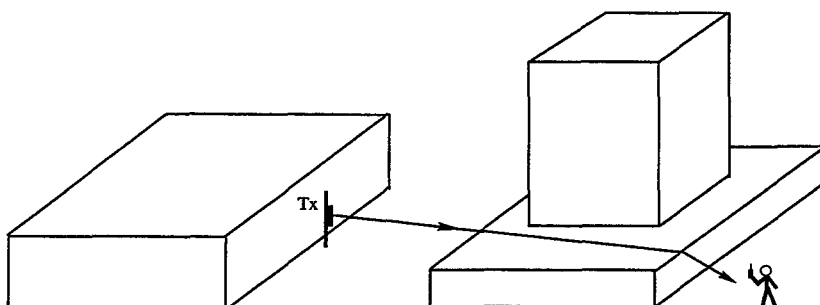


Figure 1. Propagation over a building rooftop by a single diffraction

2. Two-Dimensional Ray Tracing

The Shooting and Bouncing Ray (SBR) method is first employed to trace the ray paths through the two-dimensional building geometry as described in [5]. These ray paths are traced without regard for the location of specific field points. Rays are first traced from the source points with the rays reflecting specularly from the building walls and transmitting through the building walls with no change in the direction as shown in Fig. 2. These SBR ray paths are also used to find the diffraction points by searching for adjacent rays which have interacted differently with the building geometry and then locating the diffracting edge between these rays. Rays are then traced from all the diffracting edges. The last two steps are then repeated if higher order diffractions are to be included.

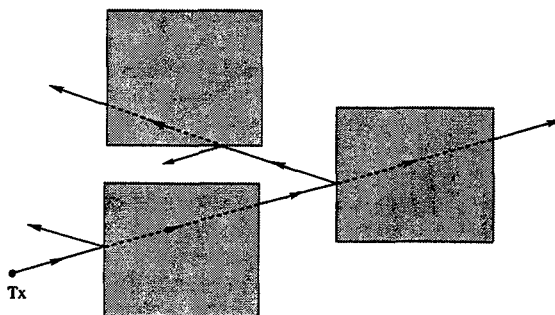


Figure 2. Two-dimensional reflected and transmitted rays

Once the SBR paths have been traced from a transmitter or edge, the next step is to construct the specific geometrical paths to each field point from the Tx or diffracting edge. This is done by enclosing each field point by a collection surface and finding the SBR rays which intersect these surfaces. Since a number of SBR rays which have followed essentially the same path through the buildings may intersect this collection surface, the rays are sorted to select just one ray for each unique geometrical path. Once the specific ray paths to each field point are found, the paths are then stored, either in RAM or on the hard disk, depending on the size of the area and the number of field points. Section 3 describes how the full three-dimensional paths are constructed from this database of two-dimensional paths.

The efficient storage and reuse of this path data allows for quickly constructing the three-dimensional propagation paths between any Tx and Rx locations. Stored paths include diffracted propagation paths from edges to Rx locations, from Tx locations to edges, and from edges to edges. By using this path database, the propagation characteristics can quickly be re-evaluated for different operating frequencies, antenna heights, antenna patterns and building materials. The reuse of diffracted paths also makes it possible to quickly calculate results for new Tx and Rx locations with a minimal amount of additional ray tracing.

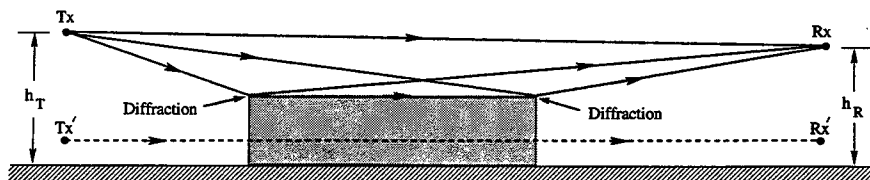


Figure 3. The four ray paths by which energy can propagate over a building when the transmitter and receiver are above the roof of the building.

3. Construction of 3-D Propagation Paths

Once the two-dimensional ray tracing is completed, the next step is to determine for the given transmitter and receiver heights whether the ray paths transmitted through the building walls would have intersected, passed overtop or diffracted from the building walls. This is done by initially assuming the ray travels from the transmitter to the receiver with a constant slope of $\tan\theta = (h_R - h_T)/R_{TR}$, from Tx to rooftop diffraction with a slope of $\tan\theta = (h_w - h_T)/R_{TW}$, and from rooftop diffraction to Rx with a slope of $\tan\theta = (h_R - h_w)/R_{WR}$, where θ is measured with respect to the horizontal, R_{TR} , R_{TW} and R_{WR} are the unfolded path lengths, and h_T , h_R and h_w are the transmitter, receiver and wall heights, respectively.

In order to illustrate how the transmitted paths are used to construct the paths which actually pass over the buildings, consider the paths shown in Fig. 3. The dashed line is the transmitted ray path found from the 2-D ray trace with the transmitter and receiver below the height of all the buildings at Tx' and Rx'. What is not shown for the sake of simplicity is that this ray may have reflected and diffracted (from a vertical edge) before and after passing through the building. If the ray is found to have passed over both sides of the building, as is case for the transmitter and receiver sites shown, four paths would be constructed: a LOS path, two singly diffracted paths, and a doubly diffracted path. But all four paths are present only when both antennas are above the building. When either the receiver or transmitter are below the roof of the building, one of the singly diffracted paths, and possibly the LOS path, will be blocked, and if both antennas are below the building the only path found to exist would be the doubly diffracted one.

The only path initially found from the 2-D ray trace would be Tx-T-T-Rx, where "T" indicates a transmission. The following candidate paths would then be constructed: Tx-T-T-Rx, Tx-O-O-Rx, Tx-D-O-Rx, Tx-O-D-Rx, and Tx-D-D-Rx, where "D" indicates a diffraction and "O" indicates that the path passes over the building wall. It is a simple matter then to determine whether the ray could have actually intersected (or not intersected in the case of an "O") the building face at each point as prescribed. Based on the outcome of these tests it is a simple matter to determine which of these candidate paths should be retained, omitting any "O"s, and which deleted. The same approach is used when there are reflections and diffractions from vertical edges in the path.

The validity of using this approach for constructing these additional paths depends on two assumptions. The first is that the actual 3-D paths do not lie far from the ones initially traced out by the transmitted rays, so the distance by which the paths are being displaced vertically is small compared to the total path length. This will be true when the vertical separation between the transmitter and receiver is small compared to the horizontal separation.

The second assumption concerns the shape of the buildings found of a typical urban environment. In this environment the buildings may often have very complex cross-sections in the horizontal plane, but will not be nearly so complex in any vertical plane. The fact that almost all buildings have flat vertical walls guarantees that the strongest paths will lie close to the horizontal plane

because there are no interactions which can scatter a significant amount of energy from a vertically propagating ray back into this plane. Ground reflections and diffractions are the exceptions to this, but these can be handled as special cases. The assumption of vertical walls makes it possible to construct the paths which have propagated over the lower buildings by simply considering the height at which the rays

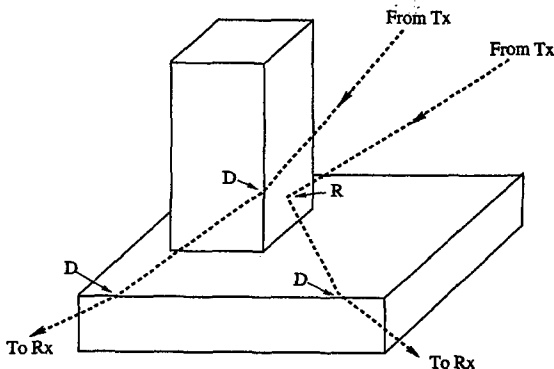


Figure 4. Rays which diffract and reflect from both the upper and lower tiers of a two tiered building. An "R" denotes a reflection and a "D" a diffraction.

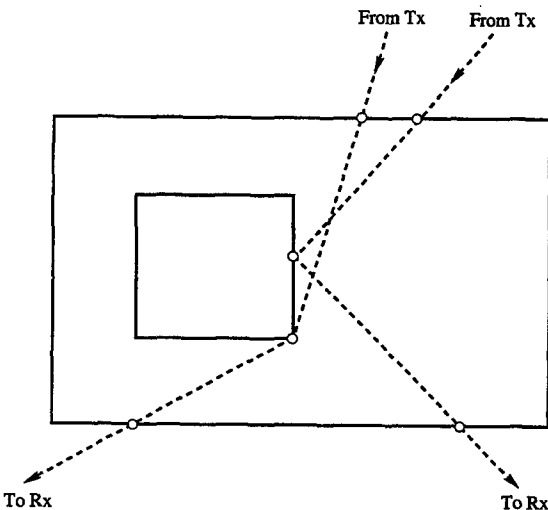


Figure 5. The two-dimensional transmitted and reflected/diffracted paths used to construct the three-dimensional paths in Figure 4.

intersect the plane of the building face. However, it is not necessary to assume that all the buildings are vertically uniform, and structures such as the tall tower in the center of the building on the right in Fig. 1 would still be found to block propagation to some receiver locations.

This approach can also be extended to include multi-tiered buildings, sometimes referred as "wedding cake" buildings, in which the footprints of the higher floors are completely enclosed by the footprint of the lower floors. Figure 4 shows an example of such a building. The initial 2-D ray trace is carried out using only the footprints of each tier. Figure 5 shows the 2-D transmitted, reflected and/or diffracted ray paths which are initially traced in order to construct the paths shown in Fig. 4.

The ray tracing and path construction algorithms can also be applied to arbitrarily complex buildings in which different parts of the buildings are at different heights and in which there are no restrictions on how the various parts can overlap. Figure 6 shows an example of this type of building. As in the previous cases considered, only the footprints of each section are used in the initial 2-D ray trace

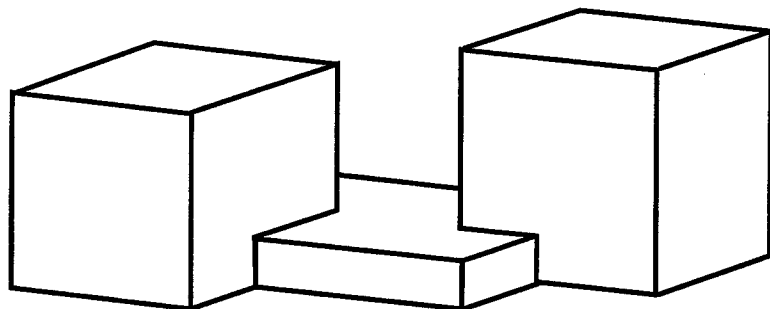


Figure 6. Complex building consisting of three overlapping sections with different heights.

4. Numerical Results

This approach has been validated by comparisons to the full 3-D calculation of the path loss and geometrical propagation paths for numerous transmitter and receiver locations within the building geometry in Fig. 7 using various building heights and Tx and Rx locations. Figure 8 shows one such comparison of the path loss predictions along line AB at a height of 5 m and with the transmitter at $x=500$, $y=325$, $z=30$ m. All antennas are vertically polarized and omnidirectional. All buildings are 75 m in height, except for building 5 which is 20 m high. To simplify the comparisons, the ground reflected paths have been eliminated for this comparison by using a flat perfectly absorbing ground plane. However, reflections and diffractions from the ground are predicted by the quasi 3-D model and were included in other comparisons.

In addition to comparing the path loss, we have also made many comparisons of the individual paths between many Tx and Rx locations. For example, Fig. 9 shows the five strongest paths as calculated by quasi 3-D between the Tx given above and the Rx at $x=275$, $y=575$, $z=5$ m. The ten strongest paths are tabulated in Table 1 for the quasi 3-D model, where an "R" denotes a reflection, a "D" denotes a diffraction from a vertical edge and a "d" denotes a diffraction from a horizontal rooftop edge, and the number after the interaction type refers to the building numbers in Fig. 9. A comparison of these paths

to the ones predicted by the full 3-D model has shown that the two models predicts the same propagation paths with nearly the same power levels.

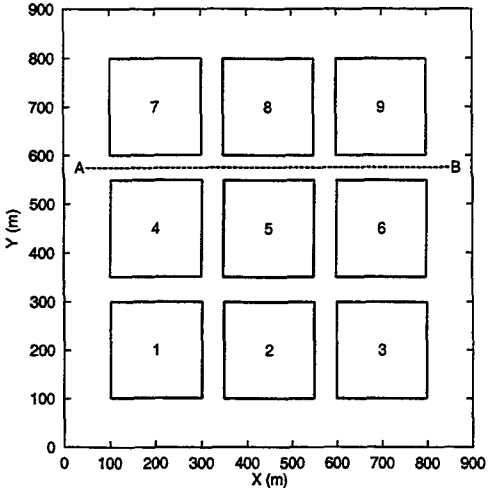


Figure 7. Building geometry used for Quasi 3-D to full 3-D comparisons.

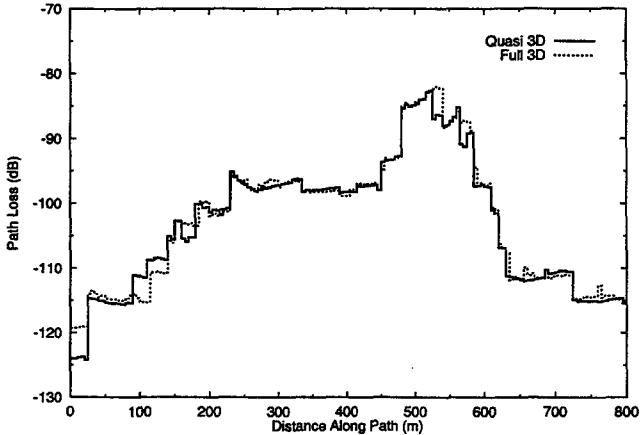


Figure 8. Path loss at 900 MHz along line A-B in Fig. 6.

Path	Building Interactions	Power (dB)	Time (μ s)
1	Tx - d(5) - R(7) - Rx	-104.6	1.271
2	Tx - d(5) - R(4) - R(5) - Rx	-106.4	1.370
3	Tx - R(6) - d(5) - Rx	-110.7	1.656
4	Tx - R(2) - d(5) - R(7) - Rx	-113.2	1.414
5	Tx - R(6) - d(5) - R(8) - R(4) - Rx	-117.8	1.845
6	Tx - d(5) - D(4) - Rx	-118.2	1.139
7	Tx - d(4) - d(4) - Rx	-120.3	1.289
8	Tx - R(2) - R(6) - d(5) - R(7) - Rx	-121.3	1.857
9	Tx - R(6) - d(5) - d(5) - Rx	-121.3	1.657
10	Tx - R(6) - d(5) - R(4) - R(5) - Rx	-124.7	1.957

Table 1. Building interactions, path loss, and arrival time of the ten strongest paths predicted by the quasi 3-D model.

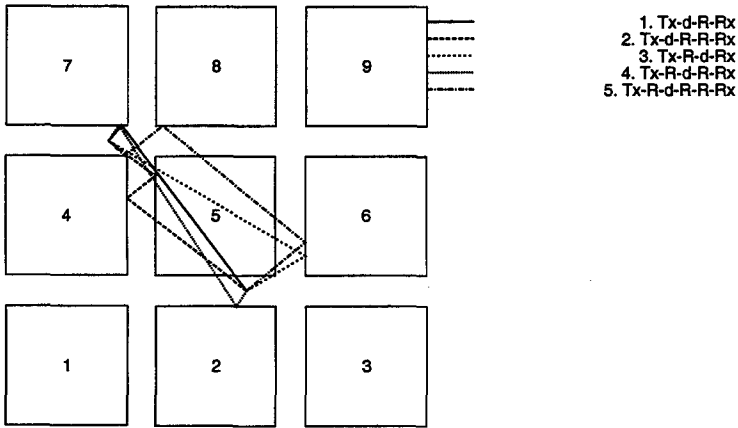


Figure 9. The five strongest ray paths predicted by the quasi 3-D model.

5. Conclusion

A propagation model for urban microcells is presented in this paper which is able to predict paths with propagate over building rooftops, but which still retains most of the speed of a purely two-dimensional model. This approach uses rays which are transmitted through the buildings to analytically construct the over the rooftop paths. An important component of this approach is the storing and reusing the 2-D geometrical path data to allow for quickly constructing the full 3-D paths for different antenna heights without any additional ray tracing. The model was shown to give nearly identical results to a full 3-D model.

References

1. S. Y. Tan and H. S. Tan, "A microcellular communications propagation model based on the uniform theory of diffraction and multiple images," *IEEE Trans. Antennas Propagat.*, vol. 44, no. 10, pp 1317-1326, Oct. 1996.
2. K. Rizik, J. Wagen and F. Gardiol, "Two-dimensional ray-tracing modeling for propagation prediction in microcellular environments," *IEEE Trans. Veh. Technol.*, vol. 46, pp. 508-517, May 1997.
3. H. Son and N. Myung, "A deterministic ray tube method for microcellular wave propagation prediction model," *IEEE Trans. Antennas Propagat.*, vol. 47, no. 8, pp 1344-1350, Aug. 1999.
4. M. C. Lawton and J. P. McGeehan, "The application of a deterministic ray launching algorithm for the prediction of radio channel characteristics in small-cell environments," *IEEE Trans. Veh. Technol.*, vol. 43, no. 4, pp. 955-969, Nov. 1994.
5. J. Schuster and R. Luebbers, "Hybrid SBR/GTD radio propagation model for site-specific predictions in an urban environment," *12th Ann. Rev. of Progress in Applied Computational Electromagnetics*, Monterey, CA, vol. 1, pp. 84-92, Mar. 1996.
6. S. C. Kim, B. J. Guarino, T. M. Willis, V. Erceg, S. J. Fortune, R. A. Valenzuela, L. W. Thomas, J. Ling and J. D. Moore, "Radio propagation measurements and prediction using three-dimensional ray tracing in urban environments at 908 MHz and 1.9 GHz," *IEEE Trans. Veh. Technol.*, vol. 48, pp. 931-936, May 1999.
7. R. J. Luebbers, "Finite conductivity uniform GTD versus knife edge diffraction in prediction of propagation path loss," *IEEE Trans. Antennas Propagat.*, vol. 32, no. 1, pp. 70-76, Jan. 1984.
8. G. Liang and H. L. Bertoni, "A new approach to 3-D ray tracing for propagation prediction in cities," *IEEE Trans. Antennas Propagat.*, vol. 46, no. 6, pp. 853-863, June. 1998.

FDTD Techniques for Evaluating the Accuracy of Ray-Tracing Propagation Models for Microcells

Joseph W. Schuster
Remcom, Inc.
State College, PA
E-mail: jws@remcom.com

Raymond J. Luebbers
Department of Electrical Engineering
The Pennsylvania State University
University Park, PA
E-mail: RayL@psu.edu

Abstract

In this paper several techniques are presented for employing a two-dimensional FDTD simulation as a tool for evaluating the accuracy of radio wave propagation models based on high-frequency asymptotic methods. In particular, comparisons are made to a GTD based method in the frequency and time domains. The GTD results are calculated using the Uniform Theory of Diffraction (UTD) wedge diffraction coefficients modified for finite conductivity. Because the 2D FDTD fields spread as cylindrical waves emitted from a line source, a simple technique is introduced for modifying the 2D FDTD time domain response to approximate the spherical wave spreading of fields emitted from a point source.

1. Introduction

A number of ray-tracing based propagation models have been developed since the early 1990's for making site-specific propagation predictions in urban microcells [1,2,3]. These models have usually been validated by comparison with measurements of received power and delay spread. However, because of the complexity of the environments in which the measurements are made it is often not clear from the comparisons why the predictions are inaccurate in some areas and how the models can be improved. The purpose of this paper is to introduce some simple techniques by which the finite difference time domain (FDTD) method can be used to evaluate the accuracy of propagation models based on ray-tracing and high frequency asymptotic methods such as GTD.

Of course, even the largest computers do not have nearly enough memory to allow for a full three-dimensional FDTD simulation of UHF propagation in a microcell. However, in high-rise urban areas the transmitting and receiving antennas will frequently be located well below the building heights, and in these situations paths which diffract over the rooftops are usually of negligible power compared to paths which propagate between buildings in the horizontal plane. This is the type of environment and antenna locations to which a two-dimensional (2D) FDTD simulation can be applied.

At UHF and microwave frequencies the buildings in a high-rise urban environment are electrically very large and this allows for the application of high frequency methods in electromagnetics. It has been demonstrated that it is essential to include diffracted fields in making predictions for an urban

environment. Diffraction is often a very important propagation mechanism in this environment, whether it is diffraction around corners into non-line-of-sight streets or diffraction over rooftops down to street level. Most site-specific models combine some type of ray-tracing procedure with geometrical optics and one of the high frequency methods for calculating diffracted field amplitudes. The most popular method is the Geometrical Theory of Diffraction originally developed by Keller in 1962; and within the framework of the GTD, the Uniform Theory of Diffraction developed by Kouyoumjian and Pathak and modified for finite conductivity as given in [4] is widely used.

The GTD results in this paper are calculated with the 2D version of the propagation model described in [5]. This model combines the Shooting and Bounce Ray (SBR) method with the GTD. The SBR method is employed as a computationally efficient ray tracing procedure to find the ray paths to the field points. After the paths are found the GTD is used to evaluate the electric field amplitudes using the UTD diffraction coefficients modified for finite conductivity surfaces that are given in [4].

2. FDTD Implementation

Although a two-dimensional approximation to the building geometry can be used in a high-rise urban environment, the fields will still attenuate with distance as spherical waves emitted from a point source. However, in the 2D FDTD simulation the fields will spread as cylindrical waves emitted from a line source, so in order to compare the FDTD fields directly to measurements or to the GTD predictions it is necessary to modify the FDTD fields to have the correct spherical wave attenuation with distance.

For non-diffracted fields which reflect only from planar surfaces the spreading is as $1/r$ for spherical waves and as $1/\sqrt{r}$ for cylindrical waves, where r is the total path length. For diffracted fields the attenuation with distance is more complicated, but according to the UTD the ratio of the spherical to cylindrical wave attenuation remains $1/\sqrt{r}$. The basic idea is to use the fact that $r=ct$, and then to introduce an additional $1/\sqrt{r}$ of attenuation into the FDTD fields by multiplying the time domain fields by $1/\sqrt{ct}$. This is implemented by exciting the FDTD simulation with a narrow pulse at the source point and then saving the complete time record at each point of interest. In post-processing the fields are multiplied by the correction factor and then Fourier transformed to obtain the amplitudes and phases of the frequency domain fields.

It is also possible to take the interference with the ground reflected wave into account. To obtain the correct interference pattern it is necessary to include the time shifts due to the different propagation distances. The field not reflected by the ground is given by

$$E(t') = E_{FDTD}(t) \frac{\sqrt{ct}}{ct'} \quad (1)$$

and the ground reflected field by

$$E_G(t'') = E_{FDTD}(t) R_G(\theta) \frac{\sqrt{ct}}{ct''} \quad (2)$$

where $R_{\theta}(\theta)$ is an angle dependent reflection coefficient, $ct' = \sqrt{(h_R - h_T)^2 + c^2 t^2}$, $ct'' = \sqrt{(h_R + h_T)^2 + c^2 t^2}$, $\tan \theta = (h_R + h_T)/ct$, h_T and h_R are the heights of the transmitter and receiver.

Figure 1 shows a simple geometry consisting of four buildings with a rectilinear street pattern. Each building consists of a perfect electrical conducting core with a 0.3 m thick lossy dielectric coating ($\epsilon_r = 4$, $\sigma = 0.05$ S/m) on all sides. A cell size of 1.5 cm (20 cells per wavelength at 1 GHz) was used in the FDTD simulation. The ground reflection is calculated using a perfectly conducting ground plane.

A vertically polarized field was excited at $x=37.5$, $y=6.2$ m. To prevent the excitation of unwanted low frequency fields which GTD cannot predict, the FDTD simulations were excited with a truncated derivative of a Gaussian having the form

$$E(t) = \begin{cases} -2A_0 \alpha (t - \beta \Delta t) e^{\alpha(t - \beta \Delta t)^2} & 0 \leq t \leq 2\beta \Delta t \\ 0 & t > 2\beta \Delta t \end{cases} \tag{3}$$

where $E(t)$ is the electric field at the source point, $\alpha = [1/(\beta \Delta t/4)]^2$ and $\beta = 48$.

3. Numerical Results

In Figures 2 and 3 the FDTD calculated fields are compared to the GTD fields at a frequency of 900 MHz. The GTD results include ray paths with up to 8 reflections and 2 diffractions. The fields are compared along the lines AB and CD with the field points at a height of 2 m. The scaling factor E_0 used in the plots is the field at 1 m from the transmitter in the absence of the buildings. The electric field in free space is also shown in order to illustrate the large attenuation produced by the buildings.

An alternative is to compare the GTD predictions directly to the FDTD calculated time domain electric fields. Comparing the results in this way makes it possible to examine properties of specific propagation paths between the source and field points. Although it is not possible to determine from the FDTD simulation the full geometrical path by which energy traveled from the transmitter to the field point, it is possible, by choosing the excitation properly, to isolate specific propagation paths in the FDTD time domain response and to compare the strength and arrival time of these paths to the values predicted by the GTD model.

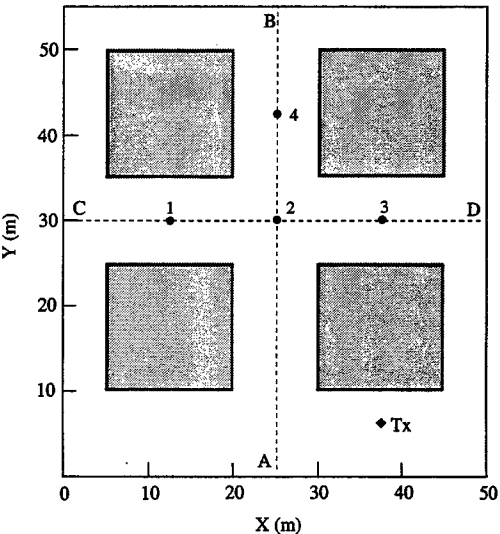


Figure 1: Four building geometry used for the numerical results

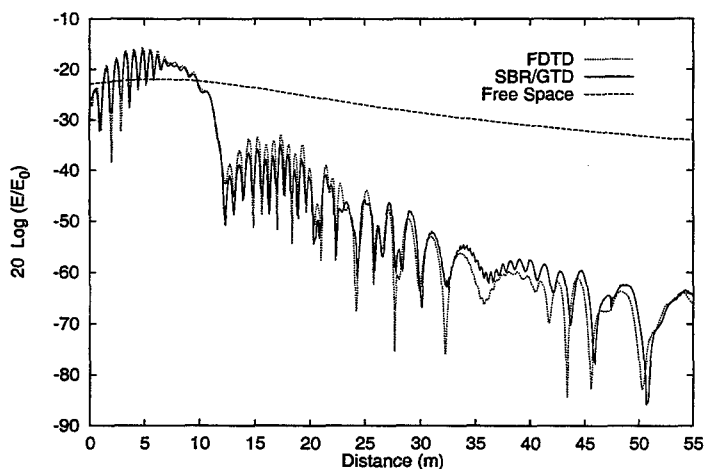


Figure 2: Comparison of the GTD and FDTD calculated electric fields at 900 MHz along line AB in Fig. 1.

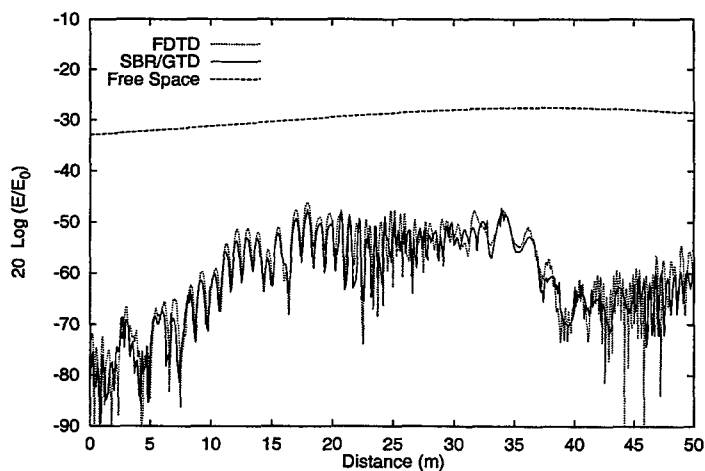


Figure 3: Comparison of the GTD and FDTD calculated electric fields at 900 MHz along line CD in Fig. 1.

To demonstrate how this can be done, we will consider the paths from the transmitter to field point 1. The building interactions and the times of arrival for the first ten significant GTD calculated paths to arrive at point number 1 are listed in Table 1, and in Fig. 4 the first five of these paths are plotted with the building geometry. Several paths (mainly double diffractions) which are of very low amplitude have been omitted from the figure and the table. To give some indication of the relative strength of each path, the power in dBm for a transmitted power of 0 dBm are given at 500 MHz, which is approximately the center frequency of the excitation pulse. These results were obtained using the model described in [5], and the diffracted fields were evaluated using the finite conductivity UTD diffraction coefficients given in [4].

The first path to arrive at point 1 is one which diffracts twice, first from the lower left hand corner of building 2 and then from the upper right hand corner of building 1. There are several paths listed in Table 1 which travel nearly the same distance and arrive at nearly the same time as other paths. For instance, paths 2 and 3 differ only by path 3 having a second diffraction from building 1. Paths 5 and 6 are another such pair which follow nearly parallel paths. It is interesting to note that path 10 is the first path to arrive at point 1 which undergoes only reflections and no diffractions, and due mainly to presence of the lossy surfaces, this path is 10 dB weaker than path 5, which undergoes a diffraction but two less reflections. This demonstrates why diffraction rather than multiple reflection is often the most important propagation mechanism in the outdoor environment

Path	Sequence of Building Interactions	Time (ns)	Power (dBm)
1	Tx - D(2) - D(1) - Rx	118	-102.5
2	Tx - D(2) - R(3) - Rx	144	-91.8
3	Tx - D(2) - D(1) - R(3) - Rx	144	-101.2
4	Tx - D(2) - D(3) - Rx	148	-129.6
5	Tx - D(2) - R(1) - R(2) - Rx	170	-81.8
6	Tx - D(2) - R(1) - R(2) - D(1) - Rx	170	-90.9
7	Tx - D(2) - R(3) - R(2) - Rx	174	-103.5
8	Tx - D(2) - R(1) - D(2) - R(3) - Rx	188	-102.3
9	Tx - D(2) - R(1) - R(2) - D(1) - R(3) - Rx	196	-110.7
10	Tx - R(1) - R(2) - R(1) - R(2) - Rx	231	-91.6

Table 1: Arrival time and building interactions for the first 10 significant paths to arrive at point 1. In the second column, "D" denotes a diffraction, "R" denotes a reflection, and the numbers refer to the buildings in Fig.1.

To compare the GTD time domain response directly to the FDTD time domain results, the GTD time domain fields are determined from

$$E_{GTD}(t) = F^{-1}\{E_{GTD}(f) \times E_1(f)\}, \quad (4)$$

where F^{-1} denotes the inverse Fourier transform, $E_1(f)$ is the Fourier transform of the excitation pulse at one meter from the source point, and $E_{GTD}(f)$ is the frequency domain response evaluated using an electric field amplitude of 1 V/m at one meter from the source. The GTD time domain predictions are compared to the FDTD time domain fields in Fig. 5. By referring to Table 1 and Fig. 4, it is possible to associate specific paths with the peaks in the FDTD response. For example, the doubly diffracted path which arrives first at point 1 at 118 ns is clearly present, and the amplitude and overall shape are in good agreement with the FDTD results.

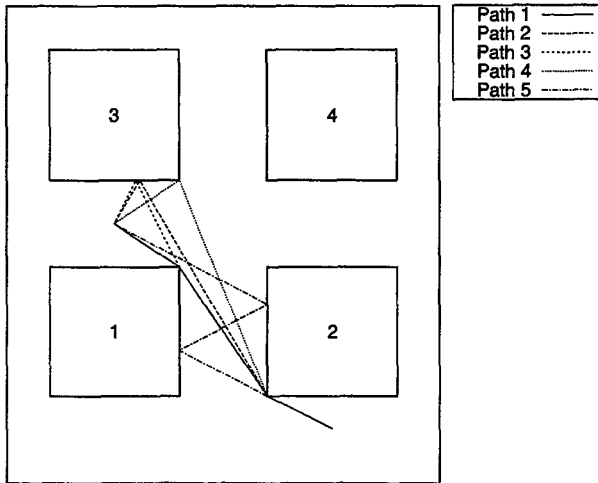


Figure 4: Ray paths to point 1

4. Conclusion

In this paper techniques are presented for introducing the correct spherical wave spreading into 2D FDTD fields and for comparing the propagation paths predicted by GTD to the FDTD calculated time domain response. An application to a simple geometry has shown that the diffracted fields calculated with the UTD finite conductivity diffraction coefficients are shown to be in good agreement with the FDTD calculated electric field strength. The FDTD calculated time domain fields are found to be in good qualitative agreement with the ray optics picture of high frequency propagation. As the propagation prediction methods are improved in the future, FDTD simulations may prove to be a useful tool for evaluating the accuracy of these methods.

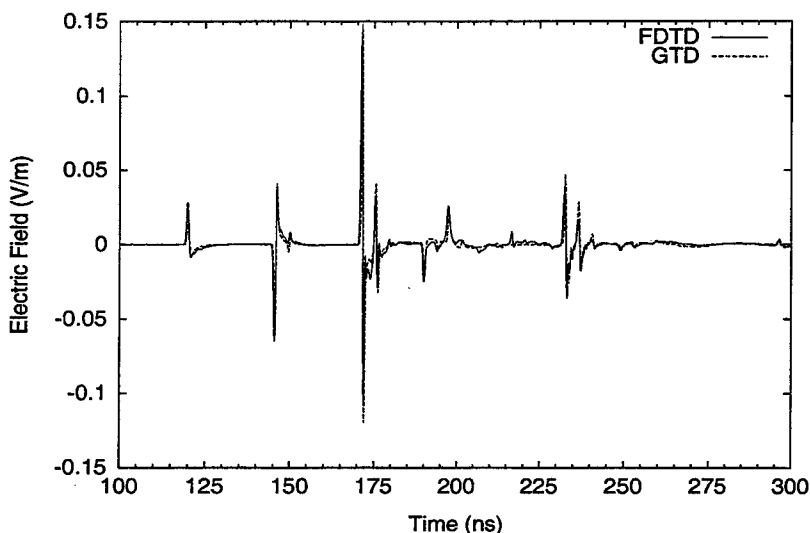


Figure 5: Comparison of FDTD and GTD time domain fields

References

1. M. C. Lawton and J. P. McGeehan, "The application of a deterministic ray launching algorithm for the prediction of radio channel characteristics in small-cell environments," *IEEE Trans. Veh. Technol.*, vol. 43, no. 4, pp. 955-969, Nov. 1994.
2. S. Y. Tan and H. S. Tan, "A microcellular communications propagation model based on the uniform theory of diffraction and multiple images," *IEEE Trans. Antennas Propagat.*, vol. 44, no. 10, pp. 1317-1326, Oct. 1996.
3. K. Rizik, J. Wagen and F. Gardiol, "Two-Dimensional Ray-Tracing Modeling for Propagation Prediction in Microcellular Environments," *IEEE Trans. Veh. Technol.*, vol. 46, pp. 508-517, May 1997.
4. R. J. Luebbers, "Finite conductivity uniform GTD versus knife edge diffraction in prediction of propagation path loss," *IEEE Trans. Antennas Propagat.*, vol. 32, no. 1, pp. 70-76, Jan. 1984.
5. J. Schuster and R. Luebbers, "Hybrid SBR/GTD radio propagation model for site-specific predictions in an urban environment," *12th Ann. Rev. of Progress in Applied Computational Electromagnetics*, Monterey, CA, vol. 1, pp. 84-92, Mar. 1996.

A Building Database Features Pre-Processor For 3-D SBR/GTD Urban EM Propagation Models

James Pickelsimer, Raymond Luebbers
Department of Electrical and Computer Engineering
The Pennsylvania State University
University Park, PA 16802
jdp202@psu.edu;RayL@psu.edu

Abstract

A software program was developed for the simplification of complex building and terrain databases. It was implemented for use in the SBR3D model. This software utilizes the Shooting and Bouncing Rays Technique along with the Geometric Theory of Diffraction for predicting the path loss of an electromagnetic wave in an urban environment. [1-3] SBR3D is designed for use at cellular phone frequencies, about 800 MHz to 2 GHz. [3]

The Features Pre-Processor reads in one of four formats of building data provided by a vendor. The software then simplifies this database by removing building features that are smaller than a user-specified length. It also combines building faces that are nearly coplanar into one large face. The simplified data is then written to a file in a format that takes into account the needs of the SBR3D software. Results are shown of path loss predictions from the SBR3D software in a section of Rosslyn, Virginia that are compared with measured data. These results are obtained from a database that has been simplified for different specified minimum lengths. They are also compared with results obtained from using the same database simplified by hand.

Introduction

There is a great need to develop analysis tools that will determine the path loss and the phase spreading of electromagnetic waves in an urban environment. An SBR/GTD method was developed for this purpose. A major difficulty that was encountered in this endeavor was the processing of complicated databases. By hand, such processing can take months for a 1 km by 1 km section of a city. The file has to be sorted through by hand and then simplified manually. The purpose of the Features Pre-Processor is to accomplish this automatically.

Problem Concerns

One difficulty in implementing a Features Pre-Processor is that the user desires it to be able to process any form of building database. Also, the data being analyzed needs to be in a form that is usable by the SBR3D software. This means that there are to be no protruding faces and the buildings need to be convex. If there are two faces that are nearly coplanar, they need to be merged into one larger face since the SBR3D software will attempt to calculate diffraction at that edge, leading to erroneous results. Finally, each face needs to have a normal vector that is pointing away from the building. This is determined by the rotation sense of the vertices.

Data Types

DXF Data Files

The first data type considered was an AutoCAD drawing exchange file (DXF). It is a text-based command file used by the AutoCAD drawing software. This file format is three-dimensional. Our example file covers a 1380 meter by 2070 meter region of

Rosslyn, Virginia. It has a precision of less than one meter. The data file is divided into separate objects which are further subdivided into individual faces. These faces are also further subdivided into their different vertices. The file does not contain any materials information. It only contains the building geometry.

MCS Data Files

The second data file type was obtained from EDX, Incorporated. This file is called MCS due to the ".mcs" extension given to their file names. This is also a text-based data format. The areas covered in the files obtained were a 400 meter by 50 meter section of Eugene, Oregon and a 700 meter by 700 meter section of Manhattan, New York. It has a precision of approximately two meters. This file format is also three-dimensional. It displays the x- and y-coordinates of each side plate and then gives the top and bottom heights of the side plate. Small structures on top of buildings, such as small maintenance buildings are entered into the data files as separate objects. This file type also lacks building materials data.

TXT Data Files

The third file type was obtained from 3D Metric, Incorporated. This file type has a simple ".txt" extension and is a text-based file. It covers a 2700 meter by 4900 meter section of Baltimore, Maryland. It has a precision of approximately two meters. This file is only extruded two-dimensional. It contains the coordinates of the top face of the building and the building height. If there are small substructures on the building, the data file places it in a separate section, but it identifies the substructure as part of the building. However, for the sake of simplicity and consistency, the Features Pre-Processor treats these substructures as separate building objects. This data file type contains materials data.

GAM Data Files

The fourth file type was obtained from GDE Systems. This type is referred to as a GAM file since they have a ".gam" extension. This data file is text-based and three-dimensional. The area covered in the file obtained is a 1300 meter by 1900 meter section of Rosslyn, Virginia. It displays the data by individual face, but organizes the faces into building objects with an index. There is no material information in this data file type.

Format of Features Pre-Processor

In order to facilitate the addition of other data types that may be acquired in the future, a modular approach was taken to the design of the Features Pre-Processor. The order of the modules is shown below in Figure 1.

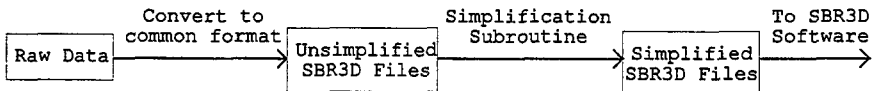


Figure 1: Simplification Process Overview

First, the raw data is converted into the format used in the SBR3D software, though it still needs to be simplified to be useful. A separate subroutine converts each

of the different raw data formats into the common format. If other data formats are obtained, one simply needs to write another subroutine to convert this format into the common format. The Features Pre-Processor then reads in this common format and simplifies it. Output files are then written which can be used by the SBR3D software.

Initial Processing of Data

The data file is read in using a different subroutine to handle each different data type. Then, if material properties are given in the data type, these properties are approximated as one of the properties embedded in the SBR3D software. A subroutine is then executed that corrects the rotational sense of the vertices of the faces that require it. A file of this data is then written in the format common to the SBR3D software.

Simplification Process

Angle Simplification

The first simplification performed is the angle simplification. The angle simplification subroutine is an aspect of the Features Pre-Processor that does not rely on the user-specified minimum length. The purpose of this section is to smooth over faces that are nearly coplanar.

The first step is to form vectors from the top edges of each pair of consecutive plates. The vectors are similar to the vectors formed in the determination of rotation sense. One has a slightly different formula since it is pointing in the opposite direction.

$$\begin{aligned}\bar{a}_j &= (x_{j+1} - x_j)\hat{e}_x + (y_{j+1} - y_j)\hat{e}_y \\ \bar{b}_j &= (x_j - x_{j-1})\hat{e}_x + (y_j - y_{j-1})\hat{e}_y\end{aligned}$$

The angle between the two plates is then determined with the formula below.

$$\theta_j = \cos^{-1}(\bar{a}_j \cdot \bar{b}_j)$$

If the magnitude of theta is less than ten degrees, then the two plates are approximated as one plate. Ten degrees was selected since coplanar faces in the data files obtained tend to have around five degrees or less difference between each other while non-coplanar faces tend to have over thirty degrees between each other. The procedure for this is to mark the j th vertex for removal if the two plates are nearly coplanar and then follow the same procedure as in the length simplification section.

Length Simplification

The main feature of the simplification process is the removal of features that are smaller than a user-specified length. This process is essentially two-dimensional. The top face is simplified and then the side faces are altered in accordance with this transformation.

The length simplifier determines the distance between a vertex in the top face and the proceeding vertex. If this distance is smaller than the user-specified minimum length, then the latter vertex is marked for removal. The simplifier will then check against the next vertex and repeat this procedure until it finds a vertex in which the distance between it and the initial vertex is greater than the user-specified

minimum length. Then, that vertex will become the new initial vertex and the whole process repeats. This process continues until the whole top face has been inspected.

The top face is then constructed by using the vertices that were not marked for removal. If this procedure results in less than four vertices for the top face, then four vertices from the original unsimplified top face are used. These four vertices are spaced at roughly equal distances around the circumference of the top face. Then, the side faces are constructed from the side edges that correspond to the vertices of the new top face.

Quadrilateral Simplification

Another form of simplification that can be performed by the Features Pre-Processor instead of the length simplification is quadrilateral simplification. This process is also essentially two-dimensional.

First, the area of the top face of the building object is determined by splitting the top face into adjacent triangles and calculating the area of each individual triangle. Then, the center point of the top face is determined.

Next, vectors are formed from each side of the top face. In the x-y plane, each vector is pointing in one of the four angular quadrants. Four vector sums are performed, one for each quadrant. For example, if the vector of an edge is pointing in the positive x and negative y directions, then the vector is added to the summation corresponding to the fourth quadrant.

After the vector summations are performed, the quadrilateral is constructed. The four vectors are placed such that the center point determined previously is the center point of the new building. The four vectors form the four edges of the quadrilateral. Using the bottom heights of the side faces in the unsimplified building object, four side faces are constructed by extruding this quadrilateral.

Area Simplification

The last procedure used to simplify the database is the area simplifier. This subroutine determines if an object is a significant reflector given the user-specified minimum length. This procedure is invoked upon building objects that have been simplified down to objects with four vertices on the top face by the previous procedures.

The area for an arbitrary quadrilateral is determined and checked against a minimum area. The minimum area is determined by the following equation.

$$\{\text{minimum area}\} = \{\text{minimum length}\}^2$$

The area is determined for the top face and two adjacent side faces. If the top face is less than the minimum area, then the object removed. If the two adjacent side faces are both less than the minimum area, then the object is also removed.

Overall Procedure

The three procedures listed above are performed on each building in the database in the order listed. After all three procedures have been performed on the building object, then they are repeated if any simplification has been done. The exceptions to this are if the building object was removed by the area simplifier or if the number of vertices of the top face is equal to four since no more simplification would be possible.

Terrain Approximation

After the building database has been simplified, a suitable terrain needs to be added. Depending on the user's preference and the flatness of the region, one of two terrain approximations can be used, either a flat plane or a pair of connected triangular plates with differing heights at their far corners.

The first terrain approximation treats the terrain as a flat plane. First, the Features Pre-Processor sorts through the simplified building data and determines the lowest z-coordinate in that set of data. A flat plane is then set one-tenth of a meter above that lowest z-coordinate. Next, the z-coordinates of all of the bottom edges of all of the ground-level objects are set to the value of z that was determined to be the lowest in the simplified building database. This way, there are no floating buildings. The bottoms of all of the buildings are sunk one-tenth of a meter into the approximated terrain.

The second terrain approximation treats the terrain as a pair of connected triangular plates. They both share an edge that passes diagonally through the region of interest. In the x-y plane, the two triangles form a rectangle that covers an area slightly larger than the region of interest. The z-coordinates of the four corners that the two triangular plates occupy are determined by first taking the average of the heights of the bottoms of the ten ground-level buildings that are closest to the corner and setting that corner to a height that is 1.2 times this value. The factor of 1.2 is due to the fact that the SBR3D software places a bounding box around the building features geometry. The coordinates for this bounding box are calculated by first finding the difference between the maximum and minimum coordinate values. The coordinates of the bounding box are then placed twenty percent of this distance beyond the maximum and minimum coordinate values. After the heights of the corners are determined, then the bottom edges of the ground-level buildings are sunk to one-tenth of a meter below the approximated terrain.

Building Simplification Examples

Length Simplification

The length simplification procedure removes jagged edges from the building database. This is important in SBR3D code since these jagged edges would require more reflections, thus greatly increasing the computation time. The required computation time increases as the cube of the number of reflections. Furthermore, both the method of Shooting and Bouncing Rays (SBR) and the Geometrical Theory of Diffraction (GTD) work only if the wavelength of the incident field is much smaller than the edge that it diffracts off of. The wavelength ranges from 0.15 meters to 0.375 meters for our region of interest, so the size of the reflecting and diffracting faces must be much larger than this. An example of the length simplification procedure is shown in figures 2-4.



Figure 2:
Unsimplified
Building



Figure 3:
minimum length =
5 meters

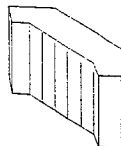


Figure 4:
minimum length =
7 meters

Figure 2 is the unsimplified building structure. Figure 3 is an example of a building that has been simplified with too small of a minimum simplification length. As can be seen, there are still many jagged edges. These causes unnecessary reflections which greatly increases the number of required reflections in the SBR3D code. Figure 4 shows a proper level of simplification, although the angle simplifier has been suppressed for demonstration purposes. The resulting geometry shows flat side faces with no protrusions. The difference in the ray path lengths for figure 4 and figure 3 is small compared to total distance that the rays will have to travel in an urban environment. However, the SBR3D program will have a considerably greater computation time for figure 3 than it will for figure 4.

Angle Simplifier

The SBR3D software searches the edges between adjacent faces for possible diffraction points. If there are two faces that are nearly coplanar, the software may attempt to diffract around what in reality is the middle of a solid wall. The angle simplifier prevents this by approximating two nearly coplanar faces as one face. An example of this procedure is given in figures 5-6 below.

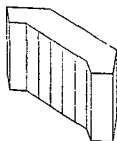


Figure 5:
Before Angle
Simplification

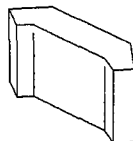


Figure 6:
After Angle
Simplification

Area Simplifier

For cellular phone frequencies, some objects are simply not significant reflectors. However, keeping these objects in the database slows down the processing time for the SBR/GTD software. Therefore, they should be removed. The small structures on top of large main structures are evaluated by the Features Pre-Processor as separate objects and removed if necessary.

Rosslyn, Virginia

The main area of interest in this study was an area of Rosslyn, Virginia. Figure 7 shows the unsimplified database. Figure 8 shows the length simplified database and figure 9 shows the quadrilateral simplified database. The minimum simplification length used in for both simplification databases was 15 meters. The minimum simplification length can be greater while still retaining a reasonable level of accuracy. A minimum simplification length of 15 meters was found to give results in both models that were comparable to the hand-simplified database while still retaining a level of simplification that would greatly reduce the needed memory and computation time. This database was then used in SBR3D to obtain path loss data for this area. How the results of both types of analysis compared with the measured data is shown in table 1.

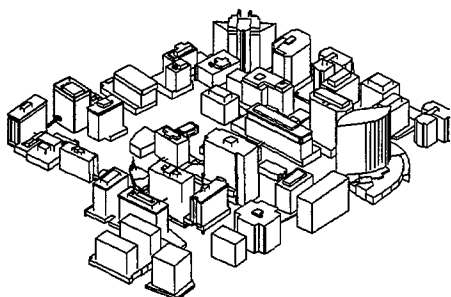


Figure 7:
Unsimplified Section
of Rosslyn, Virginia

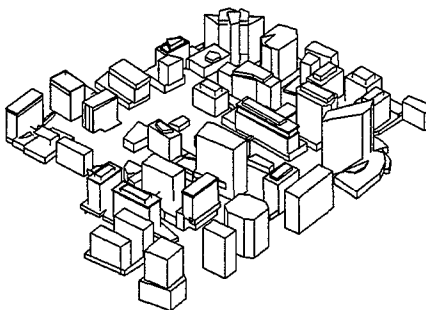


Figure 8:
Length Simplified Section
of Rosslyn, Virginia

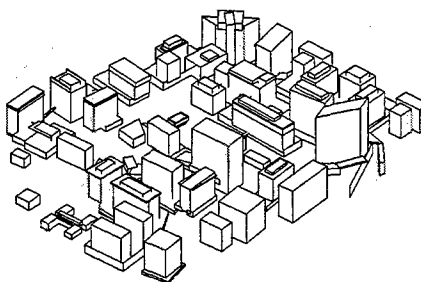


Figure 9:
Quadrilateral Simplified Section
of Rosslyn, Virginia

Results and Comparisons

Path loss results were obtained with the SBR3D software using a hand-simplified database and databases constructed by the Features Pre-Processor for both the length and quadrilateral simplification models. Results from the automatically simplified models are shown in Table 1 with minimum simplification lengths (MSL) of 15, 18 and 21 meters. Results for a minimum simplification length of 30 meters are also included in order to show a high level of simplification.

The mean difference obtained from using databases produced by the Features Pre-Processor is comparable to the mean difference obtained using the hand-simplified database when the MSL is low for both simplified database types. This worsens as the MSL increases. The standard deviation for all of the results for all three simplified database types is roughly eight decibels. This suggests that the overall trend for the path loss remains the same, but the removal of increasingly large reflectors increases the overall mean value of the field strength. The overall geometry is still the same, but fewer reflections occur as the MSL increases. In order to obtain results with the Features Pre-Processor that are comparable to using the hand-simplified database, roughly twice the number of faces are required.

Type	MSL (meters)	# Faces	Mean Diff. (dB)	Std. Dev. (dB)
Hand	(N/A)	355	1.59	7.57
Length	15.0	738	3.65	7.84
Length	18.0	623	5.20	7.53
Length	21.0	526	7.61	8.35
Length	30.0	429	10.3	7.75
Quad	15.0	708	2.14	8.13
Quad	18.0	603	3.21	7.83
Quad	21.0	518	1.23	8.08
Quad	30.0	373	5.07	8.57

Table 1: Results of Analyses
From SBR3D Software

In the hand-simplified database, it is easier to remove small features and retain larger features since one only needs to see which features are significant to a particular building. By setting a low MSL for length simplification, some small features will be retained along with some small structures that would normally be removed by someone processing the database by hand. If a high MSL is set, then even some important features may be eliminated. With many buildings in a database, it is not generally possible for the user to find a minimum simplification length that will eliminate the small features on all of the buildings while keeping the main features of all of the buildings. Therefore, a compromise must be made between the run time of the SBR3D software and the required level of accuracy. The quadrilateral simplification is not as sensitive to the MSL since its basic geometry is set without it. The area simplifier is the only subroutine that utilizes this. However, at certain MSLs, it may remove both an unused object on top of a large building along with a small building that would normally cause reflections. This would still cause a rise in the mean difference, but not one that is as pronounced as when the length simplifier is used.

Conclusions

The Features Pre-Processor has been shown to be an effective means to simplify databases for use in the SBR3D electromagnetic propagation code. The use of the Features Pre-Processor requires a larger number of building faces in the resulting database in order to obtain results comparable to simplifying the database by hand. The advantage in using this software is that it greatly reduces the time needed to process the complex database that is initially received. Furthermore, this automation allows for the simplification of the database for various minimum simplification lengths. Doing this by hand would require a great deal of time and effort.

References

1. R. Luebbers, J. Schuster, "Site-Specific Radio Propagation Prediction Methods for Urban Environments," Invited Paper presented at the NATO AGARD Sensor and Propagation Panel Meeting, Athens, Greece, September 18-21, 1995.
2. J. Schuster, R. Luebbers, "Comparison of Site-Specific Radio Propagation Path Loss Predictions to Measurements in an Urban Area," IEEE AP-S International Symposium and URSI Radio Science Meeting, Baltimore, MD, July 21-26, 1996.
3. J. Schuster, *A Hybrid SBR/GTD Approach For Predicting UHF Radio Wave Propagation Characteristics In Urban Environments*, Masters Thesis, 1997.

Toward a New Model for Indoor and Urban Propagation using Percolation Theory

G. Franceschetti

Dipartimento di Ingegneria Elettronica e delle Telecomunicazioni
Università degli Studi di Napoli "Federico II", Napoli, I-80125 Italy

S. Marano

Dipartimento di Ingegneria dell'Informazione e Ingegneria Elettrica
Università degli Studi di Salerno, Fisciano (SA), I-84084 Italy

N. Pasquino

Dipartimento di Ingegneria Elettronica e delle Telecomunicazioni
Università degli Studi di Napoli "Federico II", Napoli, I-80125 Italy
pasquino@thewavesgroup.unisa.it

I.M. Pinto

Università degli Studi del Sannio a Benevento, Benevento, I-82100 Italy

Abstract

A new method based on percolation theory is outlined which can be applied to the analysis and statistical characterization of wave propagation in general indoor and urban channels. Appropriate code based on a "ray tracing" technique has been developed in order to simulate optical propagation within the channel. Investigations on signal contributes arrival rate, reflections against obstacles and path lengths have been done. Variations of the latter quantities with propagation and physical parameters, such as lattice density and separation between transmitter and receiver, have been commented.

I. INTRODUCTION.

In the last decades telecommunications have undergone an exponentially-increasing development, mainly stimulated by uncomparated demand for fast and reliable access to information with steadily improved quality of service. When unwired cellular systems are the choice, a working knowledge of the propagation properties of the involved communication channel is needed, in order to produce reliable estimates of the coverage and therefore mean extension of a cell.

To this order, empirical approaches are usually adopted whereby measured electromagnetic fields are used to build some statistical characterization of the channel of interest [1]-[6]. On the one hand, these methods are highly time and money demanding, since extensive measurement campaigns are needed at every location to be characterized. On the other hand, they are reliable in terms of accuracy.

An alternative procedure known as the "ray tracing" method is viable when dealing with micro-cellular environments. It basically consists in tracing the trajectories of the electromagnetic energy flux from the transmitter to the receiver making some judicious use of Geometrical Diffraction Theory whenever needed [7]. To accomplish this, some *a priori* knowledge of the electromagnetic and physi-

cal properties of the propagation environment and an adequate amount of processing power is also required.

In this paper we propose a new method which is based on a physical model of the propagation channel borrowed from Percolation Theory. This will allow for a *simple* description of the channel itself and the propagation phenomena in it, which will turn into a *simple yet relatively complete* software modeling.

The paper is organized as follows: in section II the proposed model is presented, and the relevant assumptions and simplifications are discussed. In section III simulations are presented for the propagation of an ideal pulse through a channel within the frame of the proposed model.

II. THE PERCOLATIVE APPROACH.

The proposed model to investigate propagation in cellular environment is based on *percolation theory* (hereafter P.T.). This latter describes the effects that a variation in the interconnection density has over diffusion in a random system and has been widely applied to such diverse fields as medicine, fire-prevention and polymers [8]. The spirit of P.T. can be grasped by referring to a simple example: a wood on fire. Percolation describes variations in fire duration depending on tree density and cluster¹ extension. Letting a random lattice model the channel, and an electromagnetic (hereafter e.m.) wave play the role of the fire, it would be interesting to apply concepts and methods used in P.T. to study the propagation of the wave through the lattice [9]-[10]. Accordingly, the only quantities we shall have to care about are density, cell side-length and distance between source and observer, since percolation allows for the analysis of even complex phenomena using a relatively *small* number of *simple* parameters.

In order to give a better understanding of the model, we can consider a city channel and model it as a two dimensional lattice, where occupied cells represent buildings whose known density² is q . The cell side-length is fixed and denoted as a . We can neglect building heights to a first approximation. Supposing the e.m. field characteristic frequency to be much smaller than the cell side-length, and the cell itself large enough to neglect contributions from its vertexes will allow us to ignore diffraction phenomena as well. We thus assume ray propagation where each ray proceeds straight until a reflection against an obstacle changes its direction. The obstacles will be taken as opaque, and an average reflection coefficient R will be considered. Power loss due to reflection will be taken into account by means of a suitable attenuation coefficient.

A preliminary discussion of the above approximations is now in order. Firstly, we can comment on the uniform cell-distribution hypothesis. In a real city there are in fact *highly connected* structures (i.e. streets and squares) that introduce likewise some degree of correlation in the cell statistical distribution. One then needs to introduce a correlation coefficient probably depending on the separa-

¹ A cluster is defined as a polygonal area including two or more trees sharing at least one side, not just a vertex.

² Without losing generality we can imagine a completely uniform distribution of obstacles within the lattice where the status of each cell is totally independent from that of surrounding ones.

tion between different cells. Free and occupied cell locations within the lattice will be no more uniform, but will probably look like a cluster of clusters separated by large empty areas. Our hypothesis can perhaps be still maintained as referred to some Europe historical city centers.

Secondly, the model assumes a square plane obstacle acting on the propagation through simple reflection coefficients. This is the crudest assumption for cities, where instead a major role in determining channel characteristics may be played by diffraction phenomena [11].

Moreover, a two-dimensional propagation is assumed. As a matter-of-fact, transmitters are usually placed on top of buildings, and therefore contributes from floors and roofs must be taken into account in principle. This can be done by appropriate generalization.

Finally, it should be noted that no information on time-changes has been included. In a city, many moving obstacles such as buses, motorcycles and cars can take part in the propagation, modifying the instantaneous behavior eventually. Our alternative way to take into account time variations has been to average the simulations of the propagation process over different lattices featuring the same density.

III. SIMULATIONS RESULTS.

Simulation procedures have been implemented using *Matlab*[®]. The random built-in function has been used to generate the random lattice, and an isotropic set of rays modeling an ideal pulse has been considered. Well known trigonometric formulas have been used to determine ray trajectories and path lengths. Arrival times and signal amplitudes have been stored and used to get signal statistics of the simulated propagation process.

Studies have been made on the channel characteristics for different values of the lattice density q and the distance³ d between source and observation points. We can assume an *a priori* Poisson distribution for the arrival times - as usual when dealing with counting processes - and investigate the characteristic quantity $\lambda(t)$ - arrival rate at time t - also known as *parameter function* [12].

Results (see Fig.1) show that $\lambda(t)$ is not constant with time. Maxima of $\lambda(t)$ versus propagation time correspond to paths where arrivals cluster. Simulations obtained for different density values (Fig.1a) show that longer paths occur at higher densities since a larger amount of obstacles imposes longer trajectories to the rays to reach the destination cell. This result is consistent with considerations reported in [1]. No relevant differences have been noted when different values of distances are used (Fig.1b). From the same figures it is also argued that the total amount of arrivals, which is obtained integrating $\lambda(t)$ over all times, increases with density and decreases with separation.

³ According to [10] the distance to be considered in lattice propagation is the *city-block* distance defined as $d = N_x + N_y$ where N_x and N_y are the number of horizontal and vertical cells between transmitter and receiver respectively.

Further investigations have been made on the total number of reflections $N(t)$ that rays undergo before reaching the observation point. This datum is most important for a complete knowledge of pulse response properties as the signal amplitude is directly related to the number of reflections. Fig.2a shows the dependence of a linear interpolation of $N(t)$ on the lattice density. Higher values of q result in larger line slope. Rays in fact encounter more obstacles during their journey to the receiver when the density is higher. Fig.2b shows dependence of the same linear interpolation on the separation between transmitter and receiver.

The total path length covered by the different rays contributing to the received signal has also been investigated. First of all, strong dependence on lattice density has been observed (see Fig.3a). It is quite intuitive that the larger the parameter values, the larger the mean path length as the probability of finding a direct path from transmitter to receiver is lower. In this case in fact it takes more time for a ray propagating from the source to go through the larger amount of obstacles in the lattice. Fig.3a also shows that two main regimes are possible. The first one is encountered for small propagation times, where longer times to cover paths between source and destination correspond to higher density, since a higher amount of obstacles must be avoided before getting to the receiver. As propagation goes on, subsequent arrivals are closer in time for higher densities. That means that successive arrivals cover almost the same distance when density is higher. This is quite easy to understand: higher density and larger number of obstacles do not allow a ray to go too far from the observation cell before redirecting it to the receiver again, so that the time interval between two passages on the same cell decreases. Moreover, as expected an higher separation between transmitter and receiver imply longer paths (see Fig.3b).

IV. CONCLUSIONS.

A percolation model for indoor and outdoor (urban) channel propagation has been outlined. Results have been shown for a simulated propagation process of an ideal pulse through an ideal lattice. Arrival rate, number of reflections and path lengths have been investigated and, to some extent, been related to those obtained applying different channel characterization methods. The next step will be the description of the urban-lattice e.m. impulse response. Work in this direction is in progress.

REFERENCES

- [1] Turin G.L., "A statistical model of urban multipath propagation", *IEEE Transactions on Vehicular Technology*, Vol.21, no.1, pagg.1-9, Feb. 1972
- [2] Turin G.L., "Communication through noisy, random-multipath channels", *IRE National Convention Rec.*, pt.4, pagg.154-166, 1956
- [3] Suzuki H., "A statistical model for urban radio propagation", *IEEE Transactions on Communications*, Vol.25, no.7, pagg.673-680, July 1977
- [4] Suzuki H., "A statistical model for urban radio propagation", Doctoral Thesis, University of California, Berkeley, 1975
- [5] Hashemi H., "Impulse response modeling of indoor radio propagation channels", *IEEE Journal on Selectes Areas in Communications*, Vol.11, no.7, pagg.967-978, September 1993

- [6] Hashemi H., "The indoor radio propagation channel", *Proceedings IEEE*, Vol.81, no.7, July 1993
- [7] James G., *Geometrical Theory of Diffraction for Electromagnetic Waves*, P. Peregrinus, Stevenage, England, 1976
- [8] Stauffer D., Aharony A., *Introduction to Percolation Theory*, 2nd ed., Taylor & Francis, London 1992
- [9] Franceschetti G., Marano S., Palmieri F., "Propagation without wave equation. Towards a urban area model", *IEEE Transactions on Antennas and Propagation*, Vol.47, no.9, pagg. 1393-1404, Sept. 1999
- [10] Franceschetti G., Marano S., Palmieri F., "Statistical characterization of ray propagation in a random lattice", in press.
- [11] Leubbers R., "Finite conductivity uniform GTD versus knife edge diffraction in prediction path loss", *IEEE transactions on antennas and propagation*, Vol.32, no.1, pagg.70-76, Jan. 1984
- [12] Snyder D., Miller M., *Random point processes in time and space*, 2nd ed., Springer-Verlag, 1991

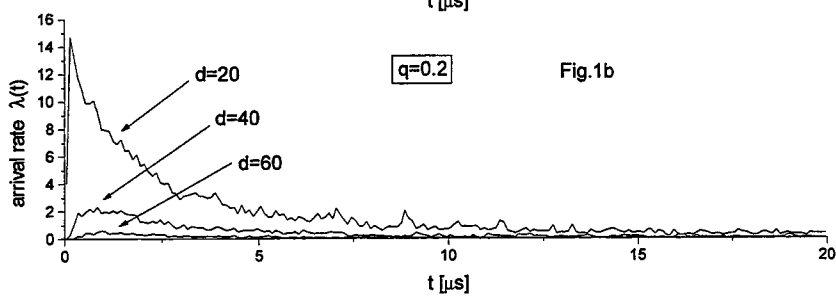
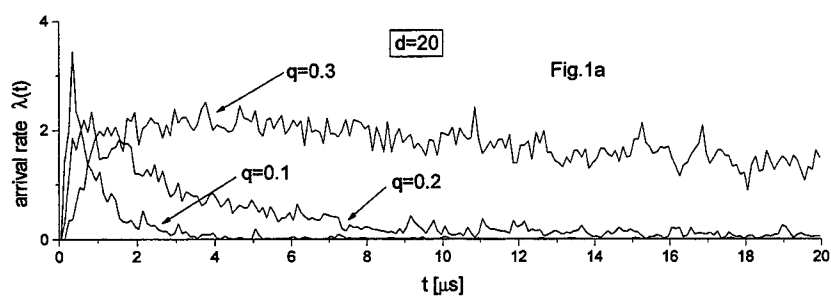


Fig. 1 - Arrival rate $\lambda(t)$ vs arrival times t

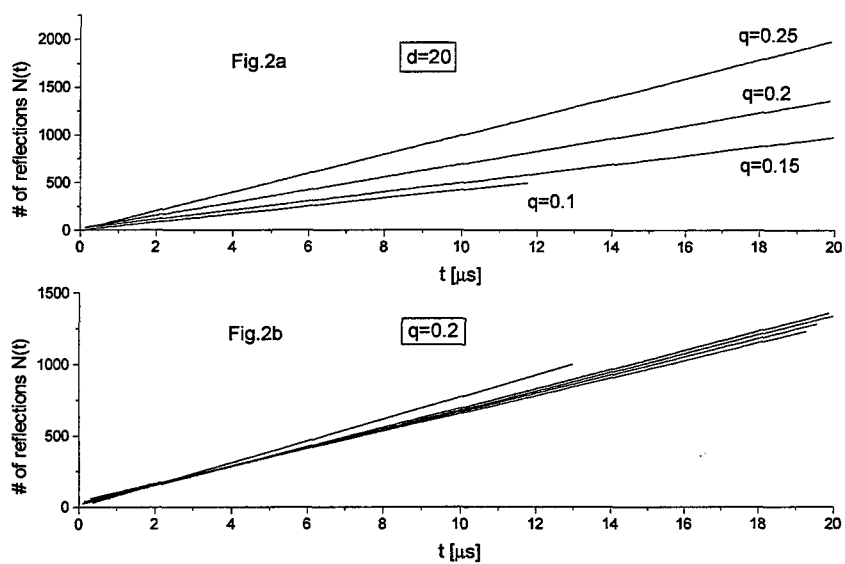


Fig. 2 - Number of reflection $N(t)$ vs arrival times t

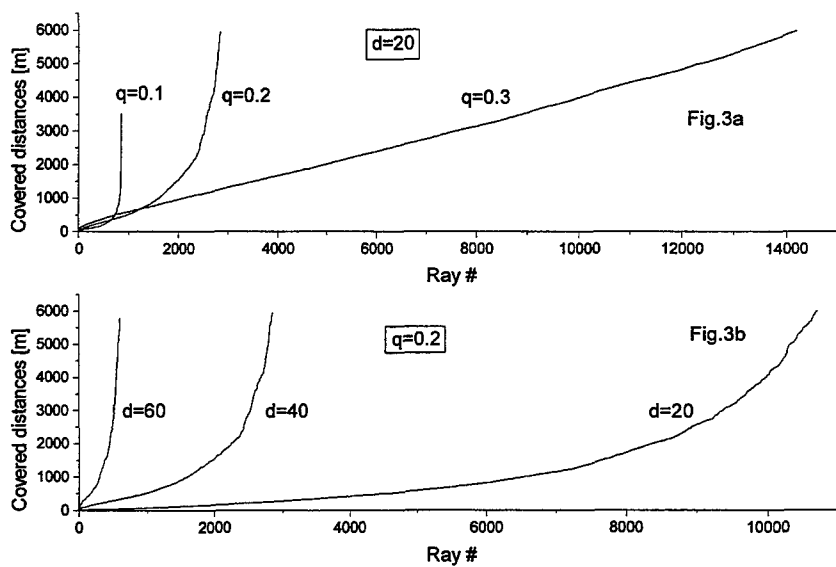


Fig. 3 - Distances covered by rays

Ray Tracing Algorithm for Indoor Propagation

C.W. Trueman, R. Paknys, J. Zhao

EMC Laboratory
Concordia University
Montreal

Trueman@ece.concordia.ca
Paknys@ece.concordia.ca
Zhao@ece.concordia.ca

D. Davis

Dept. of Electrical Engineering
McGill University
Montreal

Don@ece.concordia.ca

B. Segal

Dept. of Otolaryngology
McGill University
Montreal

Segal@med.mcgill.ca

Abstract—The fields due to a portable radio operated inside a hospital are of interest because of possible interference with hospital equipment. This paper presents an algorithm for finding ray paths from a handset to an observer using an “image tree” data structure. The algorithm finds all ray paths having field strength at the observer above a preset “threshold” value, no matter how many reflections are involved. The method is applied to compute the fields due to a handset in a small room, and the results are compared with measured field strengths.

1 Introduction

When a portable radio such as a cellular telephone is operated indoors, geometrical optics is often used to compute the handset's fields[1]. If the observer is within sight of the handset, there is a “direct” path. There are often several paths involving one reflection: from the sidewalls of the room, from the floor, from the ceiling, from the wall behind the handset, or from the wall behind the observer. There are many paths having two reflections. Construction materials have sufficiently high permittivity that they are relatively good reflectors, hence a ray can undergo many reflections from the walls and floor before its field strength is reduced to an insignificant value. Hence some ray paths can include many reflections from the surfaces of the walls, floor and ceiling.

Ray paths are calculated by determining the location of an image source in each reflecting surface; multiple reflections use images of images. The conventional approach is to decide, a priori, to account for ray paths having N or fewer reflections, say $N=3$ or 6 or 10, and to discard all other ray paths[1]. This paper presents a different approach to computing ray paths involving multiple reflections. We will decide, a priori, to include all ray paths that have field strengths larger than a “threshold” value. We then construct an “image tree”, with as many levels of images as needed to compute the field to the desired accuracy. Then for each observer, we use the pre-made image tree to compute actual ray paths from the handset to

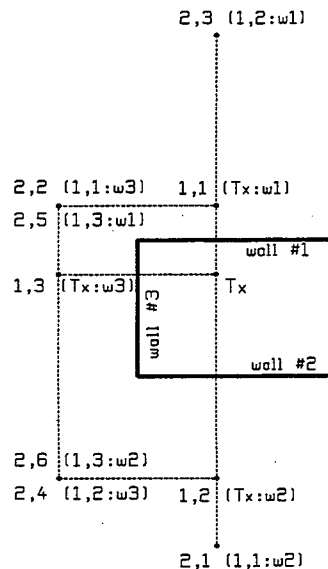


Figure 1 A system of three walls and a transmitter (Tx). The first two levels of images are shown.

that observer, and the field strength associated with each ray path.

The paper will conclude by comparing the computed field strength in a room with that obtained by direct measurement. Although there are many features of the actual room and the handset that cannot yet be included in the calculation, there is a reasonable correspondence between the measured and the computed field.

2 The Ray Tracing Algorithm

2.1 The Image Tree

Fig. 1 illustrates the construction of the set of images for a transmitter "Tx" and a system of three walls, leading to the tree structure of images shown in Fig. 2. The 1st level of the tree contains the image of the transmitter in each of the three walls, image sources (1,1), (1,2) and (1,3). Each image is uniquely identified by an ordered pair (i, j) . Images at level i in the tree are numbered sequentially, $j=1,2,3$. For our

system of three walls, these three image sources are sufficient to compute all ray paths having one reflection from the transmitter to the observer. The 2nd level of the tree contains the location of the image of each 1st level image source in each wall, except the wall that created the 1st level image. Thus for image source (1,1), which is an image in wall #1, there is image (2,1) in wall #2, and an image (2,2) in wall #3. Adding the images of sources (1,2) and (1,3) gives 6 images at the second level, as shown in Fig. 1. This is sufficient to compute all ray paths with one reflection or with two reflections from the transmitter to the observer. Note that the image tree is correct for *any* location of the observer, so the *same* image tree can be used to find the field for all possible observers.

The third level, the tree has the image of each 2nd level in two walls. Thus there are as many as twelve 3rd level images, and up to 24 images at the 4th level, and so forth. It may seem that the number of images will grow very rapidly. In fact this does not happen because the walls are not infinite planes. Consider image source S in Figure 3, which is an image in wall #S. At the next level, source S is imaged in wall #I to get image source I. Rays starting at I must lie in the solid angle between ray C and ray D in order that they pass through wall #I. These rays start at S and reflect from wall #I. But in turn rays starting at S must be reflections from wall #S. If points A and B are not within the physical area of wall #S, then we can discard image source #I. These geometrical considerations eliminate many image sources.

A stopping criterion is required, that indicates when no further images are needed. An obvious criterion is that if we try to create images at level N , but no images are created because no ray paths are

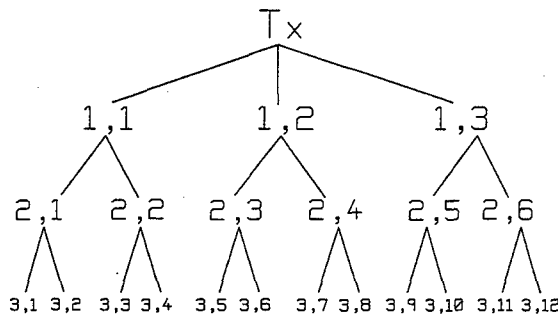


Figure 2 The image tree showing the transmitter and three levels of images.

possible, then we look no further for images. This is the case for a simple two wall system such as a corner reflector.

A more useful criterion is based on the observation in Fig. 1 that the images at level 2 are further from the walls than those at level 1. Similarly the images at level 3 are further from their associated walls than those at level 2. The largest possible field from an image is that evaluated at the nearest point on the surface of the wall giving rise to the image; since the field decreases as $1/\text{distance}$, as the images get further from the walls the maximum field goes down. Thus the user can specify a cutoff field strength for discarding images. When an image source is so far from its associated wall that the largest field falls below the cutoff, the image is discarded. The reflection coefficient is assumed to be unity during the construction of the image tree. Later, when the image location is used to find specific ray paths, the angle of incidence on each panel is known and then the reflection coefficient is fully accounted for.

On input the user specifies the radiated power P_r of the dipole antenna. The program computes the "isotropic level" field strength,

$$E_i = \sqrt{\frac{\eta_o P_r}{2\pi}}$$

where η_o is the intrinsic impedance of free space. This is the field strength that, radiated in one polarization uniformly over the radiation sphere, corresponds to a radiated power of P_r watts. The user specifies the "threshold" for discarding rays, in dB below the isotropic level. For example, to model a cellular telephone handset at 835 MHz with radiated power 600 mW, the isotropic level is 6 volts per meter at one meter from the antenna. If the user specifies a threshold of -65.56 dB, then the cutoff field strength is 3.16 mV/m, and image sources which can never yield field strengths larger than 3.16 mV/m are discarded. A larger value for the threshold would include more rays in the computation but would increase the computation time. This is a very conservative criterion because it does not account for attenuation associated with the reflection coefficients of multiple reflections. Hence more image sources are included than may actually be needed.

Ref. [1] recognizes that the hierarchy of images is a tree data structure. But in Ref. [1], the number of reflections must be decided a priori and the tree is constructed only to a pre-set depth. In the present work, the user decides a priori the minimum field strength that should be considered, by choosing the threshold in dB below the isotropic field strength. The program itself decides to what depth the image tree should be built, depending upon the maximum field strength that each image source can give rise to. For example, in finding the fields in a 150 m corridor, if the source is at one

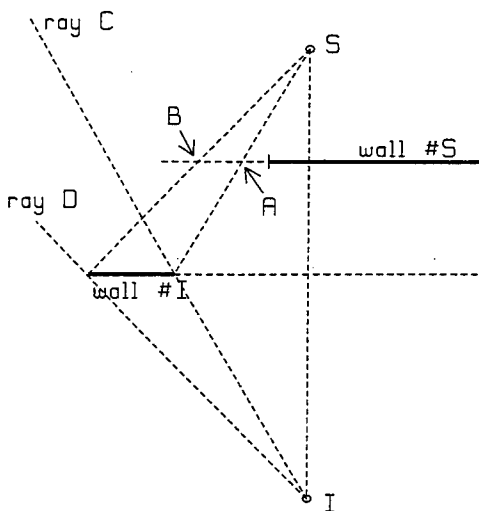


Figure 3 An image source S and its image I in wall #I

end and the receiver at the other, then many reflections from the walls can contribute to the receiver's field. Specifying the accuracy to which the field is needed is more meaningful in this case than simply deciding to include, say, up to 3 or 4 reflections in the computation.

2.2 Tracing Rays to an Observer

In a typical calculation, the field is required at many points along a line, or at many points covering a rectangular grid. Each such point is a "receiver". The image tree is constructed once, and then used to find the field at all of the receivers. Consider the image tree of Fig. 2, with three levels. To trace all possible rays with three reflections from the source to the observer, work through the tree as follows. First consider source (3,1). Trace a ray from (3,1) to (2,1), its parent in the image tree. The reflection point must lie within the physical area of the wall in which source (3,1) is an image, else discard the ray path. Then trace a ray from (2,1) to (1,1), the parent of (2,1). Again the reflection point must be physically within the area of the wall. Finally, trace a ray from (1,1) to the transmitter (Tx). If all three reflection points are real points, then calculate the field at the observer as follows. Start at the source and proceed to the reflection point associated with image (1,1). In a complex

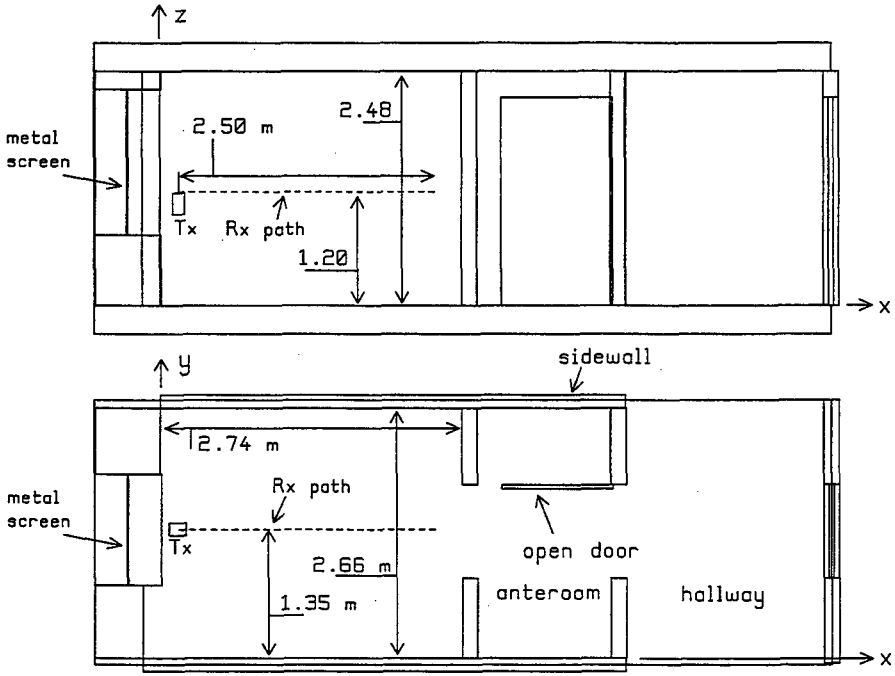


Fig. 4 The hospital clay-block room showing the location of the transmitter (Tx) and the measurement path for the receiver(dashed line).

problem, this ray may pass through one or more intervening walls; account for the transmission losses. Then account for the reflection coefficient associated with source (1,1) using the proper polarization and angle of incidence. Proceed to the reflection point for (2,1), then for (3,1). This gives us the field at the observer associated with one ray path, having three reflections.

Repeat the ray tracing outlined above for all the 3rd level image sources, (3,2), (3,3), ..., to find all possible ray paths with three reflections. Then move up one level in the image tree. Start with image (2,1) and proceed up through the image tree to image (1,1) then to the transmitter (Tx), to identify one path having two reflections. This is done for all 2nd level images to find all the two-reflection paths. Then go to the 1st level, and find paths having one reflection for image sources (1,1), (1,2), etc. In this way all the possible ray paths from the transmitter to the receiver are found, including the associated field at the observer.

The search for ray paths using the image tree is repeated for each "receiver" that the user has specified.

2.3 Algorithm Application: A Hospital Clay Block Room

A comprehensive program of measurement of the field strengths in the hospital environment has been on-going for several years[2-7]. This paper evaluates the ray-tracing algorithm by comparing simulations with field measurements made in the small hospital room of clay block construction shown in Fig. 4. The transmitter is an analog cellular telephone handset, of an older design, operating at 835 MHz. The receiver is a dipole antenna mounted on a "robot", which moves along the floor. The received signal is brought via a coaxial cable to a spectrum analyzer. The system records the field at preset intervals along the path, typically every 3.2 cm of distance traveled.

Fig. 4 shows the hospital room in which the measurement was made. At bottom, the plan view of the room shows that it is 2.74 m deep by 2.66 m wide by 2.48 m tall. The walls are clay block construction, 14 cm thick. The floor and ceiling are concrete with an embedded metal mesh. The lower half of the window at left has a metal screen outside the glass. There are walls and a doorway into a small anteroom, and then walls and a door to the hall. The door is modeled as open, made of wood and 4 cm thick. The wall on the opposite side of the hall, with its wooden door, is included in the computation.

The base of the antenna on the transmitter is located about 44 cm in front of the metal window screen, 1.2 m above the floor, and 1.35 m from the left-hand wall

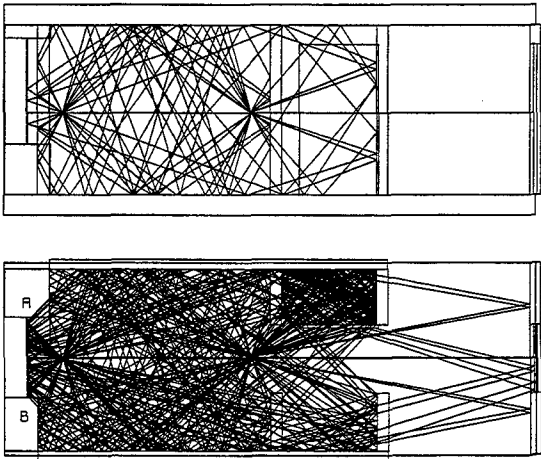


Figure 5 With the receiver positioned at the end of the 2.5 m path, the geometrical optics code computes the ray paths shown in this figure.

when the viewer is facing the window. The receiver dipole is moved by the robot along a path perpendicular to the window, displaced by 2 cm from the base of the antenna, hence 1.37 cm from the left-hand wall. The path runs from a point 44 cm from the window screen for a distance of 2.5 m.

2.3.1 Computing the Field

The geometrical optics code was run with a threshold of 65.56 dB. It creates 19 levels of images and 26,437 image sources for this problem, which has 17 wall panels including the floor and ceiling. Thus ray paths with up to 19 reflections are included in the calculation. Figure 5 shows all the ray paths used by the code, projected onto a horizontal plane in the plan view at bottom, and onto a vertical plane in the elevation at the top. Note that the surfaces of the walls near the window grille, at "A" and "B" in the figure, were not included as reflecting surfaces so some rays incorrectly pass through these surfaces. We note that many ray paths pass through the walls to the anteroom; this is correct and the transmission loss is accounted for. Rays become trapped in the rectangle formed by the sidewall, the door, the anteroom wall and the wall to the hall, and there are many, many rays bouncing around in this region before finding their way to the receiver. In the elevation view we see that there are many ray paths involving reflection from the floor and ceiling.

The handset in the measurement radiates 600 mW. An FDTD analysis of the handset shows that it radiates both an E_θ and E_ϕ component over the radiation sphere. With the handset oriented vertically, the azimuth radiation pattern in E_θ is reasonably circular, with E_ϕ having a figure-eight pattern about 17 dB down from E_θ . The handset was represented in the geometrical optics analysis as an ideal dipole antenna that radiates 600 mW into E_θ . It is intended in future work to incorporate the FDTD-computed handset fields over the radiation sphere into the geometrical optics analysis.

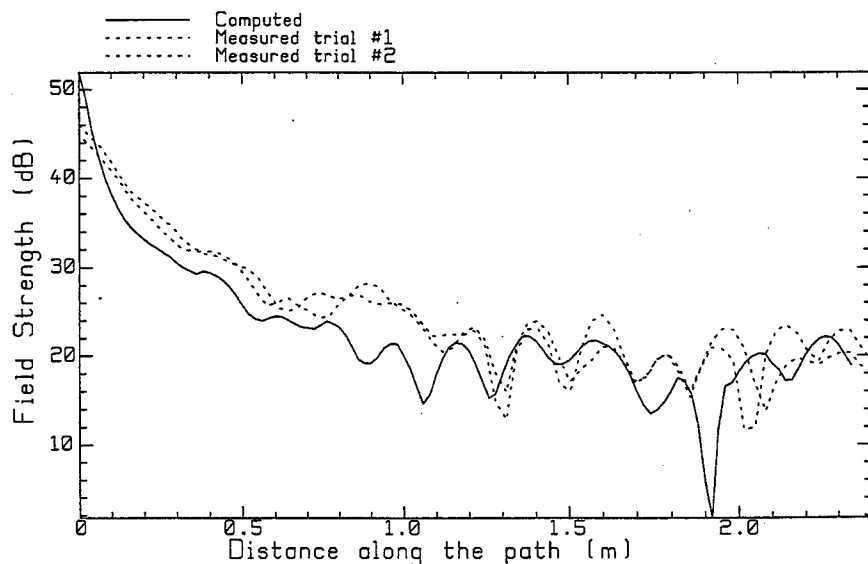


Fig. 6 Comparison of the computed and the measured field in the hospital room.

2.3.2 Computed vs. Measured Field Strength

Fig. 6 compares the computed and measured field strength along the path shown in Fig. 4, in dB above 1 volt/meter field strength. The dashed curves show two measurements done on the same day. The field strength close in to the transmitter is reasonably reproducible, to a distance of about 0.6 m. There are some differences near 0.5, 0.85 and 1.1 m. The minimum at 1.3 m differs between the two measurements. The peak at 1.35 m is reasonably consistent but that at 1.55 m differs between the two measurements. The peak at 1.8 m is almost identical. The measurements differ for distances greater than 1.9 m.

Both the measured field strength and the computed field strength correspond to 600 mW of radiated power. To a distance of about 0.8 m, the field associated with the direct ray dominates. The measured field is about 2 dB stronger than the computed field; but both decline with about the same slope. The field strength in this region is that of the transmitter plus the image of the transmitter in the metal screen covering the window. Moving the handset closer to or farther from the screen changes the phase relationship of the direct field and the field reflected from the screen, hence the net field strength.

Between about 0.8 m and 1.1 m distance, the measured field shows a maximum but the computed field has oscillations. From about 1.1 m to about 1.8 m distance the measurement and the computation both have oscillations and the locations of the maxima and the minima approximately correspond. In this region the peaks and minima are formed as the phase relationship changes between the direct ray from the transmitter, and the reflections from the two sidewalls in the room. Because of the transmitter's directional pattern in the vertical plane, the reflected ray from the floor and from the ceiling have only a minor influence on the vertical component of the field. At distances greater than about 1.8 m, the measurement and the computation correspond poorly, but the average field levels are very similar.

2.4 Conclusion

This paper uses geometrical optics to model indoor propagation. It presents a method for building a tree structure of image sources as the first step in computing the fields, and then using the same tree to find ray paths from the transmitter to each observation point. The user specifies a threshold to determine the weakest field to be accounted for, rather than the maximum number of reflections to be considered. The paper compares the computed field in a small room with measured data. It shows that the general behavior of the computed and measured fields is quite similar. Some features arising from the interference of the signal from the antenna with that from the room's sidewalls are reasonably well reproduced.

References

1. M. Kimpe, H. Leib, O. Maquelin, and T. D. Szymanski, "Fast Computational Techniques for Indoor Radio Channel Estimation", *Computing in Science & Engineering*, pp. 31-41, Jan.-Feb., 1999.
2. P. Vlach, B. Segal and T. Pavlasek, "The Measured and Predicted Electromagnetic Environment at Urban Hospitals", *Proc. 1995 IEEE International Symposium on Electromagnetic Compatibility*, pp. 4-7, Aug. 14-18, 1995.
3. B. Segal, "Medical Equipment Malfunction: Risk and Minimization". In G.L. Carlo, editor, "Wireless Phones and Health: Scientific Progress", pp. 283-295, Kluwer Academic Publishers, Boston, Ma., 1998.

4. D. Davis, B. Skulic, B. Segal, P. Vlach and T. Pavlasek, "Variation of Emergency Room Electromagnetic Interference Potential", Proc. 1998 IEEE Antennas and Propagation Society International Symposium, pp. 1996-1999, Atlanta, Ga., June 21-25, 1998.
5. P. Vlach, B. Segal, J. LeBel and T. Pavlasek, "Cross-floor Signal Propagation Inside a Contemporary Ferro-concrete Building at 454, 862 and 1705 MHz", to be published in the IEEE Trans. On Antennas and Propagation.
6. D. Davis, B. Segal, T. Pavlasek, "Can Minimal-Separation Criteria Ensure Electromagnetic Compatibility in Hospitals?", AAMI Biomedical Instrumentation and Technology Journal, Vol. 33, No. 5, September/October 1999.
7. D. Davis, B. Segal, A. Cinquino, K. Hoege, R. Mastrocola and T. Pavlasek, "Electromagnetic Compatibility in Hospital Corridors", 1999 IEEE International Symposium on Electromagnetic Compatibility, pp. 268-272, Seattle, Wa., Aug. 2-6, 1999.

Modeling Large and Small-Scale Fading on the DPSK Datalink Channel Using a GTD Ray-Tracing Model

Kent Chamberlin (Kent.Chamberlin@unh.edu), Mikhailo Seledtsov (mikhailo@cisunix.unh.edu), and
Petar Horvatic
University of New Hampshire, Dept. of Electrical & Computer Engineering

Abstract

The impetus for the work presented here arose from the need to model the impact of terrain-induced multipath interference on the narrow-band (25 KHz), airborne digital radio link. One of the software components used in this Datalink model is a GTD-based propagation model that has been proven to be effective in predicting absolute signal strength in the presence of irregular terrain. It is the practical aspects of using this ray-tracing model to estimate communication channel performance that is the topic of this paper. Specifically, it addresses the issue of how to efficiently include the effects of the relatively slowly changing multipath signal component into the information-carrying, high-frequency signal. Also included in this paper is a means for estimating small-scale fading, which occurs as the Fresnel zone migrates across varying terrain as a result of a changing receiver location. While the specific application addressed here is the airborne data link, the techniques presented should apply to any wireless digital channel.

The GTD Propagation Model

The GTD model used in this study is named GELTI, for GTD-Estimated Loss due to Terrain Interaction.

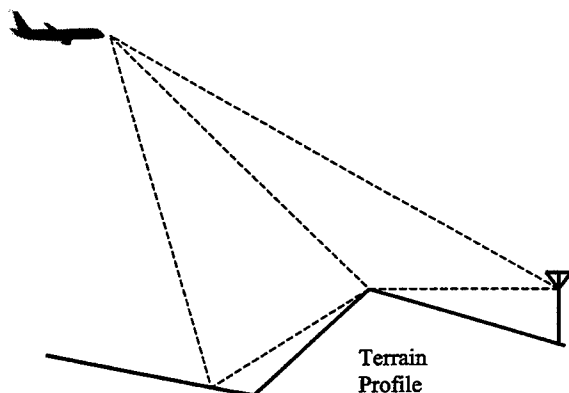


Figure 1 Example of rays contributing to the received signal for the terrain profile shown.

This model has been tested extensively and has been shown to provide good estimates of absolute signal strength for a wide range of frequencies and terrain/receiver location geometries [1,2]. GELTI estimates signal strength by calculating the existence and contributions of up to 16 different rays and ray combinations. For example, Figure 1 illustrates a case where three individual rays comprise the propagation path between the transmitter and receiver. Those rays are the direct, diffracted, and diffracted-reflected rays. The magnitudes and phases of these rays are determined by the optical path

length and the complex-valued diffraction or reflection coefficients, depending upon the type of ray involved. The complex sum of all existing rays and ray combinations provide an estimate of the received signal. This signal can be constructed in either the time or the frequency domain depending upon the data rates involved. For the narrow bandwidth application addressed here, the analyses were performed in the frequency domain, providing phase and amplitude change at the carrier frequency as a function of aircraft position.

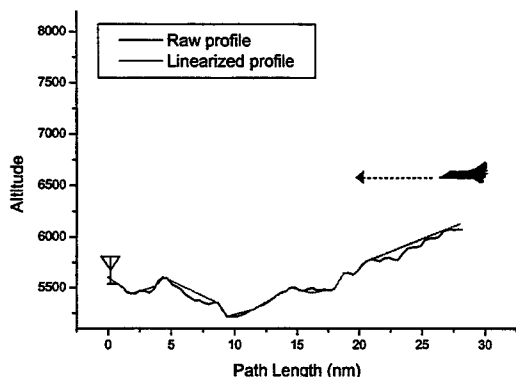
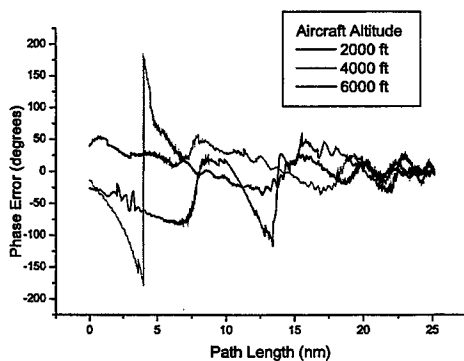
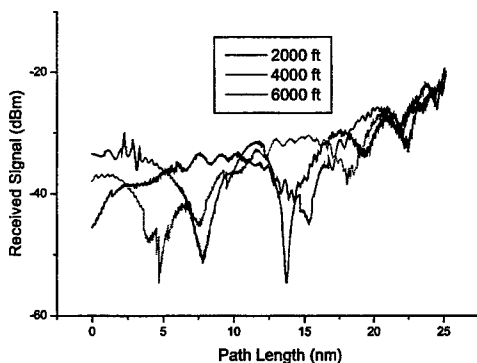


Figure 2. Example scenario for estimating multipath interference

To illustrate how the received phase and amplitude varies with position, consider figure 2 which shows an aircraft flying above an irregular terrain profile; the carrier frequency in this case is 125 MHz. The modeled phase and amplitude data for this flight scenario are plotted in Figures 3 and 4 for 3 different aircraft altitudes (AGL). It should be noted that the effects of Doppler shift have been removed from the phase plot of figure 4. As might be expected, phase and amplitude variations appear to be greatest for lower aircraft altitudes, since the receiver is closer to the scattering objects at the lower altitudes.



Figures 3 and 4. Modeled amplitude and phase for a receiver moving above the profile shown in Figure 2

To gain insight into how the phase variations plotted above might affect a DPSK waveform, consider figure 5 which plots the phase for a 33 KBaud 8-ary DPSK signal along with phase variations caused by a worst-case multipath condition and Doppler shift as a function of time. These waveforms were generated assuming an aircraft velocity of 200 knots. As seen in this figure, the phase of the in-

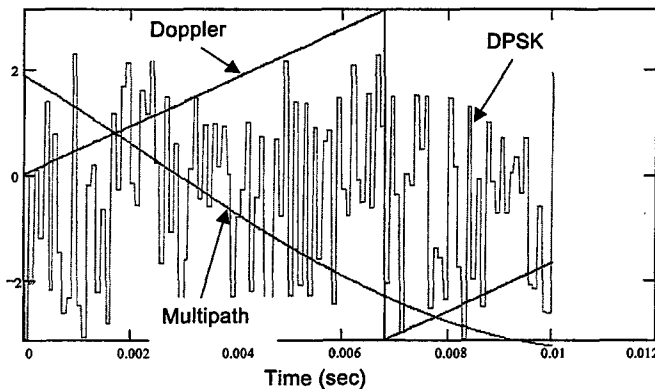


Figure 5. Phase (radians) versus time for a DPSK signal, Doppler shift, and worst-case multipath interference for a receiver traveling toward the transmitter at 200 knots

formation-carrying signal changes more rapidly than the phase changes in either the Doppler or the multipath. Because the phase change between DPSK symbols caused by Doppler or multipath is so small, it is likely that these phase variations do not contribute significantly to bit errors. More likely, it is the amplitude variations caused by multipath interference that causes errors, since the amplitude of the received signal has such a direct impact on signal-to-noise ratio. However, both of the phase and the amplitude variations induced by

multipath interference are accounted for in the modeling effort described here.

Incorporating GELTI Into the Channel Model

To effectively model the multipath effects on data link performance as the receiver moves in space, the phase and amplitude variations imposed on the carrier by the multipath must be taken into consideration. A brute force approach for obtaining these data from GELTI would be to call it several times during the carrier cycle so that the resultant signal could then be passed to a receiver model. However, because of the relatively long execution time required by GELTI, having it generate data at over twice the carrier frequency would be too computationally intensive to be viable. Fortunately, for most realistic receiver path scenarios, multipath interference is slow moving with respect to the carrier frequency and data rate, as shown above, which suggests that the effects of multipath need be applied to the modeled received signal less frequently than twice the carrier frequency rate.

To illustrate how the spatial sampling increment is determined for this application, consider Figure 6, which shows a single ray incident on the receiver that is traveling in the x direction. If N is the total number of rays incident at the receiver location, then the total received signal is given by:

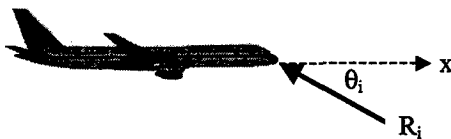


Figure 6 Depiction of i^{th} ray at a receiver traveling in the x direction.

$$S|_{x=0} = \sum_{i=1}^N R_i$$

This sum will result in a complex number, S , that represents the phase and amplitude of the received signal. Because the magnitude of a ray, R_i , and its angle of arrival, θ_i , tend to change relatively slowly compared to the data

rate, even for a fast-moving receiver, we can approximate the received signal as a function of x using the following expression:

$$S(x) = \sum_{i=1}^N R_i e^{j\beta x \cos \theta_i}$$

where β is the free-space wavenumber, and the $x\beta \cos \theta_i$ term accounts for phase shift in the i^{th} ray as a function of distance, x . Clearly, the same information can be obtained by calling GELTI at each location x , but as pointed out above, this can be prohibitively time consuming and unnecessary when updates are needed over small increments of x . A side benefit for using the above expression to define multipath is that it provides a deterministic equation which can be used to optimize the system intended to compensate for multipath effects.

A key question that needs to be answered in applying this approximation is the interval, Δx , over which it is valid. To answer that question, consider Figure 7 below which shows the receiver positioned at the GELTI sample point, $x = 0$, and at the greatest x value for which the approximation is

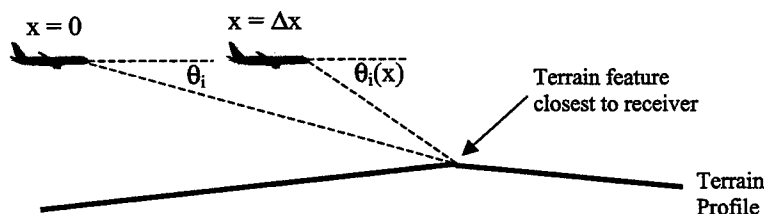


Figure 7 Geometry used to determine spatial sample interval, Δx .

valid, $x = \Delta x$. It is assumed here that the magnitude of a ray does not change in Δx , but only its phase. The assumption in the approximation is that θ_i remains constant within Δx , although it is really a function of x . The range of x for which the approximation is considered valid, Δx , is the value of x where the phase error from any ray begins to exceed 5° . The ray that will have the most rapidly changing angle of arrival will be the ray emanating from the closest terrain feature, and hence it is that ray that is used to determine Δx . The phase error is given by the difference between the actual phase at Δx and the approximated phase, which as stated above, is limited to 5° :

$$|\Delta x \beta \cos(\theta_i(x)) - \Delta x \beta \cos(\theta_i)| \leq 5^\circ$$

Finding Δx using the above requires solving a transcendental equation, but it is more than justified by the computation it saves. Using this approximation between sample points also ensures that significant multipath events are not "stepped over" in the sampling process.

Small Scale Fading Model

Small scale fading will occur with aircraft motion, since the properties of the terrain scattered signal will vary when the aircraft location changes. Because the GELTI model assumes a piecewise-linear terrain profile, modifications were necessary to enable it to account for small-scale fading. To il-

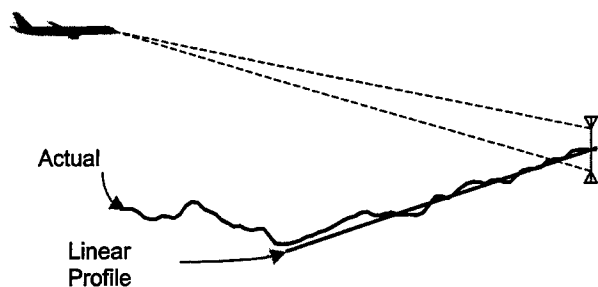


Figure 8. Aircraft Above An Actual Terrain Profile and its Linearized Representation

illustrate this phenomenon, consider Figure 8 below, which shows an aircraft above both an actual terrain profile and a linearized representation of that profile. In the example shown, the actual terrain reflection will vary with aircraft position because the properties of the first few Fresnel zones change as the Fresnel

zone migrates with aircraft position.

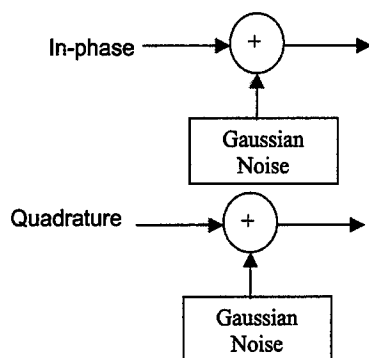


Figure 9. Small-Scale Fading Model Used in the Datalink Model

The small-scale fading model added to the Datalink model was developed using airborne data collected and analyzed by the Federal Systems Integration and Management Center. In that study [3], signal strength data were collected at a 1 kHz rate, and were used to establish the statistical properties of small scale fading. Small scale fading is modeled as Gaussian noise added independently to both the in-phase and quadrature signal components as shown in Figure 9. As seen in the figure, small-scale fading is approximated by Gaussian noise added independently to both the in-phase and quadrature components of the received signal. The magnitude and standard deviation of the Gaussian noise is a function of the direct ray magnitude, the terrain roughness, and the speed of the aircraft.

To illustrate how the addition of small-scale fading affects modeled received signal strength, consider Figure 10 below,

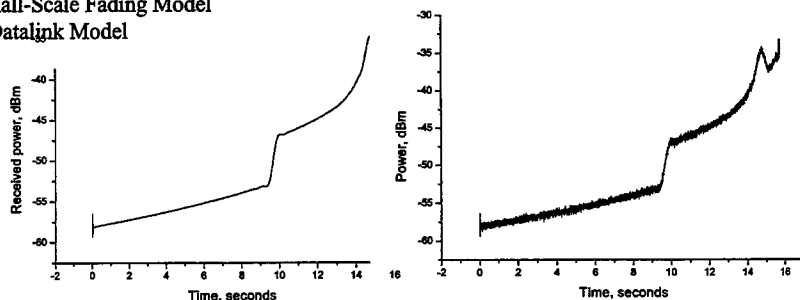


Figure 10. GELTI Output Both With and Without Small-Scale Fading

which show GELTI output both with and without small-scale fading added. The small-scale fading shown in the figure was generated assuming an aircraft velocity of 200 Knots.

The Complete Datalink Channel Model

A block diagram for the complete Datalink channel model is given in Figure 11. As seen in the figure, the large-scale fading effects, provided by GELTI, are applied equally to both the in-phase and quadrature components of the signal, while small-scale fading is added separately to those components.

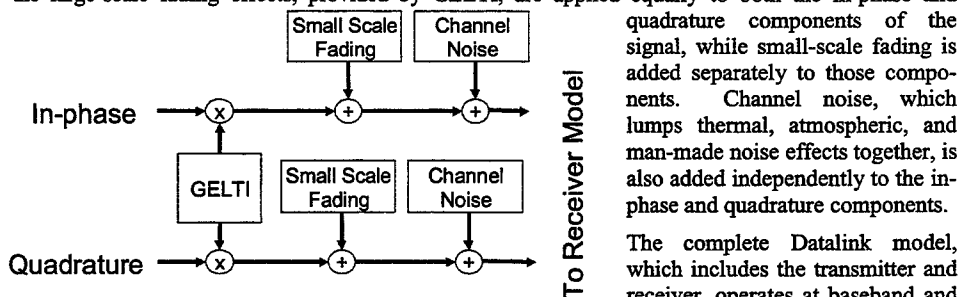


Figure 11. Complete Datalink Channel Model Block Diagram.

The complete Datalink model, which includes the transmitter and receiver, operates at baseband and hence requires signal samples at twice the bandwidth of the information-carrying signal, or 50 kHz in the application described here. The updates from GELTI are generated using the strategy described above, while the small-scale fading and channel noise values are provided by software noise routines.

For the channel model described here, perhaps the least well understood component is the channel noise module. The characteristics of channel noise are known to be somewhat impulsive, and hence exponentially or log-normally distributed [4,5]. However, measured data for the frequency range, bandwidth, and locations of interest are scarce. Consequently, we have had to estimate channel noise and its statistical characteristics using limited data. Future work will include obtaining and analyzing channel noise to identify realistic, worst-case conditions that will likely be encountered by a digital receiver.

References

1. Chamberlin, Kent A., "Terrain Effect Modeling Using the Geometrical Theory of Diffraction", Radio Science Bulletin, No 280, March, 1997.
2. Chamberlin, Kent A., "An Automated Approach for Implementing GTD to Model 2-D Terrain Effects at Microwave Frequencies", IEEE Transactions on Electromagnetic Compatibility, Vol. 38, No.1., February, 1996.
3. Federal System Integration and Management Center, "Terminal Area Channel Sounding Measurements", Subtask 038-2, January, 1998.
4. Lauber, Wilfred R. and Bertrand, Jean M., "Statistics of Motor Vehicle Ignition Noise at VHF/UHF", IEEE Transactions on Electromagnetic Compatibility, Vol. 41, No.3., August, 1999.
5. Spaulding, A. D. and Disney, R. T., "Man-made Radio Noise Part 1: Estimates for Business, Residential and Rural Areas", OT Report 74-38, Boulder, CO, June 1974.

ROUGH SURFACE FORWARD SCATTER IN THE PARABOLIC WAVE EQUATION MODEL

FRANK J. RYAN

Maritime Surveillance Division, CODE D-711
Space and Naval Warfare Systems Center
San Diego, CA. 92152-5001
e-mail: ryan@nosc.mil

ABSTRACT. A technique is described for modeling coherent forward scatter from statistically rough surfaces using the parabolic wave equation. The focus is on low grazing angle electromagnetic propagation over a rough ocean surface, but the technique is also applicable to propagation over other types of surfaces such as terrain. The method incorporates Fresnel or impedance type boundary conditions at the air-water interface and treats both horizontally and vertically polarized wave fields.

§1.0 INTRODUCTION

In many applications involving the propagation of electromagnetic fields over the ocean surface, the received signal is significantly affected by the low grazing angle (LGA) coherently forward scattered wave reflected from the sea surface. For a smooth ocean surface, the coherent scattered field, for simple plane wave incidence, is in the specular direction θ_0 . (In what follows, all angles are measured relative to the horizontal.) Neglecting diffraction phenomena, the specularly scattered field, E_s , is related to the incident plane wave field E_0 via a plane wave reflection coefficient Γ_0 : $|E_s(\theta_0)| = |E_0\Gamma_0(\theta_0)|$. The coherent Fresnel reflection coefficient for a smooth dielectric half-space with complex relative dielectric ϵ is:

$$\Gamma_0(\theta) = \begin{cases} \frac{p - \kappa}{p + \kappa}, & \text{H-pol} \\ \frac{\epsilon p - \kappa}{\epsilon p + \kappa}, & \text{V-pol} \end{cases} \quad \kappa = \sqrt{k_0^2(\epsilon - 1) + p^2},$$

where $p = k_0 \sin(\theta)$ is the vertical wavenumber, and k_0 is the wavenumber. If an impedance type boundary condition is assumed, then the equivalent reflection coefficient is

$$\Gamma_0 = (p - \alpha_s)/(p + \alpha_s), \quad \alpha_s = \begin{cases} k_0\sqrt{\epsilon - 1}, & \text{H-pol} \\ k_0\sqrt{\epsilon - 1}/\epsilon, & \text{V-pol} \end{cases}$$

When the ocean surface is rough, the surface reflected signal is modified according to the coherent surface reflectivity defined as $R_{coh} \equiv |\bar{E}/E_0\Gamma_0|$ where \bar{E} is the coherent scattered field, and E_0 is the direct wave field.

Miller and Brown⁷, employing geometrical optics theory and modeling the random sea surface elevation ζ as the stochastic process $\zeta = H \sin \phi$, with the wave height H a zero-mean, normally distributed process and the phase ϕ uniformly distributed on $[-\frac{\pi}{2}, \frac{\pi}{2}]$, derived the formula for the coherent reflectivity:

$$R_{MB} = e^{-\frac{1}{2}g^2} I_0(\frac{1}{2}g^2), \quad g = 2k_0\sigma \sin(\theta) \quad (1)$$

where g is the Rayleigh parameter, σ is the surface RMS amplitude, and I_0 is the zero-th order modified Bessel function. The Miller-Brown formula Eq. (1) better fits the experimental data of Beard² in the range $0 \leq g \leq 0.6$ than the Isakovitch-Eckart-Ament result $R_{IAE} = e^{-\frac{1}{2}g^2}$. However, neither appears to provide a satisfactory fit to Beard's data near $g \approx 0.2$.

For moderate Rayleigh parameter, $R_{MBA} \ll 1$, while for low grazing angles ($g \ll 1$)

$$R_{MBA} \sim 1 - 2(k_0\sigma \sin \theta)^2, \quad (\theta \rightarrow 0) \quad (2)$$

Following Bass and Fuks³, the reflection coefficient for a rough surface characterized by an impedance boundary condition $\frac{\partial U}{\partial N} = -ik_0\eta U$ is computed by perturbation theory for LGA to be

$$R_{msp} \sim 1 - 2\eta \sin(\theta) \quad (3)$$

where the rough surface impedance η is

$$\eta = \begin{cases} \eta_h^0 - (k_0\sigma)^2 e^{i\pi/4} \sqrt{\frac{2}{\pi k_0 l}} \int_0^\infty \frac{dx}{\sqrt{x}} \frac{d\hat{W}(x)}{dx}, & \text{H-pol} \\ \eta_v^0 + \frac{\sigma^2}{2l^2} e^{i3\pi/4} \sqrt{\frac{k_0 l}{2\pi}} \int_0^\infty \frac{dx}{x^{3/2}} \frac{d\hat{W}(x)}{dx}, & \text{V-pol} \end{cases}$$

and $\eta_{h,v}^0$ are the smooth surface impedances. The function $\hat{W}(\rho/l) = W(\rho)$ is the scaled surface roughness correlation function W defined by the horizontal correlation radius l .

Despite the popularity of the Miller-Brown(MB) theory, there are a number of problems associated with it. The LGA limit of Eq. (2) is independent of polarization, and conflicts with the results of full-wave perturbation theory Eq. (3)— under predicting the coherent surface loss at low grazing angles. The sea surface model employed to derive the MB result does not correspond to accepted oceanographic models of stochastic ocean surfaces. Another problem with the Miller-Brown type approach is that it is predicated on a geometrical optics incident wave field on the surface and hence breaks down when the incident wave field is dominated by diffractive energy—for example beyond the horizon.

§2.0 MULTIPLE FORWARD SCATTER

Computing coherent LGA forward scatter using ray theoretic methods leads to incorrect results as described earlier. Essentially this is due to a fundamental breakdown in approximating the field via geometrical optics in regions dominated by diffraction physics where full-wave methods are needed. An alternative approach to LGA propagation is to use the parabolic

wave equation coupled with the Helmholtz-Kirchoff integral representation and the Ewald-Ossen extinction theorem⁵.

Assuming a linear polarized wave field (H-pol, V-pol), the vector electromagnetic wave equations can be replaced by equivalent scalar wave equations for the non-zero transverse field component U (U = electric E_ϕ or magnetic H_ϕ) and approximated by a PWE solution⁹. A multiple forward scatter solution can be obtained by successive application of a Huygens's type solution obtained from the Helmholtz-Kirchoff integral. Consider a closed surface S enclosing a volume V containing no sources. If $\vec{P} \in V$ is an observation point inside V , and N is the normal to S , then the field $U(\vec{P})$ can be expressed in terms of the surface field on S and a Green's function \mathcal{G} :

$$U(\vec{P}) = \frac{1}{4\pi} \int_S [U(\vec{P}') \frac{\partial \mathcal{G}(\vec{P}|\vec{P}')}{\partial N} - \mathcal{G}(\vec{P}|\vec{P}') \frac{\partial U(\vec{P}')}{\partial N}] dS' \quad (4)$$

where $\vec{P}' = \{x, y\} \in S$ is a vector on the surface.

Restrict the discussion to two-dimensional propagation in the $\{x, z\}$ -plane, and suppose a surface impedance boundary condition is defined on the interface $z = h(x)$

$$\frac{\partial U(x, z)}{\partial N} + \beta U(x, z) = 0, \quad (5)$$

and a radiation condition at infinity. The surface S in Eq. (4) is decomposed into $S = S_1 + S_2 + S_3$, where S_1 is the vertical aperture along the positive z -axis, S_2 is the circular arc bounding the first quadrant $x > 0, z > 0$, and S_3 is the positive x -axis. Along S_2 the field $U \rightarrow 0$ according to the radiation boundary condition. Now construct a Green's function \mathcal{G} that: 1) satisfies the surface boundary condition Eq. (5) along S_2 , and 2) satisfies a Dirichlet boundary condition along S_1 . In this case, Eq. (4) becomes simply

$$U(\vec{P}) = \frac{1}{2\pi} \int_0^\infty U(z') \frac{\partial \mathcal{G}(\vec{P}|z')}{\partial N} dz' \quad (6)$$

The multiple-forward-scatter parabolic wave equation (MFS-PWE) method results if the exact Green's function \mathcal{G} is approximated by the parabolic Green's function G , and Eq. (6) recursively applied to the wave field at successive vertical planes. If the boundary surface $z = h(x)$ is approximated by piecewise-linear segments, such that within the i -th segment $h(x) = h_0 + gx, x \in [x_{i-1}, x_i]$ where $g = \tan \alpha$ is the local tangent slope, the Green's function G_α can be exactly represented in rotated $\{u, v\}$ -coordinates

$$G_\alpha(v, u|v_0, u_0) = i \int_{-\infty}^\infty \frac{dq}{\xi} e^{+i(\xi|v-v_0|+qu)} \left[e^{-iqu_0} + \Gamma(q) e^{+iqu_0} \right]$$

$$\xi = \sqrt{k_0^2 - q^2}, \quad q = k_0 \sin(\theta - \alpha)$$

$$u = (z - h_0) \cos \alpha - x \sin \alpha, \quad v = x \cos \alpha + (z - h_0) \sin \alpha$$

§3.0 SEA SURFACE REALIZATION

The rough ocean surface used in the MFS-PWE method is generated from a stochastic spectral ocean wave model parameterized by water properties (temperature, salinity, surfactants), surface wind fields (speed, fetch, duration, direction), and swell (distantly generated waves propagated into the observation region). The ergodic sea surface elevation profile $z = \zeta(\vec{x}, t)$ ($\vec{x} = \{x, y\}$ is a horizontal vector) has the Fourier-Stieltjes integral representation

$$\zeta(\vec{x}, t) = \iint_{-\infty}^{\infty} e^{+i(\vec{k}\cdot\vec{x} - \omega t)} d\tilde{B}(\vec{k}),$$

where $\vec{k} = (k_1, k_2) = (k, \phi)$ is the wavenumber vector, ω is the radian frequency and \tilde{B} is a stochastic process. \tilde{B} is related to the surface covariance K by

$$K(\vec{\rho}, \tau) = E[\zeta(\vec{x}, t)\zeta^*(\vec{x} + \vec{\rho}, t + \tau)] = \iiint_{-\infty}^{\infty} E\{e^{+i(\vec{k}\cdot\vec{x} - \omega t)} e^{-i(\vec{k}'\cdot(\vec{x} + \vec{\rho}) - \omega'(t + \tau))} d\tilde{B}(\vec{k}) d\tilde{B}^*(\vec{k}')\}$$

where $E[\dots]$ denotes ensemble average. The wave spectrum $X(\vec{k}, \omega)$ is the Fourier transform of the covariance⁸,

$$X(\vec{k}, \omega) = (2\pi)^{-3} \iint K(\vec{\rho}, \tau) e^{-i(\vec{k}\cdot\vec{\rho} - \omega\tau)} d\vec{\rho} d\tau, \quad \iint X(\vec{k}, \omega) d\vec{k} d\omega = \sigma^2,$$

with σ the RMS wave amplitude. $X(\vec{k}, \omega)$ represents the mean distribution of wave energy with magnitude $k = |\vec{k}|$ and frequency ω propagating in the direction \vec{k} . Oceanographers typically model ocean wave spectra in terms of the one-sided directional wavenumber spectrum $\Phi(\vec{k}) = 2 \int_0^\infty X(\vec{k}, \omega) d\omega$ which represents the actual wavenumber directional distribution of wave energy propagation. For scattering calculations, the symmetric or folded wavenumber distribution $\Phi_s(\vec{k}) = \frac{1}{2}[\Phi(\vec{k}) + \Phi(-\vec{k})]$ is required.

3.1 Elevation profile

For an instantaneous traverse of the sea surface along the line r_1 (direction = ϕ_0), the covariance $E[\zeta(\vec{x}, t)\zeta(\vec{x} + r_1, t)] = K(r_1) = \int_{k_1} \phi(k_1) dk_1$, where the one-dimensional (transverse) spectra ϕ_1

$$\phi_1 \equiv \phi(k_1) = \frac{1}{2\pi} \int K(r_1) e^{-ik_1 r_1} dr_1 = \int_{-\infty}^{\infty} \Phi(\vec{k}) dk_2$$

represents an integral of the wavenumber spectrum $\Phi(\vec{k})$ along a line $k_1 = \text{const.}$ perpendicular to the direction of the traverse. Assuming the ocean sea surface can be represented as a stationary Gaussian process, the elevation profile along the $r = r_1$ direction can be expressed as⁶

$$\zeta(r) = \int_0^\infty \cos[kr + \epsilon(k)] \sqrt{\phi_1(k)} dk \quad (7)$$

where the phase $\epsilon(k)$ is a random function uniformly distributed on $[0, 2\pi]$. In practice, Eq. (7) is implemented via a fast Fourier transform

$$\zeta(r) = \sum_{j=1}^N [a_j \cos(k_j r) + b_j \sin(k_j r)] \sqrt{\phi_1(k_j) \Delta k}, k_j = j \Delta k \quad (8)$$

where a_j and b_j are zero-mean independent Gaussian random variables with unit variance.

3.2 Ocean wave model

The 1-D spectrum ϕ_1 in Eq. (7) is obtained by collapse of a 2-D directional wavenumber spectrum $\Phi(\vec{k}) = \Phi_w(\vec{k}) + \Phi_s(\vec{k})$ consisting of a broadband wind-wave component Φ_w representing local wave generation mechanisms, and a narrowband swell component Φ_s which represents distant wave energy propagating into the observation region. The wind-wave spectrum is based on a modified Donnellan-Pierson-Banner (DPB)^{1,4} type spectrum Φ_{DPB} represented in product polar form as

$$\Phi_w(\vec{k}) = \Phi_{DPB}(k, \chi) = \Phi(k, 0) D(k, \chi),$$

where $F(k) = \Phi(k, 0)$ is the peak of the 2-D directional wavenumber spectrum in the dominant wave direction $\chi = 0$ (usually the wind direction), and D is a angular spreading function which takes into account the attenuation of wave energy propagating in directions away from the maximum. The directional spreading function has the form $D(k, \chi) = \text{sech}^2[h(k)\chi]$, where $h(k)$ is a wavenumber dependent spreading width. The DPB radial spectrum F consists of a low wavenumber component F_{gw} describing surface gravity waves and a higher wave number component F_{cw} modeling capillary waves:

$$F(k) = \begin{cases} F_{gw}, & k < 10k_p, \\ F_{cw}, & k > 10k_p \end{cases} \quad k_p = g(\Omega/U_{10})^2$$

where k_p is the wavenumber at the spectral peak, U_{10} is 10m wind speed and Ω is the inverse wave age. The gravity wave component F_{gw} has the JONSWAP form

$$F_{gw} = \alpha_p \sqrt{k/k_p} \gamma^\Gamma e^{-1.2(k_p/k)^2} k^{-4}, \quad \Gamma = e^{-\frac{1}{2}(\sqrt{k/k_p} - 1)^2 / \sigma^2}$$

where the spectral peak α_p and peak enhancement factors γ, Γ are functions of waveage Ω .

§4.0 RESULTS AND CONCLUSIONS

The method described above has been implemented in an operational computer code—VTRPE (Variable Terrain Radiowave Parabolic Wave Equation). The VTRPE model treats both forward scatter and backscatter from rough ocean surfaces. An example of a 2-D 1km x 1km sea surface realization for a fully developed sea with a 20kn wind is shown in Figure-1. A slice thru the surface in the co-wind direction is shown in Figure-2. Figures-3 and 4 show

coverage diagram results for an X-band airborne surface search radar (APS-137) near the horizon. The 1kn wind speed case shows a coverage diagram with essentially the same type of Lloyd's mirror interference pattern expected from a smooth surface. The 20kn (Figure-4) case shows a distinctly different coverage diagram—the deep nulls have been filled in and the entire pattern rotated counter-clockwise. This later phenomena is not predicted by methods using the Miller-Brown technique.

References

1. M.L. Banner, "Equilibrium spectra of wind waves," *J. Phys. Oceanogr.* **20**, 966–984 (1990).
2. C.I. Beard, "Coherent and Incoherent Scattering of Microwaves from the Ocean," *IRE Trans. Ant. Prop.* **AP-9**, 470–483 (1961).
3. F.G. Bass and I.M. Fuks, *Wave Scattering from Statistically Rough Surfaces*, (Pergamon Press, Oxford, 1979).
4. M.A. Donelan and W.J.P Pierson, "Radar scattering and equilibrium ranges in wind-generated waves with applications to scatterometry," *J. Geophys. Res.* **92**, 4971–5029 (1987).
5. A. Ishimaru, *Electromagnetic Wave Propagation, Radiation, and Scattering*, (Prentice-Hall, Englewood Cliffs, 1991).
6. B. Kinsman, *Wind Waves; their Generation and Propagation on the Ocean Surface*, (Prentice-Hall, Englewood Cliffs, 1965), Chap 8.
7. A.R. Miller, R.M. Brown, and E. Vegh, "New derivation for the rough-surface reflection coefficient and for the distribution of sea-wave elevations," *IEE Proceedings, Part H* **131**, *Microwaves, Opt. Antennas*, 483–489 (1986).
8. O.M. Phillips, *The Dynamics of the Upper Ocean*, (Cambridge University Press, Cambridge, 1977), 2nd Ed..
9. F.J. Ryan, "Analysis of electromagnetic propagation over variable terrain using the parabolic wave equation," *NOSC TR-1453*, Naval Ocean Systems Center, San Diego, CA (1991).

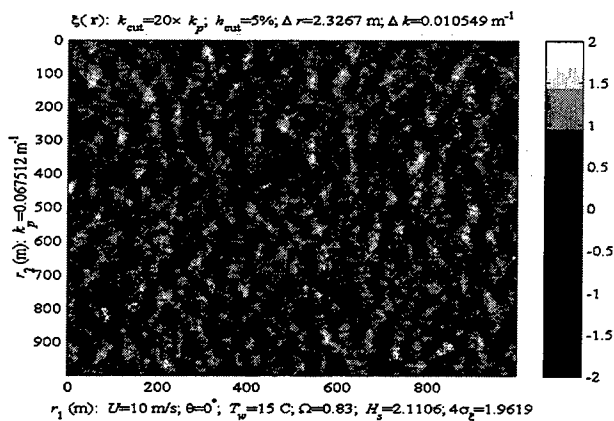


FIG. 1. Sea Surface Realization: Wind Speed=20kn

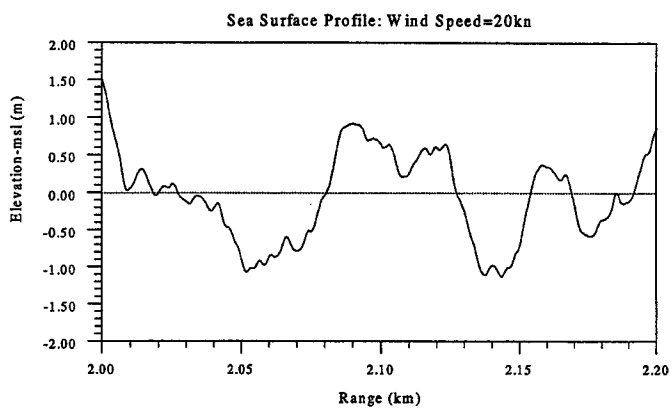


FIG. 2. Sea Surface Co-wind Traverse: Wind Speed=20kn

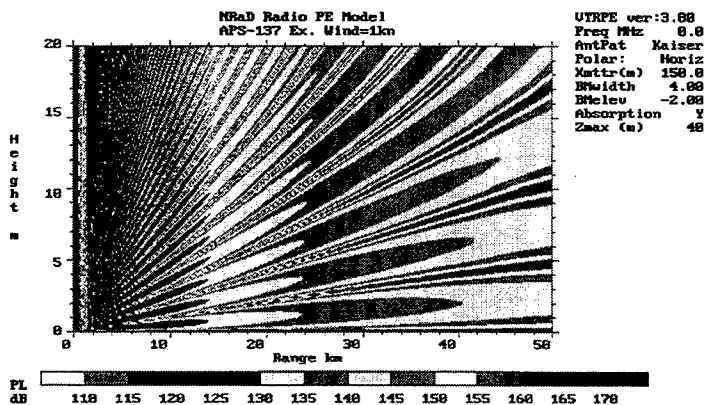


FIG. 3. VTRPE Coverage Diagram:Wind Speed= 1kn

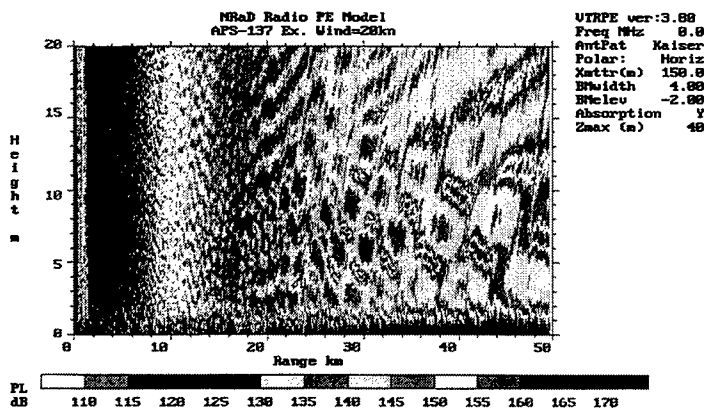


FIG. 4. VTRPE Coverage Diagram:Wind Speed= 20kn

A Comparison of Electromagnetic Parabolic Equation Propagation Models Used by the U.S. Navy to Predict Radar Performance

Donald de Forest Boyer
Naval Surface Warfare Center Dahlgren Division
Code N25
17320 Dahlgren Road, Dahlgren, Virginia 22448
(540) 653-1908, dboyer@nswc.navy.mil

Huong Pham
Technology Service Corporation, Washington Operations
962 Wayne Avenue
Silver Spring, Maryland 20910
(301) 565-2970, hpham@tscwo.com

1. Introduction

The research and development effort that produced the military radars used in World War II also produced new techniques for predicting propagation of electromagnetic waves in the atmosphere. These results are documented elegantly in the book edited by Donald E. Kerr [2], which was originally published shortly after World War II. One section in Kerr's book, entitled "Methods for Calculating Field Strength with Standard Refraction" by William T. Fishback, became the basis for modeling the effects of the earth and atmosphere on shipboard radars for the thirty years following World War II [3], [4]. Kerr's book also derived classical infinite series solutions to the full Helmholtz Wave Equation in the case of an index of refraction with only height variation. However, these solutions were only applicable in the academic community, and were not easy to employ when one needed to analyze the range performance of a shipboard radar.

By the late 1980's it was clear that in order to include range varying refractivity and rough surface effects in the analysis of range performance for shipboard radars, the Parabolic Wave Equation (PWE) approximation to the Helmholtz equation, and its implementation using the Fast Fourier Transform, was the technique that showed the most promise. The PWE approximation was introduced by the Russian physicist V.A. Fock in 1946 to simplify the classical solution of propagation of electromagnetic waves around the surface of the earth [1]. Thirty years after Fock's original work, Tappert and Hardin [5] showed how the Fast Fourier Transform could be employed to devise a very efficient computational method, called the Fourier split-step solution to the PWE. Though the PWE has been solved classically, using separation of variables, resulting in an infinite series of special functions [6], as well as numerically, using finite differences [7], the models that are under discussion in this paper use the Fourier split-step method to solve the PWE. For very careful derivations and analyses of the approximation errors which may be induced by replacing the full Helmholtz equation with the PWE model, and the numerical issues involved in with the implementation of the Fourier split-step algorithm¹ see [8], and [9].

This paper focuses on a comparison of four of the PWE models which were developed within The U.S. Navy community since the late 1980's, and are still being supported by Department of Defense sponsors. A detailed discussion of the development and application of three of these models is provided in the recent article by G. D. Dockery, [10]. So only a brief description of the latest version, (as of September 1999), of each the models, with very little historical background will be provided.

¹ From this point on, in this paper, when the acronym "PWE" is used, it will mean the "Parabolic Wave Equation implemented computationally with the Fourier split-step method".

2. General Characteristics of the Models and the Scenarios

The PWE approximation converts the Helmholtz wave equation into an initial value problem, which under the assumption that the refractivity is constant expresses the Fourier split-step solution, as an inverse Fourier transform with respect to the height variable. The split-step algorithm is initialized in the transform domain, with the antenna pattern. The inverse FFT is used to transform back to the height and range domain, and the solution is "marched" in range over a small enough rectangle to guarantee that the error involved in modeling the refractivity as constant, plus the numerical error involved in the discretization are sufficiently small. The FFT is computed at the new range step, and split-step solution begins anew. Each of the four models discussed here uses the some form of the PWE approximation. The output that most radar analysts desire is the total path loss in dB, in the form of a coverage diagram expressed in range and height. Each of the models handles range-varying refractivity profiles. The form of the Fourier transform imposes the lower boundary condition on the field. If a sine transform is used then the field will be zero at the lower boundary, etc.

1. **RPO** (Radio Physical Optics) was developed by Herbert Hitney at the SPAWAR Systems Center San Diego (SSC-SD) and released in 1992. The "Hybrid PWE Model" term is applied to RPO because it employs a ray optics technique to compute the path loss in the ray-optics region. Beyond this region the loss is computed with the PWE technique. Also an extended optics technique is used above the PWE region. Using this Hybrid method a much smaller FFT size is possible, and significant execution time saving occurs. Also RPO assumes perfect conductivity at the sea boundary, which also saves time. As a result of these assumptions, RPO executes a typical scenario in about a second compared with 20-30 seconds for models that do not use a Hybrid variation on the PWE. RPO only applies over the ocean, and does not model vertical polarization or surface roughness, except in the ray-optics region. The hybrid method restricts the antenna height to no more than 100 meters.

2. **APM** (Advanced Propagation Model) was also developed at SSC-SD by Amalia Barrios, and is now available over the SPAWAR web site. APM is a Hybrid PWE model much like RPO. However it does not assume perfect conductivity, thus it is able to model vertical polarization better than RPO. Also it operates over terrain as well as ocean, but it does not attempt to model surface roughness anywhere. APM executes at about half as quickly as RPO, but still at least ten times as quickly as the non-hybrid models. If an antenna height of more than 100 meters is specified, then APM resorts to a full PWE method.

3. **TEMPER** (Tropospheric Electromagnetic Parabolic Equation Routine) was developed at the Johns Hopkins University Applied Physics Laboratory, primarily by G. Daniel Dockery. TEMPER is a full PWE model which computes the complex field, i.e. phase and amplitude as it marches in range over both sea and land. It handles surface roughness effects over the ocean using a surface impedance boundary condition including a modified Miller-Brown technique, see [11] and [12]. The terrain heights are introduced using the Belis-Tappart technique, or the user may select an implementation of knife-edge diffraction, see[13].

4. **VTRPE** (Variable Terrain Radiowave Parabolic Equation) was developed at SSC-SD by F. J. Ryan. VTRPE, like TEMPER, is a full PWE model that marches in range producing the complex field with amplitude and phase over both sea and land. It also includes the effects of surface roughness. To model the surface roughness effects on forward scatter over the ocean, VTRPE offers two options. The user can select the Miller-Brown technique that TEMPER employs, or the model uses a realization of the rough sea surface along a propagation radial, which includes the effects of the ocean-wave spectra of both gravity waves and capillary waves. The forward scatter off the sea surface realization is computed using the E or H field from VTRPE as the incident wave. Numerical integration of the Stratton-Chu integral equation over the sea surface realization produces the representation of the forward scattered wave. Since VTRPE allows dynamic selection of the range step, a very small step may be selected when needed to account for height variations in the surface realization. A paper in these proceedings, see [14], will discuss these techniques in more detail. Also, a paper by F. J. Ryan and R. Gover will soon appear which will compare the Miller-Brown and the VTRPE techniques for modeling sea surface roughness effects on forward scatter.

The four models will only be compared relative to their performance over the ocean, even though APM, TEMPER and VTRPE model propagation over land as well as the ocean. The scenarios that will be illustrated are limited to the following conditions:

- **Frequencies:** S-Band 3.3 GHz and X-Band 10 GHz; Maximum Range: 120 km; Maximum Height: 600m
- **Antenna Heights and 3dB-Beam Widths:** 18m and 2° for S-Band; 26m and 1° for X-Band
- **Polarization:** Vertical
- **WMO Sea States:** 3, RMS-Wave Height 0.2m and 5, RMS-Wave Height 0.8m
- **Surface Ducting:** Moderate-Strong, 20 Meter Evaporation Duct; Very Strong, 35 Meter Evaporation Duct; and Extreme, a set of measured range varying profiles composed of 45 meter surface based ducts, with extremely strong height gradients

These cases were chosen to illustrate the differences between the propagation models, when used to simulate the forward propagation of a shipboard radar, performing horizon search over the ocean. The frequencies are appropriate for shipboard search radars, as are the antenna heights.

3. Ducting and Ocean Wave Height Effects on Surface Roughness Modeling

When an electromagnetic wave is propagated through free space and is incident on a plane surface, such as the earth, it is scattered by the surface specularly, so that the scattered or reflected wave has the same angle of incidence, or grazing angle, as the incident wave. For a planar ocean surface the plane wave reflection coefficient for a vertically polarized wave is the well-known Fresnel coefficient:

$$R_0 = \frac{n^2 \sin(\gamma) - \sqrt{n^2 - \cos^2(\gamma)}}{n^2 \sin(\gamma) + \sqrt{n^2 - \cos^2(\gamma)}}, \quad (1)$$

$$n^2 = \frac{\epsilon}{\epsilon_0} - 60i\lambda\sigma,$$

Where λ is the wavelength, γ is the grazing angle and ϵ and σ are the dielectric constants for salt water, while ϵ_0 is the free space dielectric constant. Of course the ocean surface must have very small waves to be meaningfully modeled as a plane surface. The varying heights and spatial distribution of the ocean waves introduce roughness onto the smooth, planar sea surface. In terms of ray theory, if the height difference, h , between two portions of the surface causes a significant change in phase of two parallel rays incident on these two portions of the surface, the surface is called rough. The phase difference is

$$\Delta\phi = \frac{4\pi}{\lambda} h \sin(\gamma) \quad (2)$$

This measure of roughness is called the Rayleigh criterion, and one usually considers a surface to be fairly smooth if

$\Delta\phi \leq \frac{\pi}{2}$. Thus a surface can be considered rough at a given frequency and smooth at lower ones, even for the same

grazing angle. If a surface is smooth then the reflected wave is identical to the incident wave except that it is multiplied by the reflection coefficient, R_0 . If the surface is slightly rough, the reflected wave is attenuated slightly due to the scattering, and power corresponding to this decrease in reflected power is scattered in other directions. The reflected power is sometimes called the *specular* component, and the scattered power the *diffuse* component. In radar applications the specular component is called *forward* scatter, and that part of the diffuse component that scatters back to the radar is called *back scatter* or *sea clutter*. In this paper only forward scatter or specular reflection is investigated.

Two of the important applications of rough surface scattering in radar range performance analysis are multipath fading in slightly rough sea conditions, see [17] and power attenuation in a surface duct, also in slightly rough sea conditions. Beckmann and Spizzochino in [15] derive the earlier theoretical results; see Ament [18], based on simple assumptions regarding the random distribution of wave heights. They assumed that the scattering reflection coefficient could be related to R_0 by

$$(R_s)_{RMS} = (\rho_s)_{RMS} R_0 \quad (3)$$

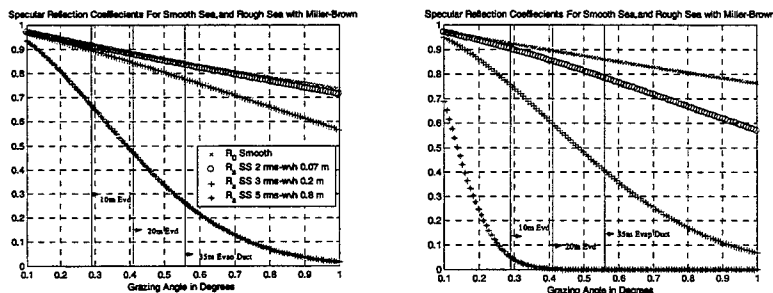
In 1974 Brown and Miller, [16], showed that if the sea wave elevation is represented as a sinusoid with Gaussian amplitude and uniform phase that

$$(\rho_s)_{RMS} = \exp\left(-\frac{(\Delta\phi)^2}{2}\right) I_0\left(\frac{(\Delta\phi)^2}{2}\right) \quad (4)$$

The RMS-wave height σ_h is substituted for h in formula (2) to obtain $\Delta\phi$. The following two plots illustrate the smooth surface and rough surface coefficients as functions of grazing angle, for sea states 3 and 5, and for an S-band as well as an X-band radar. The grazing angle in a duct is computed by TEMPER. Beyond the optical interference region the grazing angle can be approximated as:

$$grz = \sqrt{2 * \Delta M} \quad (5)$$

Where grz is the grazing angle in milliradians, and ΔM is the M-unit deficit of the profile.



Figures 1 and 2. Reflection Coefficients at S-Band (3.3 GHz) and X-Band (10GHz)

4. A Comparison of the Propagation Models over a Slightly Rough Ocean Relative to Both Moderate and Very Strong Surface Ducting

In order to include the variations in atmospheric refractivity and surface roughness into range performance analysis of shipboard radars, it is very convenient to return to Kerr's book [2], and include these effects in the *pattern propagation factor F*, defined by Kerr to be:

$$F = \left| \frac{E}{E_0} \right|, \quad (6)$$

Where E_0 is the magnitude of the free-space field at a given point, with the transmitting antenna oriented directly toward the point and E is the field which includes the antenna pattern, atmospheric refraction, diffraction, ducting, rough or smooth surface effects, etc. At that given point. Fortunately we have observed that $E(x,z)$ is what the PWE models compute so efficiently at each point in the propagation plane (x,z). In terms of F the one-way power transmission equation expressing the path loss becomes

$$PL(R, \theta, \phi) = \frac{P_r(R, \theta, \phi)}{P_t(R, \theta, \phi)} = \frac{G_r G_t \lambda^2}{(4\pi R)^2} F^2(R, \theta, \phi) \quad (7)$$

Where the antenna gains G_t and G_r , since they are constant over the entire path, and need not be included in the path loss. Thus, we can write

$$PL = \left(\frac{\lambda}{4\pi R} \right)^2 F^2 \quad (8)$$

This expresses the path loss as a product of the *free-space loss* $\left(\frac{\lambda}{4\pi R}\right)^2$ and the one-way propagation factor² F^2 . These are the factors in the equation that depend upon range and directions. The PWE model produces the *path loss* $PL_{dB}^{pwe}(x, z)$ as a function of range and height in dB, and includes all of the atmospheric, surface roughness, and antenna pattern effects that are modeled therein. The propagation factor is then obtained from model by

$$F_{dB}^{pwe}(x, z) = 20 \log \left(\frac{\lambda}{4\pi R} \right) - PL_{dB}^{pwe}(x, z) \quad (9)$$

This is the quantity that is plotted, and it is a gain. If $F_{dB}^{pwe}(x, z)$ is greater than zero then the signal strength at that point is stronger than it would for free-space at that range. Thus if this situation occurs beyond the radar horizon there must be a duct of some type present to cause the increased signal level. In the plots below, the following symbols are used: '+' for APM, '*' for RPO, 'o' for TEMPER, and ' ' for VTRPE.

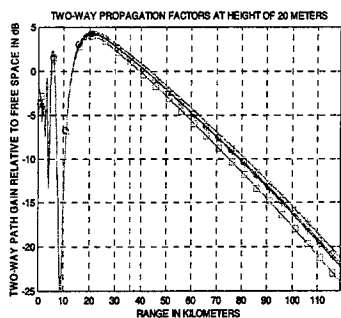


Figure 3. S-band, 20m Evaporation Duct, at 20m, Miller Brown roughness with sea state 3

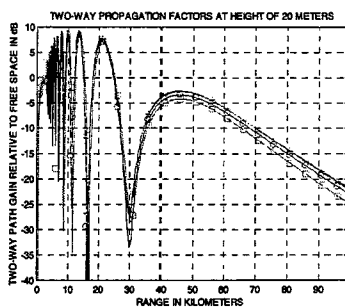


Figure 4. X-band, 10m Evaporation Duct at 20m, Miller Brown roughness with sea state 3

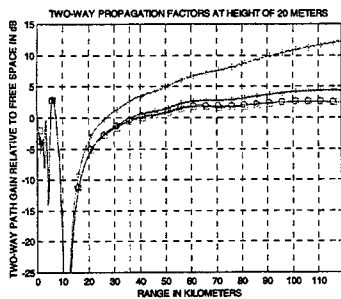


Figure 5. S-band, 35m Evaporation Duct at 20m, Miller-Brown Surface Roughness, sea state 3

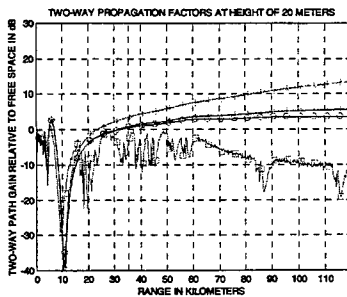
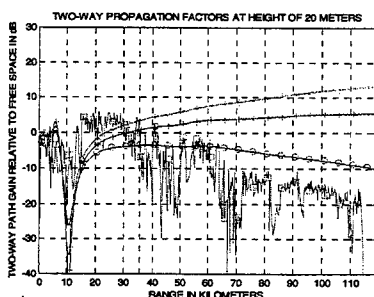
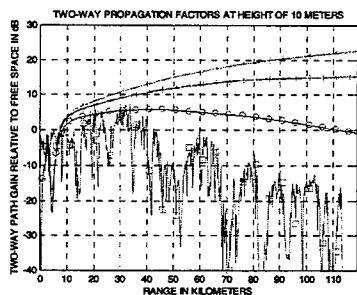


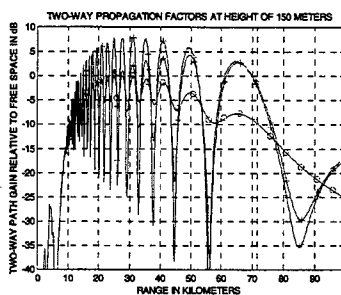
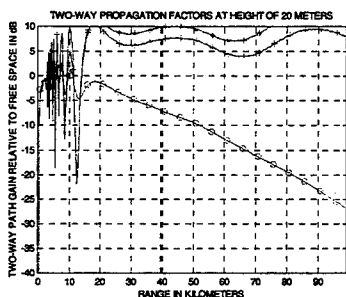
Figure 6. S-band, 35m Evaporation Duct at 20m, sea state 3, VTRPE with Sea Surface Realization

² The terms propagation factor and pattern propagation factor are used interchangeably in this context.

In Figures 3, 4 and 5 TEMPER and VTRPE use the Miller-Brown technique for rough surface attenuation, and the differences between TEMPER, VTRPE, and APM are all similar as would be expected from Figures 1 and 2. Since RPO does not model vertical polarization it deviates from the others under extreme ducting conditions shown in Figures 5 and 6. The roughness and more attenuated propagation factors in Figure 6 illustrate the different representations of roughness in VTRPE, when the sea surface realization is used, compared with Miller-Brown in TEMPER.

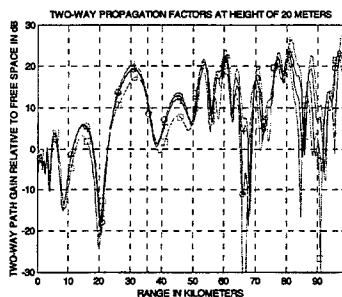
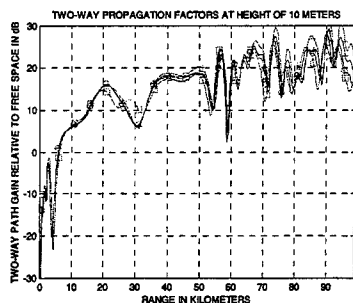


Figures 7 and 8. S-band, 35m Evaporation Duct, at 10m and 20m, sea state 5, VTRPE with sea surface realization



Figures 9 and 10. X-band, 35m Evaporation Duct at 20m and 150m, sea state 5, VTRPE not included

These sea-state 5 examples for both S-band and X-band illustrate the effects of surface roughness rather dramatically. At S-band even the Miller-Brown technique can cause TEMPER and APM to part by as much as 15 dB, while at X-band they can show a difference of more than 25 dB. The difference between TEMPER and VTRPE are due to Miller-Brown versus the sea surface realization. Figure 10 illustrates the effects of surface roughness on a higher target at 150m. The multipath peaks and nulls in TEMPER show the damping as Miller-Brown indicates. It is interesting to note that even RPO shows some multipath damping compared to APM, since RPO models roughness only in the interference region while APM does not model it anywhere.



Figures 11 and 12. S-band, Measured Profiles at 10m and 20m.

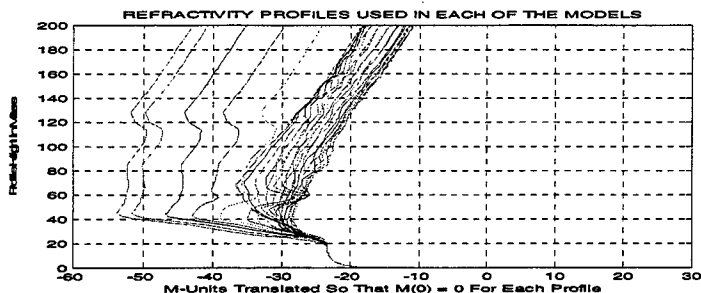


Figure 13. Measured Profiles at Wallops Island on April 02, 1998.

Figures 11 and 12 compare the four models in an S-band, sea state 3, very strong range varying surface-based ducting condition that was measured on April 02, 1998 at Wallops Island. The range-varying profiles are illustrated in Figure 13. The stronger surface based duct is at the land sea interface, and the M-deficit across the ducts decreases out to the open ocean. The 31 profiles are spaced at one nautical mile increments. The four models agree quite well even under extreme atmospheric conditions.

5. Conclusions

The four models give very similar representations of the propagation factor in the presence of a moderate evaporation duct and fairly calm sea. As the sea state is increased, the models that employ the Miller-Brown methodology for surface roughness, TEMPER and VTRPE, show the damping appropriate for multipath peaks and nulls and the attenuation expected beyond the horizon in the duct. APM and RPO do not exhibit these properties. In a 35-meter evaporation duct with sea state 5, the surface roughness attenuation in the duct is as much as 15 dB at S-band, and 25 to 30 dB at X-band, which is predicted by Figures 1 and 2. When the sea surface realization is exercised in VTRPE rather than Miller-Brown, significant differences are apparent. VTRPE also has a technique for modeling sea clutter using back scatter from the sea surface realization. This will be demonstrated in a paper by Spaulding, Nunn, and Levitas at the 2000 Radar Conference [19]. In conclusion, each of the four models has many applications. APM and RPO are easier to set up and execute 20 to 30 times faster than TEMPER and VTRPE. There is a new version of APM on the SPAWAR web site which includes the Miller-Brown technique so that APM should be very close to the other two models over the ocean. Since it is still a hybrid model, it should execute faster than the other two models, especially if the maximum altitude is well above the top of the PE region.

References

- [1] Fock, V.A. *Electromagnetic Diffraction and Propagation Problems*, Pergamon Press (1965).
- [2] Kerr, D.E. *Propagation of Short Radio Waves*, MIT Radiation Laboratory Series, Boston Technical Publishers (1964).
- [3] Blake, L.V. *Radar Range Performance Analysis*, Artec House (1986).
- [4] Blake, L.V. Chapter 2 in *Radar Handbook* by M. Skolnik, McGraw Hill (1990).
- [5] Hardin, R.H. and Tappert, F. D. "Applications of the Split-step Fourier Method to the Numerical Solutions of Nonlinear and Variable Coefficient Wave Equations," *SIAM Rev* 15, 423 (1973).
- [6] Wait, J.R. *Electromagnetic Waves in Stratified Media*, Oxford Pergamon Press (1962).
- [7] Marcus, S.W. "A Hybrid (finite difference-surface Green's function) method for computing transmission losses in an inhomogeneous atmosphere over irregular terrain," *IEEE Trans. Antenna and Propagation*, vol 40, no.12, pp.1451-1458, Dec. (1992).
- [8] Kuttler, J. R. and Dockery, G.D. "Theoretical Description of the Parabolic Approximation/Fourier Split-Step Method of Representing Electromagnetic Propagation in the Troposphere" *Radio Sci.* 26 (2), pp. 381-393 (1991).
- [9] Ryan, F. J. "RPE: A Parabolic Equation Radio Assessment Model" *AGARD Conf. Proc. No 453*, pp 19-1 to 19-10 (1989).
- [10] Dockery, G.D. "Development and Use of Electromagnetic Parabolic Equation Propagation Models for U.S. Navy Applications" **JOHNS HOPKINS APL TECHNICAL DIGEST, VOLUME 19, NUMBER 3** (1998).
- [11] Miller, A. R., Brown, R. M., and Vegh, E. "New Derivation for the Rough-Surface Reflection Coefficient and for the Distribution of Sea-Wave Elevations" **IEE PROCEEDINGS, Vol. 131, pt. H, No. 2** (1984).
- [12] Dockery, G. D. and Kuttler, J. R. "An Improved Impedance-Boundary Algorithm for Fourier Split-Step Solutions of the Parabolic Wave Equation" *IEEE Trans. Antennas and Propagation*, vol. 44, no. 12, pp-1592-1599 (1996)
- [13] Donohue, D. J. and Kuttler, J. R. "Modeling Radar Propagation over Terrain," **JOHNS HOPKINS APL TECHNICAL DIGEST, VOLUME 18, NUMBER 2** (1997).
- [14] Ryan, F. J. A Paper in These Proceedings (2000).
- [15] Beckman, P. and Spizzichino, A. *The Scattering of Electromagnetic Waves from Rough Surfaces*, Artec House (1987).
- [16] Brown, R. M. and Miller, A. R. "Geometric-Optics Theory for Coherent Scattering of Microwaves from the Ocean Surface" **NRL REPORT 7705** (1974).
- [17] Karasawa, K. and Shiokawa, T. "A Simple Prediction Method for L-Band Multipath Fading in Rough Sea Conditions" **IEEE TRANS COMMUNICATIONS**, Vol. 36, No. 10 (1988).
- [18] Ament, W. S. "Toward a Theory of Reflection by a Rough Sea Surface" *Proc. IRE* 41, pp 142-146 (1953).
- [19] Spaulding, B., Nunn, C., and Levitas, M. *Sea Clutter Reflectivity in Ducted Propagation*, 2000 Radar Conferences

AUTHORS INDEX

- Abbott, T. I-221
Akyurtlu, A. I-181
Allard, J. I-73
Amrhein, J. I-28
Andersen, L.S. II-734
Antonini, G. II-654
Arakaki, D. II-742, 944
Archambeault, B. I-423, 431, 436
Aydin, K. I-181
Balanis, C.A. I-387
Barba, I. II 534, 635
Bardali, F. II 930, 975
Barka, A. II-1006
Batchelor, J.C. II-562
Bevensee, R.M. I-214
Beyer, A. I-255
Bleszynski, E. II-874
Bleszynski, M. II-874
Bluck, M.J. 4, II-662
Borkes, J. I-255
Boyer, D. I-515
Breakall, J.K. II-814
Brench, C.E. I-410
Burkholder, R.J. II-1001
Burke, G.J. I-452
Cabrera, F.J. II-699
Canales, R.R. I-189
Cangelaris, A.C. I-108
Catedra, M.F. II-959
Chamberlin, K. I-501
Chew, W.C. II-668, 691, 838, 851
Christopoulos, C. II-587
Chitchekatourov, V. II-580
Coccetti, F. II-580
Cohen, N. II-822
Cravens, L.A. II-677
Cuevas del Rio, J.G. II-699
Cui, W. I-436
Cwik, T. I-308
Cybert, K.J. I-395, II-806
Davis, D. I-493
Dawson, T.W. I-333
DeCarlo, D. I-365
De Marco, F. II-930
De Zutter, D. II-981
Demkowicz, L. I-11, 19
Di Giampaolo, E. II-975
Ditkowski, A. II-917
Doncov, N.S. I-233
Donepudi, K. II-691, 716, 851
Drewniak, J.L. I-130, 431, 436
Dridi, K. II-917
Durantini, A. II-975
DuRieu, D. I-341
Ellingson, D. I-56
Elsherbeni, A.Z. I-294, II-924
Erdemli, J.E. II-734
Ergin, A.A. II-647
Fan, G-X II-890
Fan, K. I-130
Fear, E.C. I-310
Fonseca, L.F. I-189
Franceschetti, G. I-485
Fujii, M. II-526, 534, 1013
Gaudine, D. I-356
Georgakopoulos, S.V. I-387
Gjonaj, E. I-241
Glisson, A.W. II-683
Goldberg, D.E. I-78
Goldsmith, K. I-341, II-750
Gomez Martin, R. II-627, 995
Gres, N.T. II-647
Grothjohn, T. I-28
Guidry, R.D. II-765
Guy, A.W. I-317
Haala, J. II-936
Hagen, J.V. II-670, 758
Hagness, S.C. I-310
Hammes, P. I-247
Han, D-H. I-387
Hesthaven, J.S. II-917
Hill, K.C. II-677
Hoefler, W.J.R. II-526, 534, 635, 1013
Hohlfeld, R.G. II-822
Holtby, L. II-780
Holzheimer, T.R. I-198, II-726, 798
Hoorfar, A. I-63
Horvatic, P. I-501
Hu, B. II-838
Hu, E. II-526, 838, 1013
Huang, C-W.P. II-924
Huang, T.H. I-444
Huttunen, T. I-49
Jacobs, M.W. II-814
Jaroszewicz, T. II-874
Ji, Y. I-444
Jiang, B.N. II-604
Jiao, D. 166, II-611
Jimenez, E. II-699
Jin, J-M. I-166, II-611, 691, 716, 845, 851
Johnson, P. II-750
Kang, G. II-691, 851
Katehi, L.P.B. II-540
Kawakami, H. I-206
Kayano, T. I-349
Kempel, L. I-28, II-765, 772
Kent, W.J. II-677
Kishik, A.A. II-683
Knighten, J.L. I-130
Kogiso, S. I-206
Koning, J. II-882
Kubina, S.J. I-356
Lammers, T. I-160
Langley, R.J. II-562
Layden, R.G. II-677
Lee, Y.H. I-70
Liao, N. II-604
Li, X. I-310
Lindenmeier, S. II-587
Ling, F. II-718, 845
Liu, Q.H. II-890, 897
Liu, W. II-526, 1013
Liu, Y. I-63
Iizuka, Y. I-206
Long, B.R. I-86
Loeffler, D. II-758
Luebbbers, R.J. I-462, 470, 477
Lysiak, K. II-790
Macon, C. II-772
Magnusson, R. I-198
Manara, G. I-56
Manara, G. II-640
Mangold, T. II-570
Marano, S. I-485
Marrocco, G. II-930, 975
Martin, R.A. I-286
Marvin, A.C. I-70
Michielssen, E. I-78, II-647
Miller, E.K. I-99
Milovanovic, B.D. I-233
Mittra, R. I-2, 56, II-742, 944, 968, 995
Miyata, K. I-349
Monk, P. I-49
Monorchio, A. I-56, II-640, 968
Mueller, G. I-123
Munn, D.R. I-373, 381
Myers, C.D. I-365
Ng, M.W.R. II-562
Nott, A. I-325
Ohashi, K. I-349
Ojio, Y. I-206
Ordovas, R. I-4
Orlandi, A. II-654
Ottusch, J.J. II-867
Olyslager, F. II-981
Ouyang, C.C. II-604
Paknys, R. I-493
Pantoja, M.F. II-627
Pasquino, N. I-485
Pathak, P.H. II-1001
Paul, J. II-556
Perez, R. I-416
Pertz, O. I-255
Peterson, A.F. I-43
Petroopoulos, P.G. II-906
Pham, H. I-515
Pickelsimer, J. I-477
Piket-May, M. I-160, II-988
Pinto, I.M. I-485
Polycarpou, A.C. I-35, 387
Porter, S.J. I-70
Priest, T. I-341, II-750
Przybyszewski, P. II-951
Railton, C.J. I-115
Ramahi, O.M. I-146, 152
Rebel, J. II-570
Reiss, K. I-123
Remis, R.F. I-93
Represa, J. II-534, 635
Reuster, D.D. I-395, II-806
Rivas, F. II-959
Roa, J.P. II-959
Rodriguez-Pereyra, V. I-294
Rogier, H. II-981
Rubio Bretones, A. II-627, 995
Rummel, P. I-28
Rumsey, I. II-988
Russer, P. I-401, II-570, 580, 587, 594
Ryan, F.J. I-507
Sarris, C.D. II-540
Sato, G. I-206
Schuhmann, R. I-247
Schneider, S. II-772
Schunn, F. II-619
Schuster, J.W. I-462, 470
Segal, B. I-493
Seledtsov, M. I-501
Sertel, K. II-859
Setzer, S. I-247
Shang, J.S. II-611
Shanker, B. II-647
Shi, H. I-130
Shin, J. II-683
Shlepnev, Y.O. I-138
Singer, H. II-619
Slater, M. I-281
Smith, C.E. I-294, II-924

So, P.P.M.S. II-526, 594, 1013
 Sobhy, M.I. II-562
 Song, J. II-691, 845, 851
 Soudais, P. II-1006
 Speciale, R.A. I-263
 Staker, S.W. I-160
 Stamm, J.M., II-814
 Steich, D.J. I-452
 Stuchly, M.A. I-310, 333
 Sunderland, K.V. I-226
 Tabet, S.N. I-365
 Takahashi, N. I-349
 Tentzeris, M.M. II-548
 Thomas, C. II-662
 Thomas, D.W.P. II-556
 Trapp, B. I-247

Trenkic, V.M. I-233
 Trott, K.D. II-765, 772
 Trueman, C.W. I-281, 356, 373, 381, 493
 Tuerk, U. I-401
 van den Berg, P.M. I-93
 Vardapetyan, L. I-11
 Vietzorreck, L. II-580
 Visher, J.L. II-867
 Volakis, J.L. II-734, 859
 Walker, S.P. I-4, II-662
 Wandzura, S.M. II-867
 Wang, H. I-444
 Wasi, S. I-43
 Weiland, T. I-247
 Weile, D.S. I-78
 Wiesbeck, W. II-670, 936

Werner, D.H. I-86, 173, 181, 286, II-742,
 Werner, D.H. II-829, 944
 Werner, P.L. I-36; II-829
 White, Daniel II-882
 White, Doug I-436
 Wiesbeck, W. II-758
 Wood, Jr., W.D. II-677
 Xu, X.M. II-897
 Ye, X. I-436
 Yefet, A. II-906
 Young, P.P. I-198
 Yu, W. II-944
 Zhang, Z.Q. II-897
 Zhao, J. I-493
 Zmyslo, J.S. I-173
 Zubaidah, S. I-349
 Zypman, F.R. I-189